Wrocław University of Technology
Centre of Advanced Materials and Nanotechnology

Materials Science-Poland

Vol. 27 • No. 1 • 2009

Oficyna Wydawnicza Politechniki Wrocławskiej

Materials Science-Poland is an interdisciplinary journal devoted to experimental and theoretical research into the synthesis, structure, properties and applications of materials.

Among the materials of interest are:

- glasses and ceramics
- sol-gel materials
- photoactive materials (including materials for nonlinear optics)
- laser materials
- photonic crystals
- semiconductor micro- and nanostructures
- piezo-, pyro- and ferroelectric materials
- high-T_c superconductors
- magnetic materials
- molecular materials (including polymers) for use in electronics and photonics
- novel solid phases
- other novel and unconventional materials

The broad spectrum of the areas of interest reflects the interdisciplinary nature of materials research. Papers covering the modelling of materials, their synthesis and characterisation, physicochemical aspects of their fabrication, properties and applications are welcome. In addition to regular papers, the journal features issues containing conference papers, as well as special issues on key topics in materials science.

Materials Science-Poland is published under the auspices of the Centre of Advanced Materials and Nanotechnology of the Wrocław University of Technology, in collaboration with the Institute of Low Temperatures and Structural Research of the Polish Academy of Sciences and the Wrocław University of Economics.

All accepted manuscripts are placed on the Web page of the journal and are available at the address: http://MaterialsScience.pwr.wroc.pl

All published papers are placed on the Web page of the journal and are **freely accessible** at the address: http://MaterialsScience.pwr.wroc.pl

Materials Science-Poland is abstracted/indexed in: Chemical Abstracts, Materials Science Citation Index, Science Citation Index Expanded, Scopus.

The Journal is supported by the State Committee for Scientific Research

Editorial Office

Daniel Davies
Krzysztof Małecki

Printed in Poland

Drukarnia Oficyny Wydawniczej Politechniki Wrocławskiej
Zam. nr 217/2009.

From the Editor

The preceding issue of *Materials Science-Poland* [1] contains selected papers presented at the final meeting of the MAG-EL-MAT Scientific Network [2]. More papers presented at the meeting are available in earlier issues of this journal [3, 4]. All these papers were collated and compiled by Professors Stanisław Lipiński and Tadeusz Luciński (Institute of Molecular Physics, Polish Academy of Sciences, Poznań), who acted as Guest Editors.

[1] Materials Science-Poland, 26 (2008), No 4, 803–1104.
[2] IDZIKOWSKI B., Materials Science-Poland, 26 (2008), 803.
[3] Materials Science-Poland, 25 (2007), No 4, 1223-1294.
[4] Materials Science-Poland, 26 (2008), No 3, 641-668.

Juliusz Sworakowski
Editor-in-Chief

Materials Science-Poland, *Vol. 27*, *No. 1*, *2009*

Vibrational spectra, electronic excited states and magnetic properties of the copper(II) ions in alkylaminoacetylurea complexes

H. CIURLA[1*], J. HANUZA[1, 2], Z. TALIK[1], M. KORABIK[3], J. MROZIŃSKI[3]

[1]Department of Bioorganic Chemistry, Institute of Chemistry and Food Technology, Faculty of Engineering and Economics, University of Economics, 53-345 Wrocław, Poland

[2]Institute of Low Temperature and Structure Research, Polish Academy of Sciences, P. O. Box 1410, 50-950 Wrocław 2, Poland

Faculty of Chemistry, University of Wrocław, 50-383 Wrocław, Poland

Copper(II) complexes with alkylaminoacetylurea ligands were synthesized and studied by means of IR, Raman, electron absorption and luminescence spectroscopies, as well as by ESR and magnetic methods. The spectroscopic and magnetic studies were performed in the 4–300 K and 1.9–300 K temperature ranges, respectively. The Cu^{2+} ions in these complexes are four coordinated having distorted square-planar surroundings. The dependence of the spectroscopic parameters on the alkyl radical of the ligand is discussed. At low temperatures, very weak ferromagnetic interactions are observed for the C_3 and C_5 alkyls, and an antiferromagnetic one is observed for the remaining complexes, with C_4 and C_6–C_{18} alkyls.

Key words: *copper(II) complexes; alkylaminoacetylureas; IR; Raman; UV absorption spectra; luminescence; ESR; magnetic properties*

1. Introduction

Copper ions play a vital role in a number of biological processes. They are recognised to be plant nutrients and serve as catalysts [1] in plant enzyme systems and as urease inhibitors [2]. Cu^{2+} complexes with macrocyclic polyamines act as mimics of metalloenzyme active sites [3–8], redox-active species for electrocatalytic processes [9–14] or photoredox molecular devices for converting the light energy into other forms [15–19]. Complexes of transition metal ions with urea were the subjects of several works [20–23]. A considerable interest of these studies has been focused on their interaction with drugs administered for therapeutic purposes.

*Corresponding author: e-mail: hanna.ciurla@ue.wroc.pl

Our present work concerns the structure, spectroscopic and magnetic properties of copper(II) compounds with alkylaminoacetylureas. These ligands have been synthesised for the first time [24, 25] and their complexes have not been studied in detail. Our preliminary studies showed that these urea derivatives effectively extract Cu^{2+} ions from diluted acid solutions formed in the flotation process of very poor copper deposits [26].

2. Experimental

Synthesis of alkylaminoacetylurea copper(II) complexes. Syntheses of the copper(II) complexes with alkylaminoacetylureas have been described in our previous paper [26], where the chemical and magnetic properties were reported for a few derivatives. Their chemical compositions, colours, formulae, molecular masses and melting points are presented in Table 1.

Table 1. Complex compounds of alkylaminoacetyl ureas (Scheme 1) with copper(II)

No.	Alkyl radical (R) Molecular formula Molecular mass	Colour	Melting point [°C]	Composition	
				Calculated [%]	Found [%]
1	2	3	4	5	6
1	C_3H_7 $C_{12}H_{24}N_6O_4Cu$ 379.91	violet	193	C 37.94 H 6.37 N 22.12	C 38.08 H 6.33 N 22.03
2	C_4H_9 $C_{14}H_{28}N_6O_4Cu$ 407.95	rose	192	C 41.22 H 6.92 N 20.60	C 41.18 H 6.93 N 20.61
3	C_5H_{11} $C_{16}H_{32}N_6O_4Cu$ 436.01	violet	187	C 44.07 H 7.40 N 19.28	C 43.98 H 7.40 N 19.17
4	C_6H_{13} $C_{18}H_{36}N_6O_4Cu$ 464.07	violet-red	165	C 46.58 H 7.82 N 18.11	C 46.80 H 7.57 N 17.91
5	C_7H_{15} $C_{20}H_{40}N_6O_4Cu$ 492.12	violet-rose	163D	C 48.55 H 8.19 N 17.08	C 48.55 H 8.54 N 16.90
6	C_8H_{17} $C_{22}H_{44}N_6O_4Cu$ 520.18	violet-blue	155	C 50.79 H 8.53 N 16.16	C 50.72 H 8.98 N 15.99
7	C_9H_{19} $C_{24}H_{48}N_6O_4Cu$ 548.23	dark rose	152	C 52.28 H 8.83 N 15.33	C 52.75 H 9.12 N 15.21
8	$C_{10}H_{21}$ $C_{26}H_{52}N_6O_4Cu$ 576.28	blue	152	C 54.18 H 9.10 N 14.58	C 53.94 H 9.52 N 14.16

Table 1 continued

1	2	3	4	5	6
9	$C_{12}H_{25}$ $C_{30}H_{60}N_6O_4Cu$ 632.39	dark rose	150	C 56.98 H 9.56 N 13.29	C 56.66 H 9.91 N 13.26
10	$C_{14}H_{29}$ $C_{34}H_{68}N_6O_4Cu$ 688.59	rose	146	C 59.31 H 9.96 N 12.21	C 59.30 H 10.27 N 12.10
11	$C_{16}H_{33}$ $C_{38}H_{76}N_6O_4Cu$ 744.61	rose	143	C 61.29 H 10.29 N 11.29	C 61.60 H 10.27 N 11.40
12	$C_{18}H_{37}$ $C_{42}H_{84}N_6O_4Cu$ 800.72	light rose	137	C 63.00 H 10.57 N 10.50	C 63.30 H 10.75 N 10.80

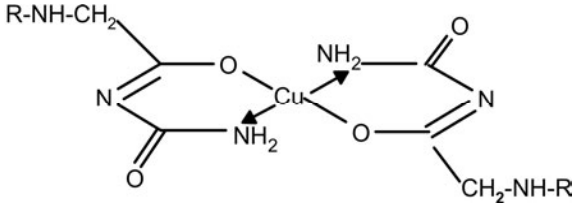

Scheme 1. Alkylaminoureas under investigation (see Table 1)

Spectroscopic studies. Electronic absorption spectra of the copper complexes and free ligands (non-coordinated alkylaminoureas) were recorded at room temperature in ethyl alcohol solutions and Nujol mulls with JASCO V-570 UV/VIS and Varian Cary 5E UV/VIS/NIR spectrophotometers with a resolution of 0.5 nm. The mulls for all samples were prepared using the same ratio (2:1) of the complex to Nujol.

The photoluminescence spectra were recorded with the 366 nm excitation (the Hg line) and the emission lifetimes with the 337 nm excitation (2 ns nitrogen laser). A spectrometer consisting of a SPM-s Carl Zeiss Jena monochromator, a cooled GaAs R 943-03 Hamamatsu photomultiplier, a gated photon counter of the SR400 Stanford research system, a box integrator of the Stanford research system and the PC were used. The emission spectra obtained in this arrangement were compared to those obtained at 260 nm excitation from the Xenon lamp and recorded with the SSF1 spectrometer (produced by LOMO, Sankt Petersburg).

Room temperature Fourier transform IR spectra (FTIR) were recorded in the 4000 –30 cm^{-1} range using the BIORAD 575 spectrophotometer with a 2 cm^{-1} resolution. Room temperature FT Raman spectra (FTRS) were recorded in the 4000–80 cm^{-1} range using a BRUKER 110/S spectrometer with the Nd:YAG excitation and 2 cm^{-1} resolution. The Gaussian deconvolution of the spectra was made using the Origin 7.0 computer program.

Magnetic studies. The ESR spectra were recorded at X-band with an ESP 300 Bruker spectrometer equipped with a ER 035M Bruker NMR gaussmeter and a HP

5350B Hewlett-Packard microwave frequency counter. The measurements were made at room temperature. The ESR measurements at 5 K were performed with a conventional X-band reflection spectrometer equipped with an Oxford Instruments ESR-900 helium flow cryostat. The magnetic studies of the polycrystalline samples were performed for 12 compounds using a quantum design SQUID magnetometer (MPMS-5 type) at the magnetic field of 0.5 T in the temperature range 1.9–300 K. The magnetization in function of magnetic field was measured in the range 0–5 T. The corrections consist in subtracting the sample holder signal and that for diamagnetism of the constituent atoms, calculated using Pascal's constants [27]. The value 60×10^{-6} $cm^3 \cdot mol^{-1}$ was used for the temperature-independent paramagnetism of copper(II) ions. The effective magnetic moment was calculated from the equation $\mu_{eff}=2.83(\chi_m T)^{1/2}$ [μ_B].

3. Results

3.1. FT-IR and Raman spectra

The FT-IR and FT-Raman spectra of the representative complex under study, namely $Cu(C_{14}H_{28}N_6O_4)$, are shown in Fig. 1. They are compared to the spectra of a free ligand recorded in the same conditions. Noticeable changes in the IR and Raman spectra are observed in the regions of vibrations of C=O and NH_2 groups. Upon coordination, these bands shift towards longer wavelengths, indicating formation of new bonds with copper ions. The most characteristic changes are observed for the following bands: $\nu(NH_2)$ Raman doublet at 3392 + 3315 cm^{-1} → 3170 cm^{-1} and the IR band at 3317 cm^{-1} → 3164 cm^{-1}; ν(C=O) Raman band at 1697 cm^{-1} → 1642 + 1612 cm^{-1}, the doublet at 1721 + 1683 cm^{-1} → 1637 cm^{-1} and the 1598 cm^{-1} band → 1567 cm^{-1}; ρ(NH) IR band at 1416 cm^{-1} → 1353 + 1347 cm^{-1}. In the 800–1200 cm^{-1} region, several bands of dicarbonylimide –CO–NH–CO– groups are observed [28].

The most informative changes occur in the 60–500 cm^{-1} region, in which the stretching and bending vibrations of the coordination polyhedron are expected. Let us assume, in the first step, that the structure of the CuO_2N_2 unit is described by the D_{2h} symmetry, i.e. the Cu–O and Cu–N bonds form two bond pairs of the same length, and the Cu ion lies on the plane formed by the oxygen and nitrogen atoms with the inversion centre in this plane. Such a structure can be derived from the electron absorption studies of the complex in the alcoholic solution (see below). The vibrational normal modes of this unit are described by the representation $2A_{1g} + B_{1g} + 2B_{1u} + 2B_{2u} + 2B_{3u}$ in which the stretching vibrations $\nu(CuN_2)$ and $\nu(CuO_2)$ correspond to the $A_{1g} + B_{3u}$ and $A_{1g} + B_{2u}$ representations, respectively. Three types of bending vibrations, δ(NCuN), δ(OCuO) and δ(NCuO), correspond to the remaining representations ($B_{1g} + 2B_{1u} + B_{2u} + B_{3u}$). Because *g* and *u* modes are Raman and IR active, respectively, two bands of the stretching vibrations are expected in both spectra. For the bending modes one Raman band and four IR bands should be observed for the considered

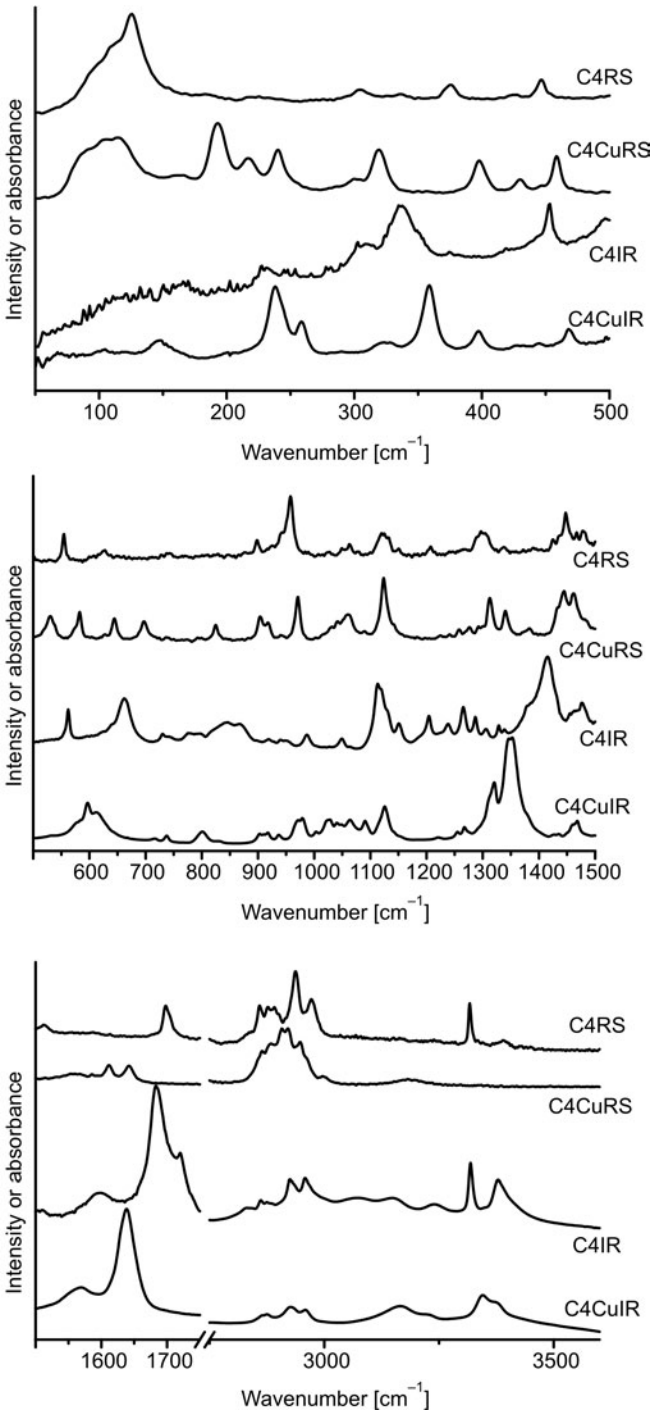

Fig. 1. FT-IR (IR) and FT-Raman (RS) spectra of the $Cu(C_{14}H_6N_4)$ complex (No. 2 in Table 1; C_4H_9 group)compared to the free ligand spectra

polyhedron of the D_{2h} symmetry. When the copper atom is situated above the N_2O_2 plane, the C_{2v} symmetry should be adopted for the discussion of the vibrational dynamics of the orthorhombic pyramidal polyhedron. The vibrations of this system are described by the representation $4A_1 + A_2 + 2B_1 + 2B_2$. These nine modes can be characterized as four stretching $\nu(CuN_2)$ ($A_1 + B_1$) and $\nu(CuO_2)$ ($A_1 + B_2$) modes, as well as five bending δ(NCuN), δ(OCuO) and δ(NCuO) ($2A_1 + A_2 + B_1 + B_2$) modes. For the C_{2v} symmetry, all modes are active in the Raman spectra, whereas the A_1, B_1 and B_2 modes are active also in the IR spectra. Therefore, four bands are expected in both spectra in the stretching mode regions whereas five Raman bands and four IR bands should be observed in the bending modes region. A further lowering of the symmetry to C_2, C_s or C_1 makes all nine bands active in the IR and Raman spectra. These considerations provide insight into a real structure of the CuN_2O_2 coordination polyhedron in the complexes studied here.

Upon comparing the FTIR and Raman spectra of the free ligand and its Cu-complex in the range 60–500 cm^{-1} (Fig. 1), it is clearly seen that several new bands appear in this region. Two Raman lines at 430 (medium) and 398 cm^{-1} (strong) and the IR counterparts at 425 (weak) and 397 cm^{-1} (medium) correspond to two $\nu(CuN_2)$ modes. Two other bands in the IR spectrum at 358 (strong), 330 cm^{-1} (weak) and 320 cm^{-1} (strong) should be assigned to $\nu(CuO_2)$ stretching modes. Bending vibrations of the considered unit can be easily assigned to the Raman lines at 249, 217, 195 and 164 cm^{-1} and IR bands at 259, 245 (shoulder), 238, 220 (shoulder) and 148 cm^{-1}. The wavenumbers of these modes are in good agreement with those reported in the literature for the copper(II) complexes with nitrogen and oxygen donor ligands ([29–32] and references therein). It should be noted that nine IR bands and eight Raman lines are observed in this region that could be assigned to the vibrations of the CuN_2O_2 unit. This result means that the coordination polyhedron of the studied complexes is a distorted orthorhombic pyramid and its symmetry could be described by the C_2, C_s or even C_1 point group.

3.2. Near infrared, visible and ultraviolet absorption spectra

The electronic spectra of the complexes studied in the solid state and in the ethyl alcohol solution are shown in Figs. 2 and 3. Figure 3 also shows deconvolution of the spectra into Gaussian components. As a representative example, a $C_{38}H_{76}N_6O_4Cu$ sample, with the $C_{19}H_{39}N_3O_2$ ligand and the R = $C_{16}H_{33}$ alkyl radical, was chosen. The reference spectrum of a free (non-coordinated) ligand is also shown for the comparison. The spectra generally consist of seven components. In order to make the discussion easier, the observed bands were labelled as $N = \nu_1$–ν_7 (in the order of increasing energy). These data are collected in Table 2. Three types of electronic transitions, appearing in different energy regions, are expected for the copper(II) complexes studied. These are d–d transitions, ligand-to-metal charge transfer (LMCT) and charge

transfer inside the electronic shell of the ligand (CT). The electronic spectrum of the free ligand (Fig. 3) reveals the CT transitions of the alkylaminoacetylureas in the UV region, i.e., above 30 000 cm^{-1}. Their energies are significantly higher than those observed for the two other types of transitions. The spectra of the free and coordinated ligands show three strong bands at ca. 45 000–49 000 cm^{-1}, 40 000 cm^{-1} and 30 000 cm^{-1}. These bands correspond to the $\pi \rightarrow \pi^*$ and $n \rightarrow \pi^*$ CT transitions inside the electron shell of the ligand. The appearance of few components for the CT transitions results from the presence of several chromophores in this molecule: two carbonyl and three amino groups.

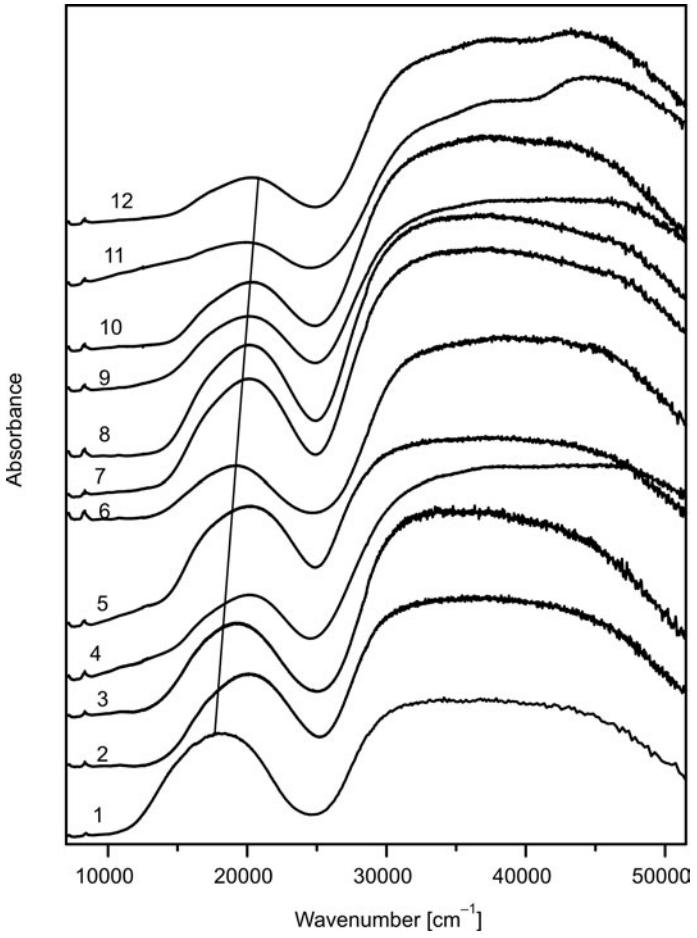

Fig. 2. Room temperature electronic absorption spectra of copper(II) complexes with alkylaminoacetylureas; in the solid state the sample specification as in Table 1. The experimental error of the determination of the positions of band maxima does not exceed 10 cm^{-1}

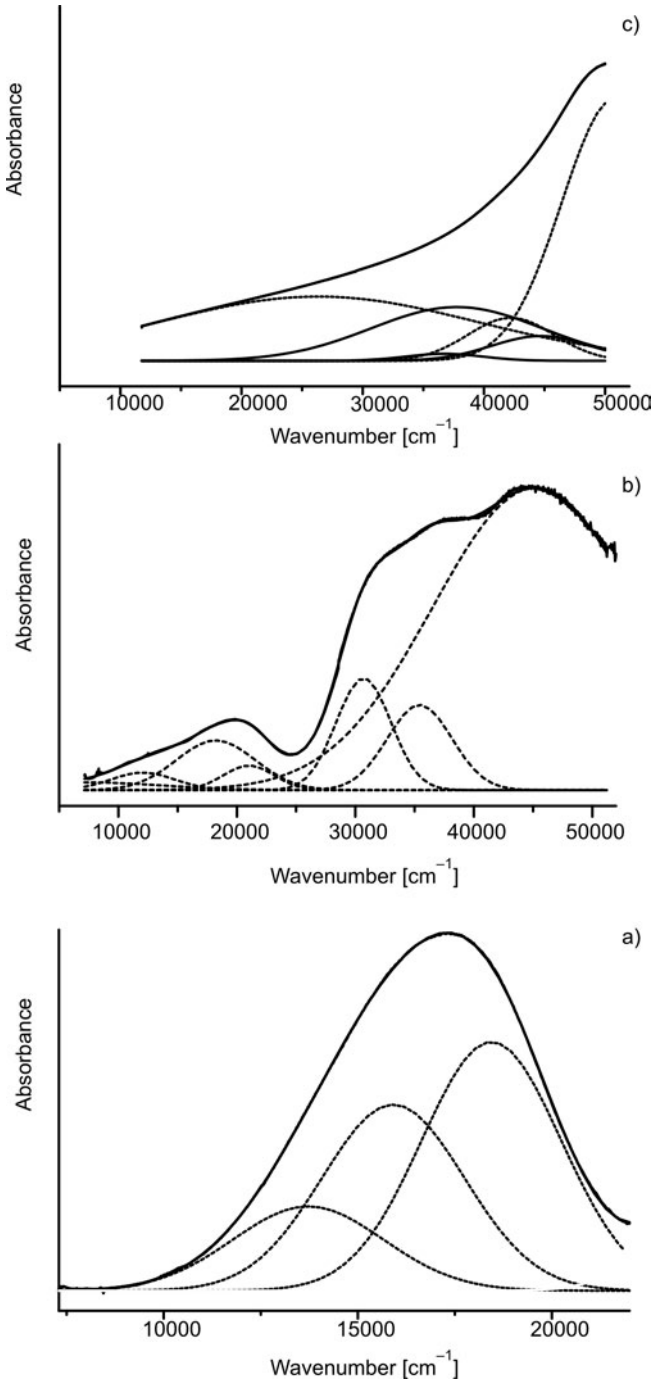

Fig. 3. The Gaussian deconvolution of the representative absorption spectrum of $C_{38}H_{76}N_6O_4Cu$ complex int the solid state (a) and ethanol (b) and its comparison with the spectrum of a free $C_{19}H_{39}N_3O_2$ ligand (c)

The LMCT transitions in the complexes studied appear at about 29 000 and 22 000 cm^{-1}. The spectra of the free ligands do not show any band in this region. For the complex compounds these transitions appear as medium intensity bands. The alkylaminoacetylureas have low lying empty orbitals of the non-bonded electrons as well as empty π-antibonding orbitals connected with double bonds of the ligand. Therefore, the components of these transitions, observed at about 29 000 and 22 000 cm^{-1}, can be denoted as N→Cu and O→Cu LMCT because the complexation of the ligand to the copper ion occurs through oxygen and nitrogen atoms.

Table 2. Positions of maxima of the absorption bands for twelve complexes studied (data obtained from their Gaussian deconvolutions)[cm^{-1}]

R	d–d transitions			N→Cu ligand to metal CT	O→Cu ligand to metal CT	$n\rightarrow\pi^*$ CT of the ligand	$\pi\rightarrow\pi^*$ CT of the ligand
C_3H_7	7680		15780	19980	29290	32710	43200
C_4H_9	8290		17840	21420	29790	34010	44550
C_5H_{11}		10350	17210	20770	29900	33620	42180
C_6H_{13}		12520	18300	21560	30120	35710	45870
C_7H_{15}		12220	17560	21410	28600	32570	43190
C_8H_{17}	7700	11340	17980	21060	30350	34040	43660
C_9H_{19}	7670	12020	18090	21830	29330	33980	45500
$C_{10}H_{21}$	8710		18120	21630	29460	34150	45180
$C_{12}H_{25}$	8130	12860	18010	21670	29710	34220	45770
$C_{14}H_{29}$	8630	12380	18290	21620	29810	33790	43130
$C_{16}H_{33}$	7290	12070	18220	21000	30690	35430	45200
$C_{18}H_{37}$	8570	12750	17410	21140	30040	33850	43790

The d-d transitions of the complexes studied are observed in the NIR region from 8000 to 18 000 cm^{-1}. The intensities of these bands are a few orders of magnitude lower than those of the CT transitions. Two clear bands appear in this region at about 17 500 and 12 000 cm^{-1}. The third component of this contour can be obtained from the Gaussian deconvolution. This procedure locates the third component at about 8000 cm^{-1}. Among the electronic transitions characteristic of the Cu^{2+} ion, the band at about 17 500 cm^{-1} is the most informative since it has relatively high intensity and is clearly visible as a shoulder on the slope of the LMCT contour.

In the discussion of the observed electron spectra, the C_{2v} symmetry derived from the vibrational studies should be taken into account in the first approximation. The order of the 3d electronic states for related systems have been established by means of polarized crystal spectra and theoretical calculations based on the angular overlap model (AOM) [33–37]. The order of the 3d orbitals, as derived by these authors, for the C_{2v} symmetry was $d_{x^2-y^2} > d_{xy} > d_{z^2} > d_{yz} > d_{xz}$. The selection rules of magnetic dipole transitions predict that the $d_{xy} \rightarrow d_{x^2-y^2}$, $d_{yz} \rightarrow d_{x^2-y^2}$, and $d_{xz} \rightarrow d_{x^2-y^2}$ transitions are allowed, while the

$d_{z^2} \rightarrow d_{x^2-y^2}$ transition is forbidden. Therefore, in the spectra recorded by us, three bands are apparently in agreement with the experiment. The bands at 17 500, 12 000 and 8 000 cm–1 can be assigned to the $d_{xz} \rightarrow d_{x^2-y^2}$, $d_{yz} \rightarrow d_{x^2-y^2}$ and $d_{xy} \rightarrow d_{x^2-y^2}$ transitions, respectively. This result indicates that symmetry of the coordination polyhedron for the studied complexes in the solid state is not higher than C_{2v}, i.e. the coordination polyhedron is a distorted CuN_2O_2 pyramid. The energy ranges of the electron transitions obtained in the present work fit well with the data presented in the literature [37–39].

The spectra of the complexes in ethyl alcohol solutions exhibit a splitting of the 17 500 cm^{-1} band into a doublet at 15 910 and 18 440 cm^{-1}. This result indicates that three components are observed in the 10 000–20 000 cm^{-1} range at 13 720, 15 910 and 18 440 cm^{-1}. The extinctions of these bands are as follows: 45.9, 80.6 and 81.2 [$dcm^3 \cdot mol^{-1} \cdot cm^{-1}$], respectively. Low intensities of these bands suggest that the *trans*-CuN_2O_2 unit may have a symmetry being a slight modification of a centrosymmetric group.

3.3. Luminescence spectra

Luminescence spectra of the complexes studied at room temperature (RT) are presented in Fig. 4. The comparison of the RT spectra with those recorded at 15 K (LT) for the representative samples is shown in Fig. 5.

The RT emission spectra consist of two transitions: a broad and strong band at ca. 14 000 cm^{-1} and another one, of weak intensity, observed at ca. 17 000 cm^{-1} as a shoulder on the slope of the former band. Its behaviour upon the temperature decrease depends on the R radical mass. For the C_{10} sample, the emission has a nearly constant position. For the C_{14} sample the maximum of the emission shifts from 14 000 cm^{-1} at RT to 15 800 cm^{-1} at LT. The largest shift is observed for the C_6 sample ranging from 10 000 to 18 000 cm^{-1}. The emissions at 17 000 and 14 000 cm^{-1} can be described, as before, by $d_x^2\text{-}_y^2 \rightarrow d_{xz}$ and $d_{xy} \rightarrow d_{xz}$, respectively. The large width of these bands suggests that more than one site could appear in the complexes studied. This problem will be discussed in the later part of this paper. The decay curves obtained for the complexes studied from the time resolved experiment are non-exponential, giving two life times of a few ns order. This suggests a different symmetry of some Cu^{2+} ions in these materials.

The electronic transitions observed in the absorption and emission spectra can be compared with the complexes studied. The dependence of their energies on the R-radical mass (i.e. the length of the R radical chain) is shown in Fig. 2 (the straight line between the band maxima for the samples 1 and 12). Energy increases according to a general trend, although the course is irregular. For the lighter ligands some differences in the transition energies are observed, and stabilization occurs for the ligands above C_{10}. This result shows that the mass and length of the radical chain in the ligand influence, to some extent, the energy of the electronic levels and the properties of the complexes studied.

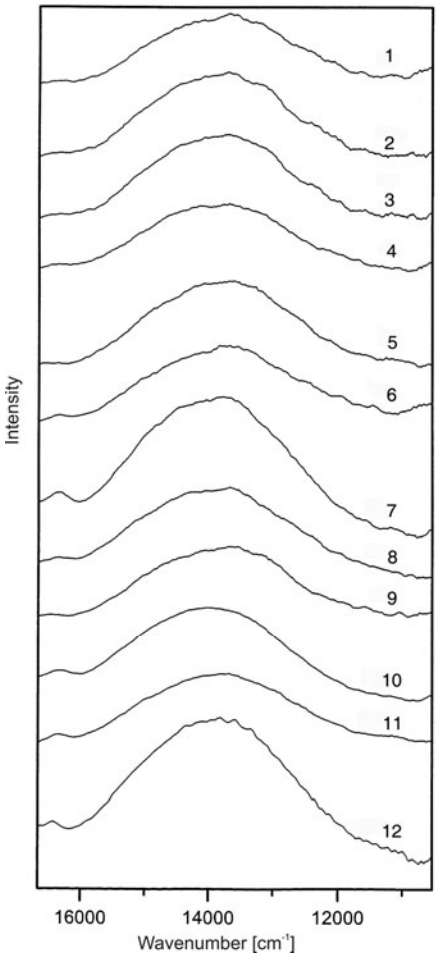

Fig. 4. Room temperature emission spectra of Cu^{2+} complexes studied (λ_{exc} = 488 nm); the sample specification as in Table 1. The experimental error of the determination of the positions of band maxima does not exceed 10 cm^{-1}

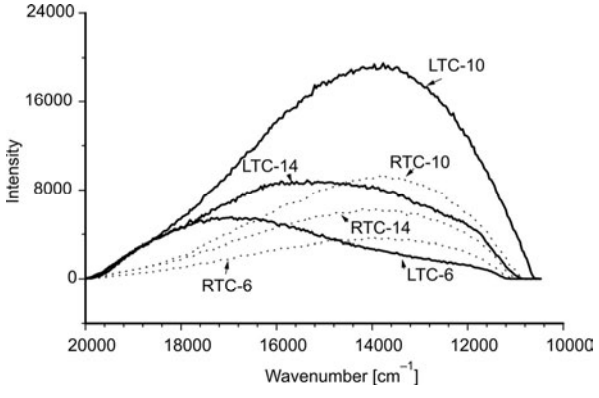

Fig. 5. Comparison of the room (RT) and liquid helium (LT) temperature emission spectra for representative samples: R = C_6H_{13}, R = $C_{10}H_{21}$ and R = $C_{14}H_{29}$ and cross-section of the energetic levels

3.4. ESR spectra and magnetic properties

The magnetic susceptibility data obtained for twelve copper(II) complexes with alkylaminoacetylurea ligands in the temperature range 1.9–300 K are collected in Table 3. It has been shown [26] that magnetic moments and susceptibilities of the compounds studied change with the length of the alkyl chain. In the present paper, syntheses of two other complexes belonging to this group with R = C_3H_7 and C_4H_9 are reported and properties of these materials are compared with the properties of the previously studied compounds.

Table 3. Magnetic data of the Cu^{2+} complexes studied

No.	R	μ_{eff}(300 K) [B.M.]	μ_{eff}(80 K) [B.M.]	μ_{eff}(1.9 K) [B.M.]	Weiss constant θ [K][a]	Curie constant C [$cm^3 \cdot K \cdot mol^{-1}$][a]
1	C_3H_7	1.80	1.78	1.81	0.13 [b]	0.410 [b]
2	C_4H_9	1.76	1.74	1.03	–2.21	0.391
3	C_5H_{11}	1.83	1.79	1.90	0.42 [b]	0.433 [b]
4	C_6H_{13}	1.75	1.73	0.98	–2.34	0.386
5	C_7H_{15}	1.71	1.69	1.01	–2.43	0.379
6	C_8H_{17}	1.74	1.74	1.01	–1.50	0.388
7	C_9H_{19}	1.87	1.80	1.69	–3.00	0.431
8	$C_{10}H_{21}$	1.73	1.74	1.05	–0.93	0.398
9	$C_{12}H_{25}$	1.81	1.72	1.06	–5.00	0.420
10	$C_{14}H_{29}$	1.70	1.68	1.02	–2.20	0.369
11	$C_{16}H_{33}$	1.85	1.73	1.05	–3.10	0.405
12	$C_{18}H_{37}$	1.99	1.81	1.10	–9.35	0.449

[a]In the temperature range 6–300 K.
[b]In the temperature range 6–40 K.

The results of susceptibility measurements for the new complexes with R = C_3H_7 and C_4H_9 are presented in Fig. 6 in the form $\chi_m T = f(T)$, where χ_m is the corrected molar magnetic susceptibility per Cu^{2+} and T is the absolute temperature. The observation of weak magnetic interactions at very low temperatures for the studied complexes suggests that copper(II) ions are not isolated in the crystal lattice. For the R = C_3H_7 complex a weak ferromagnetic interaction is observed, as evidenced through a very small increase of $\chi_m T$ and magnetic moments below 25 K, as well as a positive value of the Weiss constant (Fig. 6, Table 3). Similar results were previously observed for the complex with R = C_5H_{11} [26]. The behaviour of the complex with R = C_4H_9 is also similar to the behaviour of other compounds studied (see Table 1), i.e. below 25 K decrease of the $\chi_m T$ values is observed, and the magnetic moment decreases from 1.76 B.M. at RT to 1.03 B.M. at 1.9 K (B.M. – Bohr magneton). This behaviour suggests the existence of weak antiferromagnetic interactions between Cu^{2+} ions. The plot of χ_m versus T shows a maximum at ca. 2 K (Fig. 7). This result confirms the presence

of weak antiferromagnetic interactions. The calculated Weiss constant is negative and its value is –2.21 K (Table 3).

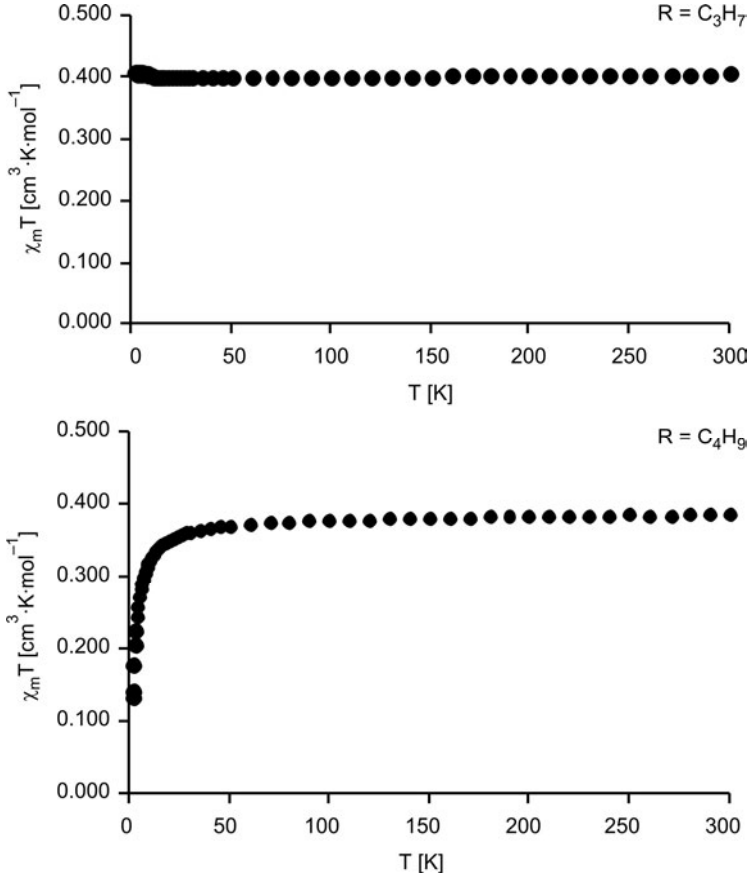

Fig. 6. Temperature dependences of the $\chi_m T$ product for the complexes with alkyls R = C_3H_7 and R = C_4H_9

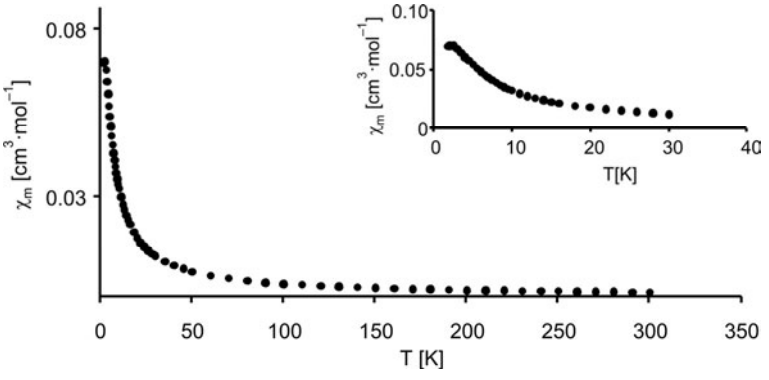

Fig. 7. Temperature dependences of the magnetic susceptibility for the sample R = C_4H_9

Figure 8 shows representative ESR spectra for three samples (R = C_3H_7, C_4H_9 and C_5H_{11}).

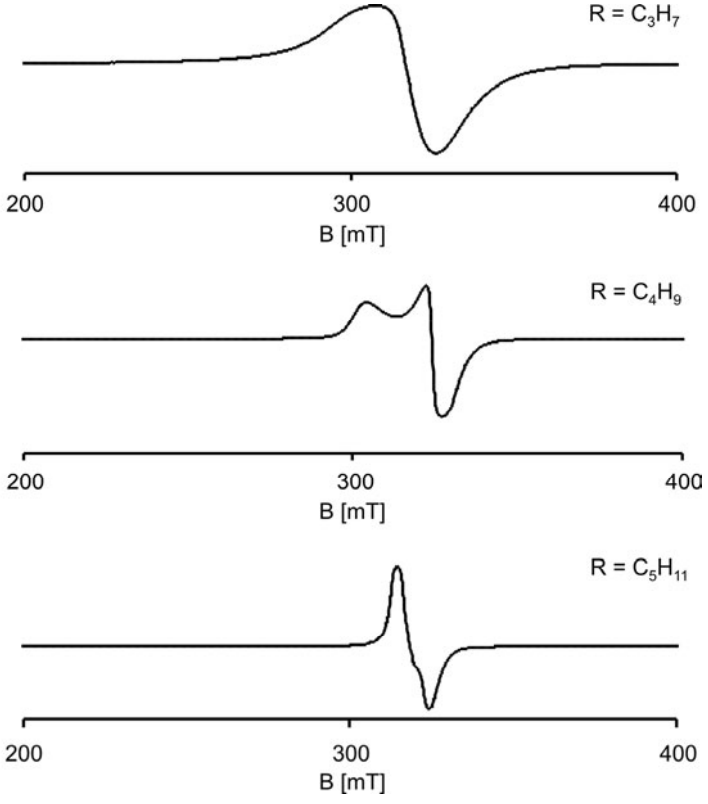

Fig. 8. ESR spectra of selected polycrystalline complexes:
R = C_3H_7, R = C_4H_9, R = C_5H_{11}, at 5 K

The ESR spectra were measured for polycrystalline samples at 300 and 5 K. Spectroscopic splitting parameters are the same for all measured complexes, $g_{av} = 2.10$. However, clear differences between the compounds with R = C_3H_7, R = C_5H_{11} and the remaining analogues are observed in the ESR spectra (Fig. 8). Since weak magnetic interactions were observed only at the lowest temperatures, we have analyzed the ESR spectra measured at 5K in order to obtain some information about these interactions. The spectrum of the complex with R = C_3H_7 exhibits only one symmetrical line at about 3000 G, whereas the spectrum of the R = C_4H_9 complex (which is representative of the remaining complexes) exhibits signal with two components. These components are characteristic of monomeric Cu^{2+} ions when the unpaired electron occupies the $d_{x^2-y^2}$ orbital and $g_{\|} = 2.18 > g_{\perp} = 2.05$. The different type of spectrum was observed for the complex with R = C_5H_{11}, with $g_{\perp} = 2.11$ and $g_{\|} = 2.05$. The reverse ($g_{\|} < g_{\perp}$) ESR spectra are obtained in complexes with a single electron in a d_z^2 orbital [40]. For the complex with R = C_5H_{11} weak ferromagnetic interaction was observed. The distance

between the Cu^{2+} centres in the crystal lattice must be long and, therefore, the observed magnetic interactions are very weak.

For all complexes the magnetization in function of the magnetic field strength was measured and the results obtained at 1.9 K are presented in Fig. 9.

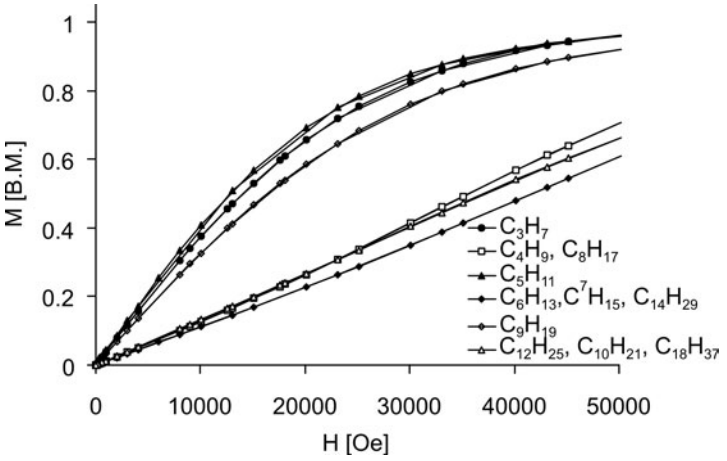

Fig. 9. Magnetic field dependence of the magnetisation for the copper(II) complexes studied at 1.9 K

For isolated magnetic ions, when H is small enough, the molar magnetization is linear and the Curie Law is valid. When H becomes large, M tends to the saturation value M_S [41]. The molar magnetization is $M = Ng\beta SB_S(y)$, where $B_S(y)$ is the Brillouin function [41]. When H becomes very large, $B_S(y)$ tends to unity and M tends to the saturation value $M_S = Ng\beta S$. If the saturated magnetization is expressed in $N\beta$ units, its value for $S = 1/2$ and $g = 2.0$ tends to 1. Figure 9 shows that for the two measured complexes, with R = C_3H_7 and C_5H_{11}, magnetization tends to the saturation value at high magnetic fields. It confirms the ferromagnetic character of magnetic interaction observed in the two complexes. For the remaining compounds, up to H = 50 000 G, the magnetization is linear.

4. Conclusion

The absorption and emission spectra as well as magnetic and ESR data obtained for the new copper(II) complexes with alkylaminoacetylurea ligands suggest that the physicochemical properties of these compounds change with the length of the alkyl chain. The coordination polyhedron of the Cu^{2+} ions in these complexes is four coordinated and pyramidal with small distortion from the square-planar. The very weak ferromagnetic interactions are observed for the C_3 and C_5 alkyls and the antiferromagnetic ones for the remaining complexes with C_4 and C_6–C_{18} alkyls. These studies will

be continued using other physicochemical and X-ray methods when on single crystals of these compounds.

References

[1] MILLER E.V., *Chemistry of the Plants*, Reinheld, New York, 1957.
[2] GEISSLER P.R., ROSENBLATT T.M., US Patent 1970, 3, 523, 018.
[3] ZHENG M., KHANGULOV S.V., DISMUKES G.C., BARYNIN V.V., Inorg. Chem., 33 (1994), 382, and references therein.
[4] RILEY D.P., WEISS R.H., J. Am. Chem. Soc., 116 (1994), 387, and references therein.
[5] LINDSEY J.S., PRATHAPAN S., JOHNSON T.E., WAGNER R.W., Tetrahedron, 50 (1994), 8941.
[6] REICHWEIN A.M., VERBOOM W., REINHOUDT D.N., Recl. Trav. Chim. Pays-Bas., 112 (1993), 595.
[7] SHIONOYA M., KIMURA E., SHIRO M., J. Am. Chem. Soc., 115 (1993), 6730 and references therein.
[8] MURAKAMI Y., KIKUCHI J., MIYAJIAMA T., HISAEDA Y., Chem. Lett. (1994), 55.
[9] HORWITZ P., Chem. Matter, 1 (1989), 463.
[10] COLLIN J.P., SAUVAGE J.P., J. Chem. Soc. Chem. Commun., (1987), 1075.
[11] BEDIOUI F., MOISY P., DEVYNK J., SALMON L., BIED-CHARRETON C., J. Mol. Catal., 56 (1989), 267.
[12] LELIJ F., MORELLI G., RICCARDI G., ROMANELLI M., ROSA A., OTTAVIANI M.F., Polyhedron, 16 (1991), 1911.
[13] SMITH C.I., CRAYSTON J.A., HAY R.W., J. Chem Soc. Dalton Trans., (1993), 3267.
[14] FUJITA E., HAFF J., SANZENBACHER R., ELIAS H., Inorg. Chem., 33 (1994), 4627.
[15] BALZANI V., Tetrahedron, 48 (1992), 10443.
[16] FUJITA E., BRUNSCHWIG B.S., OGATA T., YANAGIDA S., Coord. Chem. Rev., 132 (1994), 195.
[17] BIGNOZZI C.A., BORTOLINI O., CHIORBOLI C., INDELLI, M.T., RAMPI M.A., SCANDOLA F., Inorg. Chem., 31 (1992), 172.
[18] SETH J., PALANIAPPAN V., JOHNSON T.E., PRATHAPAN S., LINDSEY J.S., BOCIAN D.F., J. Am. Chem. Soc., 116 (1994), 10578.
[19] ODOBEL F., SAUVAGE J.P., New J. Chem., 18 (1994), 1139.
[20] YAWNEY D.G.W., DOEDENS R.J., Inorg. Chem., 9 (1970), 1626.
[21] KISHITA M., INOUE M., KUBO M., Inorg. Chem., 3 (1964), 237.
[22] BULLOCK J., J. Inorg. Nucl. Chem., 29 (1967), 2257.
[23] DALLOEY N.K., MUELLER M.H., SIMONSEN S.H., Inorg. Chem., 11 (1972), 1840.
[24] TALIK T., TALIK T.W., TALIK Z., Chemia Stosowana, 34 (1990), 301 (in English).
[25] TALIK T., TALIK Z., PUSZKO A., Scientific Works of Wroclaw Academy of Economics, Technology, 749 (1997), 67.
[26] CIURLA H., HANUZA J., TALIK T., TALIK Z., KORABIK M., MROZIŃSKI J., J. Alloys Comp., 341 (2002), 111.
[27] KÖNIG E., *Magnetic Properties of Coordination and Organometallic Transition Metal Compounds*, Springer, Berlin, 1966.
[28] CIURLA H., MICHALSKI J., HANUZA J., MACZKA M., TALIK T., TALIK Z., Spectrochim. Acta, A 64 (2006), 34.
[29] DROŻDŻEWSKI P., KORDON E., Spectrochim. Acta, A 54 (1998), 947.
[30] DROŻDŻEWSKI P., KORDON E., Spectrochim. Acta, A 56 (2000), 1299.
[31] DROŻDŻEWSKI P., PAWLAK B., GŁOWIAK T., J. Coord. Chem., 55 (2002), 735.
[32] DROŻDŻEWSKI P., BROŻYNA A., KUBIAK M., Polyhedron, 23 (2004), 1785.
[33] SCHAFFER C.E., JORGENSEN C.K., Mol. Phys., 9 (1965), 401.
[34] SCHAFFER C.E., Struct. Bonding (Berlin), 5 (1968), 68.
[35] LARSEN E., MAR G.N.L., J. Chem. Educ., 51 (1974), 633.
[36] ATANASOV M.A., HITCHMAN M.A., Inorg. Chem., 32 (1993), 3973 and references therein.

[37] AKITSU T., KOMORITA S., URUSHIYAMA A., Bull. Chem. Soc. Jpn., 74 (2001), 851.
[38] ATTANASIO D., COLLAMATI I., ERCOLANI C., J. Chem. Soc. Dalton Trans., (1974), 1319.
[39] PROTASIEWYCK G.M., NUNES F.S., Spectrochim. Acta A, 65 (2006), 549.
[40] ELLIOTT H., HATHAWAY B.J., SLADE R.C., J. Chem. Soc. A, (1966), 1443.
[41] KAHN O., Molecular Magnetism, VCH, Weinheim, Germany, 1993.

Received 14 June 2007
Revised 19 December 2008

Materials Science-Poland, *Vol. 27*, *No. 1*, *2009*

Preparation and bioactivity of embedded-style hydroxyapatite–titania nanotube arrays

X.-F. XIAO*, R.-F. LIU, T. TIAN

College of Chemistry and Materials Science, Fujian Normal University, Fuzhou 350007, China

Embedded-style hydroxyapatite–titania nanotube arrays were successfully prepared by anodic oxidation of titanium substrate and centrifugal filling hydroxyapatite precursor sol into hollow nanotubes. The morphology, microstructure and thermal stability of the samples were characterized by X-ray diffraction, environmental scanning electron microscopy, and energy dispersive X-ray analysis. The results show that the structure of titania nanotube arrays is stable at 500 °C or below, and the crystallized hydroxyapatite could be formed from hydroxyapatite precursor sol after calcining at 500 °C for 4 h. The optimum calcining temperature for this material is 500 °C. An obvious apatite layer formed on the surface of the embedded-style material after soaking in simulated body fluid for 5 days, indicating that the material possesses a good *in vitro* apatite forming ability on its surface.

Key words: *hydroxyapatite; bioactivity; composite; biomaterial; nanotube array; titania*

1. Introduction

Hydroxyapatite (HA, $Ca_{10}(PO_4)_6(OH)_2$), a major inorganic component of bones, shows high biocompatibility, bioactive and osteoconductive properties. HA, however, cannot be used in load bearing situations due to its brittleness [1, 2]. Titanium and its alloys possess favourable properties, such as good ductility, tensile and fatigue strength, modulus of elasticity matching that of bones, a similar density to that of bones, and good biocompatibility. So they are frequently used as surgical implants in load bearing situations such as hip prostheses and dental implants [3, 4]. However, it is difficult for them to bond to bones, due to their poor osteointegration properties. Thus, much attention has been focused on improving the bioactivity of titanium, using techniques such as plasma spray [5], laser fusion [6], ion sputtering [7], electrophoretic deposition [8], hydrothermal electrodeposition [9] etc. to form HA coating on titanium substrates. All these methods have respective merits but they share a common ground in that the materials derived from them are layer-style configurations, with HA

*Corresponding author, e-mail: rfliu@vip.sina.com

coating on the surface of titanium substrates. This means that the interfacial fractures may occur between HA coatings and titanium substrates, resulting in the implant migration and loss. Therefore, how to avoid loosing and scaling-off of coating is an urgent problem to resolve for HA coating materials.

In this study, a new embedded-style composite material, instead of a layer-style one, was prepared by anodizing on the titanium in HF solution to fabricate titania nanotube arrays and then affusing HA precursor sol into titania nanotubes by centrifugal force. HA precursor sol was prepared from $Ca(NO_3)_2{\cdot}4H_2O$ ethanol solution and P_2O_5 ethanol solution. Titania nanotube arrays prepared by anodic oxidation in HF [10–14] show a discrete, well-ordered, and hollow structure. Therefore, titania nanotube arrays could be used as carriers to fill HA precursor sol. Consequently, an embedded-style hydroxyapatite–titania nanotube arrays composite material could be obtained. This composite material has both excellent properties of HA and Ti being expected to improve the loosing and dislocation problems of HA coating.

2. Experimental

Preparation of titania nanotube arrays. Pure titanium foils (99.5% pure) were purchased from the Northwest Institute for Non-ferrous Metal Research (China). Prior to anodization, the titanium foils were ultrasonically cleaned in acetone and distilled water, for 5 min, respectively, then eroded in 4% HF + 5mol/dm^3 HNO_3 for 30 s, followed by ultrasonic cleaning in distilled water for 5 min and dried in air at 40 °C. A set-up with a graphite cathode was employed for the anodization of titanium in HF solution (0.5 wt. %). All electrolytes were prepared from analytical reagent grade chemicals and distilled water. The anodizing voltage was kept constant at 20 V during the entire process with a dc power supply (GOA, China) [10]. The whole course of anodization was conducted at room temperature (25 °C) with magnetic agitation. After anodization, the samples were rinsed with distilled water and then dried at 40 °C in air. The effect of the heat treatment on morphology of the titania nanotube arrays was conducted by putting the samples into a furnace at various temperatures (from 300 °C to 600 °C) for 4 h.

Preparation of the HA precursor sol. HA precursor sol was prepared using a mixed ethanol solution of calcium nitrate and phosphorous pentoxide [15], controlling the Ca/P molar ratio at 1.67 being the stoichiometric value of HA. Calcium nitrate ethanol solution was dripped into phosphorous pentoxide ethanol solution with a magnetic agitation at room temperature, and kept static for 24 h before filling into titania nanotube arrays. Furthermore, another precursor sol was dried at 100 °C for 2 h and the resulting dried gels were calcined for 4 h at various temperatures, ranging between 300 °C and 500 °C.

Preparation of embedded-style composite materials. The prepared HA precursor sol was placed in a centrifugal test-tube, and then the prepared titania nanotube arrays

were soaked in the HA precursor sol. The samples were placed as shown in Fig. 1, titanium foil was glued horizontally on the built-in sample stage and titania nanotube arrays were put upwards. Under the centrifugal force, produced by the centrifuge operating at 4000 rev./min for 30 min, HA precursor sol was filled into the titania nanotubes. The samples were then taken out, ultrasonically cleaned in pure ethanol to remove HA precursor sol on the top of titania nanotube arrays. Then, the samples were dried at 100 °C in air for 1 h and calcined at 500 °C for 4 h.

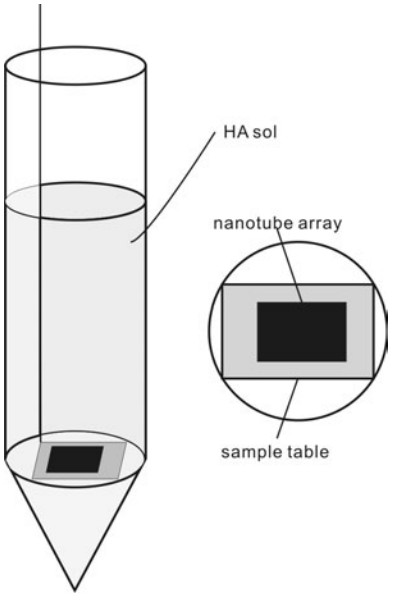

Fig. 1. Schematic diagram of the placement of the sample during centrifugal filling

In vitro bioactivity of the composite material. The composite materials were inserted into culture vials containing a simulated body fluid (SBF), which was prepared according to Kokubo et al. [16]. The composite materials were soaked in SBF for 5 days at 37 °C without stirring before they were taken out for coating characterization. Titania nanotube arrays without embedded HA were also soaked in SBF in a control experiment.

Characterization of the samples. A Philips XL30 environmental scanning electron microscope (ESEM), equipped with a Philips energy dispersive X-ray analyzer (EDAX) was employed to characterize the morphology and compositions of the composite materials. In order to obtain information on the structure of composite materials, they were mechanically bent, and in some cases a partial lift-off of the titanium substrate occurred. A Philips X'Pert MPD diffractometer system, using CuK_{α} radiation, was employed to characterize the phase of the samples. The X-ray generator operated at 40 kV and 40 mA. Data sets were collected over the range of 5–90° with a step size of 0.02° and a count rate of 4.0 $K \cdot min^{-1}$.

3. Results and discussion

Figure 2 shows SEM images of the titania nanotube arrays obtained by anodization. As shown in Fig. 2a, titania nanotube arrays with discrete, hollow, tubular features were obtained in 0.5 % HF solution. The SEM micrographs show that titania nanotubes measure about 250 nm long with an inner diameter of about 100 nm. This structure possesses larger surface areas and is different from the nonporous titania layers formed in other electrolytes such as sulfuric acid [17, 18]. In fluoride-containing electrolytes, anodization of titanium is accompanied with the chemical dissolution of titanium oxide due to the formation of TiF_6^{2-}. Highly uniform nanotube arrays, instead of porous or nonporous structures, formed [10, 14]. Although the shrinkage of the tube diameter was observed after heating at 500 °C for 4 h (Fig. 2b), the structure of the titania nanotube arrays is still intact. When increasing the heat treatment temperature to 600 °C (Fig. 2c), the nanotubes collapse into an irregularly shaped morphology, losing their tubular structures. The results indicate that the titania nanotube arrays structure could be stable at temperatures not higher than 500 °C.

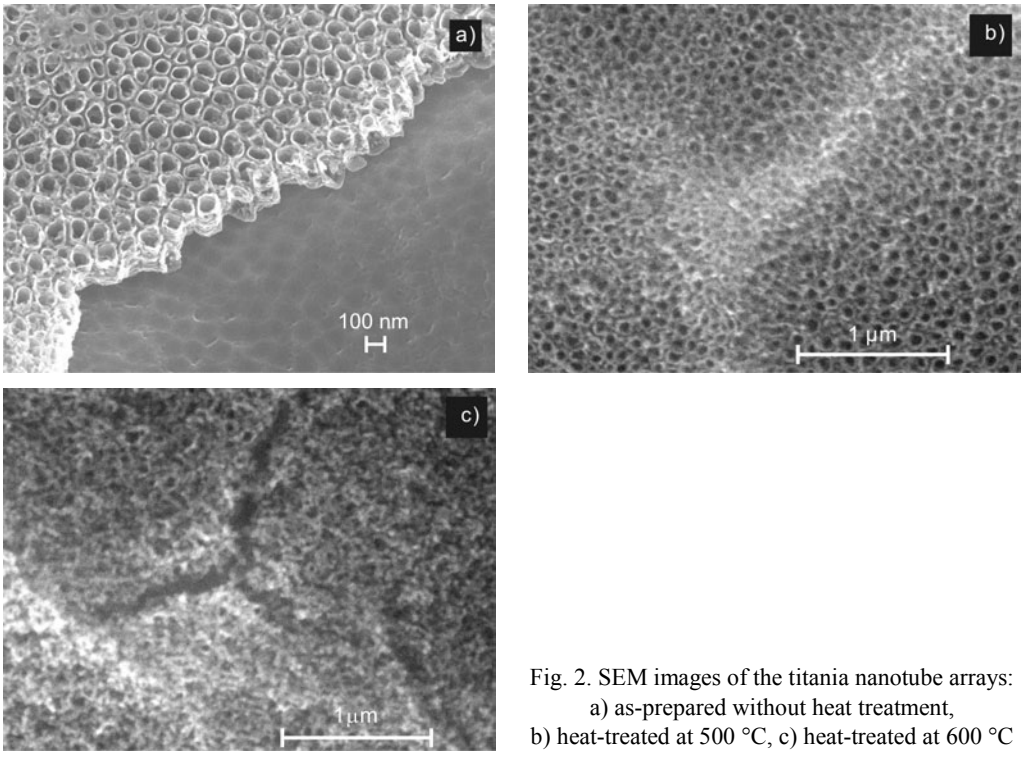

Fig. 2. SEM images of the titania nanotube arrays: a) as-prepared without heat treatment, b) heat-treated at 500 °C, c) heat-treated at 600 °C

Figure 3 shows the XRD patterns of the titania nanotube arrays without (Fig. 3a) or with heat treatment at 500 °C (Fig. 3b). Only Ti diffraction peaks can be seen in Fig. 3a, indicating that the untreated nanotubes were amorphous and were crystallized

from amorphous to anatase phase at 500 °C. In order to testify the crystallization of titania nanotube arrays, the same heat treatment was performed on pure titanium without titania nanotube arrays. There is only Ti peak appearing on the pattern at 500 °C. The results indicate that the phase transformation of the titania nanotube arrays at 500 °C is the result of their crystallization.

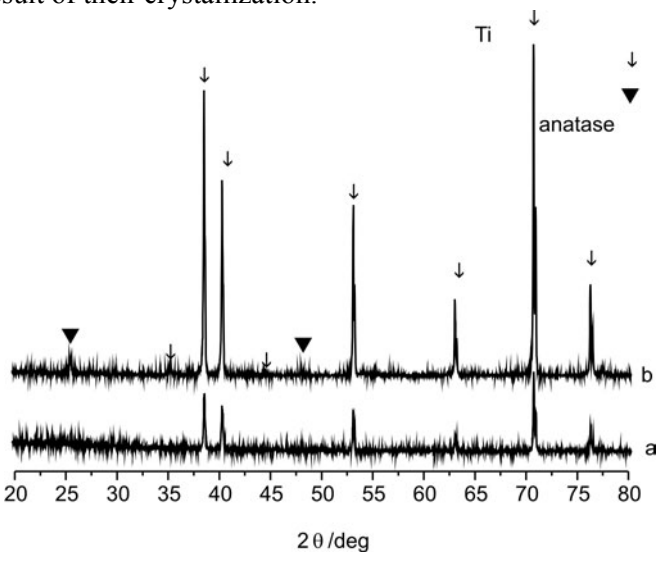

Fig. 3. XRD patterns of titania nanotube arrays: a) as-prepared without heat treatment, b) heat-treated at 500 °C

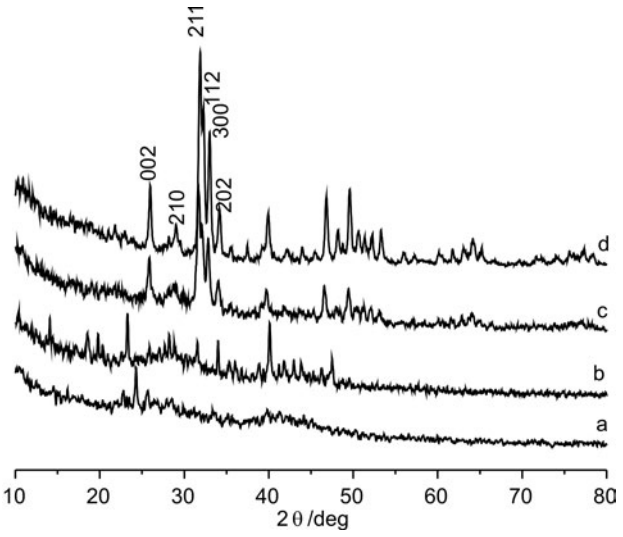

Fig. 4. XRD patterns of the powder from HA precursor sol after calcining at various temperatures: a) before calcining, b) at 300 °C, c) at 400 °C, d) at 500 °C

Figure 4 shows the XRD patterns of the powder formed from HA precursor sol after calcining at various temperatures. Figure 4a shows that the dried gel without heat treatment exhibits highly amorphous characteristics. The powder calcined at 300 °C exhibits many diffraction peaks of other phases with a considerable amount of amorphous phase (Fig. 4b). The diffraction peaks of apatite appear after heat treatment at 400 °C (Fig. 4c), and their intensity increases with increasing temperature. After calcining at 500 °C, the intensity of the main diffraction peaks of HA, such as (002), (210), (211), (112), (300) and (202), is very strong, indicating that HA has a high degree of crystallinity.

According to the morphology observation of titania nanotube arrays (Fig.2) and the XRD analysis of the powder of HA dried gel after heat treatment at different temperature (Fig. 4), an embedded-style hydroxyapatite–titania nanotube arrays composite material could be obtained by affusing HA precursor sol into titania nanotubes using centrifugal force and then calcining at 500 °C. The optimum calcining temperature for this material is 500 °C.

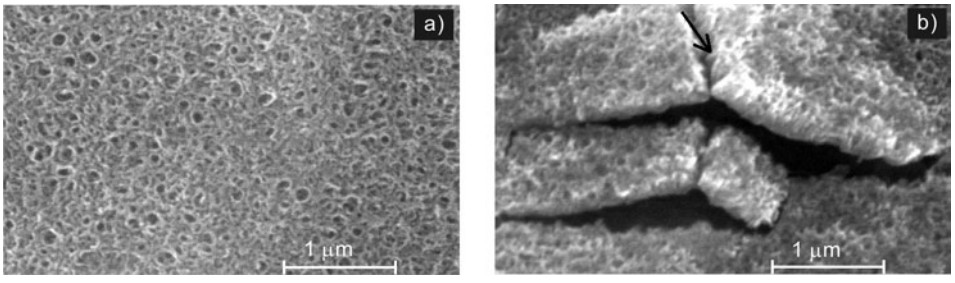

Fig. 5. SEM image of the surface and transection morphology of the embedded-style materials

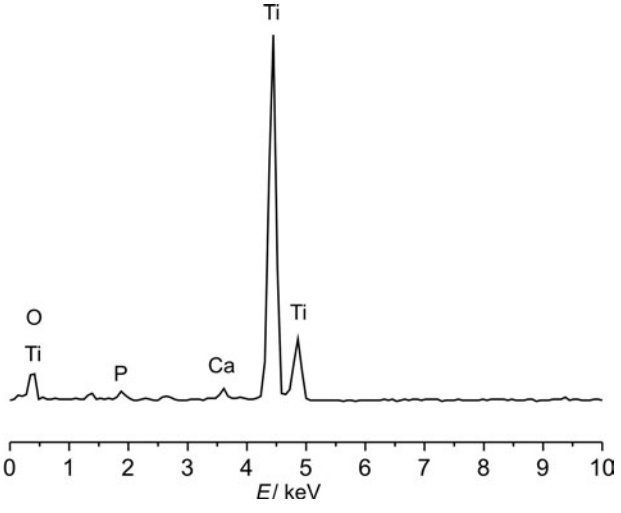

Fig. 6. EDAX analysis of the nanotube end as shown with the arrow in Fig. 5b

Figure 5 shows the surface and transection morphology of the embedded-style hydroxyapatite–titania nanotube arrays composite material. As shown in Fig. 5a, it is clear that many tubes have been filled with something, but some nanotubes still have not been filled with, the mouths of which are clearly visible. In order to confirm whether the HA precursor sol has been filled into the nanotubes, the nanotube end was characterized by EDAX, as shown in the arrow in Fig.5b. EDAX results show that titania nanotube arrays mainly consist of Ti, O and a small quantity of Ca and P element (Fig.6), which indicates that HA precursor sol could be filled into the nanotube using centrifugal force, and such embedded-style hydroxyapatite–titania nanotube arrays composite material could be obtained.

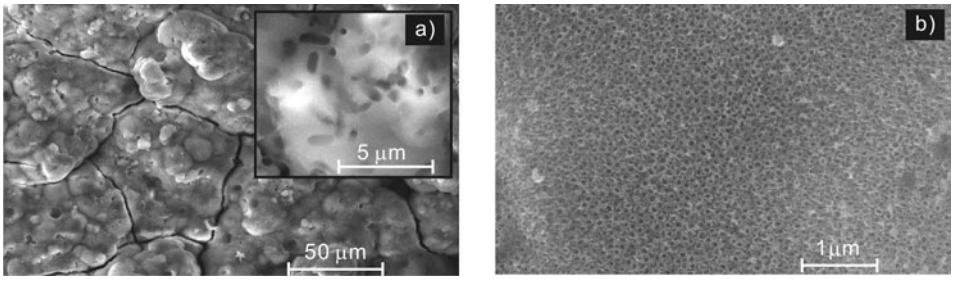

Fig. 7. Surface morphology of the sample after soaking in SBF for 5 days:
a) embedded-style composite material, b) titania nanotube arrays heat-treated at 500 °C

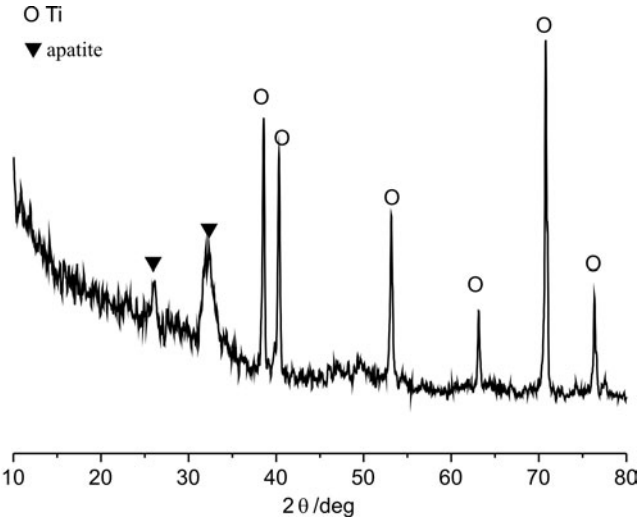

Fig. 8 XRD pattern of the new layer after soaking in SBF for 5 days

Figure 7a shows the surface morphology of the embedded-style hydroxyapatite –titania nanotube arrays after soaking in SBF for 5 days with an obvious layer formed on the surface of the titania nanotube arrays. The XRD pattern of the new layer is shown in Fig. 8, compared with the standard card (JCPDS 09-432), indicating

that the layer formed on the surface is an apatite layer. The results of a control experiment without filling HA precursor sol are shown in Fig. 7b: there is nothing on the surface of the titania nanotube arrays and the open tops of the nanotubes are clearly visible. The results show that an embedded-style hydroxyapatite–titania nanotube arrays composite material has an apatite-forming ability in SBF on its surface related to the HA contained in the nanotubes. After soaking in SBF, a trace of HA could dissolve and form PO_4^{3-} and Ca^{2+} ions which induce the nucleation of apatite. Once the apatite nuclei are formed, they spontaneously grow by consuming calcium and phosphate ions from SBF. As a result, apatite nucleates and grows on the surface of titania nanotube arrays. Therefore, they are endowed with *in vitro* bioactivity by centrifugal filling with the HA sol.

4. Conclusions

A new embedded-style hydroxyapatite–titania nanotube arrays composite material was successfully prepared by centrifugal filling HA precursor sol into the nanotubes of titania nanotube arrays, with the aid of the pressure provided by a centrifuge. The optimum calcining temperature for this embedded-style material is 500 °C. Bioactivity study indicates the obtained material possesses excellent bioactivity. It is an effective way to endow Ti with bioactivity by anodic oxidation in HF electrolyte and centrifugal filling HA precursor sol into the nanotubes.

Acknowledgements

The authors thank the National Nature Science Foundation of China (30600149), the Science Research Foundation of the Ministry of Health and United Fujian Provincial Health and Education Project for Tackling the Key Research, PR China (WKJ 2005-2-008), Fujian Development and Reform Commission of China (No. 2004 (477)), Fujian Provincial Department of Science and Technology (No. 2006I0015) and Fujian Nature Science Foundation (2007J0144).

References

[1] OSBORN J., NEWESELY H., Biomater., 1 (1980), 108.
[2] AKAO H., AOKI H., KATO K., J. Mater. Sci., 16 (1981), 809.
[3] NOORT R., J. Mater. Sci., 22 (1987), 3801.
[4] TENGVALL P., LUNDSTROM I., Clin. Mater., 9 (1992), 115.
[5] SUN L., BERNDT C.C., KHOR K.A., CHEANG H.N., GROSS K.A., J. Biomed. Mater. Res., 2 (2002), 228.
[6] PILLIAR R.M., FILIAGGI M.J., Bioceramics 6 (1993), 165.
[7] ONG J.L., LUCAS L.C., Biomater., 14 (1994), 337.
[8] DUCHEYNE P., RADIN S., HEUGHEBAERT M., HEUGHEBAERT J.C., Biomater., 11 (1990), 244.
[9] XIAO X.F., LIU R.F., ZHENG Y.Z., Mater. Lett., 59 (2005), 1660.
[10] GONG D.W., GRIMES C.A., VARGHESE O.K., HU W., SINGH R.S., CHEN Z., DICKEY E.C., J. Mater. Res., 12 (2001), 3331.
[11] BERANEK R., HILDEBRAND H., SCHMUKI P., Electrochem. Solid-State Lett., 3 (2003) B12.
[12] MOR G.K., SHANKAR K., PAULOSE M., VARGHESE O.K., GRIMES C.A., Nano Lett., 1 (2005), 191.

[13] CAI Q., PAULOSE M., VARGHESE O.K., GRIMES C.A., J. Mater. Res,. 1 (2005), 230.
[14] MOR G.K., VARGHESE O.K, PAULOSE M., MUKHERJEE N., GRIMES C.A., J. Mater. Res., 11 (2003), 2588.
[15] WENG W.J., BAPTISTA J.L., J. Mater. Sci.: Mater. Med., 9 (1998), 159.
[16] KOKUBO T., KUSHITANI H., SAKKA S., KITSUGI T., YAMAMURO T., J. Biomed. Mater. Res., 24 (1990), 721.
[17] YANG B.C., UCHIDA M., KIM H.M., ZHANG X.D., KOKUBO T., Biomater., 25 (2004), 1003.
[18] SUL Y.T., JOHANSSON C.B., JEONG Y., ALBREKTSSON T., Med. Eng. Phys., 23 (2001), 329.

Received 3 September 2007
Revised 22 August 2008

Materials Science-Poland, *Vol. 27*, *No. 1*, *2009*

Structure, magnetic and electrical transport properties of $Mn_{4-x}Ag_xN$ compounds

W.J. FENG[1, 2*], D. LI[1], Q. ZHANG[1], Y.F. DENG[2], S. MA[1], Z.D. ZHANG[1]

[1] Shenyang National Laboratory for Materials Science, Institute of Metal Research, and International Centre for Materials Physics, Chinese Academy of Sciences, Shenyang 110015, China

[2] Shenyang-Chelyabinsk Laboratory of Condensed Matter Physics, College of Physics and Technology, Shenyang Normal University, Shenyang 110034, China

$Mn_{4-x}Ag_xN$ compounds (x = 0.0, 0.3, 0.6, 1.0) were prepared by milling and subsequently annealing the mixture of $Mn_2N_{0.86}$, Mn, and Ag powders. All compounds display good single-phase characteristics. Both Mn_4N and $Mn_{3.7}Ag_{0.3}N$ exhibit ferrimagnetism, and a little Ag replacement of Mn can improve the saturation magnetization. The magnetic transition of $Mn_{3.4}Ag_{0.6}N$ and Mn_3AgN below 15 K is from triangular antiferromagnetism to non-coplanar ferrimagnetism, while the ones at 256 and 275 K ($Mn_{3.4}Ag_{0.6}N$ and Mn_3AgN, respectively) have been ascribed to the gradual transition, as temperature increases, from the triangular antiferromagnetic structure Γ^{5g} to a ferrimagnetic-like one. Two minima appear on the $\rho(T)$ curves for Mn_3AgN, with the observation of a positive magnetoresistance throughout the whole tempeature-dependent change.

Key words: *antiferromagnetism; spin reorientation; magnetoresistance*

1. Introduction

Nitrogen atoms in octohedral interstices of fcc manganese yield the cubic anti-perovskite Mn_4N and, in turn, produce a strong difference between the Mn atoms surrounding the nitrogen and those at the corners of the unit cell. Therefore, the face centred Mn forms an Mn_6N octahedron having a great chemical stability [1]. Conversely, Mn atoms at the corners have greater lability, hence can be substituted by a set of metallic atoms, giving rise to the family of the anti-perovskite Mn_3MN (M = Zn, Cu, and Sn, etc.) compounds [2–4].

Mah [5] prepared Mn_4N, with a minor impurity phase MnO, by heating Mn powders in N_2 for 31 h at 1173–1243 K, and determined the heat of combustion of Mn_4N

*Corresponding author, e-mail: wjfeng@yahoo.com.cn

as –441.4±0.2 kcal/mol. Takei et al. [6, 7] determined its magnetic structure by means of neutron diffraction. At 77 K, the Mn moments with $3.85\mu_B$, at the corner of the cubic unit cell, are anti-parallel to three face-centred moments of $0.90\mu_B$. Recently, the film of Mn_4N [8] was grown by plasma-based ion implantation, and the corresponding structural and magnetic properties were extensively investigated. On the other hand, Fruchart et al. [9] reported the preparation of Mn_3AgN compound. Their investigation revealed that the manganese moment of the Mn_3AgN compound was 3.1 μ_B below 55 K, with a coexistence of two kinds of triangular antiferromagnetic (AFM) structures, i.e. Γ^{4g} and Γ^{5g}, which indicated the presence of ferromagnetic moments. However, this compound exhibits a pure triangular AFM structure Γ^{5g} in the temperature range between 55 and 290 K, with the manganese moment of 2.8 μ_B. After considering the magneto-crystalline anisotropy energy and the Dzyaloshii–Moriya interaction, Gomonaj et al. [10] stated that the magnetic phase transition at low temperatures of Mn_3AgN should be from triangular AFM to non-complanar ferrimagnetic (FIM n.c.) ones. Moreover, Mn_4N and its various metal-doped compounds such as $Mn_{4-x}Ga_xN$ [11] and $Mn_3(Cu_{1-x}Ge_x)N$ [12, 13] display a variety of magnetic structures as well as promising applications.

From the aforementioned research, it can be inferred that $Mn_{4-x}Ag_xN$ with $x = 0 - 1$ solid solution compounds could be produced successfully. Moreover, from the ferrimagnetism of Mn_4N to a pure triangular AFM structure Γ^{5g} of Mn_3AgN, it is a significant and interesting subject to explore magnetic and transport properties of $Mn_{4-x}Ag_xN$ solid solution compounds which might lead to some new findings as well as applications.

2. Experimental details

Mn flakes were milled under an argon atmosphere for 5 h in a high-energy ball mill. The as-milled powders were firstly homogenized at 573 K in a vacuum for 20 min and then cooled down to room temperature. N_2 was introduced into the enclosed tube with the powders, before in-situ nitrogenation was carried out at 823 K for 4 h. X-ray diffraction (XRD) pattern reveals a single-phase compound $Mn_2N_{0.86}$ [14]. Mn, Ag and $Mn_2N_{0.86}$ powders were mixed evenly in an appropriate proportion. The powder mixtures were continuously milled under an argon atmosphere for 1 h before interruption at a predetermined interval of 0.5 h, so as to prevent $Mn_2N_{0.86}$ from decomposition. The total milling time was 5 h. The as-milled powders were annealed at 823 K for 30 min in a vacuum better than 2×10^{-3} Pa.

XRD analysis was performed using CuK_α radiation with a Rigaku D/max-γA rotating target diffractometer. Magnetic properties were investigated with a superconducting quantum-interference device (SQUID, Quantum Design). For the magnetic measurements, the sample was cooled from 295 K to 5 K in the absence of a magnetic field and subsequently subjected to a dc magnetic field at 5 K. The sample was then heated while the magnetization was measured in the constant field. The powders were

uniformly solidified with glue. The powders were pressed into a pellet that was ground to a rectangular parallelepiped with the dimensions of 1×0.6×8 mm^3 to fit the test holder used for electrical measurement. Temperature dependences of electrical resistivity were measured by a standard four-probe method.

3. Results and discussion

3.1. Structural properties

Figure 1 shows the XRD patterns of $Mn_{4-x}Ag_xN$ compounds. The diffraction peaks of all the compounds are broadened indicating the presence of nanocrystallites. All samples are isostructural with Mn_4N ($Pm\bar{3}m$). As mentioned above, Mn atoms at the corner of Mn_4N have greater liability than those at the face centre, and may be

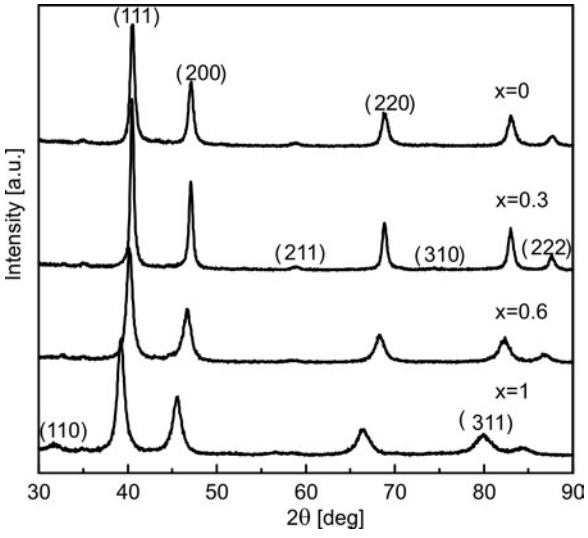

Fig. 1. X-ray diffraction patterns of $Mn_{4-x}Ag_xN$ with x = 0.0, 0.3, 0.6, and 1.0

preferentially substituted, which is confirmed by a successful preparation of $Mn_{4-x}Ag_xN$ solid solution compounds. Besides, with the increase of Ag content, the corresponding XRD peaks of the compounds shift towards lower angles which indicates lattice expansion. Due to a smaller atomic radius of Mn (0.1365 nm) than that of Ag (0.1445 nm), the change of lattice parameters of the $Mn_{4-x}Ag_xN$ compound is entirely reasonable.

3.2. Magnetic properties

Temperature dependences of magnetizations of Mn_4N and $Mn_{3.7}Ag_{0.3}N$ compounds under dc magnetic fields of 10 mT and 5 T (only for Mn_4N) are plotted in

Fig. 2. Obviously, both curves under the field of 10 mT display similar behaviour. A broad peak occurs in the range from 5 to 300 K. However, the temperature dependence of magnetization under the field of 5 T represents no abnormal behaviour in the same temperature range. The isofield magnetizations of Mn_4N, or rather $Mn_{4-x}In_xN$ with $x = 0$ with a large magnetic field [15] resemble that of ours under the field of 5 T. Therefore, the round cusp should be ascribed to a spin reorientation.

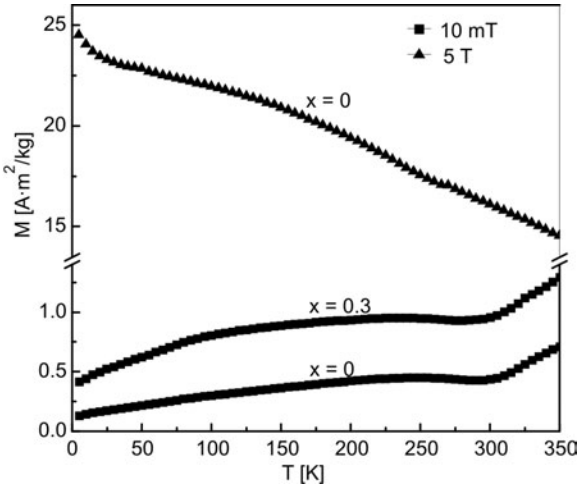

Fig. 2. Temperature dependences of magnetization of $Mn_{4-x}Ag_xN$ ($x = 0$, 0.3) measured in a dc magnetic field of 10 mT and 5 T

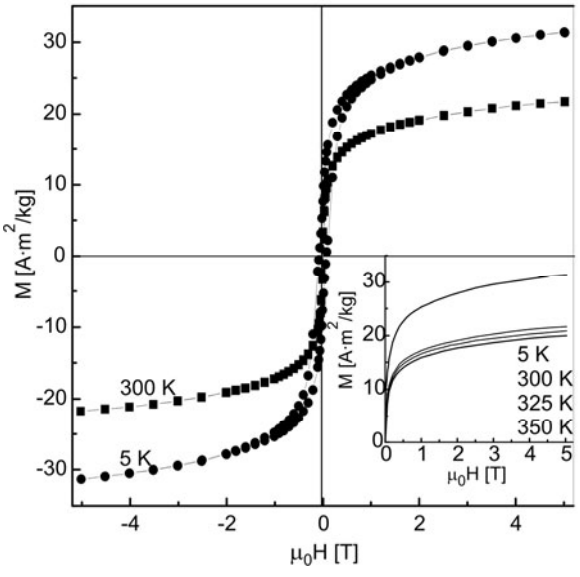

Fig. 3. Hysteresis loops of $Mn_{3.7}Ag_{0.3}N$ at 5 and 300 K. The inset shows the isothermal magnetization curves at different temperatures

The hysteresis loops of $Mn_{3.7}Ag_{0.3}N$ compounds at 5 and 300 K are shown in Fig. 3. Its inset gives isothermal magnetizations at various temperatures. Ferrimagnetic behaviour can be observed for this compound in the temperature range 5–350 K. It is well known that Mn_4N exhibits ferrimagnetism [6, 7]. Moreover, weakly Ag substituted Mn_4N compound can still display ferrimagnetism. Furthermore, as shown in Figs. 2 and 3, the saturation magnetizations at 5 K of Mn_4N and $Mn_{3.7}Ag_{0.3}N$ are 24.8 and 31.7 $A \cdot m^2/kg$.

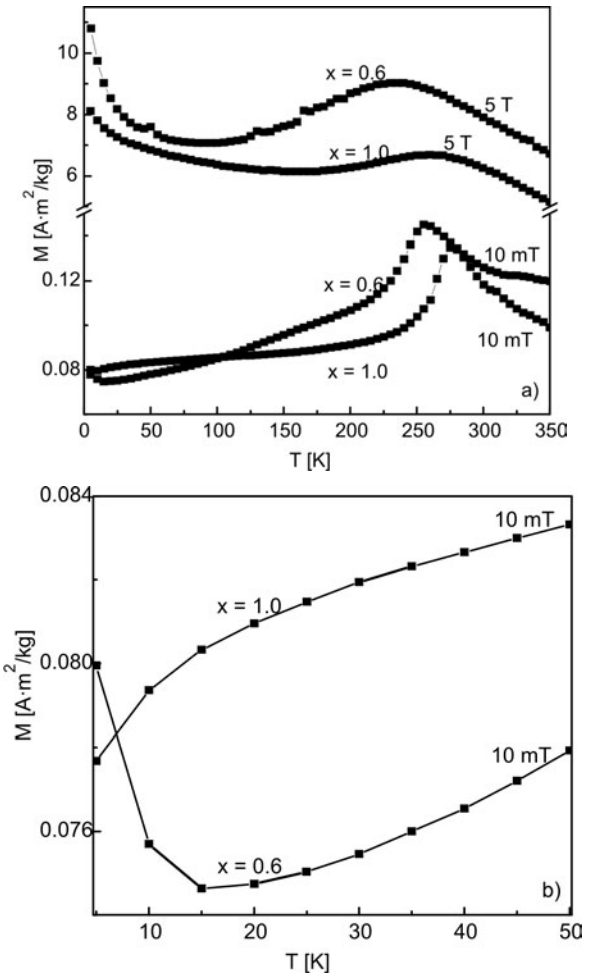

Fig. 4. Temperature dependences of magnetization of $Mn_{4-x}Ag_xN$ (x = 0.6, 1.0) measured in a dc magnetic field of 10 mT and 5 Tat a) 300 K, b) 5 K

Spin reorientation can be often observed in the Mn_3MN family (M = Ag, Ga, Ni, etc.) [10, 16, 17]. That is, the presence of weak ferromagnetism or triangular AFM is based on the symmetry of Γ_{4g} or Γ_{5g}, or their combined magnetic structures, i.e. rotation of triangular magnetic moment in the (111) crystal plane. During the rotation

process, the axis would change continuously in a wide temperature interval without changes in the magnitude of moments or in the lattice structure, and then spin reorientation occurs.

Temperature dependences of magnetization of $Mn_{3.4}Ag_{0.6}N$ and Mn_3AgN, under the dc magnetic field of 10 mT and 5 T, respectively, are plotted in Fig. 4a. The same dependences at low temperatures are shown in Fig. 4b. Under the field of 10 mT, the magnetic behaviour of Mn_3AgN is similar to that of $Mn_{3.4}Ag_{0.6}N$ above 20 K. That is, they display a cusp at 275 and 256 K, respectively. But below 20 K, the magnetization of $Mn_{3.4}Ag_{0.6}N$ becomes large again, while that of Mn_3AgN becomes continuously smaller. Under the field of 5 T, similar behaviours of both compounds can be distinctly observed throughout the whole temperature range, other than the rounder peaks (see the upper panel of Fig. 4a).

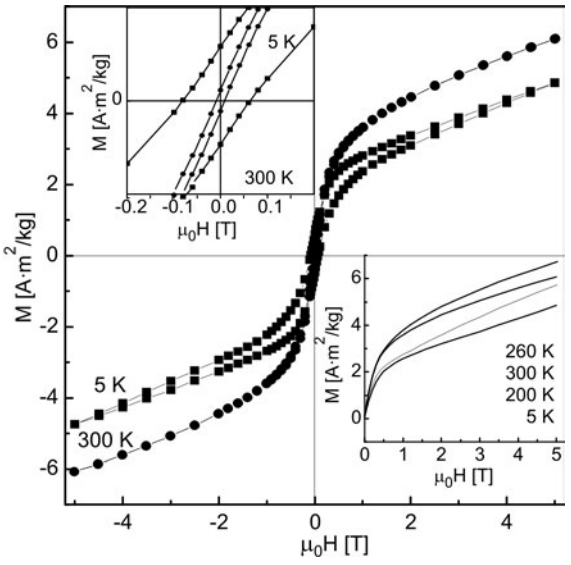

Fig. 5. Hysteresis loops of Mn_3AgN at 5 and 300 K. The top inset shows the hysteresis loops at 5 K and 300 K in a larger scale, while the bottom one isothermal magnetization curves at various temperatures

Fruchart et al. [9] reported that, for Mn_3AgN compounds, a combination of two triangular AFM structures, i.e. Γ^{4g} and Γ^{5g}, exists below 55 K, while an entirely triangular AFM Γ^{5g} structure exists between 55 and 290 K. This indicates that a magnetic change occurs at about 55 K. According to Gomonaj et al. [10] this magnetic transition should be from triangular AFM to FIM nc upon decreasing temperature. For $Mn_{3.4}Ag_{0.6}N$, below 20 K, the magnetization enhancement suggests the occurrence of the magnetic transition, essentially consistent with the findings in Refs. [9] and [10]. For Mn_3AgN under low field, the smaller magnetizations with decreasing temperatures seem to be associated with the enhancement of magneto-crystalline anisotropy which is evident as shown in the top inset of Fig. 5. Under a strong field, Mn_3AgN

displays the same behaviour as that of $Mn_{3.4}Ag_{0.6}N$ which reveals that both compounds should experience similar magnetic transitions. On the other hand, the peaks at 256 and 275 K, for the magnetizations of $Mn_{3.4}Ag_{0.6}N$ and Mn_3AgN, respectively, indicate that both the compounds exhibit different magnetisms below and above these temperatures.

The hysteresis loops of Mn_3AgN at 5 and 300 K are plotted in Fig. 5. Below 1 T, they both display ferrimagnetic-like behaviour, while AFM behaviour can be observed under a strong field, which is a common characteristic of Mn_3MN (M = Sn, Ag, Ni, et al.) [4, 10, 16]. The bottom inset represents the isothermal magnetizations of Mn_3AgN at various temperatures. As temperature increases, the magnetization becomes enhanced in the range from 5 to 260 K, and gets small again above 260 K, implying that the magnetic transition can occur at 260 K, corresponding to the observation of the isofield magnetizations. However, this magnetic transition seems to only relate to the comparative increase/decrease of the ferromagnetism component of Mn_3AgN.

Commonly, the triangular spin configuration per unit is composed of three spin vectors, with their respective angle of 120º. The triangle rotates opposite to the rotation of the field [18]. Moreover, the aforementioned triangular AFM is based on the symmetry of Γ_{4g} or Γ_{5g}, or their combined magnetic structures. When a strong magnetic field is exerted on this configuration, the three spins will be partially aligned along the direction of the field. Therefore, ferrimagnetic-like behaviour will gradually increase, based on the increasingly weakening magneto-crystalline anisotropy in function of increasing temperature. Finally, once the $M(T)$ curves achieve peak magnetization (i.e., those when a maximum vector sum is attained) under the 5T field, magnetization decreases with subsequent temperature increase. To some extent, this process is the magnetic transition from triangular AFM Γ^{5g} structure to ferrimagnetic-like one, but at a gradual pace. This argument can be used to explain the magnetic behaviour of $Mn_{3.4}Ag_{0.6}N$ and Mn_3AgN compounds above 200 K.

3.3. Transport properties

Temperature dependences of electrical resistivity of Mn_3AgN under the fields of 0 and 5 T, respectively, are shown in Fig. 6. Its inset shows the temperature dependence of magnetoresistance MR. It is noted that the electrical resistivity is rather large. Furthermore, a double minimum of resistivity occurs on the $\rho(T)$ curves. As is known, the compound experiences a magnetic transition from AFM to FIM n.c. at low temperatures. Based on the magnetic scattering mechanism, the electrical resistivity should become small, contrary to our observation. In fact, the spin-glass-like and ferrimagnetic phases of $Mn_{4-x}Ga_xN$ solid solution ($0.7 < x < 1$) [11] always coexist at low temperatures which arises from a complicated change of magnetic structures. We conjecture that the enhancement of electrical resistivity for Mn_3AgN at low temperatures is due to the presence of such disorder as spin glass or spin-glass-like phase.

Between 45 and 220 K (the temperature corresponding to the maximum electrical resistivity), the resistivity becomes enhanced with increasing temperature. In the same temperature range, the magnetization increases almost linearly, which is characteristic of triangular AFM. The increase of the resistivity reveals the enhancement of AFM. From 220 to about 350 K, the magnetic measurement reveals the gradual magnetic transition from triangular AFM Γ^{5g} structure to a ferrimagnetic-like one. Correspondingly, the resistivity exhibits the contrary process.

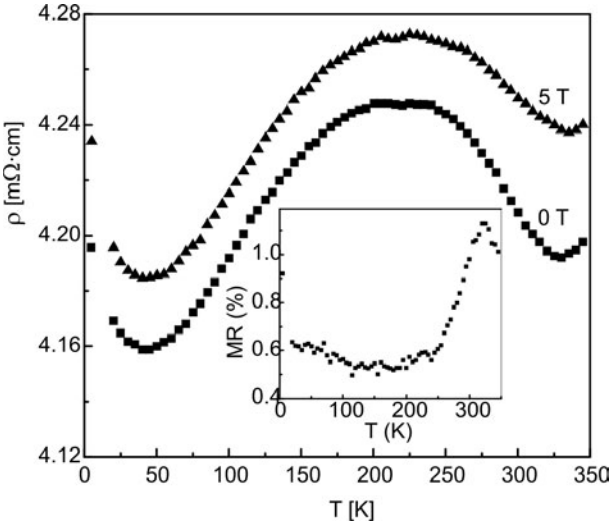

Fig. 6. Temperature dependences of electrical resistivity of Mn_3AgN at various fields. The inset represents temperature dependence of MR value, i.e. $(\rho(H) - \rho(0))/\rho(H)$, where $\rho(H)$ and $\rho(0)$ correspond to the electrical resistivities measured in dc magnetic fields of 5 T and 0 T, respectively

In terms of the above measured results, MR value can be determined, which is plotted in function of temperature in the inset of Fig. 6. The zero-field electrical resistivity curve is almost the same as that corresponding to a 5 T dc field. Furthermore, the latter is above the former in the whole temperature range, which means a positive MR value, with the maximum of 1.13%. Chi et al. [3] reported a positive MR value of $CuNMn_3$ in the whole temperature range, with the maximum of 4% at 150 K under the field of 5 T. According to Kim et al. [2], for $ZnNMn_3$ compound, the structure-induced magnetic transition can result in the increase/decrease of the electrical resistivity. That is, micro-cracks, generated from the irreversible radical lattice expansion can lead to the enhancement of resistivity and a positive MR value. Sun et al. [19] reported an anomalous, positive-valued MR in $Fe_{0.75}Mn_{1.35}As$. By combining the lattice expansion, confirmed by XRD measurement, with the magnetic measurements, they unambiguously revealed that micro-cracks resulting of radical lattice expansion are the dominant factor leading to positive MR. Our Mn_3AgN compound was prepared by milling and subsequently annealed at 823 K for 30 min. The presence of a broad XRD peak reveals that the homogenization is rather insufficient for removing the de-

fects such as dislocations, stacking faults, grain boundaries, etc., arising from the high-energy milling process. Therefore, it seems that the presence of a magnetic field is not the only factor leading to the positive MR value. The so-called magnetoresistance can also arise from other non-field contributions, such as micro-cracks.

4. Conclusions

By means of milling and subsequent annealing the mixture of $Mn_2N_{0.86}$, Mn, and Ag powders, $Mn_{4-x}Ag_xN$ (x = 0.0, 0.3, 0.6, 1.0) compounds were successfully prepared. All samples exhibit single-phase compounds. Mn_4N and $Mn_{3.7}Ag_{0.3}N$ display ferrimagnetism. Partial Ag replacement of Mn can promote the saturation magnetization. For $Mn_{3.4}Ag_{0.6}N$ and Mn_3AgN compounds, the magnetic transition below 15 K is from AFM to FIM n.c. with lowering temperature. The magnetic transitions at 256 and 275 K, respectively, can be ascribed to the gradual transition from triangular AFM Γ^{5g} structure to ferrimagnetic-like one. Two minima occur on the curves of temperature dependences of electrical resistivity which can be clearly interpreted by the magnetic scattering mechanism. Positive magnetoresistance can be observed in the whole temperature range, with the maximum of 1.13%.

Acknowledgements

This work has been supported by the National Natural Science Foundation of China under Grant No. 50331030, and by the Liaoning Province Science Foundation of China under Grant No. 20070556.

References

[1] BOUCHAUD J.P., Ann. Chim., 3 (1968), 81.
[2] KIM W.S., CHI E.O., HUR N.H., LEE K.W., CHOI Y.N., Phys. Rev. B, 68 (2003), 172402.
[3] CHI E.O., KIM W.S., HUR N.H., Solid State Commun., 120 (2001), 307.
[4] FENG W.J., LI D., REN W.J., LI Y.B., LI W.F., LI J., ZHANG Y.Q., ZHANG Z.D., J. Alloy. Compd., 437 (2007), 27.
[5] MAH A.D., J. Am. Chem. Soc., 80 (1958), 2954.
[6] TAKEI W.J., SHIRANE G., FRAZER B.C., Phys. Rev., 119(1) (1960), 122.
[7] TAKEI W.J., HEIKES R.R., SHIRANE G., Phys. Rev., 125(6) (1962), 1893.
[8] VEMPAIRE D., FRUCHART D., GOUTTEBARRON R., HLIL E.K., MIRAGLIA S., ORTEGA L., PELLETIER J., Physica A, 358 (2005), 136.
[9] FRUCHART D., BERTAUT E.F., J. Phys. Soc. Jpn., 44(3) (1978), 781.
[10] GOMONAJ E.V., L'VOV V.A., Phase Trans., 40 (1992), 225.
[11] NAVARRO R., ROJO J.A., GARCÍA J.J., GONZÁLEZ D., BARTOLOMÉ J., L'HERITIER PH., J. Magn. Magn. Mater., 59 (1986), 221.
[12] TAKENAKA K., TAKAGI H., Appl. Phys. Lett., 87 (2005), 261902.
[13] TAKENAKA K., TAKAGI H., Mater. Trans., 47 (3) (2006), 471.
[14] FENG W.J., SUN N.K., GAO M., ZHANG Q., DENG Y.F., ZHANG Z.D., Physical B, in press.
[15] MEKATA M., J. Phys. Soc. Jpn., 17 (1962), 796.

[16] GOMONAJ E.V., Phase Trans., 18 (1989), 93.
[17] GOMONAJ E.V., L' VOV V.A., Phase Trans., 38 (1992), 15.
[18] TOMIYOSHI S., YAMAGUCHI Y., J. Phys. Soc. Jpn. 51,(1982), 2478.
[19] SUN N.K., LI Y.B., LI D., ZHANG Q., FENG W.J., ZHANG Z.D., Phys. Rev. B 74 (2006), 172402.

Received 15 October 2007
Revised 19 December 2008

Materials Science-Poland, *Vol. 27*, *No. 1*, *2009*

Characterization of nanocrystalline $LiNi_{1-x}Co_xVO_4$ prepared by the polymerized complex method

T. THONGTEM[1*], A. PHURUANGRAT[2], S. THONGTEM[2]

[1]PERCH-CIC, Department of Chemistry, Faculty of Science, Chiang Mai University, Chiang Mai 50200, Thailand

[2]Department of Physics, Faculty of Science, Chiang Mai University, Chiang Mai 50200, Thailand

Nanocrystalline $LiNi_{1-x}Co_xVO_4$ (x = 0.00, 0.25, 0.50, 0.75 and 1.00) was prepared from Li_2CO_3, $Ni(NO_3)_2.6H_2O$, $Co(NO_3)_2.6H_2O$ and NH_4VO_3, using tartaric acid as a complexing agent, followed by 450 °C calcination for 12 h. TGA results show that nanocrystallites started to form at 450–550 °C. Inverse spinel $LiNi_{1-x}Co_xVO_4$ was detected using the XRD and SAED methods. The calculated lattice parameter increased upon increasing Co concentration. It was in accordance with the increase in the particle size determined using TEM images. A stretching band of VO_4 tetrahedra was detected at 651–820 cm^{-1} using FTIR. V–O vibrational bands analyzed with a Raman spectrometer were shifted to the lower wavenumbers, due to the increase of Co concentration. The selected elements were also analyzed using EDX and AAS to determine the stoichiometric values (x) of the oxides.

Key words: *nanocrystalline $LiNi_{1-x}Co_xVO_4$; polymerized complex method; tartaric acid*

1. Introduction

Lithium transition metal oxides are appropriate for use as cathode materials in Li ion batteries. To improve their electrochemical properties, cathode materials containing a variety of transition metal oxides have been developed and investigated. Among transition metal oxides with inverse spinel structures, $LiNiVO_4$, $LiNi_{0.5}Co_{0.5}VO_4$ and $LiCoVO_4$ can perform very well even at voltages as high as 4.3–4.8 V [1–4]. Currently, nanocrystals are found to exhibit novel properties by decreasing the electron path length, promoting the tunneling property of electrons, and increasing the specific surface area [5]. For the present research, nanocrystalline $LiNi_{1-x}Co_xVO_4$ was prepared by the polymerized complex method, using tartaric acid as a complexing agent, and analyzed to specify phase, morphology and other features.

[*]Corresponding author, e-mail: ttpthongtem@yahoo.com; ttpthongtem@hotmail.com

2. Experimental

Li_2CO_3, $Ni(NO_3)_2{\cdot}6H_2O$, $Co(NO_3)_2{\cdot}6H_2O$ and NH_4VO_3 were separately dissolved in water and then mixed together. pH of 5 was adjusted using HNO_3. Then tartaric acid was added. The solution was stirred at 80 °C until it became a gel consisting of tartaric complexes of the metal ions (precursors). The gel was dried at 80 °C for 12 h and calcined at 450 °C for 12 h to form powder. The final products were analyzed by the TGA at the heating rate of 20 °C/min in ambient atmosphere, XRD operated at 20 kV, 15 mA and using the K_α radiation from a Cu target, TEM as well as SAED operated at 200 kV, EDX operated at 15 kV, AAS to determine Li, Ni and Co atomic percents, FTIR with KBr as a diluting agent and operated in the range 400–4000 cm^{-1}, and a Raman spectrometer using 50 mW Ar laser with $\lambda = 514.5$ nm.

3. Results and discussion

3.1. TGA curves

Pure tartaric acid and non-calcined precursors were analyzed using TGA (Fig. 1). The curves for the different stoichiometric values (x) are very similar, showing that

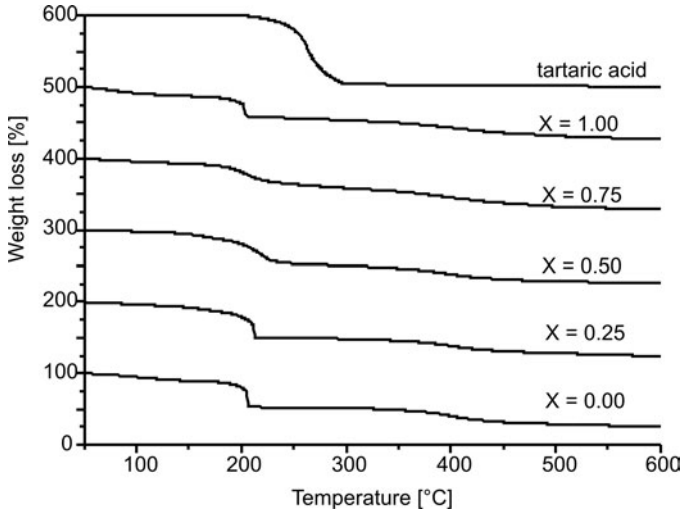

Fig. 1. TGA curves of pure tartaric acid and non-calcined precursors for $LiNi_{1-x}Co_xVO_4$

weight losses were controlled by the same processes. Their weight losses were divided into four stages over the temperature range 50–550 °C. They are the evaporation of adsorbed and lattice water at 50–200 °C, the decomposition of residual tartaric acid at 200–290 °C (compared with pure tartaric acid), and the decomposition and combustion of residual starting agents and other organic compounds at 290–450 °C. At

450–550 °C, the weights are almost constant and different atoms are arranged in a particular order or positions to form crystalline oxides.

3.2. XRD spectra

XRD spectra of the oxides are shown in Fig 2. At x = 0.00 and 1.00, they correspond to those of the JCPDS standard for $LiNiVO_4$ (38–1395) and $LiCoVO_4$ (38–1396), respectively [6]. At x = 0.25, 0.50 and 0.75, the spectra are similar to those of their pure oxides (x = 0.00 and 1.00) specified as the solid solution (mixture) of $LiNiVO_4$ and $LiCoVO_4$ [1, 3, 4].

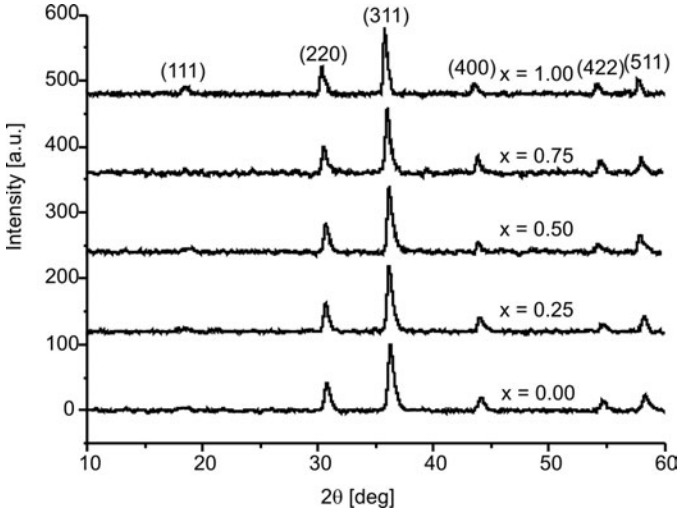

Fig. 2. XRD spectra of $LiNi_{1-x}Co_xVO_4$

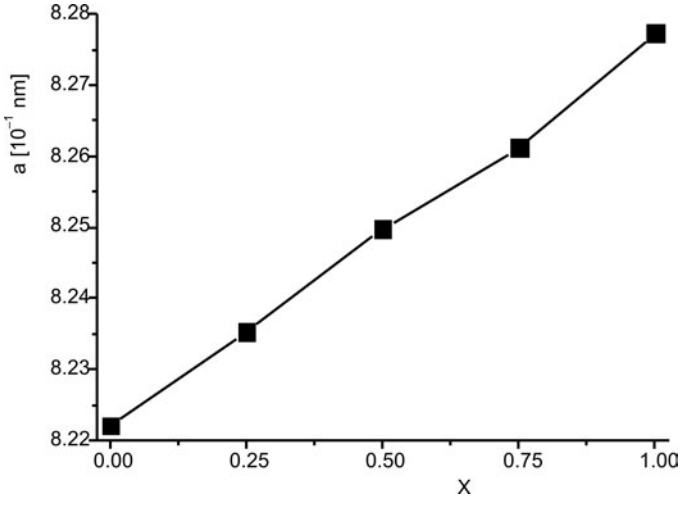

Fig. 3. Cubic lattice parameter (a) vs. stoichiometric values (x)

$LiNi_{1-x}Co_xVO_4$ (x = 0.00, 0.25, 0.50, 0.75 and 1.00) forms a single phase with inverse spinel structure identified by (111) and (220) peaks of weak and strong intensities, respectively [2, 7]. For inverse spinel structure, Li and M (M = Ni and Co) atoms equally occupy octahedral sites at random, and V atoms are in tetrahedrally coordinated 8a sites [2, 4, 7]. The cubic lattice parameter (a) of $LiNi_{1-x}Co_xVO_4$ was calculated (Fig. 3) [8]. It was monotonically increased with the increase in stoichiometric value x. At x = 0.00 and 1.00, the lattice parameters are respectively 0.8222 nm and 0.8278 nm which are very close to the values shown in the JCPDS standard (0.8220 nm for $LiNiVO_4$ and 0.8279 nm for $LiCoVO_4$) [6].

3.3. FTIR and Raman analyses

FTIR spectra of $LiNi_{1-x}Co_xVO_4$ (Fig 4) show a stretching band of VO_4 tetrahedra at 651–820 cm^{-1}. It splits into three bands (651, 722 and 820 cm^{-1}) characterized as the inverse spinel structure [4, 9–11]. The splitting extent becomes lesser when the stoichiometric values are larger, and no longer exists at x = 1.00. An asymmetric stretching band of MO_6 (M = Ni and Co) octahedrons was detected at 1136 cm^{-1} [10]. At x = 0.00 and 1.00, they are the stretching bands of Ni–O and Co–O, respectively.

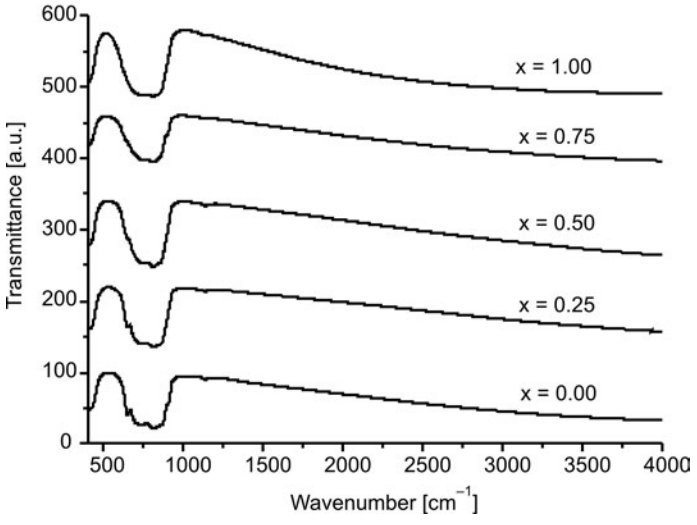

Fig. 4. FTIR spectra of $LiNi_{1-x}Co_xVO_4$

Raman spectra of $LiNi_{1-x}Co_xVO_4$ (Fig. 5) show bands of the stretching (A_{1g} symmetry) and bending (E_g symmetry) V–O modes in VO_4 tetrahedra [3, 4]. The stretching and bending modes were respectively detected at 811 and 327 cm^{-1} for $LiNiVO_4$, and at 803 and 304 cm^{-1} for $LiCoVO_4$ [3, 4]. The bands of $LiNiVO_4$ appear at higher wavenumbers than those of $LiCoVO_4$. The stretching and bending bands of $LiNi_{0.75}Co_{0.25}VO_4$, $LiNi_{0.50}Co_{0.50}VO_4$ and $LiNi_{0.25}Co_{0.75}VO_4$ are between those of

$LiNiVO_4$ and $LiCoVO_4$. The substitution of Ni in $LiNiVO_4$ by Co makes the vibration bands of all metal–oxygen in the solid solution weaker by shifting the bands from high to low wavenumbers [3].

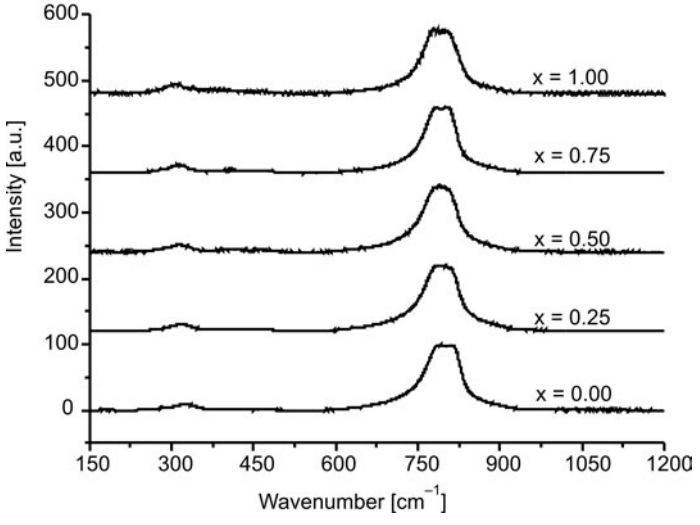

Fig. 5. Raman spectra of $LiNi_{1-x}Co_xVO_4$

3.4. TEM and SAED

TEM images and SAED patterns of $LiNiVO_4$, $LiNi_{0.50}Co_{0.50}VO_4$ and $LiCoVO_4$ are shown in Fig 6. The oxides are composed of rather round particles with dimensions of 19, 60 and 98 nm, respectively. The average particle sizes are increased with the

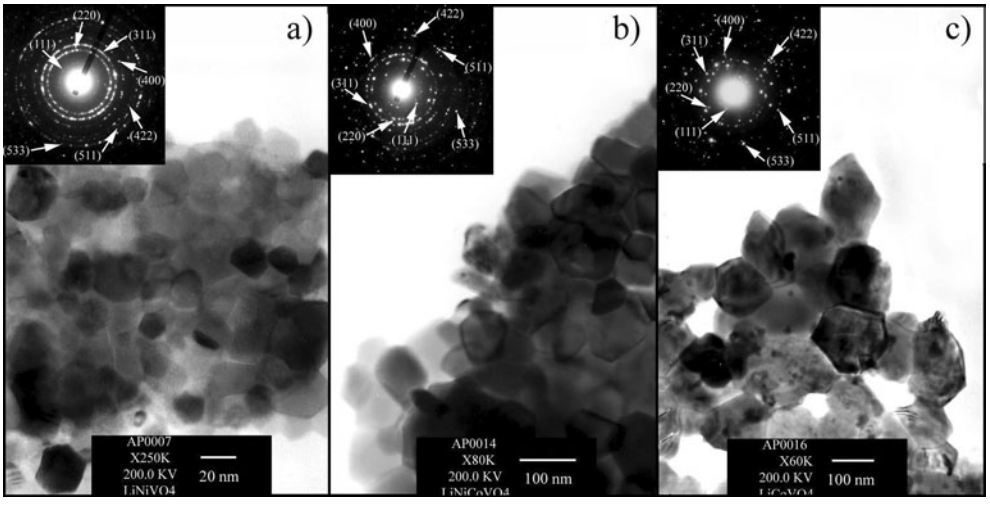

Fig. 6. TEM images and SAED patterns of: a) $LiNiVO_4$, b) $LiNi_{0.50}Co_{0.50}VO_4$, and c) $LiCoVO_4$

increase of Co concentration corresponding to the increase of the lattice parameter. SAED patterns show a number of bright spots arranged in concentric rings. They diffract from the crystallographic planes of the unit cells of the oxides. The calculated interplanar spaces (*d*) [12] of the SAED patterns in Fig. 6a and 6c are in accordance with those of the JCPDS standard of $LiNiVO_4$ and $LiCoVO_4$, respectively [6]. The diffraction planes are (111), (220), (311), (400), (422), (511) and (533). The *d* values of the SAED pattern in Fig 6b correspond to those of pure oxides (x = 0.00 and 1.00) showing that $LiNi_{0.50}Co_{0.50}VO_4$ is the solid solution of $LiNiVO_4$ and $LiCoVO_4$ [1, 3, 4].

3.5. EDX and AAS

Li is too light to be detected using the EDX. At x = 0.00, only Ni, V and O were detected. Additional Co was detected at x = 0.25, 0.50 and 0.75. The results are in accordance with those of using both Ni and Co salts as the starting agents. At x = 1.00, only Co, V and O were detected. To determine the atomic percentages of Li, Ni and Co, the oxides were analyzed using AAS. The stoichiometric values are very close to those of the expected oxides (Table 1).

Table 1. Formulas from expectation and AAS

Expected formula	Formula from AAS
$LiNiVO_4$	$Li_{1.045}Ni_{1.087}VO_4$
$LiNi_{0.75}Co_{0.25}VO_4$	$Li_{1.012}Ni_{0.779}Co_{0.263}VO_4$
$LiNi_{0.50}Co_{0.50}VO_4$	$Li_{1.025}Ni_{0.523}Co_{0.533}VO_4$
$LiNi_{0.25}Co_{0.75}VO_4$	$Li_{1.023}Ni_{0.266}Co_{0.777}VO_4$
$LiCoVO_4$	$Li_{1.034}Co_{1.065}VO_4$

4. Conclusions

Nanocrystalline $LiNi_{1-x}Co_xVO_4$ was successfully prepared by the polymerized complex method using tartaric acid as a complexing agent, with the subsequent calcination at 450 °C for 12 h. TGA shows that the oxides started to form at 450–550 °C. By using XRD, TEM, SAED, FTIR and Raman analyses, nanocrystalline $LiNi_{1-x}Co_xVO_4$ with inverse spinel structure was detected. The calculated lattice parameter and particle size were increased with the increase of the Co concentration. The vibration bands analyzed by a Raman spectrometer were also shifted to the lower wavenumbers. With the exception of Li, the elements contained in the oxides were detected using EDX. The atomic percentages of Li, Ni and Co analyzed using AAS are very close to the expected values.

Acknowledgements

The research was supported by PERCH-CIC, Department of Chemistry, Faculty of Science, Chiang Mai University, National Research Council of Thailand, and NANOTEC, a member of NSTDA, Ministry of Science and Technology, Thailand.

References

[1] VIVEKANANDHAN S., VENKATESWARLU M., SATYANARAYANA N., Mater. Chem. Phys., 91 (2005), 54.
[2] CHEN W., MAI L.Q., XU Q., ZHU Q.Y., YANG H.P., Mater. Sci. Eng., B 100 (2003), 221.
[3] FEY G.T.K., HUANG D.L., Electrochim. Acta, 45 (1999), 295.
[4] JULIEN C., MASSOT M., PÉREZ-VICENTE C., Mater. Sci. Eng., B 75 (2000), 6.
[5] PRABAHARAN S.R.S., MICHAEL M.S., IKUTA H., UCHIMOTO Y., WAKIHARA M., Solid State Ion., 172 (2004), 39.
[6] Powder Diffract. File, JCPDS Int. Centre Diffract. Data, PA 19073–3273, U.S.A., 2001.
[7] KALYANI P., KALAISELVI N., MUNIYANDI N., Mater. Chem. Phys., 77 (2002), 662.
[8] SURYANARAYANA C., NORTON M.G., *X-Ray Diffraction*, Plenum Press, New York, 1998.
[9] BHUVANESWARI M.S., SELVASEKARAPANDIAN S., KAMISHIMA O., KAWAMURA J., HATTORI T., J. Power Source, 139 (2005), 279.
[10] LAI Q.Y., LU J.Z., LIANG X.L., YAN F.Y., JI X.Y., Inter. J. Inorg. Mater., 3 (2001), 381.
[11] LIU J.R., WANG M., LIN X., YIN D.C., HUANG W.D., J. Power Source, 108 (2002), 113.
[12] ANDREWS K.W., DYSON D.J., KEOWN S.R., *Interpretation of Electron Diffraction Patterns*, Plenum Press, New York, 1971.

Received 19 October 2007
Revised 14 October 2007

Materials Science-Poland, *Vol. 27*, *No. 1*, *2009*

The effect of Cr, Co, W, Zr and Pb (M) substitution on the structure and corrosion resistance of nanocrystalline $Nd_{10}Fe_{84-x}M_xB_6$ magnets

G. PAWŁOWSKA[1], W. KASZUWARA[2*], H. BALA[1]

[1]Częstochowa University of Technology, Faculty of Materials Processing Technology and Applied Physics, Department of Chemistry, Al. Armii Krajowej 19, 42-200 Częstochowa, Poland

[2]Warsaw University of Technology, Faculty of Materials Science and Engineering, ul. Wołoska 141, 02-507 Warsaw, Poland

The effect of partial substitution of iron with Cr, Co, W, Zr or Pb in nanocrystalline $Nd_{10}Fe_{84-x}M_xB_6$ magnetic material on general corrosion in acidified sulphate environment is discussed in the paper. The materials were produced from spec pure powders of Nd, Fe, Fe–B and additive powders (Cr, Co, W, Zr or Pb) by mechanical alloying. The structural analysis was performed using a JEOL JEM 1200 TEM microscope and the stereological parameters of the microstructures were determined. The magnetic properties were measured with a pulse field hysteresigraph. The following substitutions are the most favourable in terms of the magnetic properties of nanocrystalline $Nd_{10}Fe_{84-x}M_xB_6$ magnets: cobalt (10 at. %), chromium (4 at. %), tungsten (15 at. %), lead (1.5 at. %) and zirconium (2 at. %). The samples for corrosion investigations were prepared from annealed powders by shock compaction. For electrochemical tests, electrodes made from the samples in the form of rotating discs were used. Resistance to general corrosion of the tested materials was evaluated by potentiokinetic polarisation tests. It was shown that the applied additions inhibit the corrosion process by up to 2–3 times. Chromium, cobalt and lead additives facilitate passivation of the alloys.

Key words: *corrosion; passivation; permanent magnets; nanocrystalline materials*

1. Introduction

Partial substitution, either of neodymium with other lanthanides or of iron with other transition metals, appeared to be an effective method of modifying magnetic properties of Nd–Fe–B-type magnets. A systematic classification of the elements that can substitute Fe in Nd–Fe–B magnets with more than 11.9 at. % of Nd was put forward by Fidler [1, 2]. The additives can be classified into those that dissolve in the $Nd_2Fe_{14}B$ ferromagnetic phase and those that occur in the form of inclusions. Among

*Corresponding author, e-mail: wkaszu@inmat.pw.edu.pl

the latter group of elements, one can distinguish two types of additives: (i) additives forming new phases within the grain boundary area and dissolving in the Nd-rich eutectic thereby lowering the melting temperature and (ii) additives occurring in the form of inclusions enriched with Fe or B. Although Fidler's classification is valid for high-neodymium alloys, there is, however, strong evidence that this classification can also be used for nanostructured, low neodymium magnets [3, 4]. The magnetic properties of these materials can depend on: (i) intrinsic properties of the hard magnetic phase, (ii) grain size, (iii) interaction between the domain walls and the inclusions, (iv) change of the phase composition. Some of these factors and features strongly affect the corrosion resistance [5].

In modified sintered Nd–Fe–B-type magnets, iron is usually partially substituted by other transition metals. Their alloy contents may amount to 1–20 at. %. Small additions of chromium [6, 7] and large additions of cobalt [8] are considered to be the most favourable in enhancing the corrosion resistance of the sintered material.

The corrosion behaviour of a material is influenced both by its phase structure and by its grain size. In nanocrystalline materials, the order of magnitude of the grain size is in the 10–20 nm range, and the phase structure is different from that in sintered materials. In general, nanocrystalline materials exhibit higher corrosion resistance [9–11]. Alloy additives in nanomaterials may thus have an essentially different effect on corrosion processes than in the case of sintered materials. Within the present study, the effect of partial substitution of iron with such elements as Cr, Co, W, Zr and Pb on the corrosion behaviour of $Nd_{10}Fe_{84-x}M_xB_6$ nanocrystalline materials in acidified sulphate solutions was investigated.

2. Experimental

Nanocrystalline $Nd_{10}Fe_{84-x}M_xB_6$ materials (M = Cr, Co, W, Zr or Pb; the values of x were chosen in terms of optimum magnetic properties, Table 1) were tested. The materials were produced from spec pure powders of Nd, Fe, Fe-B and additive powders (Cr, Co, W, Zr or Pb) by mechanical alloying (MA). The mixture of the powders was milled in a high energy ball mill in a protective argon atmosphere for 90 h. The powders thus obtained, composed of an amorphous phase and Fe crystallites, were annealed in vacuum of 10^{-3} Pa at the temperature of 650 °C for 0.5 h. The magnetic properties were measured with a pulse field hysteresigraph, using the field of 4 T. The samples for investigations of corrosion were prepared from annealed powders by shock compaction. The details of the compacting systems are described in [12]. In our experiments, we used a two-stage process that included preliminary and final compaction carried out at detonation wave speeds of 3800 and 5240 m/s, respectively. The structural analysis was performed using a JEOL JEM 1200 TEM microscope and the stereological parameters of the microstructures were determined. For electrochemical tests, electrodes made from the above-mentioned samples in the form of rotating discs with an operating surface area of 0.1 cm^2 were used.

Table 1. Effect of the iron substitution in $Nd_{10}Fe_{84-x}M_xB_6$ (M = Cr, Co, W, Zr or Pb) nanocrystalline material on coercivity (H_c) and remanence (B_r)

Substitution	Coercivity H_c [kOe]	Remanence B_r [T]
–	2.90	0.83
1 at. % Cr	2.67	0.50
4 at. % Cr	3.65	0.61
7 at. % Cr	2.87	0.57
5 at. % Co	3.95	0.83
10 at. % Co	4.53	0.88
20 at. % Co	3.22	0.86
2 at. % W	3.48	0.74
15 at. % W	6.79	0.47
28 at. % W	10.78	0.22
2 at. % Zr	4.30	0.69
5 at. % Zr	4.17	0.98
0.5 at. % Pb	2.87	0.68
1.5 at. % Pb	2.11	0.70
3 at. % Pb	0.82	0.67

The resistance to general corrosion of the tested materials was evaluated by potentiokinetic polarisation tests. Polarisation measurements were carried out in deaerated (argon saturated) acidified sulphate solutions (pH = 3.0) at the temperature of 25 °C, at the disc rotation speed of 16 rps and at the potential scanning rate of 10 mV/s. A CHI 680 potentiostat (CH Instruments, Austin, Texas, USA) was used to record potentiokinetic polarisation curves. The values of electrode potentials were measured with respect to a saturated calomel electrode (SCE).

3. Results and discussion

The effect of the M = Cr, Co, W, Zr or Pb additives on the magnetic properties (coercivity and remanence) of nanocrystalline $Nd_{10}Fe_{84-x}M_xB_6$ magnets has been described in our earlier papers [3, 4, 13]. Co is the most frequently used substituent, which substitutes Fe in the $Nd_2Fe_{14}B$ phase. Zr, Cr, and W are substituents of type II, whereas Pb is a substituent of type I [1, 3, 4, 13]. The experiments with the Nd–Fe–Co–B magnets processed by mechanical alloying (MA) show that an addition of Co improves both the remanence and coercivity [13]. This improvement is due to the reduction of the grain size, which enhances magnetic exchange interactions. The TEM observations were performed with the $Nd_{10}Fe_{84}B_6$ and $Nd_{10}Fe_{64}Co_{20}B_6$ magnets (Figs. 1a, c). Although the microstructure was heterogeneous (larger and smaller grains), the substitution of 20 at. % Fe with Co results, in general, in the reduction of

the mean equivalent diameter from 18.9 nm in the Co-free magnets to 7.9 nm in the Co-enriched material [4]. The effect of tungsten content has been described in [3].

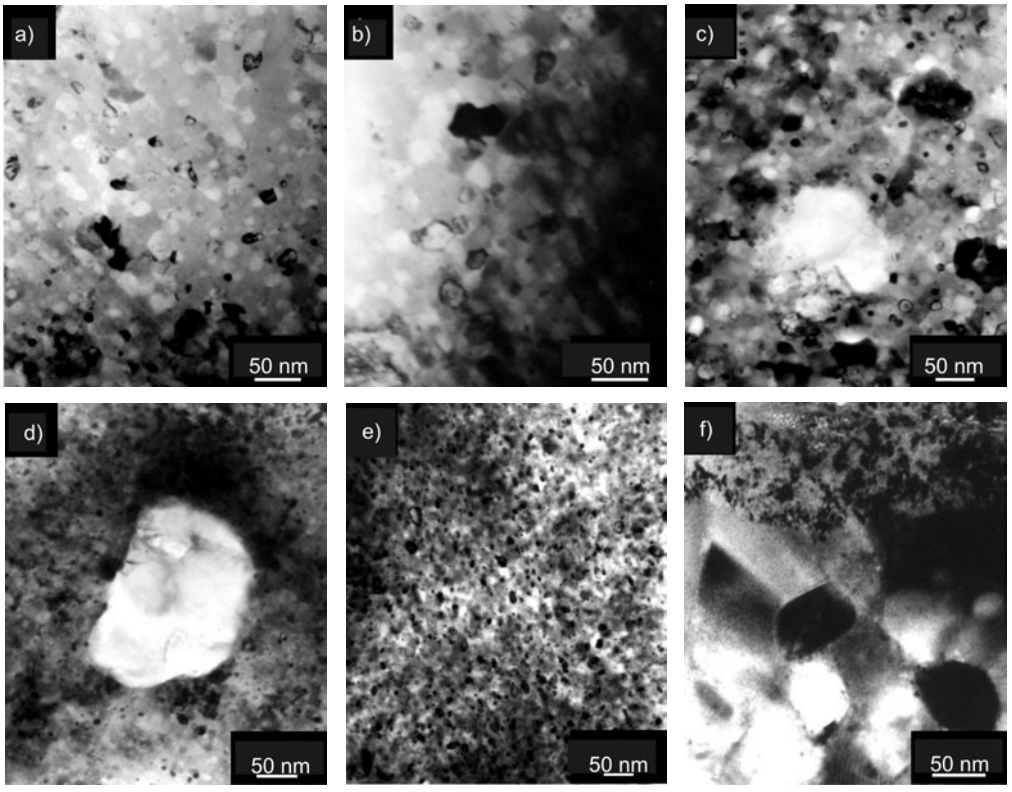

Fig. 1. TEM images of shock compacted samples with optimal magnetic properties: a) $Nd_{10}Fe_{84}B_6$, b) $Nd_{10}Fe_{80}Cr_4B_6$, c) $Nd_{10}Fe_{64}Co_{20}B_6$, d) $Nd_{10}Fe_{56}W_{28}B_6$, e) $Nd_{10}Fe_{79}Zr_5B_6$, f) $Nd_{10}Fe_{82}Pb_{1,5}B_6$

It was found that the addition of W leads to a substantial increase in the coercivity and a decrease in the remanence. An X-ray phase analysis showed that the material annealed at 650 °C contained practically pure W inclusions (magnets annealed at 850 °C contained the FeWB phase). The mean equivalent grain diameter in the magnets containing 28 at. % W was 10.2 nm and was smaller than that in the W free material which was 18.9 nm (compare Figs. 1a and d). An addition of Cr [4] results in the formation of Fe containing inclusions, and a decrease in the mean equivalent grain size diameter (in the $Nd_{10}Fe_{80}Cr_4B_6$ magnet, its measured value was 13.9 nm). However, the TEM studies also revealed the presence of large precipitates, testifying that Cr reacted with the basic alloying elements (Fig. 1b). A similar microstructure was observed in the microcrystalline magnets with a Zr content [4]. The Zr addition results in a strong reduction of the grain size and the effect is more distinct than that observed with Cr, Co and W. The mean equivalent diameter in the $Nd_{10}Fe_{79}Zr_5B_6$ magnets was as small as 7.2 nm. As with the magnets containing Cr, the magnets with Zr additive

contain large Zr-rich inclusions (above 50 nm in size, Fig. 1e). TEM observations of the material with Pb additive confirm that a new phase component has appeared (Fig. 1f). Fine grain areas occur together with a typical 80 nm grain structure. The microstructure evidently contains the Nd_5Pb_3 or Nd_2Pb phase, probably formed as a result of decomposition of the hard magnetic phase, and, thus, it also contains small Fe crystals [4]. The fine grain areas were about 100 nm wide. The addition of Pb increases the mean equivalent diameter (for the magnet with 1.5 at. % Pb it was evaluated to be 81.6 nm).

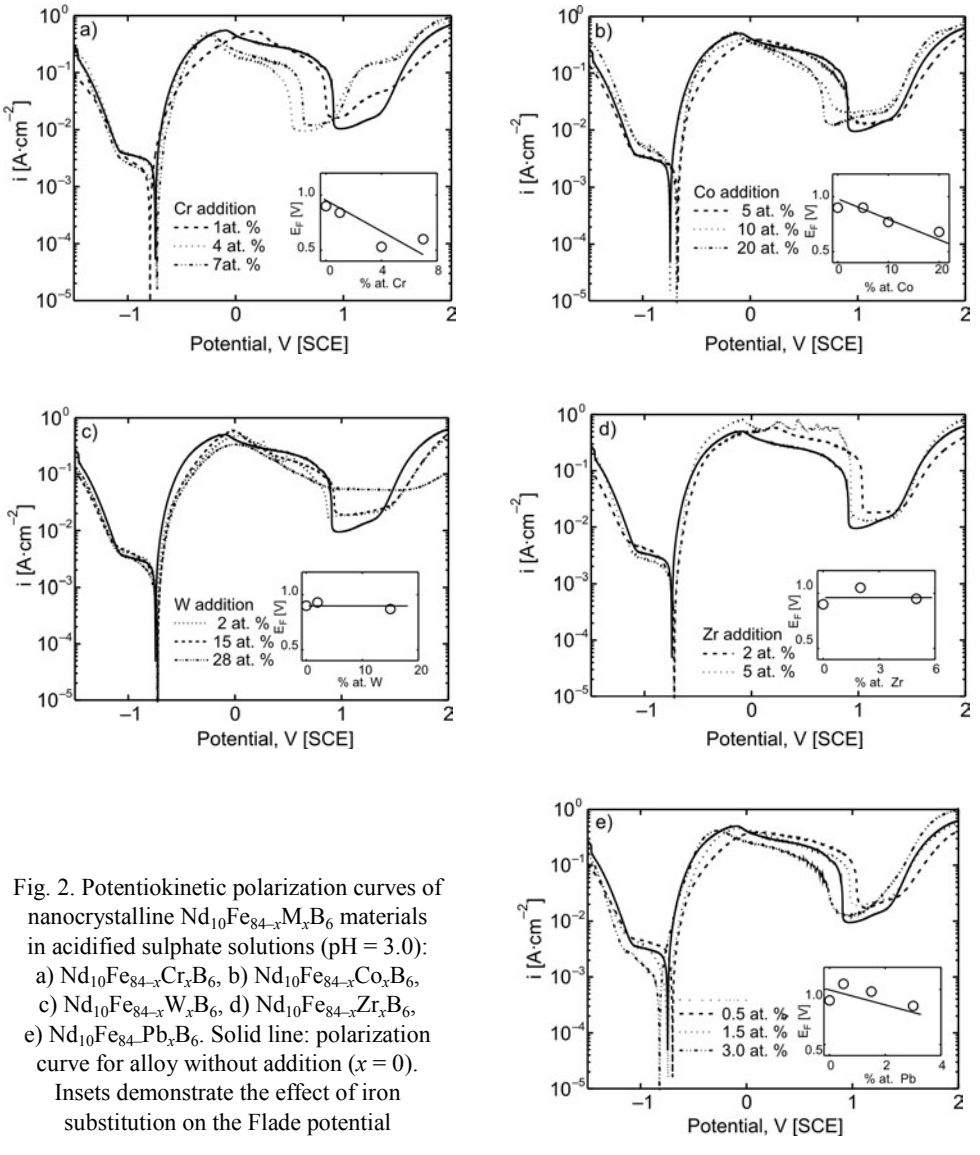

Fig. 2. Potentiokinetic polarization curves of nanocrystalline $Nd_{10}Fe_{84-x}M_xB_6$ materials in acidified sulphate solutions (pH = 3.0): a) $Nd_{10}Fe_{84-x}Cr_xB_6$, b) $Nd_{10}Fe_{84-x}Co_xB_6$, c) $Nd_{10}Fe_{84-x}W_xB_6$, d) $Nd_{10}Fe_{84-x}Zr_xB_6$, e) $Nd_{10}Fe_{84-}Pb_xB_6$. Solid line: polarization curve for alloy without addition ($x = 0$). Insets demonstrate the effect of iron substitution on the Flade potential

In strongly acidic sulphate environments (pH = 0.3), where the corrosion behaviour of Nd–Fe–B-type sintered materials results from the electrochemical activity of rare earth metals, no major differences in the corrosion behaviour of Nd-(Fe,M)-B materials were established [6], therefore a less aggressive environment was chosen for corrosion tests within the present study. In medium acid solutions the mass loss of specimens is smaller, while the differences in the shape of the polarization curves are more distinct. The electrochemical tests were carried out in acidified sulphate solutions with pH = 3.0, due to, among others, a good repeatability of polarization curves and small changes in pH at the corroding surface during the experiment [6]. The sulphate solution of pH = 3.0 is, for the specimens tested, an environment, where the corrosion is controlled by diffusion (H^+ ion reduction current in the potential range from –1.2 to –0.8 V at the electrode rotation speed of 16 rps takes on the form of a limiting current with the density of 2–3 $mA \cdot cm^{-2}$). In this environment, the materials tested exhibit a tendency to passivation, being dependent on the type and amount of the additive in the material. The most significant tendency to passivation is observed for the addition of chromium (Fig. 2). Figure 2a shows that the addition of 1 at. % of Cr does not considerably affect the shape of the curves. On the other hand, the additions of 4 and 7 at. % of Cr shift the Flade potential (the potential of transition into a passive state, E_F) of $Nd_{10}Fe_{84-x}Cr_xB_6$ material to a more negative value. This potential is 0.90 V for the specimen with no addition of Cr and 0.52 V (SCE) for the specimen containing 4 at. % Cr (compare the inset in Fig. 2a). Although Cr addition facilitates passivation, the width of the passive range for alloys containing 4 and 7 at. % Cr decreases due to the transpassive dissolution of Cr for $E > 1.0$ V ($2Cr + 7H_2O - 12e \rightarrow Cr_2O_7^{2-} + 14\ H^+$). The beneficial effect of Co is visible for the additions of 10 and 20 at. % (Fig. 2b). Although pure Co and RE-Co alloys do not passivate in either acid or neutral environments [14, 15], the increase in Co content facilitates the transition into the passive state of the nanocrystalline materials tested, similarly as it was in the case of sintered materials [8]. As can be seen from Fig. 2c, tungsten additions of up to 15 at. % have little effect on the corrosion behaviour of the Nd–(Fe,W)–B material. The additions up to 15 at. % W practically do not affect the value of E_F and only slightly increase (from 0.01 to 0.02 $A \cdot cm^{-2}$) the value of the minimum current in the passive region. However, further increase in the tungsten content to 28 at. % unexpectedly decreases the material tendency to passivation: the transition into the passive state becomes poorly pronounced for this material, and the minimum current densities in the potential range from 1.0 to 1.5 V are comparatively high (0.05 $A \cdot cm^{-2}$). The additions of 2–5 at. % of Zr slightly worsen the tendency to passivate the material (Fig. 2d) similarly as small additions of Pb (Fig. 2e). A greater amount of Pb in the alloy (3 at. % Pb) enhances the passivation process.

In Figure 3, the linear polarisations for potentials close to E_{cor} are presented. Based on the determined polarization resistances* $R_p = (\Delta E/\Delta i)_{E \rightarrow E_{cor}}$ it has been established

*According to Stearn and Geary [16,17], at potentials close to E_{cor} the dependence $E = f(i)$ is linear and the greater slope of $\Delta E/\Delta i$, the smaller is corrosion rate $i_{cor} = B(\Delta i/\Delta E)$, where B is a constant dependent on anodic and cathodic Tafel slopes.

that all additions investigated inhibit corrosion processes in the tested sulphate environment. The polarization resistance of the material without additions is 7.7 Ω·cm^2.

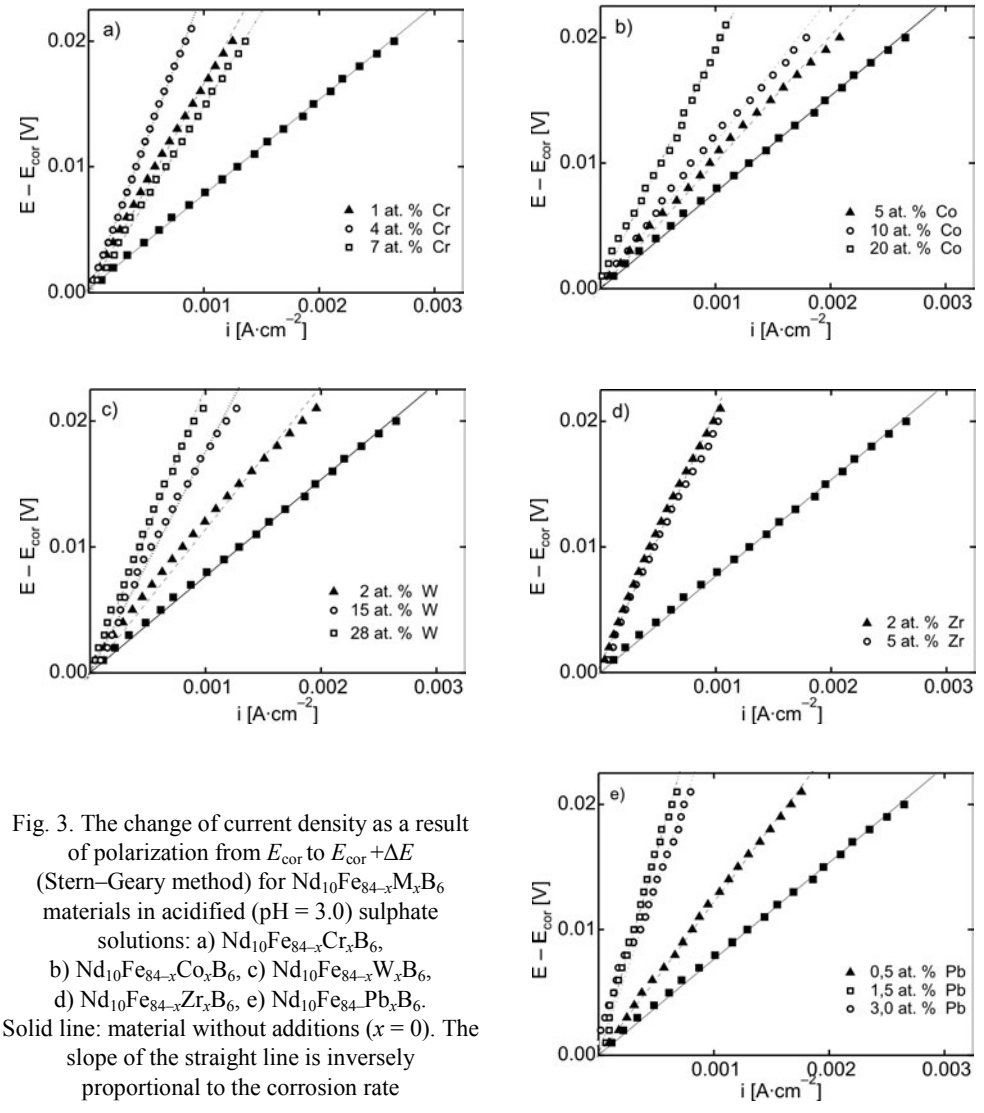

Fig. 3. The change of current density as a result of polarization from E_{cor} to $E_{cor}+\Delta E$ (Stern–Geary method) for $Nd_{10}Fe_{84-x}M_xB_6$ materials in acidified (pH = 3.0) sulphate solutions: a) $Nd_{10}Fe_{84-x}Cr_xB_6$, b) $Nd_{10}Fe_{84-x}Co_xB_6$, c) $Nd_{10}Fe_{84-x}W_xB_6$, d) $Nd_{10}Fe_{84-x}Zr_xB_6$, e) $Nd_{10}Fe_{84-}Pb_xB_6$. Solid line: material without additions ($x = 0$). The slope of the straight line is inversely proportional to the corrosion rate

A particularly clear corrosion inhibition effect is visible for 1.5 at. % of Pb (R_p = 27 Ω·cm^2), and for 4 at. % Cr (R_p = 24 Ω·cm^2). However, in the case of greater amounts of Co and W, the corrosion resistance is also very high and equal to 19-22 Ωcm^2. It should be noted, however, that such high contents of the above-mentioned alloying additives cannot be used in practical applications because the additives worsen the magnetic properties of the nanocrystalline material (see Table 1). If the considered additives are used in smaller quantities, the inhibition of corrosion is rather

negligible. The results obtained for nanocrystalline magnets are similar to those found for sintered Nd(Fe,M)B materials [18, 19]: the additives improve the corrosion behaviour of the magnets, however improvement is generally insufficient.

4. Conclusions

The following substitutions for iron are the most favourable in terms of the magnetic properties of nanocrystalline $Nd_{10}Fe_{84-x}M_xB_6$ magnets: cobalt (10 at. %), chromium (4 at. %), tungsten (15 at. %), lead (1.5 at. %) and zirconium (2 at. %).

The most pronounced tendency to passivation was observed for the magnets containing chromium (> 4 at. %), cobalt (>10 at. %) and lead (3 at. %). Tungsten has no effect on the tendency to passivate in the acidified sulphate environment, while zirconium slightly impairs the passivation ability of the material.

The metals substituting iron in the present study inhibit the corrosion process in an acidified medium by a factor of 2–3.

Acknowledgement

This paper was partly supported by the State Committee for Scientific Research, MNiSW Poland, Grant No. T08C00828

References

[1] FIDLER J., Proc. 7th Inter. Symp. *Anisotropy and Coercivity in Rare-Earth Transition Metal Alloys*, Canberra, Australia, 1992, p. 11.
[2] FIDLER J., BERNARDI J., SCHREFL T., KRONMŰLLER H., Proc. 8th Int. Symp. *Anisotropy and Coercivity in Rare-Earth Transition Metal Alloys*, Birmingham, UK, 1994, p. 37
[3] KASZUWARA W., LEONOWICZ M., KOZUBOWSKI J., Proc. 16th Int. Workshop *Rare Earth Magnets and Their Applications*, Sendai, Japan, 2000, p. 711.
[4] KASZUWARA W., LEONOWICZ M., J. Mag. Mag. Mater., 242–245 (2002), 1366.
[5] PAWŁOWSKA G., BALA H., KASZUWARA W., KUCHARSKA B., Inż. Mater., 26 (2005), 27.
[6] SZYMURA S., BALA H., RABINOVICH YU.M., SERGEEV V.V., PAWŁOWSKA G., J. Magn. Magn. Mater., 94 (1991), 113.
[7] SZYMURA S., BALA H., PAWŁOWSKA G., RABINOVICH YU.M., SERGEEV V.V., POKROVSKII D.V., J. Less Common Met., 175 (1991), 195.
[8] PAWŁOWSKA G., BALA H., SZYMURA S., Proc. 4th Polish Corrosion Conference KOROZJA'93, Warsaw, Poland, 1993, p. 279.
[9] JING X.P.,WANG X.Y., LI J.X., LI D.Y., MAN C.S., SHEPARD M.J., ZHAI T., Mater Sci. Eng., A 429 (2006), 30.
[10] KRÓLIKOWSKI A., Ochrona przed Korozją, 4 (2007), 140.
[11] PAWŁOWSKA G., Ochrona przed Korozją, 4–5 (2008), 144.
[12] KASZUWARA W., LEONOWICZ M., JANUSZEWSKI D., MENDOZA G., DAVIES H.A, PASZULA J., J. Mater. Sci. Mater. Electr., 9 (1998), 17.
[13] KASZUWARA W., LEONOWICZ M., Proc. 18th Int. Workshop *High Performance Magnets and Their Applications*, Annecy, France, 2004, p. 193.
[14] BALA H., SZYMURA S., Appl. Surf. Sci., 32 (1988), 233.

[15] BALA H., SZYMURA S., RABINOVICH YU.M., SERGEEV V.V., PAWŁOWSKA G., POKROVSKII D.V., Arch. Nauk. Mater., 12 (1991), 27.
[16] STEARN M., Corrosion, 14 (1958), 440t.
[17] BALA H., Proc. *Korozja materia*łów – *teoria i praktyka*, Częstochowa, Poland, 2002, p. 239 (In Polish).
[18] BALA H., PAWŁOWSKA G., SZYMURA S., SERGEEV V.V., RABINOVICH YU.M., J. Magn. Magn. Mater., 87 (1990), 255.
[19] BALA H., SZYMURA S., PAWŁOWSKA G., RABINOVICH YU.M., J. Appl. Electrochem., 23 (1993), 1017.

Received 23 October 2007
Revised 14 July 2008

Materials Science-Poland, *Vol. 27*, *No. 1*, *2009*

Methacryloyl functionalized hydrazones as hole-transporting materials for electrophotography

R. BUDRECKIENE[1*] V. ANDRULEVICIUTE[1], G. BUIKA[1],
J.V. GRAZULEVICIUS[1**], V. JANKAUSKAS[2], V. GRAZULEVICIENE[3]

[1]Department of Organic Technology, Kaunas University of Technology,
Radvilėnų pl. 19, LT-50254 Kaunas, Lithuania

[2]Department of Solid State Electronics, Vilnius University,
Sauletekio al. 9, LT-10222, Vilnius, Lithuania

[3]Department of Chemistry, Lithuanian University of Agriculture,
Studentu g. 11, LT-4324, Akademija, Kauno r. Lithuania

Syntheses and thermal, optical as well as photoelectrical properties of carbazolyl-, triphenylamino- and 2-hydroxy-4-diethylaminophenyl-based hydrazones with reactive methacryloyl groups have been reported. All the synthesized materials form glasses with glass transition temperatures ranging from 9 to 50 °C. They absorb electromagnetic radiation in the 250–440 nm range. Ionization potentials of the amorphous films of the synthesized materials, established by electron photoemission technique range from 5.20 to 5.71 eV. The lowest ionization potential and the best charge transport properties were observed for 2-(methacryloyl)oxy-4-diethylaminophenyl-1-carbaldehyde *N*,*N*-diphenylhydrazone. Time-of-flight hole mobilities in its 50% solid solution in bisphenol Z polycarbonate reach 10^{-5} cm^2/(V·s) at high electric fields.

Key words: *reactive hydrazone; glass; ionization potential; charge mobility*

1. Introduction

Materials accepting charges generated in adjacent materials and transporting them towards appropriate electrodes are called charge transport materials or semiconductors [1]. Most of known charge transport materials are photoconductive in UV light, and conversely, all truly photoconductive materials can act as transporting media for

[*]Present address: Department of Biological Chemistry, Lithuanian Veterinary Academy, Tilzes str. 18, LT-47181, Kaunas, Lithuania.
[**] Corresponding author, e-mail: Juozas.Grazulevicius@ktu.lt

charges generated extrinsically. Organic photoconductors or charge transport materials are used in photoreceptors of most modern copying machines, laser printers, and fax machines. They are also used in commercial organic light emitting diodes. The forthcoming fields of application of organic semiconductors are solar cells and field effect transistors. Most of the practical electrophotographic photoreceptors are multilayer devices in which every layer has its own function. Organic semiconductors are used for the fabrication of charge transport layers of devices usually several micrometers thick and represent so called molecularly doped polymers, i.e. solid solutions of low-molar-mass organic semiconductors in inert polymers such as polycarbonates [2].

One of the frequent requirements for charge transport layers of electrophotographic photoreceptors is that they be resistant to organic solvents. This requirement is particularly important if liquid developers are used in electrophotographic processes. Solvent resistant charge transport layers can be prepared by (photo)crosslinking. For this, charge transporting materials with reactive functional groups are required. The aim of this work was to synthesize and study methacryloyl functionalized hydrazones as hole transport materials for electrophotographic photoreceptors. Hydrazones are very effective hole transport materials widely used in electrophotography [3–5]. Earlier, hydrazones containing reactive epoxy- [4, 6] and vinyloxyethyl- [7, 8] groups were reported. However the reactivity of epoxy- and vinyloxyethyl-substituted hydrazones has appeared to be not too high, particularly in cationic polymerization reactions. Therefore it was of interest to synthesize methacryloyl-substituted hydrazones as radically (photo)polymerizable or (photo)crosslinkable compounds, which can be used for the preparation of solvent resistant charge transport layers.

2. Experimental

Materials. All required chemicals: N-phenylhydrazine, 97% (Aldrich), potassium carbonate, 99% (Aldrich), potassium hydroxide, 86% (Lachema), phosphorus oxychloride, 99% (Aldrich), triethylamine, 99% (Acros), sodium chloride, 99% (Lachema), magnesium sulphate, 97% (Aldrich), sodium sulphate, 98% (Aldrich) were used as received without further purification. Methacryloylchloride, 97% (Fluka) was distilled (water pump vacuum) before use collecting the fraction with the boiling point 92 °C. Organic solvents were purified and dried by the standard methods [9]. 4-(Diphenylamino)benzaldehyde (**4**) (yield of $C_{19}H_{15}N_1O_1$ (*FW* = 273.26) was 72% (5.57 g of yellowish crystals); m.p. 126–126.5 °C)) [10]; di(4-formylphenyl)phenylamine (**4a**) (yield of $C_{20}H_{15}N_1O_2$ (*FW* = 301.26) was 44% (8.2 g of yellow-orange crystals); m.p. 126–126.5 °C)) [10], 9-ethylcarbazole-3-carbaldehyde (**1**) (yield of the product $C_{15}H_{15}N_1O_1$ (*FW* = 223.21) was 80% (4.57g of grey crystals); m.p. 84.5–85 °C)) [11], 9-ethylcarbazole-3,6-dicarbaldehyde (**1a**) (yield of $C_{16}H_{15}N_1O_2$ (*FW* = 251.22) was 60% (11.5 g of brown crystals); m.p. 146.5–148 °C)) [11], were prepared by the known procedures.

*9-Ethylcarbazole-3-carbaldehyde N-phenylhydrazone (**2**).* 9-Ethylcarbazole-3-carbaldehyde (**1**) (10.0 g, 0.045 mol) was dissolved in 300 ml of methanol under mild heating. Then a solution of 7.25 g (0.067 mol) of N-phenylhydrazine in methanol was added. The reaction mixture was refluxed for 2 h and stopped when no starting materials were left (TLC control). After recooling, yellow-grey crystals were separated by filtration, washed with a large amount of methanol and dried. The yield of $C_{21}H_{19}N_3$ (*FW* = 313.32) was 92% (13.12 g); m.p. 136–137 °C. IR (KBr) (in cm^{-1}): ν(N–H) 3306, ν(C–H in Ar) 3051, ν(C–H) 2972, ν(C=C, C–N in Ar) 1602; 1494; 1475; 1237, ν(C–N) 1256, γ(Ar) 815; 747; 731. MS (APCI$^+$, 20 V), *m*/*z* = 314 ($[M + H]^+$); 222. ^{1}H NMR (100 MHz, $CDCl_3$, δ, ppm): 1.34 (*t*, *J* = 7.0 Hz, 3H, CH_3); 4.23 (*q*, *J* = 7.0 Hz, 2H, CH_2); 6.90–7.64 (*m*, 8H, Ar); 7.60 (*s*, 1H, Ar); 7.81 (*d*, 1H, Ar); 8.08 (*d*, 2H, Ar); 8.15(*d*, 1H, =CH).

*9-Ethylcarbazole-3-carbaldehyde-N-(methacryloyl)-N-phenylhydrazone (**3**).* 9-Ethylcarbazole-3-carbaldehyde-N-phenylhydrazone (**2**) (5.0 g, 0.0157 mol) was dissolved in 40 ml of dry dichloromethane under nitrogen atmosphere and 2.61 ml (0.0188 mol) of triethylamine and 1.82 ml (0.0188 mol) of freshly distilled methacryloylchloride was added dropwise. The reaction mixture was stirred and heated at ca. 40 °C for 10 h and cooled down. Then the product was extracted using chloroform and distilled water. The organic layer was dried using anhydrous sodium sulphate and filtered. The solvent was removed from the filtrate with a rotary evaporator. The product was purified by column chromatography using an eluent mixture of hexane and ethyl acetate in the volume ratio of 3:1. The solvents were rotary evaporated and the product was washed with a large amount of benzene, filtered and dried. Yield of the product was 23.45% (1.4 g of brownish powder). IR (KBr) (in cm^{-1}): (C–H in Ar) 3062, 3033, ν(C–H) 2970, ν(C=O) 1671, ν(C=C in Ar) 1598, 1491, ν(C–N) 1238, 1202, γ(Ar) 747, 679. MS (APCI$^+$, 20 V), *m*/*z* = 382.37 ($[M+H]^+$), 288.36, 260.39, 221.40, 149.16. ^{1}H NMR (100 MHz, $CDCl_3$, δ, ppm): 3.50 (*s*, 3H, CH_3–C); 4.19–4.27 (*q*, *J* = 6.5 Hz, 1H, CH_2=), 5.40–5.54 (*q*, *J* = 6.0 Hz, 1H, CH_2=), 7.19–8.15 (*m*, 13H, Ar, –CH=). Elemental analysis for $C_{25}H_{23}N_3O_1$ (*FW* = 381.38): calculated: C 78.71%; H 6.08%; N 11.02%; O 4.20%; found: C 78.87%; H 6.52%; N 10.92%.

*4-(Diphenylamino)benzaldehyde N-phenylhydrazone (**5**).* 4-(Diphenylamino)benzaldehyde (**4**) (10.0 g, 0.037 mol) was dissolved in 300 ml of methanol under mild heating. Then, a solution of 5.94 g (0.055 mol) of N-phenylhydrazine in 5 ml of methanol was added. The reaction mixture was refluxed for 0.5 h until no starting materials were observed (TLC control). After recooling and crystallisation, yellowish crystals were filtered, washed with a large amount of methanol and dried. The yield of $C_{25}H_{21}N_3$ (*FW* = 363.36) was 86.7% (11.7 g); m.p. 168–169 °C. IR (KBr) (in cm^{-1}): ν(N–H) 3294, ν(C–H in Ar) 3026, ν(C=C in Ar) 1595; 1489, ν(C–N) 1282; 1257, γ(Ar) 750; 731. MS (APCI$^+$, 20 V), *m*/*z* = 364 ($[M+H]^+$), 314, 223, 159. ^{1}H NMR (100 MHz, $CDCl_3$, δ, ppm): 6.55–7.64 (m, 21H, Ar, = CH, –NH).

*4-(Diphenylamino)benzaldehyde N-(methacryloyl)-N-phenylhydrazone (**6**).* 4-(Diphenylamino) benzaldehyde N-phenylhydrazone (**5**) (5.0 g, 0.0135 mol) was dissolved

in 40 ml of dry dichloromethane in a nitrogen atmosphere, and 2.26 ml (0.0163 mol) of triethylamine was added. The reaction mixture was cooled down to 0 °C. Then 1.58 ml (0.0163 mol) of freshly distilled methacryloylchloride was added dropwise into the reaction mixture. The reaction mixture was stirred for 3 h and the second portion of methacryloylchloride (1.58 ml) and TEA (2.26 ml) was added. After 4 h the reaction was terminated when no starting materials were left (TLC control). The product was extracted using chloroform and distilled water. The organic layer was dried using anhydrous sodium sulphate and filtered. The solvent was removed from the filtrate with a rotary evaporator. The product was purified by the column chromatography using an eluent mixture of hexane and ethyl acetate in the volume ratio of 3:1. Finally, the solvent was rotary evaporated and the product was freeze dried. The product yield was 22.77% (1.33 g of yellowish brown powder). IR (KBr) (in cm^{-1}): ν(C–H in Ar) 3036, ν(C–H) 2829, 2742, ν(C=O) 1689, ν(C=C in Ar) 1585, 1489, ν(C–N) 1287, 1220, 1155, γ(Ar) 757, 696. MS (APCI$^+$, 20 V), m/z = 432.25 ([M+H]$^+$), 162.22. ^{1}H NMR (100 MHz, $CDCl_3$, δ, ppm): 2.2 (s, 3H, CH_3–C); 5.39–5.57 (m, 2H, CH_2=), 6.79–7.81 (*m*, 20H, Ar, –CH=). Elemental analysis for $C_{29}H_{25}N_3O_1$ (*FW* = 431.42): calculated: C 80.71%; H 5.48%; N 9.74%; O 3.71%; found: C 80.91%; H 6.02%; N 9.16%.

Di{4-[(N-phenylamino)iminomethyl]phenyl}phenylamine (7). Di(4-formylphenyl)-phenylamine (**4a**) (7.6 g, 0.025 mol) was dissolved in 150 ml of methanol under mild heating. Then, a solution of 6.75 g (0.0625 mol) of N-phenylhydrazine in 5 ml of methanol was added. The reaction mixture was refluxed for 2 h and stopped when no starting materials were observed (TLC control). After recooling and crystallisation, yellow-orange crystals were filtered off, washed with a large amount of methanol and dried. The yield of $C_{32}H_{27}N_5$ (*FW* = 481,48) was 84.1% (10.21 g); m.p. 131.5–132 °C. IR (KBr) (in cm^{-1}): ν(N–H) 3295, ν(C–H in Ar) 3027, ν(C=C in Ar) 1597; 1499, ν(C–N) 1287; 1253, γ(Ar) 749; 723. MS (APCI$^+$, 20 V), m/z = 482.24 ([M+H]$^+$), 392.28, 180.24, 112.99. ^{1}H NMR (100 MHz, $CDCl_3$, δ, ppm): 3.34 (*s*, 2H, –NH), 6.72–7.84 (*m*, 25H, Ar, =CH).

*Di(4-{[(N-methacryloyl)-N-phenylamino]iminomethyl}phenyl)phenylamine (**8**)*. Di{4-[(N-phenylamino)iminomethyl]phenyl}phenylamine (**7**) (5.0 g, 0.0104 mol) was mixed with 50 ml of dry dichloromethane (CH_2Cl_2) in a nitrogen atmosphere. 3.48 ml (0.025 mol) of triethylamine was added and the heterogeneous reaction mixture was cooled to 0 °C. Then 2.42 ml (0.025 mol) of freshly distilled methacryloylchloride was dropped into the reaction mixture. The reaction mixture was stirred at 40 °C and stopped after 18 h when no starting materials were left in the reaction mixture (TLC control). After recooling, the product was extracted using chloroform and distilled water. The organic layer was dried using anhydrous sodium sulphate and filtered. The solvent was removed from the filtrate with a rotary evaporator. The product was purified by the column chromatography using an eluent mixture of hexane and acetone in the volume ratio of 6:1. Finally, the solvent was rotary evaporated and the product was freeze dried. Yield: 23% (1.7 g of yellowish powder). IR (KBr) (in cm^{-1}): ν(arene C –H) 3284, 3063, ν(C–H) 3008, 2973; 2924; ν(C=O) 1673, ν(C=C, in Ar) 1594; 1509;

1490, ν(C–N) 1283; 1233, 1183, γ(Ar) 755; 696. MS (APCI$^+$, 20 V), *m*/*z* = 618.17 ([M+H]$^+$), 458.25, 298.36, 297.35, 134.14. ^{1}H NMR (100 MHz, $CDCl_3$, δ, ppm): 2.20 (*s*, 6H, CH_3), 5.35–5.44 (*m*, 2H, CH_2=); 5.48–5.59 (*m*, 2H, CH_2=), 7.03 (s, 2H, –CH=); 7.1–7.6 (*m*, 23H, Ar). Elemental analysis for $C_{40}H_{35}N_5O_2$ (*FW* = 617.59): calculated: C 77.77%; H 5.71%; N 11.34%; O 5.18%; found: C 78.29%15.0 g (0.0776 mol); H 4.92%; N 10.96%.

*2-Hydroxy-4-diethylaminophenyl-1-carbaldehyde N,N-diphenylhydrazone (**9**).* 2-Hydroxy-4-diethylaminophenyl-1-carbaldehyde (15.0 g, 0.0776 mol) was dissolved in 50 ml of methanol under mild heating. Then a solution of 25.69 g (0.1164 mol) of *N*,*N*-diphenylhydrazine hydrochloride dissolved in ca. 50 ml of methanol was added. The reaction mixture was stirred at ca. 30 °C for 2 h and cooled down. Then the reaction product was extracted and shaken in a separatory funnel with diethyl ether and distilled water. The organic layer was dried using anhydrous sodium sulphate and filtered. The solvent was removed by rotary evaporation. The product was purified by the column chromatography using an eluent mixture of hexane and chloroform in the volume ratio of 1:1 and crystallized from the eluent. The yield of $C_{23}H_{25}N_3O_1$ (*FW* = 359.38) was 74.73% (20.85 g of grey crystals); m.p. 100.5–101 °C. IR (KBr) (in cm^{-1}): ν(O–H) 3218, ν(C–H in Ar) 3057, ν(C–H) 2971; 2932; 2894, ν(C=C in Ar) 1633, 1596, 1495, ν(C–N) 1298, 1245, γ(Ar) 751, 700. MS (APCI$^+$, 20 V), *m*/*z* = 360.4 ([M+H]$^+$), 206.4, 120.1. ^{1}H NMR (100 MHz, $CDCl_3$, δ, ppm): 1.15 (*t*, *J* = 7.0 Hz, 6H, CH_3); 3.33 (*q*, *J* = 7.0 Hz, 4H, CH_2); 6.73 (*d*, *J* = 9.0 Hz, 1H, =CH); 7.05–7.45 (*m*, 13H, Ar), 11.25 (*s*, 1H, –OH).

*2-(Methacryloyl)oxy-4-diethylaminophenyl-1-carbaldehyde N,N-diphenylhydrazone (**10**).* 2-Hydroxy-4-diethylaminophenyl-1-carbaldehyde-*N*,*N*-diphenylhydrazone (**9**) (7.0 g, 0.019 mol) was dissolved in 10 ml of dry dichloromethane in a nitrogen atmosphere and 3.2 ml (0.023 mol) of triethylamine was added. The reaction mixture was cooled down to 0 °C. Then 2.22 ml (0.023 mol) of freshly distilled methacryloylchloride was added dropwise. The reaction mixture was stirred for 10 min and terminated, since no starting materials were left (TLC control). The product was extracted using chloroform and distilled water. The organic layer was dried with anhydrous sodium sulphate and filtered. The solvent was removed by rotary evaporation. The product was purified by column chromatography using diethyl ether as an eluent. Finally, the solvent was rotary evaporated and the product was freeze dried. The yield of the product was 89.54% (7.45 g of yellowish brown resin). IR (KBr) (in cm^{-1}): ν(C–H in Ar) 3061, 3023, ν(C–H) 2973, 2929, 2895, ν(C=C in Ar) 1783, ν(C=O) 1736, ν(C–O) 1319, 1290, 1273, γ(Ar) 749, 701. MS (APCI$^+$, 20 V), *m*/*z* = 428.4 ([M+H]$^+$). ^{1}H NMR (100 MHz, $CDCl_3$, δ, ppm): 1.2 (*t*, *J* = 7.0 Hz, 6H, CH_3);1.8 (*s*, 3H, CH_3–C=), 3.23 (*q*, *J* = 7.0 Hz, 4H, CH_2); 5.49 (s, 1H, H_2C=), 5.98 (*s*, 1H, H_2C=), 6.99–7.42 (m, 13H, Ar), 7.9(*d*, *J* = 9.0 Hz, 1H, –CH=). Elemental analysis for $C_{27}H_{29}N_3O_2$ (*FW* = 427.44): calculated: C 75.84%; H 6.84%; N 9.83%; O 7.49%; found: C 75.43%; H 7.24%; N 9.59%.

2.2. Measurements

IR spectra were recorded with Bio-Rad Digilab FTS-40 and Perkin Elmer Spectrum GX spectrophotometers. The spectra were obtained from KBr pellets. UV/VIS spectra were recorded with a Spectronic Unicam Genesys^{TM} 8 spectrophotometer. Fluorescence emission spectra were recorded with a Hitachi MPF-4 luminescence spectrometer. ^{1}H NMR spectra were obtained using a Bruker AC 250 (250 MHz), Varian Unity Inova (300 MHz) and JOEL FX 100 (100 MHz) apparatus. All the data are given as chemical shifts in δ (ppm), multiplicity, integration downfield from $(CH_3)_4Si$. Electron impact mass spectra were obtained on a Waters 2Q 2000. Thermogravimetric analysis (TGA) was performed on a Netzsch STA 409. Differential scanning calorimetry (DSC) measurements were carried out using a Perkin-Elmer DSC-7 calorimeter.

Ionization potential (I_p) was measured by the electron photoemission in air method as described earlier [12]. The samples for the measurements were prepared by casting the solutions of the compounds on Al plates pre-coated with methylmethacrylate and methacrylic acid copolymer as adhesive layer.

Charge carrier mobility (μ) was measured by the xerographic time of flight method [13, 14]. The samples for the measurements were prepared by casting the solutions of the compounds or solutions of the mixtures of these compounds with the polymer host, i.e. bisphenol Z polycarbonate (PC-Z) at the mass proportion 1:1 in THF. The substrate was polyester film with an Al layer. The thickness of the charge-transporting layer varied in the range of 3–10 μm.

3. Results and discussion

New charge transport compounds bearing methacryloyl function groups **3**, **6**, **8**, **10** have been synthesized by the procedures described in Schemes 1–3**.** These procedures are similar to that reported earlier by Strohriegl [15]. The key starting materials aldehyde N-phenylhydrazones **2**, **5**, **7** and **9** were synthesized by multi-step synthesis, as described in previous works [7, 8, 16].

The first step was the formylation of arylamine, using $POCl_3$/DMF complex as a catalyst, by the Vilsmeier method [17] to get mono- and diformyl compounds **1**, **1a**, **4** and **4a**. The second step was condensation of aldehydes with N-phenylhydrazine, and the third step was the nucleophilic substitution reactions of 9-ethylcarbazole-3-carbaldehyde-N-phenylhydrazone (**2**), 4-(diphenylamino)benzaldehyde N-phenylhydrazone (**5**) and di{4-[(N-phenylamino)iminomethyl]phenyl}phenylamine (**7**) with methacryloylchloride in the presence of triethylamine in nitrogen atmosphere.

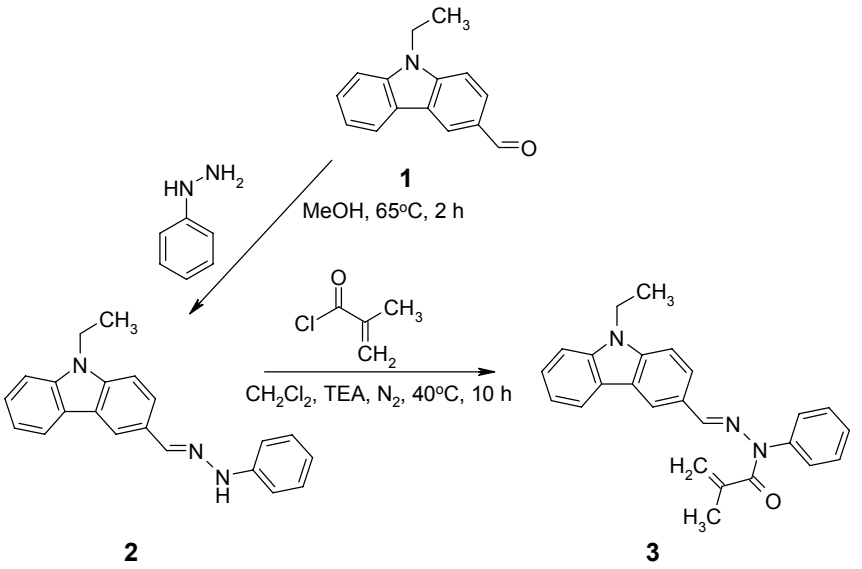

Scheme 1. Synthesis of 9-ethylcarbazole-3-carbaldehyde-N-(methacryloyl)-N-phenylhydrazone (**3**)

2-(Methacryloyl)oxy-4-diethylaminophenyl-1-carbaldehyde *N*,*N*-diphenylhydrazone (**10**) was synthesized by a two-step procedure as shown in Scheme 3. The first step was condensation of 2-hydroxy-4-diethylaminophenyl-1-carbaldehyde with *N*,*N*-diphenylhydrazine hydrochloride and the second step was alkylation of 2-hydroxy-4 -diethylaminophenyl-1-carbaldehyde *N*,*N*-diphenylhydrazone (**9**) with methacryloyl-chloride in the presence of triethylamine in a nitrogen atmosphere.

All the products were purified by the column chromatography to obtain pure and well defined compounds. All the synthesized materials were characterised by IR, ^{1}H NMR spectroscopy, mass spectrometry and elemental analysis.

IR spectra of compounds **3**, **6**, **8**, **10** have characteristic absorption of C=O groups at ca. 1725 cm^{-1}.

The signals in ^{1}H NMR spectra of all the newly synthesized hydrazone compounds can be exactly assigned to the characteristic hydrogen atoms of these compounds. The well distinguished signals of CH_3–C protons are at 1.8–3.5 ppm in the spectra of all methacryloyl substituted hydrazones. Characteristic signals of the protons of CH_2= group of methacryloyl group are observed at 4.19–4.27 and 5.26–5.98 ppm in the spectra of compounds **3**, **6**, **8**, **10**. The signals at 6.99–8.15 ppm can be assigned to the aromatic and heterocyclic protons.

Mass spectra of all the synthesized hydrazones show the corresponding molecular ion peaks and peaks due to alkyl and respective aryl fragments.

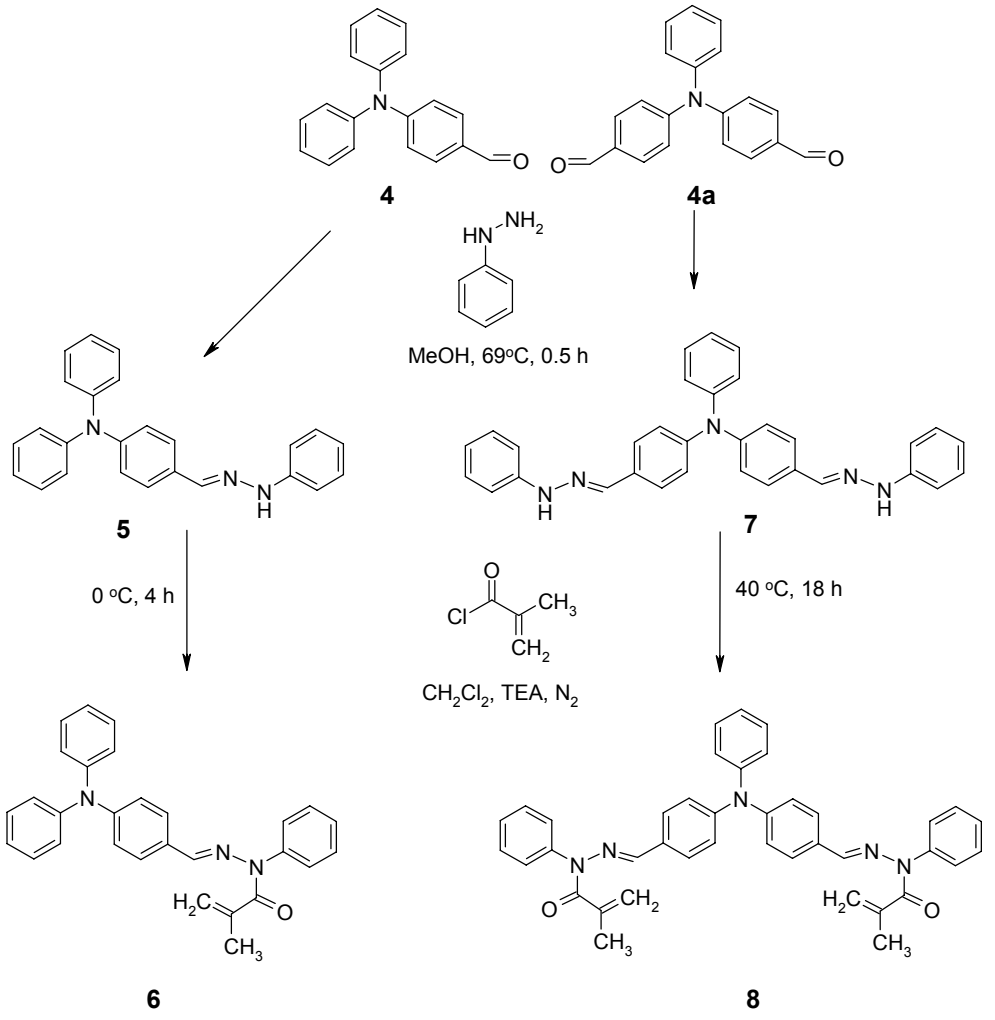

Scheme 2. Synthesis of triphenylamine-based hydrazones containing methacryloyl functional groups

Compounds **3**, **6**, **8**, **10** were studied by UV/VIS spectrometry. They absorb electromagnetic radiation in the region of 200–420 nm. The wavelengths of the absorption maxima for methacryloyl-substituted hydrazones are given in Table 1.

Table 1. Wavelengths of absorption maxima for compounds **3**, **6**, **8** and **10** [nm]

Compound	**3 (2)**	**6 (5)**	**8 (7)**	**10 (9)**
λ	298, 326 (348)	354 (376)	381 (394)	368 (370)

Methacryloyl-substituted hydrazones **3**, **6**, **8**, **10**, owing to the electron withdrawal effect of the carbonyl group, exhibit hypsochromic shift (up to 22 nm) with respect to

the corresponding nonsubstituted hydrazones. In the case of the substitution of one hydrazone group (**3** and **6** compounds), the shift is the same, i.e., is 22 nm. Substitution of two hydrazone groups results in a smaller hypsochromic shift of 13 nm. This indicates stronger electron withdrawal into delocalization when a chromophore contains two hydrazone groups. In the case of the substitution of the OH group, the spectrum exhibits 2 nm hypsochromic shift of the longwave peak, that means only negligible distortion of the system in hydrazone **10** conjugated by the methacryloyl group.

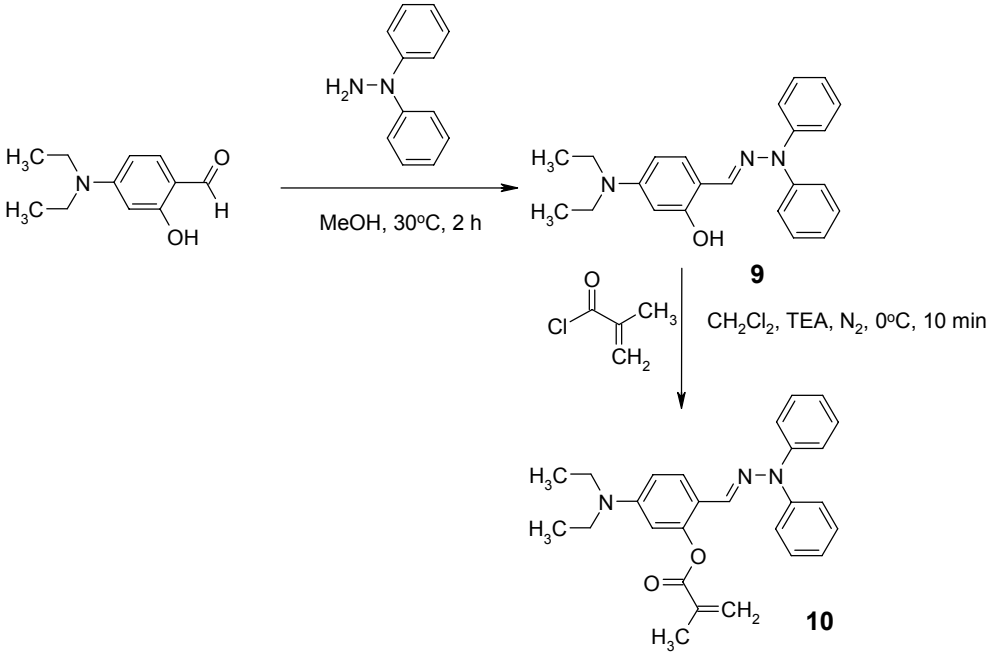

Scheme 3. Synthesis of 2-(methacryloyl)oxy-4-diethylaminophenyl -1-carbaldehyde *N*,*N*-diphenylhydrazone (**10**)

Fluorescence emission spectra of dilute solutions of compounds **3**, **6**, **8**, **10** are presented in Fig. 1. The wavelengths of the maximum fluorescence intensities are 382 nm for carbazole containing compound **3**, 475 nm and 448 nm for triphenylamine bearing compounds **6** and **8**, 425 nm for 2-hydroxy-4-diethylaminophenyl-1-carbaldehyde moiety containing compound **10**. The large Stokes shifts of 112 nm for **3**, 185 nm for **6**, 68 nm for **8**, and 85 nm for **10** can be explained by vibrational relaxation and internal conversion in excited state of these compounds.

The thermal stability of the synthesized materials was estimated by TGA. The temperatures of their initial thermal degradation are given in Table 2. The initial mass loss temperatures (T_{ID}) for these materials range from 260 to 280 °C. The highest thermal stability was observed for triphenylamine based compound **6**. Its T_{ID} is 280 °C.

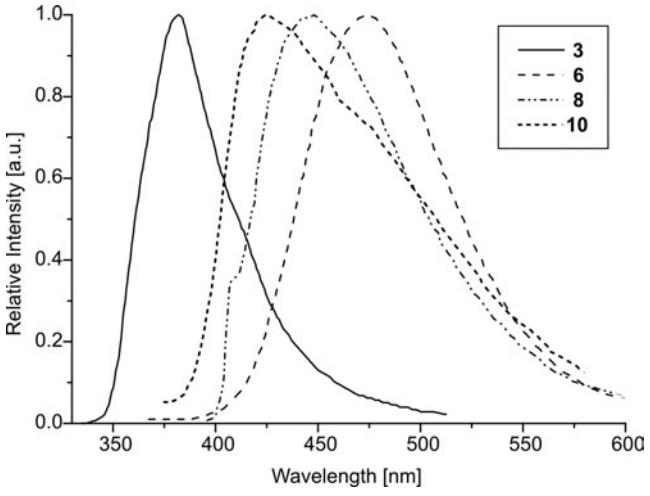

Fig. 1. Fluorescence spectra of diluted THF solutions (10^{-5} M) of hydrazones **3** (λ_{ex} = 270 nm), **6** (λ_{ex} = 290 nm), **8** (λ_{ex} = 380 nm) and **10** (λ_{ex} = 340 nm)

Table 2. Thermal characteristics of compounds **3**, **6**, **8** and **10**

Compound	T_g [°C]	T_m [°C]	T_{ID} [°C]
3	43	84	260
6	41	128	280
8	50	85	260
10	9	–	260

Compounds **3, 6** and **8** were isolated as crystalline materials. The first DSC heating scans of these compounds revealed endothermic melting signals with the maxima at 84 °C for **3**, 124 °C for **6**, and at 85 °C for **8**. Cooling did no reveal any crystallization peaks and only glass-transitions were observed in the DSC second heating scans of these compounds at 43 °C, 41 °C and 50 °C respectively. Compound **10** was isolated as a viscous resin. It showed only glass transition in all DSC heating and cooling scans. Comparison of glass transition temperatures (T_g) of methacryloyl substituted hydrazones with their vinyloxyethyl substituted analogues reported earlier [7, 8, 16] show that metacrylolyl substituted hydrazones display higher glass transition temperatures from 9 °C to 23 °C. This observation can be explained by the presence of more polar methacryloyl groups in these compounds which predetermines stronger intermolecular interaction. All materials reported in this paper are soluble in common organic solvents such as acetone, chloroform, THF, etc. The values of I_p are given in Table 3. They range from 5.20 eV to 5.70 eV. The lowest value of I_p was observed for 2-methacryloyloxy-4-diethylaminophenyl-1-carbaldehyde hydrazone **10**. It was of interest to compare I_p of methacroyl substituted hydrazones with those of their corresponding vinyloxyethyl substituted analogues reported earlier [7, 8, 16]. In all cases methacryloyl substituted hydrazones exhibit slightly higher I_p values.

Table 3. Ionisation potentials of the amorphous films of compounds **3**, **6**, **8** and **10**

Compound	**3**	**6**	**8**	**10**
I_p [eV]	5.70	5.60	5.70	5.20

Figure 2 shows electric field dependences of hole drift mobilities of solid solutions of methacryloyl substituted hydrazones **6**, **8**, **10** in PC-Z. The linear dependences of holes drift mobility on the square root of the electric field are observed for all the systems.

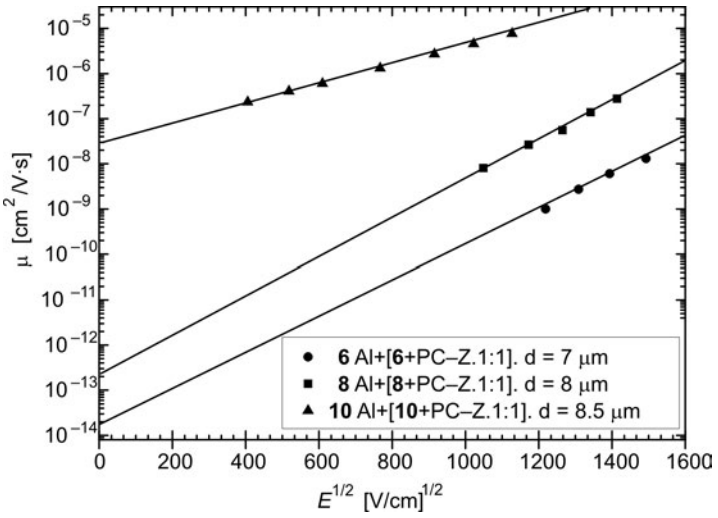

Fig. 2. Electric field dependences of holes drift mobilities of the solid solutions of compounds **6**, **8**, **10** in PC-Z

The highest hole drift mobilities were observed for the solid solution of compound **10** in PC-Z. At high electric fields, they reach 10^{-5} cm^2/(V·s). Hole drift mobilities in PC-Z doped with compound **10** are close to those observed in PC-Z doped with the vinyloxyethyl substituted analogue of **10** [16]. In other cases the systems containing methacryloyl substituted hydrazones show lower charge mobilities than the systems containing vinyloxyethyl substituted hydrazones [8].

4. Conclusions

We have synthesized hydrazones containing carbazole, triphenylamino and 2-hydroxy-4-diethylaminophenyl moieties with reactive methacryloyl groups as polymerizable or cross-linkable hole transport materials for electrophotographic photoreceptors. We have also studied thermal, optical and photoelectrical properties of the synthesized materials. All the materials form glasses with glass transition temperatures ranging from 9 °C to 50 °C. They absorb electromagnetic radiation in the 250–440 nm

range. Ionization potentials of the amorphous films of the synthesized materials, established by electron photoemission technique, range from 5.20 to 5.71 eV. The lowest ionization potential and the best charge transport properties were observed for 2-(methacryloyl)oxy-4-diethylaminophenyl-1-carbaldehyde *N*,*N*-diphenylhydrazone. Time of flight hole mobilities in its 50% solid solution in bisphenol Z polycarbonate reach 10^{-5} $cm^2/(V \cdot s)$ in high electric fields.

Acknowledgements

This research was supported by the Lithuanian Science and Studies Foundation. Habil. Dr. Valentas Gaidelis from the Department of Solid State Electronics, Vilnius University is thanked for the ionisation potential measurements.

References

1] STOLKA M., [in:] *Special Polymers for Electronics and Optoelectronics*, J.A. Chilton, M.T. Goosey (Eds.), Chapman and Hall, London, 1995, p. 284.
[2] BORSENBERGER P.M., WEISS D.S, *Organic Photoreceptors for Xerography*, M. Dekker, New York, 1998, p. 768.
[3] JIANG K.J., SUN Y.L., SHAO K.F, YANG L.M., Chem. Lett., 33 (2004), 50.
[4] GETAUTIS V., STANISAUSKAITE A., MALINAUSKAS T., STUMBRAITE J., GAIDELIS V., JANKAUSKAS V., Monatsh. Chem., 137 (2006), 1401.
[5] GETAUTIS V., DASKEVICIENE M., MALINAUSKAS T., GAIDELIS V., JANKAUSKAS V., TOKARSKI Z., Synth. Met., 155 (2005), 599.
[6] GETAUTIS V., DASKEVICIENE M., MALINAUSKAS T., STANISAUSKAITE A., STUMBRAITE J., Molecules, 11 (2006), 64.
[7] BUDRECKIENE R., BUIKA G., GRAZULEVICIUS J.V., JANKAUSKAS V., STANISKIENE B., J. Photochem. Photobiol. A. Chem., 181 (2006), 257.
[8] BUDRECKIENE R., BUIKA G., GRAZULEVICIUS J.V., JANKAUSKAS V., TOKARSKI Z., Synth. Met., 156 (2006), 677.
[9] LIDLE D.R., *Handbook for Organic Solvents*, CRC Press, Boca Raton, 1995.
[10] LEE H.J., SOHN J., HWANG J., PARK S.Y., CHOI H., CHA M., Chem. Mater., 16 (2004), 456.
[11] OSTRAUSKAITE J., VOSKA V., ANTULIS J., GAIDELIS V., JANKAUSKAS V., GRAZULEVICIUS J.V., J. Mater. Chem., 12 (2002), 3469.
[12] MIYAMOTO E., YAMAGUCHI Y., YOKOYAMA M., Electrophotography, 28 (1989), 364.
[13] MONTRIMAS E., GAIDELIS V., PAZERA A., Lithuanian Journal of Physics, 6 (1966), 569.
[14] VAEZI-NEJAD S.M., Int. J. Electronics, 62, (1987) 361.
[15] STROHRIEGL P., Mol. Cryst. Liq. Cryst. 183, (1990), 261.
[16] BUDRECKIENE R., GRAZULEVICIUS J.V., JANKAUSKAS V., VEDEGYTE J., SIDARAVICIUS J., J. Optoelectronics Adv. Mater., 8 (2006), 1533.
[17] VILSMEIER A., HACK A., Ber. 60 (1927) 119.

Received 23 October 2007
Revised 8 July 2008

Materials Science-Poland, *Vol. 27*, *No. 1*, *2009*

Synthesis in aqueous phase and characterization of silver nanorods and nanowires

J. ZHOU[1,2], G. ZHOU[3], R. WANG[1], M. LU[3*]

[1]School of Life Science, Shandong University, Jinan 250100, P.R.China

[2]Center for Disease Prevention and Control of Jinan Military Command, Jinan 250014, P.R.China

[3]State Key Laboratory of Crystal Materials, Shandong University, Jinan 250100, P.R.China

Silver nanorods and nanowires have been synthesized via a chemical process in aqueous phase by using ascorbic acid as a reducing agent and anionic surfactant dodecyl benzene sulfonic acid sodium (SDBS) as a capping agent. The products were characterized by X-ray diffraction (XRD) techniques and transmission electron microscopy (TEM). Experimental results indicated that the concentration of ascorbic acid played a critical role in the formation of the silver nanorods and nanowires. The optical properties were investigated. The prepared nanostructures displayed a very strong absorption band at room temperature.

Key words: *nanomaterials; optical properties; X-ray technique*

1. Introduction

One-dimensional (1D) nanostructures are expected to play an important role in fabricating nanoscale devices. As a result, the synthesis and characterization of 1D nanostructures have recently attracted much attention due to their interesting physical properties and their potential applications in fabricating optoelectric, thermoelectric, and magnetic devices [1–7]. Silver nanorods and nanowires with well-defined dimensions and aspect ratios are particularly interesting to fabricate and study because they exhibit high electrical conductivity, thermal conductivity and unusual optical properties among all the metals. Recently, much effort has been devoted to syntheses of silver nanorods and nanowires. For example, silver nanorods and nanowires have be prepared by using DNA [8], carbon nanotubes [9, 10], polymers [11, 12] and mesoporous silica [13] as templates, respectively. Murphy and co-workers have successfully synthesized high-quality silver and gold nanorods and nanowires by using a rod-like micellar template of cetyltrimethylammonium bromide

*Corresponding author, e-mail: mklu@sdu.edu.cn

(CTAB) instead of hard template [14, 15]. Tian and his collaborators have synthesized silver nanorods and nanowires by using a surfactant-assistant route [16]. They used sodium dodecylsulfonate as a capping agent but not as a soft template. Xia and Sun have demonstrated a polyol process that generated silver nanowires by reducing silver nitrate with ethylene glycol in the present of poly (vinyl pyrrolidone) (PVP) [17]. Murphy reported a seedless and surfactantless wet chemical approach to produce silver nanowires in the present of NaOH [18]. However, the final products of all these chemical methods were characterized by problems such as relatively low yields, low aspect ratios, irregular morphologies, non-uniformity size, or polycrystalline domain structure.

In this paper, we report a solution-phase method that generated silver nanorods and nanowires by reduced silver nitrate with ascorbic acid in the presence of anionic surfactant SDBS, which served as a capping agent. It was found the ascorbic acid concentration plays a key role in the formation of these nanocrystals.

2. Experimental

$AgNO_3$ and ascorbic acid (Shanghai Chemistry Co.) of analytical grade purity were used as starting materials without further purification. All solutions were made with distilled water. In a typical experiment, 1 dm^3 of 10 mM $AgNO_3$ solution and 1 dm^3 of 50 mM SDBS solution were added to 48 dm^3 of distilled water in a flask. 10 min of vigorous stirring was necessary to ensure that all the reagents were dispersed homogeneously at room temperature. 6 dm^3 of 10 mM ascorbic acid solution was then added drop-wise to the above solution under a continuous stirring. After the ascorbic acid addition was completed, the mixture was heated to 100 °C and refluxed for 30 min. The colour of the reaction solution changed to orange-yellow due to formation of silver nanorods and nanowires. Prior to characterization, the precipitate was separated by a centrifuge at 3000 rpm for 20 min and carefully washed repeatedly with distilled water and absolute ethanol to remove the remaining SDBS, and then dried in a vacuum oven at 60 °C for 5 h. The X-ray diffraction (XRD) patterns were recorded using a Japan Rigaku D/Max 2200PC diffractometer with graphite monochromatized CuK_α radiation (λ = 1.5418 Å). Transmission electron microscopy (TEM) studies were carried out using a Japan JEM-100CX Ⅱ transmission electron microscope. UV-visible spectra were measured on a Varian Cary-100 spectrophotometer. All the measurements were carried out at room temperature.

3. Results and discussion

The X-Ray diffraction (XRD) pattern (Fig. 1) taken from the sample prepared using 1.2 mM ascorbic acid in the presence of 1 mM SDBS (the final concentration) indicates that the crystal structure of the nanorods and nanowires is face-centred cubic (fcc), space group *Fm*3*m*, and cell lattice parameters: a = 4.086 Å (JCPDS file number: 04-0783). The high peaks indicate that the as-prepared samples are well crystallized.

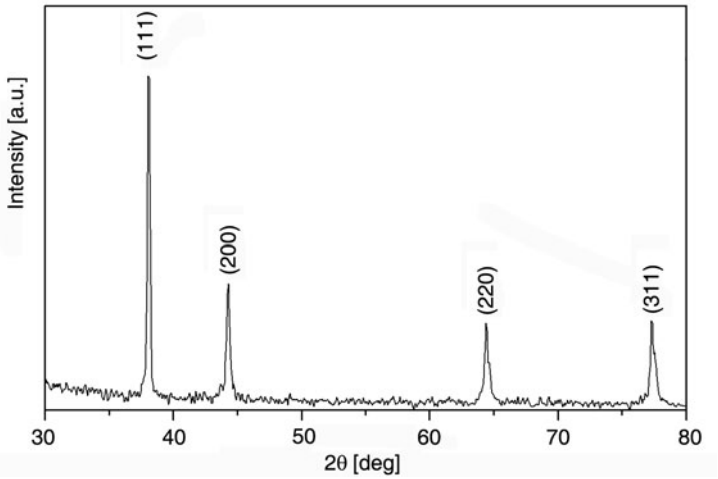

Fig. 1. XRD pattern of the as-prepared silver samples

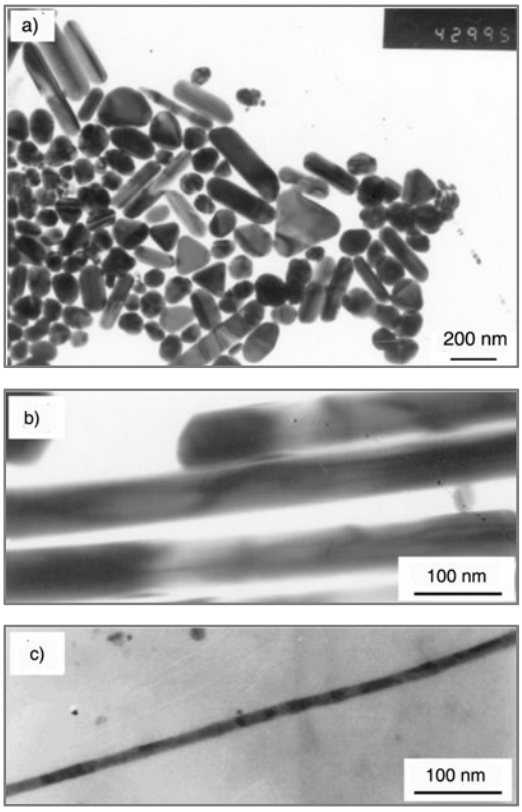

Fig. 2. TEM images of silver nanorods and nanowires prepared with 1.2 mM ascorbic acid in the presence of 1mM SDBS (a) and typical SEM image of individual nanorods (b) and nanowires (c)

The morphologies and structures of the products were investigated by the transmission electron microscopy (TEM); Figure 2a shows a typical TEM image taken from the orange-yellowish colloidal solution obtained using 1.2 mM ascorbic acid. It was clearly seen that the as-prepared samples consisted of an abundance of nanorods and nanowires, and relatively few spherical nanoparticles. The length of the nanorods ranges from 500 nm to 1.5 μm. The TEM of individual nanorods (Fig. 2b) shows that the average width of the nanorods is ca. 50–60 nm. The smallest aspect ratio of the rods is about 10 and the largest exceeds 40. The length of the nanowires ranges from 600 nm to 2.5 μm. The TEM of individual nanowires (Fig. 2c) shows that the average width of the nanowires is about 10–15 nm.

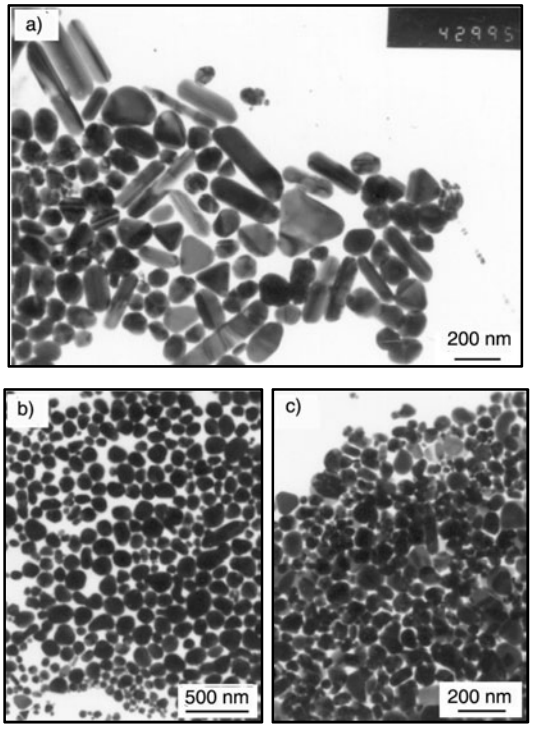

Fig. 3. TEM images of silver samples prepared using: a) 0.2 mM ascorbic acid in the presence of 1mM SDBS, b) 1.8 mM ascorbic acid in the presence of 1mM SDBS, c) 1.2 mM ascorbic acid in the presence of 10 mM SDBS

In the present study, the concentration of ascorbic acid plays a critical role in the formation of silver nanorods and nanowires. The silver nanoparticles with various morphologies were obtained as shown in Fig. 3 by changing the concentration of ascorbic acid from 1.2 mM to 0.2 mM and 1.8 mM. When the concentration of ascorbic acid was decreased to 0.2 mM, many nanorods, with a few triangular prisms and some nanoparticles were found in the products (Fig. 3a). It can be clearly seen that the aspect ratio of nanorods decreases upon decreasing concentration of ascorbic acid.

When it was increased to 1.8 mM, the products were dominated by spherical or irregular nanoparticles (Fig. 3b).

In addition, the SDBS concentration is another important parameter influencing the information on silver nanorods and nanowires. When no SDBS was introduced, $AgNO_3$ cannot be reduced by ascorbic acid and the reaction solution was still transparent after refluxing for 30 min at 100 °C. No silver nanoparticles were found in the solution by TEM. When the SDBS concentration is increased to 10 mM, spherical nanoparticles are the major products (Fig. 3c).

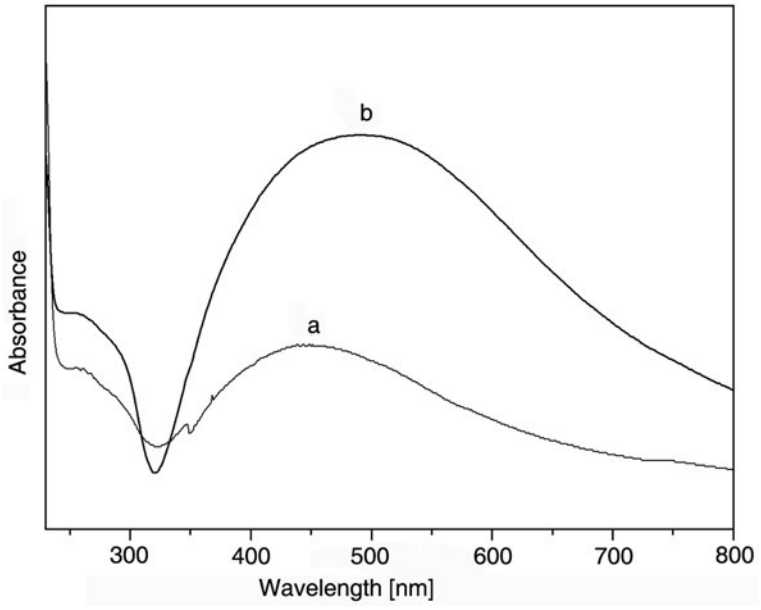

Fig. 4 UV-Vis absorption spectrum of silver nanocrystals prepared using:
a) 0.2 mM, b) 1.2mM ascorbic acid in the presence of 1 mM SDBS.

It is well known that gold, silver, and copper nanoparticles display plasmon absorption in the visible region, and silver nanoparticles usually have an absorption maximum at 404 nm [19]. The UV-visible spectra of the silver nanocrystals fabricated using various concentrations of ascorbic acid (0.2 mM and 1.2 mM) are shown in Figs. 4a, b, respectively. The optical properties of silver nanoparticles depend on shape, as shown in Fig. 4. This is due to the absorption of visible light both along the length of the nanorods (the longitudinal plasmon band) and along the width of the nanorods (the transverse plasmon band). The larger the aspect ratio, the more red-shifted the longitudinal plasmon band, as theory predicts [20] and experiment confirms [21–23]. Figure 4a displays an absorption maximum at 447 nm red-shifted by about 43 nm compared to the reported results. The reason is that the obtained nanocrystals consisting of some spherical nanoparticles and nanorods, which have smaller aspect ratio, are abundant. Since the silver nanorods and nanowires prepared

using 1.2 mM ascorbic acid have larger aspect ratio, Figure 4b shows absorption maximum at 495 nm, which is red-shifted by about 91 nm. As the shape of silver nanocrystals changed from spheres to rods and wires, the red-shift increased with the increasing aspect ratio. These experimental results strongly confirm the results predicted by the theory.

Acknowledgements

This work is supported by the awarded funds of excellent state key laboratory (No. 50323006).

References

[1] HUANG Y., DUAN X.F., WEI Q.Q., LIBER C.M., Science, 291 (2001), 630.
[2] VION D., AASSIAME A., COTTET A., JOYEZ P., POTHIER H., URBINA C., ESTEVE D., DEVORET M.H., Science, 296 (2002), 886.
[3] SUN X.M., LI Y.D., Chem. Eur. J., 9 (2003), 2229.
[4] MARTIN B.R., ANGELO S.K.ST., MALLOUK T.E., Adv. Funct. Mater., 12 (2002), 759.
[5] XIA Y., YANG P., SUN Y., WU Y., MAYERS B., GATES B., YIN Y., KIM F., YAN H., Adv. Mater., 15 (2003), 353.
[6] LIU Z., LIANG J., LI S., PENG S., QIAN Y., Chem. Eur. J., 10 (2004), 634.
[7] LI L.S., ALIVISATOS A.P., Adv. Mater., 15 (2003), 408.
[8] BRAUN E., EICHEN Y., SIVAN U., BEN-YOSEPH G., Nature, 391 (1998), 775.
[9] SLOAN J., WRIGHT D.M., WOO H., BAILEY G.S., BROWN G., YORK A.P.E., COLEMAN K.S., HUTCHISON J.L., GREEN M.L.H., Chem. Commun. (1999), 690.
[10] GOVINDARAJ A., SATISHKUMAR B.C., NATH M., RAO C.N.R., Adv. Mater., 12 (2000), 202.
[11] SUN Y.G., GATES B., MAYERS B., HERRICKS T., XIA Y.N., Nano Lett., 2 (2002), 165.
[12] ZHANG D.B., QI L.M., YANG J.H., MA J.M., CHENG H.M., HUANG L., Chem. Mater., 16 (2004), 872.
[13] HUANG M.H., CHOUDRY A., YANG P.D., Chem. Commun., (2000), 1063.
[14] JANA N.R., GEARHEART L., MURPHY C.J., Chem. Commun., (2001), 617.
[15] MURPHY C.J., JANA N.R., Adv. Mater., 14 (2002), 80.
[16] HU J.Q., CHEN Q., XIE Z.X., HAN G.B., WANG R.H., REN B., ZHANG Y., YANG Z.L., TIAN Z.Q., Adv. Funct. Mater., 14 (2004), 183.
[17] SUN Y., XIA Y., Adv. Mater., 14 (2002), 833.
[18] CASWELL K.K., BENDER C.M., MURPHY C.J., Nano Lett., 3 (2003), 667.
[19] ITAKURA T., TORIGOE K., ESUMI K., Langmuir, 11 (1995), 4129.
[20] EL-SAYED M.A., Acc. Chem. Res., 34 (2001), 257.
[21] FOSS C.A., HORNYAK G.L., STOCKERT J.A., MARTIN C.R., J. Phys. Chem., 98 (1994), 2963.
[22] LINK S., MOHAMED M.B., EL-SAYED M.A., J. Phys. Chem. B, 103 (1999), 3073.
[23] JANA N.R., GEARHEART L., MURPHY C.J., J. Phys. Chem. B, 105 (2001), 4065.

Received 2 November 2007
Revised 8 July 2008

Materials Science-Poland, *Vol. 27*, *No. 1*, *2009*

Structure and crystallization kinetics of amorphous Al–Ni–Si alloy

M. GÖGEBAKAN*, M. OKUMUS

[1]Department of Physics, Faculty of Art and Science,
Kahramanmaras Sutcu Imam University, Kahramanmaras, 46000, Turkey

In the present work, the structure and crystallization kinetics of rapidly solidified $Al_{70}Ni_{13}Si_{17}$ amorphous alloy have been investigated by a combination of differential scanning calorimetry (DSC) and X-ray diffractometry (XRD). Amorphous ribbons were obtained by melt spinning at wheel speeds higher than 10 m/s. Crystallization of amorphous $Al_{70}Ni_{13}Si_{17}$ alloy during continuous heating in DSC, takes places in three stages: (1) formation of fcc-Al and hexagonal phases; (2) growth of fcc-Al and hexagonal phases; (3) formation of fcc-Si and orthorhombic Al_3Ni phases. Isothermal annealing DSC traces for this amorphous alloy, the first crystallization peak showed a clear incubation period, and the Avrami time exponent *n* has been determined to be 2.4–2.8 using the Johnson–Melh–Avrami analysis. This suggested that the transformation reaction involved continuous nucleation and three dimensional diffusion-controlled growth. Electrical resistivity of the alloy was measured as 33×10^{-6} Ω·cm for the amorphous structure and 1×10^{-6} Ω·cm for the crystalline one. This study describes the structure and crystallization kinetics of a rapidly solidified $Al_{70}Ni_{13}Si_{17}$ amorphous alloy.

Key words: *amorphous alloys; rapid solidification; X-ray diffraction; calorimetry*

1. Introduction

Amorphous alloys are metallic alloys with no long range atomic order, in contrast to crystalline alloys showing long range order with a repeating unit cell. Amorphous alloys are usually produced by rapid solidification of the alloying constituents from the liquid phase at such high cooling rates that the atoms are frozen into their liquid configuration to form a metastable glass-like structure. For the last three decades, amorphous alloys have attracted great interest because of their good mechanical properties, useful physical properties and good chemical properties resulting from their new alloy composition and new atomic configurations. Particularly, great effort has

*Corresponding author, e-mail: gogebakan@ksu.edu.tr

been devoted to the production of Al-rich amorphous alloys, with the aim of utilizing a high strength material with light weight which may lead to applications in a number of fields [1–4]. Recently, Al-rich amorphous alloys have been produced in various Al–TM–RE ternary alloy systems, where TM is Fe, Co, Ni and RE is Y, La, Ce, by rapid solidification technique, and the resulting amorphous alloys exhibit high mechanical strength combined with low density, large glass-forming ability and distinctly appreciable glass transition phenomenon [5–10]. Although Al–TM–RE alloys systems could be easily amorphized by rapid solidification technique, these amorphous alloys contain expensive rare earth elements such as Y, La, Ce, and it is necessary to replace them with cheaper elements such as Si and Ni. Furthermore, the density of Si (2.3 g/cm^3) is lower than that of Y (4.45 g/cm^3), La (6.17 g/cm^3) and Ce (6.77 g/cm^3). Hence, rapidly solidified Al–Ni–Si amorphous alloys are better choice for practical application as materials with high strength, low density and useful physical properties.

In this study, we present the structure, crystallization kinetics and electrical resistivity of rapidly solidified $Al_{70}Ni_{13}Si_{17}$ amorphous alloy by a combination of differential scanning calorimetry (DSC), X-ray diffractometry (XRD) and four-probe techniques.

2. Experimental

Ternary alloy ingot with nominal composition $Al_{70}Ni_{13}Si_{17}$ (at. %) has been fabricated by melting of appropriate proportions of high purity Al, Si and Ni elements in a graphite crucible under an argon atmosphere. Rapidly solidified ribbons were manufactured by the single roller melt-spinning technique. By this technique, it is possible to quench the molten alloy at a cooling rate of 10^4–10^6 K/s. In order to obtain rapidly solidified ribbons, the ingot was re-melted in a quartz crucible and then molten alloy ejected through an orifice onto a single Cu wheel with a wheel surface velocity of 10–40 m/s. The resulting ribbons were typically 60–100 μm thick, 3–5 mm wide and up to several meters long. The amorphous/crystalline natures of the as-melt-spun and annealed ribbons were characterized by X-ray diffractometry (XRD) technique. The XRD experiments were performed using a Philips X'Pert Pro diffractometer with filtered CuK_α ($\lambda = 0.154$ nm), 35 kV and 50 mA. For phase identification, measurements were scanned for a wide range of diffraction angles (2θ) from 20° to 100° with the scanning rate of 5 deg/min. The crystallization of rapidly solidified ribbons was investigated by DSC (Perkin-Elmer DSC-7) using both continuous heating and isothermal annealing under a pure argon atmosphere. In order to ensure reliable temperature and heat release values, the DSC was calibrated using In (99.999 wt. % of pure In) and Pb (99.999 wt. % of pure Pb) standard. Continuous heating was performed at a constant heating rate of 20 K/min. Isothermal DSC measurements were carried out by annealing to various temperatures 5–15 K lower than their first crystallization peak temperatures with the heating rate of 20 K/min, and the heating duration of 3.5 h. For resistiv-

ity measurements, rapidly solidified ribbons were annealed for 30 min at various temperatures from 300 to 650 K, and then electrical resistivities of the samples were measured by the four-probe method.

3. Results and discussion

Formation of amorphous alloys by melt-spinning technique is strongly dependent on the processing parameters. The most important processing parameters are the wheel surface velocity, ejection pressure and ejection temperature. These parameters can modify the cooling rate, the viscosity of the melt and also the microstructure of the resulting ribbons. In the present work, we changed the surface velocity while keeping other parameters nominally constant. Figure 1 shows XRD spectra of the rapidly solidified $Al_{70}Ni_{13}Si_{17}$ alloys prepared using circumferential wheel speeds in the range 10–40 m/s. At the wheel speed of 10 m/s, the melt spun ribbon was very brittle and XRD trace showed the presence of peaks corresponding to elemental Al, Si phases and intermetallic Al_3Ni phases (as seen in Fig.1a). At wheel speeds greater than 10 m/s, the diffraction peaks from Al, Si and intermetallic Al_3Ni phases disappeared, and the XRD traces showed the broad halo peak indicating that the structure of the melt spun ribbon produced is amorphous.

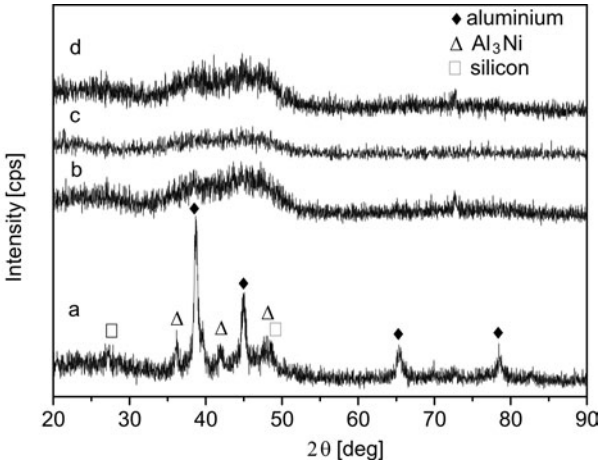

Fig. 1. XRD spectra of the $Al_{70}Ni_{13}Si_{17}$ alloys prepared at various wheel speeds: a) 10 m/s, b) 20 m/s, c) 30 m/s, and d) 40 m/s

Figure 2 shows a series of continuous DSC traces obtained from the rapidly solidified $Al_{70}Ni_{13}Si_{17}$ alloy which exhibited a broad halo peak in Fig. 1b–d. As seen in Fig. 2, the crystallization behaviour of amorphous $Al_{70}Ni_{13}Si_{17}$ alloys is very similar. The DSC traces of these amorphous alloys exhibit three exothermic peaks, indicating that structural transformation into final phase takes places in three single steps. It can

be seen that the crystallization onset temperature T_x and the first peak temperature T_1 are dependent on the wheel speed. T_x and T_1 decreased from 451 K to 442 K and from 463 K to 452 K, respectively, with increasing wheel speed from 20 m/s to 40 m/s.

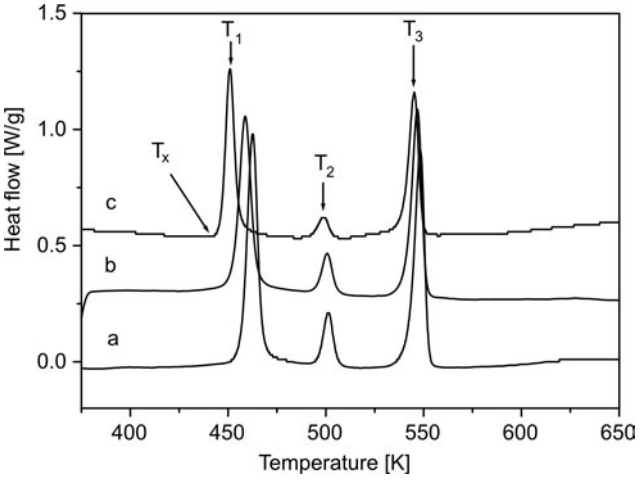

Fig. 2. Continuous DSC traces from an amorphous $Al_{70}Ni_{13}Si_{17}$ alloy manufactured at various wheel speeds: a) 20 m/s, b) 30 m/s, and c) 40 m/s

However, the crystallization peak temperature for other exothermic peaks (the second and third peak) remained constant and independent of wheel speed (Fig. 2). The crystallization onset temperature (T_x) and the three crystallization peak temperatures (T_1, T_2, T_3) are listed in Table 1.

Table 1. The crystallization onset temperature T_x and three crystallization peak temperatures T_1, T_2, T_3 of $Al_{70}Ni_{13}Si_{17}$ alloys manufactured using various wheel speeds

Wheel speed [m/s]	T_x [K]	T_1 [K]	T_2 [K]	T_3 [K]
20	451	463	501	548
30	447	459	501	547
40	442	452	500	545

The crystallization onset temperature and the three crystallization peaks temperatures are in good agreement with those reported by McKay et al. [11] for a similar alloy, as determined from their continuous DSC results. On the other hand, at temperatures below the first exothermic crystallization peak, there was no clear evidence of a glass transition effect, as would be expected for a marginal glass former. The absence of the feature characteristic of glass transition temperature could be explained assuming that during rapid solidification, a significant number of cluster distributions is formed. Under continuous heating, the clusters that are above the critical nucleation size grow even at lower temperatures. Therefore, glass transition temperature is hidden underneath the first

crystallization peak. In continuous heating analyses, the dependence of crystallization temperature on the heating rate can be used to estimate the associated crystallization activation energy by means of the Kissinger method [12]. The activation energies are presented in Table 2.

Table 2. Activation energies E_a (kJ/mol) for crystallization in $Al_{70}Ni_{13}Si_{17}$ alloys manufactured using different wheel speeds

Wheel speed [m/s]	1st peak [kJ/mol]	2nd peak [kJ/mol]	3rd peak [kJ/mol]
20	240	170	145
30	247	179	151
40	238	173	142

As seen in Table 2, the measured values of the overall activation energy for the first exothermic peaks (240±10 kJ/mol) were higher than those of the second (175±10 kJ/mol) and third exothermic peaks (145±10 kJ/mol), indicating a relatively stable amorphous structure. A similar result was reported by McKay et al [11] for Al–Ni–Si alloy. The higher activation energy implies that the energy barrier for the glass-to-crystallization phase transformation is higher, and that the amorphous structure is more stable at temperatures lower than the crystallization temperature.

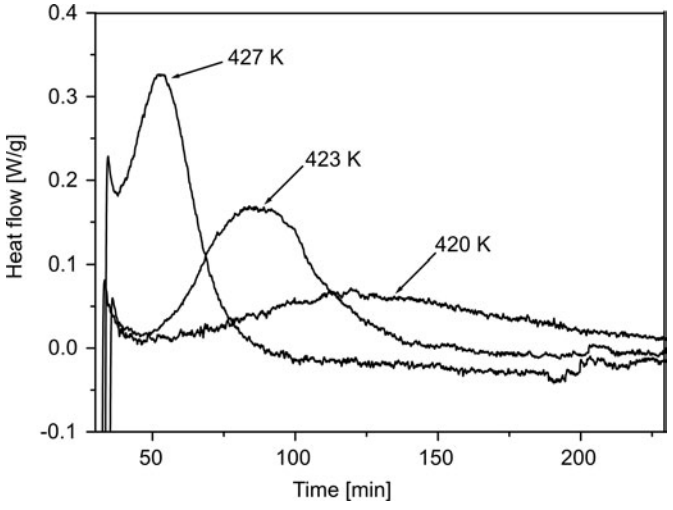

Fig. 3. DSC traces from amorphous $Al_{70}Ni_{13}Si_{17}$ alloys obtained after isothermal annealing at various temperatures

Figure 3 shows typical isothermal annealing DSC traces of amorphous $Al_{70}Ni_{13}Si_{17}$ alloy prepared at a wheel speed of 40 m/s. As seen in Fig. 3, isothermal annealing DSC traces occurred with a clear incubation period, followed by an exothermic peak. Then

a decrease in the reaction occurred, which is typical of a nucleation and growth mechanism. This suggests that the crystallization should take place by nucleation and growth, since the existence of the time dependent incubation period indicates a thermal activation nucleation barrier. The kinetics of crystallization can be expressed by the Johnson–Mehl–Avrami (JMA) equation [13] and the corresponding Avrami plots were made. This is shown in Fig. 4. From these plots, Avrami exponents n were obtained in the range 2.4–2.8. The Avrami exponent with $n = 2.5$ is associated with nucleation at a constant rate and diffusion-controlled growth [13]. Similar crystallization behaviour and Avrami exponents were reported by Gögebakan et al. for Al–Y–Ni alloy [14] and McKay et al. [11] for Al–Ni–Si alloy.

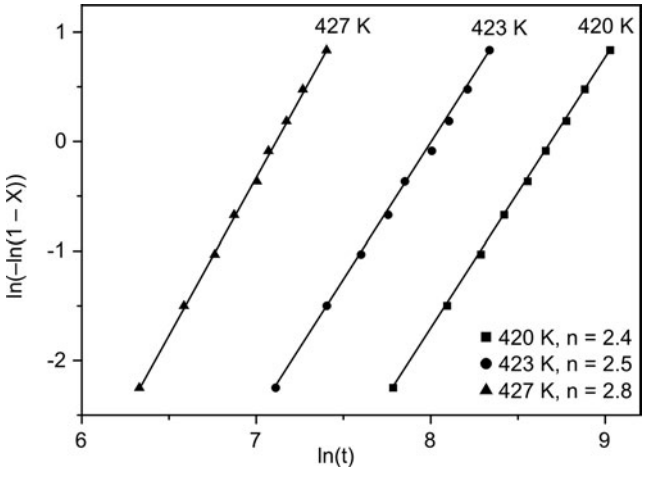

Fig. 4. Avrami plots for the amorphous $Al_{70}Ni_{13}Si_{17}$ alloy

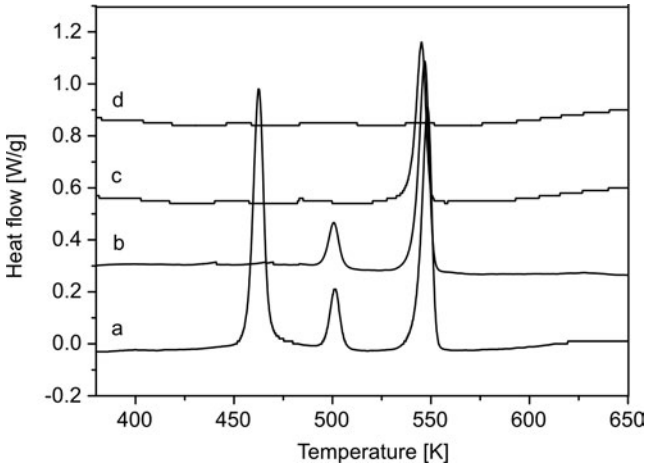

Fig. 5. DSC traces obtained during continuous heating of $Al_{70}Ni_{13}Si_{17}$ alloys as melt spun (a), and annealed for 30 min at: b) 475 K, c) 525 K, d) 575 K

To investigate the crystallization behaviour during the exothermic reactions, amorphous ribbons were heated up to the end temperatures of each exothermic reaction peak, and then cooled rapidly to freeze the microstructure for subsequent DSC and XRD analysis. Figure 5 shows a typical DSC trace obtained during continuous heating of $Al_{70}Ni_{13}Si_{17}$ alloys (prepared at a wheel speed of 40 m/s), as melt spun and annealed for 30 min at various temperatures from 475 to 575 K. The DSC traces of the as melt spun ribbon consisted of three exothermic peaks. At the annealing temperature of 475 K, the first exothermic peak disappeared and the DSC traces showed two exothermic peaks. However, the second and third exothermic peaks were not affected by the heat treatment. The DSC traces of the alloys annealed at 525 K showed only one exothermic peak. The DSC trace from alloys annealed at 575 K did not show any exothermic peak. Similar crystallization behaviour was reported by Kim et al. [4] for their Al–Y–Ni alloys.

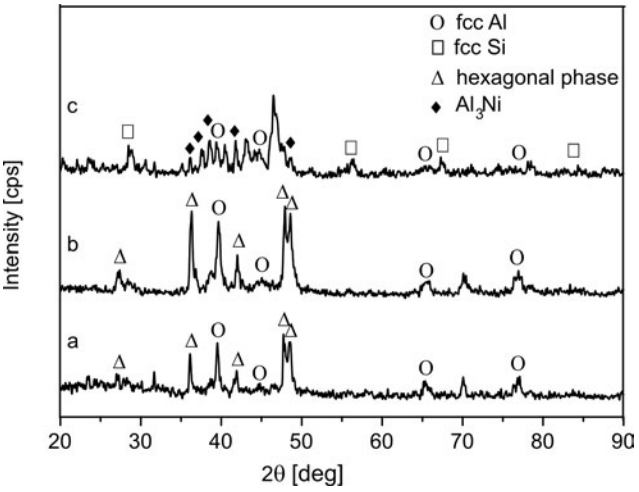

Fig. 6. XRD traces from amorphous $Al_{70}Ni_{13}Si_{17}$ alloys annealed for 30 min at: a) 475 K, b) 525 K, and c) 575 K

Figure 6 shows the XRD traces obtained from rapidly solidified $Al_{70}Ni_{13}Si_{17}$ alloys (prepared at a wheel speed of 40 m/s) after heated up to 475, 525 and 575 K, respectively. XRD results revealed that, after annealing to 475 K, fcc-Al and a hexagonal phase were formed. This hexagonal phase has been previously identified by Schumacher [15] and Legresy [16]. Therefore, this is an indication that, for amorphous $Al_{70}Ni_{13}Si_{17}$ alloys, the first crystallization peaks correspond to the formation of fcc-Al and hexagonal phases. After heating to 525 K, no new phase in the XRD traces were observed, and the intensities of present phases were increased. Therefore, the second exothermic peak in DSC corresponds to the growth of the fcc-Al and hexagonal phases. However, after annealing to 575 K, fcc-Al, fcc-Si and orthorhombic Al_3Ni phases were observed, at this stage of heating the hexagonal phase was no longer pre-

sent and this is indicating that it is metastable. This observation is in agreement with that of McKay et al [11] for Al-Ni-Si alloy.

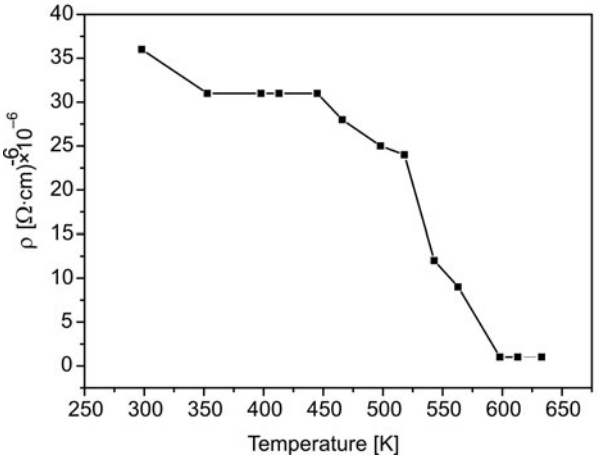

Fig. 7. Changes of electrical resistivity of $Al_{70}Ni_{13}Si_{17}$ alloys annealed at various temperatures

In order to understand the variation of the electrical resistivity with annealing temperature, amorphous ribbons were annealed for 30 min at various temperatures from 300 to 650 K. The changes in electrical resistivity with annealing temperature are shown in Fig. 7. As seen from the figure, the electrical resistivity remains nearly the same up to 450 K, which is about $33\times10^{-6}\Omega\cdot$cm. Therefore the electrical resistivity of the amorphous $Al_{70}Ni_{13}Si_{17}$ alloy is higher than that of pure Al (2.82×10^{-6} Ω·cm) and Ni (7.12×10^{-6} Ω·cm), and lower than that of Si (640×10^{2} Ω·cm). However, the highest resistivity value decreases significantly from 33×10^{-6} Ω·cm to 1×10^{-6} Ω·cm, on de-compositions of the amorphous phase to a fully crystalline phase. This suggests that, in Al–Si–Ni alloy, amorphous structure is responsible for the high resistivity.

4. Conclusions

The as-spun ribbon prepared at wheel speeds higher than 10 m/s is ductile, and the XRD traces showed a broad halo peak corresponding to the amorphous structure. At the wheel speed of 10 m/s, the melt spun ribbon was very brittle and XRD trace showed the presence of peaks corresponding to elemental Al, Si phases and intermet-allic Al_3Ni phase. Crystallization of amorphous $Al_{70}Ni_{13}Si_{17}$ alloy during continuous heating in DSC, takes places in three stages: (1) formation of the fcc-Al and hexagonal phases from the amorphous phase; (2) growth of the fcc-Al and hexagonal phases; (3) formation of fcc-Si and orthorhombic Al_3Ni phases. Crystallization of amorphous $Al_{70}Ni_{13}Si_{17}$ alloy during isothermal annealing at in the range 420–27 K show JMA

kinetics with the Avrami exponent of 2.4–2.8, corresponding to continuous nucleation and three dimensional diffusion-controlled growth. Electrical resistivity of the alloy was measured as 33×10^{-6} Ω·cm for the amorphous structure and as 1×10^{-6} Ω·cm for the crystalline structure.

Acknowledgements

We would like to thank the Turkish State Planning Organization (DPT) for its financial support, Project No. 103K-120-730, and Dr. Umit Alver for his technical assistance with electrical resistivity measurements.

References

[1] KIM Y.H., HIRAGA K., INOUE A., MASUMOTO T. , JO H.H., Mater. Trans. JIM., 35 (1994), 293.
[2] KIM Y.H., INOUE A. , MASUMOTO T., Mater. Trans. JIM., 31 (1990), 747.
[3] CHANG I.T.H., BOTTEN R.R., Mater. Sci. Eng. A, 226-228 (1997), 183.
[4] KIM W.T., GOGEBAKAN M., CANTOR B., Mater. Sci. Eng. A, 226–228 (1997),178.
[5] GÖGEBAKAN M., UZUN O., KARAASLAN T., KESKIN M., J. Mater. Proc. Techno., 142 (2003), 87.
[6] MUNOZ-MORRIS M.A., SURINACH S., GICH M., BARO M.D., MORRIS D.G., Acta Mater., 51 (2003), 1067.
[7] GANGOPADHYAY A.K., KELTON K.F., Philos. Mag. A, 80 (2000), 1193.
[8] BASSIM N., KIMINAMI C.S., KAUFMAN M.J., OLIVEIRA M.F., PERDIGÃO M.N.R.V., BOTTA FILHO W.J., Mater. Sci. Eng. A, 304–306 (2001), 332.
[9] GLORIANT T., PING D.H., HONO K., GREER A.L., BARO M.D., Mater. Sci. Eng. A, 304–306 (2001), 315.
[10] HONG S.J., WARREN P.J., CHUN B.S., Mater. Sci. Eng. A, 304–306 (2001), 362.
[11] MCKAY B.J., CIZEK P., SCHUMACHER P., O'REILLY K.A.Q., Mater. Sci. Eng. A, 304–306 (2001), 240.
[12] KISSINGER H.E., Anal. Chem., 29 (1957), 1702.
[13] CHRISTIAN J.W., *The Theory of Transformation in Metals and Alloys*, Pergamon Press, Oxford, UK, 1975.
[14] GÖGEBAKAN M., WARREN P.J., CANTOR B., Mater. Sci. Eng. A, 226–228 (1997), 168.
[15] SCHUMACHER P., *Nucleation in Aluminium Alloys Studied Using Devitrifation*, Ph.D. Thesis, University of Cambridge, Cambridge, UK, 1993.
[16] LEGRESY J.M., *Characterization and Kinetics of the Crystallization of Al–Ni–Si Amorphous* Alloys, Ph.D. Thesis, Institut National Polytechnique de Grenoble, 1987.

Received 8 October 2007
Revised 29 August 2008

Materials Science-Poland, *Vol. 27*, *No. 1*, *2009*

Preparation and pressureless sintering of nanostructured zirconia–titania composite powders

Y. ZHANG[1, 2], L. HU[1*], T. HU[1, 2], J. CHEN[1]

[1]State Key Laboratory of Solid Lubrication, Lanzhou Institute of Chemical Physics, Chinese Academy of Sciences, Lanzhou 730000, China

[2]Graduate School of the Chinese Academy of Sciences, Beijing 100039, China

TiO_2 doped yttria–zirconia nanosized powders were prepared by the coprecipitation method, with particle sizes of 10–15 nm. The effects of TiO_2 content and calcining temperature on the phase structure and grain size of powders were studied. Nanopowders were compacted uniaxially and densified in a muffle furnace. Densification studies show that the dense pellet of yttria stabilized tetragonal zirconia polycrystal (Y-TZP)–TiO_2 is obtained after sintering at 1200 °C. The presence of TiO_2 inhibits grain growth and suppresses the densification process of pure Y-TZP. Ceramics with a mean grain size of 39 nm can be obtained based on the powder that has been doped with 30 mol % TiO_2.

Key words: *ZrO_2–Y_2O_3–TiO_2; crystallization; nanocomposites; pressureless sintering*

1. Introduction

Nanostructured materials, characterized by an ultrafine grain size, have stimulated much research interest by virtue of their unusual mechanical, electrical, optical, and magnetic properties. Nanocrystalline ceramics, in which grain sizes smaller than 100 nm occur, are believed to have special characteristics, such as superplasticity at low temperature [1–4]. However, fabrication of a dense bulk nanocrystalline ceramics is very challenging, since an inevitable grain growth occurs at relatively high sintering temperatures needed for densification. Nanocomposites constructed by dispersing second-phase nanosize particles within the matrix grains and on the grain boundaries, lead to a new concept of material design which significantly improves strength and also provides moderate enhancement in fracture toughness [5]. On the other hand, the nano/nano-type composites which were composed of the dispersoids and matrix grains (both of nanometer size) showed additionally attractive properties, due to a peculiar

* Corresponding author, e-mail: lthu@lzb.ac.cn, zhysh@lzb.ac.cn

role of nanosized phases in physical and mechanical properties [5, 6]. Therefore, nanocomposites have been the subject of intensive research in recent years.

ZrO_2–Y_2O_3 systems find a wide variety of applications in many advanced structural, high-temperature and electrical applications due to their unique properties such as high hardness, low wear resistance, low coefficient of friction, high elastic modulus, chemical inertness, low thermal conductivity, high fracture toughness and high melting point [7, 8]. Nevertheless, their mechanical properties at room temperature do not deliver guaranteed results. It is well known that the strength of yttria stabilized tetragonal zirconia polycrystal (Y-TZP) may decrease drastically during ageing in air at temperatures between 100 °C and 400 °C [9–11]. At these temperatures, the tetragonal–monoclinic (t–m) phase transformation is activated by the environment, and the volume expansion that takes place can generate microcracks in the transformed surface, thereby degrading the strength and surface properties of the material. It has been reported that the uniform distribution of Al_2O_3 to ZrO_2 matrix can suppress the low-temperature degradation of mechanical properties. In addition, a dopant can control the microstructure by a prevention of the abnormal grain growth and refinement of matrix grains [12–14]. Thus it seemed interesting to prepare Y_2O_3 doped ZrO_2 (Y-ZrO_2) based mixed oxides and to study their structural and morphological behaviour. Similar materials are also of interest in the field of the preparation of Y-TZP based ceramics as engineering materials.

In earlier studies, ZrO_2–Y_2O_3–Al_2O_3 and ZrO_2–Y_2O_3–CuO nanocrystalline powders were prepared using the chemical coprecipitation method. On this basis, Y-TZP/Al_2O_3 and Y-TZP/CuO nanoceramics were prepared successfully by the authors [15–18] by pressureless sintering. Tetravalent dopants such as Si^{4+}, Ce^{4+} etc., were also found to be effective agents to stabilize t-ZrO_2 forming cationic networks and high-energy surface layers [19, 20]. In the zirconia-rich end of the titania phase equilibrium diagram, TiO_2 is known to dissolve into tetragonal ZrO_2 up to 18 mol % at high temperatures and act as a stabilizing agent in a manner similar to Y_2O_3 and CeO_2 [21]. Therefore, ZrO_2–Y_2O_3–TiO_2 could be an interesting challenge. In this work, ZrO_2 –Y_2O_3–TiO_2 nanosized powders with various TiO_2 contents were synthesized by chemical coprecipitation. The sintering behaviour and microstructure of the bulk ceramics prepared by pressureless sintering was investigated.

2. Experimental

Homogeneous 3Y-ZrO_2 and TiO_2 powder mixtures with nanosized particles were synthesized by coprecipitation [15, 16]. $ZrOCl_2 \cdot 8H_2O$, $Y(NO_3)_3 \cdot 6H_2O$ and $TiCl_4$, selected as starting materials, were dissolved in deionized water to prepare a transparent metal salt solution with TiO_2 content from 5 mol % to 30 mol% relative to 3Y-ZrO_2. $NH_3 \cdot H_2O$ solution was prepared separately with deionized water. The two solutions were then mixed and continuously stirred to obtain a homogenous solution, and the pH of the solution was adjusted to 9–10 by adding ammonia. The precipitate was filtered

and washed repeatedly with deionized water to remove NO_3^- and Cl^- anions and then washed with ethanol for three times. Then the precipitates were dried in an oven for 24 h and calcined at various temperatures for 2 h. The product was ground in an agate mortar, and nanosized powders were obtained. The products were referred to as ZT05, ZT10, ZT15 and ZT30 for 3Y-ZrO_2–TiO_2 binary oxide samples with TiO_2 contents from 5 mol % to 30 mol% relative to 3Y-ZrO_2. X-ray powder diffraction (XRD) for the powders was recorded on a D/max-RB diffractometer using CuK_α radiation (λ = 0.15406 nm). The EDS analysis of powders was performed on a scanning electron microscope (SEM, JEOL JSM-5600LV). The grain size was estimated from the full width at half maximum (FWHM) by the Scherrer equation and confirmed by a transmission electron microscope (TEM, JEM1200EX).

The green compact pellets were obtained by uniaxial pressing of the 3Y-ZrO_2 and 3Y-ZrO_2–TiO_2 powders at 1000 MPa for 5 min in air at room temperature. The nanocomposites were prepared by heating the green compacts in air at the rate of 5 °C/min up to a predetermined temperature and sintering for 4 h at that temperature. Archimedes' principle was used to measure the bulk density. XRD (D/max-RB) was used to deduce the crystalline phases and grain size of the sintered samples. The fracture surfaces of the sintered pellets were examined by scanning electron microscopy (SEM, JEOL JSM-6701F).

3. Results and discussion

3.1. Morphological properties and phase structure of the powders

The XRD patterns of 3Y-ZrO_2, and four mixed oxides with various TiO_2 contents after calcination at 600 °C are shown in Fig. 1. It is seen that the ZT30 and ZT15 after calcination at 600 °C were in an amorphous form. For the ZT10, the XRD shows a line at 30° corresponding to tetragonal ZrO_2. Although the XRD patterns of ZT10 have a feature line of tetragonal ZrO_2, the sample exhibits mostly the characteristics of amorphous phase. Relatively speaking, the ZT05 exhibits stronger tetragonal phase structure.

Figure 2 shows the XRD patterns of binary oxide samples after calcination at 800 °C. One can see that the XRD patterns of the five mixed oxides show the strongest diffraction peak of t-ZrO_2 phase. The 3Y-ZrO_2, ZT05 and ZT10 samples also show other diffraction peaks corresponding to the monoclinic phase structure, except for the ZT15 and ZT30 samples with a single t-ZrO_2 phase. The inset in Fig. 2 represents the relationship between TiO_2 content and phase composition. The volume fraction of the monoclinic phase (V_m) was determined by the empirical formula [22]:

$$V_m = \frac{[I_m(111) + I_m(11\bar{1})]}{[I_m(111) + I_m(11\bar{1}) + I_t(111)]}$$

where I_m denotes the intensities of the monoclinic peaks, and I_t denotes the intensities of the tetragonal peaks.

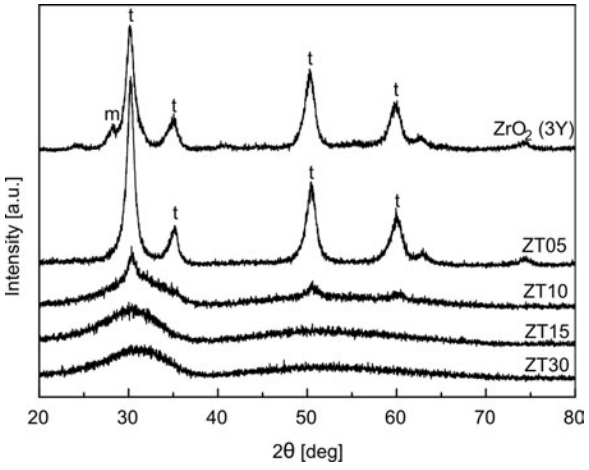

Fig. 1. XRD patterns of 3Y-ZrO_2 and 3Y-ZrO_2–TiO_2; t – tetragonal, m – monoclinic

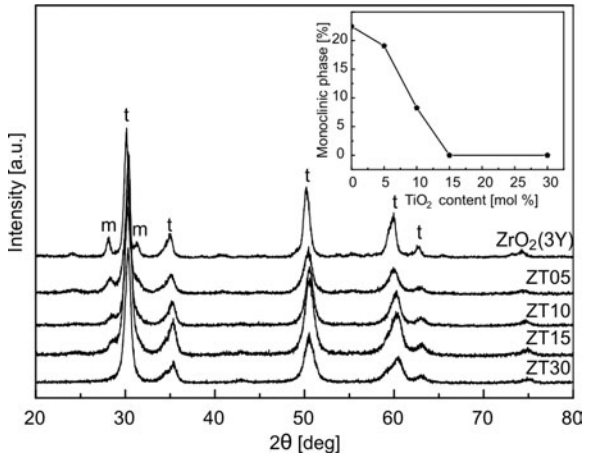

Fig. 2. XRD patterns of 3Y-ZrO_2 and 3Y-ZrO_2–TiO_2 powders calcined at 800 °C; t – tetragonal, m – monoclinic. The inset represents the relationship between TiO_2 content and phase composition

It can be seen that the phase composition follows a decreasing trend in monocline volume fraction as TiO_2 content increases. The monocline volume fraction of ZT05 powders is 19.1 vol. %. In the ZT10 sample, the monocline content decreases to 8.3 vol. %. The peak of monoclinic phase disappeared when the TiO_2 content increased further. It seems that the addition of TiO_2 delayed the phase transformation of zirconia from the tetragonal metastable phase to thermally stable monoclinic phase at 800 °C.

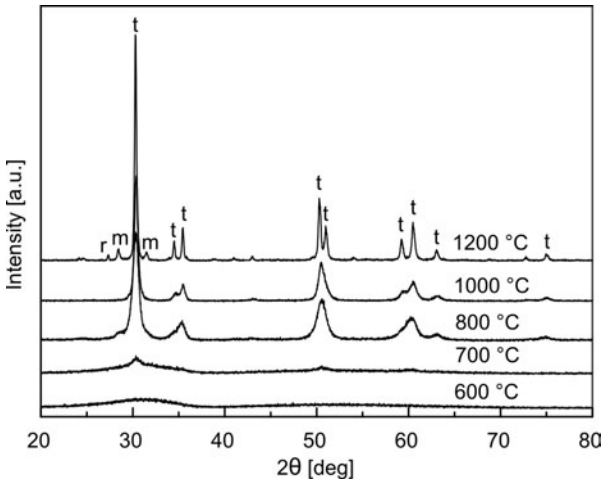

Fig. 3. XRD patterns of ZT15 powders calcined at various temperatures; t – tetragonal, m – monoclinic, r – rutile

The crystallization process with increasing temperature for the dried 3Y-ZrO_2 powder with 15 mol % TiO_2 was studied by the XRD technique, as shown in Fig. 3. It indicates that the dried gel existed as a totally amorphous mixture, and heating at temperatures lower than 700 °C did not cause any crystallization of the gels. Above 700 °C, there appeared crystallization peaks of the tetragonal ZrO_2 phase. The t-ZrO_2 peaks, with large full widths at the half maximum, indicate that the average crystallite size was small. With increasing temperature, the higher intensity and much sharper ZrO_2 peaks were observed. The XRD pattern after calcination at 1000 °C shows only t-ZrO_2. But rutile-TiO_2 and m-ZrO_2 were found to appear at 1200 °C.

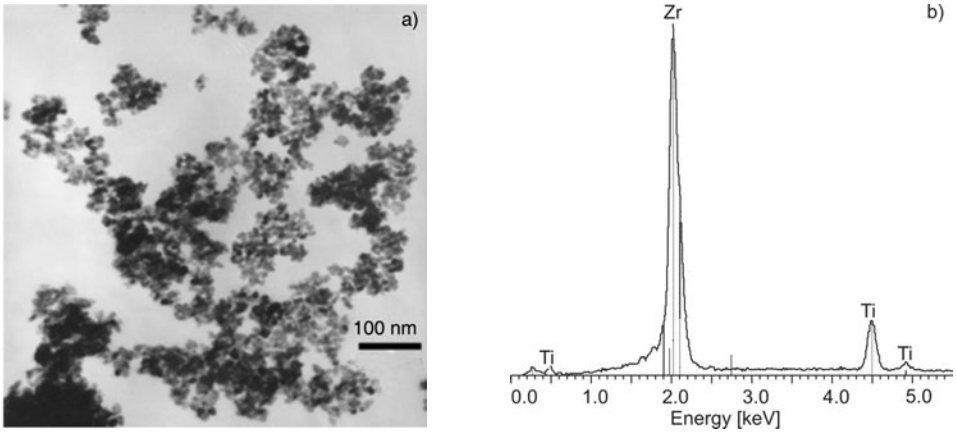

Fig. 4. TEM image (a) and EDX spectrum (b) of the ZT15 powder after calcination at 800 °C

Figure 4 shows the TEM photograph and EDS profile for ZT15 powders after calcination at 800 °C. It is seen that the agglomerates in Fig. 4a consist of almost spheri-

cal primary crystalline particles with the sizes of 10–15 nm. The EDS analysis exhibited clear peaks of Zr and Ti from any detected site. These results indicate that the homogeneous nanosized composite powder could be obtained by this coprecipitation process.

3.2. Sintering behaviour and microstructures

Figure 5 shows relative densities of specimens of various compositions in function of sintering temperatures. It can be seen that the presence of TiO_2 suppresses the densification process of Y-TZP. In samples without addition of TiO_2, densification starts at 600 °C and increases continuously [17, 18].

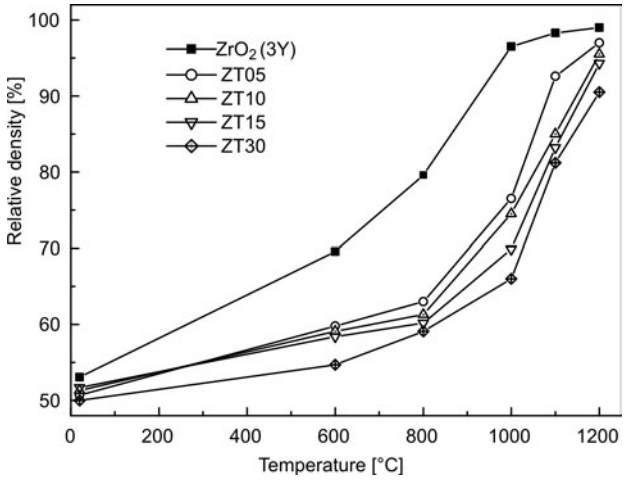

Fig. 5. Relative density in function of the sintering temperature

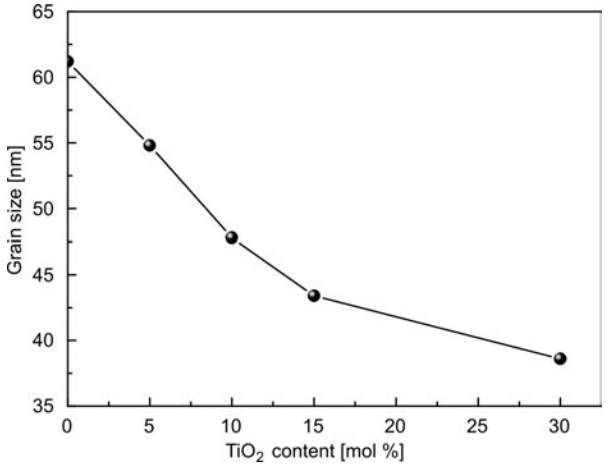

Fig. 6. Effect of TiO_2 content on the grain size of Y–TZP–TiO_2 sintered at 1200 °C

The powder doped with TiO_2 exhibits a lower sintered density at the same temperature. Note that, after sintering at 600 °C, low densities (about 60%) are obtained for the samples doped with TiO_2, but all 3Y-ZrO_2–TiO_2 oxides can be densified above 90% at 1200 °C. Effect of TiO_2 content on the grain size of Y-TZP sintered at 1200 °C is presented in Fig. 6. Grain size was calculated from X-ray line broadening. Obviously, the presence of TiO_2 inhibits grain growth dramatically. The powder that has been doped with 30 mol % TiO_2 and sintered at 1200 °C has a very small grain size (only 39 nm): the SEM micrograph of this specimen is shown in Fig. 7. Some uniaxial grains and polyhedral morphology are found in the SEM micrograph. The grains have a primary diameter of about 50–100 nm, which is larger than that determined from the corresponding X-ray peak broadening. The grains in the SEM photograph could be agglomerates comprised of several individual grains [18].

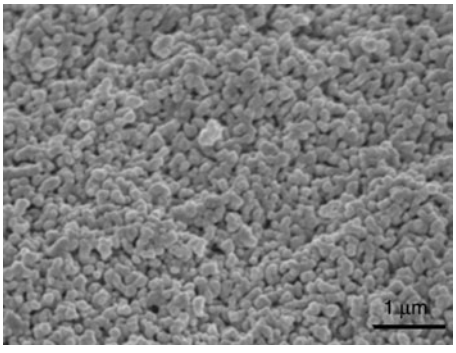

Fig. 7. SEM fractograph of Y-TZP/30mol %TiO_2 sintered at 1200 °C

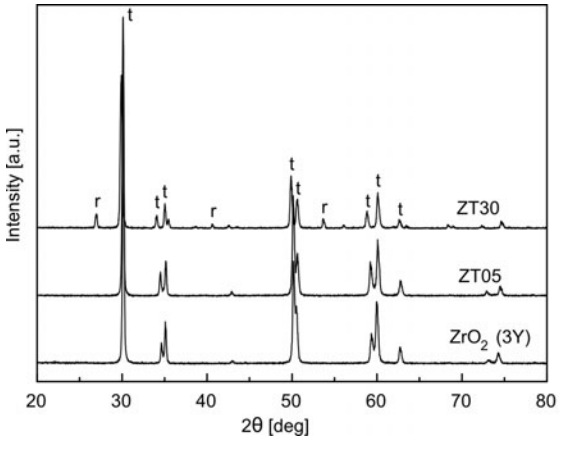

Fig. 8. The XRD patterns of the zirconia based nanocomposites sintered at 1200 °C; t – tetragonal, r – rutile

Evolutions of phases were investigated in function of sintering temperature, using X-ray diffraction. The phase composition of the Y-TZP/TiO_2 nanocomposites re-

mains almost unchanged after sintering at temperatures up to 1200 °C (see Fig. 8). The XRD patterns of the three samples show the strongest diffraction peak of t-ZrO_2 phase. The sintered sample doped with 30 mol % TiO_2 also showed the other diffraction peaks for the rutile phase structure.

4. Conclusions

Homogeneous 3Y-ZrO_2–TiO_2 nanosized particles can be obtained by a coprecipitation process. The presence of TiO_2 inhibits grain growth and suppresses the densification process. The dense zirconia based nanocomposites with a fine grained microstructure can be pressurelessly sintered in air using a powder prepared by coprecipitation. The sintered bodies (1200 °C) of doped TiO_2 (30 mol %) were composed mainly of tetragonal and a small amount of rutile phase, with a very small grain size (only 39 nm) calculated by X-ray line broadening.

Acknowledgement

Financial support from the Innovative Group Foundation from NSFC (Grant No. 50721062) and the China National Science and Technology Program 973-2007CB607606 is acknowledged.

References

[1] KARCH J., BRRINGER R., GLEITER H., Nature, 330 (1987), 556.
[2] MAYO M. J., Int. Mater. Rev., 41 (1996), 85.
[3] MAYO M. J., Mater. Design., 16 (1993), 323.
[4] SAKKA Y., SUZUKI T.S., MORITA K., NAKANO K., HIRAGA K., Scr. Mater., 44 (2001), 2075.
[5] CHOI S. M., AWAJI H., Sci.Techn. Adv. Mater., 6 (2005), 2.
[6] YOSHIMURA M., OH S.T., SANDO M., NIIHARA K., J. Alloys Compds., 290 (1999), 284.
[7] AI D.S., KANG S.H., Ceram. Int., 30 (2004), 619.
[8] SHUKLA S., SEAL S., Int. Mater. Rev., 50 (2005), 45.
[9] FEDER A., ANGLADA M., J. Eur. Ceram.Soc., 25 (2005), 3117.
[10] MASAKI T., Int.J.High Technol.Ceram., 2 (1986), 85.
[11] KOBAYASHI K., KUWAJIMA H., MASAKI T., Solid State Ionics, 3-4 (1981), 489.
[12] TSUKUMA K., UEDA K., J. Am. Ceram. Soc., 68 (1985), 4.
[13] SRDIC V.V., WINTERER M., HAHN H., J.Am.Ceram.Soc., 83 (2000), 1853.
[14] ANTSIFEROV V.N., SEVASTIANOVA I.G., Nanostructured Materials, 6 (1995), 683.
[15] ZHANG Y.S., HU L.T., YUAN S.L., CHEN J.M., LIU W.M., Mater. Mech.Eng., 30 (2006), 75.
[16] ZHANG Y.S, HU L.T., ZHANG H.S, CHEN J.M., LIU W.M., J. Mater. Process. Technol., 198 (2008), 191.
[17] ZHANG Y.S., CHEN J.M., HU L.T., LIU W.M., Mater.Lett., 60 (2006), 2302.
[18] ZHANG Y.S., HU L.T., LI H.K., CHEN J.M., J. Am. Ceram. Soc., 91(2008),1332.
[19] DEL MONTE F., LARSEN W., MACKENZIE J.D., J. Am. Ceram. Soc., 83 (2000), 628.
[20] LI P., CHEN I.W., HAHN J. E.P., J. Am. Ceram. Soc., 77 (1994), 118.
[21] NAWA M., BAMBA N., SEKINO T., NIIHARA K., J.Eur.Ceram.Soc., 18 (1998), 209.
[22] ZHANG Y.S., HU L.T., CHEN J.M., LIU W.M., Adv. Eng. Mater., 8 (2006), 271.

Received 22 November 2007
Revised 14 October 2008

Materials Science-Poland, *Vol. 27*, *No. 1*, *2009*

Construction of the master sintering curve for submicron size α-Al_2O_3 based on non-isothermal sintering containing lower heating rates only

W. SHAO, S. CHEN*, D. LI, H. CAO, S. ZHANG

College of Physics Science, Qingdao University, Qingdao 266071, P. R. China

The master sintering curve (MSC) is quite useful for analyzing the shrinkage behaviour of ceramics. In this study, the shrinkage behaviour for α-Al_2O_3 with a mean particle size of 350 nm during constant-heating-rate sintering were evaluated based on the MSC theory. An MSC for the above powder has been constructed using dilatometry data containing heating rates lower than 5 °C/min only with the help of combined-stage sintering model. The validity of the MSC has been verified by a few experimental runs. A comparison between predicted and experimental shrinkage curves showed good consistency, thus confirming that it is possible to control shrinkage behaviour using the MSC. The concept of the MSC has been used to evaluate the apparent activation energy for the above powder, and a high value of 1035 kJ/mol was obtained.

Key words: *low heating rate; master sintering curve; apparent activation energy; α-Al_2O_3*

1. Introduction

Sintering is a crucial step in the fabrication of α-Al_2O_3 ceramic components from a powder compact and involves microstructure evolution through the action of several different mechanisms [1]. Analysis of densification during non-isothermal sintering with constant heating rates allows one to follow more closely microstructure evolution.

Since the 1940s, many researchers have proposed sintering theories that have been verified by experimental examinations [2, 3]. These theories are, however, limited to a single transportation process and a single stage. Such theories are insufficient for evaluating sintering behaviours. Hansen et al. [4] proposed a generalized model with a sintering equation for the shrinkage rate, quantifying sintering as a continuous process from the beginning to the end. The microstructure is characterized by two separate parameters representing the geometry and scale (average grain size). Based on the generalized model, Su and Johnson [5] extended a classic sintering theory and proposed the master sintering curve (MSC).

*Corresponding author, e-mail: shaouchen@126.com

The MSC is empirically derived from densification data obtained over a range of heating rates [6]. When a proper activation energy is used, all the data converge onto a single curve, the MSC. The activation energy can be readily estimated with just a few dilatometer experiments if it is unknown beforehand. Once established, the MSC makes it possible to predict the final density after arbitrary temperature-time excursions. It is particularly useful when considering alternative sintering methods [7]. This curve is sensitive to such factors as the starting morphology of the powder, fabrication route, dominant diffusion mechanism and heating condition used for sintering. Thus the MSC curve can also be used as an aid to compare the sinterability of various powders [8–10] and to know the effects of additives, atmosphere and fabrication procedure of sintering [6]. In the MSC theory, $\Phi(\rho)$ which is function only of density, is given as the function of temperature and time:

$$\Phi(\rho)=\Theta(t,T(t))=\int_0^t \frac{1}{T}\exp\left(-\frac{Q}{RT}\right)dt \tag{1}$$

where Q is the apparent activation energy for sintering, R – the gas constant, T – the absolute temperature, t – the time. In this case, if one dominant diffusion mechanism exists and the microstructure is a function only of density, a unique MSC can be obtained dependent on the powder and green body characteristics, which are independent of the heating profile.

The relationship between the density ρ and Θ is defined as the master sintering curve. For the construction of MSC, a series of runs at constant heating rates over a range of heating rates is needed. In the past, the heating rate used for the construction of the MSC for α-Al_2O_3 inevitably contains higher values (higher than the heating rate of 5 °C/min) [6, 11, 12], little attention was paid to the sintering process containing heating rates lower than 5 °C/min only.

It is well known that surface diffusion inhibits sintering, particularly at low temperatures and during the earliest stages of sintering. In constant heating rate sintering, this inhibition diminishes with time and increased temperature. Estimates of the activation energy of densification are biased upward by this surface diffusion effect, particularly at low heating rates. The MSC for low heating rates in the presence of low activation energy surface diffusion would be biased to higher temperatures from those at higher heating rates.

In ceramic powder processing, high heating rates are often used to enhance sintering and reduce grain growth. The essence of this concept is that fast heating rates favour densification instead of grain growth in coarsening sensitive systems (i.e., with higher activation energy for densification than for grain growth). In these systems, a slow heating rate results in grain coarsening by surface diffusion which is able to operate through low temperature ranges. Conversely, a high heating rate takes the system to high temperatures where a high densification rate is favoured before surface diffusion causes grain growth. Moreover, a slower heating rate produced a higher densification of samples because time available for densification in this case was longer.

The objectives of this study were to construct the MSC for α-Al_2O_3 based on non-isothermal sintering containing lower heating rates only, to determine whether the MSC can be applied to predict and control the α-Al_2O_3 sintering, and to apply the MSC to determine the sintering activation energy.

2. Experimental

For constant-heating-rate sintering, α-Al_2O_3 powder (99.9% purity, Dalian Luming Nanometer Material Ltd, Dalian, China) having an average particle size of 350 nm was mixed with 1 wt. % adhesion agent, dried, granulated, and screened to –60 mesh. The powder was pressed using a uniaxial pressure of 80 MPa and then further consolidated by cold isostatic pressing at 250 MPa to create bars of ca. 5×5×45 mm^3. The binder was burned out at 500 °C. This resulted in negligible densification but provided green strength and minimized contamination from any adsorbed species in the raw powder. The green density was measured by the geometric method. The green density of α-Al_2O_3 powder compacts was 2.08±0.03 g/cm^3. The value of 3.98 g/cm^3 was used as the theoretical density (ρ_0), which was the single crystal density.

The shrinkage of α-Al_2O_3 samples was measured with a push rod type dilatometer in the axial direction. The length change measurements were made with a linear voltage differential transducer (LVDT) which was maintained at a constant temperature by means of water circulation from a constant temperature bath. The accuracy of the measurement of the change in length was within ±0.1 μm. The temperature was measured using a calibrated thermocouple placed directly above the sample. A small force of 0.2 N was applied to the sample through the push rod.

First, two green compacts were heated to the peak temperature (the temperature corresponding to the end of the sintering) at the heating rate of 2 and 5 °C/min. Secondly, three green compacts were sintered by heating up to 1200, 1350 and 1500 °C with holding time for 6 h at the heating rate of 5 °C/min. Finally, other runs for non-isothermal sintering were carried out in the same system by heating at 1 °C/min to 1115 °C, 2 °C/min to 1250 °C, 3 °C/min to 1420 °C, 4 °C/min to 1575 °C and 5°C/min to 1650 °C without holding dwell time, respectively. Apparent densities of the sintered samples were determined by the Archimedes method.

3. Results and discussion

3.1. Construction of the master sintering curve

Figure 1 shows temperature dependence of the $\Delta L/L_0$ of α-Al_2O_3 under two heating rates. The dilatometric curves of Fig. 1 were replotted as the relative density ver-

sus temperature (Fig. 2). The $\Delta L/L_0$ (shrinkage) values were converted into the time-dependent relative density ρ using the following dependence [13]:

$$\rho = \frac{\rho_G}{\left(1-\frac{\Delta L}{L_0}\right)^3}\frac{1}{\rho_0} \tag{2}$$

where ρ_G is the density of the green compact, ρ_0 is the theoretical density. The curves have the familiar sigmoidal shape and generally shifted to higher temperatures with increasing heating rate.

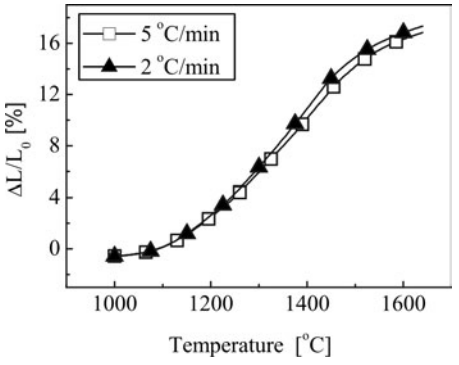

Fig. 1. Sintering curves for α-Al_2O_3 powder compacts at two heating rates

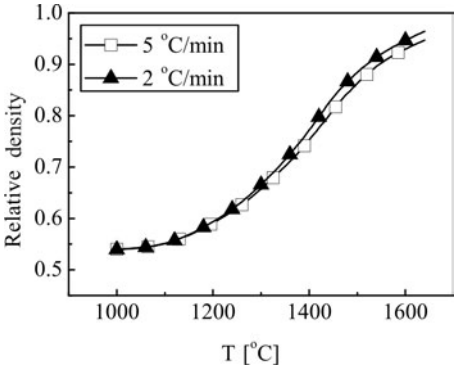

Fig. 2. Relative density in function of sintering temperature

For the construction of MSC, the integral of Eq. (1) and the experimental density should be known. The dilatometry can be conveniently used to determine the density since the instantaneous density at all times can be obtained from the dilatometric data [14]. For the calculation of Θ, the activation energy (a characteristic quantity that elucidates the fundamental diffusion mechanisms during the sintering process) should be

known. If the activation energy is unknown, it can be estimated with a good precision from Θ vs. density ρ data [6, 15].

For this purpose, initially, an estimate is made for the activation energy Q, and the MSCs for all the heating profiles are computed using Eq. (1). If the correct value of Q has been given, all the data converge to a single curve. A curve (a polynomial function) can be fitted to all the data points, and then the convergence of the data to the fitted line can be quantified through the sum of the residual squares of the points with respect to the fitted line. Another estimate of Q is made, and the process is repeated (Fig. 3a–d). When the best estimate of Q is found, the mean of residual (sum of residual squares divided by total number of data points) is a minimum.

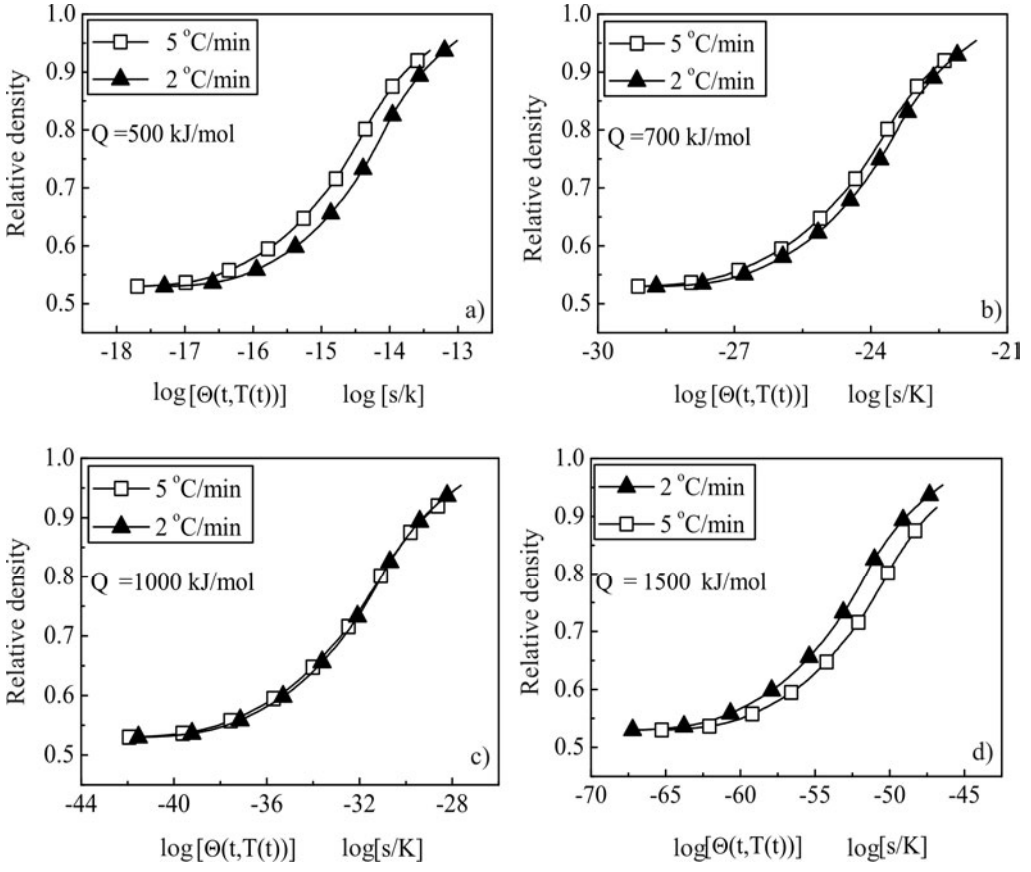

Fig. 3. Construction of a ρ–Θ curve for various heating profiles for a chosen value of activation energy: a) 500 kJ/mol, b) 700 kJ/mol, c) 1000 kJ/mol, d) 1500kJ/mol

The results for such an exercise for the alumina sintering data of Fig. 2 are shown in Fig. 4.The minimum is reached at ca. 1035 kJ/mol, indicating the estimated sintering activation energy. It is a high estimate, considering the reported activation energies for alumina in the literature [11, 12].

The activation energy of α-Al_2O_3 obtained by Tatami et al. [11] for heating rates 7.5–20 °C/min was 555 kJ/mol based on the MSC theory. In their experiments, the powder was uniaxially molded at 50 MPa, followed by cold isostatic pressing at 200 MPa. Shrinkage behaviour during sintering of the green bodies was evaluated using an electric furnace equipped with a dilatometer. The samples were heated to 1400 °C at constant heating rates (7.5, 10, 15, 20 °C/min). The shrinkage ranging from 2.5 to 17.5% was analyzed. It was found that the MSCs obtained by sintering at the heating rate of 3–5 °C/min did not correspond to that based on the heating rate of 7.5–20 °C/min [11]. It can be presumed that contribution of the surface diffusion for the slow heating rate becomes large. For this reason, in firing at 3–5 °C/min, densification proceeded by a diffusion mechanism different from the others. In other words, the activation energy at 3–5 °C/min sintering differed from that at 7.5–20 °C/min firing.

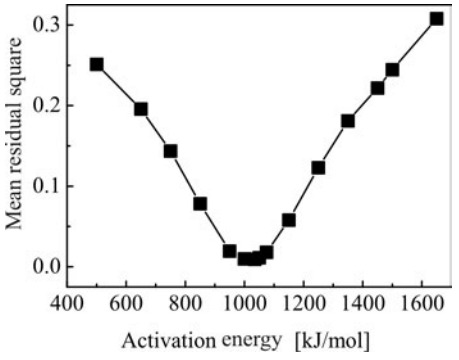

Fig. 4. Dependence of mean of residual squares on the activation energy; minimum at 1035 kJ/mol

In the α-alumina (with the average particle size of 0.27 μm) sintering experiments by Wang and Raj [12], the activation energy was determined to be 440 kJ/mol from an Arrhenius plot of $\ln(\dot{\varepsilon}T)$ vs. the reciprocal of the absolute temperature. Five values of density ranging from 0.65 to 0.85 are used. The cylindrical samples themselves were prepared by uniaxial pressing in a steel die at 40 MPa and then by isopressing cylindrical green compacts at 100 MPa. The samples were 12 mm in diameter and 10 mm high. Their relative green density was 55±1%. The temperature of the specimen was raised to 800 °C in 1 h and held at that temperature for 10 min. Thereafter three different heating rates (5, 10, and 20 °C/min) were used to increase the temperature from 800 °C to 1600 °C. The experiments were terminated when the temperature reached 1600 °C.

In the ZnO sintering experiments by Chu et al. [5], all the powder compacts were heated first to 500 °C at 10 °C/min and then heated to 1100 °C at a wide range of heating rates (0.5, 2, 5, 10 and 15 °C/min). Closer inspection of the MSCs derived from the experimental data showed that the points calculated from the data of the lowest heating rate (0.5 °C/min) experiment were a little lower than those from higher heating rate

experiments. i.e., using 0.5–15 °C/min, yields an apparent activation energy of 310 kJ/mol. Excluding the lowest and the two lowest heating rate data from the analysis results in estimates of 300 and 285 kJ/mol, respectively. This could be ascribed to a surface diffusion effect, which would have a more significant effect at lower heating rates.

It should be noted that the activation energy value obtained in the present work is quite high (almost twice as high as 555 kJ/mol obtained by Tatami et al. [11] for heating rates 7.5–20 °C/min or Wang and Raj [12] of 440 kJ/mol) and differs much more significantly than that in the discussed case of ZnO.

During sintering, surface transport mechanisms (evaporation condensation, E-C; surface diffusion, SD) provide for neck growth by moving mass from surface sources. Bulk transport processes (grain boundary diffusion, GB; volume diffusion, VD; plastic flow, PF) provide for neck growth using internal mass sources. Only bulk transport mechanisms cause shrinkage. However, a major complication arises due to multiple mechanisms contributing simultaneously to shrinkage. The activation energy for sintering is equal to the activation energy for the rate-controlling diffusional mechanism since the sintering rate is proportional to the diffusion coefficient. However, the value obtained for Q can vary drastically, depending on the conditions (i.e., the characteristics of the raw materials, the preparation procedure of green compacts, the sintering procedure, etc.) under which the sintering data are obtained.

As has been shown, the condition under which the activation energy was obtained in the literature [5, 11, 12] differs significantly from that in the present work, especially the heating rate (heating rates lower than 5 °C/min only employed in the present work). According to the sintering theory, the activation energy of sintering should be consistent with that of the apparent diffusion coefficient of the rate-limiting species of sintering. In sintering polycrystalline ceramics, it is common that both grain boundary and lattice diffusion of the rate-limiting species can simultaneously contribute to densification. Some reports [16, 17] have suggested that the change of the relative contribution of D_l and D_b (D_l is the lattice diffusion and D_b is the grain boundary diffusion) due to the difference of the impurity level or grain size can affect not only the pre-exponential factor but also the activation energy of the apparent diffusion coefficient. However, the relative contribution of D_l and D_b also is different at different temperatures even impurity level and grain size are the same because these two diffusivities have different temperature-dependences. Thus, heating rate would have a significant influence on the non-isothermal kinetic processes due to the fact that it can change the relative contribution of D_l and D_b from low to high temperatures. Therefore, the higher activation energies evaluated based on the non-isothermal sintering can be attributed to the effect of heating rate [18]. Especially for the small-grain-size powder, due to the fact that its densification can occur at lower temperatures. Thus, the contribution of D_b to densification will be higher because of the higher degree of densification in the lower temperatures using lower heating rates, which in turn would influence the evaluation of the activation energy.

Moreover, German [19] pointed out that diffusivities could vary widely with impurity content and atmosphere. In the present work, the increase in carbon content is due to the binder residue left behind after the debinding process. Thus, the presence of binder residue and impurities on the particle surfaces after the binder has decomposed may also be a cause leading to the higher activation energies found in the present research.

It is obvious that in the present work the samples have not achieved full density (about 96% of the theoretic density) and that the activation energy value is similar to the one obtained by Fang et al. [18] (1080 kJ/mol) for classified α-Al_2O_3 compacts in the intermediate stage of sintering.

In the literature [18], the classified powder had an average diameter of 0.21 μm. Sintering was performed in air using a dilatometer. For nonisothermal sintering, four heating rates of 3, 5, 10, and 20 °C/min were used to reach the desired temperature (1700 °C) without holding. The activation energy of sintering could essentially be evaluated from the Arrhenius plot of $\ln(\dot{\varepsilon}T)$ vs. the reciprocal of the absolute temperature. Five values of density ranging from 0.70 to 0.90 were used.

For the classified powder, three values of activation energy in the intermediate stage of sintering can be evaluated based on different heating rates, i.e., 478 kJ/mol for 10 and 20 °C/min, 640 kJ/mol for 5, 10, and 20 °C/min, and 1080 kJ/mol for 3, 5, and 10 °C/min, respectively. It indicated that a higher value of the evaluated activation energy will be obtained when the Arrhenius plot involves low heating rates, which further supports that the relative contribution of D_l and D_b to densification is different at the same density level for high and low heating rates. Comparing the activation energy of 1080 kJ/mol in the literature and 1035 kJ/mol obtained in the present work, this kind of similarity can be attributed to the similar heating rates used in the literature and the present work.

3.2. Validation of the master sintering curve

From the knowledge of the activation energy of sintering as obtained above, MSC for α-Al_2O_3 has been constructed (Fig. 5). In Figure 6, the shrinkage versus isothermal hold time of ca. 6 h is shown for the samples sintered at 1200, 1350 and 1500 °C, respectively. In this plot, the abscissa represents the isothermal hold on time. From the dilatometric data of a particular run, the Θ values are calculated for the isothermal hold by Eq. (1). These values are shown on the master sintering curve as shown in Fig. 7. It can be seen that the values for all the three temperatures with different periods of time lie on the MSC, validating the concept of MSC. For clarity only a few representative data points are shown.

In addition, based on the experimental data (the density determined by the Archimedes method with different heating procedure), the relationship of ρ and Θ, shown in Fig. 8, was highly consistent with the MSC. The constructed MSC agreed

well with the densities determined by the Archimedes method under different heating history, which further verified its validity.

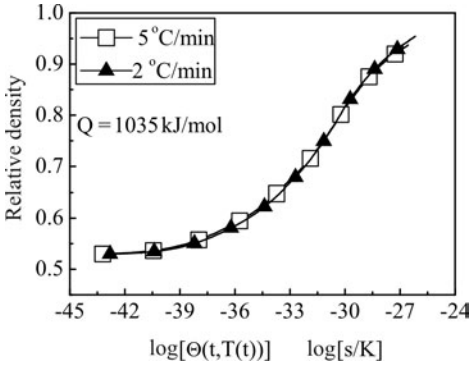

Fig. 5. MSC constructed from the sintering data shown in Fig. 2 using the activation energy of 1035 kJ/mol

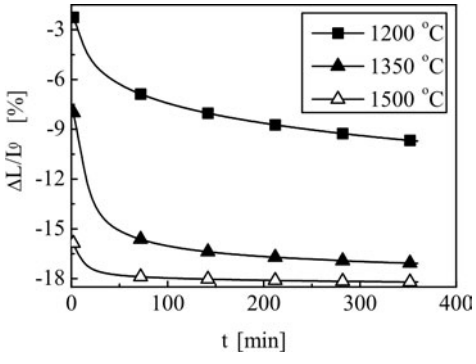

Fig. 6. The shrinkage curves for α-Al_2O_3 compacts during the isothermal heating

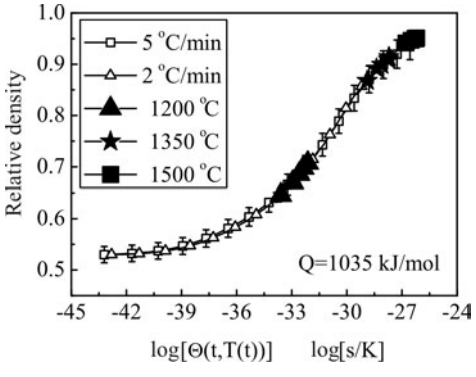

Fig. 7. Validation of MSC for α-Al_2O_3. The experimental values for three temperatures are shown (including error bars)

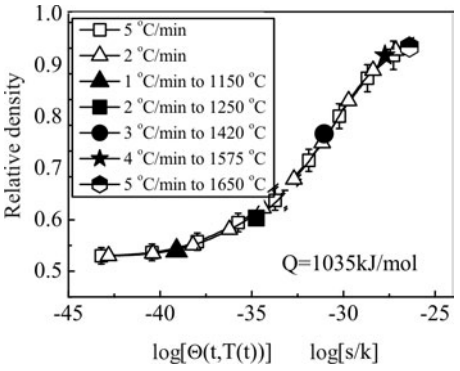

Fig. 8. Validation of MSC for α-Al_2O_3. The densities determined by the dilatometer trace are in a good agreement with the Archimedes densities (including error bars)

Thus it can be regarded that integration of the proposed sintering time –temperature profile yields a point on the MSC curve. The expected density can be obtained by finding the ordinate value at that point. On the other hand, if the final desired density is known, it is possible to find out the corresponding Θ value from the abscissa of the master sintering curve and thereafter to plan the sintering schedule [20, 21]. Thus MSC can be a characteristic measure of the sinterability of a powder compact over a wide range of densities.

4. Conclusions

Based on the constant heating rate sintering containing low heating rates only, the master sintering curve for α-Al_2O_3 has been constructed with the help of a combined-stage sintering model. A comparison between the predicted and the experimental shrinkage curves showed good consistency, thus confirming that it is possible to control shrinkage behaviour using the MSC. With one experimentally determined temperature dependent parameter Θ, the densification behaviour for α-Al_2O_3 can be described from the early to the final stages of sintering.

The concept of MSC has been used to calculate the apparent activation energy for densification during sintering for sub-micron-sized α-Al_2O_3 powders. The activation energy was determined to be 1035 kJ/mol, which is higher than the value reported by other researchers. So the evaluation of sintering activation energy based on MSC will be influenced by the heating rates.

Acknowledgements

Great thanks to the financial support of Nature Science Foundation of Qingdao (05-1-JC-89), P.R. China.

References

[1] RAHAMAN M.N., JONGHE L.C., BROOK R.J., J. Am. Ceram. Soc., 69 (1986), 53.
[2] KUCZYNSKI G.C., Trans. Am. Inst. Mining. Met. Eng., 185 (1949), 169.

[3] COBLE R.L., J. Appl. Phys., 2 (1961), 787.
[4] HANSEN J.D., RUSIN R.P., TENG M.H., JOHNSON D.L., J. Am. Ceram. Soc., 75 (1992), 1129.
[5] SU H., JOHNSON D.L., J. Am. Ceram. Soc., 79 (1996), 3211.
[6] DIANTONIO C.B., EWSUK K.G., Ceram. Trans., 157 (2005), 15.
[7] JOHNSON D.L., Ceram. Trans., 157 (2005), 3.
[8] LI D., CHEN S., JING Y., SHAO W., ZHANG Y., LUAN W., Sci. Sinter., 39 (2007), 103.
[9] EWSUK K.G., ELLERBY D.T., DIANTONIO C.B., J. Am. Ceram. Soc., 89 (2006), 2003.
[10] NIKOLIC M.V., PAVLOVIC V.P., LABUS N., STOJANOVIC B., Mater. Sci. Foru., 494 (2005), 417.
[11] TATAMI J., SUZUKI Y., WAKIHARA T., MEGURO T., KOMEYA K., Key Eng. Mater., 317–318 (2006), 11.
[12] WANG J.D., RAJ R., J. Am. Ceram. Soc., 73 (1990), 1172.
[13] XIONG X.D., Rare. Metal. Mater. Eng., 28 (1999), 298.
[14] KUTTY T.R., HEGDE P.V., KHAN K.B., PILLAI S.N., SENGUPTA A.K., JAIN G.C., MAJUMDAR S., KAMATH H.S., PURUSHOTHAM D.S., J. Nucl. Mater., 305 (2002), 159.
[15] JOHNSON D.L., SU H., Ceram. Bull., 76 (1997), 72.
[16] DOSDALE T., BROOK R., J. Am. Ceram. Soc., 66 (1983), 392.
[17] HODGE D., J. Am. Ceram. Soc., 66 (1983), 216.
[18] FANG T.T., SHIVE J.T., SHIAU F.S., J. Mater. Chem. Phys., 80 (2003), 108.
[19] GERMAN R. M., *Sintering Theory and Practice*, MPIF, Princeton, 1997.
[20] SOHN D., Cement. Concr. Res., 29 (1999), 241.
[21] JOHNSON D.L., HOST J.J., TENG M.H., ELLIOTT B.R., HWANG J.H., MASON T.O., WEERTMAN J.R., DRAVID V.P., J. Mater. Res., 12 (1997), 1268.

Received 22 December 2007
Revised 8 July 2008

Materials Science-Poland, *Vol. 27*, *No. 1*, *2009*

Study of the electrical properties of polystyrene–foliated graphite composite

N. K. SRIVASTAVA, R. M. MEHRA*

Department of Electronic Science, University of Delhi South Campus, New Delhi – 110 021, India

The present paper reports the development of polystyrene–foliated graphite composites via a hot compression moulding technique. Foliated graphite, as obtained by the sonication of expanded graphite, was used as a filler. A distinct percolative behaviour was observed in the variation of conductivity of the composites as a function of graphite concentration. At the percolation concentration of graphite content (0.02 vol. fraction), the conductivity is found to be ca. 10^{-5} S/cm. The percolation behaviour was analyzed using the generalized effective media equation. An estimation of the interparticle distance between the filler particles/clusters in the composites was made. The analysis of current–voltage characteristics revealed that near the percolation threshold the electrical transport is due to tunnelling of charge carriers, while above the threshold it is ohmic in nature.

Key words: *polymer composites; electrical properties; percolation threshold; scanning electron microscopy (SEM)*

1. Introduction

The electrical insulating behaviour of most polymeric materials is well known. However, conductive fillers can be incorporated as a second phase into these matrices, leading to an increase in the conductivity of the resulting composites [1–3]. The properties of these composites are mainly varied with the filler content [4–6]. When the filler content reaches a critical value (the so-called percolation threshold), a sharp transition in the conductivity of the composites occurs with a slight increase of the filler content [7, 8]. Nanosize fillers significantly modify the properties of polymer composites and even generate certain new properties that cannot be derived from conventional fillers [9]. The incorporation and dispersion of nanosize conducting fillers is assumed

*Corresponding author, e-mail: rammehra2003@yahoo.com.

to be better as compared with conventional microsize fillers and thus a low percolation threshold and higher conductivity are achieved.

Naturally abundant graphite flakes have been widely used as conducting fillers for polymer composites. Conventional graphite fillers are usually microsize powders. In order to fabricate a composite with a satisfactory conductivity, loadings of fillers are usually as high as 20 wt. % or even higher. This often results in poor mechanical properties of the material. Polymer composites made from graphite nanosize powder or nanosheets may possess promising properties, especially good electrical conductivity at low filler loading, corresponding to low percolation concentration of the filler. Various theories/models have been proposed to interpret the electrical conductivity behaviour of polymer composites [3, 8, 10].

The percolation threshold concentration of filler depends on the dispersion of the conducting filler into the polymer matrix and the preparation technique of such composites. The conducting polymer composite can be prepared using either hot compression moulding or in-situ polymerization. In hot compression moulding [11–13], the filler particles are pre-localized [14, 15] onto the polymer particles before compression. In the case of in-situ polymerization, the polymer particles are dispersed into the monomer before polymerization. The monomer is gradually polymerized with the addition of an initiator, along with proper sonication of filler particles to achieve better dispersion. The effect of filler content on the conductivity of the composite is generally analyzed by using percolation theory for both types of composites. In the hot compression mouding technique, the conductivity of the composites depends on various parameters of the individual polymer and graphite particles. The main parameters which are primarily responsible for the electrical behaviour of the composites are (i) conductivity, (ii) size, (iii) structure and (iv) orientation. For such a system, McLachlan [16, 17] has given a generalized effective media (GEM) equation. The conduction mechanism of various polymers/graphite nanosheets fabricated using in-situ polymerization process has been reported earlier by several groups [18, 19]. The schematic representation of the dispersion of nanosize filler has been reported by Chen et al. [20] using a poly(methyl methacrylate)–exfoliated graphite composite system.

This paper deals with the preparation of polystyrene–foliated graphite composites by the hot compression moulding. Foliated graphite (FG) was used as filler. The foliated graphite was characterized using scanning electron microscopy (SEM) and X-ray diffraction (XRD). Variation of room temperature conductivity of the composite with filler content was investigated. The percolation concentration was estimated using a power law model of conductivity. The electrical conductivity versus filler volume fraction data was also analyzed using the GEM equation. The interparticle distance between the filler particles/clusters using the sizes of the insulating and conducting components of the system was calculated. These results were ascertained by SEM morphology of fractured composites. The effect of filler content on the current–voltage (I–V) characteristics was also investigated. The mechanical strength of the composites was estimated in terms of the D-shore hardness.

2. Experimental

Materials. The matrix polymer used in the present study is a commercial grade polystyrene (PS) manufactured by the Reliance Industry Ltd., Bangalore, India, supplied in the form of granules. The PS granules were ground to obtain finer particles using an Aurther H. Thomas type Willey grinder. The scanning electron micrographs (SEM) of PS particles and foliated graphite coated PS particles are shown in Fig. 1. It is seen from the images that the PS particles have an average size of 212–250 μm and the shape close to an ellipsoid. It is also seen from Fig. 1b that there is no significant change in the shape of the polymer due to tumble mixing or after pre-localization of filler. The glass transition temperature (T_g) of PS, as determined from differential scanning calorimetric measurements, was found to be 100 °C.

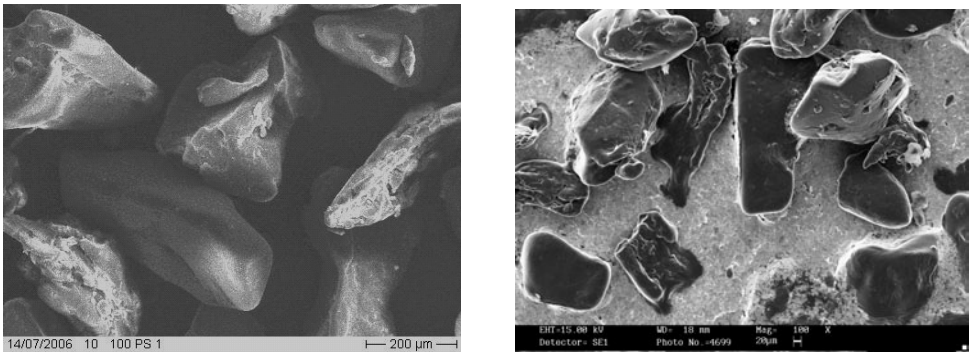

Fig. 1. SEM images of PS particles (left) and FG coated PS particles (right)

Natural graphite flakes (NFG) with average particle size of 10–20 μm, supplied by the Graphite India Ltd., were used as the source of foliated graphite. Conductivity of the graphite flakes was 1.33×10^4 S/cm with the density of 1.75 g/cm^3. FG is used as the conducting filler to prepare PS/FG composites.

Expansion of graphite. Graphite is a form of carbon where the carbon atoms are bonded in layers with van der Waals forces in between the layers. This structure allows intercalation by additional atoms or molecules which occupy spaces between the carbon layers. Graphite can be intercalated by exposure to an appropriate chemical reagent. Intercalation can be performed by immersing NFG in the mixture of concentrated HNO_3 and H_2SO_4. The reaction is as follows [21]:

$$n(\text{graphite}) + n(H_2SO_4) + 0.5n(O) \rightarrow n(\text{graphite}\cdot HSO_4) + 0.5nH_2O \qquad (1)$$

where (O) is the oxidant and (graphite·H_2SO_4) is the graphite intercalated compound (GIC). The resulting GIC comprises carbon layers and intercalated layers stacked on top of one another in a periodic fashion. The number of carbon layers between each pair of intercalated layers is the stage number. To obtain GIC from NFG, concentrated sulfuric and nitric acid (4:1, v/v) were mixed with NFG at room temperature and

stirred continuously for 16 h. Acid-treated natural graphite was then washed with water and dried at 100 °C to obtain GIC. The expansion of GIC can be achieved by using a thermal shock [22]. In the present case, GIC was exposed in a microwave oven for 20 s to obtain expanded graphite (EG). The SEM image of EG is shown in Fig. 2 at higher magnification (×4000). The inset in Fig. 2 shows the SEM image at lower magnification (×15). It is seen from the inset that the GIC has expanded about hundred times along the *c*-axis. The EG is a loose and porous vermicular product of greatly decreased density. The structure of EG basically comprised parallel boards which were completely torn into sheets 80–150 nm thick.

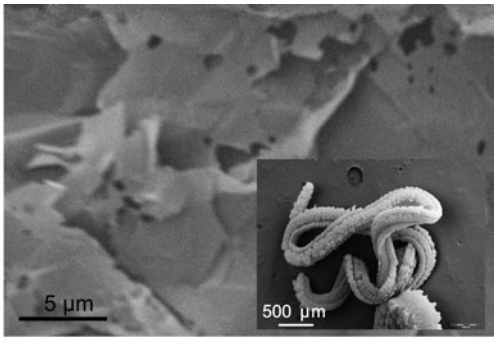

Fig. 2. SEM images of expanded graphite. The magnification of the main photograph is 4000×, that of the inset 15×

Structure of foliated graphite. Foliated graphite was obtained by sonication of 70% aqueous–alcohol solution of EG in an ultrasonic bath for 8 h [23, 24]. The resulting dispersion was then filtered and dried to get FG. Figure 3 shows a SEM image of FG at magnification of 5000×. It is seen from the image that the foliated graphite has a sheet type structure. The range of thickness and diameter of FG is estimated to be 80–150 nm and 5–10 μm, respectively. The sheet structure of foliated graphite, shown in Fig. 4, was also observed by the transmission electron microscopy (TEM) in a normal mode. The selected area diffraction (SAD) of the FG (the inset of Fig. 4) indicates the polycrystalline nature of foliated graphite.

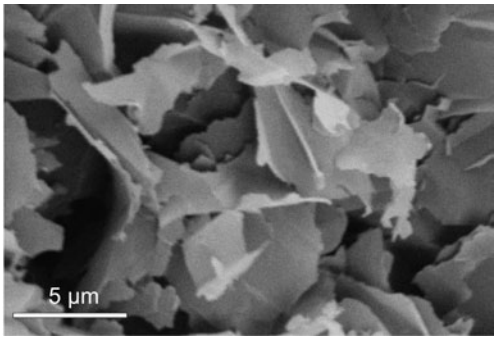

Fig. 3. SEM image of foliated graphite

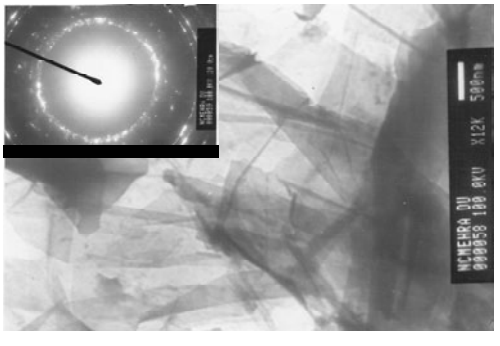

Fig. 4. TEM images of foliated graphite in normal mode and in diffraction mode (inset)

Preparation of composites. Initially, the as obtained foliated graphite was mixed with the polymer by pastel mortar. The mixture was further tumble mixed [13] thoroughly for 4 h at room temperature. This process involves coating of conducting foliated graphite on the surface of PS particles, referred as pre-localization of the conductive phase. Prolonged mixing improves the homogeneity of the spatial distribution of the conductive particles. The localized foliated graphite onto the PS particles was compacted by hot compression moulding in a piston cylinder assembly using a hydraulic press (Shimadzu Corp. Kyoto, Japan) having the ram diameter of 42.7 mm. The compression moulding operation was performed first at 90 °C for 15 min under 105 MPa (curing), then at 120 °C for 15 min under 20 MPa (baking). A series of disk shaped specimens of PS/FG conductive composites with varying filler contents from 0 to 0.115 volume fraction of FG were prepared. The density of the compression moulded pure PS and pure FG pellet was found to be 1.02 g/cm^3 and 1.97 g/cm^3, respectively. The sample diameters were 1.004 cm while thicknesses were ca. 0.3 cm for electrical measurements and ca. 0.5 cm for accurate and reliable hardness measurements.

Characterization and measurements. Both surfaces of the pellets were polished with sandpaper to remove a graphite rich surface layer and to eliminate surface irregularities. The conducting silver paint 'conductrox 3347 AG conductor' coatings supplied by the Ferroelectric Materials, USA, were used as the electrical contact. Pellets were sealed in air free polyethylene bags prior to testing in order to avoid atmospheric and humidity effects. A digital multimeter was used for samples having electrical resistance lower than 200 MΩ. However, for the samples having resistance higher than 200 MΩ, a Keithley Pico ammeter (Model DPA III) was used. Current-voltage measurements were performed with a Keithley 2400 source meter. The JEOL JSM 840 SEM was used for the analysis of morphology of the foliated graphite and composite polymer. X-ray diffraction measurements were done using CuK_α radiation (λ = 0.154 nm) operated at 40 kV and 40 mA in the 2θ range of 20–80°. A Scientico Hardness tester (Durometer, model No. SRHT-501D), conforming to ASTM 1706-61 and D 676-59T specifications, was used to determine the hardness of the samples.

3. Theory

The most popular theory used to explain the electrical conductivity of polymer composites is the percolation theory, based on the power law model [25, 26].

$$\sigma_{pc} = \sigma_{fg}(\phi - \phi_c)^t \tag{2}$$

where σ_{pc} is the electrical conductivity of the polymer composite, ϕ is the filler content in volume fraction, ϕ_c is the percolation threshold concentration of the filler, t is the universal exponent determining the power of the conductivity increase above ϕ_c and σ_{fg} is considered to be the conductivity of the filler, i.e. foliated graphite in the present

case. The value of t is found to be in the range 1.5–2.0 [25–28] which is invariant on the polymer matrix, conducting filler, magnitude of the two different components, structure of the resulting composite, etc. Various research articles with different polymer matrix and filler, such as low density polyethylene and carbon black [29], poly(vinylidene fluoride) and stainless steel fibre [30], ethylene butylacrylate and carbon black [31] and polyurethanes and single walled carbon nanotubes [32], show the range of the composite conductivity (10^{-15} – 10 S/cm) along with filler volume fraction (0–0.5). Almost entirely the same range of conductivity as well as the filler volume fraction is assumed to be responsible for the so-called universal nature of t. In some cases, a higher amount of filler content is required to achieve the above-mentioned conductivity; however, t has not been affected due to the relative value of ($\phi - \phi_c$) with conductivity. The nature of the electrical behaviour is more or less similar beyond ϕ_c with a sharp increase of 6–8 orders in conductivity against filler content. No further information has been disclosed from the power law model.

The variation of conductivity of the composite as a function of filler content can be critically examined by the GEM equation since it takes into account the intrinsic conductivities, geometries and arrangement of the filler and polymer particles along with their orientations to an applied electric field. Prior to applying the GEM equation, it is assumed that (i) the binary system is homogeneous, (ii) the particles are in contact with each other (no voids) and (iii) the electrical contact potential between insulating and conducting particles is negligible. McLachlan postulated a generalized effective medium (GEM) equation [16, 17] for the electrical conductivity of the binary composite polymer system. The GEM equation is written as

$$\frac{f\left(\sigma_{ps}^{t} - \sigma_{pc}^{t}\right)}{\sigma_{ps}^{t} + A\sigma_{pc}^{t}} + \frac{\phi\left(\sigma_{fg}^{t} - \sigma_{pc}^{t}\right)}{\sigma_{fg}^{t} + A\sigma_{pc}^{t}} = 0 \tag{3}$$

where σ_{ps}, σ_{pc} and σ_{fg} are the conductivities of the polymer composite, the polymer matrix (polystyrene) and the conducting filler (foliated graphite) respectively, f and ϕ are the volume fractions of the polymer and conducting filler, thus $f + \phi = 1$. A is defined as

$$A = \frac{\left(1 - \phi_c\right)}{\phi_c} = \frac{f_c}{\left(1 - f_c\right)} \tag{4}$$

In the extreme limiting condition, the low component conductivity tends to zero, causing Eq. (3) to reduce to

$$\frac{\sigma_{pc}}{\sigma_{fg}} = \left(1 - \frac{f}{f_c}\right)^{t} \tag{5}$$

For the critical filler volume concentration $\phi_c << 1$, Eq. (5) reduces to Eq. (2).

The critical filler concentration is related to the geometries and orientations of both the components [16];

- for an oriented ellipsoid

$$\phi_c = \frac{L_\phi}{(1 - L_f + L_\phi)} \tag{6}$$

- for a random ellipsoid

$$\phi_c = \frac{m_f}{(m_f + m_\phi)} \tag{7}$$

where L_ϕ and L_f are the demagnetization constants of foliated graphite and polystyrene particles, respectively. L stands for the combination of particle shape and orientation to the applied field. The value of L is 1/3 for spherical particles; 1 and 0 for the fiber/layer-shaped component oriented along and perpendicular to the compaction direction, respectively. m_ϕ and m_f are parameters for a random case. Exponent t in Eq. (3) is also related to oriented and random ellipsoids, respectively, by the following equations [16]

$$t = \frac{1}{1 - L_f + L_\phi}, \qquad t = \frac{m_f m_\phi}{m_f + m_\phi} \tag{8}$$

From Eqs. (6)–(8), L and m are given as

$$L_\phi = \frac{\phi_c}{t}, \qquad L_f = 1 - \frac{1 - \phi_c}{t} \tag{9}$$

$$m_\phi = \frac{t}{\phi_c}, \qquad m_f = \frac{t}{(1 - \phi_c)} \tag{10}$$

The electrical conductivities in function of filler content for the composite under study were fitted to the GEM equation by four-parameter computer programming [33].

4. Results and discussion

4.1. X-Ray diffraction of foliated graphite

The X-ray diffraction pattern of foliated graphite is shown in Fig. 5. A strong c-axis oriented diffraction peak (002) is observed at 26.78º. The diffraction pattern confirms the polycrystalline nature of foliated graphite. The full width at half maximum (FWHM) of the peak is 0.240º. The crystallite size of the FG was also estimated from the FWHM of the (002) diffraction peak by using Scherrer's relation [34]

$$l = \frac{0.94\lambda}{\beta \cos\theta} \tag{11}$$

where λ is the wavelength of X-ray radiation, θ is the Bragg angle of the (002) peak and β is the angular width of the (002) peak at a half of its maximum intensity (FWHM). The grain size of the polycrystalline foliated graphite was found to be 34 nm.

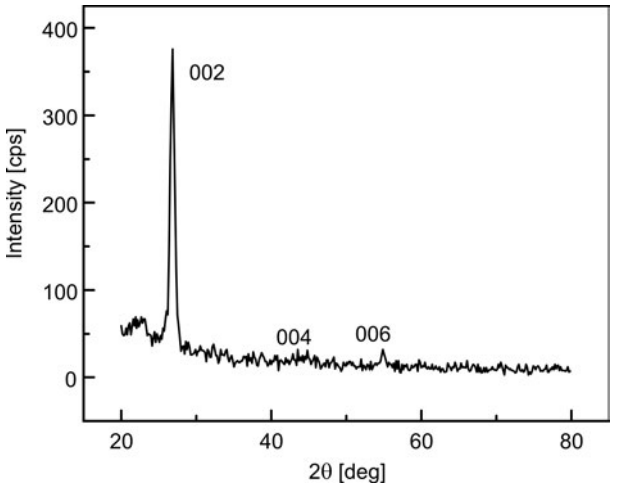

Fig. 5. X-ray diffraction pattern of foliated graphite

4.2. Electrical properties of composites

The electrical conductivity σ_{pc} of FG filled PS composites as a function of graphite volume fraction ϕ is shown in Fig. 6. It is seen from the figure that σ_{pc} increases by more than six orders of magnitude when the graphite content reaches 0.017 volume fraction (3 wt. %) of FG. The electrical conductivity reached 10^{-1} S/cm at the graphite content of 0.041 volume fraction (5 wt. %) and thereafter saturation in conductivity was observed for higher concentrations of filler.

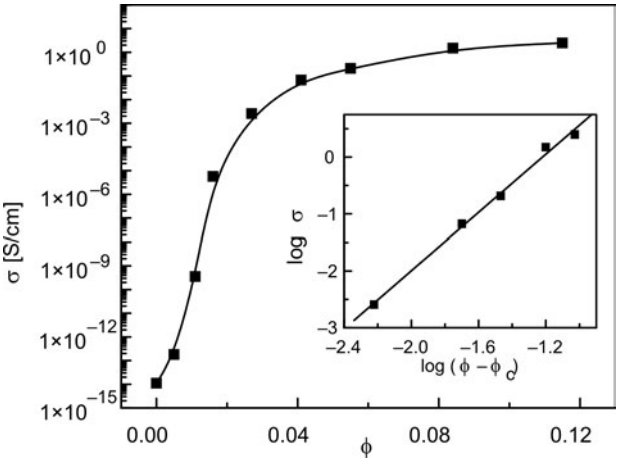

Fig. 6. Dependence of electrical conductivity on the filler content and in the inset dependence of $\log\sigma_{pc}$ on $\log(\phi - \phi_c)$ of PS/foliated graphite composites

4.3. Power law model

The conductivity data with the filler volume fraction were analyzed using the power law model (Eq. (2)). The plot of log σ_{pc} in function of log ($\phi - \phi_c$) is shown in the inset of Fig. 6. The best linear fit was found for $\phi_c = 0.02$ volume fraction of graphite with minimum standard deviation ($\delta = 0.101\%$). The values of t and σ_{fg} as estimated from the slope and intercept of the line, are found to be 2.56 and 1.33×10^3 S/cm, respectively. The value of σ_{fg}, as obtained from the power law model, is one tenth of the conductivity of filler particles (1.33×10^4 S/cm). The observed value of t = 2.56 is higher than as predicted by the power law model. Probably the easy and fine dispersion of two-dimensional foliated graphite is responsible for the better segregated chains which causes a large increase in conductivity beyond the critical filler concentration, giving rise to higher values of t. Liu et al. [32] and Yuen et al. [35] have found large t values for polyurethanes and single walled carbon nanotube systems, and for epoxy and multi walled carbon nanotube systems, respectively.

4.4. GEM analysis

Using the four-parameter computer fitting program, t, ϕ_c, σ_{pc} and σ_{fg} were evaluated from the best fits and, finally, L_ϕ, L_f, m_ϕ, and m_f were calculated where L and m, as mentioned above, are the orientation based parameters. The composite conductivity, as estimated from the GEM equation with filler concentration, was further compared with the experimental conductivity in Fig. 7. Various parameters, as fitted and estimated from the GEM equation, are compared with the results obtained from the power law model in Table 1.

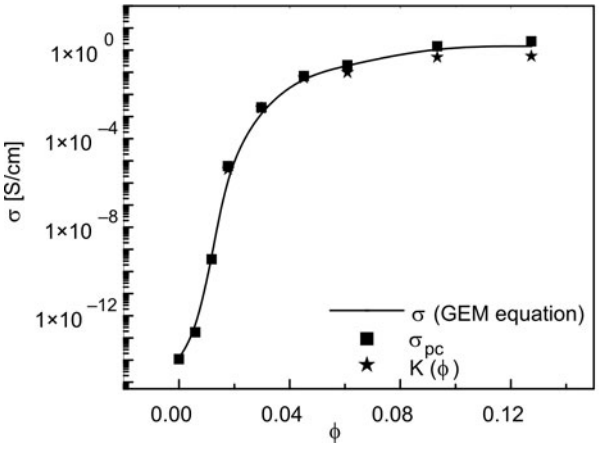

Fig. 7. Comparison of $\sigma_{pc}(\phi)$ with GEM conductivity and K of PS/foliated graphite composites

Table. 1. Parameters fitted and estimated from GEM equation compared with the power law model

Parameter	GEM equation	Power law model
t	1.83	2.56
Φ_c	0.019	0.02
σ_{ps} [S/cm]	1.354×10^{-14}	–
σ_{fg} [S/cm]	176.881	1.33×10^{3}
L_ϕ	0.01	–
m_ϕ	96.316	–
L_f	0.47	–
m_f	1.865	–
δ[%]	0.85	0.101

In the PS–foliated graphite composite, the smaller particles, i.e. FG, play the conducting role and are thus responsible for the percolation phenomenon as well as for the electrical conductivity of the system. Based on the preparation of the composite, filler particles get coated onto the matrix during dry mixing, referred as pre-localization of the filler [36], followed by compaction in a hot compression moulding, causing orientation of the filler particles during moulding, and thus forming a segregated network. A high aspect ratio between the insulating and conducting particles further ensures the segregated distribution. The value of L_ϕ as estimated from the GEM equation is very low, suggesting that almost all the filler particles are oriented perpendicular to the compaction direction, and was also confirmed from the SEM images, as shown in Fig. 8.

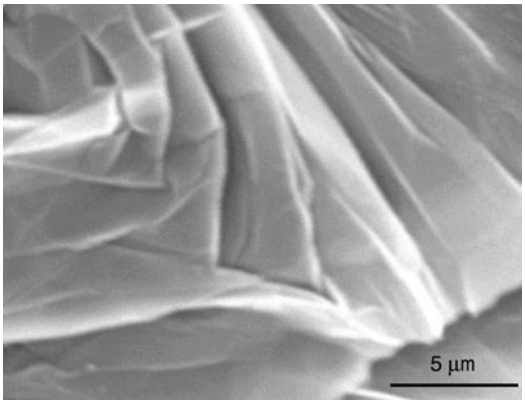

Fig. 8. SEM image of freeze fractured PS–foliated graphite composite for 0.115ϕ

Apparently, a layered type of structure of the filler particles as seen in the SEM morphology, further justifies a low value of L_ϕ. The estimated value of L_ϕ is 0.01 (close to 0), ensures the layered type of filler structure is oriented perpendicular to the compaction direction. The value of L_f is found to be 0.47. It may be mentioned that for spherical particles the GEM theory assumes L_f to be 0.333. The higher value of L_f, in

the present case, as estimated from the parameters of the GEM equation, could be attributed to a non-spherical shape (close to ellipsoid) of the polymer, as seen in Fig. 1a. The percolation threshold concentration of the filler is 0.019 volume fraction of FG from the four-parameter fittings of the GEM equation with the minimum standard deviation (δ = 0.85%). The value of ϕ_c obtained from both the power law model and GEM equation is almost the same as the content of filler and is close to the experimental volume fraction (0.017, 3 wt. %).

It is seen from Table 1 that there is a considerable difference in the values of t as obtained from the GEM equation and power law model. However, the value of t obtained from the GEM equation is close to the universal value of the exponent.

4.5. Interparticle distance

The motivation behind the concept of a percolation threshold is the creation of a connected network of filler particles in between the polymer matrix by forming a direct contact or very small interparticle distance between the filler particles. The interparticle distance (d_{fg}) is estimated using the expression [37]

$$d_{fg} = r_{fg}\left(3.95\left(\frac{r_{ps}}{r_{fg}}\right)^{-1/2} f^{1/6}\phi^{-1/2} - 2\right) \tag{12}$$

where r_{ps} and r_{fg} are the average radii of polymer and filler particles, respectively. The above equation has been obtained under the assumption of spherical polymer and filler particles. In the present case, polymer particles can be assumed to be spherical; however, the filler particles (graphite) are in the form of sheets. The average sheet thickness (0.115 μm) is the value used for r_{fg}. Using the average radius of the polymer (ca. 115 μm), the interparticle distance was found to be negative for $\phi \geq \phi_c$. A negative interparticle distance represents the direct contact of the filler particles with each other. Below the percolation concentration of the filler, the interparticle distance becomes positive.

The cross-sectional SEM image (magnification 5000×) of the freeze-fractured PS–foliated graphite composite for $\phi > \phi_c$ (volume fraction of FG 0.115) is shown in Fig. 8. The image clearly shows the layers of connected FG over the polymer matrix. The higher particle size ratio of the PS resin and foliated graphite ensures segregated distribution of filler onto the polymer matrix pertaining to a much lower percolation threshold concentration. Below ϕ_c, the filler particles are far apart with no connectivity amongst each other giving rise to very low conductivity.

4.6. Current–voltage characteristics

Current–voltage (I–V) characteristics can be expressed as [38]

$$I(\phi,V) = K(\phi)V^n \tag{13}$$

where $K(\phi)$ represents the conductivity of the composite at a given value of ϕ, and n is the slope in the log$I$–log$V$ plot. In Equation (13), Ohm's law is fulfilled in the system at $n = 1$.

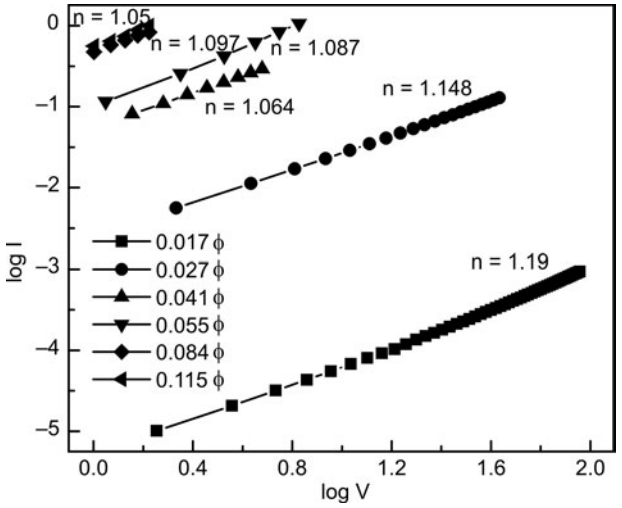

Fig. 9. log$I$(V) of PS/foliated graphite composites

Figure 9 illustrates the log I–log$V$ plots of PS–foliated graphite composite with different compositions. It is seen from the figure that the value of $n = 1.23$ at ϕ_c decreased to 1 at $\phi \approx 0.041$. The transition of the conduction mechanism from non-linear to ohmic is generally understood in terms of the distance and the number of tunnelling gaps in the percolating network [39]. At a sufficiently higher filler concentration for $\phi >> \phi_c$, the tunnelling gaps start to change into ohmic contacts. This effect is clearly visible in the SEM image of the polymer composite for $\phi = 0.115$ (Fig. 8). The variation of $K(\phi)$ and σ_{pc} with ϕ is also shown in Fig. 7. It is seen from the figure that both $K(\phi)$ and σ_{pc} closely match each other. A scaling behaviour in the I–V characteristics (Eq. (13)) was observed from the typical behaviour of current from non-linear to linear nature with increase in filler loadings as compared to conductivity variation from the power law model (Eq. (2)).

4.7. D-shore hardness

D-shore hardness of PS–foliated graphite composite with respect to ϕ is shown in Fig. 10. The hardness of the composites is found to decrease sharply from 89.5 to 85 up to the percolation concentration of the filler. However, beyond the percolation threshold, the hardness decreases slowly to 79.5 for $\phi = 0.115$. It is evident that using foliated graphite as filler, the degradation in the hardness of the PS/FG composite is only 12% at the highest achieved conductivity of ca. 10^{-1} S/cm. The decrease in hard-

ness with increase in the FG content may be due to the decreased particle-to-particle interaction among PS particles in the presence of graphite conducting channels in the composite.

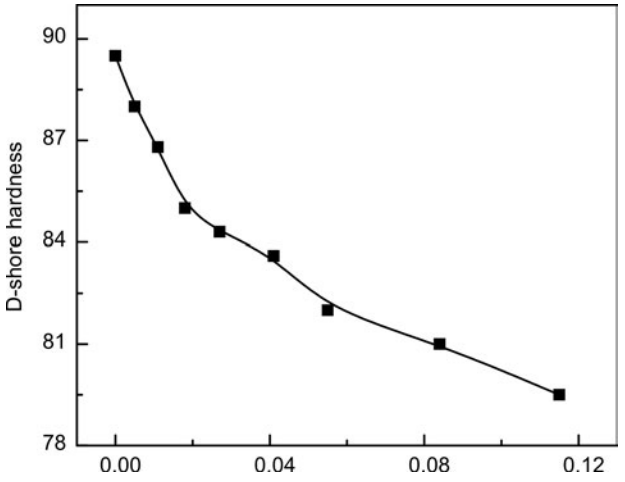

Fig. 10. D-shore hardness of PS/foliated graphite composites in a function of ϕ

5. Conclusion

The use of foliated graphite as filler was found to lower the percolation threshold. Electrical conductivity as high as 10^{-1} S/cm was obtained, without significantly affecting the hardness. The electrical conductivity data could be well understood in terms of the GEM equation. The dominant transport mechanism of charge carriers near and above the percolation threshold are found to be tunnelling and ohmic conduction, respectively.

Acknowledgement

Financial support from DRDO, Govt. of India under the project No. ERIP/ER/0503529/M/01/850 is thankfully acknowledged. Thanks are also due to the University of Delhi for providing funds for strengthening the R&D infrastructure.

References

[1] CARMONA F., Physica A, 157 (1989), 461.
[2] CELZARD A., FURDIN G., MARECHE J.F., MCRAE E., J. Mater. Sci., 32 (1997), 1849.
[3] DZIEDZIC A., Microelectron. Reliab., 47 (2007), 354.
[4] RUSCHAU G.R., YOSHIKAWA S., NEWNHAM R.E., J. Appl. Phys., 72 (1992), 953.
[5] DZIEDZIC A., KITA J., MACH P., Vacuum, 50 (1998), 125.
[6] CELZARD A., MARECHE J.F., FURDIN G., Carbon, 40 (2002), 2713.

[7] HUANG J.C., Adv. Polym. Technol., 21 (2002), 299.
[8] CELZARD A., MARECHE J.F., PAYOT F., FURDIN G., Carbon, 40 (2002), 2801.
[9] FISCHER H., Mater. Sci. Eng. C, 23 (2003), 763.
[10] KIRKPATRICK S., Rev. Mod. Phys., 45 (1973), 574.
[11] OUYANG M., CHAN C.M., Polymer, 39 (1998), 1857.
[12] CHUNG K.T., SABO A., PICA A.P., J. Appl. Phys., 53 (1982), 6867.
[13] SACHDEV V.K., MEHRA N.C., MEHRA R.M., Phys. Stat. Solidi a, 201 (2004), 2089.
[14] OUYANG M., CHAN C.M., Polym. Eng. Sci., 36 (1996), 2676.
[15] GUBBELS F., BLACHER S., VANLATHEM E., JEROME R., DELTOUR R., BROUERS F., TEYSSIE P., Macromolecules, 28 (1995), 1559.
[16] MCLACHLAN D.S., J. Phys. C: Solid State Phys., 18 (1985), 1891.
[17] MCLACHLAN D.S., J. Phys. C: Solid State Phys., 20 (1987), 865.
[18] CHEN G.H., WENG W., WU D., WU C., LU J., WANG P., CHEN X., Carbon, 42 (2004), 753.
[19] SEMKO L.S., DZYUBENKO L.S., KOCHEROV V.L., J. Ther. Anal. Calorimetry, 62 (2000), 485.
[20] CHEN G.H., WU D.J., WENG W.G., YAN W.L., Polym. Eng. Sci., 41 (2001), 2148.
[21] CHEN G.H., WU D.J., WENG W.G., HE B., YAN W., Polym. Int., 50 (2001), 980.
[22] CHUNG D.D.L., J. Mater. Sci., 22 (1987), 4190.
[23] CHEN G.H., WENG W., WU D., WU C., Eur. Polym. J., 39 (2003), 2329.
[24] ZHENG W., WONG S.C., SUE H.J., 73 (2002), 6767.
[25] SCHER H., ZALLEN R., J. Chem. Phys., 53 (1970), 3759.
[26] CHEN X.B., DEVAUX J., ISSI J.P., BILLAUD D., Polym. Eng. Sci., 35 (1995), 637.
[27] FLANDIN L., PRASSE T., SCHUELER R., SCHULTE K., BAUHOFER W., CAVAILLE J.Y., Phys. Rev. B, 59 (1999), 14349.
[28] HU J.W., LI M.W., ZHANG M.Q., XIAO D.S., CHENG G.S., RONG M.Z., Macromol. Rapid Commun., 24 (2003), 889.
[29] DANG Z., SHEN Y., FAN L., CAI N., NAN C., J. Appl. Phys., 93 (2003), 5543.
[30] LI Y.J., XU M., FENG J.Q., DANG Z., Appl. Phys. Lett., 89 (2006), 072902-1.
[31] JAGER K. M., MCQUEEN D. H., TCHMUTIN I. A., RYVKINA N. G., KLUPPEL M., J. Phys. D: Appl. Phys., 34 (2001), 2699.
[32] LIU Z., BAI G., HUANG Y., FENG D., LI F., GUO T., CHEN Y., Carbon, 45 (2007), 821.
[33] PAN Y., WU G.Z., YI X.S., J. Mater. Sci., 29 (1994), 5757.
[34] SAGALOWICZ L., FOX G.R., J. Mater. Res., 14 (1999), 1876.
[35] YUEN S.M., MA C.C.M., WU H.H., KUAN H.C., CHEN W.J., LIAO S.H., HSU C.W., WU H.L., J. Appl. Polym. Sci., 103 (2007), 1272.
[36] PANWAR V., SACHDEV V.K., MEHRA R.M., Eur. Polym. J., 43 (2007), 573.
[37] BHATTACHARYYA S.K., BASU S., DE S.K., J. Mater. Sci., 13 (1978), 2109.
[38] MAMUNYA Y.P., MUZYCHENKO Y.V., PISSIS P., LEBEDEV E.V., SHUT M.I., Polym. Eng. Sci. 42 (2002), 90.
[39] NAKAMURA S., SAITO K., SAWA G., KITIGAWA K., Jpn. J. Appl. Phys., 36 (1997), 5163.

Received 22 December 2007
Revised 22 August 2008

Materials Science-Poland, *Vol. 27*, *No. 1*, *2009*

Synthesis and characterisation of SnO_2 films obtained by a wet chemical process

S. MAJUMDER*

Department of Physics, Asansol Engineering College, Asansol 713304, India

SnO_2 thin films, being n-type semiconductors, have wide application in the field of sensor technology. They are obtained by a wet chemical process, using $SnCl_2 \cdot 2H_2O$ as a tin containing precursor. The films thus obtained were subjected to optical, X-ray diffraction (XRD), microstructural, FTIR and Raman studies.

Key words: *SnO_2; Raman spectra; FTIR*

1. Introduction

Metal oxide gas sensors have been the subject of many investigations during the past [1–7]. These materials change their conductivity due to adsorption and desorption of oxygen on the surface of metal oxide (MOX) and surface reactions between the absorbed oxygen and the detecting gases. Oxygen from air is chemisorbed as O^-, O_2^-, or O^{2-}. This adsorbed oxygen gets trapped at the grain boundary trap states, thereby increasing the grain boundary potential barrier. This culminates in an increase in resistivity of the material. For reducing gases, the trap states get depleted of charge carriers and thereby reduce the resistance through lowering of the potential barrier at the grain boundaries.

Among various metal oxides studied for gas sensor applications, SnO_2 has emerged as one of potentially the most useful materials. Numerous reports described how various properties of the material have relevance to various aspects of gas sensor applications. Tin oxide has the unique property of being both transparent and conducting material. Different techniques [1, 8, 9] were adopted to deposit SnO_2 coatings for sensor applications. The wet chemical method became the most favoured one due to scalability and cost-effectiveness.

*E-mail: smajumderaec@gmail.com

In this study, all wet chemical routes were adopted to deposit SnO_2 films onto soda lime glass substrates. Optical, FTIR and Raman studies were also carried out on these films.

2. Experimental details

Tin oxide films were deposited from a sol by the spin coating method. Soda lime glass slides were used as the substrates. The substrates were cleaned thoroughly with liquid detergents and distilled water followed by boiling in distilled water. The substrates were then subject to ultrasonic treatment in 2-propanol for 15 min, and finally degreased with 2-propanol vapour before drying.

Sol preparation and the colour of the sol are important for getting a reproducible final product. Analytical reagent grade $SnCl_2{\cdot}2H_2O$ was used as a starting material. 0.837 g of $SnCl_2{\cdot}2H_2O$ was refluxed and stirred with 10 ml of dehydrated ethanol at around 353 K for 3 h. The resultant sol was then allowed to cool down to room temperature. Stirring was continued till the cooling down process was completed. SnO_2 films were deposited onto cleaned glass substrates by the spin coating technique, and the films were immediately annealed at 773 K for 20 min in air. The films were taken out after being cooled down to room temperature. This process produced transparent and adherent SnO_2 films.

Scanning electron microscopy (SEM) and X-ray diffraction (XRD) using CuK_α line were used to obtain the microstructural data. The crystallinity of each film was calculated from XRD spectra by Scherrer's formula:

$$D_m = \frac{0.9\lambda}{\beta \cos\theta} \tag{1}$$

where D_m is the crystallite size, β the full-width at half maximum (FWHM) of a distinctive peak (rad), θ the Bragg angle and $\lambda = 0.154$ nm.

Optical studies were performed by measuring the transmittance and the absorbance in the wavelength region 200–900 nm at room temperature using a spectrophotometer Hitachi-U3410. The spectra were recorded with the resolution of $\lambda \approx 0.07$ nm, along with a photometric accuracy of ±0.3% for transmittance measurements. Raman spectra were recorded using a Renishaw inVia micro-Raman spectrometer, equipped with a 514 nm Argon laser. FTIR spectra were recorded in the 4000–400 cm^{-1} range, using a Nicolet^{TM}-380 FTIR.

3. Results and discussion

Figure 1 shows the scanning electron micrograph (SEM) of a representative SnO_2 film. The film appeared to be compact and rougher surface in nature. The average

grain sizes were measured to be between 200 nm and 250 nm for the films. It was noticed that there was a tendency of grain growth with increase in annealing temperature, which was a general physical phenomenon. The XRD spectra (Fig. 2) are characterized by the presence of stronger but broader characteristic peaks for SnO_2 located at 2θ =26.61°, 33.89°, 51.79° and 61.87° arising out of reflections from (110), (101), (211) and (310) planes, respectively. Crystal size was computed from Eq. (1) and from XRD data; it was found that the size was ca. 40 nm for deposited SnO_2 thin film.

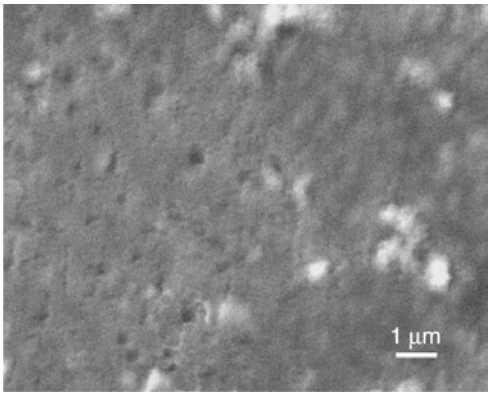

Fig. 1. SEM picture of as-deposited SnO_2 film

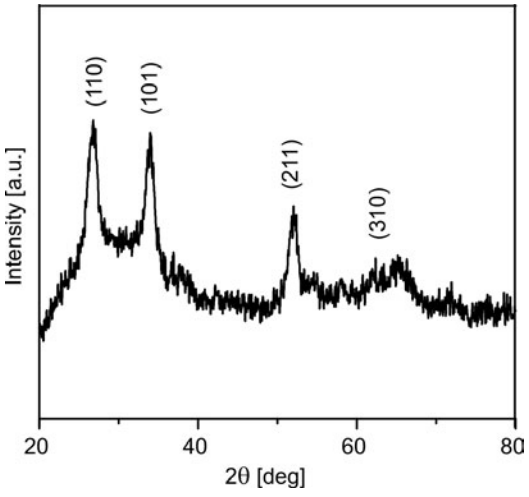

Fig. 2. XRD spectrum of the film
whose SEM picture shown in Fig. 1

The films were transparent in the visible region. The variation of the optical absorption coefficient α with photon energy $h\nu$ was obtained using the transmittance data for various films. The absorption coefficients α of the SnO_2 films were deter-

mined by measuring transmittance T_r and reflectance R in these films [10, 11]. The absorption coefficient α may be written as a function of the incident photon energy $h\nu$

$$\alpha = \frac{A}{h\nu}\left(h\nu - E_g\right)^m \tag{2}$$

where A is a constant which is different for different transitions indicated by different values of m, and E_g is the corresponding band gap. Equation (2) may be rewritten as:

$$\frac{d\left(\ln \alpha h\nu\right)}{d\left(h\nu\right)} = \frac{m}{h\nu - E_g} \tag{3}$$

A plot of $d(\ln(\alpha h\nu))/d(h\nu)$ vs. $h\nu$ will show a divergence at $h\nu = E_g$, from which a rough estimate of E_g may be obtained. Thus, by using Eq. (2), the value of m can easily be evaluated from the slope of the plot of $\ln(\alpha h\nu)$ vs. $\ln(h\nu - E_g)$. The inset of Fig. 3 shows the plot of $\ln(\alpha h\nu)$ vs. $\ln(h\nu - E_g)$ for a representative SnO_2 film. The value of m obtained from the slope is 0.46, which indicates that an allowed direct transition is present in deposited SnO_2 film. The band gap was determined by extrapolating the linear portion of the plot of $(\alpha h\nu)^2$ vs. hν (Fig. 3) which indicated $E_g \approx 3.66$ eV for the film.

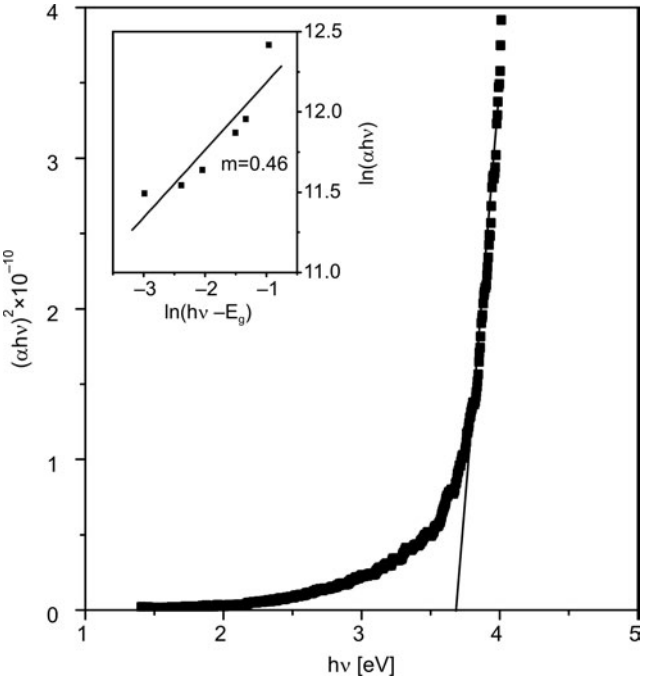

Fig. 3. Plots of $(\alpha h\nu)^2$ vs. hν for representative as-deposited SnO_2 film

FTIR and Raman studies were performed at room temperature on the SnO_2 film. The above studies reflected the bonding environment in these films. Figure 4 shows the FTIR spectra of the film. It may be observed that the SnO_2 film showed characteristic FTIR absorption peaks at ca. 511 cm^{-1} and 800 cm^{-1} which are due to Sn–O vibrational and O–Sn–O stretching modes, respectively. There are absorption peaks due to –CH, CO_2 and –OH modes. This observation is consistent with that reported by Chen and Gao [12].

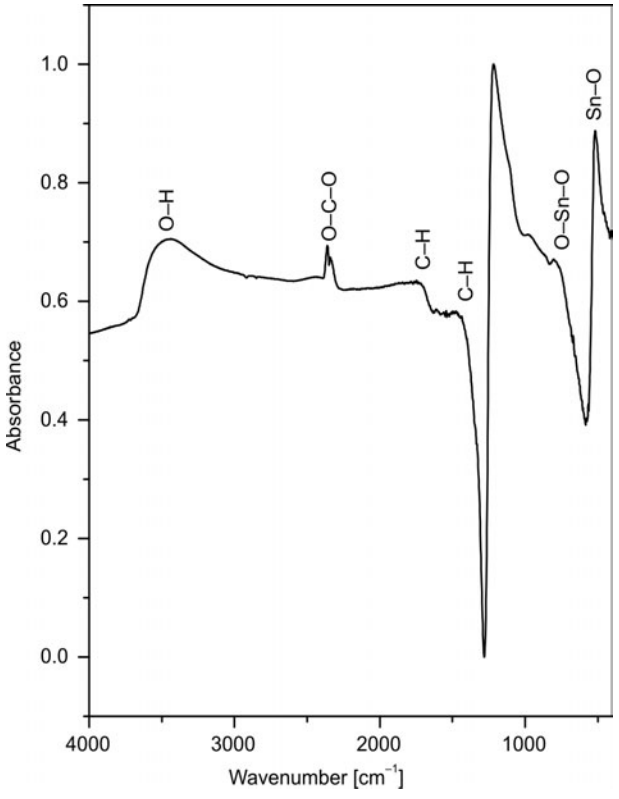

Fig. 4. FTIR for as-deposited SnO_2 film

Figure 5 shows typical Raman spectra for as-deposited SnO_2 film. The spectra for as-deposited SnO_2 is dominated by the presence of a broad and strong peak at ca. 560 cm^{-1} along with a peak of a smaller intensity at ca. 782 cm^{-1}. The peak at ca. 560 cm^{-1} has a shoulder and this peak, when deconvolved (inset of Fig. 5a), shows the existence of two peaks at ca. 567 cm^{-1} and 452 cm^{-1}. These two peaks could correspond to S1 and S2 bands of SnO_2 , while the peak at ca. 782 cm^{-1} is due to B_{2g} mode of SnO_2. Similar Raman spectra of SnO_2 films have been reported in Refs. [13–15].

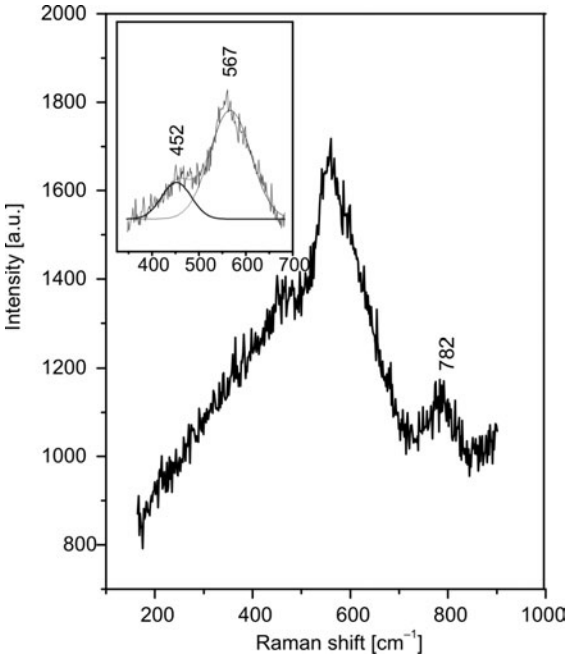

Fig. 5. Raman spectra for as-deposited SnO_2 film

4. Conclusion

SnO_2 films can be successfully obtained by the sol-gel technique. X-ray diffraction confirmed the presence of crystalline SnO_2 in these films. Tin (IV) oxide is non-stochiometric and is deficient in oxygen atoms. Charge neutrality is maintained by the presence of Sn^{2+} ions instead of Sn^{4+} ions. The Sn^{2+} ions act as electron donors during the process. At an elevated temperature, adsorption of atmospheric oxygen takes place by forming O_2^- , O^- or O^{2-} anions, thus decreasing the concentration of electrons near the surface and resulting in a depletion layer of higher resistance. Under exposure to reducing gases, the co-adsorption and interaction between gas and absorbed oxygen result in oxydation at the surface and a decrease in chemisorbed oxygen concentration, inducing an increase in conductance. Thus, SnO_2 may be used as a cheap gas sensing device for gases like methane, LPG, CO, NO_2. FTIR analysis indicated that the peaks for Sn–O at ca. 511 cm^{-1} became prominent and the peak due to stretching modes for O–Sn–O at ca. 800 cm^{-1} is prominent. This may possibly be due to the presence of very few oxygen vacant sites.

References

[1] SALEHI A., Thin Solid Films, 416 (2002), 260.
[2] KOHL D., J. Phys. D. Appl. Phys., 34 (2001), R125.

[3] MO Y., OKAWA Y., NAKAI T., TAJIMA M., NATUKAWA K., Thin Solid Films, 416 (2002), 248.
[4] GARDNER J.W., Sensors Actuators B, 4 (1991), 109.
[5] IMAWAN C., SOLZBACHER F., STEFFES H., OBERMEIER E., Sensors Actuators B, 68 (2000), 184.
[6] SCHWEBEL T., FLEISCHER M., MEIXNER H., Sensors Actuators B, 65 (2002), 176.
[7] HAHN S.H., BARSAN N., WEIMAR U., Sensors Actuators B, 78 (2001), 64.
[8] COBIANU C., SARANIU C., CICILIANO P., CAPONOE S., UTRIANIEN M., NINISTO L., Sensors Actuators B, 77 (2001), 496.
[9] GORDILLO G., MORENO L.C., DELA CRUZ W., TEHERAN P., Thin Solid Films, 252 (1994), 61.
[10] BHATTCHARYYA D., CHAUDHURI S., PAL A.K., Vacuum 4 (1992), 313.
[11] MOSS T.S., *Optical Properties of Semiconductors*, Butterworths, London, 1959, p. 34.
[12] CHEN D., GAO L., J. Colloid Interface Sci., 279 (2004), 137.
[13] PEERCY P.S., MOROSIN B., Phys. Rev. B, 7 (1973), 2279.
[14] DIEGUEZ A., ROMANO-RODRIGUEZ A., VILA A., MORANTE J.R., J. Appl. Phys., 90 (2001), 1550.
[15] YU K.N., XIONG Y., LIU Y., XIONG C., Phys. Rev. B, 55 (1997), 2666.

Received 23 December 2007
Revised 2 June 2008

Materials Science-Poland, *Vol. 27*, *No. 1*, *2009*

Prediction of the thermal shock resistance of refractory materials using *R* values

M. R. IZADPANAH[1*], A. R. A. DEZFOLI[2]

[1]Department of Materials Engineering and Metallurgy, Shahid Bahonar University of Kerman, Iran

[2]Department of Mechanical Engineering, Shahid Bahonar University of Kerman, Iran

Knowledge of the thermal shock resistance of refractory materials is of particular importance in a variety of applications. To meet the needs of these various applications, a number of thermal shock parameters based on material properties have been developed. The area of thermal shock resistance of refractories is often one of conflicting results in terms of agreement between experimental observations and predictions based on parameters of materials. The current study presents the temperature and stress distributions in magnesite samples. This information plus other results obtained from thermal and mechanical properties of these materials are used to develop a model which predicts the number of quench cycles for various refractory materials. The comparison of the theoretical values using the solution of the presented model with experimental data for materials having different thermal resistances shows a close agreement.

Key words: *thermal shock resistance; refractory material; modelling*

1. Introduction

Refractory materials have various applications in many industries such as cement, iron and steel, non-ferrous, ceramic, glass and power generation. Among other properties, which are very important in manufacturing and the consumer market, thermal shock resistance is still a challenge for refractory community. Thermal shock is the direct result of exposing the surface of refractory installations to rapid heating and cooling conditions which cause temperature gradients within the refractory blocks. Such gradients, in the case of uneven cooling or heating, may cause failure of the material [1, 2].

The thermal shock resistance of refractory materials is determined using standard quench tests [3, 4] in which the material is heated and cooled subsequently, and the number of quench cycles that a material can withstand prior to failure is taken as its

*Corresponding author, e-mail: mizadpanah@yahoo.com

resistance to thermal shock. However, the experimental method of evaluation of this property is both time consuming and expensive [1]. Hence, presentation of a model which could predict this property using other properties, being easier and less expensive to perform would be valuable.

Several research works have been carried out to study thermal shock behaviour of ceramics [5–8]. A limited number of attempts have been made to model thermal shock resistance of refractories [9, 10]. Therefore, information regarding the assessment of thermal stability of refractory materials is scarce.

In the present work, the temperature distribution and the resulted stresses in samples made of magnesite have been studied. Upon analyzing the results, a comprehensive model capable of predicting the thermal stability of refractory materials has been presented.

2. Experimental setup and procedure

Experimental set up. Experiments were carried out using the test rig shown in Fig. 1. The test rig consists of a sample holding table which is designed so that the heat transfer due to conduction is reduced to its minimum value. Stainless steel sheathed K type insulated junction thermocouples, 0.5 mm in diameter, 150 mm long were used to measure the surface and the centre temperatures. These thermocouples can measure temperatures ranging from 0 to 1100 °C.

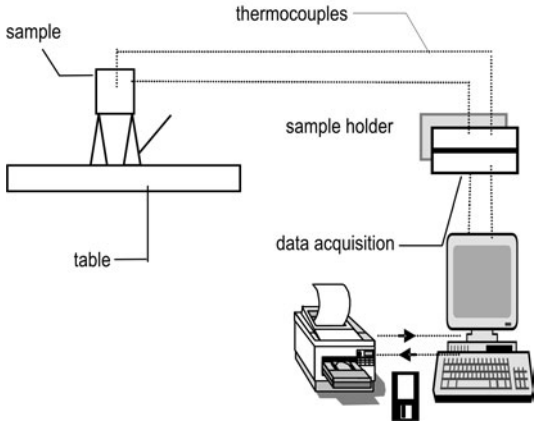

Fig. 1. Schematic diagram of the test rig

A data acquisition system consisting of two boards, namely the CIO-DAS08 and the CIO-EXP32 cards that are connected to a desktop computer is used to collect the data. The CIO-DAS08 card turns the PC into a medium speed data acquisition and control station suitable for data collection. A menu driven computer code is used to process the acquired raw data. The processed data are then saved in a file for each test.

Samples. Refractory materials used in this investigation are magnesite with different chemical compositions. The samples of the size 6×6×6 cm^3 were supplied by the Pars Refractories Company, a leading refractory manufacturer in Iran. The chemical compositions of these samples are given in Table 1. Acronyms describing the samples will be used further in the paper.

Table 1. Chemical composition of the samples [wt. %]

Component	Sample				
	70DL	70DR	70S	80S	80D
MgO (min.)	60	70	67.5	75	76
Cr_2O_3 (min.)	16–18	10	10	8	8
Al_2O_3	13–15	–	–	–	–
Fe_2O_3	6–8	–	–	–	–
CaO	0.5–1	–	–	–	–
SiO_2 (max.)	2	2.5	3.5	3	2

Procedure. The samples were heated in an electric furnace to 950 °C and then quenched in still air while placed on the table. The above procedure was repeated until failure occurred. The number of cycles withstood by a sample is taken as a measure of its thermal shock resistance. The results are presented in Table 2. While the samples are cooled, the thermocouples measure the temperatures at the surface and in the centre of the samples. Other relevant parameters are given in Table 3. These have been evaluated according to standard test methods [3, 4]. The tests were carried out at laboratories of Pars Refractories Company.

Table 2. Number of quench cycles

Sample	70DL	70DR	70S	80S	80D
Number of cycles	41	30	35	22	20

Table 3. Thermal and mechanical properties of the samples

Parameter	Sample				
	70 DL	70 DR	70 S	80 S	80 D
Density [g /cm^3]	3.00	2.95	2.96	2.95	3.00
Thermal conductivity [W/(m·K)]	2.53	2.45	2.47	2.43	2.32
Thermal expansion [%]	1.00	1.10	0.90	1.25	1.25
Compressive strength [MPa]	66	57	60	45	40
Heat capacity, c [J/kgK]	1	0.922	0.907	0.968	0.97
Poisson ratio, ν	0.2	0.2	0.2	0.2	0.2
Young modulus [GPa]	16	18	17	20	23
Biot number	3.24	3.31	3.28	3.33	3.49
Fourier number	23×10^{-5}	21×10^{-5}	23×10^{-5}	22×10^{-5}	20×10^{-5}

3. Formulation of the model

Taking into consideration the importance of temperature distribution and its role in developing thermal stresses, one can infer the significance of temperature distribution in predicting thermal shock resistance of refractory materials.

The modelling procedure starts with a simplification of the volume averaged energy equation. The unsteady state energy equation in a cubical sample in three dimensions assuming homogeneous properties yields [11]:

$$\frac{\partial^2 T}{\partial x^2}+\frac{\partial^2 T}{\partial y^2}+\frac{\partial^2 T}{\partial z^2}=\frac{1}{\kappa}\frac{\partial T}{\partial t} \tag{1}$$

The initial and boundary conditions applicable to the solution of the above partial differential equation with respect to the test bed under consideration are as follows:

$$T(x,y,z,0)=T_0 \tag{2}$$

$$\frac{\partial T(0,y,z,t)}{\partial x}=0 \tag{3}$$

$$\frac{\partial T(L,y,z,t)}{\partial x}=\frac{h}{k}\left(T(L,y,z,t)-T_\infty\right) \tag{4}$$

$$\frac{\partial T(x,0,z,t)}{\partial y}=0 \tag{5}$$

$$\frac{\partial T(x,L,z,t)}{\partial y}=\frac{h}{k}\left(T(x,L,z,t)-T_\infty\right) \tag{6}$$

$$\frac{\partial T(x,y,0,t)}{\partial z}=0 \tag{7}$$

$$\frac{\partial T(x,y,L,t)}{\partial z}=\frac{h}{k}\left(T(x,y,L,t)-T_\infty\right) \tag{8}$$

The overall heat transfer coefficient h used in the boundary conditions is given by

$$h=h_{\text{conv}}+h_{\text{rad}} \tag{9}$$

where heat lost through convection is given by [11]

$$h_{\text{conv}}=0.52\left(Gr\,Pr\right)^{0.25}\left(\frac{k}{l}\right) \tag{10}$$

In the above equations, T stands for temperature, t is time, κ is the thermal diffusivity, k – thermal conductivity, L – the sample length, and Gr and Pr stand for the Grashof and Prandtl numbers, respectively.

The amount of heat lost through radiation is [11]:

$$h_{\text{rad}} = \varepsilon\sigma\left(T_1^2 + T_2^2\right)\left(T_1 + T_2\right) \tag{11}$$

where ε and σ are the emissivity and Stefan–Boltzman constant, respectively.

The analytical solution of Eq. (1) yields the following general solution for the temperature distribution in the test piece.

$$\begin{aligned} T\left(x,y,z,t\right) = T_0 + 8(T_0 - T_\infty)\sum_{n=1}^{\infty}\sum_{m=1}^{\infty}\sum_{p=1}^{\infty}\frac{\sin(\lambda_n L)\cos(\lambda_n x)}{\lambda_n L + \sin(\lambda_n L)\cos(\lambda_n L)} \\ \times\frac{\sin(\beta_m L)\cos(\beta_m y)}{\beta_m L + \sin(\beta_m L)\cos(\beta_m l)} \\ \times\frac{\sin(\gamma_p L)\cos(\gamma_p z)}{\gamma_p L + \sin(\gamma_p L)\cos(\gamma_p L)}\mathrm{e}^{\left(-\kappa\tau\left(\lambda_n^2+\beta_m^2+\gamma_p^2\right)\right)} \end{aligned} \tag{12}$$

To find the stress S distribution, the above solution of the temperature distribution is substituted in the following equation [9]:

$$S(x,y,z,t) = \frac{\alpha E}{1-\nu}\left(T_m(x,y,z,t) - T(x,y,z,t)\right) \tag{13}$$

where

$$T_m(x,y,z,t) = \frac{1}{8L^3}\int_{-L}^{L}\int_{-L}^{L}\int_{-L}^{L} T(x,y,z,t)\,dx\,dy\,dz \tag{14}$$

ν is the Poisson coefficient, and α is the thermal expansion coefficient. Equation (13) gives the stress distribution in the samples under the test conditions.

4. Results and discussion

A comparison of one and three dimensional temperature distributions at the centre and surface of the 70DL sample with experimental data is shown in Fig. 2. As suggested by the aforementioned figure, there is a considerable difference between the 1D distributions with the experimental data; and therefore it can be concluded that the one dimensional solution results in appreciable errors when analyzing the thermal behaviour of the samples. Hence, the analytical procedures are considered and solved using 3D forms.

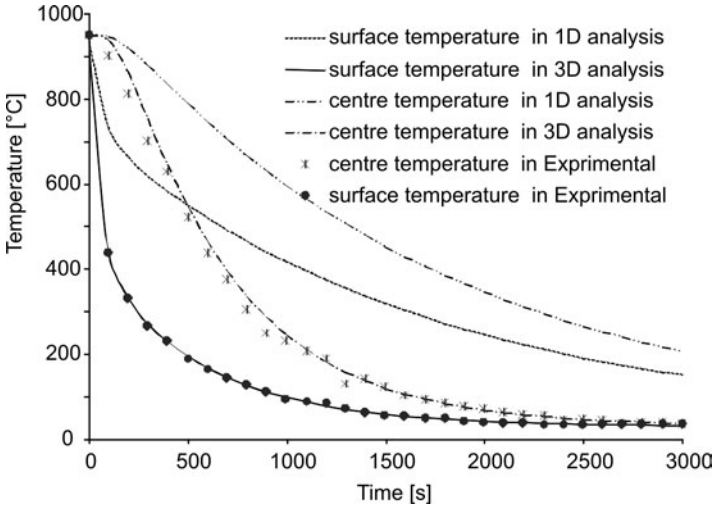

Fig. 2. Dependences of theoretical and experimental temperature distributions on time for 70DL sample

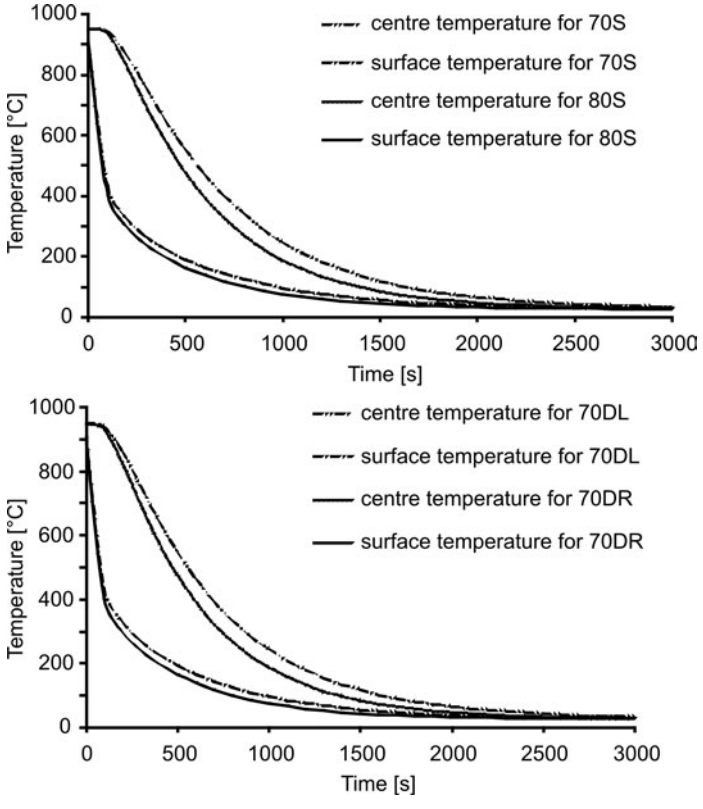

Fig. 3. Dependences of three dimensional temperature distributions on time for various samples subject to thermal shock in still air

Time dependences of temperatures at the surface and the centre for the 70 DL,70S and 80S samples are presented in Fig. 3. As can be seen, there is a significant difference between the two temperature profiles at different time intervals. This is due to the low thermal conductivity which is responsible for the existence of thermal stresses and hence sample failure [6].

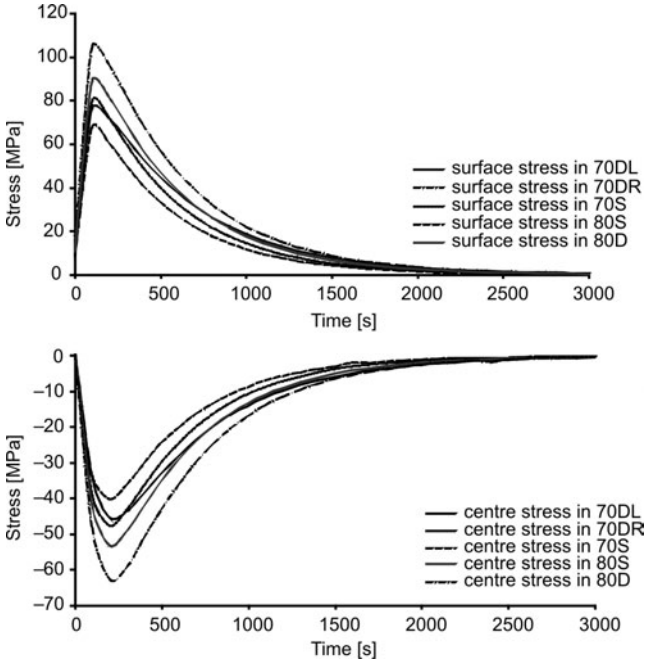

Fig. 4. Dependences of three dimensional stress distributions on time for various samples subject to thermal shock in still air

In Figure 4, the theoretical stress distributions at the surface and the centre of the samples are shown. These graphs emphasize the fact that the existence of a non-uniform temperature distribution will result in different stresses at the surface and the centre of the samples. Comparison of thermal shock behaviour of the samples can therefore be related to material thermal stability.

5. Modelling

Thermal stability of refractory materials is measured using standard laboratory tests. The ability of the material to withstand the thermal shock corresponds to the number of cycles that the material can stand the cooling–heating cycles before it fails.

It has long been the practice to use the fracture resistance parameter R to represent the thermal shock ability of these materials. R depends on various thermal and me-

chanical properties. However, the dependence of this parameter on the aforementioned properties only classifies them in order of their thermal resistance which is given by

$$R = \frac{S_M (1-\nu)}{\alpha E} \tag{15}$$

where S_M is the strength and E stands for the Young modulus.

The fracture resistance parameter, however, could be used as a criterion to correlate thermal shock behaviour of refractory materials in terms of the number of quench cycles. Considering the dependence of the number of quench cycles on various properties, the following correlation can be suggested in terms of resistance parameter R and the Biot number for various materials used in the present investigation.

$$\Omega = a + b \ln \Re \tag{16}$$

where Ω is the number of quench cycles, a and b are constants and their values are determined from experimental data, and $\Re$ is given by:

$$\Re = \frac{RkBi^{0.28}}{\kappa} \tag{17}$$

where Bi is the Biot number. The values of constants in Eq. (16) are calculated using non-linear regression. Therefore, Eq. (16) becomes:

$$\Omega = -113 + 22 \ln \Re \tag{18}$$

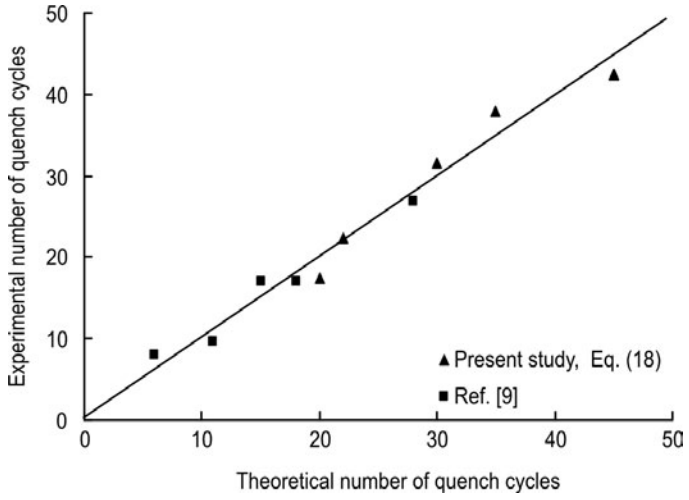

Fig. 5. Comparison of theoretical number of quench cycles with experimental data

Table 4. Results of non-linear regression

Comparison Ω with number of quench experiments	R^2
Present study	0.9837
Present study and [9]	0.9706
Ref. [9]	0.9616

Figure 5 represents the comparison of the theoretical values using Eq. (18) with experimental data. The comparison establishes an excellent agreement between the experimental data and the predicted values.

A comparison of the results published by Volkov–Husovic et. al. [9] as indicated in Fig. 5 and the R^2 values given in Table 4 suggests that the presented model can be used to predict the thermal stability of other refractory materials.

6. Conclusions

Based on the results and discussions presented in the current research it can be concluded that the thermal shock resistance of refractory materials is a very important feature of these materials, and its dependence on the temperature as well as stress distributions is of greatest significance.

Traditional use of R parameters only sorts this property in order of magnitude and cannot give a quantitative measure of thermal shock resistance of refractory materials. However, this factor can be correlated with the number of quench cycles so that thermal stability can be predicted with a suitable accuracy.

The current work presents an equation for predicting the number of quench cycles in terms of other available properties of refractory materials. A comparison of the values obtained using the correlation suggests that it can predict the experimental data obtained by the present authors as well as other researchers with exceptionally good accuracy.

References

[1] SHAW K., *Refractories and Their Uses*, Applied Science Publishers Ltd., London, 1972.
[2] CHANDLER H. W., *Thermal Shock of Refractories*, Proc. Tehran Int. Conf. of Refractories, 2004, 28–39.
[3] American Society of Testing and Materials Standards, Sect. 15, Vol. 15.01, 1990.
[4] British Standard Testing of Engineering Ceramics, BS 7134, Section 1.2, 1989.
[5] HASSELMAN D. P. H., J. Am. Ceram. Soc., 52 (1969), 600.
[6] HASSELMANN D.R., Ceram., 49 (1970), 1033.
[7] NAKAYAMA J., ISHIZUKA M., Am. Ceram., 45 (1965), 666.
[8] KINGERY W. D., J. Am. Ceram., 40 (1955), 38.
[9] VOLKOV-HUSOVIC T., JANCIC R. M., CVETKOVIC M., MITRAKOVIC D., POPOVIC Z. Mater. Lett., 38 (1999), 372.

[10] ANDREEV K., HARMUTH H., J. Mat. Proc. Tech., 143–144 (2003), 72.
[11] HOLMAN J. P., *Heat Transfer*, McGraw-Hill, London, 2002.

Received 31 December 2007
Revised 19 December 2008

Materials Science-Poland, *Vol. 27*, *No. 1*, *2009*

Characterization of oxidic and organic materials with synchrotron radiation based XPS and XAS*

D. SCHMEISSER[1**], M. TALLARIDA[1], K. HENKEL[1], K. MÜLLER[1], D. MANDAL[1], D. CHUMAKOV[2], E. ZSCHECH[2]

[1]Applied Physics Sensors, Brandenburg Technical University Cottbus, 03046 Cottbus, Konrad-Wachsmann-Allee 17, Germany

[2]AMD Saxony, Wilschdorfer Landstr. 101, 01109 Dresden, Germany

The use of synchrotron radiation (SR) based X-ray absorption spectroscopy (XAS) and X-ray induced photoelectron spectroscopy (XPS) is demonstrated for the analysis of thin films. In the first part we report on oxidic films used for high-*k* dielectric films in Si technology and focus on a recent in-situ approach to study the atomic layer deposition growth of HfO_2 films. We demonstrate that even hidden layers can be characterized by using fluorescence technologies. In the second part, we demonstrate the suitability of SR based techniques for the analysis of organic thin films. Here, the first example deals with P(VDF-TrFE), a ferroelectric polymer, with possible applications in non-volatile memory devices. Another example concerns the analysis of C_{60} based low-*k* polymers for use in Cu interconnect systems.

Key words: *synchrotron radiation spectroscopy; HfO_2; high-k oxide; ultralow-k polymers*

1. Introduction

Analysis of materials using synchrotron based spectroscopy techniques is a field with many possible applications. The main field of research in our group at the BTU Cottbus is in the materials science of thin functional films [1]. In our studies, we combine both, electrical and spectroscopic studies for their characterization. We have focused on two classes of materials, oxidic thin films – some of which are used as high-*k* dielectrics in MIS stacks and on organic thin films – some of which are used as low-*k* dielectrics to isolate around Cu interconnects.

We have prepared thin films of Pr_2O_3 and HfO_2 on Si and SiC substrates to build MIS structures for their electrical characterization. We optimized the films in terms of

---

* Presented at the 3rd Workshop *Hybrid Nanostructured Materials*, Prague, Czech Republic, 5–6 November, 2007.

**Corresponding author, e-mail: dsch@tu-cottbus.de

their dielectric properties (k value) and their insulating properties (leakage current densities). In particular, we stress that the studied oxide films are always controlled in their stoichiometry and thickness by spectroscopic means [2–10].

The intrinsic properties of the oxide thin films are monitored by XPS when optimizing the deposition parameters. This ensures control over stoichiometry, phase stability, and defined film thickness. Another investigation controls the temperature stability of the deposited oxide films. Such studies were done for pure but also for some mixed oxide systems [11–14].

Our studies concerned, in particular, the interface stabilities of the ultra thin oxide layers. The interface towards the metal electrodes turned out to be very important, as most metals penetrate into the oxides upon mild annealing. We observed a high mobility of Au, Ag, and Al which could be controlled only by the insertion of a thin Ti diffusion barrier [15].

Interface reactions also occur on the interface towards the substrates. Here in particular the mobility of Si is crucial and causes the formation of silicates [16, 17]. This turned out to be the case for Pr_2O_3 as well as for HfO_2 and Al_2O_3 thin films.

In our systems, we always combine the spectroscopically controlled films with electrical characterization (capacitance–voltage (CV) and current–voltage (IV) measurements). With both approaches, we learned that the introduction of an AlON layer as a buffer layer between the Si substrate and a high-k oxide delivers much better properties than those obtained for the bare system. In particular, the thickness of a silicate rich interface layer could be reduced significantly [4, 15, 18–20].

2. Experimental

Our synchrotron radiation (SR) based spectroscopic studies are performed using the BTU owned beam line U49/2 at BESSY, Berlin [1]. We briefly describe the most important features of the two main techniques applied.

X-ray induced photoemission spectroscopy (XPS) enables a quantitative determination of the elements contained in an investigated sample. The technique may be used with synchrotron radiation (SR) or laboratory X-ray sources. For low-k materials and for organic films in general, this technique is very promising because of the ease of sample preparation. Also, this technique does not suffer from X-ray induced radiation damage. The advantage of using SR as an excitation source is the higher sensitivity and better energy resolution. The higher sensitivity arises from the fact that the photo ionization cross sections are largest close to the ionization threshold. Hence, by using a tunable X-ray source, the excitation energy can be optimized.

The XAS technique again needs a tunable X-ray source, and therefore, this technique is exclusively used at synchrotron radiation sources. Very conveniently, the element-specific absorption coefficient can be determined by recording the total current of the emitted photoelectrons by tuning the energy of the incident photons around a particular ionization threshold (absorption edge). The most intense signal appears

near the absorption edge, the respective technique is referred to as near-edge absorption fine structure spectroscopy (NEXAFS). The method is more bulk-sensitive compared with XPS, since the total photoyield is primarily determined by the secondary electrons. Their mean free path is larger (up to 10 nm) than that of typical XPS photoelectrons. Thereby, the analysis of thicker films is feasible. The absorption coefficient can be determined either by recording the total electron yield (TEY) or by the total fluorescence yield (TFY). Using TFY, even higher bulk-sensitivity is obtained, as the X-ray photons are significantly less attenuated when penetrating through the films. The TFY mode can be beneficial when analyzing oxidic materials, as this mode is less sensitive to sample charging than the TEY mode. Elemental composition can be analyzed quantitatively in thin films. The technique is often used to analyze the chemical bonding, as the shape of the absorption profile differs characteristically for different oxidation states (finger printing) of inorganic compounds. In particular, the XAS spectra of transition and rare earth oxides show very sharp and structured features which can be used to analyze the particular charge state of the atom investigated. Because of the high sensitivity, such studies can also be performed on diluted or mixed oxide systems.

Electrical measurements have been carried out on MIS capacitors at room temperature in dark conditions. For further details of the MIS stack preparation refer to [20]. CV and conductance–voltage (GV) characteristics have been recorded with an Agilent 4284 LCR meter. IV characteristics were recorded using Agilent E3649A, HP34401, PREMA4001 and/or Keithley487 meters, respectively. Permittivity and capacitance equivalent thickness (CET) values were deduced from the oxide capacitance in the accumulation regime of the CV loop. Densities of interface states (D_{it}) were determined by AC conductance maxima [21].

3. Oxidic thin films

3.1. In-situ ALD setup for synchrotron radiation based spectroscopy

Among the possible growth methods, atomic layer deposition (ALD) is the most promising when considering very thin films conformal to three dimensionally structured substrates. As this is the typical request in the newest DRAM technology node, where thin capacitors have a very high aspect ratio (up to 60:1), the ALD growth method has an important industrial potential.

ALD growth contrasts with the chemical vapour deposition (CVD) technique, both of which are frequently used for the preparation of ultra-thin functional films. In both methods, two or more precursors react with each other, producing the targeted material. The difference between the two methods is that the ALD is based on a self-limiting process characterized by the adsorption of the metal precursor on the surface of a substrate. As a consequence of that surface reaction a layer-by-layer growth is achieved. On the other hand, in the CVD growth, the reactions take place in the gas

phase and are not controlled by the surface. Here, it has to be noted that the layer-by-layer growth of ALD does not necessarily correspond to one layer after every cycle but in most of the cases one layer is achieved after several cycles, as the surface coverage at every metal precursor exposure is usually not complete.

The ALD growth of metal oxides consists in the chemisorption of the metal precursor onto the substrate and the subsequent oxidization of the chemisorbed species. The two steps are separated by the introduction of a purging inert gas, which is needed to remove the non-reacted molecules of the metal precursor and the byproduct of the reacted molecules. In this way, with the introduction of the oxidant, the reactions take place only at the surface of the substrate, avoiding the CVD growth.

Up to now most of the investigations of ALD grown, high-*k* films were made ex situ, with the samples prepared in the ALD reactor and analyzed in a separated chamber, implying the transportation in air. This procedure involves the contamination of the high-*k* film and in some cases the formation of SiO_2 in very thin films, which make the interpretation of the experimental results difficult [22]. We show here the first results of our in-situ experiments, where the ALD reactor (base pressure 2×10^{-7} mbar) and the measurement UHV chamber (2×10^{-10} mbar) were connected together through an interface chamber maintained at an intermediate pressure of about 2×10^{-9} mbar. With respect to the ex situ experiments, our procedure assures the measurement of contamination-free surfaces. There is another important advantage of making measurements in situ: with our equipment we can study the film after every cycle and also after any single step of every cycle. This could be important for studying in detail the most important deposition step represented by the oxidation of the chemisorbed metal precursor.

The results presented here were obtained by using $HfCl_4$ as a metal precursor and H_2O as an oxidant, while the purging gas was N_2. The pressure reached by the metal precursor was 2×10^{-5} mbar and that of H_2O was 2×10^{-2} mbar, with one cycle consisting of 6 min exposure to $HfCl_4$ and 20 s exposure to H_2O, with a purging time of 2 min. After the oxidation step, another purging exposure was made before moving the sample into the interface chamber. The maximum value of deposition rate found for the ALD growth with the $HfCl_4$ as a metal precursor is about 1 ML every 3 cycles [23]. The temperature of the Si substrate was maintained at 300 °C during the complete cycle, and the ALD reactor was maintained at 140 °C during the experiment to avoid the condensation of $HfCl_4$ on the walls of the reactor. The $HfCl_4$ source was heated also at ca. 140 °C during the metal precursor step and then fast cooled to about 50 °C. The Si(001) substrate was cut from an n-type doped wafer, covered with a 2.2 nm thick oxide. The oxide was partially removed by etching the sample in a diluted HF solution, leaving the surface with an OH group termination. The remaining oxide thickness was determined to be 0.5 nm by the relative intensity of the peaks of the Si^{0+} and Si^{4+} species in the Si2p core level.

The photoemission and NEXAFS experiments were all performed at the synchrotron source BESSY in Berlin, at the beam line U49/2. The synchrotron light can be

made to have high photon intensity in a wide range of energy, leading to a high surface sensitivity and high energy resolution of the photoemission experiments, much higher compared with the usual AlK_α lab source. This is important because the films under investigation are of the order of less than a few nanometers and a detailed analysis requires both high sensitivity and good energy resolution.

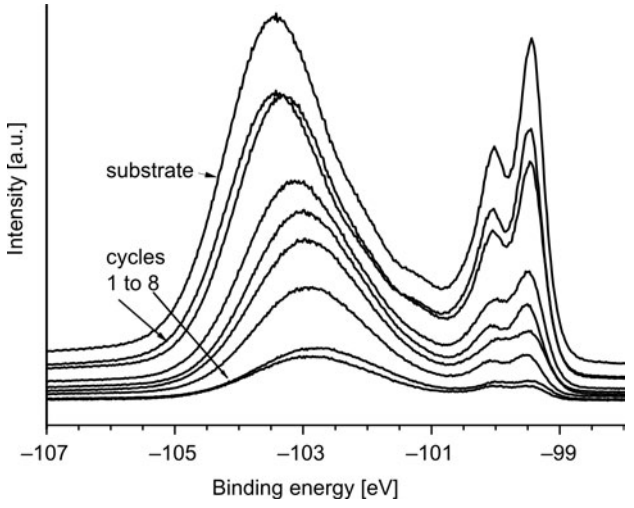

Fig. 1. In-situ growth of HfO_2 on a SiO_2/Si(001) substrate. The Si2p core levels are measured with the photon energy of 150 eV after the initial etch and after 8 consecutive ALD cycles

In Figure 1, we show the Si2p variation for the etched substrate and after 8 successive ALD cycles. The photon energy used to obtain these spectra was 150 eV, i.e. the spectra are very surface sensitive. The resolution was set to about 50 meV, giving the possibility to observe the spin-orbit splitting of the substrate related (Si^{0+}) component of the Si2p at about 99.6 eV, which is about 0.6 eV. Also, the intermediate oxidation components (Si^{+1}, Si^{+2}, and Si^{3+}) can be observed at binding energies between 100 eV and 103 eV. The intensities of the spectra are divided by the incoming photon flux, which is a function of the residence time in a synchrotron.

In Figure 2, we report on the corresponding NEXAFS spectra at the Si2p edge, measured in the photon energy range from 95 eV to 120 eV. Also, here, the intensities of the absorption spectra were divided by the incoming photon flux, because of the time dependence and, in this case, the photon energy dependence.

By increasing the deposition of HfO_2, the overall intensity of the Si2p core level changes because of the increasing thickness of the oxide. Electrons from the substrate have to travel into the Hf-oxide film before escaping into the vacuum. The elastic scattering of those electrons produce an intensity attenuation which is exponentially dependent on the overlayer thickness d as expressed in the equation $I = I_0\exp(-\lambda/d)$, where λ represents the mean free path of the electrons in the oxide. This is a function of the electron kinetic energy, with a minimum at about 0.5 nm for electrons with

a kinetic energy of 50 eV. It is therefore possible to determine the thickness of the oxide film through the intensity weakening of the Si oxide and the substrate components.

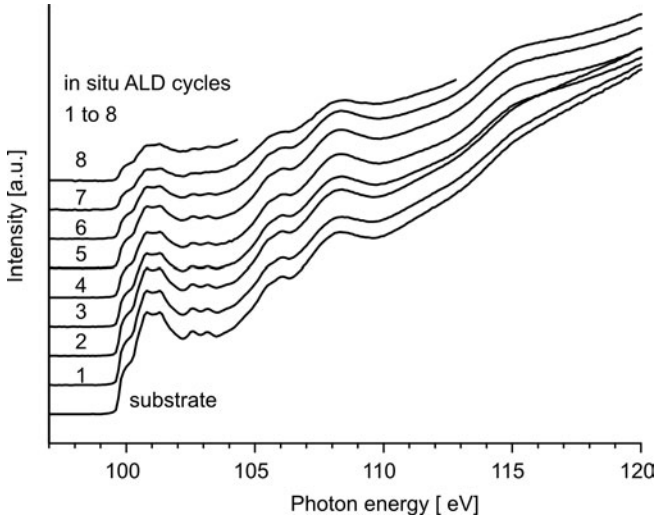

Fig. 2. In-situ growth of HfO_2 on a SiO_2/Si(001) substrate. The total electron yield spectra are taken at the Si2p edge of the sample after the initial etch and after every ALD cycle.

In Table 1, we report the Hf-oxide thickness extracted from the photoemission data after every cycle. The estimation was made by considering a homogenous oxide layer and by adopting the value 0.5nm for the mean free path of the electrons with a kinetic energy of about 50 eV in HfO_2. The simple assumption of a homogeneous oxide layer could be misleading for the interpretation of our results, as in the ALD growth the coverage of the surface is not necessarily homogeneous. Nevertheless, we are developing a mathematical model to take into account the deviation of the experimental results from a simplified homogeneous growth.

Table 1. Thickness of the initial SiO_2 and of the HfO_2 as determined from the XPS intensities after every ALD cycle

Film	Etched SiO_2	HfO_2							
		1 cycle	2 cycles	3 cycles	4 cycles	5 cycles	6 cycles	7 cycles	8 cycles
Thickness [nm]	0 .54	0.13	0.20	0.53	0.69	0.86	1.06	1.49	1.62

After the 8th cycle the substrate is covered with a Hf-oxide film about 1.5 nm thick, showing an excellent sensitivity of our technique to films with a thickness in the nanometer range. At such a thickness, the contamination of the sample due to the transport in air certainly would considerably distort the interpretation of the experi-

mental data. However, with our in situ facility, we can assure the measurement of thickness and analyze the chemical state after each cycle.

The Si2p photoemission spectra change also in shape with increasing HfO_2 deposition. This is especially evident in the energy range between 102 eV and 104 eV, where the contributions from Si^{3+} and Si^{4+} are expected. In the etched sample, the most intense peak is centred at 103.4 eV due to the Si^{4+} component from SiO_2. After the first three cycles, the peak shifts evidently towards lower binding energies, meaning an increase of the Si^{3+} component. After the first three cycles the shift is still present up to the 6th cycle but is much smaller, and it is undetectable in the last two cycles. The strong shift observed in the first cycles is due to the formation, during the early stages of the growth, of Hf-silicate (Hf–O–Si bonds), while in the next cycles the growth is converted to HfO_2. Also here, the observation of the transition between the Hf silicate growth and the HfO_2 growth were possible only because the sample was transferred into the measurement chamber without breaking the vacuum and without contaminating it with external agents.

Also the NEXAFS spectra recorded at the Si2p edge show variations with the growth of Hf oxide. The two main structures are those between 100 eV and 105 eV, ascribed to the substrate Si, and those between 105 eV and 115 eV, derived from SiO_2. The oxide growth induces an attenuation of the absorption spectra in a similar way as for the photoemission spectra. Anyway, the attenuation observed in the energy range of the substrate Si is slightly different from that observed in the energy range of SiO_2. That deviation could be due to either formation of an extra silicon oxide during the Hf oxide deposition or to the transformation of the initial SiO_2 into Hf silicate. The latter possibility is in accordance with the broadening of all peaks in the range 105–115 eV due to smearing of the silicate signal into the silicon dioxide one. From the present status, no definitive answer can be given, but more accurate measurements, at the O1s edge for example, should clarify this point.

3.2. Band gap determination by combined XAS and RIXS measurements

In this section, we report on a study of a hidden layer of AlON deposited between the Si(001) substrate and a Pr_2O_3 layer. In the particular sample used for the studies, the thickness of the AlON layer was 1.5 nm, and the thickness of the Pr_2O_3 layer was 5 nm. The AlON films were prepared by reactive ion sputtering from an Al target; details have been published elsewhere [19]. Pr_2O_3 films were obtained by thermal evaporation in an e-beam evaporator; for details see [15].

In Figure 3, the resonant inelastic X-ray spectroscopy (RIXS) data are shown obtained by excitation above the N1s edge. In a RIXS spectrometer (also called X-ray emission spectroscopy XES), upon resonant excitation, the emitted X-ray fluorescence photons are collected and recorded in function of their detected energy. This method yields a partial density of states of the valence band. Photons of 405 eV were used to excite emission and the emitted photons in the energy range between 370 eV and

400 eV were collected. The observed bands correspond to the N2p valence states in the hidden AlON layer. The triple shaped valence features are very similar to the valence band features of other 2p systems such as O2p in SiO_2 or C2p in C-based compounds reported by RIXS as well as by XPS valence band studies.

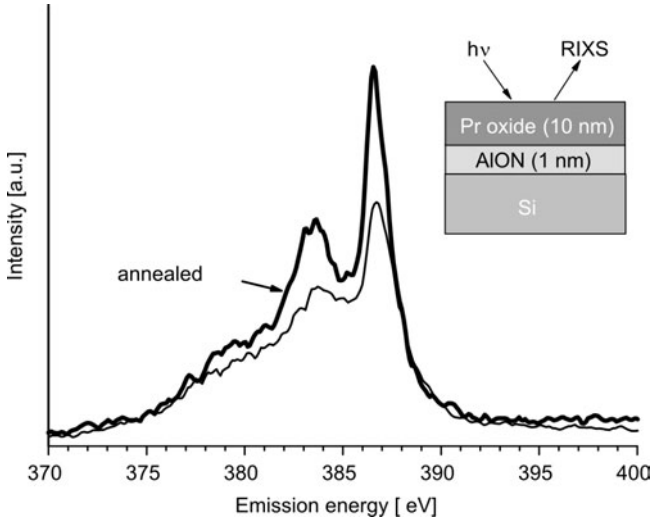

Fig. 3. RIXS spectrum taken at the resonant excitation (405 eV) from a hidden AlON layer in a Pr_2O_3/AlON/Si sandwich structure. Thin line: as deposited sample, bold line: sample annealed at 800 °C, 10 min in nitrogen

In Figure, 3 two spectra are shown. One spectrum is obtained from a sample where the AlON–Pr oxide stack was investigated as prepared, while the other curve is from a sample taken out of the same run but after annealing the stack at 800 °C for 10 min in nitrogen. The difference in the data indicates that upon annealing some crystallites within the Pr oxide film form causing a reduction of the film thickness. Consequently, the N1s signal from the hidden AlON layer appears stronger in the annealed sample. Another difference is very evident: in the annealed sample the valence features appear more sharpened. Another difference is also very evident: in the annealed sample the valence features are more sharply profiled. This is an argument which indicates some ordering in the otherwise more amorphous layers right after the sputtering deposition.

For a further analysis of the RIXS data in Fig. 4 we have used the spectrum of the annealed sample but now have included the XAS spectrum recorded on an AlON film before depositing the Pr_2O_3 layer. The purpose of this figure is to combine the valence band state density with the density of the empty conduction band states. In addition, we have marked the position of the Fermi energy which we obtained from independent measurements of metallic systems.

As a consequence, these combined data may be used to derive a band gap value for the hidden AlON buffer layer. A value of ca. 7 eV was determined and that value

considers only the N2p derived partial density of states. It should be mentioned that our results are taken upon resonant excitation and we therefore probe selectively only the N2p states. However, with this value we have demonstrated that our choice to use AlON as a buffer material is quite reasonable. The band gap is smaller than that of Al_2O_3 (ca. 9 eV) but still large enough to ascertain a proper dielectric behaviour of that buffer layer. The band offset with respect to the Si-substrate amounts to 4 eV for the VB and 2 eV for LB.

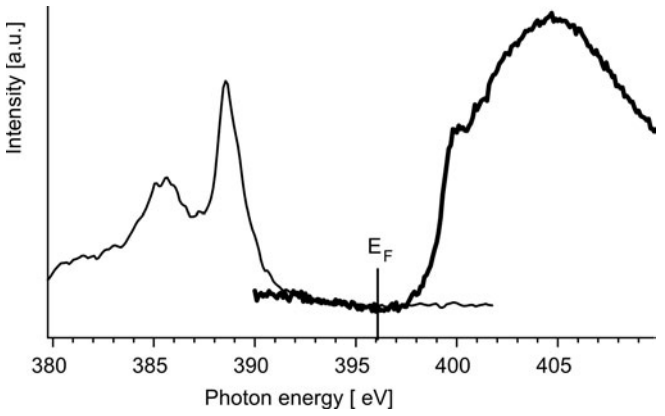

Fig. 4. Combined RIXS (thin line) and XAS (bold line) data from AlON layers plotted on a common energy scale which is referred to the Fermi energy

Determining the VBM from the slope of the sharp feature yields the value of ca. 5 eV below E_F. However, there are still some states appearing above that value. These states are due to hybridization of the N2p levels with the oxidic valence states. In Pr_2O_3 films the value of the VBM is about 3 eV below E_F. This is in agreement with the width of the hybridized states shown in Fig. 4.

To summarize, in this section we demonstrated the combination of RIXS and XAS data upon resonant excitation to obtain the partial density of states for both the valence and conduction bands. In addition, if the position of the Fermi energy can be obtained from independent measurements, the absolute values of the valence band maximum and of the band gap of the investigated system can be derived. Furthermore, we have demonstrated that the use of X-ray fluorescence spectroscopy enables the analysis of hidden layers with sufficient data quality.

3.3. Improved electrical parameters by using an aluminum oxynitride (AlON) buffer layer

Chemical reactivity of the Pr_XO_Y/SiC and Pr_XO_Y/Si interfaces causes a deleterious interaction yielding graphite and silicate formation after direct deposition of Pr_XO_Y onto SiC and Si, respectively [9, 17]. This leads to high leakage currents [4] and it limits the reduction of the CET as well.

Using an approximately 1–1.5 nm thick buffer layer of AlON, we found leakage current values improved by several orders in comparison to the stacks without the buffer. At a CET of 4 nm we could observe a leakage current density of 10^{-7} A/cm^2 (at 1 V above flat band condition) on silicon based stacks (Pr_XO_Y/AlON/Si). Furthermore, we found, for this system, that the introduction of the AlON buffer layer combined with subsequent annealing in nitrogen at 800 °C results in a decrease of the density of interface states D_{it}. Values of 5×10^{11}–1×10^{12} eV$^{-1}\cdot$cm^{-2} are observed. Using a plot of the CET versus the physical thickness of Pr_XO_Y and fitting it to a simple model of capacitors in series, we can deduce the thickness of an interfacial layer and the permittivity values of the high-*k* material. Permittivity values of the high-*k* material in the range of 17–20 were calculated in this way, the values are not influenced significantly by the buffer layer. But we could also show that the interfacial layer CET value could be reduced from 3.9 nm to 1.3 nm by using the AlON buffer, where we have to point out that this value already contains the buffer layer CET value, so the unintentional interfacial layer thickness is even smaller. Also on SiC the insertion of the buffer layer leads to better electrical characteristics. For further details of these investigations refer to [4, 19, 20].

Summarizing this section, AlON provides a suitable buffer layer between high-*k* Pr_XO_Y and Si as well as between Pr_XO_Y and wide band gap SiC. This is evident from our spectroscopic investigations (reduced silicon out-diffusion [20], higher Pr_2O_3 fractions [20], stable interface [18]), and from improved electrical parameters (low values of leakage current, D_{it}, and interfacial layer thickness). A better band alignment and reduced interfacial reactions might be responsible for these improvements.

4. Characterization of organic materials

In this paragraph, the use of synchrotron radiation (SR) based spectroscopic and microscopic techniques is demonstrated for the analysis of organic materials. We present data from a ferroelectric polymer which is a candidate for non-volatile memory devices, and we report on studies of fullerene based thin films which may be used as low-*k* materials.

4.1. Ferroelectric polymer P(VDF-TrFE)

Non-volatile ferroelectric polymer random access memory devices based on ferroelectric polymers have the potential to overcome many of the fabrication issues faced in the inorganic semiconductor industry [24]. Ferroelectric properties of copolymers of vinylidene fluoride with trifluoroethylene (P(VDF-TrFE)) have become of great interest due to potential use in non volatile memory technology [25]. It was found that in a compositional range from 50/50 to 80/20 mol % ratio of VDF/TrFE, copolymers have ferroelectric phase at room temperature [26]. In addition, these copolymers are

soluble in non toxic reagents. The most common solvent for preparing P(VDF-TrFE) thin films is 2-butanone, or cyclohexanone [27, 28]. The P(VDF-TrFE) solution is available for spin coating, ink jet printing, or roll to roll printing [29]. Spin cast films of P(VDF-TrFE) are not only available as a ferroelectric material but also usable as an organic high-*k* insulation for organic transistors [30, 31].

For electrical contacts, thermally evaporated aluminium has been widely used, compared with other metals such as Cu or Ag, because of its good adhesive strength on the copolymer film [32, 33]. But due to interactions at the interface, even at room temperature, a thin layer of AlF_3 is formed. If poly (3,4-ethylenedioxydi-thiophene):poly(styrenesulfonic acid) (PEDOT:PSS) is used, no interface reaction takes place, as revealed by XPS [34-36].

Here, we like to focus on some fundamental investigations of the copolymer molecular structure, performed by polarization dependent X-ray absorption spectroscopy (XAS) at the U49/2-PGM beam line of the BESSY-II synchrotron. As a copolymer, we used P(VDF-TrFE) in mol% ratio of 70:30, delivered by Piezotech S.A., France. The solvent was 2-butanone, the substrate a Si(100) wafer covered with PEDOT:PSS to prevent possible interface reactions. After spin coating, the copolymer film was annealed for 2 h at 135 °C to improve crystallinity [37].

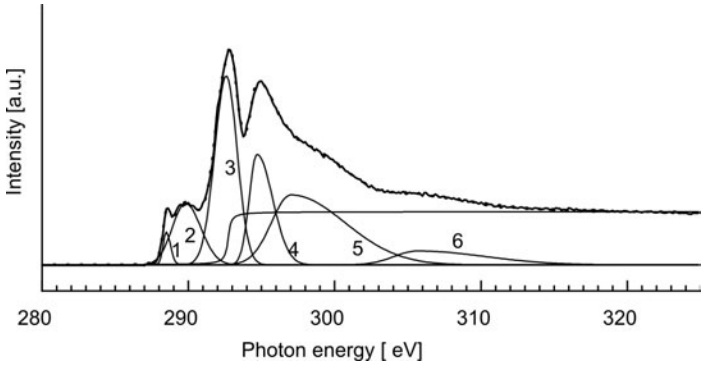

Fig. 5. C-K edge XAS spectra of a thick P(VDF-TrFE) film (~ 100 nm) on SiO_2/Si(100). Details of the peak deconvolution are given in the text

Figure 5 shows the results of XAS measurement of a thick copolymer film (100 nm, measured with a profilometer). The C-K edge is shown in the photon energy range from 280 eV to 325 eV, where various peaks can be isolated by a curve fitting procedure [38]. The peaks 1 and 2 at 287.2 eV and 289 eV are due to a σ^*(C–H) resonance, the peak 3 at 292 eV has to be attributed to a σ^*(C–F) resonance, and the peaks 4, 5, and 6 above 294 eV should be due to σ^*(C–C) resonances [38, 39]. The π^* resonances are not observed as the P(VDF-TrFE) copolymer does not contain unsaturated C–C bonds. It is also evident that no beam damage of the copolymer thin film occurred.

In Figure 6, The C-K edge of a thin copolymer film is shown. The film of the thickness of about 0.4 nm was deposited again on the PEDOT:PSS/Si(100) substrate.

This copolymer film thickness was measured by the attenuation of the XPS signal of PEDOT:PSS [34] and corresponds to the thickness of one monolayer (0.5 nm) [40].

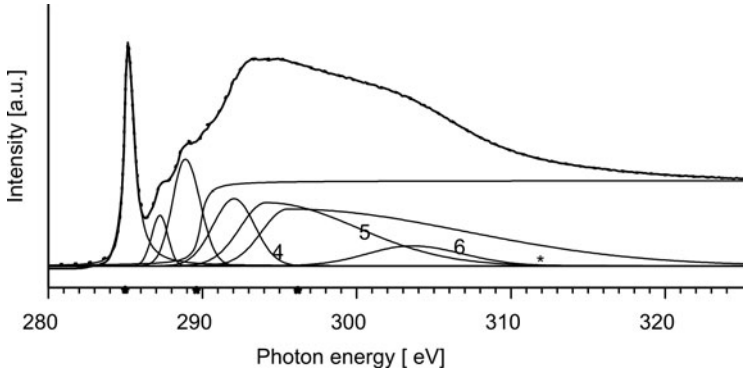

Fig. 6. C-K edge XAS spectra of very thin P(VDF-TrFE) film (ca. 0.4 nm) on PEDOT:PSS SiO_2//Si(100). For details of the peak deconvolution refer to the text. Peaks marked by a star are attributed to the substrate

Obviously, now there is a very sharp peak at 285.0 eV, which is due to π^*(C=C) resonances of PEDOT:PSS. This signal is not observed for the thicker film in Fig. 5 as it is attenuated by the PVDF film. The peak at the photon energy of 287.2 eV is due to a σ^*(C–H) resonance, and the peak at 288.9 eV is again attributed to the substrate with the σ^*(C–S) resonance of PEDOT:PSS. The rest of the peaks are only identifiable by a curve fitting procedure (see figure 6). In the curve fitting procedure, the π^*(C=C) resonance fits to Gaussian profile which match the height of the experimental peaks.

The Gaussian function matched well because of the limitation of instrumental resolution, while the Lorentzian fit is poor because the base is too broad [38]. If the instrumental resolution is comparable with the intrinsic lifetime-related width of the peak, then the peak is fitted by a Lorentzian profile. In our spectra, the σ^*(C–H), σ^*(C–S), and σ^*(C–F) resonances are fitted with Lorentzian profiles. The other peaks are fitted with an asymmetric Gaussian profile. The increase in width of resonances with increasing energy can be simply attributed to lifetime broadening. That means, the higher the energy of the final state, the shorter its lifetime and hence the broader the peaks [41, 42]. In addition to the peaks, near edge spectra of XAS contain one or sometimes more step-like features referred to as continuum steps. These steps are the result of the excitation of the core electron to a continuum or quasi-continuum of final states, e.g. to the smooth density of states [38].

Based on this peak identification, we present an analysis of angle dependent linear dichroism. In order to understand the ferroelectric nature of the PVDF copolymer the existence of oriented dipoles is a question of special interest. Here, we show an analysis of our NEXAFS measurement of an ultrathin (0.4 nm) copolymer film deposited on a PEDOT:PSS/Si substrate. Due to linear dichroism, we have to expect a modula-

tion of the intensity of specific absorption signals, if they can be attributed to a preferred orientation of dipole moments inside the copolymer film. In such cases, using the dipole approximation, this intensity should be proportional to $\cos^2\theta$, if an idealized alignment of the dipoles perpendicular to the surface is assumed [38]. In our experiment, the angle θ is the angle between the direction of the incident beam and the normal to the surface of the sample (inset in Fig. 7).

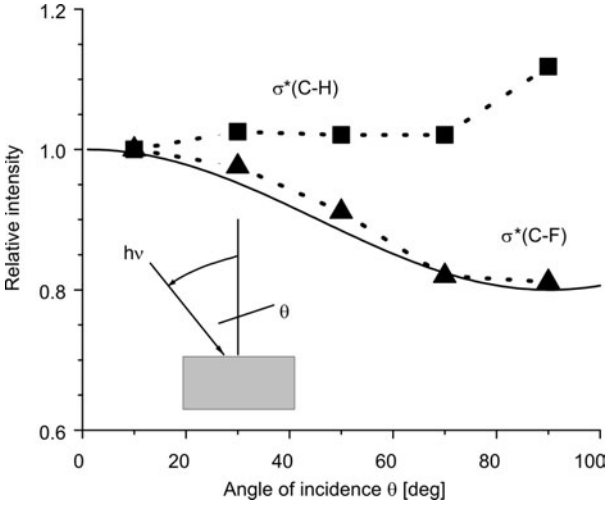

Fig. 7. Angle dependent spectra of P(VDF-TrFE) on a PEDOT/Si(100) substrate, 0.1 wt. % P(VDF-TrFE) in 2-butanone (thickness ca. 0.4 nm); the intensities of the σ^* (C–F) excitation at 292.04 eV (triangles, dotted line) and of the σ^* (C–H) excitation at 287.28 eV (squares, dotted line) normalized to the value at near-normal incidence (10°). The solid line presents the $\cos^2\theta$ modulation of intensities for an idealized alignment of dipoles (100% perpendicular to the surface of the substrate)

In Figure 7, we show the intensity of the σ^*(C–F) resonance at 292.04 eV compared with the σ^*(C–H) excitation at 287.28 eV. The observed intensity values are normalized to the peak intensity at 10°. For the σ^*(C–F) excitation (the C–F dipole) clearly an angular dependence of the intensity is visible. In contrast, for the σ^*(C–H) excitations we have no angular dependence at all. The highest dipole moment has to be attributed to the σ^*(C–F) resonance, caused by the electronegativity of fluorine atoms. Consequently we assign the σ^*(C–F) excitations to represent the ferroelectric dipole moments while the σ^*(C–H) excitations have no contribution to the ferroelectric moments, as expected. The observed angular variations can be modelled according to $I = 0.2\cos^2\theta + 0.8$ with a reasonable agreement. This means that about 20% of the ferroelectric dipoles are oriented with respect to the polarization of the incoming light. This quantity is remarkable as we have not applied an external field to the film. The $\cos^2\theta$ dependence certainly is just an approximation. Nevertheless, the measurements show a clear linear dichroism indicative of an alignment of C–F dipoles, even without the application of an external field. It seems that self alignment and ferroelectric order-

ing occurs even for ultrathin and spin-coated films, if we avoid reactive interfaces and use an inert substrate such as PEDOT:PSS.

4.2. Fullerene thin films as low-*k* materials

The low-*k* materials investigated so far include examples from organosilicate glasses (OSG) and of fullerene based porous ultra low-*k* (ULK) films. OSG materials that are used as low-*k* materials to isolate on-chip interconnects are investigated and we use the chemical sensitivity of the X-ray absorption signal around the C1s and Si2p edges to describe the chemical stability of such materials against UV curing and plasma treatment. In our XAS studies we are able to distinguish the individual σ-orbitals based on the C1s absorption features, i.e. the bonds of individual groups of the material investigated. In general, in the data for OSG the C–C, the C–O, and the C–H groups can be identified by different transition energies of the corresponding excitations. If one of the groups is modified, only this particular contribution of the XAS spectrum changes, which makes the technique very sensitive and selective for analysis of materials.

For fullerene based polymers, being candidates for ultra low-*k* materials [43], we demonstrate the stability of fullerene complexes after incorporation in sol-gel processed films. In the case of C_{60} derived components, there is a particular mechanism causing a characteristic feature in the absorption data. Based on the electronic properties of the C_{60} molecules in all C_{60} derived compounds, there is a characteristic split in the lowest absorption band causing a three-peak structure.

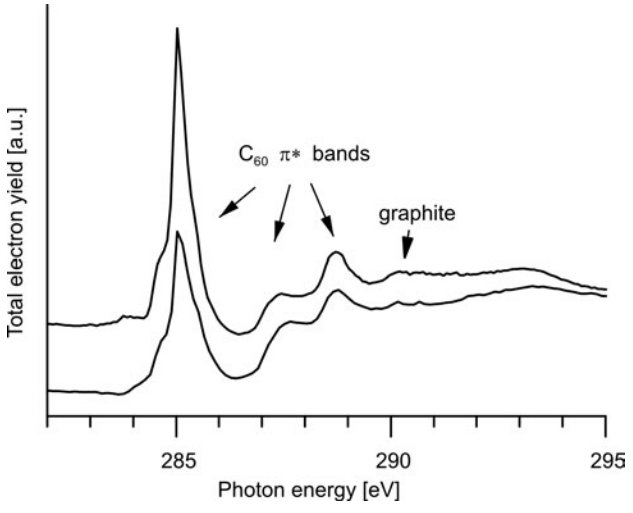

Fig. 8. XAS spectrum at the C1s edge of a thin film of a fullerene based low-*k* material taken at two different positions of the sample

These features represent transitions into the triple π^* orbitals of C_{60} and range between 285 eV and 289 eV. In Fig. 8 we show the total electron yield (TEY) spectra of

C_{60} derived films in the energy range between 282 eV and 295 eV. In line with expectation, we find the characteristic features of the C_{60} molecule are well pronounced and resolved for these C-cage ULK films. The observed features peak around 285 eV, 287.8 eV, and around 289 eV. In particular, the middle band appears at a higher transition energy than in pure C_{60} films. We attribute the differences in the peak position to the specific bonding of the C_{60} polymer.

Still, we have problems in recording such data. The films seem to be inhomogeneous and our spectroscopic observations indicate that at some positions there is a higher content of graphite in the films. In previous ULK films the amount of graphite was even larger and this made a clear detection of the split π^* bands almost impossible.

We have also investigated the XAS data of the preliminary obtained C-cage based ULK films at the N1s and O1s edges, respectively. At the N1s we identified absorption features that we attribute to residuals of the solvents used for the preparation of the films. At the O1s edge we find very unusual features, as there is a sharp absorption band at 531 eV which is well separated from the main absorption band rising at around 537 eV. Such an absorption pattern is usually observed for conducting oxides such as NiO and CrO_2.

5. Summary

We demonstrated some recent examples of synchrotron radiation based analysis of materials. We report on XPS, XAS, and RIXS studies on HfO_2 thin films and on Pr_2O_3 /AlON/SiO_2 multilayer stacks. The SR based techniques are used to learn about the growth mechanism, chemical stability, and interface reactions in such systems. In addition, the electronic properties such as the band-offsets and the band gap, are determined, as demonstrated, for the latter system.

For organic systems, we report on the usage of the linear dichroism in the absorption signal to learn about the existence of ferroelectric dipole moments in such films. Finally, the fine structure of the absorption spectra at the C1s edge is used, in particular, for detailed analysis of the composition of films. As a specific example, it is shown how this method can be used to identify C_{60} building blocks of a polymer which is to represent an ultralow-*k* prototype material.

Acknowledgements

We would like to acknowledge the skillful assistance of G. Beuckert, I. Paloumpa, and P. Hoffmann. This work was supported in part by the DFG SPP 1157 (SCHM 745/11-1-2 and SCHM 745/9-1-3) and BMBF (13N9431).

References

[1] SCHMEISSER D., HOFFMANN P., BEUCKERT G., *Electronic Properties of the Interface formed by Pr_2O_3 growth on Si(001), Si(111) and SiC(0001) surfaces* [in:] *Materials for Information Technology,*

Devices, Interconnects and Packaging, *Series: Engineering Materials and Processes*, E. Zschech, C. Whelan, T. Mikolajick (Eds.), Springer, Berlin, 2005, 449–460.
[2] SCHMEISSER D., ZHENG F., HIMPSEL F.J., ENGELMANN H.J., ZSCHECH E., Mat. Sci. Semicond. Proc., 9 (2006), 934 – 939.
[3] SCHMEISSER D., ZHENG F., PEREZ-DIESTE V., HIMPSEL F.J., LONIGRO R., TORO R.G., MALANDRINO G., FRAGALÀ, I.L., Mater. Sci. Eng., C 26 (2006), 1122.
[4] HENKEL K., TORCHE M., SOHAL R., SCHWIERTZ C., HOFFMANN P., SCHMEISSER D., MRS Proceedings, 911 (2006), B10-11.
[5] LUPINA G., SCHROEDER T., DABROWSKI J., WENGER CH., MANE A.U., MÜSSIG H.-J., HOFFMANN, P., SCHMEISSER D., J. Appl. Phys., 99 (2006), 114109.
[6] SCHMEISSER D., LUPINA G., MÜSSIG, H.-J., Mater. Sci. Eng., B 118 (2005), 19.
[7] SCHMEISSER D., MÜSSIG H.-J., *Pr-silicate formation on SiO_2 covered 3C–SiC(111),* AIP Conference Proceedings, 772 (2005), 75.
[8] LUPINA G., SCHROEDER T., DABROWSKI J., WENGER CH., MANE A.U., LIPPERT G., MÜSSIG H.-J., HOFFMANN P., SCHMEISSER D., Appl. Phys. Lett. 87 (2005), 092901
[9] GORYACHKO A., PALOUMPA I., BEUCKERT G., BURKOV Y., SCHMEISSER D., Phys. Stat. Solidi, C 1 (2004), 265 – 268.
[10] SCHMEISSER D., Mater. Sci. Semicond. Proc., 6 (2003), 59.
[11] SCHROEDER T., LUPINA G., SOHAL R., LIPPERT G., WENGER CH., SEIFARTH O., TALLARIDA M., SCHMEISSER D., J. Appl. Phys., 102 (2007), 014103.
[12] HOFFMANN P., GORYACHKO A., SCHMEISSER D., Mater. Sci. Eng., B 118 (2005), 270.
[13] SCHMEISSER D., MÜSSIG H.-J., Solid State Electronics, 47 (2003), 1607.
[14] SCHROEDER T., LUPINA G., SOHAL R., LIPPERT G., WENGER CH., SEIFARTH O., TALLARIDA M., SCHMEISSER D., J. Appl. Phys., 102 (2007), 014103.
[15] TORCHE M., HENKEL K., SCHMEISSER D., Mater. Sci. Eng., C 26 (2006), 1127.
[16] SCHMEISSER D., MÜSSIG H.-J., J. Phys. Cond. Matter, 16 (2004), 153.
[17] SCHMEISSER D., MÜSSIG H.-J., DABROWSKI J., Appl. Phys. Lett., 85 (2004), 88.
[18] SOHAL R., TORCHE M., HENKEL K., HOFFMANN P., TALLARIDA M., SCHMEISSER D., Mater. Sci. Semicond. Proc., 9 (2006), 945.
[19] HENKEL, K., SOHAL R., SCHWIERTZ C., BURKOV Y., TORCHE M., SCHMEISSER D., MRS Proc., 996 (2007), H05-23.
[20] HENKEL K., KARAVAEV K., TORCHE M., SCHWIERTZ C., BURKOV Y., SCHMEISSER D., J. Phys.: Conf. Ser., 94 (2008) , 012004.
[21] NICOLLIAN E.H., BREWS J.R., *MOS Physics and Technology,* Wiley, New York, 1982.
[22] MACK P., WHITE R.G., WOLSTENHOLME J., CONARD T., Appl. Surf. Sci. 252 (2006), 8270.
[23] DELABIE A. ET AL., J. Electrochem. Soc., 153 (2006), F180.
[24] FORREST S.R., Nature, 428 (2004), 911.
[25] PARASHKOV R., BECKER E., RIEDL T., JOHANNES H., KOWALSKY W., Proc. IEEE 93 (205), 1321.
[26] ZHANG Q.M., XU H., FANG F., CHENG Z.-Y., XIA F., YOU H., J. Appl. Phys., 89 (2001), 2613.
[27] NABER R.C.G., BLOM P.W.M., MARSMAN A.W., DE LEEUW D. M., Appl. Phys. Lett., 85 (2004), 2032.
[28] NABER R.C.G., DE BOER B., BLOM P.W.M., DE LEEUW D.M., Appl. Phys. Lett., 87 (2005), 203509.
[29] ZHANG S., LIANG Z., WANG Q., ZHANG Q., Mater. Res. Soc. Symp. Proc., 889 (2005), W05-02.1.
[30] MÜLLER K., PALOUMPA I., HENKEL K., SCHMEISSER D., J. Appl. Phys., 98 (2005), 056104.
[31] MÜLLER K., PALOUMPA I., HENKEL K., SCHMEISSER D., Mat. Sc. Eng., C 26 (2006), 1028.
[32] XIA F., ZHANG Q.M., Appl. Phys. Lett., 85 (2004), 1719.
[33] WU P., YANG G.-R., MA X. F., LU T.-M., Appl. Phys. Lett., 65 (1994), 508.
[34] MÜLLER K., MANDAL D., SCHMEISSER D., MRS Proc., 997 (2007), I6-02.
[35] MÜLLER K., MANDAL D., SCHMEISSER D., Thin solid films, submitted.

[36] MÜLLER K., BURKOV Y., MANDAL D., HENKEL K., PALOUMPA I., GORYACHKO A., SCHMEISSER D., Physica Status Solidi (A) 205 (2008), 600 – 611.
[37] FURUKAWA T., Phase Transitions, 18 (1989), 143.
[38] STÖHR J., NEXAFS Spectroscopy, 2nd ed. Springer, Berlin, 2003.
[39] JOLLY W.L., BOMBEN K.O., EYERMANN C.J., At. Data Nucl. Data Tables, 31 (1984), 433.
[40] PALTO S., BLINOV L., DBOVIK E., FRIDKIN V., PETUKHOVA N., SOROKIN A., VERKHOVSKAYA K., YUDIN S., ZLATKIN A., Europhys. Lett., 34 (1996), 465.
[41] DEHMER J. L., DILL D., WALLACE S., Phys. Rev. Lett., 43 (1979), 1005.
[42] SETTE F., STÖHR J., HITCHCOCK A.P., J. Chem. Phys., 81 (1984), 4906.
[43] ZAGORODNIY D., CHUMAKOV D., TÄSCHNER C., LUKOWIAK A., STEGMANN H., SCHMEISSER D., GEISLER H., ENGELMANN H.J., HERRMANN H., ZSCHECH E., IEEE Trans. Semicond. Manuf., 21 (2008), 646.

Received 15 January 2008
Revised 19 December 2008

Materials Science-Poland, *Vol. 27*, *No. 1*, *2009*

The influence of the prefiring temperature on the structure and surface morphology of sol-gel derived ZnO film

K. S. HWANG[1] S. HWANGBO[2], J. T. KIM[3*]

[1]Department of Applied Optics and Institute of Optoelectronic Technology,
Nambu University, 864-1 Wolgye-dong, Gwangsan-gu, Gwangju 506-824, Republic of Korea

[2]Major in Photonic Engineering, Division of Electronic and Photonic Engineering,
Honam University, 59-1 Seobong-dong, Gwangsan-gu, Gwangju 506-714, Korea

[3]Department of Photonic Engineering, College of Engineering,
Chosun University, 375 Seosuk-dong, Dong-gu, Gwangju 501-759, Korea

C-axis oriented ZnO thin films were prepared on silica glass substrates by the sol-gel method using a zinc naphthenate precursor. As-deposited films were prefired at 250 °C for 60 min, at 350 °C for 30 min, and at 500 °C for 10 min, followed by final annealing at 600–900 °C in air. Crystal structure, surface morphology, surface roughness and transmittance at the visible range were analyzed by high resolution X-ray diffraction, field emission scanning electron microscopy, scanning probe microscopy, and ultraviolet spectrophotometry. (002)-oriented ZnO films were obtained by annealing at 600 °C, and at higher temperatures for the films prefired at 350 °C and 500 °C. All the films exhibited a high transmittance, above 80%, in the visible region, and showed a sharp fundamental absorption edge at 0.38–0.40 μm. The most highly *c*-axis oriented ZnO with a homogeneous surface was observed at a prefiring temperature of 350 °C.

Key words: *ZnO thin film; sol-gel method; zinc naphthenate*

1. Introduction

The wet sol-gel method provides a simple and versatile alternative for crystalline thin film preparation [1–5]. In terms of stability in air and ease of handling, metal naphthenates are more advantageous as starting materials than metal alkoxides [6, 7]. Preparation of the coating solution using zinc naphthenate was easy by the addition of toluene, while a complicated procedure was needed for coating a metal alkoxide-

*Corresponding author, e-mail: kimjt@mail.chosun.ac.kr

derived solution. Furthermore, it should be noted that vaporization of additives such as alcohol, H_2O and catalyst etc. during prefiring and final heat treatment might cause cracks and pores in the product layer, and this disturbs the preparation of high quality oxide layers. However, the sol-gel method is relatively new and requires a greater understanding of the relation between processing and defects in order to optimize the film quality. Although the film shows a high orientation, pores and cracks due to vaporization of organics in film are easily recognizable in highly oriented films [8].

The authors suspected that the films might be excessively locally heated to high temperatures such as 600–900 °C because organic compounds that decompose and evolve during the pyrolysis are rapidly burned out. This may cause random nucleation and heterogeneous crystal growth, thus disturbing high orientation or epitaxy. Thus, comparison between the prefiring temperatures was considered to be important in order to achieve homogeneous nucleation resulting in high orientation.

In order to develop high quality ZnO films for devices with good performance, it is necessary to clarify the effect of heating conditions on growth. This will result in different microstructures suitable for various applications. The thermal analysis on zinc naphthenate shows that pyrolysis begins at 200 °C and is completed below 500 °C. Thus in the presented study prefiring temperatures were varied at 250–500 °C in order to clarify the effect of organics on the properties of ZnO.

2. Experimental

Zinc naphthenate (Nihon Kagaku Sangyo Co., Ltd., Japan) was used as a precursor in the sol-gel process by diluting the sol with toluene. The concentration of metal ions in the coating solution was about 4 wt. %.

Thin films were fabricated by spin coating onto 2.5 cm×2.5 cm×1 mm substrates made of silica glass at the rotation speed of 1500 rpm for 10 s. After each deposition, the coating film was pyrolyzed in air at 250 °C for 60 min, 350 °C for 30 min, and 500 °C for 10 min to decompose the organic species. For multiple coatings, the above-mentioned processes were repeated five times to obtain the resultant films approximately 0.5– 0.6 μm thick. The resultant films were directly annealed in a preheated furnace at 600–900 °C for 30 min in air. Table 1 shows the symbols used for the products.

Table 1. Symbols of the product films

Final annealing	Prefiring		
	250 °C	350 °C	500 °C
600 °C	A1	B1	C1
700 °C	A2	B2	C2
800 °C	A3	B3	C3
900 °C	A4	B4	C4

Thermogravimetric analysis (TGA, DTG-60, Shimadzu, Japan) was performed using an α-alumina reference and the heating rate of 10 °C/min in the range 16–600 °C. The phase evaluation of the films was examined by a high resolution X-ray diffractometer (HRXRD, X'pert-PRO, Philips, Netherlands) using CuK_α radiation in θ–2θ geometry. The surface morphology and composition of the films were evaluated from the field emission scanning electron microscopy (FE-SEM, S-4700, Hitachi, Japan) micrographs and energy dispersive X-ray spectrometry (EDS). The growth mechanism and surface roughness of the films were studied with a scanning probe microscope (SPM, Nanoscope IV, Digital Instruments, U.S.A.). All the SPM measurements were performed in air using the tapping mode. The transmittance in the visible spectra range was measured with an ultraviolet–visible–near infrared spectrophotometer (CARY 500 Scan, Varian, Australia). The transmittance was automatically calibrated against a bare glass substrate as a reference sample, and the absorption coefficient was obtained from the transmittance curve.

3. Results and discussion

Figure 1 shows the TGA curve of the starting solution dried at 80 °C for 24 h to remove the solvent. Weight loss corresponding to pyrolysis of the metal naphthenate began at around 160 °C and was completed at below 500 °C. Therefore, it was concluded that pyrolysis of the starting metal naphthenate solution is completed below 500 °C. Thus, to investigate the effects of conditions of the pyrolysis on metal naphthenate during the final heat treatment, we prepared ZnO thin films via the prefiring conditions described in the Experimental.

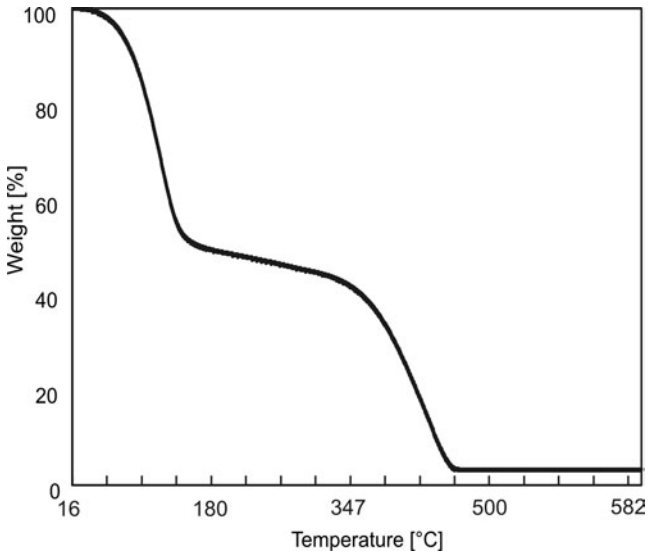

Fig. 1. TGA curve of the coating solution used in this work

All the precursor films, pyrolyzed through three paths, were found to be amorphous by XRD, and have smooth surfaces without cracks or voids as confirmed by FE-SEM observation. No significant difference was identified among these films. There were differences, however, in the content of residual carbon or carbon hydroxides in the precursor films. Residual carbon content in the films was investigated by EDS.

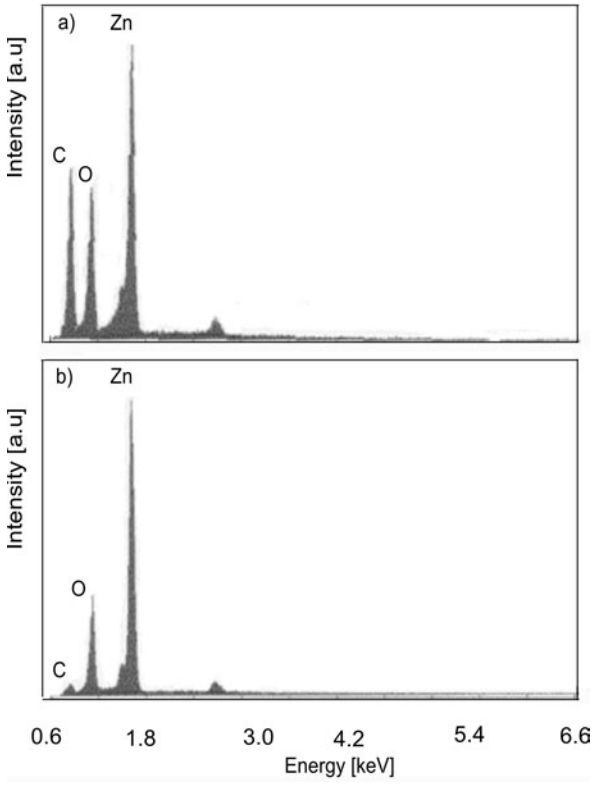

Fig. 2. EDS spectra for the surfaces of the films after prefiring:
a) at 250 °C for 60 min, b) at 500 °C for 10 min

Figures 2a, b show EDS spectra of the precursor films pyrolyzed at 250 °C for 60 min and at 500 °C for 10 min, respectively. Comparing these spectra, a large peak of CK_α was recognized in Fig. 2a. It is apparent that precursor films pyrolyzed at 250 °C for 60 min contained a larger amount of carbon than those pyrolyzed at 500 °C for 10 min.

Figure 3 shows XRD θ–2θ scans of the ZnO thin films pyrolyzed at 250 °C for 60 min (3a), at 350 °C for 30 min (3b), and at 500 °C for 10 min (3c), followed by final heat treatment at various temperatures. The (002) oriented ZnO thin films were obtained by final heat treatment at 600 °C and at higher temperatures for the films pyrolyzed at 350 °C and 500 °C. When the pyrolysis temperature was too low, at 250 °C, crystallization and orientation of ZnO thin films was very difficult to induce:

the resultant ZnO thin films A1–A4 were found to be amorphous or non-oriented. By contrast, in the films B1–B4, a distinct (002) peak of ZnO was recognized. Upon increasing the final heat treatment temperature to 800 °C and 900 °C, a strong ZnO (002) peak was seen. It should be noted that the peak intensity of ZnO thin films was significantly affected by the pyrolysis temperature, although the final heat-treatment temperature was the same. The lower peak intensity of resultant films, shown in Fig. 3a, may be attributed to the presence of residual organic components.

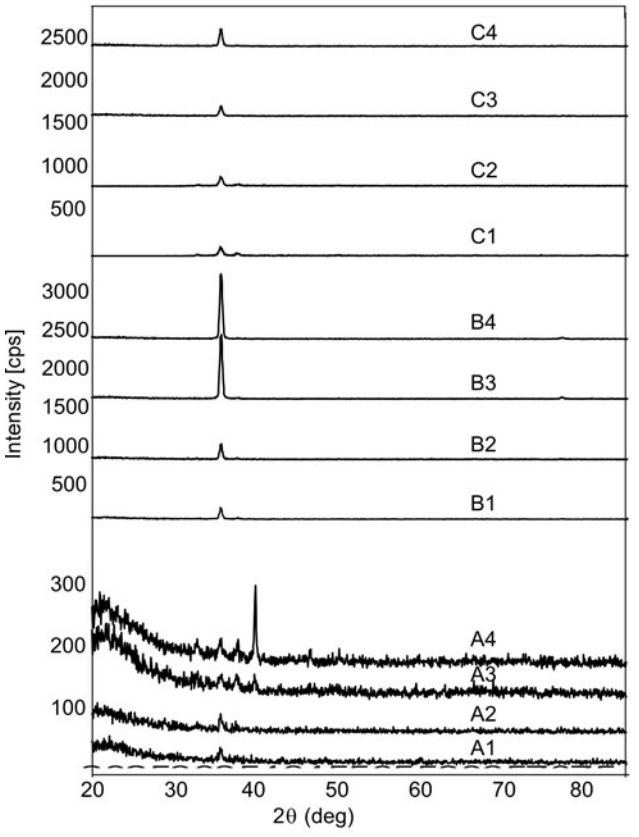

Fig. 3. XRD spectra of finally annealed films prefired:
a) at 250 °C for 60 min, b) at 350 °C for 30 min, c) at 500 °C for 10 min

EDS analysis indicated that the ZnO thin films which had been pyrolyzed at 250 °C contained much residual carbon or carbon hydroxides. In this case, crystallization of the film and decomposition of organic compounds proceeded concurrently during the final heat treatment. Crystal growth may be suppressed by residual carbon during the final heat treatment, resulting in the low peak intensity of ZnO thin films A1–A4 [9].

From the report of Ohyama et al. [10], for ZnO thin films prepared by using sol-gel with zinc acetate–2 methoxyethanol–monoethanolamine solution, when the heating rate is low, the gel film is given enough time to structurally relax before crystallization, resulting in denser ceramic films. Moreover, when the prefiring temperatures are too high (higher than 300 °C), vaporization of the solvents, and thermal decomposition of zinc acetate may take place abruptly and simultaneously with the crystallization, disturbing the unidirectional crystal growth [10]. However, in our work ([11] and present work), highly *c*-axis-oriented ZnO films were obtained by prefiring at higher temperatures, specifically at 350 °C and 500 °C. Previously, we reported that structural relaxation of the precursor gel before crystallization, by employing solvents having high boiling points about 200 °C is unessential for obtaining oriented ZnO thin films when using a zinc naphthenate precursor [11]. We prepared ZnO thin films exhibiting a strongly preferred orientation by using toluene which has a relatively low boiling point.

However, it should be noted that when the prefiring temperatures are too high, such as 500 °C, crystallinity of the ZnO thin films is decreased. This result suggests that abrupt and simultaneous thermal decomposition of zinc naphthenate, probably due to a high prefiring temperature, may slightly corrupt unidirectional crystal growth. In the sol-gel process, several actions occur simultaneously in the thermal treatment process, such as the evaporation of the dissolvent, the decomposition and evaporation of organics and the growth of ZnO grain, etc. [12]. At an excessively high prefiring temperature, the decomposition process is hastened and less time is left for gel films to undergo structural relaxation which induces a decrease in the quality of ZnO.

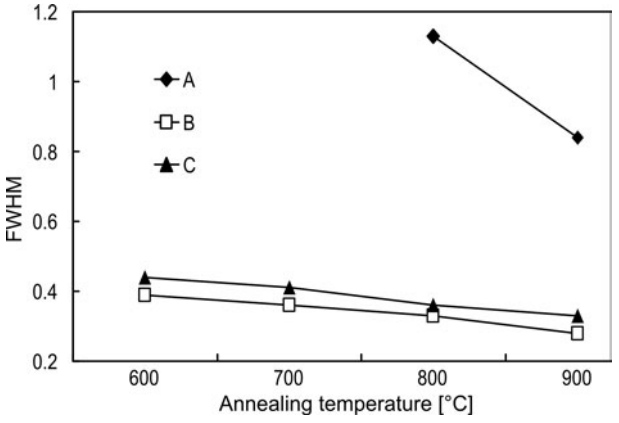

Fig. 4. FWHMs of finally annealed films in function of prefiring temperature

We also observed that with an increase in heat treatment temperature, the full width at half-maximum (FWHM) decreases, as shown in Fig. 4. In addition, the highest crystallinity is observed for the films pyrolyzed at 350 °C. These results indicate that ZnO thin films prepared with zinc naphthenate and prefired at 350 °C can be ex-

pected to have high crystallinity. For the films prefired at 350 °C, the (002) peak intensity of the ZnO films markedly improves with an increase in the annealing temperature. The increase in intensity of the (002) orientation may be attributed to reorientation of the crystallites obtaining sufficient energy at higher annealing temperature. This results in obtaining ZnO with superior crystallinity and a higher degree of orientation. More research for the relation between the crystallization and the exact organic species and contents will be done.

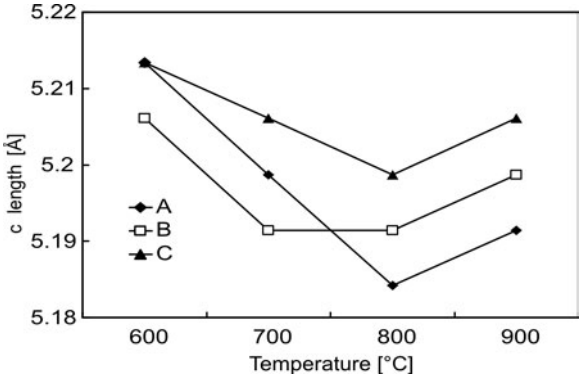

Fig. 5. Length of the *C* period of finally annealed films in function of prefiring temperature

Based on the XRD data, the lattice *c* parameter has been estimated to be 5.1842 –5.2134 Å, as shown in Fig. 5. These values are similar to the ASTM value of 5.2066 Å for the bulk ZnO. The larger value of the lattice constant for the thin film at 600 °C as compared with the standard powder value shows that the unit cell is elongated along the *c* axis, and that compressive forces act in the plane of the ZnO thin film. These compressive forces disappear as the heat treatment temperature is increased.

In order to more exactly investigate the structural properties of ZnO thin film, we calculated the stress in the film. The calculation is based on the biaxial strain model [13]. The strain $\varepsilon = [(c_{\text{bulk}} - c_{\text{film}})/c_{\text{bulk}}]$ in the direction of the *c* axis, i.e., perpendicular to the substrate surface, was measured by XRD. To derive the stress of film parallel to the film surface, the following formula has been used [13], which is valid for a hexagonal lattice:

$$s_{\text{film}} = \frac{2c_{13}^2 - c_{33}\left(c_{11} + c_{12}\right)}{2c_{13}} \frac{c_{\text{film}} - c_{\text{bulk}}}{c_{\text{bulk}}} \tag{1}$$

Thee following elastic constants c_{ij} of single crystalline ZnO have been used: $c_{11} = 208.8$, $c_{33} = 213.8$, $c_{12} = 119.7$ and $c_{13} = 104.2$ GPa [14]. Stress in the film can be estimated using Eq. (1) and is plotted in function of final heat treatment temperature in Fig. 6. The negative sign for the films A1 and C1 heat treated at 600 °C indicates that the lattice constant *c* is elongated as compared with unstressed powder, and therefore the film is compressed in the direction parallel with the surface, i.e., when a film is constrained and compressed by a substrate, the normal direction to the substrate sur-

face is elongated. After a further heat treatment above 700 °C, films enter into a state of compression as compared with the normal lattice state of bulk ZnO.

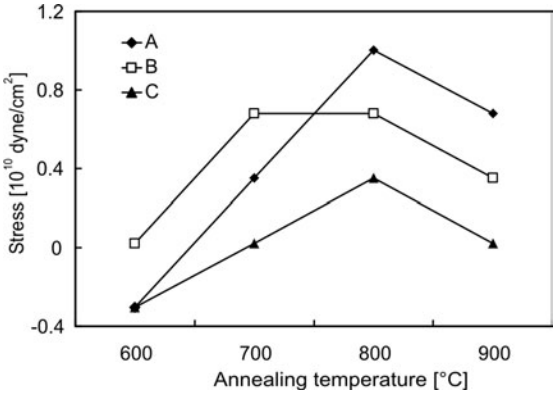

Fig. 6. Variation of stress induced in the finally annealed films in function of prefiring temperature

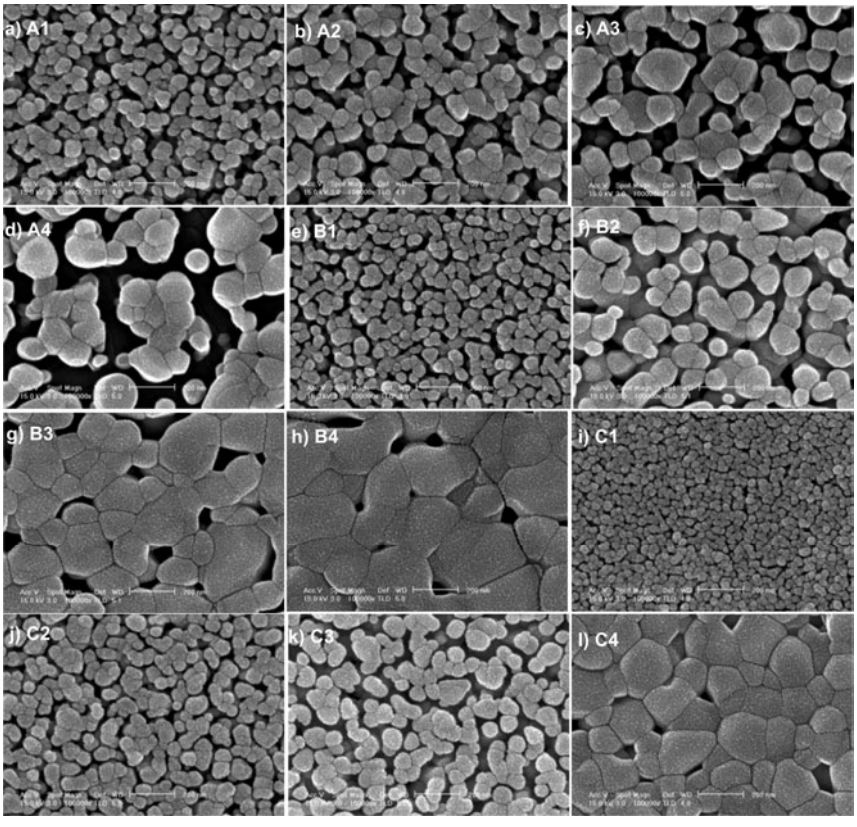

Fig. 7. FE-SEM images of the finally annealed films prefired at 250 °C for 60 min (a–d), at 350 °C for 30 min (e–h), and at 500 °C for 10 min (i–l)

Figure 7 shows the FE-SEM photographs of the ZnO thin films pyrolyzed at 250 °C for 60 min (a–d), at 350 °C for 30 min (e–h), and at 500 °C for 10 min (i–l), followed by final heat treatment at 600–900 °C for 30 min in air. Particulate structure is evident in all the films. The particle size increases with increase of the heat treatment temperature. It is obvious that the particle size increased with the increased annealing temperature which is consistent with the ZRD results. According to Hsieh et al. [15], the atoms would obtain enough energy to occupy proper sites in the crystal lattices, and grains with lower surface energy would become larger at higher temperatures. However, formation of polycrystalline films with grain boundary micropores, prefired at 250 °C, A3 and A4, is quite obvious from the micrographs. As the prefiring temperature decreases, the amount of organics in the prefired film increases, and therefore the decomposition and the crystallization may occur almost simultaneously. Since the structural relaxation of the prefired film induced by the decomposition can take place only before the crystallization, the simultaneous decomposition and crystallization may give the film less chance to be structurally relaxed, resulting in a microporous structure (see Fig. 7c and d).

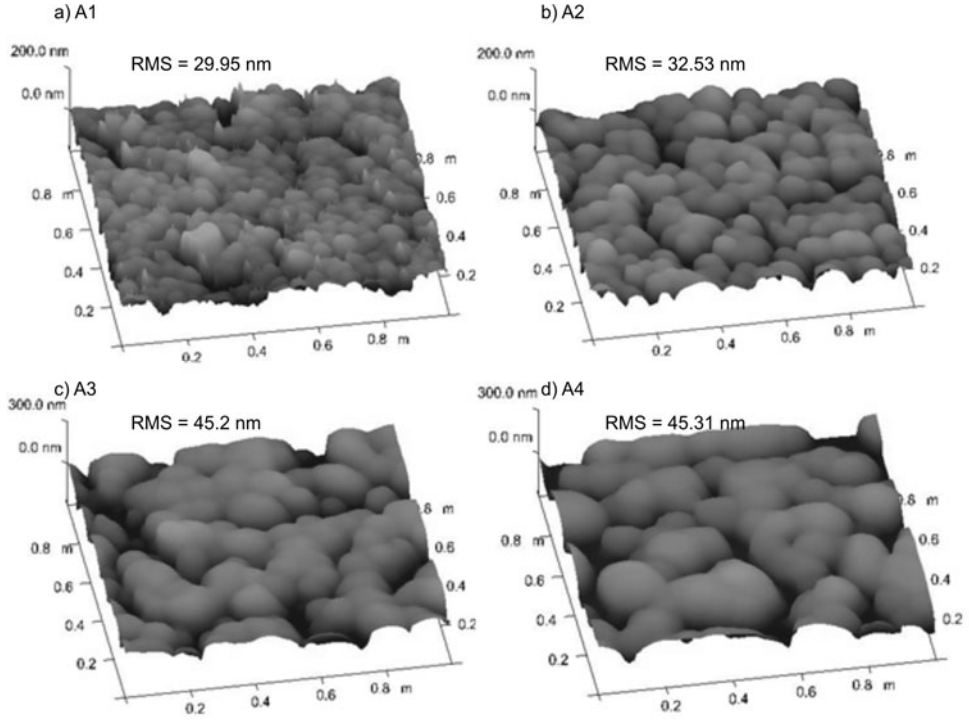

Fig. 8. SPM images (1×1 μm^2) of the finally annealed films prefired at 250 °C for 60 min

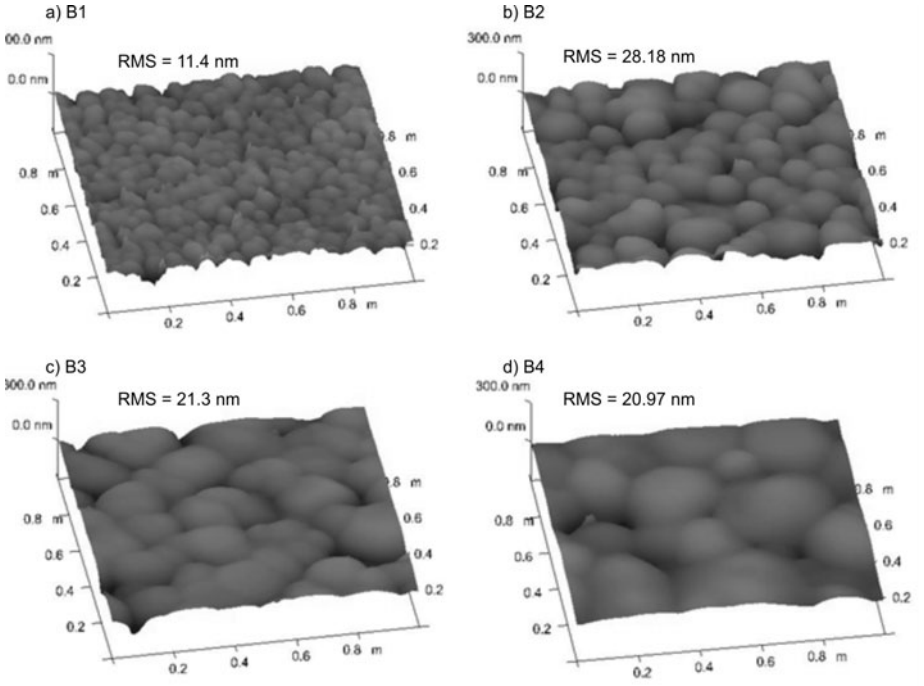

Fig. 9. SPM images (1×1 μm^2) of the finally annealed films prefired at 350 °C for 30 min

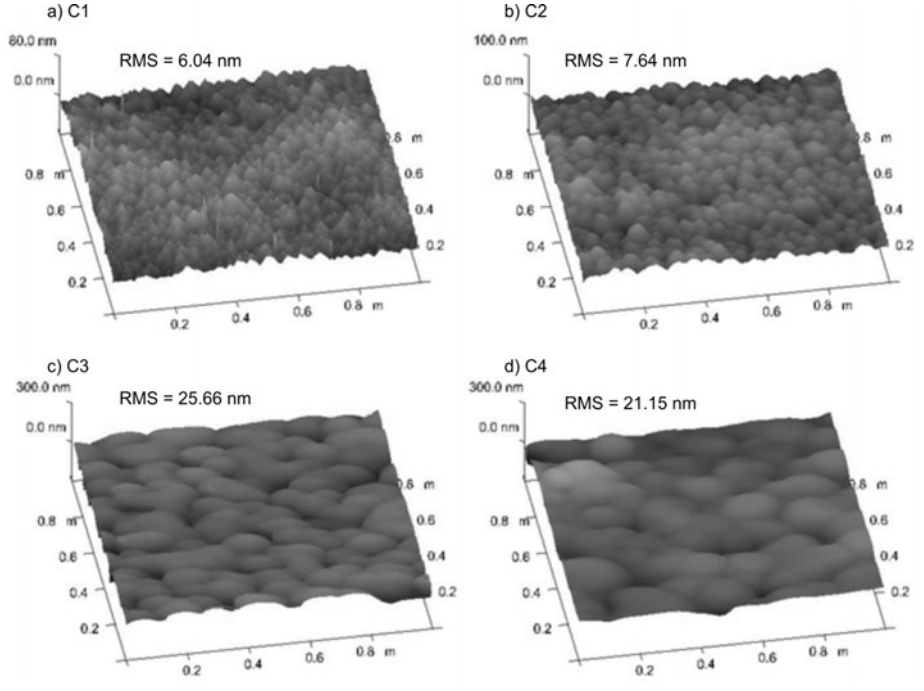

Fig. 10. SPM images (1×1 μm^2) of the finally annealed films prefired at 500 °C for 10 min

To evaluate the surface roughness and morphology of the films, SPM analysis was performed. Figures 8–10 show the SPM images (1×1 μm^2) of ZnO thin films pyrolyzed at various temperatures, followed by final heat treatment at 600–900 °C. With increasing heat-treatment temperature to 800 °C, nanosized grain growth is observed to gradually increase. At 900 °C, large grain growth is easy to identify, although the grain size uniformly increased with increasing heat treatment temperatures for all the pyrolysis temperatures. Furthermore, with an increase in annealing temperature, the root-mean-square (RMS) roughness increased to 45.2 and 45.31 nm for the films A3 and A4 pyrolyzed at 250 °C. This may be because of the pores between grains, which were confirmed by FE-SEM. On the other hand, for the films B3, B4, C3 and C4 pyrolyzed at 350 °C and 500 °C, the surface roughnesses of the annealed ZnO thin films at 800 °C and 900 °C were decreased. With increase in temperature, a smoother surface might be expected, due to an increased surface mobility of the species [16].

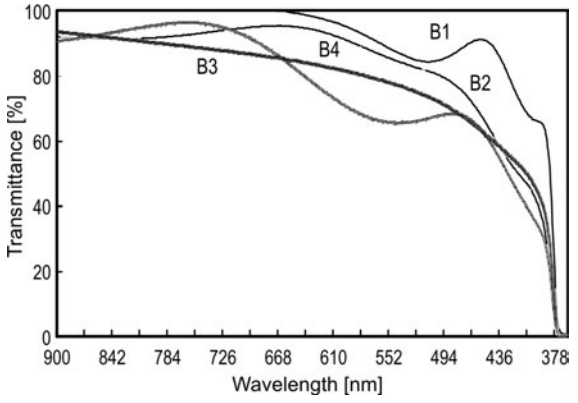

Fig. 11. Transmittance of the finally annealed films prefired at 350 °C for 30 min

Figure 11 shows transmission spectra of the annealed ZnO thin films pyrolyzed at 350 °C for 30 min. All the films exhibit transmittance higher than 80%) in the visible range and show a sharp fundamental absorption edge at about 0.38–0.4 μm which is very close to the intrinsic band gap of ZnO (3.2 eV). With an increase in annealing temperature, the transmittance decreased gradually. The high transmittance of all the films is attributed to small particle size minimizing light scattering, and low surface roughness. The optical band gap (E_g) is in the range between 3.26 eV and 3.28 eV. The estimated values of the band gap for all the films are within the range reported for such films [17]. Homogeneous transparent ZnO thin films having a high *c* axis orientation were observed at the pyrolysis temperature of 350 °C for 30 min.

4. Conclusions

Highly *c* axis oriented ZnO thin films were prepared on silica glass substrates by a sol-gel process using zinc-naphthenate as a precursor. When the prefiring tempera-

ture was too low, at 250 °C, crystallization and orientation of the films were very difficult to induce. The XRD peak intensity of ZnO films was significantly affected by the prefiring temperature, although the final annealing temperature was the same. With an increase in annealing temperature, the RMS roughness abruptly increased for the films prefired at 250 °C, while for the films prefired at 350 °C and 500 °C, the RMS roughness was somewhat decreased at 800 °C and 900 °C. Homogeneous and transparent ZnO thin film showing a high *c*-axis orientation was observed at a prefiring temperature of 350 °C for 30 min.

References

[1] HWANG K.S., KANG B.A., JEON Y.S., AN J.H., KIM B.H., NISHIO K., TSUCHIYA T., Surf. Coat. Tech., 190 (2005), 331.
[2] RYU H.W., PARK J.S., HONG K.J., HWANG K.S., KANG B.A., OH J.S., Surf. Coat. Tech., 173 (2003), 19.
[3] HWANG K.S., YUN Y.H., KANG B.A., KIM S.B., JANG S.W., KIM C.K., OH J.S., J. Mater. Sci.: Mater. in Med., 14 (2003), 761.
[4] HWANG K.S., LEE S.O., KANG B.A., YUN Y.H., SHIM Y.A., OH J.S., YANG S.H., J. Mater. Sci. Lett., 22 (2003), 307.
[5] HWANG K.S., JEON Y.S., KIM S.B., KIM C.K., OH J.S., AN J.H., KIM B.H., J. Kor. Phys. Soc., 43, (2003), 754.
[6] HWANG K.S., JEONG J.H., JEON Y.S., JEON K.O., KIM B.H., J. Sol-Gel Sci. Tech., 35 (2005), 237.
[7] KIM B.H., AN J.H., KANG B.A., HWANG K.S., OH J.S., J. Ceram. Proc. Res., 5, (2004), 53.
[8] HWANG K.S., MIN S.S., PARK Y.J., Surf. Coat. Tech., 137 (2001), 205.
[9] HWANG K.S., PhD., Tokyo Univ. of Sci. (2003),.
[10] OHYAMA M., KOZUKA H., YOKO T., Thin Solid Films, 306 (1997), 78.
[11] KIM B.H., AN J.H., JEON Y.S., JEONG J.T., KANG B.A., HWANG K.S., J. Mater. Sci. Lett., 40 (2005), 237.
[12] LAN W., PENG X., LIU X., HE Z., WANG Y., Front. Mater. Sci. China 1 (2007), 88.
[13] SHON S.Y., KIM H.M., PARK S.H., KIM J.J., J. Kor. Phys. Soc., 44 (2004), 1215.
[14] CEBULLA R., WENDT R., ELLMER K., J. Appl. Phys., 83 (1998), 1087.
[15] HSIEH P.T., CHEN Y.C., KAO K.S., LEE M.S., CHENG C.C., J. Euro. Ceram. Soc., 27 (2007), 3815.
[16] KHANDELWAL R., SINGH A.P., KAPOOR A., GRIGORESCU S., MIGLIETTA P., STANKOVA N.E., PERRONE A., Optics Laser Tech., 40 (2008), 247.
[17] SHIMONO D., TANAKA S., TOTIKAI T., WATARI T., MURANO M., J. Ceram. Proc. Res., 2 (2001), 184.

Received 17 January 2008
Revised 19 December 2008

Materials Science-Poland, *Vol. 27*, *No. 1*, *2009*

The effect of electromagnetic stirring on the microstructure and corrosion of mischmetal modified AZ91D magnesium alloy

Y. X. JIN[1, 2], L. HUA[2*], X. XU[2], Q. PENG[2]

[1]School of Materials Science and Engineering, Taiyuan University of Technology, 030024 Taiyuan PR China

[2]School of Materials Science and Engineering, Wuhan University of Technology, 430070 Wuhan, PR China

The microstructure and corrosion behaviour of mischmetal modified AZ91D magnesium alloy in the presence or absence of a rotating electromagnetic field have been investigated. The study suggests that the size and volume fraction of the β ($Mg_{17}Al_{12}$) phase in the alloy decreases as magnetic field intensity increases. The immersion test results show that the mass loss for the alloy solidified in the absence of a magnetic filed is always larger than that for the alloy solidified under magnetic field. The electrochemical corrosion experiments indicate that the corrosion potential of the alloys increases from –1.56 to –1.51 V, while the corrosion current density decreases from 6.31 to 1.58 mA·cm^{-2}, and the charge transfer resistance increases from 3.17 to 11.32 kΩ·cm^2 as the excitation voltage increases from 0 to 120 V. The enhancement of the corrosion resistance is attributed to the grain refinement, and to the volume fraction reduction of the β ($Mg_{17}Al_{12}$) phase under a rotating electromagnetic field.

Key words: microstructure; corrosion; magnesium alloy; mischmetal

1. Introduction

Magnesium alloys exhibit an attractive combination of low density and high strength/weight ratio. Therefore, magnesium alloy parts are used in a variety of applications, such as in automotive, materials handling and aerospace equipment [1,2]. Among various magnesium alloys, the Mg–9Al–1Zn (AZ91) alloy is most widely used because of its excellent cast ability and mechanical properties. However, poor corrosive resistance of AZ91 magnesium alloy limits its potential use in further applications [3–5].

Achieving finer grain size generally leads to improved mechanical properties and structural uniformity of most metals and alloys [6]. Thus, a fine grain size in castings

*Corresponding author, e-mail: kingyaxu@yahoo.com.cn

is important for the service performance of cast products and is also important for the final properties of semifabricated products. Many grain-refining methods have been developed for magnesium alloy such as superheating, agitation, the additions of nucleant particles and solute elements [7–16]. Owing to the requirement for rapid cooling from the treatment temperature to pouring temperature, grain refinement by superheating is less practical for a large pot of melt on a commercial scale. Other shortcomings include excessive consumption of time and fuel/electricity and shortened life of the alloying vessels. The additions of nucleant particles can lead to obvious grain refinement but these particles are difficult to be consistently introduced into molten alloys. Generally, among the above-mentioned refinement techniques, electromagnetic agitation and the addition of rare earth elements to molten AZ91 alloys offer more practical advantages. Emadi et al. reported that adding Sr to AZ91D alloy significantly reduced its grain size from 225 to 75–150 μm [15]. Similar results were reported by other researchers[16]. However, a wide grain size distribution obtained in these investigations does not improve corrosion resistance. Thus, a suitable grain refiner for magnesium alloys is still elusive. The two general directions of resolving the grain refinement problem of magnesium alloys are therefore either to find a new additive that will perform the task or to significantly improve the efficiency of an existing casting process [6].

Electromagnetic processing of materials is an important technology developed by combining the magnetohydrodynamics and the casting engineering to improve the properties and performances of materials [17, 18]. Electromagnetic stirring (EMS) is one of the important magnetohydrodynamic applications, and is an alternative to the widespread high pressure die-casting and sand-casting methods for developing magnesium alloys. The use of the EMS is supported by a good quality of the casting alloy with fine non-dendritic structure, the lower shrinkage and uniform distribution of the grain size. Shijie Guo et al. reported that applying the electromagnetic vibration during the casting of the AZ80 magnesium alloy billet led to significant grain refinement [11]. However, their works mainly concentrated on the effects of an electromagnetic field on mechanical properties. Therefore, the present investigation is aimed at the fabrication of AZ91D magnesium alloy alloyed with mischmetal (Ce, La, Nd and other minor rare earth elements) and solidified by electromagnetic stirring generated with various excitation voltages. The main analysis is devoted to the microstructure and corrosion resistance.

2. Experimental

Material preparation and microstructural observation. Figure 1 shows the schematic diagram of a home-made electromagnetic stirring apparatus used in the present article. This apparatus is mainly made up of an electromagnetic stirrer, heating equipment, teeter chamber and smelting crucible. The rotating electromagnetic field is produced through the coil winding of asynchronous motor with excitation voltage ranging

from 0 to 120 V while maintaining the excitation frequency at 10 Hz. A resistance wire is placed in the gap space between the teeter chamber and refractor brick to heat the magnesium alloy. A graphite crucible for loading magnesium alloy is 60 mm in inner diameter, 70 mm in outer diameter, and 150 mm in height.

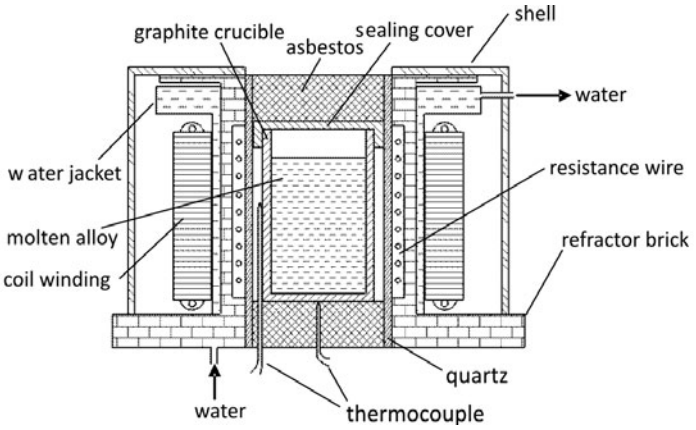

Fig. 1. Schematic diagram of the electromagnetic stirring apparatus

The chemical composition of the AZ91D magnesium alloy used in this study is as follows: Al – 9.1 wt. %, Zn – 0.85 wt. %, Mn – 0.27 wt. %, Mg – balance. Mischmetal (Ce – 50 wt. %, La – 20 wt. %, Nd – 10 wt. %, and balance other rare earths) is added at 1.0 wt. % levels. The AZ91D ingots were melted in an electric furnace and further refined at 730 °C under a protective gas mixture of 0.3% SF_6 and 99.7% CO_2. Mischemtal was added to the melt at 690 °C, held for 30 min. The melt was then transferred to the graphite crucible preheated to 200 °C. Finally, the current of the resistance wire was turned off at 640 °C, the excitation voltage of coil winding was turned on, and the molten alloy was cooled and solidified in the rotating electromagnetic field to ambient temperature.

Characterization of the grain size and qualitative analysis were conducted using an Olympus-BHM363U optical microscope (OM) and a JSM-5600LV scanning electron microscope (SEM) equipped with an Oxford energy dispersive X-ray (EDX) detector. The linear intercept method was used to measure the average grain size.

Immersion test. Immersion corrosion experiments were carried out to measure the corrosion rates of the modified alloys. The alloys were cut into rectangular specimens with dimensions of 10×10×2 mm^3. All the specimens were polished successively with SiC paper up to 4000 grit and cleaned by ethanol. The specimens were immersed in a 5 wt. % NaCl aqueous solution saturated with $Mg(OH)_2$ for up to 5 days. The tests were conducted at room temperature. After immersion testing, corrosion products were removed by immersing the specimens in an aqueous solution of 20% CrO_3 + 1% $AgNO_3$.

Electrochemical tests. Specimens for electrochemical tests were cut into cubes with dimensions of 10×10×10 mm^3. The electrochemical tests were conducted in a 100 cm^3 submarine type cell using a typical three electrode fitting in which the working electrode was facing the counter electrode. The counter electrode was platinum, and a saturated calomel electrode (SCE) was used as reference. The working electrodes consisted of a cylindrical rod embedded in an epoxy resin to provide insulation, leaving 1.0 cm^2 alloy surface in contact with the electrolyte. Polishing was carried out on samples with SiC paper up to 4000 grit before measurements.

Potentiodynamic polarization curves for the investigated alloys in the 5 wt. % NaCl solutions saturated with $Mg(OH)_2$ at ambient temperature were determined using an CS300UA model electrochemistry analysis system at a scan rate of 1 $mV \cdot s^{-1}$. Before each polarization curve measurement, the sample was immersed in the test solution for 30 min to allow the open circuit potential to become stable.

The electrochemical impedance spectroscopy (EIS) measurements were carried out using an AUTOLAB PGSTA301 model electrochemical measuring device. The EIS measurements were obtained by applying a small-amplitude perturbation of 10 mV in a sine wave form, and by scanning the modulus of impedance and the phase shift over the frequency range from 10^{-2} Hz to 10^4 Hz. The electrode potential of each specimen was controlled at the relevant open circuit potential. The EIS data analysis was performed using the Zview software.

3. Results

3.1. Measured microstructures

Because microstructure determines the final properties of the alloy, an understanding of the microstructure formed is an essential part of the casting technology. Examination of the microstructures of the mischmetal modified AZ91D alloys shows that this is different when the alloys are solidified under different excitation voltages (Fig. 2). The view shows some agglomerate particles and acicular particles in the α magnesium matrix of alloy solidified in the absence of an electromagnetic field (Fig. 2a). A typical high multiple SEM image of the alloy for the EDX analysis is shown in Fig. 3, and composition of various compounds found in the alloy are listed in Table 1. The EDX result confirms that the agglomerate phases have compositions consistent with the $Mg_{17}Al_{12}$ phase. Acicular compounds are formed between Al and Ce or La, and contribute to the increased corrosion resistance of the alloy [3]. Hamana et al. reported that most of the rare earth elements added to Mg–Al alloys react with Al to form intermetallic compounds such as AlCe and Al_4La [19]. The result in the present study suggests a stoichiometric formula of Al_4(Ce, La). Thus the major elements (Ce and La) present in mischmetal satisfy the requirement of a modifying element as suggested by Ravi et al. [10].

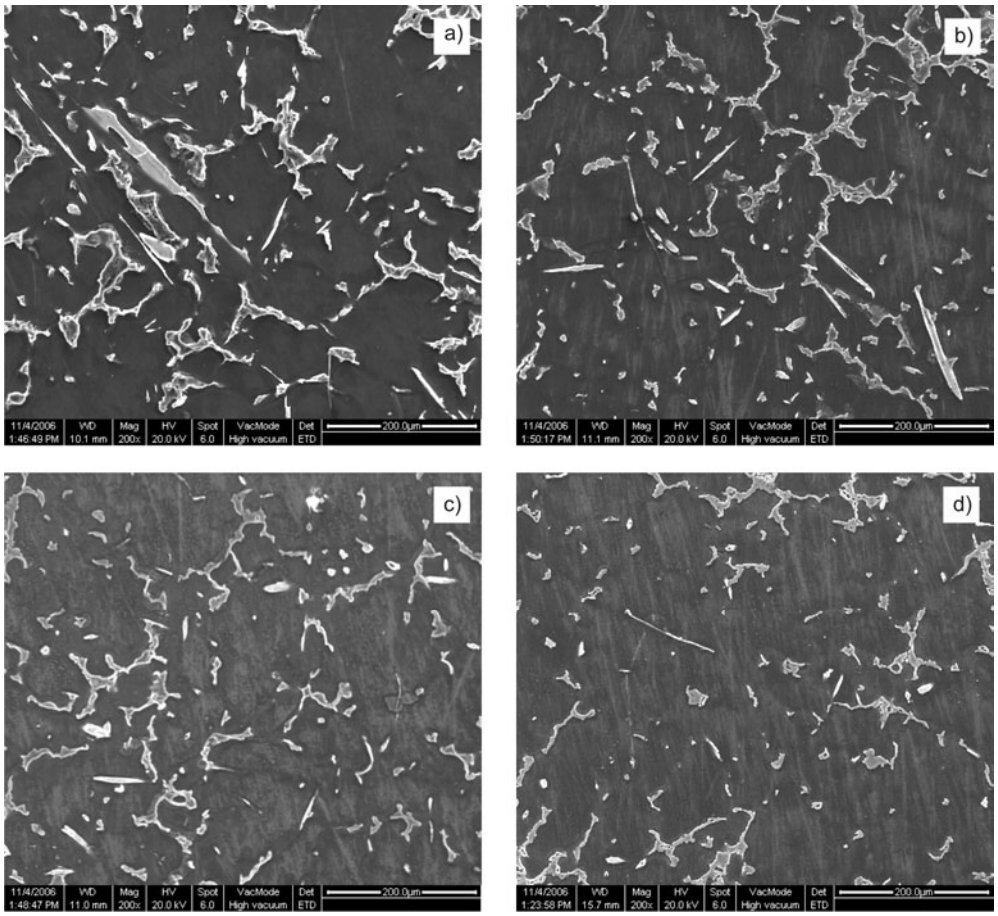

Fig. 2. SEM micrographs of mischmetal modified AZ91D magnesium alloys solidified under various excitation voltages: a) 0 V, b) 50 V, c) 80 V and d) 120 V

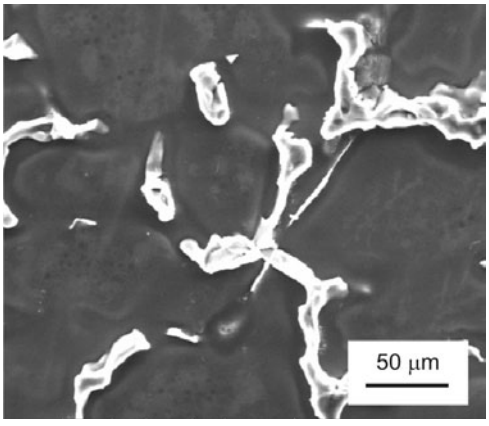

Fig. 3. High multiple SEM image of mischmetal modified AZ91D magnesium alloy solidified under the excitation voltage of 80 V

Table 1. Chemical compositions of phases of mischmetal modified AZ91D magnesium alloy solidified under the excitation voltage of 80 V (mole %)

Phase	Mg	Al	Zn	Mischmetal
$\beta(Mg_{17}Al_{12})$	56.32	38.28	5.4	
$Al_4(Ce, La)$	8.01	36.45	1.98	53.55

In the case of electromagnetic stirring casting, the grain refinement occurs, and the amount of irregular-shaped β ($Mg_{17}Al_{12}$) phase on grain boundaries decreases. When the exaction voltage is 50 V, the primary α magnesium grain size has no significant reduction, but agglomerate β ($Mg_{17}Al_{12}$) grain is obviously broken up and the volume fraction of Al_4(Ce, La) phase increases (Fig. 2b). Increasing the intensity of the electromagnetic field results in a further grain refinement. Figure 3d shows the microstructure of the alloy specimen when the exaction voltage is increased to 120 V. Significant differences in grain size and homogeneity are observed. Due to a high intensity of the stirring, the structures of the alloy are greatly refined and become homogeneous. Large dendritic β grains are deformed into insular structure, and the grain boundaries are discontinuous.

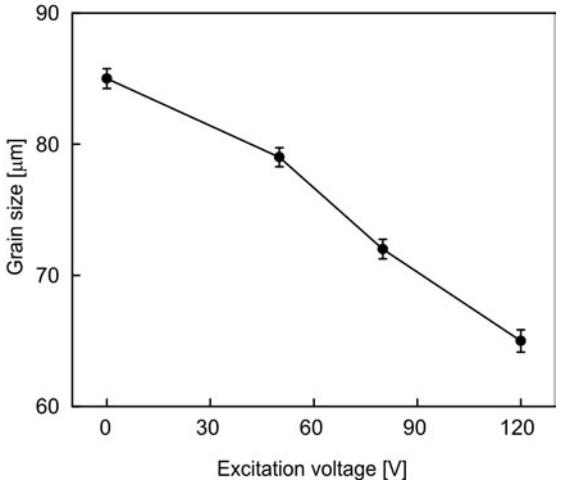

Fig. 4. Dependence of the α grain size of mischmetal modified AZ91D magnesium alloy on the excitation voltage

Figure 4 shows the relationship between the average grain size of the primary α magnesium and excitation voltage for the investigated alloys. The grain size gradually decreases from 85±0.7 μm to 65±0.8 μm on increasing the excitation voltage from 0 to 120 V. This confirms the modification of microstructure by the electromagnetic stirring during the solidification of the alloys. Considering that each grain is of a different size, the distribution of α magnesium grain size is investigated using an ImageTool software, and the results are listed in Table 2. Clearly, increasing the exci-

tation voltage results in a concentrated size distribution in the range of 40–80 μm. When the excitation voltage is 120 V, the percentage of α magnesium grain with the size range of 40–80 μm is 75%.

Table 2. Influence of electromagnetic field intensity on the distribution of α magnesium grain size

Excitation voltage [V]	< 40 μm	40–80 μm	> 80 μm
0	9%	36%	55%
50	11%	61%	28%
80	15%	63%	22%
120	18%	75%	7%

3.2. Immersion test

The mass loss curves recorded on the mischmetal modified alloys solidified under various excitation voltages are shown in Fig. 5. The mass loss of all the alloys increases with time but the values for the alloy solidified without magnetic filed are always larger than those for the alloys solidified under a magnetic field. Furthermore, the mass loss decreases with the increase in excitation voltage at any time between 1 and 5 days.

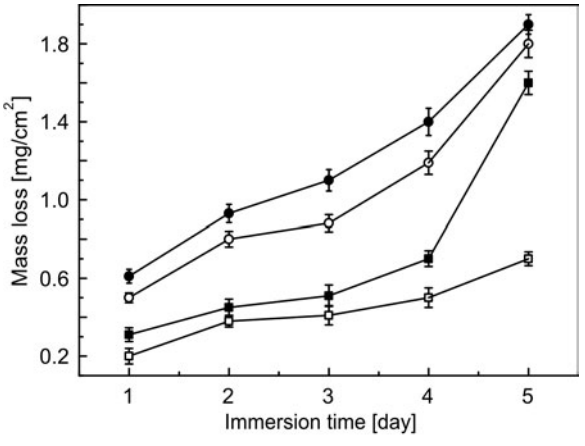

Fig. 5. Corrosion mass loss curves of the mischmetal modified AZ91D magnesium alloys solidified under various excitation voltages immersed in NaCl solution for up to 5 days: ● – 0 V, ○ – 50 V, ■ – 80 V, □ – 120 V

The effect of intensity of the electromagnetic field on the corrosion morphologies of the investigated alloys can be visualized from Fig. 6. The most outstanding characteristic of the morphology of the samples after being immersed in NaCl aqueous solution saturated with $Mg(OH)_2$ for 5 days is that all the corroded areas are adjacent to

the intermetallic precipitates, indicating that the corrosion is caused by the galvanic effect of the intermetallics. Figure 6a reveals that there existed serious general corrosion on the surface of the alloy solidified in the absence of an electromagnetic field. Moreover, some areas, perhaps originally surrounding the intermetallic precipitates, are completely corroded, and the intermetallic particles already fall off from there, leaving cavities in the α matrix. However, most areas of the alloys solidified in an electromagnetic field are not corroded or only a few areas are slightly corroded as shown in Fig. 6b–d. The results also indicate that upon increasing the intensity of the magnetic field, the surfaces of the samples remain more and more corrosion-free.

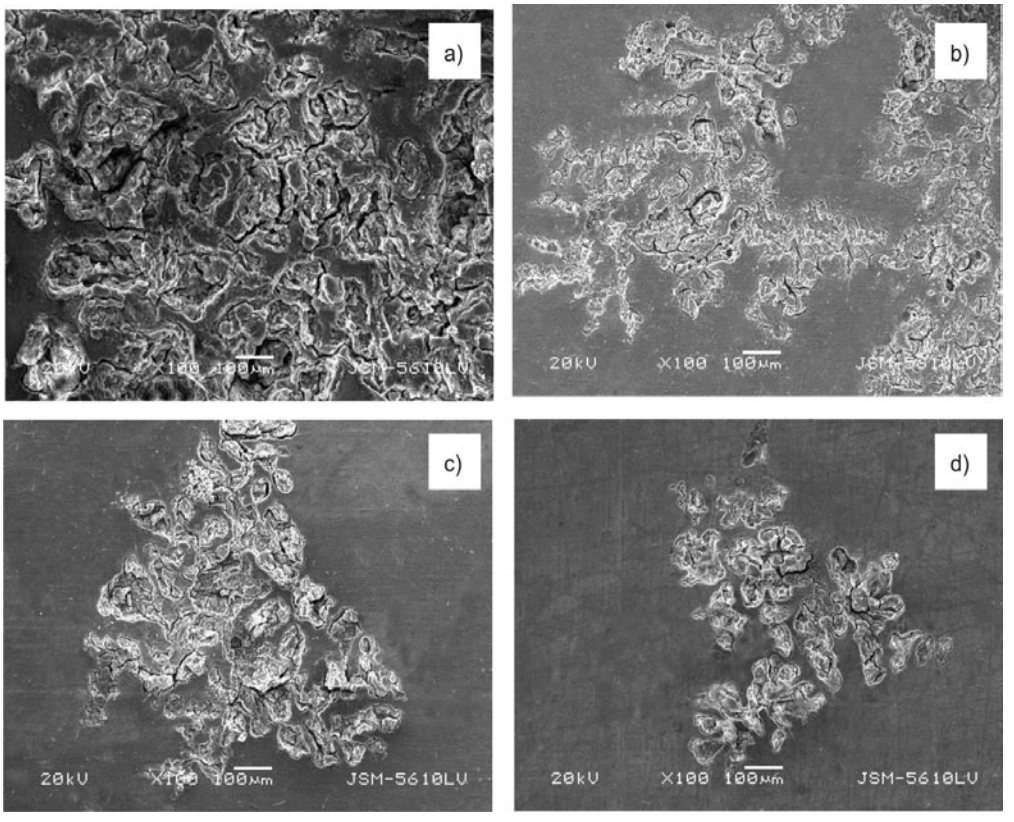

Fig. 6. SEM morphologies of corrosion surface of alloys solidified under various excitation voltages: a) 0 V, b) 50 V, c) 80 V and d) 120 V

3.3. Electrochemical tests

Figure 7 shows the potentiodynamic polarization curves of the investigated alloys. Obviously, the corrosion potential is shifted toward the active direction and the density of anodic current decreases rapidly at potentials just above –1.56 V for the alloy solidified in the absence of an electromagnetic field. It is noticed that the passivation

phenomena are invisible in the anodic regions of all the curves in the present study. In an earlier work by Mathieu et al., a plateau extending on a large anodic potential domain of the polarization curve in ASTM D1384 solution saturated with $Mg(OH)_2$ was obtained for the semi-solid cast AZ91D alloy [5]. The different results are mostly ascribed to the influence of the different corrosion media used in the experiments. In the present study, $Mg(OH)_2$ in the surface of magnesium alloy reacted with chloride anion in the NaCl solution, leading to the formation of soluble $MgCl_2$. The destructive effect of the chloride anion on the $Mg(OH)_2$ membrane makes the passivation phenomena invisible.

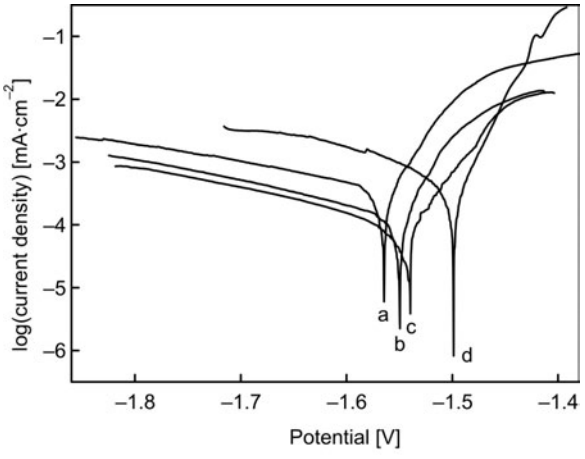

Fig. 7. Polarization curves of the mischmetal modified AZ91D magnesium alloys solidified under various excitation voltages: a) 0 V, b) 50 V, c) 80 V and d) 120 V

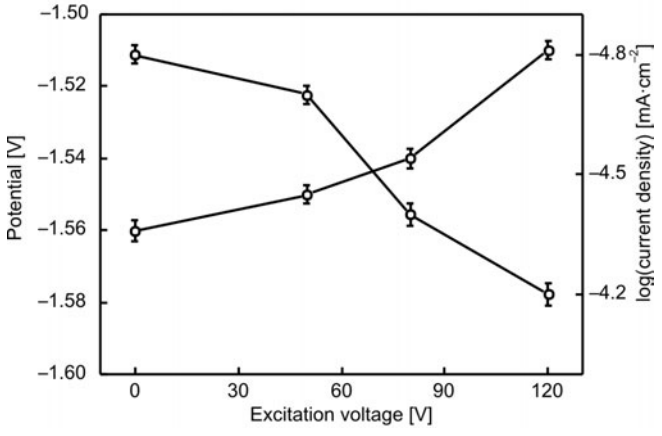

Fig. 8. Dependence of corrosion potential and corrosion current density of the mischmetal modified AZ91D magnesium alloys on the excitation voltage

Figure 8 shows the changes of corrosion potential and corrosion current density with the excitation voltage of the electromagnetic field. When the excitation voltage is

120 V, the corrosion potential is –1.51 V, being 3.52% higher than –1.56 V for the alloy solidified without electromagnetic field. The results indicate that the corrosion potential increases with the increase of the excitation voltage but at that time, the corrosion current density becomes reduced. Because the corrosion current density is directly proportional to the corrosion rate, the corrosion resistance of the mischmetal modified AZ91D magnesium alloy under the effects of rotating electromagnetic field is significantly enhanced.

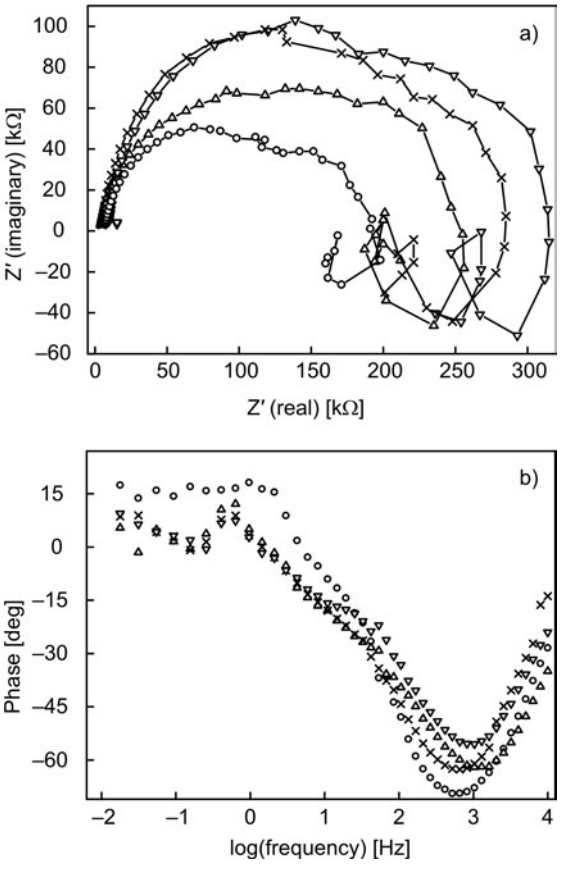

Fig. 9. EIS diagram of the mischmetal modified AZ91D magnesium alloys solidified under various excitation voltages in NaCl solution: a) Nyquist plots, b) Bode plots: ○ – 0 V, Δ – 50 V, × – 80 V, ∇ – 120 V

The EIS results of the present work are displayed in the form of Nyquist and Bode plots in Fig. 9. The Nyquist plots of the alloys at the open circuit potential display three arcs, which are capacitive arcs at both high and low frequency, and inductive arc at low frequency, respectively (Fig. 9a). The results are consistent with the prior work by Duan et al. [20]. It is believed that the corrosion process of magnesium alloy is irreversible, because the inductive arc only exists in the Nyquist plot of irreversible

electrode process. The impedance Bode plots display three extrema, including two maximum phase lags and one minimum phase lag (Fig. 9b). This implies that there exist three time constants (two capacitive responses and one inductive response) for mischmetal modified AZ91D magnesium alloys in NaCl solutions.

The corresponding equivalent circuit is shown in Fig. 10 which simulates the electrochemical behaviour of alloys in NaCl solution. The equivalent circuit contains elements corresponding to the solution resistance R_s, double-layer capacitance C, charge transfer resistance R_t, inductance component L, film surface resistance R_a, absorbing resistance R_c, and constant phase angle element CPE. The main electrochemical parameters derived from these experimental data are reported in Table 3.

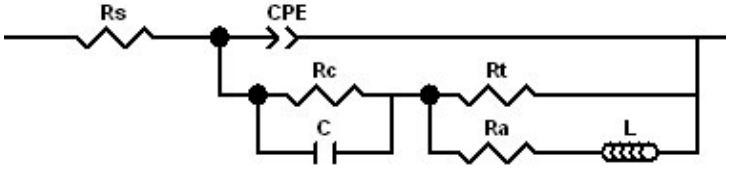

Fig. 10. Equivalent circuit of the mischmetal modified AZ91D magnesium alloys in NaCl solutions

Table 3. Equivalent circuit parameters of mischmetal modified AZ91D magnesium alloys solidified under various excitation voltages

Excitation voltage [V]	R_s [kΩ·cm^2]	C [μF·cm^{-2}]
0	3.17	3.14
50	4.28	2.56
80	6.41	1.52
20	11.32	1.33

The results show that the excitation voltage has a significant effect on the charge transfer resistance R_t and double-layer capacitance C. As the excitation voltage increases from 0 to 120 V, R_t increases from 3.17 to 11.32 kΩ·cm^2, but C decreases from 3.14 to 1.33 μF·cm^{-2}. The corrosion current density is inversely proportional to R_t. Therefore, the higher the R_t values, the more resistant the alloy is expected to be against corrosion. Moreover, the reduction of C indicates that the width of the electric double layer becomes broader. As a result, the hydrogen evolution reaction becomes slower, which is beneficial to the corrosion resistance enhancement of the alloys.

4. Discussion

4.1. The effect of an electromagnetic field on the microstructure of mischmetal modified AZ91D magnesium alloys

From the results obtained in our experiments, it can be seen that applying the electromagnetic stirring during solidification significantly refines the structure of the

mischmetal modified magnesium alloy. A review of the literature indicates that the structural refinement can be carried out by means of increased fluid flow induced by a magnetic field, an electric field, or a combination of both [11–14]. The effect is better appreciated with increasing superheat and solute element concentration. It is known that the molten undercooling during solidification increases under the influence of either an electric or a magnetic field [12]. This has been interpreted as the result of two competing processes: (1) fast growth of crystallites due to higher rate of mass transfer around each crystallite resulting in reduced superheating by accelerated release of latent heat of fusion and reduced nucleation, and (2) fast removal of heat along the solidification front, the effect of which is to enhance the tendency of the undercooling of the liquid metal and, hence, accelerate the process of nucleation.

In our experiments, the electromagnetic stirring was generated by application of a rotatory magnetic field in the molten metal. Under the effect of an alternative current of a certain frequency, the coil generates a time varying magnetic field in the melt, which in turn gives rise to an induced current in the molten metal. Therefore, the melt is subject to an electromagnetic body force (Lorentz force) caused by the interaction of the induced current and the magnetic field. The Lorentz force density consists of two parts, expressed as follows [11]

$$F = J \times B = -\nabla\left(\frac{1}{2}\mu B^2\right) + \frac{1}{\mu(B\cdot\nabla)B} \tag{1}$$

where B and J are the magnetic induction intensity and current density generated in the melt, and μ is the permeability of the melt. The first term on the right-hand side of Eq (1) is a rotational component which results in a forced convection and flow in the melt. The second term is potential forces balanced by static pressure of the melt, resulting in the formation of a convex surface and a decrease in the contacting pressure on the mold. Recent work by Fang et al. suggested that the electromagnetic body force of liquid metal in a rotating magnetic field is a sinusoidal function of the stirring time [18]. Therefore, the liquid metal in the rotating electromagnetic field experiences radial and tangential forces cyclically variable both in direction and magnitude.

Generally, a nucleus growth process can be divided into three phases: global growth, dendritic growth, and ripened rosette; and more nuclei imply a finer microstructure of the ingots [12]. According to the phase diagram of Mg–Al alloy, there should be a great amount of fine dispersed intermetallic particles such as $ZnAl_4$, $MnAl_6$, and $FeAl_3$ in a properly undercooled liquid metal being potential substratum for nucleation. When the electromagnetic pressure wave is imposed on the melt, some cavities form. Around the cavity, the melt is subject to a compressed stress; some atom clusters may form in this area. During the nucleation process, the atom clusters can easily attach to the particles to reduce the energy barrier for nucleation, thereby leading to the increased amount of nuclei. It was reported that the temperature field of the molten alloy with the rotating magnetic field was much lower and more uniform than that alloy without the magnetic field [11]. The merit of this uniform temperature field

is that the melt can be undercooled and nucleation can take place almost simultaneously in the mold resulting in an enlarged mushy zone. The subsequent result of this is that the microstructure of the alloy is fine and uniform. The structural differences shown in Fig. 2 are explained by the arguments put forward in the above discussion.

A molten alloy is a system consisting of atomic nuclei surrounded by electrons. The atomic nuclei make an irregular, thermal motion with a velocity. Under the electromagnetic field, they will revolve around the lines of the electromagnetic field; the radius of revolution and angular velocity are as follows [12]

$$r_c = \frac{mv_\perp}{|q|B} \tag{2}$$

where r_c is the revolution radius of the atomic nuclei in the electromagnetic field, q is the charge quantity of atomic nuclei, $v_\perp$ is the velocity in the vertical direction of the line of electromagnetic field, m is the mass of atomic nuclei, ω_c is the revolution angular velocity. Mg, Al, Zn and Ce ions are Mg^{2+}, Al^{3+}, Zn^{2+} and Ce^{3+}. Their radii of revolution and angular velocities are different because of the difference in m and q. Thus, a relative movement among Mg^{2+}, Al^{3+}, Zn^{2+} and Ce^{3+} will occur. As a result, the diffusion of rare earth elements in α matrix is strengthened which leads to an increase in the concentration of rare earth elements in the α matrix, and a decrease of the amount of $Mg_{17}Al_{12}$ phase on grain boundaries.

From the preceding discussion, it is clear that increasing the electromagnetic field intensity can result in a drastic forced convection of the melt and a relative movement among metal ions that will synchronously refine the structure and increase the content of rare earth elements within grains. This effect can be seen in Fig. 2.

4.2. The effect of an electromagnetic field on the corrosion behaviour of mischmetal modified AZ91D magnesium alloys

The manufacturing processes for magnesium alloy components have a great influence on the corrosion properties, since they determine the distribution of phases in the alloy. To some extent, the corrosion resistance of the AZ91D magnesium alloy depends on the morphology of the α magnesium and β phases. Numerous researchers investigated the role of the α magnesium and β grains in the corrosion, and have recognized that the β phase serves a dual purpose in the corrosion [3, 20]. When the α grain size is small, the gaps between the β precipitates are narrow and the distribution of the β phase is nearly continuous. In this case, the β phase acts as a barrier to corrosion. On the other hand, if the α grain size is large and the β phase is discontinuously distributed along the boundaries of the α phases, the β phase acts as a galvanic cathode because of the larger potential difference between the α and β phases. Moreover, the galvanic corrosion is intensified if the area ratio of cathode to anode is large.

In the alloy solidified without magnetic field, due to the larger size of the α and β grains, the β phase serves as an active cathode during corrosion. The galvanic corrosion inevitably occurs, owing to the galvanic current between the α and β phases. Applying electromagnetic stirring apparently decreases the grain size and also reduces the volume fraction of the β phase in AZ91D alloy by forming the Al_4(Ce, La) intermetallic compound which reduces the eutectic reaction between the α and β phases by consuming Al in the alloys. The change in the microstructure of the investigated alloy decreases the cathode-to-anode area ratio during corrosion. As a consequence, the galvanic current density of the alloy solidified under rotating electromagnetic field is obviously reduced. Some researchers also believed that the presence of the Al-rare earth intermetallic compound is responsible for the significantly enhanced corrosion resistance of the Mg–Al alloys [3, 9, 20]. Another factor for the corrosion resistance enhancement is that the grains are refined and the distribution of mischmetal composition and β phase is more uniform along the α grain boundaries. Even if a certain alloy grain is entirely corroded, the anti-corrosive mischmetal composition in the grain boundary can restrain the expansion of the corrosion process. In addition, there is not enough space in a single grain for a successful expansion of the corrosion pit. So the corrosion resistance of alloys solidified in the rotating electromagnetic field is enhanced.

5. Conclusion

By studying the fabrication and the properties of AZ91D magnesium alloy, alloyed with mischmetal, and solidified by electromagnetic stirring, the following conclusions can be drawn:

Electromagnetic stirring greatly refines the structure of the mischmetal modified alloys. The formation of the acicular Al_4(Ce, La) particles leads to a decrease in the volume fraction of $Mg_{17}Al_{12}$ phase. Increasing the electromagnetic stirring intensity leads to further grain refinement.

The corrosion resistance of the mischmetal modified AZ91D magnesium alloy solidified by electromagnetic stirring was significantly enhanced. The results of immersion test show that the mass loss for the alloy solidified in the absence of a magnetic field is always larger than the mass loss for the alloys solidified under a magnetic field. The electrochemical corrosion experiments indicate that the corrosion potential of the alloys increases, while the corrosion current density decreases, and the charge transfer resistance increases with the excitation voltage of the rotating electromagnetic field increasing from 0 to 120 V.

Acknowledgements

The authors acknowledge the financial support of the National Natural Science Foundation of China (Grant No. 50335060) and the Excellent Young Teacher Award of the Education Ministry of China (Grant No. [2002]383).

References

[1] HUTCHINSON C.R., NIE J.F., GORSSE S., Metall. Mater. Trans., A 36 (2005), 2093.
[2] WABUSSEG H., GULLO G.C., UGGOWITZER P.J., STEINHOFF K., KAUFMANN H., J. Mater. Sci., 37 (2002), 1173.
[3] SONG Y.L., LIU Y.H., YU S.R., ZHU X.Y., WANG S.H., J. Mater. Sci., 42 (2007), 4425.
[4] WAN Y., TAN J., SONG G.L., YAN C.W., Metall. Mater. Trans., A 37 (2006), 2313.
[5] MATHIEU S., RAPIN C., HAZAN J., STEINMETZ P., Corrosion Sci., 44 (2002), 2737.
[6] STJOHN D.H., QIAN M., EASTON M.A., CAO P., HILDEBRAND Z., Metall. Mater. Trans., A 36 (2005), 1669.
[7] YAO X.D., DAHLE A.K., DAVIDSON C.J., STJOHN D.H., J. Mater. Sci., 42 (2007), 9756.
[8] TAMURA Y., KIDA1 Y., TAMEHIRO H., KONO N., SODA H., MCLEAN A., J. Mater. Sci., 43 (2008), 1249.
[9] WANG Q.D., CHEN W.Z., DING W.J., ZHU Y.P., MABUCHI M., Metall. Mater. Trans., A 32 (2001), 787.
[10] RAVI M., PILLAI U.T.S., PAI B.C., DAMODARAN A.D., DWARAKADASA E.S., Metall. Mater. Trans., A 27 (1996), 1283.
[11] GUO S.J., LE Q.C., HAN Y., ZHAO Z.H., CUI J.Z., Metall. Mater. Trans., A 37 (2006), 3715.
[12] DONG J., CUI J.Z., YU F.X., BAN C.Y., ZHAO Z.H., Metall. Mater. Trans., A 35 (2004), 2487.
[13] MING X.G., BAO W.P., CUI J.Z., ZUO Y.B., Trans. Nonferrous Met. Soc. China, 13 (2003), 1270.
[14] MIZUTANI Y., KAWATA J., MIWA K., YASUE K., TAMURA T., SAKAGUCHI Y., J. Mater. Res., 19 (2004), 2997.
[15] EMADI D., GRUZLESKI J.E., TOGURI J.M., Metall. Mater. Trans., A 24 (1993), 1055.
[16] CLOSSET B., GRUZLESKI J.E., Metall. Mater. Trans., A 13 (1982), 945.
[17] GAO Y.L., LI Q.S., GONG Y.Y., ZHAI Q.J., Mater. Lett., 61 (2007), 4011.
[18] FANG C.F., ZHANG X.G., JI S.H., HAO H., JIN J.Z., Rare Metal Mater. Eng., 36 (2007), 170.
[19] HAMANA D., BOUCHEAR M., DERAFA A., Mater. Chem. Phys., 57 (1998), 99.
[20] DUAN H.Q., WANG S.L., CAI Q.Z., ZHANG S.C., WEI B.K., China Mech. Eng., 14 (2003), 1789.

Received 6 December 2008
Revised 19 December 2008

Materials Science-Poland, *Vol. 27*, *No. 1*, *2009*

The growth morphology of ZnO hexangular tubes synthesized by the solvothermal method

Y. LI*, X. LIU, Y. ZOU, Y. GUO

College of Science, Civil Aviation University of China, Tianjin, 300300, P.R. China

A novel hexangular tube structure of ZnO has been successfully synthesized via the solvo-thermal method, using $Zn(NO_3)_2 \cdot 6H_2O$ and NaOH as starting materials. The results showed that the supersaturation near the surface of ZnO crystal is higher than that inside the crystal, which leads to a preferential growth along *c*-axis of the side surface. The strain between the surface and the bulk of ZnO rods drives ZnO rods into tubular structure. The spectroscopic results show that ZnO tubes possess the wurtzite structure. Three emission peaks have been detected, a violet peak at about 399.9 nm, a blue emission at about 448.5 nm and a green emission at about 549.8 nm.

Key words: *zinc oxide; solvo-thermal method; electron microscopy; X-ray diffraction; photoluminescence*

1. Introduction

Zinc oxide, a wide-gap II–VI semiconductor with a direct band gap of about 3.37 eV at room temperature, is a well known material suitable for generating ultraviolet (UV) light [1]. Furthermore, a large exciton binding energy of about 60 meV in ZnO, significantly larger than the thermal energy at room temperature (26 meV), can ensure an efficient exciton emission at room temperature under low excitation energy [2, 3]. Because of these properties, zinc oxide is widely used in various applications such as photonic devices, transparent conductors, solar cell windows, surface acoustic devices and gas sensors [4, 5]. The optical, electrical and magnetic properties of zinc oxide are affected by its particle size, morphology, purity and chemical composition [6–9]. Thus, necessary efforts should be made to synthesize zinc oxide and undertake morphological studies. Various morphological crystallites of zinc oxide such as nanorods and microflowers have been synthesized by various methods [10–12]. Nanotubes of ZnO are expected to improve the luminescence efficiency of electro-optic devices and the sensitivity of chemical sensors. Wang et al. [13] prepared ZnO nanotubes by

*Corresponding author, e-mail: liyan01898@163.com

the sol-gel method within the pores of an anodic aluminum oxide template. Kong et al. [14] have prepared single-crystal nanorings by a solid-vapour process. Yan et al. [15] have synthesized aligned ZnO taper-tubes under hydrothermal conditions, using a zinc foil as a deposition substrate of ZnO. However, complex procedures, sophisticated equipment, rigid experimental conditions or a low yield are involved in these methods. Large-scale use will require the development of simple, low-cost approaches to the synthesis of inorganic, functional nanomaterials. ZnO nanotube bundles were successfully synthesized by Yu et al. [16] using a single solution method, but ZnO tubes in clusters were obtained, not in dispersive conditions. To our knowledge, solvohydrothermal synthesis of ZnO nanotubes has been rarely reported. In this work, hexangular ZnO tubes have been successfully synthesized by a simple and effective solvothermal method, without any catalysts, templates or substrates. The morphologies, structure and the photoluminescence properties of zinc oxide tubes were characterized by scanning electron microscopy (SEM), fluorescence spectrophotometry (FR) and X-ray diffraction (XRD).

2. Experimental

All analytical grade reagents: zinc nitrate hexahydrate ($Zn(NO_3)_2 \cdot 6H_2O$), sodium hydroxide (NaOH), absolute alcohol (C_2H_5OH) and sodium chloride (NaCl) were purchased from the commercial market without further purification.

ZnO crystalline powder was prepared according to the following procedure. Aqueous solutions of zinc nitrate hydrate (0.01–0.1 M) and sodium hydroxide (0.02–0.2 M) were prepared using deionized water. NaOH solution was added drop-by-drop into $Zn(NO_3)_2$ solution at room temperature under vigorous stirring which resulted in the formation of a white suspension. The suspension was separated with a centrifuge, thrice washed with distilled water, and finally washed with absolute alcohol. The separated powder was dried at 60 °C for 24 h in an oven to obtain the precursor. Subsequently, 3 g of the precursor material and 0.15 g NaCl were added into 30 ml of absolute alcohol, the mixture was mixed, and then sealed in a Teflon-lined autoclave with an interior volume filled in 35%. The autoclave was treated solvothermally at 180 °C for 72 h. Afterwards, the resulting white precipitate was washed with distilled water and alcohol for several times to obtain ZnO crystallites.

The morphology of ZnO particles was examined by 1530VP model field emission scanning electron microscopy (SEM) in the China National Academy of Nanotechnology Engineering. X-ray diffraction (XRD) with CuK_α radiation ($\lambda = 0.1542$ nm) on a DX-2000 X-ray diffractometer was used for checking the formation and identification of compounds in the obtained particles. Photoluminescence (PL) spectra of ZnO nanocrystals were recorded with a WGY-10 fluorescence spectrophotometer equipped with a Xe lamp (150 mW). The excitation wavelength was fixed at 325 nm. The emission spectrum of solid zinc oxide powder samples at room temperature was observed in the wavelength range of 300–600 nm by using a monochromator and a photomultiplier.

3. Results and discussion

Figure 1 shows the X-ray diffraction (XRD) patterns of the as-obtained ZnO crystallites synthesized solvothermally at 180 °C for 72 h. The obtained ZnO crystals possess a wurtzite structure. The diffraction peaks can be well indexed to hexagonal ZnO with lattice parameters of a = 0.324982 nm and c = 0.520661 nm (JCPDS Card No. 36-1451). All diffraction peaks with high intensity imply that ZnO crystals can grow very well in a solvent of alcohol containing little water.

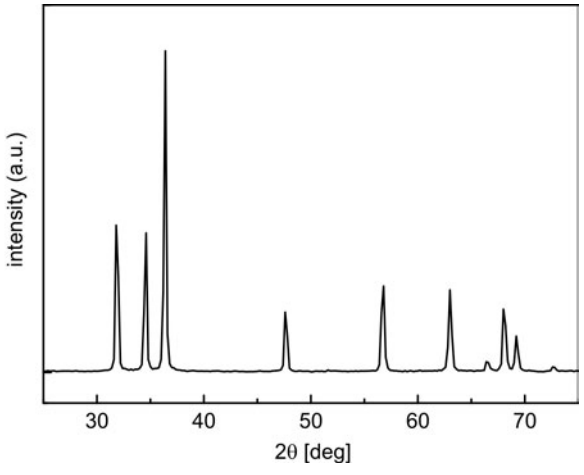

Fig. 1. XRD pattern of the synthesized ZnO tubes

The SEM images in Fig. 2 give a general overview of the synthesized products, which are hexangular pillars, hexangular tapers, or a combination of the both, with holes on their surface and an empty interior. The dimensions of the ZnO hexangular tubes are 1–2 μm in length, 400–600 nm in external diameter and 100–300 nm in inner diameter. The local wall thickness of the tube is ca. 100–150 nm. The top (0001) and bottom $(000\bar{1})$ surfaces are partly or completely open and the side faces can also have some holes, as shown in Fig. 2a, b and d. It implies that the bottom face breaks earlier, and more easily than the side faces during the growth. Interestingly, for some tubes, it can be clearly seen that the cracks in the bottom face are ready to collapse downward (Fig. 2f), and a special structure of a thick tube holding a thin tube or a hexangular pillar in its cavity was observed in some tubes (Fig. 2d, e). We also found that the surface layer density and the firmness of the synthesized ZnO tubes are higher than those of the bulk due to the faster growth and higher supersaturation along *C*-axis in the side surface, leading to a preferential nucleation and growth at 180 °C, a relative high temperature. It is understood that the strain, coming of the inner shrink of ZnO rods during its overgrowth for a long time (72 h) causes a collapse or crack between the surface layer and the inner of ZnO rods, which prompts the ZnO rods to be tubes. Meanwhile sodium chloride crystallites, not dissolving in alcohol, play an

important role as initial growth nuclei of ZnO rods, and a pipeline was left behind rinsing during the next procedure. Figure 2 shows two stages in the mechanism of a single tube growth on the surface of sodium chloride crystallite. In the first stage, an initially grown sheet along the surface of sodium chloride crystal turns into a roll or a hexangular pillar. In the second stage, a hexangular pillar or a roll transforms into a hexangular tube with a simultaneous collapse or a shrink inside ZnO rods. We may suggest that these are nanotubular type rods with polycrystalline walls consisting of wurtzite-type ZnO nanograins, rather than the well known nanotubes of the multisheet carbon nanotube type.

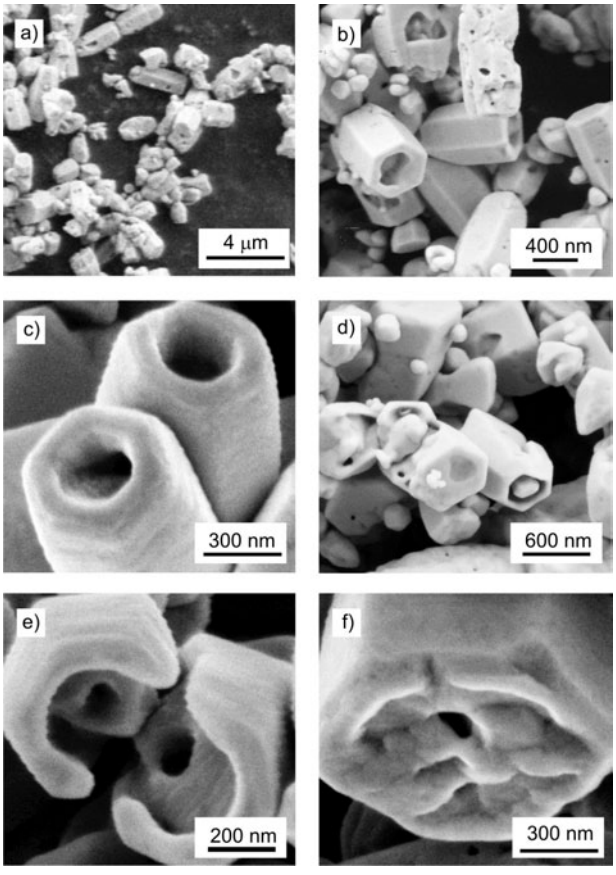

Fig. 2. SEM images of the synthesized ZnO tubes

The room temperature photoluminescence spectra of the as-prepared ZnO crystallites fabricated for 72 h at 180 °C were recorded, as shown in Fig. 3. A weak violet peak at about 399.9 nm was observed exhibiting a red shift compared to that of the reported 380 nm [17]. In addition, a broad blue emission at about 448.5 nm and a green emission centred at about 549.8 nm are also observed for these samples.

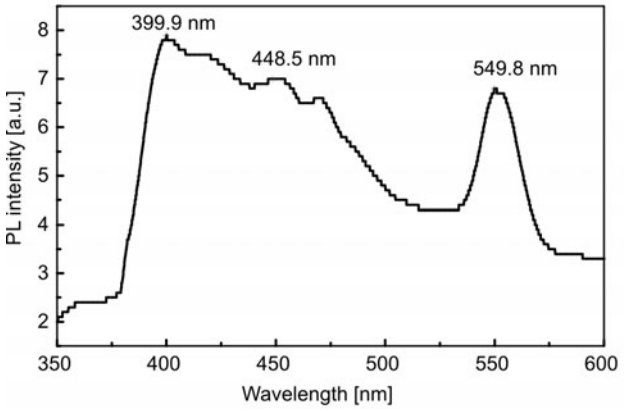

Fig. 3. Photoluminescence spectrum of the synthesized ZnO tubes

It is commonly accepted that the violet emission originates from the contribution of the near-band-edge emission of wide band gap ZnO, while the green peaks result from the recombination of electrons in single oxygen vacancies with photoexcited holes in the valence band. The stronger intensity of the green luminescence indicates a higher defect density due to oxygen vacancies in this material.

4. Conclusion

Hexangular tube structure of ZnO can be successfully synthesized by a solvohydrothermal treatment. SEM photos reveal that dimensions of the hexangular tubes of ZnO are 1–2 μm in length, 400–600 nm in the external diameter and 100–300 nm in the inner diameter. The local wall thickness of a tube is about 100 nm to 150 nm. The supersaturation near the side surface of the growing ZnO crystal is higher than that at its centre, leading to a preferential nucleation and growth along *c*-axis direction of the side surface than the inside. The strain between the surface and the inside of ZnO rods could drive the ZnO rods to be tubes. The XRD and PL results show that the ZnO tube crystallites possess a wurtzite structure, and a weak violet emission at about 399.9 nm, a broad blue emission at around 448.5 nm and a green emission centred at about 549.8 nm are observed for these samples. The ZnO tube structure may be promising in developing novel devices.

Acknowledgements

This project is supported by the Natural Science Foundation of Tianjin, China, No. 043602911, 05yfJMTC 12900.

References

[1] KIM D.K., MANZOOR U., Scr. Med., 54 (2006), 807.
[2] CHEN Z., GAO Q.M., RUAN M., SHI J.L., Appl. Phys. Lett., 87 (2005), 93113-1-3.

[3] VOROBEV V.A., J. Optic. Tech., 7 (2005), 690-247-9.
[4] UMAR A., RAHMAN M.M., KIM S.H., HAHN Y.B., Chem. Commun., 2 (2007), 166.
[5] WAMA R., UTIYAMA M., PLASHNITSA V.V., MIURA N., Electrochem. Commun., 9 (2007), 2774.
[6] WANG Q.X., YOU L.P., ZHANG X.Z., WANG R.M., LV Y.Z., GUO L., Rare Metals, 25 (2006), 193.
[7] POKROPIVNY V.V., KASUMOV M.M., Tech. Phys. Lett., 33 (2007), 44.
[8] XIE X.H., LI X.J., YAN H.H., Mater. Lett., 60 (2006), 3149.
[9] LAZARECK A.D., CLOUTIER S.G., KUO T.F., TAFT B.J., KELLEY S.O., XU J.M., Nanotechn., 17 (2006), 2661.
[10] SINGH J., TIWARI R.S., SRIVASTAVA O.N., Nanosci. Nanotechnol., 7 (2007), 1783.
[11] XU F.S., LIU X.F., TSE S.D., COSANDEY F., KEAR B.H., Chem. Phys. Lett., 449 (2007), 175.
[12] SHANG T.M., SUN J.H., ZHOU Q.F., GUAN M.Y., Cryst. Res. Technol., 42 (2007), 1002.
[13] WANG Z., LI H.L., Appl. Phys. A, 74 (2002), 201.
[14] KONG X.Y., DING Y., YANG R., WANG ZH.L., Science, 303 (2004),1348.
[15] YAN CH.L., XUE D.F., Electrochem. Comm., 9 (2007), 1247.
[16] YU Q.J., FU W.Y., YU C.L., YANG H.B., WEI R.H., LI M.H., LIU SH.K., SUI Y.M., LIU ZH.L., YUAN M.X., ZOU G.T., WANG G.R., SHAO CH.L., LIU Y.CH., J. Phys. Chem. C, 111 (2007),17521.
[17] KAUR M., BHATTACHARYA S., ROY M., DESHPANDE S.K., SHARMA P., GUPTA S.K., YAKHMI J.V., Appl. Phys A-Mater., 87 (2007), 91.

Received 31 January 2008
Revised 19 December 2008

Materials Science-Poland, *Vol. 27*, *No. 1*, *2009*

The effect of paramagnetic doping on the dielectric response of $K_{1.85}Na_{0.15}Ti_4O_9$ layered ceramics

S. V. VIKRAM[1*], D. MAURYA[2], V. S. CHANDEL[1]

[1]Department of Physics, Integral University, Lucknow, India-226026

[2]Department of Materials and Metallurgical Engineering, IIT Kanpur, India-208016.

Ceramic samples of layered polycrystalline $(K_{1.85}Na_{0.15})Ti_4O_9$:$x$Cu ($0 \le x \le 0.8$) have been prepared using high temperature solid state reaction. Room temperature X-ray diffratograms confirm the phase evolution. Room temperature electron paramagnetic resonance (EPR) data show that Cu^{2+} occupies Ti^{4+} lattice sites giving rise to electric dipoles which increases electric permittivity. The absorption peak in EPR spectra gets broadened due to increased exchange interaction in heavily doped derivatives. Dielectric data reveal that occupancy of Cu^{2+} on Ti^{4+} leads to a decrease in dielectric losses and an increase in the electric permittivity as well.

Key words: *layered ceramics; dielectric properties; electron paramagnetic resonance*

1. Introduction

The formula of alkali titanates crystallizing in a monoclinic phase is generalized by $A_2O \times nTiO_2$ ($3 \le n \le 8$, A is an alkali metal) [1]. Titanate nanotubes and nanowires have many important applications as photocatalysts, gas sensors, high-energy cells and in the field of environmental purification [2, 3]. Layered titanates are usually composed of slipped or corrugated host layers of edge-shared TiO_6 octahedra and interlayer alkali metal cations (Na^+, K^+ or H^+/H_3O^+ in protonic form) which are exchangeable with a variety of inorganic and organic cations [4]. Alkali metal titanates have been synthesized at nanoscale and studied on account of their robust applicability in biophysics [5]. Papp et al. [6] reported that the tendency of titanates to self-assemble makes them suitable candidates for utilization as efficient photocatalysts. Due to their TiO_2 derived structural origin, the nanotubes offer a potential in photocatalysis, solar

[*]Corresponding author, e-mail: svv28srf@gmail.com

energy conversion, as electrochromic materials, and self-cleaning devices [7]. The photochemical properties of Cu^{2+} doped layered hydrogen titanate have been presented elsewhere [8]. Cation exchange property has been studied for protecting environment against lethal radiation of highly radioactive liquid wastes [9].

In this array, Kikkawa et al. [10] reported that Nb^{5+} ions doped into $K_2Ti_4O_9$ naturally occupy Ti^{4+} sites and create cation vacancies leading to increased ionic conductivity. Pillaring and photo-catalytic properties of $Na_2Ti_{3-x}M_xO_7$ and $K_2Ti_{4-x}M_xO_9$ (M = Mn, Fe, Co, Ni, and Cu) have also been reported [11]. Recently, the influence of copper doping on mixed alkali titanates has also been reported [12]. Hence, it is interesting now, to synthesize and investigate the influence of copper doping ($0 \le x \le 0.8$) on the dielectric features of layered $K_{1.85}Na_{0.15}Ti_4O_9$ ceramics.

2. Experimental

The ceramic sample of $K_{1.85}Na_{0.15}Ti_4O_9$ has been prepared via conventional solid-state reaction route as reported earlier [13]. To prepare copper doped derivatives of $K_{1.85}Na_{0.15}Ti_4O_9$ ceramics, the desired molar percentages (x = 0.0, 0.02, 0.2, 0.8; hereafter referred to as PT, CPT-1, CPT-2, CPT-3) of CuO powder (99.9% pure, AR grade) were added to the mixture of alkali carbonates and titanium oxide. The mass so obtained was then calcined at 1200 K for 10 h. After grinding, the powder was compressed using a hydraulic press at 16 MPa to yield pellets, which were covered under the powder of the same composition and then sintered at 1200 K for 1 h, followed by furnace cooling to room temperature (RT).

RT XRD for $K_{1.85}Na_{0.15}Ti_4O_9$ and for all its copper doped derivatives have been obtained on an X-ray powder diffractometer ISO-Debyeflex 2002, Richseifert and Co. (Germany) using CuK_α radiation with the sweep of 3.0 deg/min, range (CPM) = 5 K, time constant = 10.0 s, current = 20 mA, and voltage across the cathode and target 30 kV.

The conventional first derivative of X-band (9.447 GHz) EPR absorption spectra were recorded on a Brucker EMX X-band EPR spectrometer with 100 KHz and 10.0 G modulations. The maximum calibrated power available was 0.201 mW. The high frequency modulation field amplitude ranged typically from 5×10^{-3} mT to 0.50 mT with rectangular TE_{102} cavity (unloaded $Q \approx 7000$) at 100 kHz field modulation. The samples for recording the EPR spectra were kept in a quartz tube (outer diameter ca. 5 mm) which was then placed at the centre of the resonant cavity. An incident microwave power level of 10 mW was used for most of the cases to give levels of 10^5. The magnetic field was calibrated using a central field at 3400 G.

The dielectric-spectroscopic measurements have been performed on an HP 4194A impedance analyzer in the frequency range 100–1000 kHz at RT with an ac bias of 0.5 V superposed. To avoid the effect of moisture, the samples were heated up to 150 °C before experiments. For this, the pellets were mounted on a sample holder kept in an evacuated (10^{-3} mbar) chamber.

3. Results and discussion

Powder X-ray diffraction patterns obtained at RT for $K_{1.85}Na_{0.15}Ti_4O_9$ are shown in Fig. 1. The room temperature XRD patterns for all copper doped derivatives are similar to that of $K_{1.85}Na_{0.15}Ti_4O_9$. These patterns are in good agreement to that reported in the literature and thus confirm the formation of polycrystalline layered alkali titanates in a monoclinic phase with $P2_1/m$ symmetry [4, 13]. Layered titanates are composed of stepped or corrugated host layers of edge shared TiO_6 octahedra and interlayered alkali metal cations (K^+, Na^+) [13]. Two kinds of interlayer spaces exist due to shifting of neighbouring layers relative to each other in amount of *b* spacing [14].

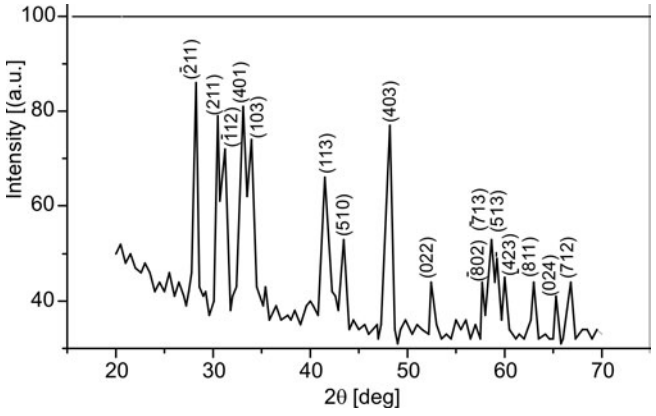

Fig. 1. Powder X-ray diffraction patterns showing indexed peaks which fairly coincide with those of a pure sample

The first derivative of X-band EPR absorption spectra recorded at RT, shown in Figs. 2a–c has a peak (with $g \approx 2.0$) at ca. 3300 G (quartets) along with intensive asymmetric lines. Therefore the data represents a superposition of two spectra corresponding to different surroundings of the copper ions. The characteristic spectrum may be explained by an isotropic spin-Hamiltonian, given by $\mathcal{H} = g\beta$ (B.S.) + A (I.S.), where notations have their usual meaning. For the fine structure spectrum, the $g_\parallel$ (g_z, quartet lines or hyperfine structures) and $g_\perp$ (($g_x + g_y$)/2, intensive asymmetric lines) components of the *g* tensor correspond to the quartet lines and intensive asymmetric lines pertaining to this peak. The hyperfine spectra have not been resolved in these materials. Also on heavy doping, the characteristic peak in the higher field side gets broadened due to increased exchange interaction (dipole–dipole). As anticipated, analysis of the calculated *g* values ($g_\parallel$ and $g_\perp$) listed in Table 1 indicates that the splitting occurs in the octahedral symmetry, and the copper site attains Cu^{2+} ($3d^9$, $S = 1/2$, and $I = 3/2$) state at the host site of Ti^{4+} ion [15, 16]. Furthermore, Cu^{2+} inclusion at the Ti^{4+} site modifies the crystal field around it into an orthorhombic one, which eventually attains axial symmetry on heavy doping [17]. Moreover, this acceptor doping activates a

charge compensation mechanism, dependent upon the evolution of oxygen vacancies in the lattice, producing electric dipoles consisting of a Cu^{2+} ion (effectively negative charge) and an oxygen vacancy site (effectively positive charge).

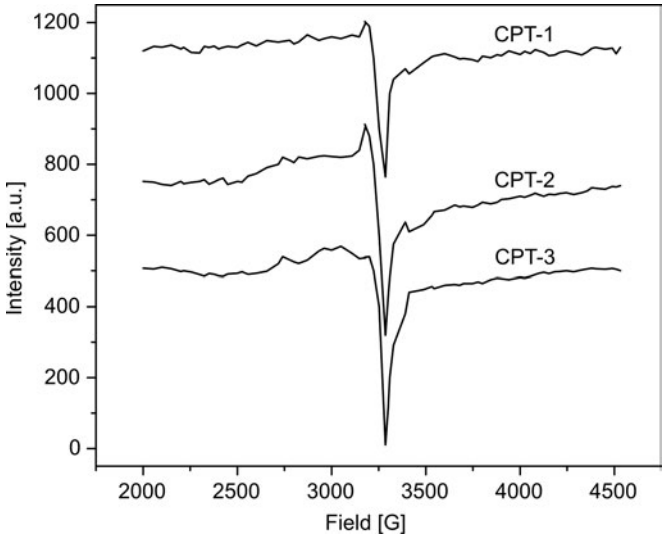

Fig. 2. First order derivative of EPR absorption spectra recorded at RT showing the characteristic Cu^{2+} peak (ca. 3300 G)

Table 1. Spin Hamiltonian parameters calculated for peak B using centre field at ca. 3400 G showing the presence of Cu^{2+} ions at Ti^{4+} sites

Sample	$g_{\parallel}$	$g_{\perp}$
CPT-1	2.3151	2.0278
CPT-2	2.3072	2.0165
CPT-3	2.3472	2.0929

The loss tangent ($\tan\delta$) and parallel capacitance (C_p) have been measured directly from the impedance analyzer. However, the relative permittivity (ε_r) has been calculated using relation $\varepsilon_r = C_p/(\varepsilon_0(a/t))$, where t is the thickness and a is the area of cross-section of the pellet. In Figure 3, room temperature $\tan\delta(\omega)$ plots are shown in the frequency range of 100–1000 kHz. These plots reveal that on copper doping (x = 0.02, 0.2), dielectric losses decrease primarily due to inhibition of domain wall motion [18] and then slightly increase for heavy doping (x = 0.8) of copper, due to a higher leakage current. Moreover, it can be seen from these plots that the loss tangents have very low frequency dispersion. The low value of dielectric loss at high frequency is the outcome of the low reactance offered by ceramic samples [19]. The trend of variation of dielec-

tric losses with frequency is a feature of dielectric losses due to dipole orientation and space charge polarization [20–22].

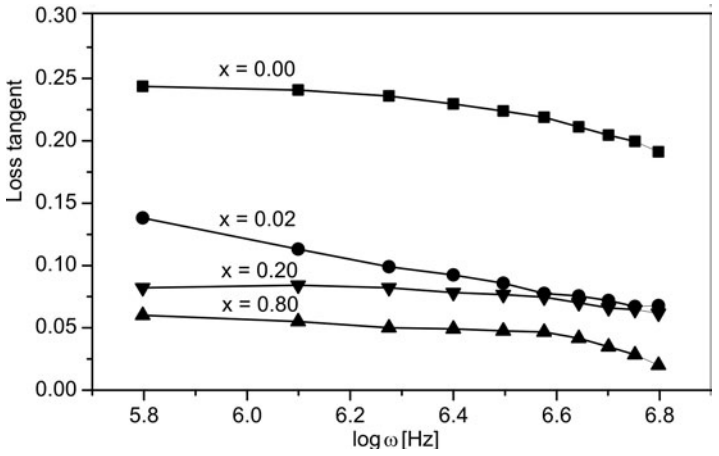

Fig. 3. Loss tangent in function of frequency for pure and doped derivatives of $(K_{1.85}Na_{0.15})\ Ti_4O_9$ ceramics

Figure 4 shows $\varepsilon(\omega)$ plots at room temperature for various pure and copper doped derivatives. These plots show almost frequency-independent behaviour of the electric permittivity. On copper doping, relative permittivity first increases for $x = 0.02$ but decreases for heavy doping ($x = 0.2$ and 0.8).

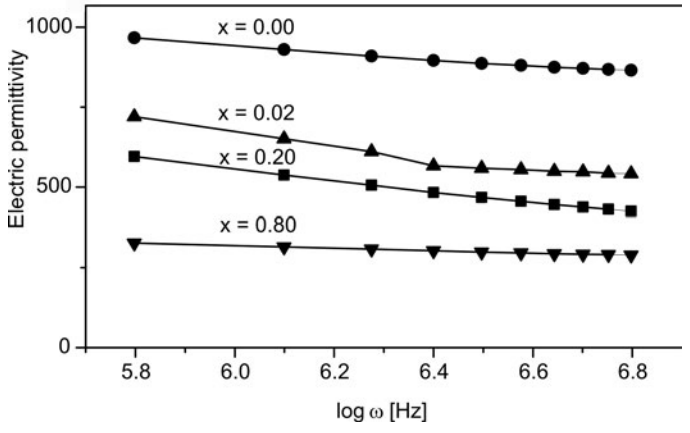

Fig. 4. Electric permittivity in function of frequency for pure and doped derivatives of $(K_{1.85}Na_{0.15})Ti_4O_9$ ceramics

Thus, for slight copper doping ($x = 0.02$), the increase in the values of the electric permittivity is accompanied by a simultaneous rapid decrease in tanδ values, which may be ascribed to the pinning of domain wall motion due to oxygen vacancies. The

acceptor doping activates a charge compensation mechanism dependent upon the evolution of oxygen vacancies in the lattice, producing electric dipoles constituted by a Cu^{2+} ion (effectively negative charge) and an oxygen vacancy site (effectively positive charge). However, heavy doping increases leakage current due to the orientation of dipoles created by the acceptor doping.

4. Conclusions

Polycrystalline layered ceramics $(K_{1.85}Na_{0.15})Ti_4O_9$:$x$Cu ($0 \leq x \leq 0.8$) have been synthesized via solid state reaction and characterized using electron paramagnetic resonance and dielectric spectroscopy. The EPR spectra show the characteristics of Cu^{2+} and confirm the occupancy of the Ti^{4+} sites by Cu^{2+}. Moreover, these peaks broaden due to increased exchange interaction for increased dopant densities. Copper doping is found to increase the electric permittivity along with a decrease in loss tangent in lightly doped compositions.

Acknowledgements

The authors acknowledge financial aid provided by the Council of Scientific and Industrial Research India, New Delhi.

References

[1] FEIST T.P., MOCARSKI S.J., DAVIES P.K., JACOBSON A.J., LEWANDOWSKI J.T., Solid State Ionics, 28–30 (1998), 1338.
[2] FUJISHIMA A., HONDA K., Nature, 238 (1972), 37.
[3] DAGON G., TOMKIEWICZ M., J. Phys. Chem., 97 (1993), 12651.
[4] VERBAERE A., TOURNOUX M., Bull. Soc. Chem. France, 4 (1973), 1237.
[5] LING Y.H., QI J.J., ZOU X.F., ZHAO X.M., BAI X.D., FENG Q.L., Key Engg. Mater., 280–283 (2005), 707.
[6] PAPP S., DEKANY I., Coll. Polym. Sci., 283 (2005), 1116.
[7] SESHADRI R., MARTIN C., HERVIEU M., RAVEAU B., Chem. Mater., 9 (1997), 270.
[8] YANAGISAWA M., UCHIDA S., SATO T., J. Inorg. Mater., 2 (2000), 339.
[9] KIKKAWA S., KOIZUMI M., SATO S. (Eds.), *Fine Ceramics*, Elsevier, USA, 1988, 83–90.
[10] KIKKAWA S., YASUDA F., KOIZUMI M., Mater. Res. Bull., 20 (1985), 1221.
[11] MACHIDA M., MA X.W., TANIGUCHI H., YABUNAKA J., KIYINA J., J. Mol. Cat. A: Chem., 155 (2000),131.
[12] MAURYA D., KUMAR J., SHRIPAL, J. Appl. Phys., 100 (2006), 034103.
[13] VIKRAM S.V., CHANDEL V.S., Proc. Int. INCCOM-6 Conf. on Future Trends in Composite Materials and Processing, IIT Kanpur, India, 12–14 December 2007, p. 319.
[14] OGURA S., SATO K., INNOVE Y., Phys. Chem. Chem. Phys., 2 (2000), 2449.
[15] ABRAGRAM A., BLEANEY B., *Electron Paramagnetic Resonance of Transition Ions*, Clarendon, Oxford, 1970.
[16] POONGUZHALI E., SRINIVASAN R., VENKATESAN R., RAVIKUMAR R.V.S.S.N., SAMBASIVA RAO P., J. Phys. Chem. Solids, 64 (2003), 1139.

[17] HEADLAM H., HITCHMAN M.A., STRATEMEIER H., SMITS J.M.M., BEURSKENS P.T., DE BOER E., JANSSEN G., GATEHOUSE B.M., DEACON G.B., WARD G.N., RILEY M.J., WANG D., Inorg. Chem., 34 (2005), 5516.
[18] MOULSON A.J., HERBERT J.M., *Electroceramics*, Chapman and Hall, London, 1990, 265.
[19] LINGWAL V., SEMAL B.S., PANWAR N.S., Bull. Mater. Sci., 26 (2003), 619.
[20] BOGORODITSKY N.P., PASYNKOV V.V., TAREEV B., *Electrical Engineering Materials*, Mir Publ., Moscow, 1979, 23 and 54.
[21] TAREEV B., *Physics of Dielectric Materials*, Mir Publication, Moscow, 1979, 67 and 140.
[22] MAJUMDAR S.B., ROY B., KATIYAR R.S., KRAPANIDHI S.B., J. Appl. Phys., 90 (2001), 2975.

Received 11 February 2008
Revised 19 December 2008

Materials Science-Poland, *Vol. 27*, *No. 1*, *2009*

Structure studies on nanocrystalline powder of MgO xerogel prepared by the sol-gel method

G. DERCZ[1,*], K. PRUSIK[1], L. PAJĄK[1], R. PIELASZEK[2], J. J. MALINOWSKI[3], W. PUDŁO[4]

[1]University of Silesia, Institute of Materials Science, ul. Bankowa 12, 40-007 Katowice, Poland

[2]Polish Academy of Sciences, High Pressure Research Center, ul. Sokołowska 29/37, Warsaw, Poland

[3]Polish Academy of Sciences, Institute of Chemical Engineering, ul. Bałtycka 5, 41-100 Gliwice, Poland

[4]Silesian Technical University, Faculty of Chemistry, ul. M. Strzody 9, 41-100 Gliwice, Poland

Structure studies were performed on nanocrystalline powder of MgO xerogel prepared by the sol-gel technique, producing high purity, chemically homogeneous materials of relatively high specific surface area. Magnesium methoxide was used as an MgO precursor. The wet gel was dried under conventional conditions, yielding xerogel with periclase phase; the only crystalline form of magnesium oxide. The X-ray diffraction, scanning and transmission electron microcopies were used as the tools of structure analysis. The Toraya PRO-FIT procedure and the Rietveld refinement method were applied for X-ray data analysis. Both techniques apply the Pearson VII function for the description of line profiles. The gamma crystallite size distribution was determined using the FW(1/5)/(4/5)M method proposed by Pielaszek. The obtained values of $<R>$ and σ (measure of polydispersity) of particle size parameters are equal to 7.1 nm and 2.1 nm, respectively, whereas the average crystallite size, estimated by the Williamson-Hall procedure, was equal to 7.5 nm. The *Rwp*, and *S* fitting parameters obtained from the Rietveld refinement were equal to 6.4% and 1.8, respectively. This would seem the most satisfactory result, when considering the nanosize of MgO crystallites and a very probable presence of amorphous phase.

Key words: *MgO; xerogel; nanocrystalline material; Rietveld refinement; Toraya procedure; XRD; TEM; SEM*

1. Introduction

There is currently a revolution in new materials that deals with the synthesis of nanoparticles of inorganic substances. Nanostructured materials with high surface area, high porosity, and particle sizes in the 1–10 nm range are becoming more available. These materials have shown great promise as adsorbents and catalysts [1].

[*]Corresponding author, e-mail: grzegorz.dercz@us.edu.pl

Magnesium oxide is an interesting basic oxide that has many applications in catalysis, adsorption and in the synthesis of refractory ceramics [2–5]. It is a unique solid because of its highly ionic character, simple stoichiometry and crystal structure, and it can be prepared in widely variable particle sizes and shapes [6]. It has been documented that the shape and size of nanocrystalline magnesium oxide particles endow them with high specific surface and reactivity, because of the high concentration of edge/corner sites and structural defects on their surface [7]. All these factors play a role in high efficiency of these materials in various heterogeneous reactions, e.g., with organophosphorous [8] and halogenated compounds [9].

The sol-gel synthetic route based on the use of magnesium alkoxide precursor, followed by drying under different conditions, has proved to be an efficient and successful approach to the production of nanocrystalline magnesium oxide particles [5, 7, 10].

The present work involves the structure analysis of nanocrystalline powder of MgO xerogel prepared by the sol-gel method with conventional drying procedure applied during synthesis. This analysis was performed by X-ray diffraction (XRD), scanning electron microscopy (SEM) and transmission electron microscopy (TEM) techniques. The above methods are standard ones used in studies of nanocrystalline materials [11–15].

2. Experimental

As the precursors, commercially available magnesium methoxide solution (Aldrich, 8.96 wt. % in methanol), methanol (POCh), and toluene (POCh) were used. The applied molar hydrolysis ratio was equal to 2 and the hydrolysis of magnesium methoxide solution was conducted in the presence of toluene. The volume ratio of toluene to methanol was 0.94. The gelling process was visually monitored by gently tilting the vials from time to time, to observe any change in the viscosity of the alcogel. Prior to drying, the wet gels were conventionally aged for 3 days. After ageing, the caps of vials containing alcogels were loosened for a few days to allow slow evaporation of the solvents. Next, the alcogels were vacuum-dried at room temperature for 12 h. Finally, the vials were transferred to an oven and heated at 60 °C for 48 h until constant weight was obtained. Heat treatment of magnesium hydroxide xerogel samples at 723 K under dynamic vacuum yielded the dehydrated magnesium oxide.

The Toraya PRO-FIT procedure and Rietveld refinement method were applied in X-ray data analysis. The PRO-FIT procedure enables the determination of parameters of individual diffraction lines, and applies the Pearson VII function for the description of line profiles [16]. This function appeared to be the most useful also in the Rietveld refinement procedure. The Rietveld analysis was performed using the DBWS-9807 program, which is an updated version of the DBWS programs for the Rietveld refinement with PC and mainframe computers [17]. The crystallite sizes and lattice distortions were analyzed using the Williamson-Hall method [18]. The crystallite size distribution was determined using the Pielaszek procedure [19].

X-ray diffraction patterns were collected by an X-Pert Philips diffractometer equipped with a curved graphite monochromator on diffracted beam, and with the following slits (in the sequence from copper tube to proportional counter): Soller (2°), divergence (1/2°), antiscatter (1/2°), Soller (2°) and receiving (0.15 mm). The powder morphology was analyzed using the SEM (JEOL JSM-6480) and TEM (JEOL 3010) techniques. A nitrogen adsorption-desorption isotherm measured at 77 K with a Micromeritics ASAP 2000 instrument was used to obtain the value of the specific surface area, S_{BET}.

3. Results and discussion

The X-ray diffraction pattern presented in Fig. 1 clearly shows that in the studied powder sample periclase is present, the only crystalline form of magnesium oxide. The broadening of diffraction lines is clearly seen.

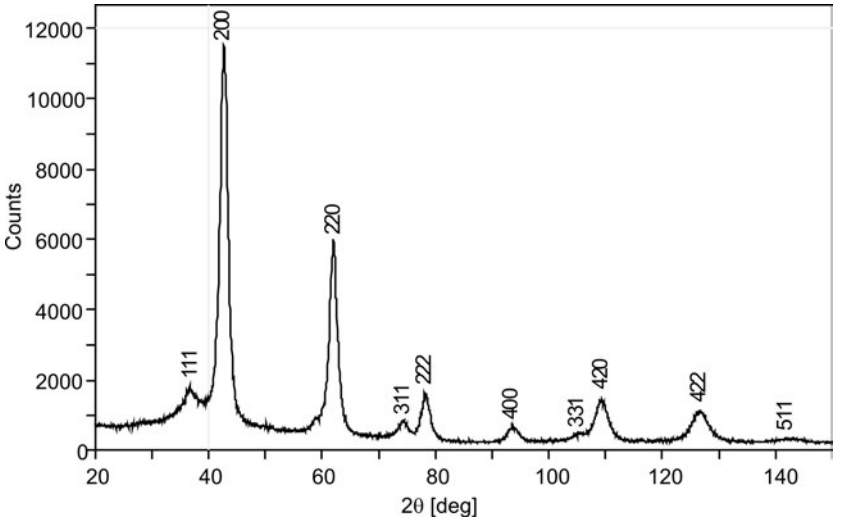

Fig. 1. X-ray diffraction pattern of MgO powder

From the analysis of the Williamson-Hall plot (not presented here) it can be concluded that the size-broadening is the main component of physical line broadening. The estimated average size of MgO crystallites is equal to 7.5 nm, whereas the lattice distortion is negligible (0.11%). The Pielaszek procedure [19] was applied to determine the size distribution of MgO nanocrystallites. The measurement of two widths of the same diffraction line at 1/5 and 4/5 of the peak maximum (FW1/5M and FW4/5M, respectively) allows the determination of the average crystallite size $<R>$ and the dispersion of sizes σ, which is more informative. From these parameters the gamma crystallite size distribution [19] can be drawn. The dispersion parameter σ, a measure of the crystallite size polydispersity, is as

$$\sigma = \sqrt{< R^2 > - < R >^2} \tag{1}$$

The procedure proposed by Pielaszek bears the same limitations as the Scherrer method. This means that only size-broadening of diffraction lines appears, whereas stacking fault, twinning probabilities and lattice strains are negligible. The applied sol -gel preparation procedure, high symmetry of crystal structure (diffraction lines do not overlap) and ionic binding of MgO are very convenient in fulfilling the above limitations. The crystallite size distribution, as calculated by the Pielaszek procedure, is presented in Fig. 2. A 200 diffraction line profile was applied in calculations; relatively large polydispersity of crystallite sizes was observed.

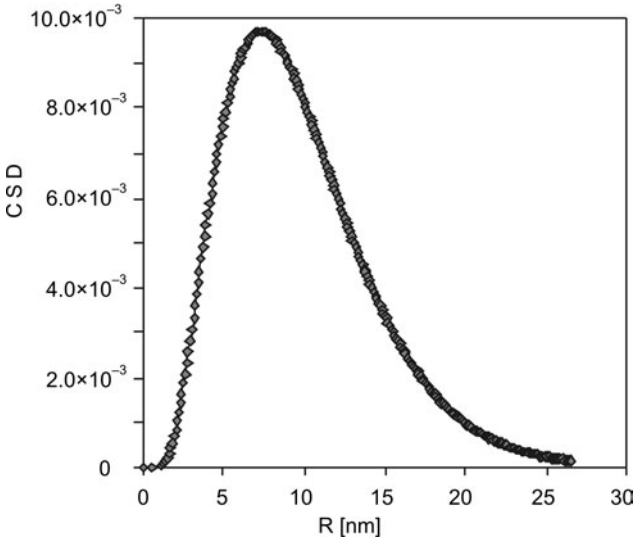

Fig. 2. Gamma crystallite size distribution (CSD) with average crystallite size $<R>$ = 7.1 nm ± 0.6 nm and dispersion σ = 2.1 nm±0.2 nm

The Rietveld refinement method was used for the determination of the lattice parameter of MgO nanocrystalline phase (Table 1).

Table 1. Lattice (a_0), crystallite size (D, $<R>$, σ) and lattice distortion ($<\Delta a/a>$) parameters for studied MgO powder

Space group	a_0, lattice parameter		Williamson – Hall		FW(1/5)/(4/5)M	
	Rietveld [nm]	ICDD [nm]	D [nm]	$<\Delta a/a>$ [%]	$<R>$ [nm]	Σ [nm]
$Fm\bar{3}m$	0.4226(1)	0.4213	7.5(9)	0.11(2)	7.1(6)	2.1(2)

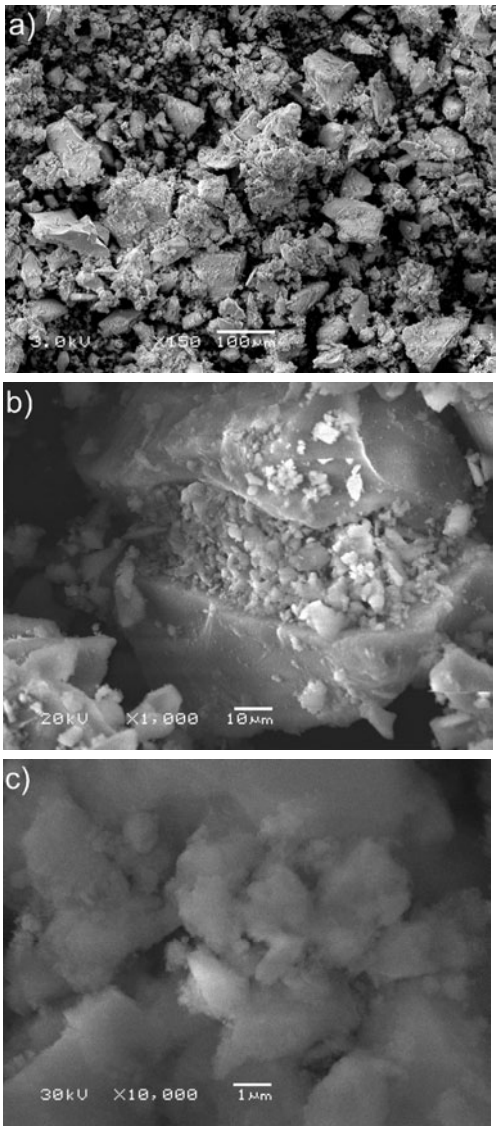

Fig. 3. SEM images of the MgO powder

Scanning and transmission electron microscopy images are presented in Figs. 3 and 4, respectively. These images indicate that the powder sample is an agglomerate of particles. From the analysis of TEM images and the X-ray diffraction pattern, it can be concluded that the amorphous phase is also present. Thus the values of R_{wp} and the S fitting parameters obtained from the Rietveld refinement, equal to 6.41% and 1.81, respectively, seem to be satisfactory. The electron microscopy images indicate an extended surface of powder particles. The specific surface area, as determined by the BET method, is equal to 138 m^2/g.

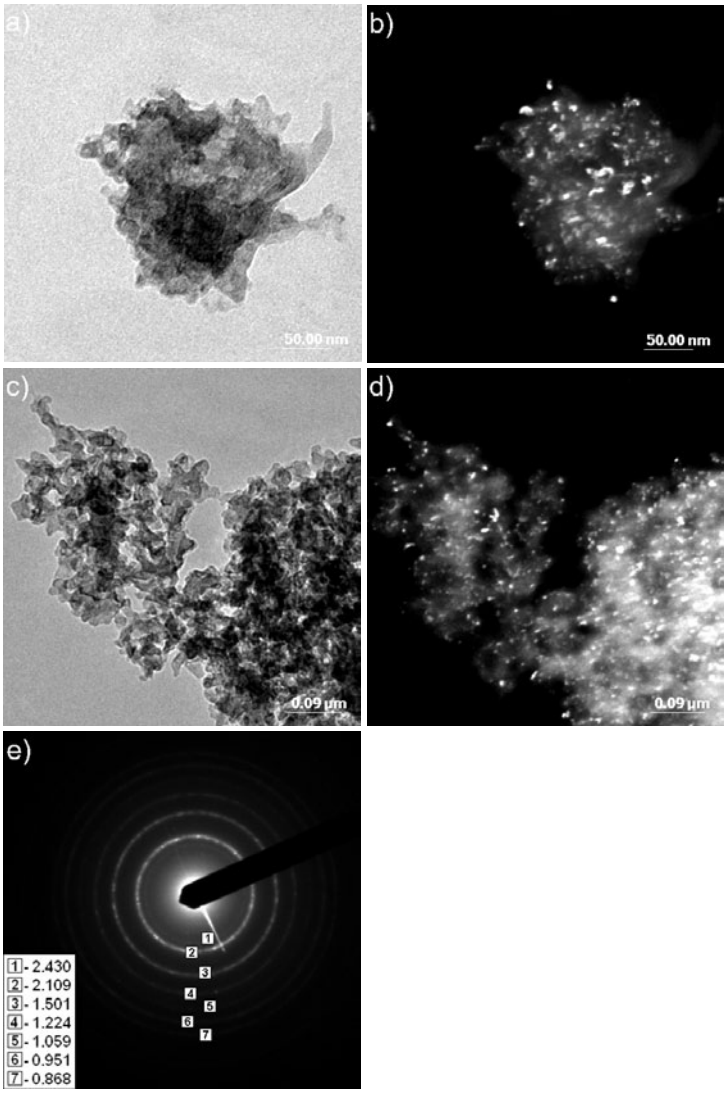

Fig. 4. TEM images of the MgO sample:
a, c) bright field, b, d) dark-field and e) electron diffraction pattern

4. Conclusions

The observed diffraction line broadening from MgO phase can be attributed to fine crystallite size. Good agreement between the average crystallite sizes, as determined by the Williamson–Hall analysis and by the Pielaszek procedure, was obtained. From the Williamson–Hall analysis, the lattice distortion ($<\Delta a/a>$) is relatively low and equal to 0.11 %, whereas the average crystallite size is estimated to be 7.5 nm.

The average crystallite size determined by the Pielaszek procedure is equal to 7.1 nm, with dispersion σ (measure of crystallite size polydispersity) equal to 2.1 nm. Despite the nanosize of MgO crystallites and the presence of amorphous phase, a good fit was found between the calculated X-ray pattern and the experimental one from the Rietveld refinement. Scanning and transmission electron microscopy images show the agglomerate nature of the powder sample, and an unfolded surface. The specific surface area, determined by the BET method, is equal to 138 m^2/g.

References

[1] LUCAS E., DECKER S., KHALEEL A., SEITZ A., FULTZ S., PONCE A., LI W., CARNES C., KLABUNDE K.J., Chem. Eur. J,. 7 (2001), 2505.
[2] CHOUDHARY V.R., RANE V.H., GADRE R.V., J. Catal., 145 (1994), 300.
[3] RAJAGOPALAN S., KOPER S., DECKER S., KLABUNDE K.J., Chem. Eur. J., 8 (2002), 2602.
[4] XU B.Q., WEI J.H., WANG H.Y., SUN K.Q., ZHU Q.M., Cat. Today, 68 (2001), 217.
[5] UTAMAPANYA S., KLABUNDE K.J., SCHLUP J.R., Chem. Mater., 3 (1991), 175.
[6] MORRIS R.M., KLABUNDE K.J., Inorg. Chem., 22 (1983), 682.
[7] KLABUNDE K.J., STARK J., KOPER O., MOHS C., PARK D.G., DECKER S., JIANG Y., LAGADIC I., ZHANG D., J. Phys. Chem., 100 (1996), 12142.
[8] LI Y.X., SCHLUP J.R., KLABUNDE K.J., Langmuir, 7 (1991), 1394.
[9] HOOKER P.D., KLABUNDE K.J., Environ. Sci. Technol., 28 (1994), 1248.
[10] ŠTENGL V., BAKARDJIEVA S., MAŘIKOVÁ M., BEZDIČKA P., ŠUBRT J., J. Mater. Sci., 57 (2003), 3998.
[11] JUNG H.S., LEE J.K., KIM J.Y., HONG K.S., J. Sol. State Chem., 175 (2003), 278
[12] WANG J.A., NOVARO O., BOKHIMI X., LÓPEZ T., GÓMEZ R., NAVARRETE J., LLANOS M.E., LÓPEZ -SALINAS E., Mater. Lett., 35 (1998), 317.
[13] NAKAMURA Y., OGURO K., UEHARA I., AKIBA E., J. Alloys Compd., 298 (2000), 138.
[14] DERCZ G., PRUSIK K., PAJĄK L., GORYCZKA T., FORMANEK B., J. Alloys Compd., 423 (2006), 112.
[15] DERCZ G., FORMANEK B., PRUSIK K., PAJĄK L., J. Mater. Proc. Tech., 162–163 (2005), 15.
[16] TORAYA H., J. Appl. Cryst., 19 (1986), 440.
[17] YOUNG R.A., SAKHIVEL A., MOSS T.S., PAIVA-SANTOS C.O., J. Appl. Cryst., 28 (1995), 366.
[18] WILLIAMSON G.K., HALL W.H., Acta Metall., 1 (1953), 22.
[19] PIELASZEK R., J. Alloys Compd., 382 (2004), 128.

Received 18 February 2008
Revised 2 June 2008

Materials Science-Poland, *Vol. 27*, *No. 1*, *2009*

The effect of DCJTB concentration on the photoluminescent and electroluminescent properties of PVK–PBD–perylene–DCJTB thin films

C. C. YAP[1*], M. YAHAYA[1], M.M. SALLEH[2]

[1]School of Applied Physics, Faculty of Science and Technology,
Universiti Kebangsaan Malaysia, 43600 UKM Bangi, Selangor, Malaysia

[2]Institute of Microengineering and Nanoelectronics, Universiti Kebangsaan Malaysia,
43600 UKM Bangi, Selangor, Malaysia

The paper reports a study of photoluminescent (PL) and electroluminescent (EL) properties of PVK–PBD–perylene–DCJTB thin film with variation of DCJTB doping concentrations. Poly(9-vinylcarbazole) (PVK) functioned as polymeric hole-transporting host, 2-(4-biphenylyl)-5-phenyl-1,3,4-oxadiazole (PBD) as electron-transporting molecule, perylene as blue dopant, and 4-(dicyanomethylene)-2-t-butyl-6(1,1,7,7-tetramethyljulolidyl-9-enyl)-4H-pyran (DCJTB) as a red dopant. The relative intensity of the blue emission from perylene decreased and that of the red emission from DCJTB increased with the increase of DCJTB concentration in both PL and EL spectra. However, the EL spectrum showed stronger DCJTB emission compared to the PL spectrum at the same DCJTB doping concentration, due to the carrier trapping effect. Interestingly, white light emission with C.I.E. coordinates of (0.31, 0.36) was observed in the EL spectrum when 0.05 wt. % of DCJTB was doped into PVK–PBD–perylene blend film. As a result, PVK–PBD–perylene–DCJTB thin film has potential application in white organic light emitting diodes.

Key words: *photoluminescence; electroluminescence; perylene; DCJTB; OLED*

1. Introduction

An organic light emitting diode (OLED) is a thin film device in which the emitting organic material is sandwiched between two electrodes. It emits light when a current is passed through it. OLEDs, using either small molecules or polymers, have attracted considerable interest due to their easy processability, flexibility, low cost, low operating voltages, wide viewing angles, tunability of the colour emission, fast response time, and ease of forming large areas [1, 2].

[*]Corresponding author, e-mail: chichin83@yahoo.co.uk

Recently, white OLEDs have attracted intense interest due to their potential applications in full colour displays combined with a colour filter, in backlights for liquid crystal displays as well as general illumination purposes. White emission from an OLED can be obtained by mixing two complementary colours (e.g., blue and orange) or three primary colours (red, green, and blue) where different emitting components are stacked in a multilayer structure [3, 4] or mixed within a single layer by doping or blending [5–7]. The latter approach is preferred because of its relatively simple fabrication and relatively stable colour coordinates with respect to the bias voltage.

Although much research has addressed the fabrication of white OLEDs utilizing blue polymer host doped with an orange-red dopant, few studies on dual fluorescent dyes white OLEDs have been reported [5, 6]. Park et al. reported OLEDs fabricated by co-doping perylene and 4-(dicyanomethylene)-2-t-butyl-6(1,1,7,7-tetramethyljulolidyl -9-enyl)-4H-pyran (DCJTB) into poly(methylphenylsilane) (PMPS) [8]. However, no white light emission was observed from their devices. In this paper, poly(9-vinylcarbazole) (PVK), one of the most frequently used polymeric hosts due to its excellent film-forming and hole-transporting properties, was used as a host for perylene and DCJTB. Since PVK is mainly hole-transport material, possessing very limited electron-transport capabilities, it is expected that in a single-layer structure, due to the highly unbalanced transport properties of holes and electrons, the recombination of carriers will be inefficient and the carrier recombination zone will also be closer to the cathode where the luminescence quenching occurs [9]. Therefore, an electron-transporting agent, 2-(4-biphenylyl)-5-phenyl-1,3,4-oxadiazole (PBD) was blended with PVK to improve the charge balance in the emitting layer [10].

The paper reports a study of photoluminescent (PL) and electroluminescent (EL) properties of PVK–PBD–perylene–DCJTB thin film with various DCJTB doping concentrations.

2. Experimental

The host polymer PVK, having a high weight-average molecular weight of 1 100 000 g/mol, electron-transporting molecule, PBD, blue dopant, perylene and the hole buffer material, PANI-EB were purchased from the Aldrich Chemical Company. The red dopant, DCJTB was purchased from the E-light Corporation. All materials were used as received without further purification. Molecular structures of the materials used in this study are shown in Fig. 1.

In order to study the EL property of PVK–PBD–perylene–DCJTB thin films, typical OLEDs with ITO/PANI-EB/PVK–PBD–perylene–DCJTB/Al structure were fabricated as shown in Fig. 2. The ITO-coated glass substrates were etched and patterned to serve as an anode. The substrates were each cleaned with 2-propanol and acetone in an ultrasonic bath for 15 min. It has been reported that the use of non-doped polyaniline (emeraldine base), PANI-EB as the insulating layer between ITO and the emitting layer resulted in significant reduction of the operating voltage [11].

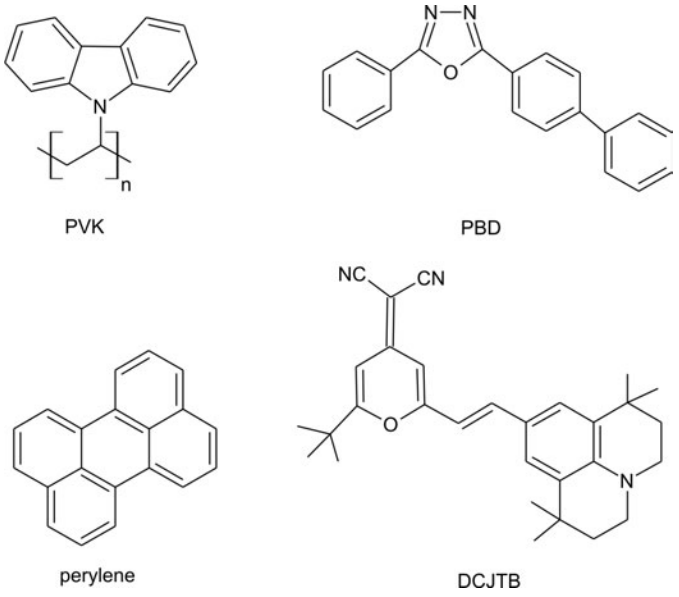

Fig. 1. Chemical structures of the organic materials used

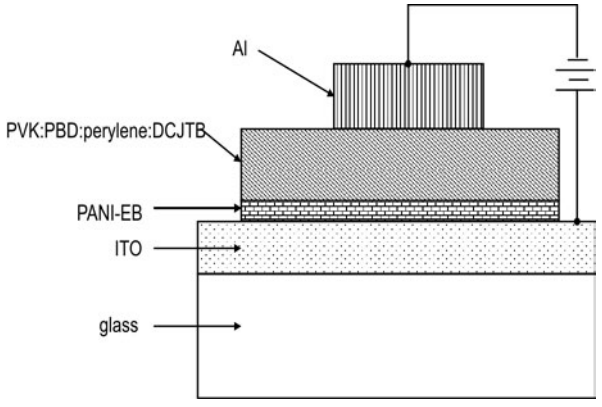

Fig. 2. The OLED with ITO/PANI-EB/PVK–PBD–perylene–DCJTB/Al structure

PANI-EB dissolved in dimethyl sulfoxide (DMSO) was spin-coated onto the ITO-coated glass substrates with a typical spinning speed and time of 2000 rpm for 40 s. After having been spun onto the substrates, the resulting PANI-EB films were dried in a vacuum oven at 80 °C for 30 min to remove excess solvent. 1,2-dichloroethane solutions each containing 8 mg/mL of PVK and PBD were prepared. For a precise doping of the host (PVK–PBD) with a very small amount of the dopants (3 wt. % of perylene and 0.025-0.25 wt. % of DCJTB), the dopants were first dissolved homogeneously in 1,2-dichloroethane. After that, the precalculated portions of the solutions were mixed with the host. The weight percentage of perylene and DCJTB (wt. %) was determined as the ratio of perylene and DCJTB to PVK. The solutions were then spin-coated onto

PANI-EB with a typical spinning speed and time at 2000 rpm for 40 s. The polymer film thickness was about 100 nm as determined by using a scanning electron microscope. Lastly, 150 nm aluminium was deposited as a cathode by using the electron gun evaporation technique.

The absorption and photoluminescence (PL) properties were investigated by depositing the corresponding thin films on pre-cleaned quartz substrates with a Perkin Elmer LAMBDA 900 UV-VIS spectrophotometer and a Perkin Elmer LS55 luminescence spectrometer, respectively. In addition, a Keithley 238 source measurement unit was used to measure the electrical characteristics of the devices, while the EL spectra were obtained with an Ocean Optic HR2000 spectrometer. All organic thin film preparation and measurements were carried out at ambient atmosphere.

3. Results and discussion

Figure 3 shows the absorption spectra of PVK–PBD host, perylene (1 wt. % in PMMA) and DCJTB (1 wt. % in PMMA) thin films. The maximum absorption wavelength for PVK–PBD, perylene and DCJTB was 298 nm, 439 nm and 505 nm, respectively. On the other hand, Figure 4 shows the PL spectra of the organic materials used. The emission of PVK–PBD, perylene and DCJTB peaked at 429 nm, 457 nm and 606 nm, respectively.

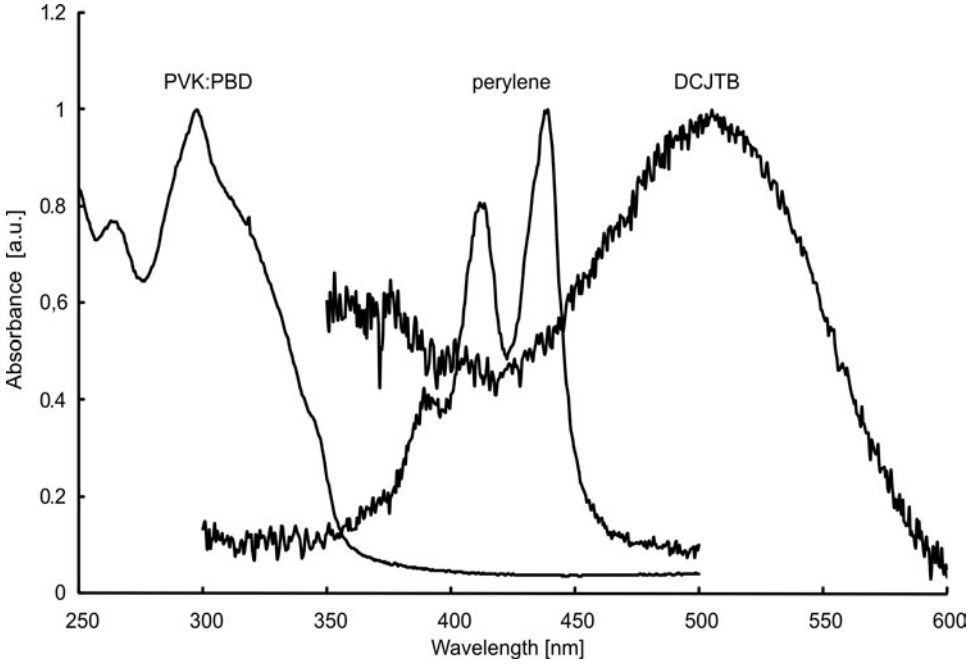

Fig. 3. UV-Vis absorption spectra of the PVK–PBD film,
PMMA–1 wt. % perylene film, and PMMA–1 wt. % DCJTB film

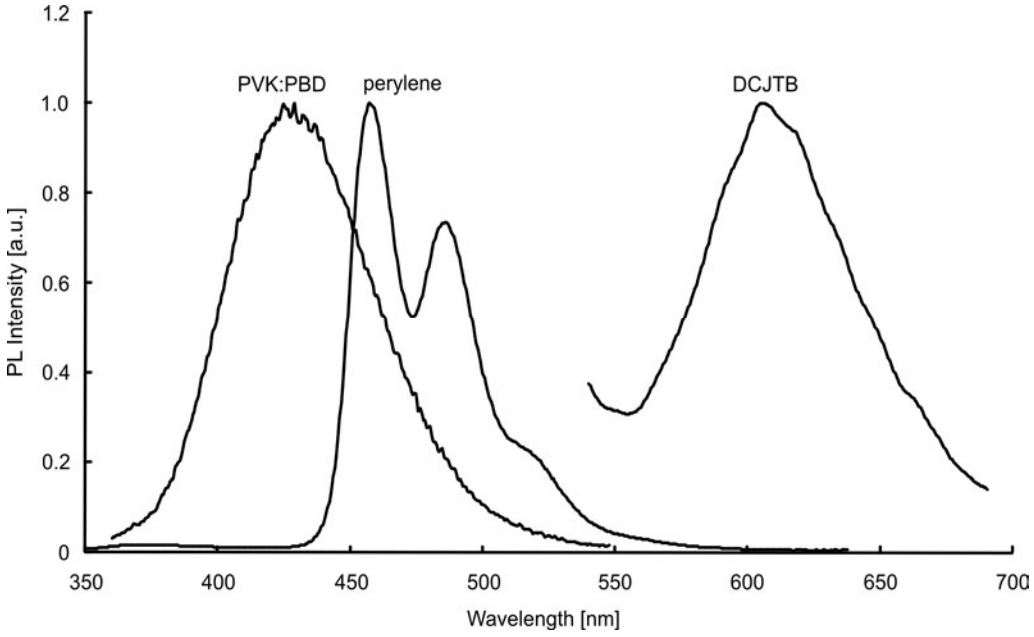

Fig. 4. Photoluminescence (PL) spectra of the PVK–PBD film,
PMMA–1 wt. % perylene film, and PMMA–1 wt. % DCJTB film

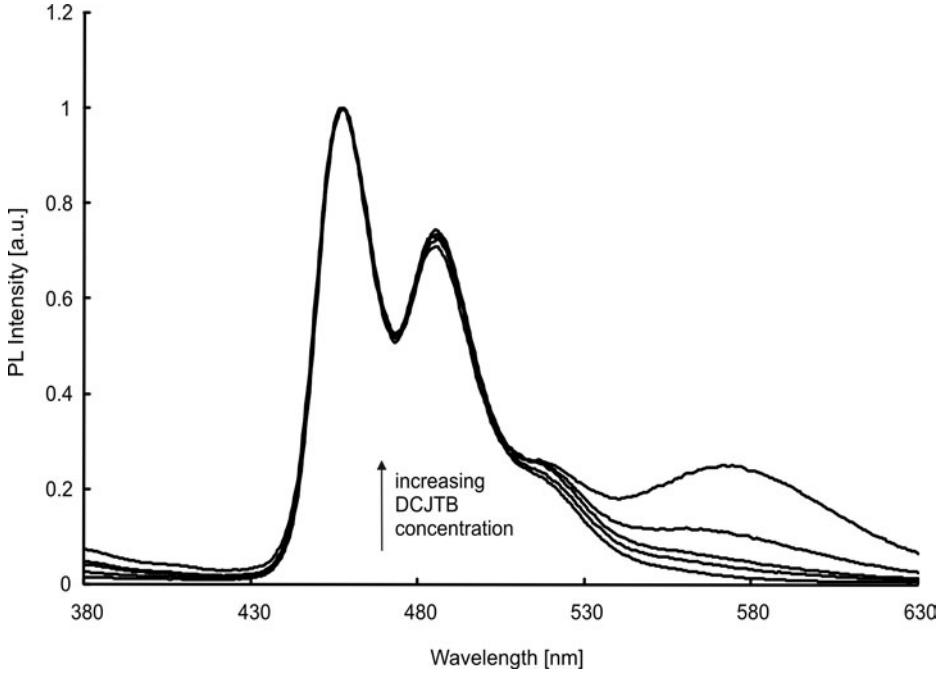

Fig. 5. PL spectra of PVK–PBD–3 wt. % perylene–DCJTB
films with various DCJTB doping concentrations

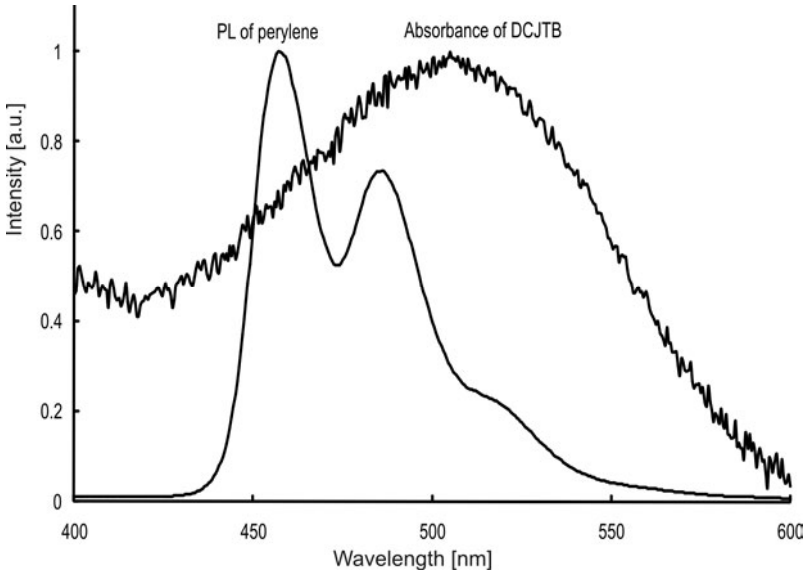

Fig. 6. Spectral overlapping between absorption of PMMA–1 wt. % perylene film and PL of PMMA–1 wt. % DCJTB film

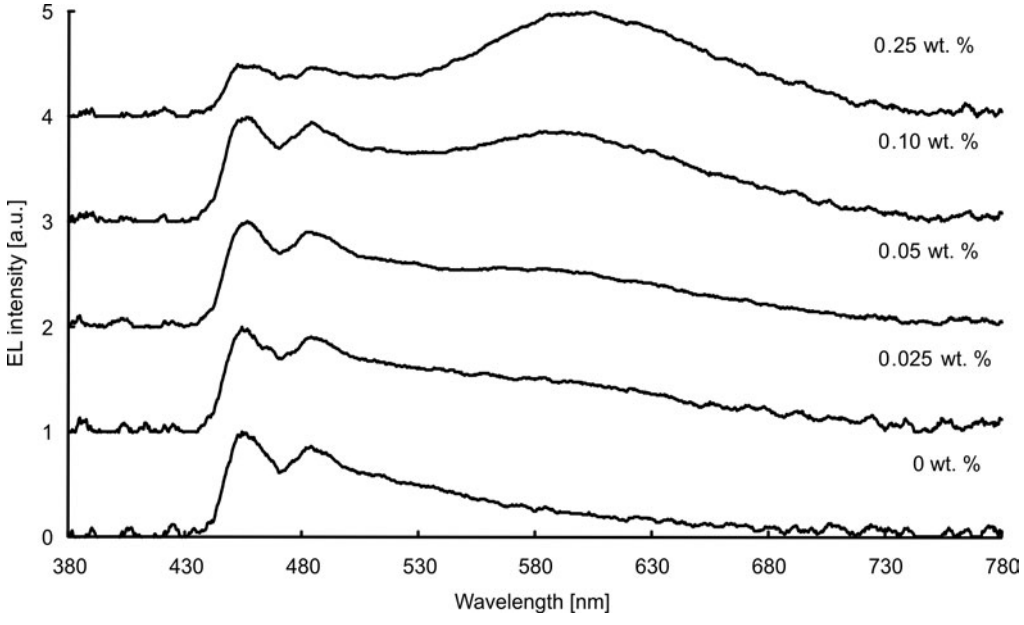

Fig. 7. EL spectra of devices with various DCJTB doping concentrations at 24 V

The PL spectra of PVK–PBD–3 wt. % perylene–DCJTB films with various DCJTB doping concentrations are shown in Fig. 5. The excitation wavelength of the spectra was 330 nm, which lies above the absorption onset of PVK–PBD and only

little absorption by perylene and DCJTB will take place at the point as is shown in Fig. 3. For a device without DCJTB, almost all emission was from perylene even though almost all excited energy was absorbed by PVK–PBD. This indicates that the energy transfer from the host to perylene was nearly complete. Exciton formation under photoexcitation in a guest emitter could result from radiative energy transfer or non-radiative energy transfer from the host. Radiative energy transfer normally can be neglected in emitter-doped OLED systems because it is a relatively slow and inefficient process [12]. Besides, Dexter energy transfer is a dominant mechanism in triplet–triplet energy transfer which can be observed in phosphorescent-based OLED [13, 14]. As a result, the most likely energy transfer mechanism between different molecular species in this study was Forster-type energy transfer [12, 15, 16]. In the case of DCJTB-doped devices, there are two emission bands in the spectra: a blue band from perylene and a red band from DCJTB. The absorption spectrum of DCJTB partially overlaps with the PL spectrum of perylene (Fig. 6), which implies a possibility of the Forster-type energy transfer from perylene to DCJTB [8]. The red band increased with the increase of DCJTB concentration from 0.025 to 0.25 wt. %. The probability for excitation transfer from perylene to DCJTB not only depends on the energy overlapping between them, but also on their spatial distance [17]. As the concentration of DCJTB was reduced (molecules of DCJTB decreased as well), the spatial distance between perylene and DCJTB became larger. As a result, less energy from perylene could be transferred to DCJTB.

Figure 7 shows the EL spectra of the devices with various doping concentrations of DCJTB at an applied voltage of 24 V. With increasing DCJTB concentration, the relative intensity of the blue emission decreased and that of the red emission increased, which indicates more energy from perylene transferred to DCJTB. The trend was similar to that observed in the PL spectra. The incomplete energy transfer from perylene to DCJTB at lower concentration of DCJTB enables the production of white light emission through control of the blend ratio. Figure 8 gives the C.I.E. coordinates of (0.24, 0.33), (0.30, 0.36), (0.31, 0.36), (0.36, 0.38) and (0.44, 0.40) for 0, 0.025, 0.05, 0.10, and 0.25 wt % DCJTB-doped devices, respectively. Among all the EL devices tested in this experiment, the device using the 0.05 wt. % DCJTB exhibited the C.I.E. coordinates (0.31, 0.36) closest to the standard CIE coordinates for white light emission (0.33, 0.33). Obviously, this is a fairly white emission. Importantly, the emission spectrum remained in the white emission region for DCJTB doping concentration from 0.025 wt. % to 0.10 wt. %.

It was also found that the shapes of EL spectrum are different from those of PL spectrum at the same DCJTB doping concentration. For example, at 0.25 wt. % DCJTB loading level, PL from DCJTB was quite low, but for EL the emission from DCJTB was very strong. This phenomenon is common in the doped systems. The main reason for the observation of this phenomenon lies in the different excitation mechanisms of PL and EL. The PL spectra are excited by photons. There is no carrier injected in this process, the emission spectra of a doped system are only determined by

the energy transfer. However, in EL spectra, besides energy transfer, carrier trapping also plays an important role [18–20]. This also can be deduced from the energy level scheme, as shown in Fig. 9 [7, 21, 22]. Since the LUMO (lowest unoccupied molecular orbital) and HOMO (highest occupied molecular orbital) energy levels of DCJTB are located inside the energy gap of other materials, some of the electrons and holes will be trapped or even directly injected and recombine directly in DCJTB molecules when an electric field is applied.

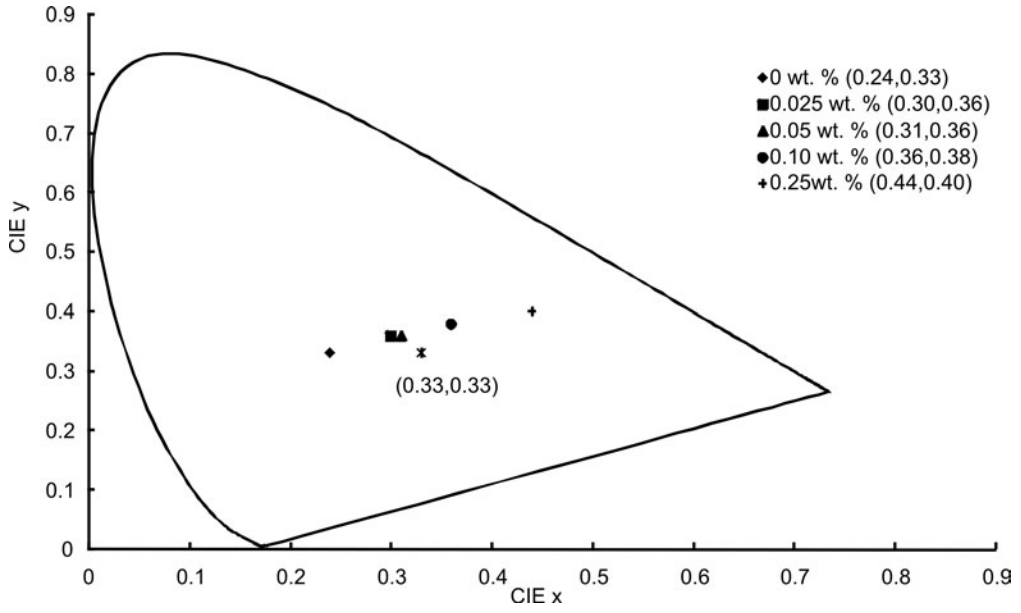

Fig. 8. CIE coordinates of devices with various DCJTB doping concentrations at 24 V

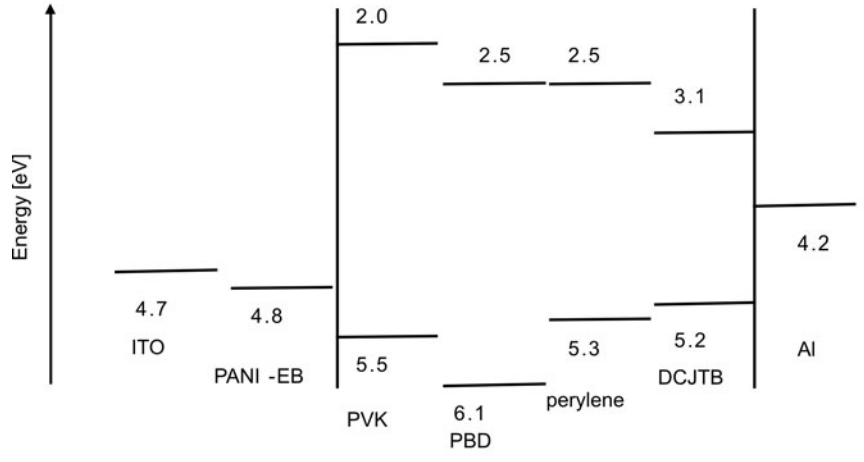

Fig. 9. Energy level diagram of ITO/PANI-EB/PVK–PBD–perylene–DCJTB/Al device

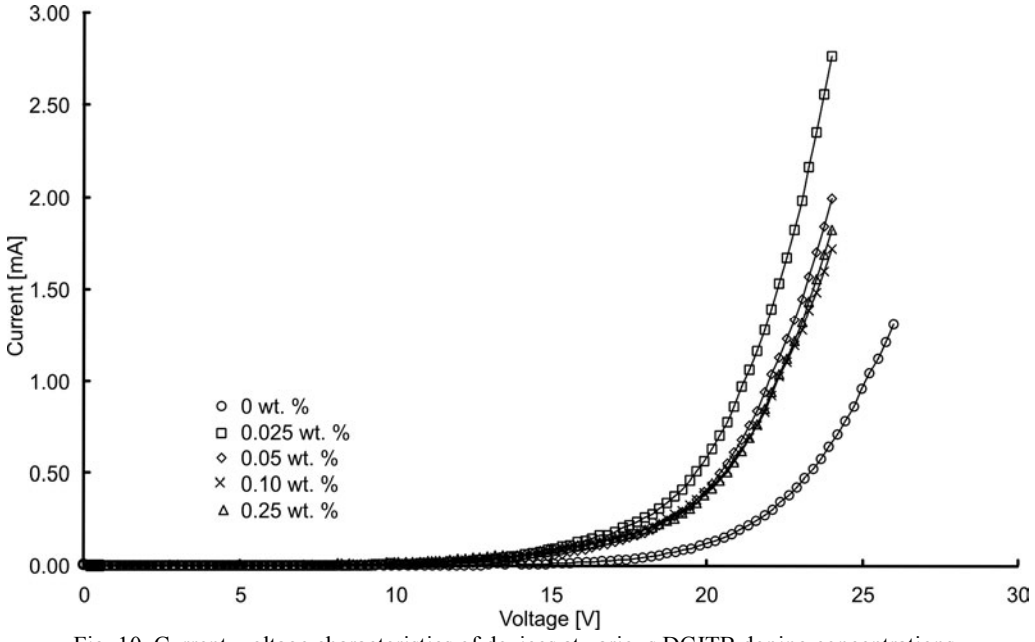

Fig. 10. Current–voltage characteristics of devices at various DCJTB doping concentrations

Figure 10 shows the current-voltage characteristics of the white light emitting devices at room temperature. The forward current was found to increase with increasing forward bias voltage, and the curve has the same characteristics as those of a typical diode. In general, current turn-on voltages for DCJTB-doped devices are lower than those for devices without DCJTB. The current turn-on voltage for DCJTB-doped devices was around 15 V. DCJTB can facilitate both electron and hole injection into the blend layer in the OLEDs due to their lower LUMO and higher HOMO relative to the work function of the Al and ITO, respectively, as shown in Fig. 6. Besides high current turn-on voltage, the luminance of the devices was also very low (< 1 cd/m^2) due to a high energy barrier for electron injection at the cathode-emitting layer interface (1.7 eV). After optimizing the structure of the devices such as adjusting the thickness of emitting layers and the blend ratio of PVK and PBD, using a low work function metal cathode, such as Ca, and introducing electron injection layers etc., further reduction in turn-on voltage and increase in luminance are expected [22–24].

4. Conclusion

The relative intensity of the blue emission from perylene decreased and that of the red emission from DCJTB increased with the increasing of DCJTB concentration in both PL and EL spectra. However, stronger DCJTB emission was observed in the EL spectrum compared to the PL spectrum at the same DCJTB doping concentration due

to carrier trapping effect. Interestingly, white light EL emission with C.I.E. coordinates of (0.31, 0.36) was achieved when 0.05 wt. % of DCJTB was doped into PVK–PBD–perylene blend film. Clearly, PVK–PBD–perylene–DCJTB thin film is suitable to be used as emitting layer in white OLEDs.

Acknowledgements

This work has been carried out with the support of the Malaysian Ministry of Science, Technology and Innovation (MOSTI), under the IRPA grant No. 03-02-02-0067-SR0007/04-04. The author would also like to acknowledge MOSTI for the University Postgraduate Research Scholarship (PGD).

References

[1] TANG C.W., VANSLYKE S.A., Appl. Phys. Lett., 51 (1987), 913.
[2] BURROUGHHES J.H., BRADLEY D.D.C., BROWN A.R., MARKS R.N., MACKAY K., FRIEND R.H., BURNS P.L., HOLMES A.B., Nature, 347 (1990), 539.
[3] DESHPANDE R.S., BULOVIC V., Appl. Phys. Lett., 75 (1999), 888.
[4] LIU Z., NAZARÈ H., Synth. Met., 111 (2000), 47.
[5] KIDO J., SHIONOYA H., NAGAI K., Appl. Phys. Lett., 67 (1995), 2281.
[6] YANG J.P., JIN Y.D., HEREMANS P.L., HOEFNAGELS R., DIELTIENS P., BLOCKHUYS F., GEISE H.J., VAN DER AUWERAER M., BORGHS G., Chem. Phys. Lett., 325 (2000), 251.
[7] ZHENG X.Y., ZHU W.Q., WU Y.Z., JIANG X.Y., SUN R.G., ZHANG Z.L., XU S.H., Display, 24 (2003), 121.
[8] PARK J., SEOUL C., KIM T., Curr. Appl. Phys., 5 (2005), 293.
[9] KIDO J., HONGAWA K., OKUYAMA K., NAGAI K., Appl. Phys. Lett., 63 (1993), 2627.
[10] JOHNSON G.E., MCGRANE K.M., STOLKA M., Pure Appl. Chem., 67 (1995), 175.
[11] WANG H.L., MACDIARMID A.G., WANG Y.Z., GEBLER D.D., EPSTEIN A.J., Synth. Met., 78 (1996), 33.
[12] LYONS B.P., WONG K.S., MONKMAN A.P.J., Chem. Phys. 118 (2003), 4707.
[13] O'BRIEN D.F., BALDO M.A., THOMPSON M.E., FORREST S.R., Appl. Phys. Lett. 74 (1999), 442.
[14] ADACHI C., BALDO M.A., THOMPSON M.E., FORREST S.R., J. Appl. Phys. 90 (2001), 5048.
[15] VIRGILI T., LIDZEY D.G., BRADLEY D.D.C., Synth. Met., 111–112 (2000), 203.
[16] OHMORI Y., KAJII H., SAWATANI T., UETA H., YOSHINO K., Thin Solid Films, 393 (2001), 407.
[17] GUILLET J. E., *Polymer Photophysics and Photochemistry*, Cambridge University Press, London, 1985.
[18] UCHIDA M., ADACHI C., KOYAMA T., TANIGUCHI Y., J. Appl. Phys., 86 (1999), 1680.
[19] TAO Y.T., KO C.W., BALASUBRAMANIAM E., Thin Solid Films, 417 (2002), 61.
[20] SHEN F., XIA H., ZHANG C., LIN D., LIU X., MA Y., Appl. Phys. Lett. 84 (2004), 55.
[21] YAMAGUCHI M., NAGATOMO T., Thin Solid Films, 363 (2000), 21.
[22] WU C.C., STURM J.C., REGISTER R.A., TIAN J., DANA E.P., THOMPSON M.E., IEEE Trans. Electron Dev., 44 (1997), 1269.
[23] PARKER I.D., J. Appl. Phys. 75 (1994), 1656.
[24] SHAHEEN S.E., JABBOUR G.E., MORRELL M.M., KAWABE Y., KIPPELEN B., PEYGHAMBARIAN N., NABOR M.F., SCHLAF R., MASH E.A., ARMSTRONG N.R., J. Appl. Phys., 84 (1998), 2324.

Received 4 March 2008
Revised 27 August 2008

Materials Science-Poland, *Vol. 27*, *No. 1*, *2009*

Enhancement of ferromagnetic properties in Ni-doped $BiFeO_3$

Y. WANG[1], G. XU[1], L. YANG[2], Z. REN[1],
X. WEI[1], W. WENG[1], P. DU[1], G. SHEN[1], G. HAN[1*]

[1]State Key Laboratory of Silicon Materials, Department of Materials Science and Engineering, Zhejiang University, Hangzhou 310027, PR China

[2]Shandong Research and Design Institute of Industrial Ceramics, Zibo 255031, PR China

Ni-doped $BiFeO_3$ samples were successfully synthesized by a hydrothermal method. The as-prepared samples were characterized by X-ray diffraction (XRD), and energy dispersive X-ray spectroscopy (EDS). It was found that the magnetization can be controlled by the Ni doping concentration. The magnetization of Ni-doped $BiFeO_3$ was greatly enhanced when the Ni doping concentration was 0.5%. Therefore, it would be interesting to fabricate thin films with similar composition and study their properties with the aim of identifying new device applications.

Key words: *Ni-doped $BiFeO_3$; ferromagnetic property; hydrothermal method*

1. Introduction

Multiferroic materials exhibiting simultaneously ferroelectricity and ferromagnetism gain much attention due to their promising multifunctional device applications [1–4]. Besides the potential applications, the fundamental physics of multiferroic materials is also fascinating. However, there is a scarcity of materials showing multiferroic behaviour because the usual atomic level mechanisms driving ferromagnetism and ferroelectricity are mutually exclusive [5]. Bismuth ferrite ($BiFeO_3$) which shows ferroelectric (T_C = 1103 K) and antiferromagnetic properties (T_N = 643 K) at room temperature, has attracted great attention since its discovery in 1960 [6].

Recently, enhancement of the ferroelectric property in $BiFeO_3$ film has been realized [7] making it attractive from the point of view of possible applications. However, $BiFeO_3$ (BFO) shows the presence of a weak magnetic moment at room temperature

*Corresponding author, e-mail: hgr@zju.edu.cn

because of the canting of the Fe sublattice moment [8]. Therefore, if the material is to be exploited in device applications, it is essential that its magnetic properties be improved. Several groups have enhanced the magnetic properties of BFO by ion substitutions [9–11] such as Mn substituting for Fe ions. To our knowledge, there is no report on the substitution of Ni for Fe ions. In this paper, the magnetization of BFO has been noticeably enhanced by the substitution of Ni for Fe ions. The doping concentration of Ni was set as the molar ratio of Ni/(Ni +Fe) (in the form of Ni^{2+} ions).

2. Experimental

The chemical reagents were bismuth nitrate ($Bi(NO_3)_3{\cdot}5H_2O$), iron nitrate ($Fe(NO_3)_3{\cdot}9H_2O$), nickel nitrate ($Ni(NO_3)_2{\cdot}6H_2O$), and potassium hydroxide (KOH). All the chemicals were of analytical grade and were used as received without further purification. Stoichiometric proportions of $Bi(NO_3)_3$, $Fe(NO_3)_3$ and $Ni(NO_3)_2$ were dissolved in diluted HNO_3 to form aqueous solutions. Then, the KOH solution was slowly added to the above solution to coprecipitate Fe^{3+}, Ni^{2+} and Bi^{3+} ions by constant stirring and a brown precipitate was formed. The precipitate was filtered, and washed with distilled water to remove NO_3^- and K^+ ions. Then, the precipitate was mixed with KOH solutions under constant magnetic stirring for 5 min. The suspension was poured into a stainless-steel Teflon-lined autoclave for hydrothermal treatment. The autoclave was sealed and maintained at 200 °C for 9 h. Finally, it was cooled down naturally to room temperature. The products were filtered, washed several times with distilled water and absolute ethanol, and then dried at 70 °C for 4 h for characterization. X-ray diffraction was performed on an ARL XTRA X-ray diffractometer with high-intensity CuK_α radiation. The EDS spectroscopy pattern was performed by X-ray energy dispersion spectroscopy using a GENENIS4000 spectrometer. Magnetic measurements were carried out using a Quantum Design superconducting quantum interference device (SQUID, MPMS XL-5).

3. Results and discussion

Figure 1 shows XRD patterns of the BFO samples doped with Ni of various concentrations. The XRD results showed that the obtained Ni-doped BFO samples were single phase with perovskite structure when the Ni doping concentration varied from 0% to 1%. However, an impurity phase ($Bi_{12}NiO_{19}$) can be detected in the case of the 1.5% Ni doping concentration, which is an indication of the saturation level of Ni substitution in BFO. An expanded view on the location of (110) diffraction peaks in the range of 30°–35° (Fig. 2) shows that the peak position of the sample obviously shifts toward a lower 2θ value in the case of Ni doping. Energy dispersive X-ray (EDS) patterns checked from the obtained products clearly demonstrate the presence

of Ni in the prepared products (Fig. 3). According to the above results, it is evident that Ni ions have been effectively incorporated into the crystal structure of $BiFeO_3$ and the lattice parameter a of $BiFeO_3$ is enlarged because of the larger radius of Ni^{2+} cations relative to that of Fe^{3+} cations.

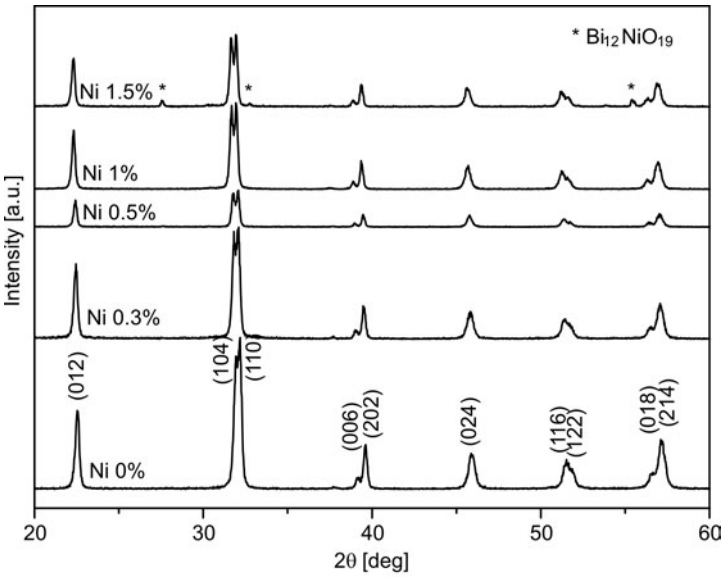

Fig. 1. XRD patterns of the Ni-doped BFO samples
with Ni doping concentrations ranging from 0% to 1.5%,

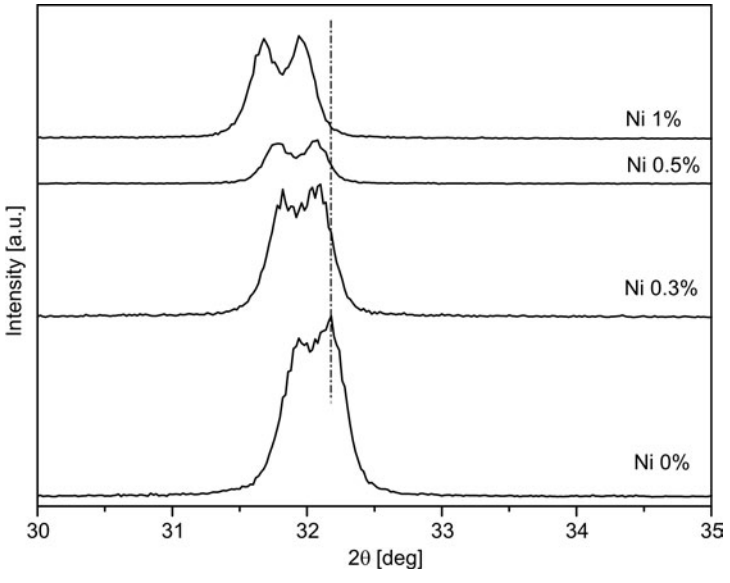

Fig. 2. Dependence of the (110) diffraction
peak positions in the patterns on Ni concentration

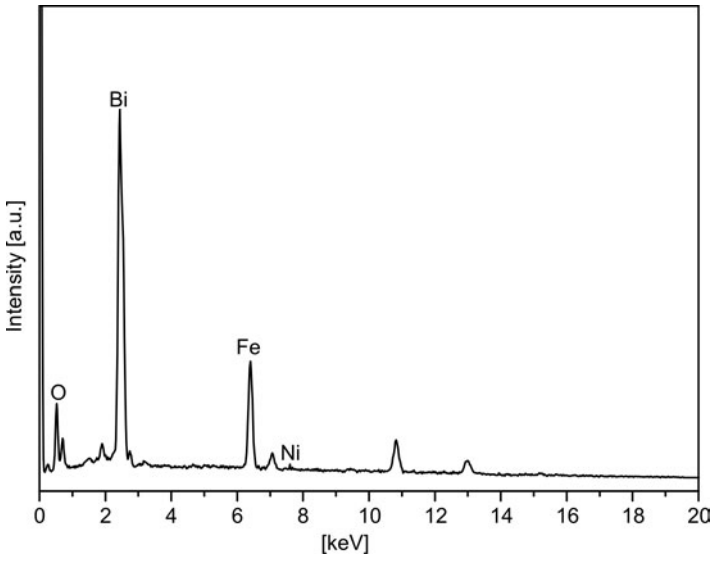

Fig. 3. The EDS spectroscopy pattern for the as-obtained Ni-doped BFO sample with a 0.5% Ni doping concentration

The lattice parameters of Ni-doped BFO samples are given in Table 1. It is clear that with the increase in Ni doping concentration there is an increase in both, *a* and *c* parameters of the unit cell. This is as expected, since the ionic radius of Ni^{2+} is slightly larger than that of Fe^{3+}. Since there is an increase in both, *a* and *c* parameters, the ratio *c*/*a* remains more or less unaffected, which is important for maintaining the ferroelectric properties in Ni-doped BFO samples.

Table 1. Lattice parameters of Ni-doped BFO samples

Ni doping concentration [%]	*a* [Å]	*c* [Å]	*v* [Å]^3	*c*/*a* ratio
0	5.571	6.911	185.78	1.241
0.3	5.577	6.914	186.28	1.240
0.5	5.578	6.926	186.68	1.241
1	5.586	6.937	187.46	1.242

Magnetic properties of the obtained Ni-doped BFO samples of various doping concentrations have been determined (Fig. 4). In pure BFO, the magnetization varies linearly with the applied magnetic field up to 20 kOe, similar to that of La-doped BFO powders [9]. There is no obvious increase of magnetization in the case of a 0.3% Ni doping concentration, but magnetization is greatly enhanced when the Ni doping concentration increases to 0.5%. Compared with the method to enhance ferromagnetic properties in BFO ceramic by La doping [10], Ni-doped BFO samples (with Ni doping

concentration 0.5%) show larger magnetization at room temperature. In addition, magnetization decreases when the Ni doping concentration is further increased to 1%. This indicates that the ferromagnetism of Ni-doped BFO does not increase with the increase of the Ni doping concentration.

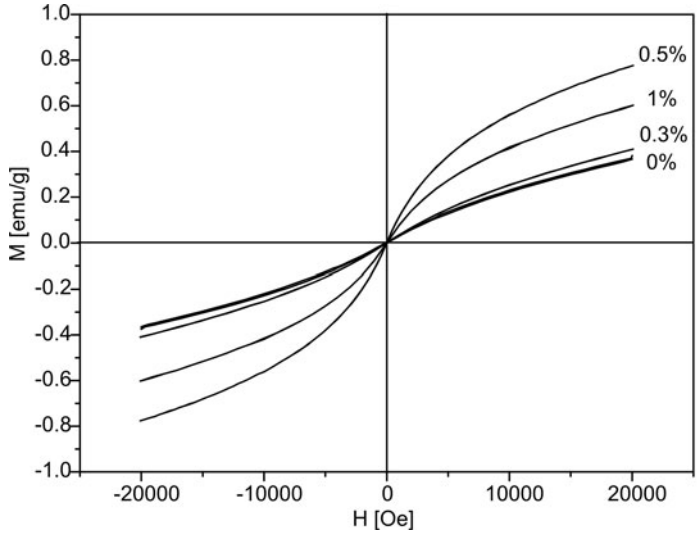

Fig. 4. *M–H* recorded at room temperature for the as-prepared Ni-doped BFO samples with Ni doping concentrations ranging from 0 % to 1 %

The dependence of the magnetization on the Ni doping concentration provides strong evidence that the noticeable enhancement in the ferromagnetism is not due to any precipitating secondary phase, such as nickel oxides. If nickel oxides are responsible for the enhancement of ferromagnetic behaviour, a stronger Ni concentration increasing up to 1% would presumably improve the corresponding magnetization. Instead, the opposite behaviour is observed.

4. Conclusions

In Ni substituted $BiFeO_3$, the magnetization varies with Ni doping concentration and the magnetization of Ni-doped $BiFeO_3$ is greatly enhanced when the Ni doping concentration is 0.5%. Therefore, it is an important task to produce thin films with similar compositions and to study their properties, in order to identify new applications in devices. Such investigations are in progress and will be reported elsewhere.

Acknowledgement

This work is supported by the National Science Foundation of China (No. 50452003).

References

[1] HUR N., PARK S., SHARMA P.A., AHN J.S., GUHA S., CHEONG S.W., Nature, 429 (2004), 392.
[2] KIMURA T., KAWAMOTO S., YAMADA I., AZUMA M., TAKANO M., TOKURA Y., Phys. Rev. B., 67 (2003), 180401.
[3] DHO J., LEUNG C.W., MACMANUS-DRISCOLL J.L., BLAMIRE M.G., J. Cryst. Growth, 267 (2004), 548.
[4] ZHU W.M., YE Z.G., Ceram. Int., 30 (2004), 1435.
[5] SPALDIN N.A., FIEBIG M., Science, 309 (2005), 391.
[6] SMOLENSKII G.A., CHUPIS I., Sov. Phys. Usp., 25 (1982), 475.
[7] WANG J., NEATON J.B., ZHENG H., NAGARAJAN V., OGALE S.B., LIU B., VIEHLAND D., VAITHMANATHAN V., SCHLOM D.G., WAGHMARE V.V., SPALDIN N.A., RABE K.M., WUTTIG M., RAMESH R., Science, 299 (2003), 1719.
[8] SMOLENSKII G.A., CHUPIS I., Sov. Phys. Usp., 25 (1982), 475.
[9] PALKAR V.R., KUNDALIYA D.C., MALIK S.K., J. Appl. Phys., 93 (2003), 4337.
[10] LIN Y.H., JIANG Q.H., WANG Y., NAN C.W., CHEN L., YU J., Appl. Phys. Lett., 90 (2007), 172507.
[11] PALKAR V.R., GANESH KUMARA K., MALIK S.K., Appl. Phys. Lett., 84 (2007), 2586.

Received 10 March 2008
Revised 19 December 2008

Materials Science-Poland, *Vol. 27*, *No. 1*, *2009*

Investigations of highly conducting and transparent Sc doped ZnO films grown by the sol-gel process

R. SHARMA[1], P. K. SHISHODIA[2], A. WAKAHARA[3], R. M. MEHRA[1*]

[1]Department of Electronic Science, University of Delhi South Campus, New Delhi – 110 021, India

[2] Department of Physics & Electronics, Zakir Husain College,
University of Delhi, New Delhi 110 002, India

[3]Department of Electrical and Electronic Engineering,
Toyohashi University of Technology, Tempaku-cho, Toyohashi 441 8580, Japan

Highly transparent and conductive scandium doped zinc oxide (ZnO/Sc) films were prepared on Corning glass 7059 substrates by the sol-gel technique. The influence of scandium concentration (0–1.5 wt. %) and annealing temperature (300–500 °C) on the structural, optical and electrical properties was investigated. The average transmittance was found to be above 89% in the visible region. ZnO/Sc film having 0.5 wt. % of Sc and annealed at 400 °C exhibited a minimum resistivity of 3.52×10^{-4} ohm·cm. The surface morphology of these films examined by SEM and AFM revealed formation of nano rods.

Key words: *zinc oxide; scandium doping; sol-gel method; thin films*

1. Introduction

Zinc oxide (ZnO) is a technologically important material exhibiting multifunctional properties for various applications in optoelectronic devices such as solar cells [1], transparent conducting electrodes [2], heat mirrors [3] and surface acoustic wave devices [4]. Nanoscale porous structures of ZnO with a high surface area find their application in chemical sensors [5] and dye-sensitised solar cells [6]. Indium tin oxide (ITO) or tin oxide (SnO_2) materials have long been established as transparent conducting materials. Recently, ZnO has been considered as a potential alternative to ITO and SnO_2, owing to a number of advantages, namely low cost, high mechanical stability, non-toxic nature and stability under reducing hydrogen atmosphere [7, 8]. ZnO is a wide-band-gap semiconductor material with a direct band gap of 3.37 eV [9] at room temperature and an exciton binding energy of 60 meV. Its electrical and optical prop-

*Corresponding author, e-mail: rammehra2003@yahoo.com

erties can be controlled by either selecting the nonstoichiometry and/or by appropriate dopants [10]. The effect of doping with In, Al , Y, N and Ga in ZnO has been frequently reported by various research groups [11, 12] but the effect of a rare-earth impurity such as Sc has been scarcely reported [13]. The ionic radius of Sc is very close to that of Zn and this makes it compatible for doping [11]. Various techniques have been used to deposit undoped and doped ZnO films on various substrates, including spray pyrolysis [14], organometallic chemical vapour deposition [15], pulsed laser deposition [16], sputtering [17] and sol-gel process [18]. Among these, the sol-gel technique offers many advantages for the deposition of thin coatings due to its excellent control of the stoichiometry of precursor solutions, ease of compositional modifications, homogeneity, low cost, low temperature and a non-vacuum requirement [19].

This paper reports a detailed investigation of transparent and conducting scandium doped zinc oxide (ZnO/Sc) films. The films are deposited by the sol-gel technique using 2-methoxyethanol as a solvent and monoethanolamine (MEA) as a stabilizer. The effect of Sc doping on structural (preferred orientation, surface morphology), electrical (resistivity, carrier concentration and Hall mobility) and optical (transmittance, band gap) properties are reported. The variation of band gap with doping and annealing is analyzed using band gap widening and narrowing phenomena.

2. Experimental

The precursor solution was prepared from $Zn(CH_3COO)_2 \cdot 2H_2O$ (99.95%, GR, Hayashi Pure Chemical Ind. Ltd, Japan), anhydrous 2-methoxyethanol (AR, Ajax Chemicals, Australia) and monoethanolamine (MEA, CP, Bio-Lab, London). The solution containing MEA/Zn with the molar ratio of 0.2 was stirred for 5 min. An appropriate amount (0–1.5 wt. %) of $ScNO_3 \cdot 6H_2O$, purity 99.9% was introduced as a dopant. This mixture was sonicated for about 2 h. The resultant clear, transparent and homogeneous solution was used after 48 h for film deposition. Microscopic Corning glass (7059) slide substrates were cleaned ultrasonically, first in acetone and then subsequently in methanol for ten minutes each. They were further cleaned with deionised water for 20 min and finally dried in nitrogen atmosphere. The spinning speed and spin duration were 3200 rpm and 30 s, respectively. The wet films were kept to hydrolyze in air at room temperature for 5 min, then dried at 200 °C for the next 10 min and finally heated at 280 °C for 20 min in air atmosphere with the heating rate of about 10 °C/min. Thus, the drying process removes the residual organic solvents and organic groups in the deposited gel film and converts the organic precursor film into a dense inorganic film. An approximate thickness of 0.02 μm was obtained for each spin. The above process of coating and drying was repeated several times to increase the film thickness. In the present work, the thicknesses of the films were in the range of 450–500 nm. Finally the deposited films were annealed in air in the tempera-

ture range of 300–500 °C for 1 h. A slow cooling rate was maintained to avoid the possibility of stress in the films as expected in rapid cooling. Crystallite phase and orientation were evaluated by the X-ray diffraction method (XRD, Philips PW 1830 Geiger counter diffractometer, PW 1830) using a monochromatized X-ray beam with nickel-filtered CuK_α radiation (λ = 1.5418 Å). A continuous scan mode was used to collect 2θ data between 30–40°, with a 0.02 sample pitch and 4 deg/min scan rate. Microstructure was investigated by the scanning electron microscopy (SEM, JEOL JSM-6300). Average surface roughness of the films was obtained by an atomic force microscopy (AFM, Burleigh-SPI 3700) with scanned area of 5×5 μm^2. The thickness of the films was determined with a DEKTECK3-ST surface profilometer. Optical transmittance was obtained in the 300–800 nm range using a Shimadzu UV-3150 spectrophotometer. The electrical resistivity ρ and the Hall coefficient R_H were measured by the van der Pauw [20] technique. The sign of the Hall coefficient confirmed the n-type conduction of the films. The composition of scandium doped ZnO films was determined by the elemental dispersion analysis using X-ray (EDAX) measurements.

3. Results and discussion

3.1. Structural properties

Figure 1 represents the XRD patterns of ZnO/Sc (Sc – 0.5 wt. %) films as a function of annealing temperature (300 - 500 °C). It is seen from the figure that as-deposited film exhibited an amorphous nature, whereas the films annealed at 300 °C showed evidence of polycrystalline structure with (100), (002) and (101) peaks. With the increase of annealing temperature from 300–400 °C, the intensity of the (002) peak increases, indicating a c-axis preferential growth, implying an improvement in the crystalline quality of the film. With further increase in temperature > 400 °C there was a decrease in the intensity (002) peak suggesting a degradation of the films at higher annealing temperature.

Figure 2 shows the X-ray diffraction patterns of the (ZnO/Sc) films annealed at the optimized temperature of 400 °C and having different Sc concentrations. The films exhibit a dominant peak at 2θ = 34.44° corresponding to the (002) plane of ZnO and other peaks corresponding to (100) and (101), indicating the polycrystalline nature of the films. It is seen from the figure that the relative intensity of the (002)-reflection peak decreases with increasing Sc concentration greater than 1.0 wt. %. No peaks corresponding to either Sc or Sc oxides appear in the diffraction pattern of the samples, suggesting that Sc is incorporated at the Zn lattice site in the hexagonal wurtzite structure of ZnO.

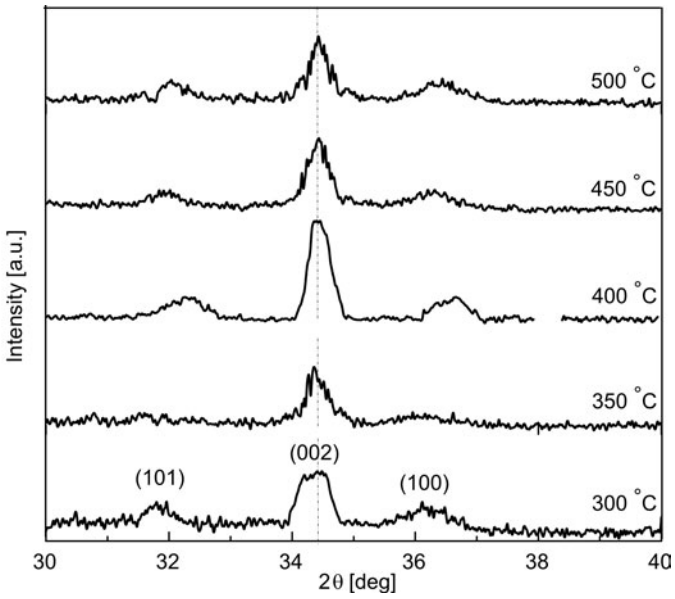

Fig. 1. Effect of annealing temperature on the XRD patterns of ZnO/Sc (Sc – 0.5 wt. %) thin films

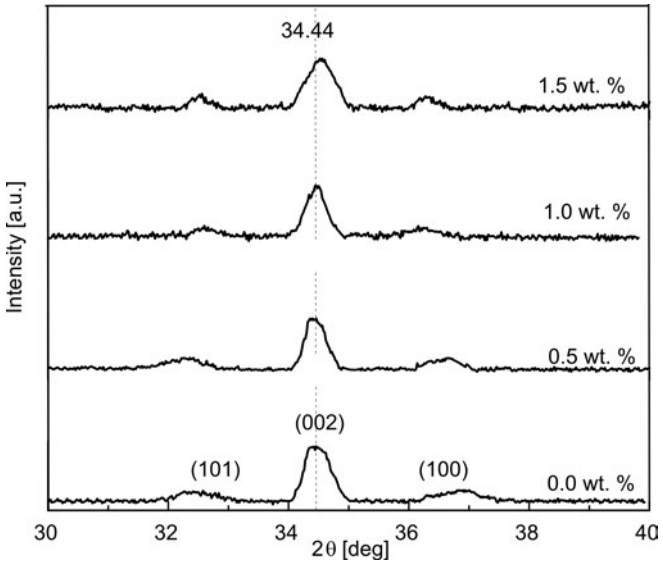

Fig. 2. Effect of doping concentration on the XRD patterns of ZnO/Sc films annealed at 400 °C in air for 1 h

Figure 3 shows the variation of grain size D and lattice constant c with annealing temperature for ZnO/Sc (0.5 wt. %) films. The grain size D of the films was calculated using the Debye–Scherrer formula [21]

$$D = \frac{0.9\lambda}{\beta\cos\theta} \tag{1}$$

where λ is the wavelength of CuK_α line, and β is the full width at half maximum (FWHM) of the (002) reflection peak.

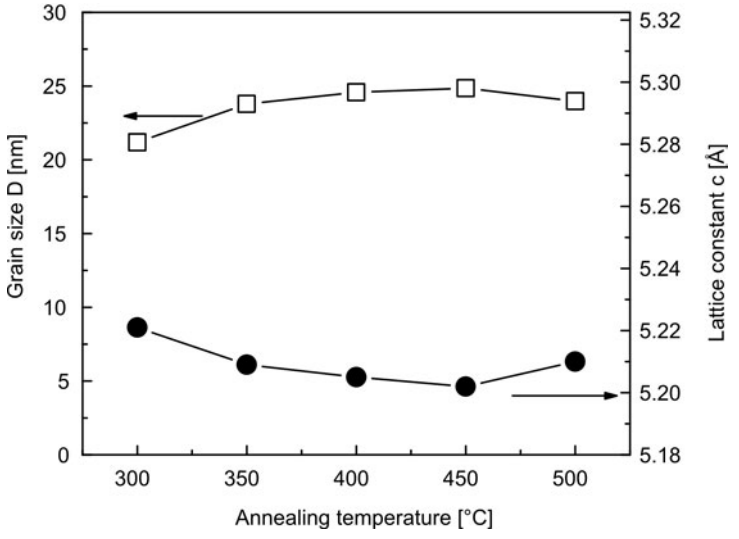

Fig. 3. Effect of annealing temperature on grain size and lattice constant of ZnO/Sc (Sc – 0.5 wt. %) thin films

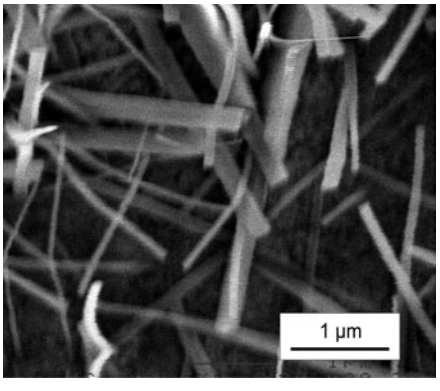

Fig. 4. SEM image of ZnO/Sc (Sc – 0.5 wt. %) thin films annealed at 400 °C in air for 1 h

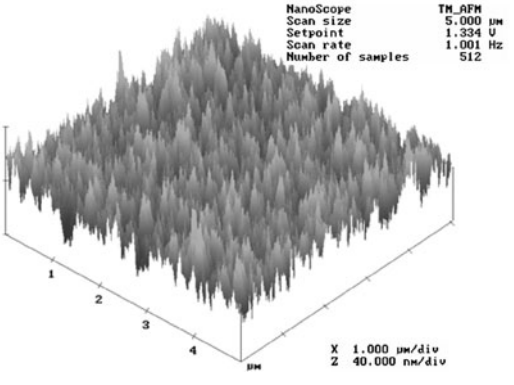

Fig. 5. AFM Image of ZnO/Sc (Sc – 0.5 wt. %) thin films annealed at 400 °C in air for 1 h

It is observed that grain size improves with the increase in annealing temperature indicating an improvement in crystallinity [22]. However, a further increase in annealing temperature above 450 °C results in a decrease in intensity and an increase in FWHM which indicate a decrease in *c* axis orientation and the grain size. It is impor-

tant to note that the value of *c* for the as deposited ZnO/Sc films is large in comparison with the unstressed bulk value of 5.2066 Å. Correspondingly, the value of *c* decreases with an increase in annealing temperature. This indicates a reduction in the tensile stress with annealing [23], which may be due to a large coefficient of linear expansion of ZnO/Sc films in comparison with the glass substrate. Thus with the increase in annealing temperature, shrinkage of *c* along with the improvement in *c* axis orientation is seen. Matsuoka et al. [24] have observed a similar shrinkage of lattice constant in Al doped ZnO films with increase of the substrate temperature.

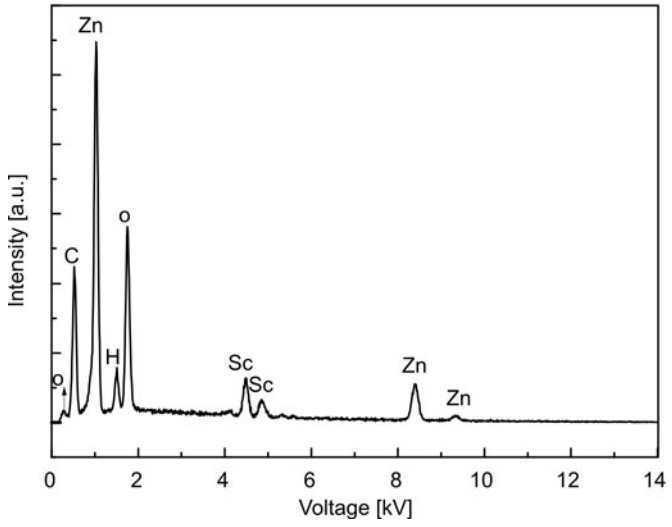

Fig. 6. Compositional analysis of ZnO/Sc (Sc – 1.5 wt. %) film annealed at 400 °C in air for 1 h

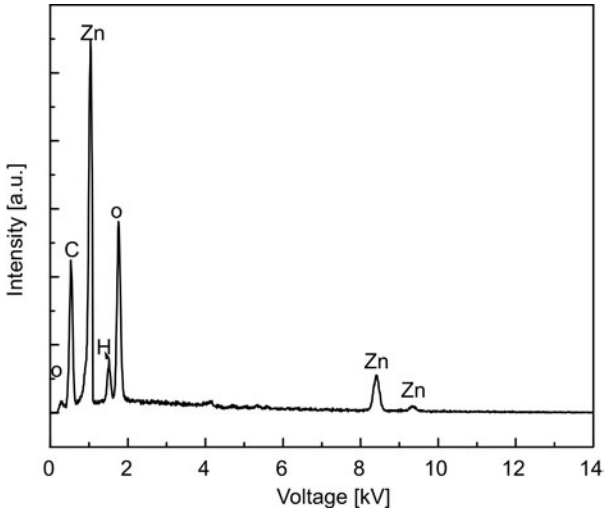

Fig. 7. Compositional analysis of ZnO film annealed at 400 °C in air for 1 h

Figures 4 and 5 show typical SEM and AFM images, respectively, of ZnO/Sc (Sc – 0.5 wt. %) annealed at the optimum temperature of 400 °C in air atmosphere for 1 h. The SEM micrograph of the film revealed the formation of nanorods. The AFM image exhibits a uniformly distributed needle type structure. The average surface roughness of the film ZnO/Sc (Sc – 0.5 wt. %) is found to be 4.81 nm.

Compositional analysis of ZnO/Sc (Sc – 1.5 wt. % and 0.0 wt. %) films, annealed at 400 °C for 1 h in air, is shown in Figs. 6 and 7, respectively. As seen from Fig. 6, the Sc doped film showed the presence of Zn, Sc and oxygen only. No other impurity was found within the EDAX detection limit. The composition (the atomic ratio of Sc to Zn) of deposited rare earth-doped ZnO films is found to be approximately equal to that in the solution. The compositional analysis of undoped (ZnO film (Fig. 7) reveals the presence of Zn and oxygen only.

3.2. Transmittance and bandgap

Transmittance spectra were recorded in the 300–800 nm range to study the influence of annealing temperature and the effect of Sc concentration on the optical properties of ZnO/Sc films. As shown in Figs. 8 and 9, all the films deposited on glass substrate exhibited high optical transparency throughout the entire visible range.

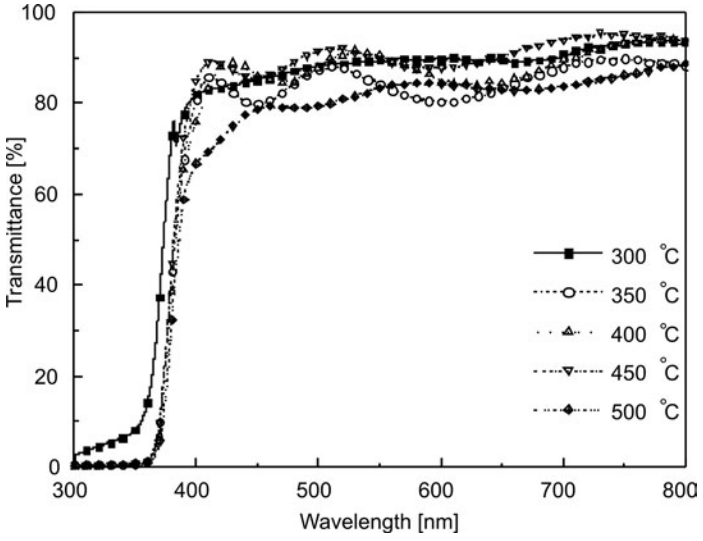

Fig. 8. Transmittance (*T*, %) in function of annealing temperature of ZnO/Sc (Sc – 0.5 wt. %) thin films

As shown in Fig. 8, all samples showed interference fringe patterns in the visible region of transmission spectra with an average transmittance *T* not lower than 89% indicating good optical quality of the deposited films with low scattering or absorption losses. The higher optical transmittance in annealed films may be due to the increased

crystal size, which reduces the inter-grain shadowing. It is observed that T increases with increase in annealing temperature up to 400 °C but with further increase in temperature it decreases. The initial increase in T is due to the improvement in the crystallinity and microstructure with an increase in annealing temperature (Fig. 8). The decrease in T with further increase in annealing temperature is due to the degradation of crystallinity of ZnO/Sc films as indicated by our XRD analysis. The transmittance is maximum for pure ZnO film and decreases with an increase in Sc concentration. The decrease in optical transmission is generally associated with the loss of light due to oxygen vacancies and scattering at grain boundaries [25]. Since all the films are deposited under similar oxygen environments and processing conditions, the loss of transmittance due to oxygen defects is assumed to be the same for all samples. The increase in scattering centres due to increased grain boundaries with an increase in Sc dopant content may be responsible for the loss of transmittance. A characteristic difference in the absorption edge has been observed with Sc incorporation in ZnO. The sharp absorption edge observed for ZnO (Sc – 0.0 wt. %) sample at 375 nm was found to shift towards blue with an increase in Sc concentration.

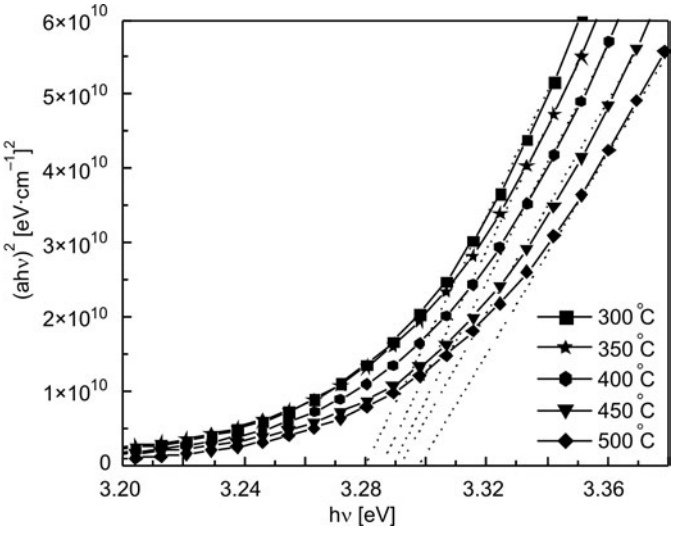

Fig. 9. Tauc's plots of ZnO/Sc (Sc – 0.5 wt. %) thin films in function of annealing temperature

The optical absorption coefficient α of a direct band gap semiconductor near the band edge, for photon energy $h\nu$ greater than the band gap energy E_g of the semiconductor, is given by [26]

$$\alpha h\nu = A\left(h\nu - E_g\right)^{1/2} \tag{2}$$

where h is Planck's constant and v is the frequency of the incident photon.

The value of α is determined from the transmittance spectra. The plot of $(\alpha h\nu)^2$ in function of photon energy $h\nu$ (Tauc's plot) for ZnO/Sc (Sc – 0.5 wt. %) films annealed at various temperatures is shown in Fig. 9 while the absorption coefficient in function of the dopant concentration for the films annealed at 400 °C is shown in Fig. 10. E_g was obtained by extrapolating the linear part of the Tauc's plot to intercept the energy axis at $((\alpha h\nu)^2 = 0$.

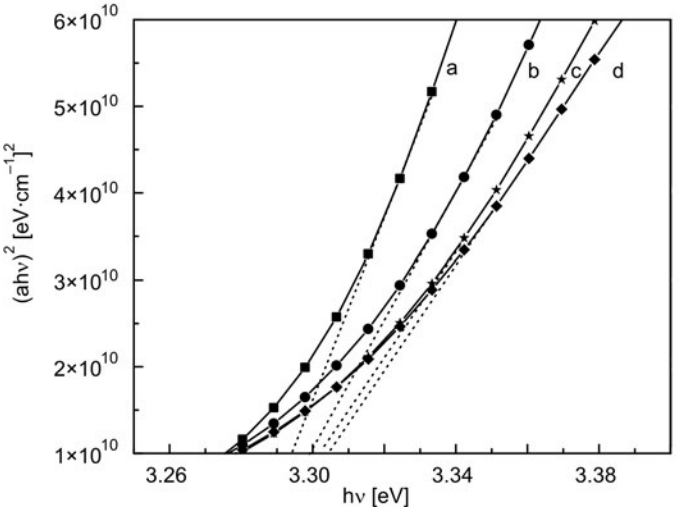

Fig. 10. Tauc's plots of ZnO/Sc films annealed at 400 °C in air:
a – 0.0 wt. %, b – 0.5 wt. %, c – 1.0 wt. % and d – 1.5 wt. %

E_g was found to increase continuously from 3.28 to 3.30 eV with an increase in annealing temperature for ZnO/Sc (Sc – 0.5 wt. %) films. The increase in E_g may be attributed to the increase in the grain size and the stress relieving process in ZnO/Sc films. An increase in E_g has also been observed with Sc doping. It increases from 3.29 to 3.31 eV as the dopant concentration is increased from 0 to 1.0 wt. %.

3.3. Electrical properties

The influence of the annealing temperature from 300 °C to 500 °C on resistivity ρ, carrier concentration n and the Hall mobility μ_H of ZnO/Sc (Sc – 0.5 wt. %) films is shown in Fig. 11. The resistivity is found to decrease with increasing annealing temperature up to 400 °C and thereafter it increases with annealing temperature. The observed decrease in resistivity can be interpreted in terms of enhanced crystallite structure of the films. A minimum resistivity of 3.52×10^{-4} ohm·cm, as well as a highest mobility value of 35.3 $cm^2/(V\cdot s)$ and carrier concentration of 3.27×10^{20} cm^{-3} annealed at 400 °C is obtained for ZnO/Sc (Sc – 0.5 wt. %).

The increased resistivity at higher annealing temperature might be due to the formation of oxygen vacancies by oxygen annihilation from the ZnO [27]. Further, the increase in resistivity of the films at temperatures above 400 °C may be due to the structural degradation as well. The mobility is found to increase with the annealing temperature up to 400 °C, which is due to the improvement of crystalline structure of the films as observed by the XRD analysis. It is also observed that *n* increases with the increase in annealing temperature.

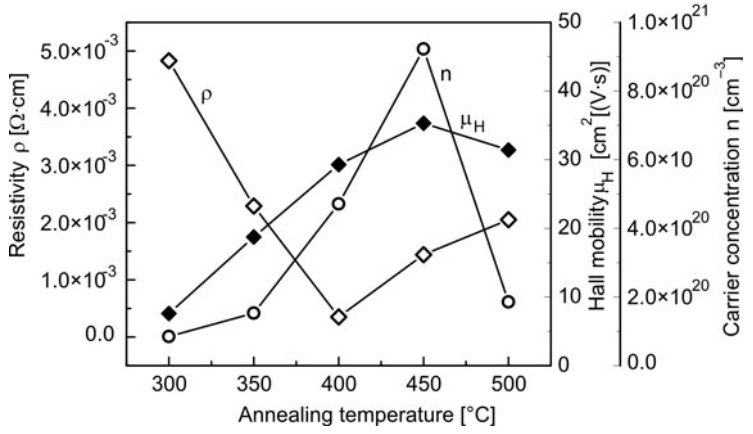

Fig. 11. Temperature dependences of σ, n and μ in ZnO/Sc (Sc – 0.5 wt. %) thin films annealed in air

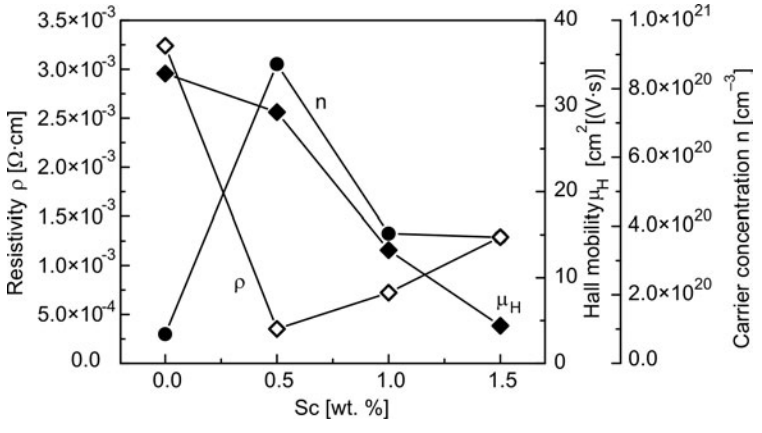

Fig. 12. Dependences of σ, n and μ of ZnO/Sc thin films annealed at 400 °C in air on Sc concentration

The variations of ρ, n and μ_H of ZnO/Sc films in function of Sc concentration are shown in Fig. 12. It is also seen from Fig. 9 that ρ decreases sharply as the Sc concentration is increased up to 0.5 wt. %, correspondingly n is found to increase while there is a gradual reduction in μ_H. The increase in n confirms that Sc acts as an effective

donor in ZnO films. The increased carrier concentration is due to the contribution from doping ion Sc^{3+}on the substitution site of Zn^{2+} ions and/or from interstitial zinc atoms. However, after 0.5 wt. % of Sc doping, the carrier concentration tends to saturate and resistivity starts increasing. This is probably because of the limited solubility of Sc in ZnO/Sc. Tang and Cameron [28] have shown a similar effect in ZnO/Al films. The impurity content dependence of mobility is not related to the crystallinity estimated by the intensity and full width at half-maximum of the (002) diffraction peak; the crystallinity did not change with increasing impurity content. The decrease in mobility at higher doping may be due to scattering from grain boundaries and defects produced by doping, which is also supported by the XRD analysis [29].

3.4. Variation of bandgap

The variation of E_g with annealing temperature and dopant concentration has been analyzed in terms of band gap widening ΔE^{BM} due to the Burstein–Moss effect and bandgap narrowing ΔE^{EX} due to many body effects. In the model of Burstein and Moss, the absorption edge shift in an n-type semiconductor is shown to be dependent on carrier concentration and is given as [30]

$$\Delta E^{BM} = \left(3\pi^2 N\right)^{2/3} \frac{\hbar^2}{2m_{vc}^*} \tag{3}$$

where m_{vc}^* is a reduced effective mass given by

$$\frac{1}{m_{vc}^*} = \frac{1}{m_c^*} + \frac{1}{m_v^*} \tag{4}$$

where m_c^* is the effective mass in the conduction band, and m_v^* is the effective mass in the valence band. The calculated value is shown in Fig. 13, which corresponds to $m_c^* = 0.38m_0$ and $m_v^* = 1.8m_0$ [31]. At higher concentrations above the Mott critical density, such as in heavily doped and highly excited semiconductors, electronic states of the crystal are modified because of carrier–carrier interaction and carrier–impurity interaction. That is, many body effects such as exchange and Coulomb interactions lead to a narrowing of the band gap [32, 33]. According to Wolf [34], in heavily n-type doped semiconductors the conduction band is shifted downwards by a quantity equal to ΔE^{EX}.

$$\Delta E^{EX} = -\frac{e}{2\pi\varepsilon_0\varepsilon_r}\left(\frac{3N}{\pi}\right)^{1/3} \tag{5}$$

where $\varepsilon_r = 8.5$ [35] is the relative electric permittivity. This band gap shrinkage represents the exchange energy due to the electron–electron interaction. The expected absorption edge shift is therefore calculated as $\Delta E = \Delta E^{BM} - \Delta E^{EX}$.

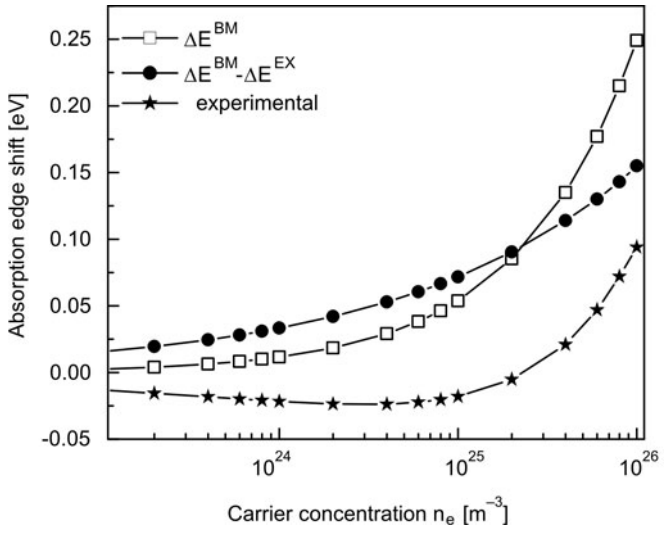

Fig. 13. Absorption edge shift ΔE in function of the carrier concentration

The theoretical and experimentalvalues of E_g in function of n are shown in Fig. 13. It is evident from the figure that the observed variation of E_g with n could not be explained by using the above mentioned two effects.

4. Conclusions

High quality c axis orientation Sc doped ZnO films have been deposited via the sol-gel route. The resistivity as low as 3.52×10^{-4} ohm·cm and transmittance 91% in the visible range have been achieved in these films. Such highly conducting and transparent films could be used as solar cell windows similar to ITO films.

Acknowledgement

One of the authors, Ruchika Sharma, gratefully acknowledges the financial assistance of AIEJ, Japan, during her visit to Toyohashi University of Technology, Toyohashi, Japan. The financial support of DRDO, Govt. of India, under the project No. ERIP/ER/0103325/M01 is gratefully acknowledged.

References

[1] RONOVICH J.A., GOLMOYA D., BUBE R.H., J. Appl. Phys., 51 (1980), 4260.
[2] SRIKANT V., CLARKE D.R., J. Appl. Phys., 81 (1997), 6357.
[3] MINAMI T., NATO H., TAKAT A.S., Thin Solid Films, 124 (1985), 43.
[4] CHOPRA K.L., MAJOR S., PANDYA D.K., Thin Solid Films, 102 (1983), 1.
[5] WEIBENRIEDER K.S., MULLER J., Thin Solid Films, 300 (1997), 30.
[6] SEOK-SOON K., JUN-HO Y., YUNG-EUN S., Solar Energy Mat. Solar Cells, 79 (2003), 495.
[7] MAJOR S., KUMAR S., BHATNAGAR M., CHOPRA K.L., Appl. Phys. Lett., 49 (1986), 394.

[8] HU J., GORDON R.G., J. Appl. Phys., 72 (1992), 5381.
[9] BIXIA L., ZHUXI F., YUNBO J., Appl. Phys. Lett., 79 (2001), 943.
[10] MALIK A., SECO A., NUNES P., VIEIRA M., MRS Displays Technologies, 471 (San Francisco, USA, 2–8 April 1997).
[11] TANG W., CAMERON D.C., Thin Solid Films, 238 (1994), 83.
[12] CHANG J.F., LIN W.C., HON M.H., Appl. Surf. Sci., 183 (2001), 18.
[13] MINAMI T., YAMAMOTO T., MIYATA T., Thin Solid Films, 366 (2000), 63.
[14] NUNES P., FORTUNADEO E., MARTINS R., Thin Solid Films, 383 (2001), 277.
[15] ROTH A.P., WILLIAMS D.F., J. Appl. Phys., 52 (1981), 6685.
[16] LU Y.F., NI H.Q., MAI Z.H., REN Z.M., J. Appl. Phys., 88 (2000), 498.
[17] JIANG X., WONG F.L., FUNG M.K., LEE S.T., Appl. Phys. Lett., 83 (2003), 1875.
[18] JIMÉNEZ-GONZÁLEZ A.E., SOTO URUETA J.A., SUÁREZ-PARRA R., J. Crystal Growth, 192 (1998), 430.
[19] CHATELON J.P., TERRIER C., BERNSTEIN E., BERJOAN R., ROGER J.A., Thin Solid Films, 247 (1994), 162.
[20] VANDER P., Philips Res. Repts., 13 (1958), 1.
[21] AZAROFF L.V., *Elements of X-ray Crystallography*, McGraw Hill, New York, 1968.
[22] MINAMI T., SATO H., TAKAT A.S., OGAWA N., MOURI T., Jpn. J. Appl. Phys., 31 (1992) , L 1106.
[23] TAKADA S., J. Appl. Sci., 73 (1993), 4739.
[24] MATSUOKA M., HOSHI Y., NAOE M., J. Appl. Phys., 63 (1998), 2098.
[25] SARKAR A., GHOSH S., PAL A.K., Thin Solid Films, 204 (1991), 255.
[26] SZEYRBOWSKI J., DIETRICH A., HOFFMANN H., Phys. Stat. Sol. a,78 (1983), 243.
[27] MINAMI T., YAMAMOTO T., MIYATA T., Thin Solid Films, 64 (2000), 63.
[28] TANG W., CAMERON D.C., Thin Solid Films, 238 (1994), 83.
[29] MINAMI T., NANTO H., TAKATA S., Jpn. J. Appl. Phys., 71 (1992), 880.
[30] MOSS T.S., Proc. Phy. Soc. London., B 67 (1954), 775.
[31] DIETZ R.E., HOPFIELD J.J., THOMOS G.D., J. Appl. Phys., 32 (1961), 2282.
[32] AUVERGNE D., CAMASSEL J., MATHIEU H., Phys. Rev. B, 11 (1975), 2251.
[33] MINAMI T., YAMANISHI M., KAWAMURA T., KUBO U., Jpn. J. Appl. Phys., 15 (1976), 1117.
[34] WOLF P.A., Phys. Rev., 126 (1962), 405.
[35] MAJOR S., BANERJEE A., CHOPRA K.L., Thin Solid Films, 125 (1985), 179.

Received 12 March 2008
Revised 4 September 2008

Materials Science-Poland, *Vol. 27*, *No. 1*, *2009*

A new composite, Co–Sn metal oxide anode for lithium ion batteries

F. HUANG[1*], X.-Z. LU[1, 2], Y.-F. ZHANG[1], X.-Y. LUO[1], C. YU[1], R. WU[1]

[1]College of Materials Science and Metallurgical Engineering,
Wuhan University of Science and Technology, Wuhan, Hubei, 430081, P.R. China

[2]Wuhan Iron and Steel Mechanic Making Co., Ltd, Wuhan, Hubei, 430083, P.R. China

The structural and morphological evolution of cobalt–tin (Co–Sn) metal composite oxides, synthesized by the decomposition of $CoSn(OH)_6$ precursor at various temperatures, were investigated by X-ray diffraction (XRD) and high-resolution transmission electron microscopy (HRTEM). The precursor was also studied by thermal analysis (TG/DTA). The electrochemical performance of nanosized Co–Sn composite metal oxides was investigated to evaluate their suitability for use as anode materials for Li ion batteries. The results revealed that the samples heat-treated at low temperatures consisted of amorphous $CoSnO_3$, and the samples heat-treated at high temperatures comprised crystalline Co_2SnO_4 and SnO_2. The charge capacity and cyclability were sensitive to the structure and composition of the electrode active materials. The samples heat-treated in the phase transition temperature range exhibited relatively worse electrochemical properties.

Key words: Co–Sn composite oxides; anode materials; lithium ion batteries; liquid precipitating method

1. Introduction

Graphite based anode materials are widely used in commercial lithium ion batteries, owing to their excellent charge and discharge cycling behaviour. However, the theoretical Li storage capacity of graphite is limited to 372 mAh/g [1]. Recently, there has been considerable interest to develop alternative anode materials for lithium ion batteries. Tin oxides have been considered the most promising anode materials for lithium ion batteries, due to their high volumetric and gravimetric capacities [2–4]. According to Courtney and Dahn [5], the reaction of tin oxides with lithium can be described in two steps; for SnO_2, they are:

$$SnO_2 + 4Li^+ + 4e^- \rightarrow 2Li_2O + Sn \quad (1)$$

*Corresponding author, e-mail: hgxlu@163.com

$$Sn + xLi^+ + xe^- \rightarrow Li_xSn \quad (0<x<4.4) \tag{2}$$

Initially, tin oxides are reduced to form small clusters of tin metal, dispersed in a Li_2O framework. Li^+ ions are then reversibly inserted in tin to form Li/Sn alloys. Alloying of Li with tin causes a large volume expansion, leading to cracking of the electrode, and a rapid loss of capacity [5]. The oxides permit the use of Li_2O as a matrix, constraining the volume expansion and contraction [6] during cycling. The cycling performance is enhanced if the active material is finely dispersed in the matrix [7]. Idota et al. [2] suggested a new class of tin-based amorphous composite oxide containing SnO as the active centre for lithium insertion and other glass forming elements such as B, P, Al as an oxide network structure; during charge and discharge, the cyclability of the glass materials had been improved largely.

Recently, Irvine et al. [3, 8, 9] prepared Zn_2SnO_4, Mg_2SnO_4, Co_2SnO_4 and Mn_2SnO_4 spinel metal composite oxides by milling and solid-state reaction at high temperatures. Huang and Yuan [10–13] synthesized a series of amorphous $MgSnO_3$, $CoSnO_3$, $MnSnO_3$ and $ZnSnO_3$ composite metal oxides by the liquid precipitation method and studied their electrochemical properties, in order to try and assess their potential for use as anode materials for lithium ion batteries. In this paper, we report the structural/morphological characteristics and lithium insertion properties of Co–Sn composite metal oxides synthesized from the precursor $CoSn(OH)_6$ by heat-treatment at various temperatures.

2. Experimental

Analytical chemical reagents of Na_2SnO_3 and $CoSO_4$ were used. Solutions of Na_2SnO_3 and $CoSO_4$ in 1:1 molar ratio were mixed under continuous stirring. The pink precipitates were washed with distilled water to remove Na^+ and SO_4^{2-} ions, and then dried in an oven at 120 °C to obtain the pink $CoSn(OH)_6$ precursor. The chemical stoichiometric equation can be expressed as:

$$CoSO_4 + Na_2SnO_3 + 3\ H_2O \rightarrow CoSn(OH)_6 + Na_2SO_4 \tag{3}$$

The precursor powder was heated subsequently at various temperatures for 4 h in air to form Co–Sn metal composite oxide.

Thermogravimetric and differential thermal analyses (TG/DTA) were carried out using a Shimadzu DT-40 thermal analyzer at the heating rate of 10 °C/min in air. XRD was measured on a Shimadzu XRD-6000 diffractometer (Cu-K_α radiation) with the scanning rate of 4°/min, to investigate the phase evolution of $CoSn(OH)_6$ precursor upon heat-treatment at various temperatures. Microstructure (JEM-2100F) of samples was studied by the high-resolution transmission electron microscopy (HRTEM).

The electrochemical cells consisted of a working electrode made of a nanosized Co–Sn metal composite oxides and a counter electrode made of lithium foil. The cells

were assembled in an Ar-filled glove box with both moisture and oxygen concentrations below 5 ppm. The working electrodes were prepared by pressing a film composed of Co–Sn composite metal oxide powders, acetylene black and polytetrafluoroethylene (PTFE) binder (weight ratio of 85:10:5) onto a stainless steel current collector. The electrolyte was 1 M $LiClO_4$ in a mixture of ethylcarbonate (EC) and dimethyl carbonate (DMC) (1:1 in volume ratio), Cellgard 2400 polyethylene was used as the separator. The cells were discharged and charged between 0–2 V versus Li^+/Li at the constant current of 50 mA/g using the Arbin BT 2000 testing system.

3. Results and discussion

3.1. Thermal analysis of the $CoSn(OH)_6$ precursor

The transformation of $CoSn(OH)_6$ precursor during heat-treatment was revealed by DTA and TG data. Figure 1 shows that a sharp endothermic peak occurred on the DTA curve at the temperature of about 300 °C.

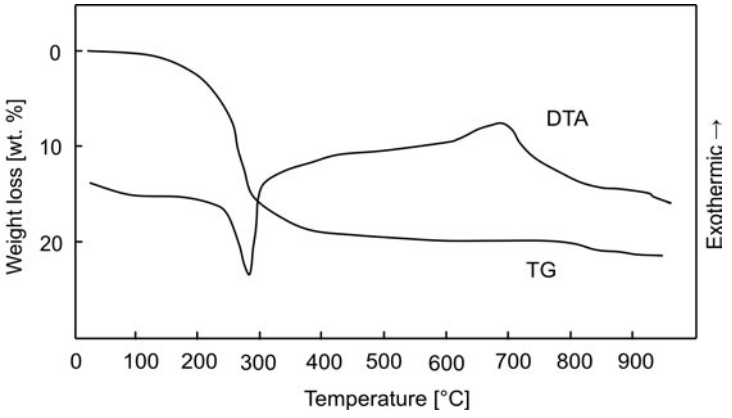

Fig. 1. DTA and TG curves of the $CoSn(OH)_6$ precursor

It also can be seen from the TG curve that the weight loss of the precursor was about 19% in this temperature range, which was due to the reaction:

$$CoSn(OH)_6 \rightarrow CoSnO_3 + 3H_2O \tag{4}$$

The weight loss calculated according to Eq. (4) was 19.3%, which is consistent with the experimental result. A small broad exothermic peak was observed on the DTA curve at the temperature of about 660 °C , but no weight loss was observed from the TG curve at temperatures above 350 °C. This indicates that the phase transition from the amorphous to the crystalline state occurred at this temperature.

3.2. Structural and phase change during heat-treatment

Figure 2 shows the XRD patterns of the $CoSn(OH)_6$ precursor (Fig. 2a) and the final products heat-treated at various temperatures (Fig. 2b). From Figure 2a, it can be seen that there is no evidence of any other phases, as all the diffraction peaks can be indexed for the tetragonal phase $CoSn(OH)_6$ (JCPDS card NO. 20-1455).

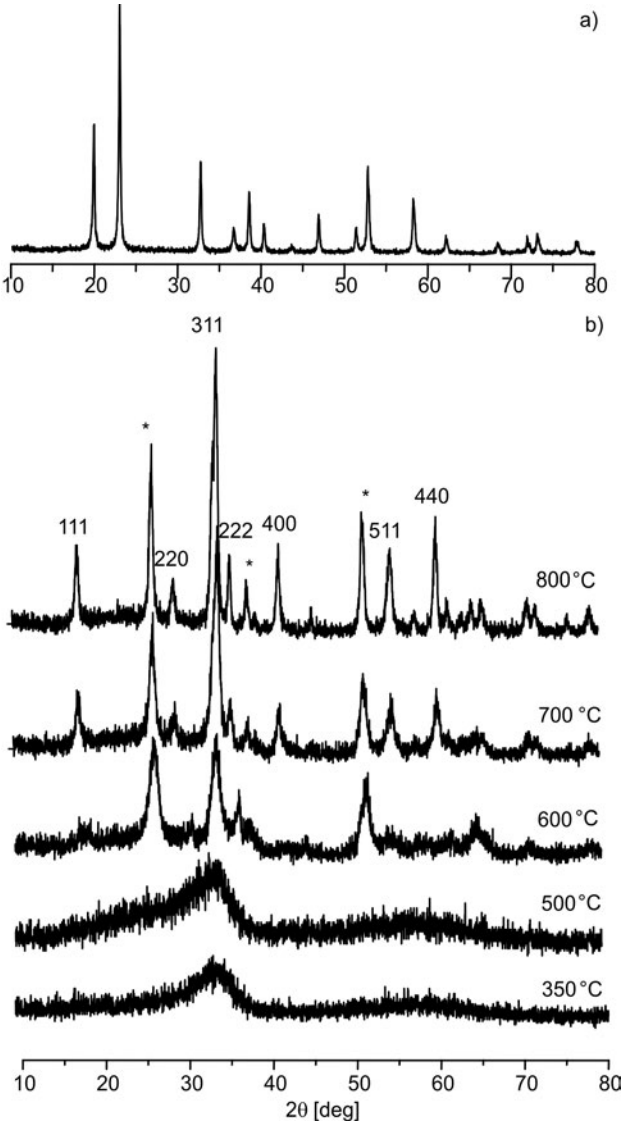

Fig. 2. The XRD patterns of the precursor $CoSn(OH)_6$ (a), and of the final products heat-treated at various temperatures (b). SnO_2 peaks are marked with asterisks

For the samples heat-treated at 350 °C and 500 °C, only one broad peak, related to amorphous $CoSnO_3$, can be observed, and there is no diffraction line assigned to any crystalline phases. This indicates that amorphous or amorphous-like $CoSnO_3$ formed at these temperatures. The XRD patterns shown in Fig. 2b changed sharply after heat-treatment at 600 °C; three diffraction peaks of crystalline SnO_2 were observed, indicating that a phase transition from an amorphous state to a crystalline state occurred during the heat treatment process. However, the XRD peaks of the samples heat-treated at 700 °C were completely different from those of the samples heat-treated at lower temperatures with the appearance of the characteristic peaks of spinel Co_2SnO_4. It suggests that the amorphous $CoSnO_3$ was decomposed spinel Co_2SnO_4 and tetragonal phase SnO_2 when the samples were heated to 700 °C, which is consistent with the results of TG/DTA measurements. In addition, upon further increase in the heat-treatment temperature to 800 °C, the diffraction peaks become stronger and sharper, indicating an increase in the amount of the crystalline phases.

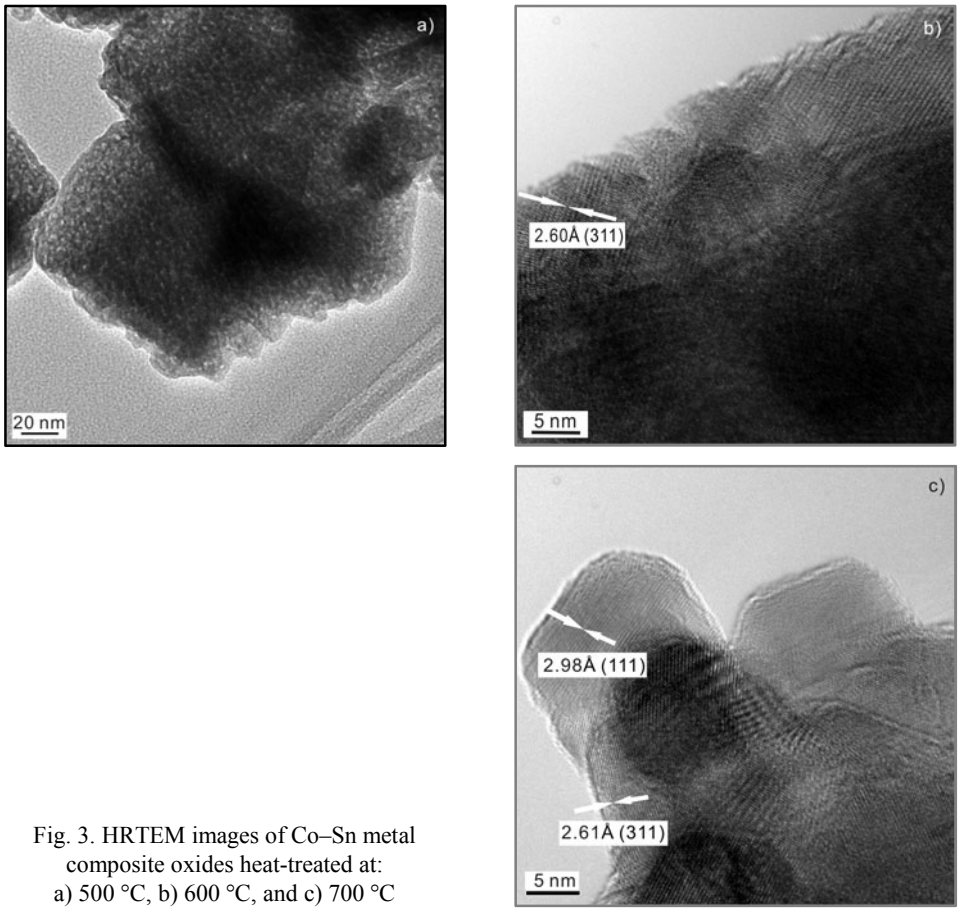

Fig. 3. HRTEM images of Co–Sn metal composite oxides heat-treated at: a) 500 °C, b) 600 °C, and c) 700 °C

Considering all these observations, a three-step process during $CoSn(OH)_6$ heat treatment at various temperatures may be proposed:

$$CoSn(OH)_6\,(\text{crystalline}) \rightarrow CoSnO_3\,(\text{amorphous}) + 3H_2O \quad (5)$$

$$2CoSnO_3\,(\text{amorphous}) \rightarrow Co_2SnO_4\,(\text{amorphous}) + SnO_2\,(\text{crystalline}) \quad (6)$$

$$Co_2SnO_4\,(\text{amorphous}) \rightarrow Co_2SnO_4\,(\text{crystalline}) \quad (7)$$

These results are consistent with the HRTEM images (Fig. 3a–c) showing the structure of nanosized Co–Sn composite oxides samples. The samples after heat-treatment at 500 °C are amorphous $CoSnO_3$, existing as cotton wadding agglomerates. When the heat treatment temperature was increased to 600 °C, the amorphous $CoSnO_3$ was transformed crystalline SnO_2 with the lattice parameter of tin oxide ($d_{hkl}\{311\} = 2.61$ Å) and amorphous Co_2SnO_4 as indicated as some anomalous arranged crystal lattice in the Fig. 3b. 700 °C, more crystalline particles were separated out from the cotton wadding agglomerates with some of the particles showing the lattice parameter of tin oxide ($d_{hkl}\{311\} = 2.61$ Å) and others the lattice parameter of spinel Co_2SnO_4 ($d_{hkl}\{111\} = 2.98$Å). Therefore, the structure and crystal phase of the Co–Sn composite metal oxides are strongly dependent on the heat-treatment temperature of the $CoSn(OH)_6$ precursor.

3.3. Electrochemical performance

First discharge curves of the Li /Co–Sn composite metal oxides cells prepared from the products of $CoSn(OH)_6$ heat-treated at various temperatures are shown in Fig. 4.

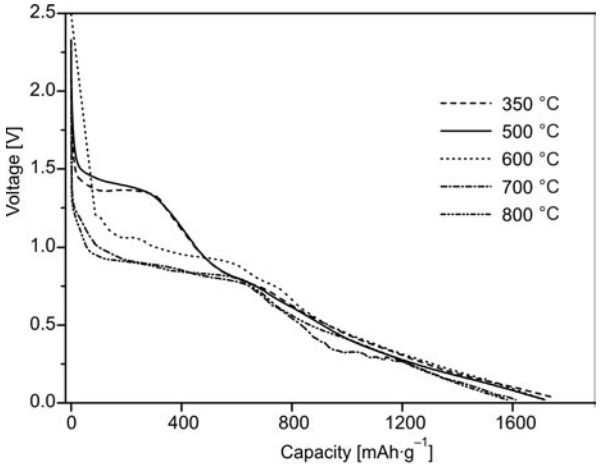

Fig. 4. The first discharge curves of Co–Sn composite oxides heat-treated at various temperatures

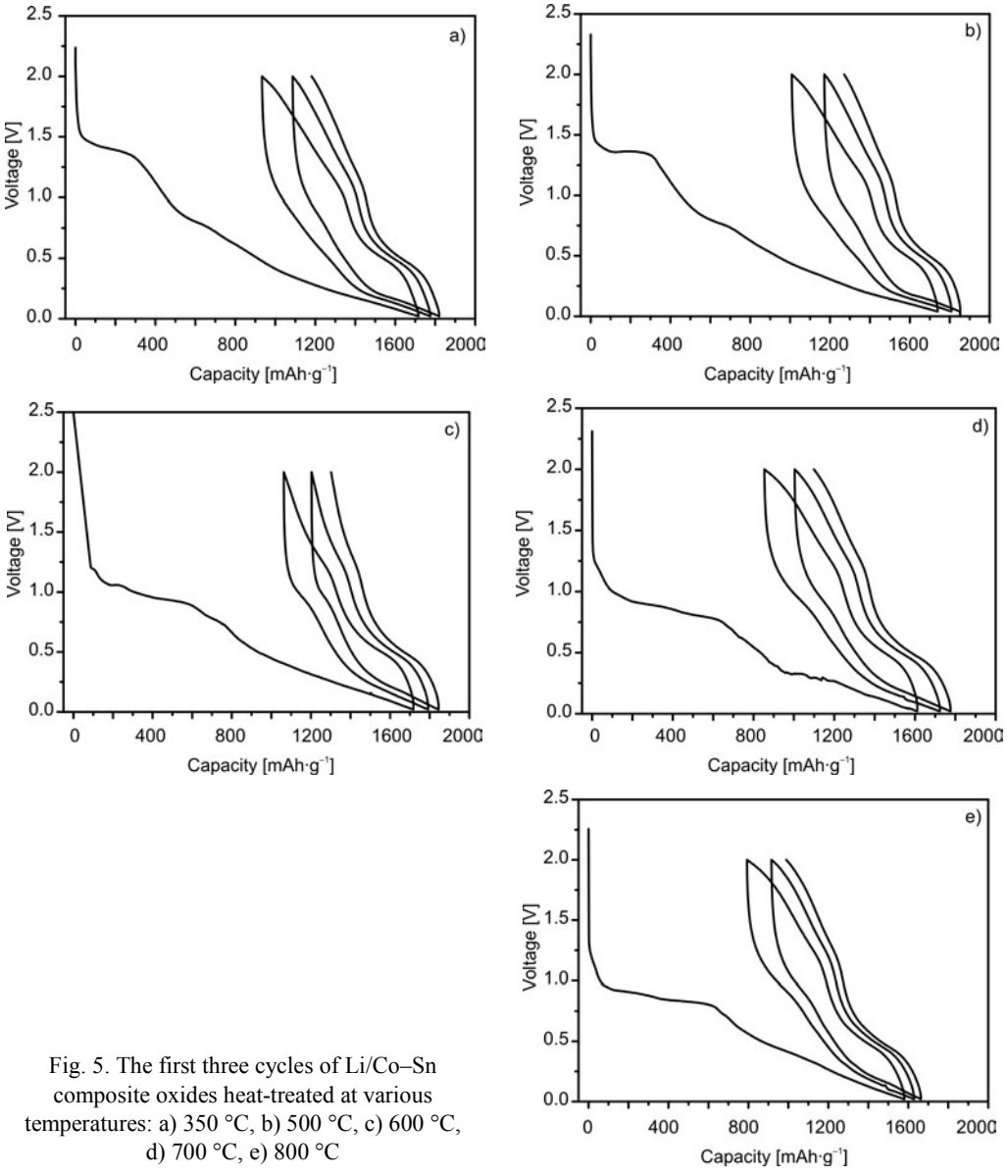

Fig. 5. The first three cycles of Li/Co–Sn composite oxides heat-treated at various temperatures: a) 350 °C, b) 500 °C, c) 600 °C, d) 700 °C, e) 800 °C

Two voltage plateaus at about 1.35 V and 0.8 V, respectively, can be observed in the first discharge curves for the samples heat-treated at 350 °C and 500 °C. With the increase in heat-treatment temperature, only one voltage plateau can be observed, at about 0.95 V, for the samples heat-treated at 600 °C and 700 °C, and two voltage plateaus, at about 0.95 V and 0.4 V, respectively, for the sample heat-treated at 800 °C. Therefore, this suggests that the formation and voltage of the plateau is closely related to the heat-treatment temperature. Figure 5 shows the voltage profiles of the Li/Co–Sn

composite metal oxide cells with $CoSn(OH)_6$ heat-treated at various temperatures for the first three cycles between 0 and 2.0V. For all the samples, the first discharging curves are different from the subsequent discharging curves. After the first cycle, the plateau at about 1.35 V and 0.8 V for the samples heat-treated at 350 °C and 500 °C and the plateau at about 0.9 V for the samples heat-treated at 600 °C, 700 °C and 800 °C all disappeared in the subsequent discharge curves, And the disappearance of the plateau should be responsible for the irreversible capacity [4, 5, 11, 12]. One voltage plateau located at about 0.5 V can be observed clearly in the charging curves for all the samples.

Table 1. Electrochemical properties of the nanosized Co–Sn composite metal oxides formed by heat treatment of $CoSn(OH)_6$ precursor at various temperatures

Property	Heat-treating temperature [°C]				
	350	500	600	700	800
The first discharge capacity [mAh/g]	1739	1716	1718	1612	1581
The first charge capacity [mAh/g]	782	731	655	758	788
Capacity loss in the first cycle [%]	55.0	57.4	61.9	53.0	50.1
$R_{20/1}$ [%]	45.4	39.4	32.7	48.3	50.5

Table 1 shows the relationship between the electrochemical properties of all Co–Sn composite metal oxides and the heat treatment temperature of $CoSn(OH)_6$. It can be seen that as the heat treatment temperature increases, the first discharge specific capacity of Co–Sn composite oxides anodes decreases. However, the lowest initial charge specific capacity obtained was as high as 655 mAh/g for the sample heat-treated at 600 °C. This is much higher than the theoretical capacity of graphite (372 mAh/g). However, for the Co–Sn composite metal oxide anodes, the problem associated with other tin oxide based systems exists, i.e. about half of the initial lithium capacity is lost due to irreversible changes in the oxide matrix. To help quantify the cycling stability of various samples, a parameter called the capacity retention index $R_{20/1}$is defined. This parameter is the capacity in the 20th charge cycle divided by the capacity in the first charge cycle. Cells that cycle without capacity loss, therefore, will have $R_{20/1}$ equal to unity [14]. As can be seen in Table 1, the samples heat-treated at the phase transition temperature (600 °C) exhibited poorer cycling performance. Taking into account all the above results, it is certain that the samples heat-treated at phase transition temperature range exhibit relatively worse electrochemical properties.

The differential capacity plots obtained at the first cycle for all Co–Sn composite metal oxide samples heat-treated at various temperatures are shown in Fig. 6. Two cathodic peaks at about 1.35 V and 0.8 V, respectively, can be observed for the samples heat-treated at 350 °C and 500 °C. Only one cathodic peak occurring at about 0.95 V can be observed for the samples heat-treated at higher temperatures (600 °C, 700 °C and 800 °C). Compared with the results published in Refs [3, 14], it

can be concluded that the change in cathodic peaks positions is due to the formation of the spinel Co_2SnO_4 phase seen from XRD patterns.

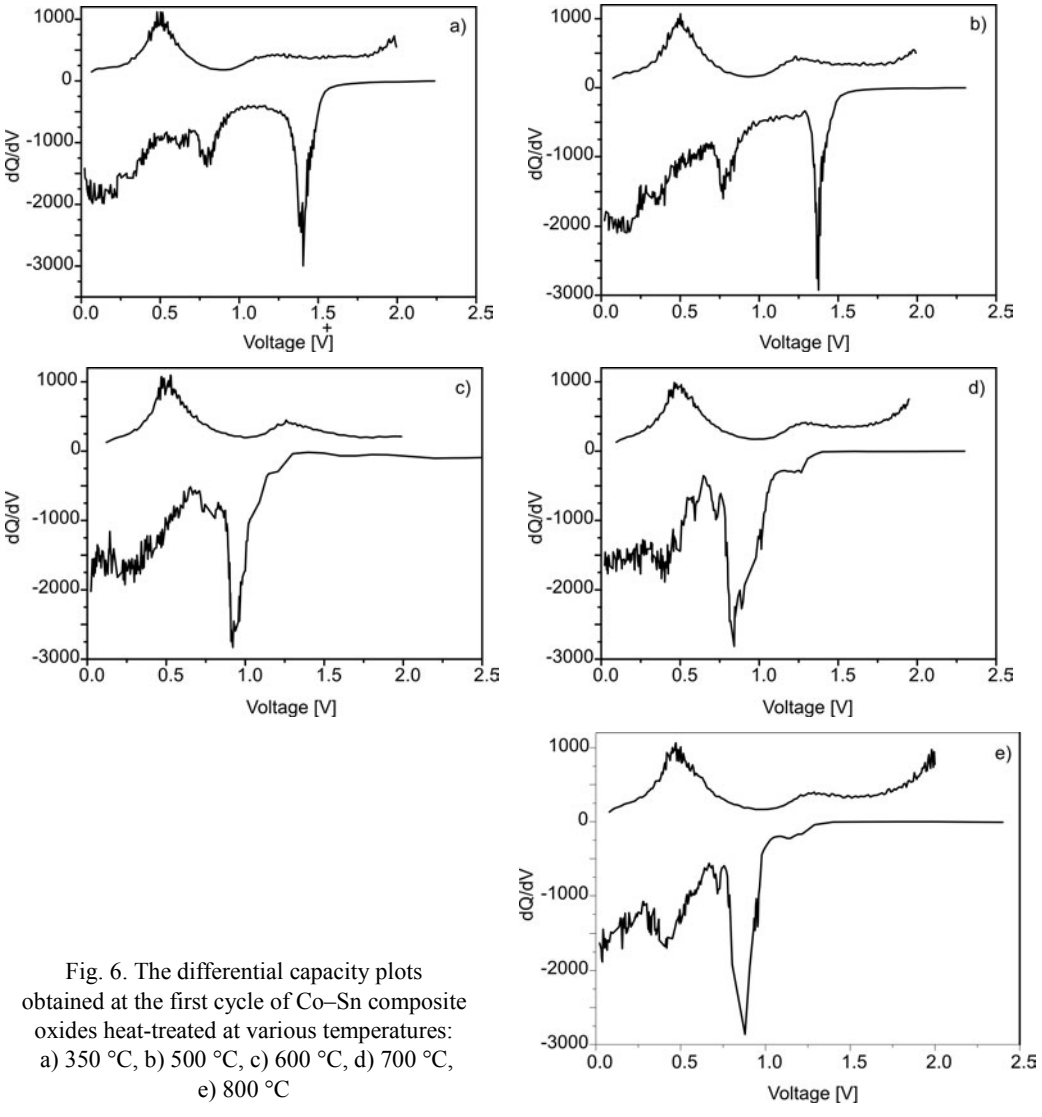

Fig. 6. The differential capacity plots obtained at the first cycle of Co–Sn composite oxides heat-treated at various temperatures: a) 350 °C, b) 500 °C, c) 600 °C, d) 700 °C, e) 800 °C

For all the samples, there are two anodic peaks located at about 0.5 V and 1.25 V, respectively, suggesting that, besides the alloying reaction involving Sn and Li, Co also participated in the electrode reaction [15]. All the anodic and cathodic peaks in differential capacity plots are consistent with the voltage plateaus in the charge and discharge curves. In addition, the shape of cathodic peaks for the 350 °C and 500 °C heat-treated samples is different from the shape of cathodic peaks for the samples heat-treated at higher temperatures. At the stage of phase transition from amorphous to

crystalline state or at the formation stage of the new phase, non uniform particle distribution results in worse electrochemical characteristics. Therefore it is believed that the phase transition is responsible for the worse electrochemical performance of the cells.

4. Conclusions

A series of nano-sized Co–Sn composite metal oxides have been prepared by heat treatment of $CoSn(OH)_6$ precursor at various temperatures. With the increase in temperature, $CoSn(OH)_6$ decomposes to form amorphous $CoSnO_3$ firstly, which is progressively converted to crystalline Co_2SnO_4 and SnO_2. The electrochemical characteristics of these composite oxides as anode materials for lithium ion batteries are closely related to their structure and composition. In the phase transition process, slight changes in temperature can greatly alter the electrochemical performance. The Co–Sn composite oxides show good possibilities as anode materials for lithium ion batteries. Future work should focus on the reaction processes involving lithium and anode materials, and on reducing the problem of irreversible changes.

Acknowledgement

This work was supported by the Natural Science Foundation of Hubei Province (No. 2007ABA320) and National 973 key research program.

References

[1] YING Z., JUN Y., WANG J.L, . Electrochim. Acta, 52 (2007), 5863.
[2] IDOTA Y., KUBOTA T., MATSUFUJI A., MACKAWA Y., Science, 276 (1997), 1395.
[3] BELLIARD F., CONNOR P.A., IRVINE J.T.S., Solid State Ionics, 135 (2000), 163.
[4] YUAN Z.Y., HUANG F., SUN J.X., ZHOU Y.H., Chem. Lett., 3 (2002), 408.
[5] COURTNEY L.A., DAHN J.R., J. Electrochem. Soc., 144 (1997), 2943.
[6] WINTER M., BESENHARD J.O., Electrochim. Acta, 45 (1999), 31.
[7] LI H., HUANG X.J., CHEN L.Q., Electrochem. Solid-State Lett., 1 (1998), 241
[8] BELLIARD F., IRVINE J.S., J. Power Sources, 97–98 (2001), 219.
[9] CONNOR P.A., BELLIARD F., IRVINE J.S., J. Power Sources, 97–98 (2001), 223.
[10] YUAN Z.Y., HUANG F., SUN J.X., ZHOU Y.H., Chem. Lett., 3 (2002), 408.
[11] HUANG F., YUN Z.Y., ZHAN H., YUAN Z.Y., SUN J.T., Mater. Lett., 57 (2003), 3341.
[12] HUANG F., YUAN Z.Y., ZHAN H., YUAN Z.Y., Mater. Chem. Phys., 83 (2004), 16.
[13] YUAN Z.Y., HUANG F., FENG C.Q., J. Mater. Sci. Lett., 22 (2003), 143.
[14] MAO O., TURNER, R.L., COURTNEY L.A., FREDERICKSEN B.D., DAHN J.R., Electrochem. Solid-State Lett., 2 (1999), 3.
[15] HUANG F., ZHAN H., YUAN Z.Y., Chinese J. Chem., 21 (2003), 1275.

Received 17 March 2008
Revised 7 August 2008

Materials Science-Poland, *Vol. 27*, *No. 1*, *2009*

Damage to TGS crystals caused by hydrostatic pressure

J. STANKOWSKI, S. WAPLAK*

Institute of Molecular Physics, Polish Academy of Sciences, ul. Smoluchowskiego17, 60-179 Poznań, Poland

In this letter we address a particular aspect of the finite size effect on ferroelectric instability: the polarization suppression under high hydrostatic pressure. We have shown that in TGS ($[NH_3^+CH_2COOH)_2(NH_3^+CH_2COO^-)SO_4^{2-}]$) single crystals under high pressure the critical temperature T_C of ferroelectric –paraelectric phase transition grows monotonically up to about 1.8 GPa. Above the critical pressure $p_C \geq 2.4$ GPa, the ferroelectricity disappears and the coefficient γ becomes negative for small ferroelectric regions which appear due to crystal break up.

Key words: *TGS crystal; ferroelectric instability; crystal braek-up*

1. Introduction

The investigation of finite-size effects on ferroelectricity is an interesting problem from both a scientific viewpoint as well as for practical reasons. The reduction in the physical sizes of ferroelectrics, from the macroscopic regimes down to mesoscopic ones results in a change in the polarization stability [1, 2]. Small ferroelectric particles exhibit dielectric properties different from those of bulk crystals, because the Coulomb long-range force plays a crucial role in them. For ferroelectrics of perovskite structure, it has been shown experimentally [3] that there is a critical crystal dimension D above which finite-size effects disappear. We have also shown that crystal damage under high hydrostatic pressure leads to finite-size dielectric properties.

2. Experimental and results

The effect of hydrostatic pressure was measured in a standard three-layer steel vessel [4, 5] up to the pressures of 3 GPa. Our data show that up to p = 1 GPa the critical temperature T_C increases linearly with pressure in accordance with the relation:

*Corresponding author, e-mail: waplak@ifmpan.poznan.pl

$$T_c(p) = T_c^0(1+\gamma p) \tag{1}$$

The change in the value of spontaneous polarization is equal to

$$\Delta P_S = P_S^P - P_S^{T_c}$$

where P_S^P and $P_S^{T_c}$ are the values of spontaneous polarization obtained at given p values and resulting from a change in ΔT_C (Fig. 1).

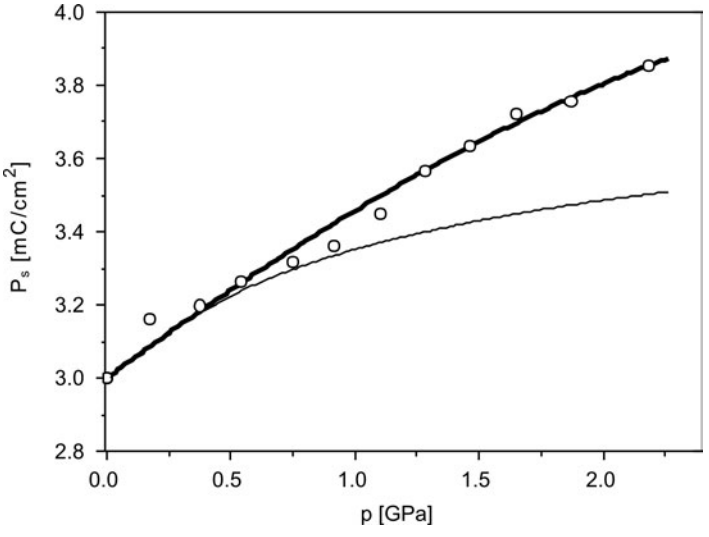

Fig. 1. Pressure dependence of the spontaneous polarization P_s (bold line) and P_s value only from T_C change (thin line)

The ΔP_S value results from additional tilting of glycine I (GI) from the *ac* crystal plane. This tilt comes from a slowing down of the rotation frequency of the NH_3 group in a double-well potential [6, 7].

Ferroelectricity appears when both potential minima are nonequivalent. High hydrostatic pressure leads to a rising potential barrier ΔU between the two minima. The monotonic growths of P_S and E_C values were recorded up to the pressure of 2.1 GPa. Below this p value all results were reproducible for a good sample quality. Above the pressure of 2.1 GPa, the samples started to be "milk-white" because pressure liquid penetrates and destroys single crystals having nanometric dimensions.. This mechanism explains recent results by Kobayashi et al. [5] for the sign change in the coefficient $\gamma = dT_C/dp$ at high pressure.

The dependence of T_C on pressure for a non-distorted crystal structure is shown in Fig. 2 and the shift of T_C can be described by linear and quadratic pressure dependences up to about 1.8 GPa (T_C in K, p in GPa)

$$T_C(p) = 322 + 22.5p - 1.73p^2 \tag{2}$$

The $\gamma(p)$ value in the range from 0 to 1 GPa is constant. For $p \geq 1$ GPa, $T_C(p)$ shows a nonlinear behaviour. Above 1.5 GPa, the observed plateau in the $T_C(p)$ profile is a signature of the damage process in TGS crystal due to the penetration of liquid into the crystal structure: for pressures up to 2.1 GPa this process is reversible.

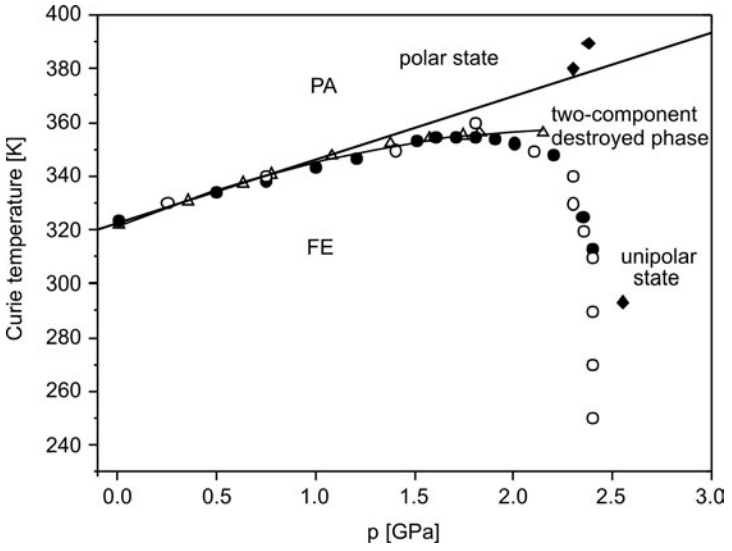

Fig. 2. The ferroelectric phase transition temperature T_C obtained under various pressure–temperature conditions: filled circles – p = const [5], open circles – T = const [5], triangles – T = const [4], diamonds – T = const > T_c^0 [5]

Upon approaching the critical pressure $p_C = 2.4$ GPa, the crystal damage process becomes of the avalanche type. Samples form a two component system, and dimension of the crystalline regions decreases with time. This confirms the data of Kobayashi et al. [5], namely that above some pressure, $T_c^{\max}(p)$, the γ coefficient changes its sign from $\gamma > 0$ at ferroelectric phase to $\gamma < 0$.

The destruction of the sample above the p_C value, where pressure liquid penetrating inside the crystal diminishes dipole–dipole interaction between GI molecules, is responsible for spontaneous polarization. The value of the Curie–Weiss constant $C = \mu^2 N/3$ is diminished. A similar effect in a distorted crystal has been observed for irradiated TGS crystals [8]. X-irradiation leads to disintegration of ferroelectric crystals into regions of the order of 100 Å and a decrease of T_C. In our experiments [4, 5] crystal disintegration on small regions of the order of nanometers leads to a decrease in T_C. The transition under $p_C \geq 2.4$ GPa does not depend on dielectric dipole ordering but reveals a transition to an amorphic mixture of pressure liquid and nanosized TGS particles.

Kobayashi et al. data [5] show that, starting from the ferroelectric phase ($T < T_C$), high pressure can transfer ferrolectric order to higher temperatures. Conversely, for

$T > T_C$ high pressure leads to nonferroelectric phase transition at p_C (Fig. 2). In accordance with the theoretical data of Shaoping et al. [10], the limitation of critical size is strongly correlated with the dimension along the spontaneous polarization direction. Relatively stronger dipole–dipole interaction leads to the formation of long dipole chains. In TGS crystals with lamelar structure at RT [6], it is strongly expected that, above a critical pressure, the TGS system changes its dimensionality.

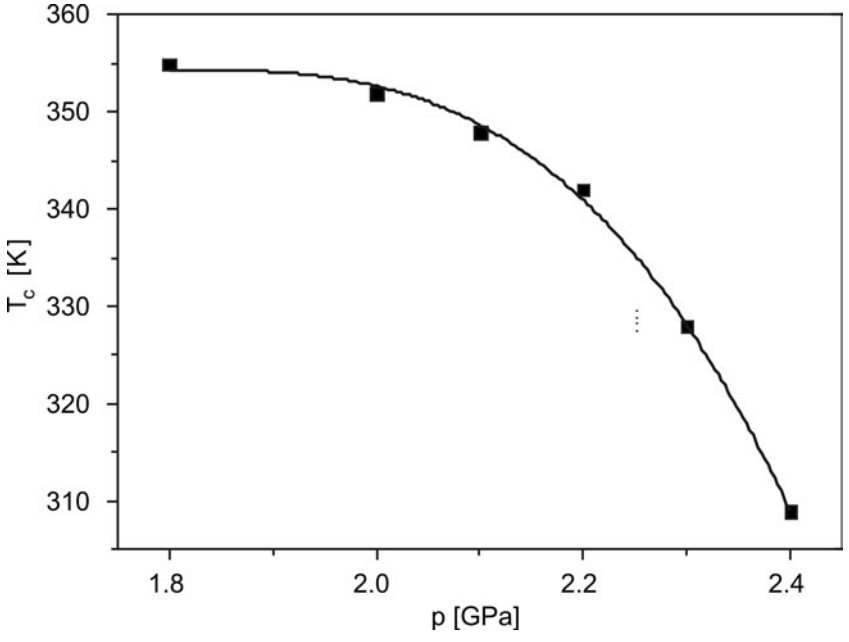

Fig. 3. $T_C(p)$ dependence above critical pressure of 1.8 GPa:
squares – experimental values, solid line –fitting curve in accord with Eq. (3)

In Figure 3, the behaviour of $T_C(p)$ for $T_C^{\max}(p) = 355$ K and $p_C = 1.8$ GPa is described by the equation:

$$T_C(p) = T_C^{\max}\left(1 - A\left(\frac{p - p_C}{p_C}\right)^{1/n}\right) \tag{3}$$

The best fit is found for $n = 0.33$ which may suggest the occurrence of a 3D–2D transition.

3. Discussion

Based on the high pressure results of Stankowski et al. [4] and Kobayashi et al. [5] it is evident that at $p_C \approx 2.4$ GPa ionic TGS crystal, with molecular dynamics driven

by NH_3 rotation groups and flipping of GI molecules, experiences a structural phase transition which consists in breaking up of ordered ferroelectric phase in amorphous pressure liquid with the unit size volume to be proportional to $p - p_C$. Because of the γ-coefficient anisotropy $\left(\gamma_{\|} \approx 1.9\ \mathrm{K{\cdot}GPa^{-1}}, \nu_{\perp} = 0.8\ \mathrm{K{\cdot}GPa^{-1}}\right)$ with an axial symmetry: $1 - \cos^2 Q$ (Q is the tilt angle of GI) the unit cell catastrophe may be reached by two ways:

- ferroelectric units preserve their own anisotropy and the T_C temperature depends linearly on pressure up to critical value p_C,
- ordered areas under high-pressure lose their own anisotropy, and above $p = 2.1$ GPa the T_C value is suppressed monotonically versus p, and dimensional effects are dominant: $T_C \propto d^{-1}$[9].

Destruction of the crystal structure essentially depends on ferroelectric dipole –dipole interactions near a "structural catastrophe" of the TGS structure and an anisotropy of unit cell compressibility.

Acknowledgement

This work was financed as a research project supported by Grant Nr. N N202 1206 33.

References

[1] WANG C.L., SMITH S.R.P., J. Phys.: Cond. Matter, 7 (1995), 7163.
[2] RÜDIGER A., SCHNELLER T., ROELOFS A., TIEDKE S., SCHMITZ T., WASER R., Appl. Phys. A, 80 (2005), 1247.
[3] WADA S., YASUNO H., HOSHINA T., NAM S-M., KAKEMONO H., TSURUMI T., Jap. J. Appl. Phys., 42 (2003), 6188.
[4] STANKOWSKI J., GAŁĘZEWSKI A., WAPLAK S., GRUSZCZYŃSKA U., GIERSZAL H., Feroelecrtics, 6 (1974), 209.
[5] KOBAYASHI Y., SAWADA S., FURUTA H., ENDO S., DEGUCHI K., J. Phys.: Cond. Matter, 14 (2002), 11139.
[6] STANKOWSKI J., Phys. Rep., 77 (1981), 1.
[7] CHOUDHURY B.R., CHITRA R., RAMANADHAM M., Phase Trans., 77 (2004), 385.
[8] PAWLACZYK CZ., Ferroelectrics 9 (1975), 17.
[9] RYSIAKIEWICZ-PASEK E., POPRAWSKI R., POLANSKA J., SIERADZKI A., RADAJOWSKA E.B., J. Non-Crystal. Solids, 351 (2005), 2703.
[10] SHAOPING LI, EASTMAN J.A., LI Z., FOSTER C.M., NEWNHAM R.E., CROSS L.E., Phys. Lett., A 212 (1996), 341.

Received 10 April 2008
Revised 19 December 2008

Materials Science-Poland, *Vol. 27*, *No. 1*, *2009*

Physically and chemically bound H_2O in the gyrolite structure

K. BALTAKYS*, R. SIAUCIUNAS

Department of Silicate Technology, Kaunas University of Technology,
Radvilenu 19, LT – 50270 Kaunas, Lithuania

Synthetic pure gyrolite prepared under hydrothermal conditions (32 h, 200 °C) from a stoichiometric composition ($CaO/SiO_2 = 0.66$) of calcium oxide and a fine-grained $SiO_2 \cdot nH_2O$ mixture can easily adsorb water vapour. The equilibrium quantity of adsorbed water vapour was estimated from desorption thermograms. It was determined that the thermal effect of desorption is close to the steam-heat of water vapour at temperatures up to 175 °C. This part of water vapour adsorption can be described by a physical adsorption model, only a small quantity of water vapour being chemisorbed. The crystal structure of gyrolite under a pressure of water vapour and at low temperatures (–197 °C) was stable.

Key words: *gyrolite; adsorption; thermal analysis; calcium silicate hydrate; X-ray diffraction*

1. Introduction

Calcium silicate hydrates, occurring in nature as hydrothermal alteration products of calcium carbonate rocks and as vesicle fillings in basalts, include many chemically and structurally distinct phases [1]. Many calcium silicate hydrates are structurally very similar, consisting of similar arrangements and modifications of the same types of structural units, i.e. dreierketten chains. Intrinsic disorder within the crystal structure of even the most crystalline natural C–S–H mineral samples can affect the crystallographic and physical characteristics of these phases [2, 3]. Moreover, the hydrothermal formation of these phases is complicated, and crystallization usually occurs via a semi-crystalline precursor and intermediate phases [4–13]. These phases can be very stable, and a long synthesis (months) may be required before the system reaches an equilibrium. This makes the exact crystallization mechanism and kinetics difficult to determine. The dehydration and recrystallization processes of these phases are also complex and vary from phase to phase, due to the different structures and varying

*Corresponding author, e-mail: kestutis.baltakys@ktu.lt

amounts of OH and/or H_2O. A few of these compounds contain molecular water, some hydroxyl, and others contain both hydrous species.

Recently, Allen et al. presented an obvious schematic diagram of the nanoscale C–S–H particles containing liquid H_2O in nanopores, adsorbed H_2O, interlayer space with physically bound H_2O and calcium silicate sheets with OH^- groups [14].

However, some properties, e.g. sorption capacity, depend not only on the crystal lattice of a porous body but also on the surface microstructure and specific surface area, as well as on the dominant pore size and their differential distribution in the compound relative to the radius. In the case of gyrolite crystal lattice, these properties usually depend on the proportion of crystalline (SiO_4 tetrahedral and CoO_6 octahedral sheets) and amorphous parts. However, no data was found on the influence of partial pressure of water vapour on the gyrolite crystal lattice.

Recently, the interest in gyrolite has increased because new possibilities of its application have been found; it may be used to educe heavy metal ions and remove them from wastewaters [15, 16]. Of specific interest is the purported ability of gyrolite to separate supercoiled plasmid, opencircular plasmid, and genomic DNA [17].

The aim of the present work was to elucidate the influence of partial pressure of water vapour on the gyrolite crystal lattice. Based on experimental measurements, the form of adsorbed water in the gyrolite structure was highlighted.

2. Experimental

In this work, the following reagents were used as starting materials: fine-grained $SiO_2 \cdot nH_2O$ (Reachim, Russia, ignition losses 21.43 %, specific surface area S_a = 1560 m²/kg by Blaine's) and CaO (99.6 % Reachim, Russia) additionally burned at 1000 °C for 0.5 h.

Pure gyrolite was synthesized after 32 h at 200 °C from a stoichiometric composition of calcium oxide and $SiO_2 \cdot nH_2O$ mixture (CaO/SiO_2 = 0.66). The dry primary mixture was mixed with water in stainless steel vessels (water/solid ratio of the suspension W/S = 10.0). The product was filtered, dried at 50 ± 5 °C and sieved through a sieve with the mesh size of 80 μm. These synthesis conditions were chosen based on previously published data [12, 13].

Experiments of adsorption of water vapour by gyrolite were carried out at room temperature. Samples of gyrolite were kept in desiccators with sulfuric acid for 60 h. Variation of sulfuric acid solution concentrations made it possible to achieve a desired relative pressure of water vapour p/p_0 (p – partial pressure of adsorbate, p_0 – saturated vapour pressure of adsorbate) (Table 1). The quantity of adsorbed water vapour was determined from data of a simultaneous thermal analysis.

In order to evaluate the stability of gyrolite structure at low temperatures and to estimate the influence of the adsorbed water vapour (adsorbate) on the structure of its crystal lattice, gyrolite samples were first saturated with water vapour, i.e. kept in a desiccator for 60 h at various relative pressures p/p_0 (1, 0.877, 0.753, 0.56, 0.355).

Later, these samples were cooled in liquid nitrogen (–197 °C) for 15 min each and heated to room temperature (20 °C). The stability of gyrolite structure was estimated from X-ray powder diffraction data.

Table 1. Partial pressures of H_2O vapour in the air above H_2SO_4 solutions at 25 °C

No.	Relative pressure (p/p_0) of water vapour	Concentration c of H_2SO_4 solutions [%]
1	0.355	50
2	0.56	40
3	0.753	30
4	0.877	20
5	1	0

The X-ray powder diffraction results were collected with a DRON-6 X-ray diffractometer with the Bragg–Brentano geometry using Ni-filtered CuK_α radiation and a graphite monochromator operating at the voltage of 30 kV and emission current of 20 mA. The step-scan covered the angular range 2–60° (2θ) in steps of $2\theta = 0.02°$. The computer program X-fit [18] was used for diffraction profile refinement under the pseudoVoid function and for description of the diffractional background under the 3rd degree Tchebyshev polynomial.

Simultaneous thermal analysis (STA, differential scanning calorimetry – DSC and thermogravimetry – TG) was carried out on a Netzsch instrument STA 409 PC at the heating rate of 15 °C/min. The temperature ranged from 30 °C up to 1000 °C in an ambient atmosphere. The ceramic sample handlers and Pt–Rh crucibles were used.

IR spectra were carried out with a Perkin Elmer FT–IR system spectrum X spectrometer. The specimens were prepared by mixing 1 mg of a sample with 200 mg of KBr. Spectral analysis was performed in the range of 4000–400 cm^{-1}, with the spectral resolution of 1 cm^{-1}.

The specific surface area of raw materials was determined by Blaine's method with an air permeability apparatus (Model 7201, Toni Technik Baustoffprufsysteme GmbH).

3. Results and discussions

Water vapour adsorption by gyrolite was studied in function of the partial pressure of water vapour in the air. The latter parameter was controlled by changing the concentration of sulfuric acid in H_2SO_4–H_2O solutions (Table 2). The equilibrium quantity of water vapour ($\sum X_p^{H_2O}$) adsorbed on gyrolite was estimated from desorption termograms (Fig. 1). We can see from Fig. 1 that the largest change of mass (Δm) occurs in the temperature range 50–150 °C and is attributed to the desorption of free water.

Table 2. Dependence of adsorbed water vapour quantity on p/p_0 in the temperature range 50–200 °C [mg]

p/p_0	t [°C]															
	50	60	70	80	90	100	110	120	130	140	150	160	170	180	190	200
1.000	0.18	0.27	0.48	0.83	1.45	2.53	4.21	6.22	8.11	9.26	9.57	9.80	10.03	10.19	10.32	10.40
0.877	0.10	0.19	0.37	0.66	1.14	1.81	2.66	3.42	3.75	3.97	4.18	4.40	4.61	4.78	4.91	5.02
0.753	0.10	0.18	0.29	0.44	0.72	1.14	1.58	1.84	2.03	2.23	2.43	2.63	2.80	2.92	2.95	3.04
0.560	0.10	0.15	0.25	0.43	0.80	1.07	1.33	1.51	1.66	1.81	1.96	2.12	2.26	2.37	2.46	2.55
0.355	0.05	0.09	0.16	0.30	0.48	0.67	0.86	1.02	1.18	1.34	1.48	1.65	1.85	1.98	2.11	2.23
0.000	0.11	0.13	0.17	0.23	0.33	0.45	0.63	0.76	0.87	0.98	1.14	1.31	1.50	1.65	1.81	1.96

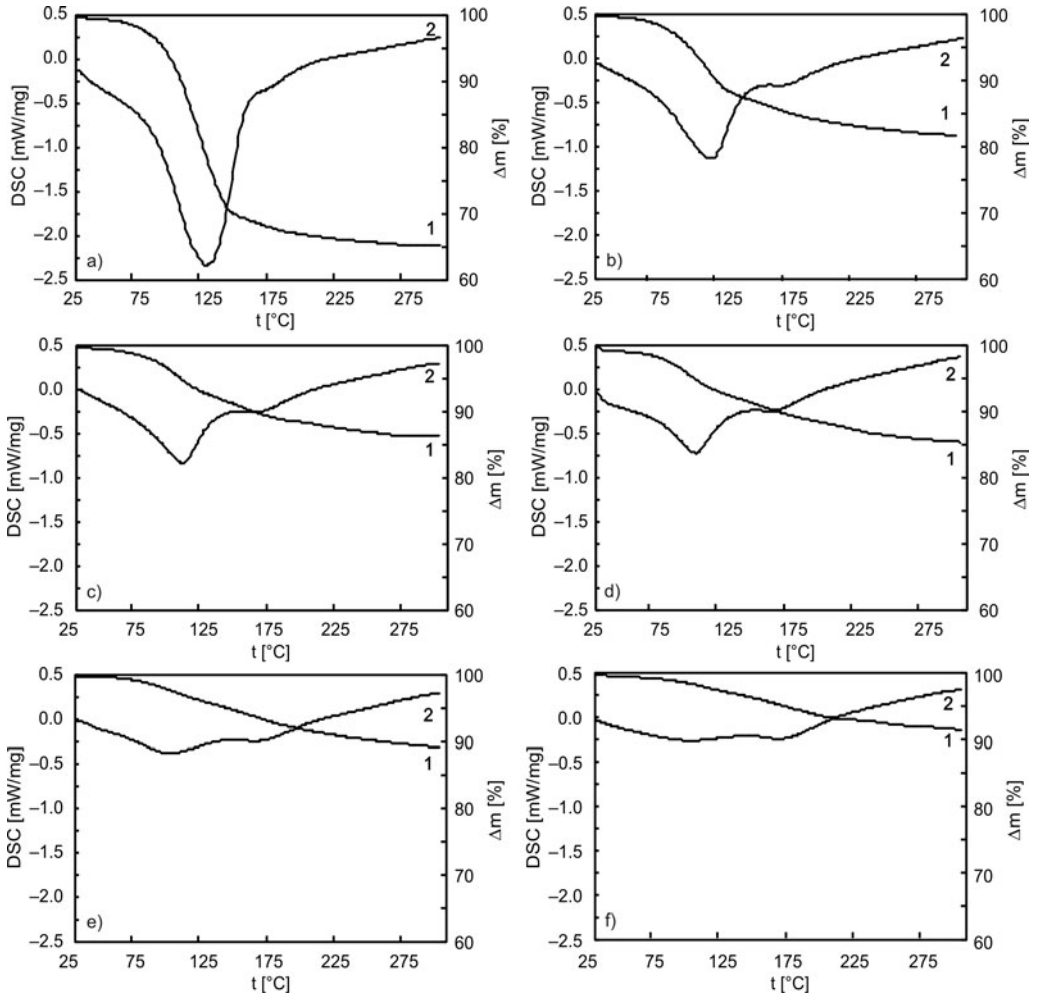

Fig. 1. TG (1) and DSC (2) curves of gyrolite at the p/p_0 ratio:
a) 1, b) 0.877, c) 0.753, d) 0.56, e) 0.355, f) reference sample

It should be emphasized that the value of $\sum X_p^{H_2O}$ changes most significantly, i.e. increases from 0.18 to 10.40 mg, when the p/p_0 ratio is equal to 1.0 (saturated water vapour) in the temperature range 50–200 °C (Fig. 2).

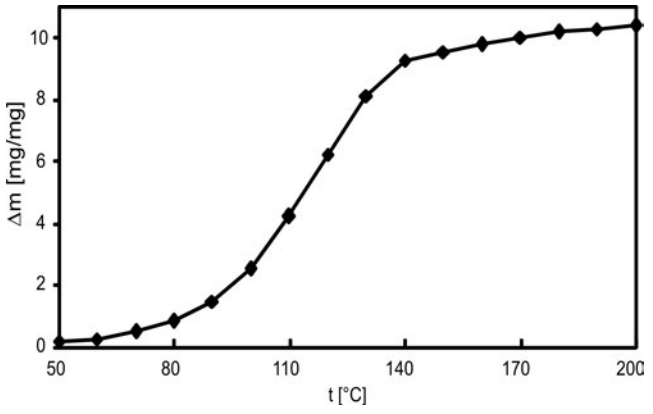

Fig. 2. Increment of the quantity of adsorbed water vapour on gyrolite surface at the p/p_0 ratio equal to 1.0 in the temperature range 50–200 °C

Experimental data and the theoretical hypothesis were also confirmed by thermodynamic calculations. It was determined that the thermal effect of water vapour desorption on gyrolite structure is close to the steam-heat of water vapour at a temperature up to 150 °C (Fig. 3). This part of adsorption of water vapour can be described by a physical adsorption model: no strong bands are formed and the adsorbed water is equilibrated. In this case, the humidity at a certain temperature has no influence on the amount of adsorbed water. However, at a low temperatures the amount of adsorbed water is related to a change of humidity (Fig. 4).

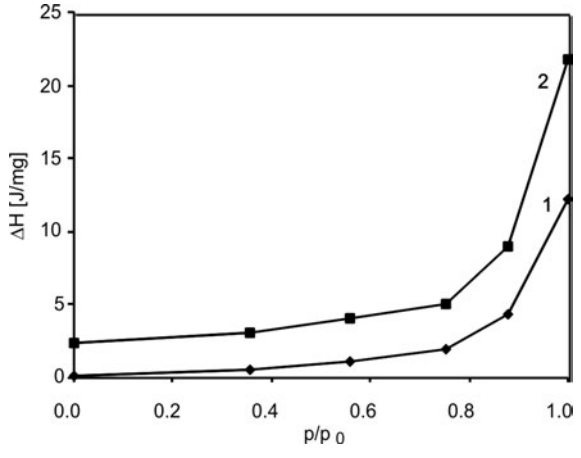

Fig. 3. Calculated isotherm (1) by steam-heat of H_2O vapour and measured isotherm (2) by desorption of H_2O vapour on gyrolite surface in the temperature range 50–150 °C

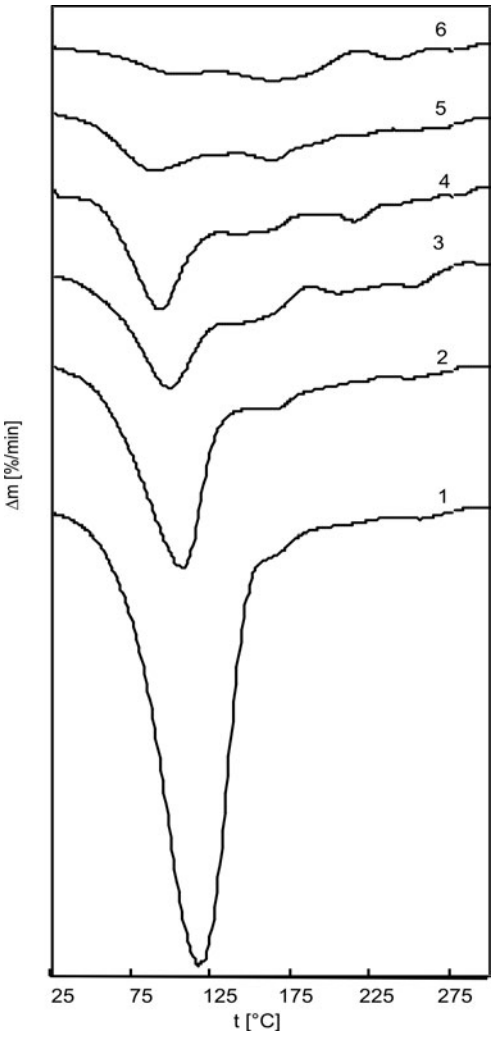

Fig. 4. DTG curves of gyrolite at the p/p_0: 1 – 1, 2 – 0.877, 3 – 0.753, 4 – 0.56, 5 – 0.355, 6 – reference sample

Moreover, a small variation of Δm was determined at 175 °C (Fig. 4). It should be emphasized that this adsorbed water is not balanced with the content of H_2O vapour in the gyrolite environment, and remains almost the same in all ranges of p/p_0. Thus, in this case the influence of the p/p_0 ratio on the adsorption process is negligible (Fig. 4, endothermic peak at 175 °C). This fact means that only a small quantity of adsorbed water is chemisorbed.

FT-IR spectroscopy is very well suited for investigating structural properties of adsorbed or chemisorbed water. Figure 5 presents FT-IR spectra of gyrolite samples, saturated (60 h) with water vapour at different p/p_0 ratios.

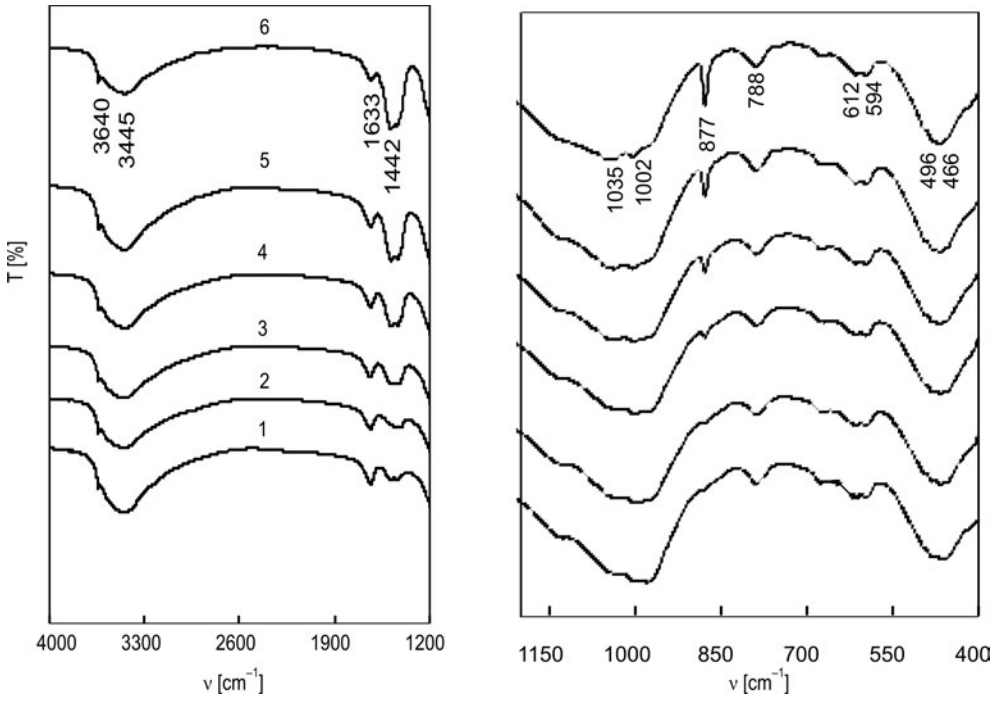

Fig. 5. FT-IR spectra of gyrolite at the p/p_0 ratio:
1 – reference sample, 2 – 0.355, 3 – 0.56, 4 – 0.753, 5 – 0.877, 6 – 1

It should be noted that the intensity of bands near 3637, 3450 and 1634 cm^{-1} does not depend on the p/p_0 ratio. Thus, chemisorption bands may appear only during synthesis at high temperatures. Besides, a sharp band near 3637 cm^{-1} proves that clearly distinguished OH positions exist in the structure of gyrolite, the OH groups being connected only with Ca atoms and not influenced by hydrogen bridge links. A wide band near 3450 cm^{-1} means the opposite – molecular water forms hydrogen bridge links in the interlayers. The bands in the 1634 cm^{-1} frequency range are assigned to $\delta(H_2O)$ vibrations, and confirm this presumption (it can be assigned to chemisorbed water). The intensity of absorption bands near 873 and 1442 cm^{-1} significantly increases during the adsorption process. Thus, analysis of absorption band profiles leaves us to conclude that water vapour was adsorbed close to the physical adsorption model. It should be underlined that chemisorption bands in the gyrolite structure can be created only during synthesis at a high temperature. The obtained experimental data on the stability of gyrolite structure at a low temperature (–197 °C) are summarized in Fig. 6. The results of XRD studies confirmed that adsorbed water has no influence on the structure of gyrolite crystal lattice, because the intensity and profile of the main peak with *d* spacing – 2.2 nm of gyrolite remains essentially unchanged. Moreover, in the X-ray diffraction pattern there were peaks determined having the *d* spacing 1.1262, 0.8371, 0.4197, 0.3732, 0.3511, 0.2803, 0.2141 nm, which are also typical of gyrolite (Fig. 6).

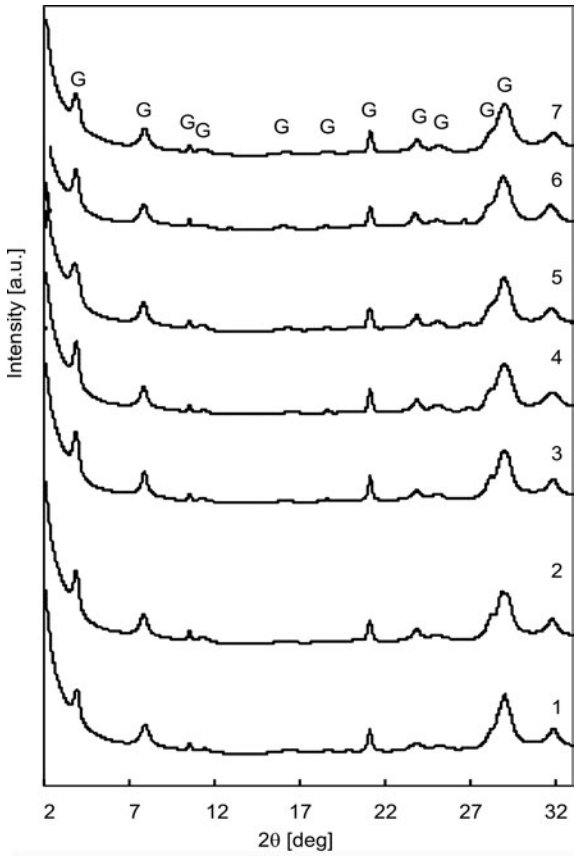

Fig. 6. X-ray diffraction patterns of gyrolite samples saturated (60 h) with water vapour, frozen in liquid nitrogen (–197 °C) for 15 min each and heated to room temperature (20 °C) at p/p_0: 1 – pure sample, 2 – 0.355, 3 – 0.56, 4 – 0.753, 5 – 0.877, 6 – 1, 7 – references sample, G – gyrolite

Thus, our research has shown that gyrolite can easily adsorb water vapour by the physical adsorption. The adsorption has no influence on the structure of gyrolite at liquid nitrogen temperature. It should be emphasized that this part of water is balanced with the content of H_2O vapour in the gyrolite environment, and its variation depends upon the p/p_0 ratio. The obtained data explain why many authors [19] indicate different chemical formulas of gyrolite with an unlimited content of water.

5. Conclusions

The equilibrium quantity of water adsorbed on gyrolite structure increases when the p/p_0 ratio of relative pressure of water vapour varies from 0.355 to 1.0. It was determined that the thermal effect of desorption is close to the steam-heat of water va-

pour. This part of water vapour adsorption can be described by the physical adsorption model.

It was observed that only a small quantity of water vapour is chemisorbed, and this water is not balanced with the content of H_2O vapour in the gyrolite environment: it remains almost constant throughout the p/p_0 range. Bands due to chemisorbed water in the gyrolite structure can be created only during hydrothermal treatment.

It was found that the crystal structure of gyrolite is stable under conditions of extreme cold (especially if in liquid nitrogen), and its stability does not depend on the quantity of adsorbed water.

References

[1] MERLINO S., BONACCORSI E., ARMBRUSTER T., Am. Miner., 84 (1999), 1613.
[2] TAYLOR H.F.W., *Cement Chemistry*, Thomas Telford Publishing, London, 1997.
[3] GARBEV K., PhD. Thesis, Faculty of Geology and Geography, St. Kliment Ohridski University, Sofia, 2004.
[4] SASAKI K., MASUDA T., ISHIDA H., MITSUDA T., J. Am. Ceram. Soc., 80 (1996), 472.
[5] NOCUN-WCZELIK W., Cem. Concr. Res., 27 (1997), 83.
[6] NOCUN -WCZELIK W., Cem. Concr. Res., 29 (1999), 1759.
[7] SHAW S., HENDERSON C.M.B., CLARK S.M., Am. Mineral., 87 (2002), 533.
[8] GARD J.A., MITSUDA T., TAYLOR H.F.W., Mineral. Mag., 43 (1975), 325.
[9] KALOUSEK G.L., NELSON E.B., Cem. Concr. Res., 8 (1978), 283.
[10] ŠTEVULA L., PETROVIČ J., Cem. Concr. Res., 13 (1983), 684.
[11] OKADA Y., MASUDA T., ISHIDA H., J. Ceram. Soc. Japan., 103 (1995), 124.
[12] BALTAKYS K., SIAUCIUNAS R., J. Mater. Sci., 41 (2006), 4799.
[13] BALTAKYS K., SIAUCIUNAS R., Mater. Sci.-Poland, 25 (2007), 185.
[14] ALLEN A.J., THOMAS J.J., JENNINGS H.M., Nature Materials, 6 (2007), 311.
[15] EL-KORASHY S.A., J. Ion Exchange, 15 (2004), 2.
[16] EL-KORASHY S.A., AL-WAKEEL E.I., EL-HEMALY S.A., RIZK M.A., Egypt J. Chem., 45 (2002), 723.
[17] WINTERS M.A., RICHTER J.D., SAGAR S.L., LEE A.L., LANDER R.J., Biotechnol. Prog., 19 (2003), 440.
[18] CHEARY R.W., COELHO A.A., Programs XFIT and FOURYA, deposited in CCP14 Powder Diffraction Library, Engineering and Physical Sciences Research Council, Daresbury Laboratory, Warrington, England, (1996) (http://www.ccp14.ac.uk/tutorial/xfit-95/xfit.htm).
[19] MERLINO S., Mineral. Mag., 52 (1988), 377.

Received 11 April 2008
Revised 16 october 2008

Materials Science-Poland, *Vol. 27*, *No. 1*, *2009*

Characterization of polypyrrole films deposited on aluminum surfaces from oxalic acid aqueous solution

A. S. LIU*, M. A. S. OLIVEIRA

Departamento de Química, Instituto Tecnológico de Aeronáutica (ITA),
Pça Mal Eduardo Gomes, 50 – CTA, São José dos Campos, SP, Brasil, CEP 12228-900

Electrochemical synthesis of polypyrrole films (PPy) on aluminum surfaces from oxalic acid aqueous solutions was performed using the cyclic voltammetry and galvanostatic technique. SEM micrographs of aluminum surfaces coated with PPy films showed that the galvanostatically deposited films were more homogeneous than those deposited by cyclic voltammetry. The presence of bands at 1170 and 1630 cm^{-1} in the FTIR spectra of the PPy films indicate that the films are overoxidised. The corrosion protection of aluminum surfaces coated with polypyrrole films was investigated by potentiodynamic polarization curves and electrochemical impedance spectroscopy in a chloride medium. A poor corrosion protection performance of the PPy films was observed and it was associated with the overoxidation process, resulting in defects and pores along the polymeric chain that allows penetration of corrosive species.

Key words: *polypyrrole; aluminum; oxalic acid; overoxidation*

1. Introduction

Polypyrrole (PPy) is a material extensively investigated because of its high conductivity, environmental stability, wide range of applications such as membranes, sensors, batteries, anti-corrosion films, etc. [1–4]. Polymeric films can be synthesized from aqueous or organic media by chemical and electrochemical methods. Electrochemical synthesis is more advantageous, since the coating properties (thickness, conductivity and adherence) can be controlled by varying parameters such as current density, monomer concentration, electrolyte solution nature and pH [5–8].

Various research groups reported the electrodeposition of PPy on aluminum surfaces in various electrolytes such as sulfuric acid, sulphonates, sulfosuccinate, saccharin and nitric acid [9–13]. The formation of an Al/Al_2O_3 /PPy sandwich structure during the PPy electrodeposition has been suggested. Since the PPy films are deposited onto aluminum oxide, the nature of this layer (porous or compact) influences the electrodeposition process [10, 14, 15]. This mechanism suggests that pores and defects on

*Corresponding author, e-mail: dora@ita.br

aluminum oxide should act as active growth sites of the PPy film, and therefore a compact layer should hinder charge transfer reactions, inhibiting the monomer oxidation and consequently the PPy growth.

In the previous work, the authors showed that the formation of adherent and homogeneous PPy films on aluminum surfaces from aqueous solutions containing pyrrole and tartrate depends on the synthesis parameters such as the pH, monomer concentration, and the current density [16]. Even though oxalic acid medium has been studied for depositing polypyrrole on aluminum substrates [17–20], the corrosion protection of aluminum surfaces coated with PPy films have been little investigated.

In this work the influence of the conditions of synthesis on the properties of the PPy films deposited on 99.89 % wt. aluminum from aqueous solution containing oxalic acid was investigated. Additionally, the corrosion behaviour of aluminum surfaces coated with PPy films was investigated by potentiodynamic polarization and electrochemical impedance spectroscopy.

2. Experimental

Pyrrole (Merck) was distilled prior to use, and the electrolytes, oxalic acid (Baker) and sodium chloride (Reagen) were used as received. The electrochemical experiments were performed at room temperature in a one-compartment cell containing three electrodes. The working electrode was 99.89 wt. % aluminum, inlaid on Teflon®, with a disc shape exposed area of 0.53 cm^2. The reference electrode was a saturated Ag|AgCl, Cl^- electrode and the auxiliary electrode was a platinum wire. The solutions of electrolytes were prepared by dissolving 0.2 $mol \cdot dm^{-3}$ oxalic acid and 0.5 $mol \cdot dm^{-3}$ pyrrole in distilled water (pH = 0.8). The aluminum surfaces were polished with abrasive paper (220, 400, 600 and 1200 grits) and rinsed with distilled water before each electrochemical experiment. The PPy electrodeposition was carried out by cyclic voltammetry by scanning the potential between –1.0 and 2.0 V vs. Ag/AgCl at a sweep rate of 5.0 $mV \cdot s^{-1}$. The PPy film growth was also performed using the galvanostatic technique, namely by applying current densities ranging between 1.0 and 10.0 $mA \cdot cm^{-2}$ to the working electrode. The morphology of aluminum surfaces polished and coated with PPy films was analyzed using a Jeol JXA-840A scanning electron microscope (SEM). The micrographs were obtained using an electron beam of 15 keV.

FTIR was used to analyze the composition of the PPy films. The spectra were obtained using a spectrometer model Spectrum-2000 (Perkin Elmer) in the range of 4000–400 cm^{-1}, with 4 cm^{-1} resolution, 40 scans, at 25 °C. KBr pellets were prepared with solid oxalic acid and with the PPy films removed from aluminum surfaces. The corrosion resistance of aluminum surfaces, polished and coated with PPy films, was investigated using the potentiodynamic polarization technique and electrochemical impedance spectroscopy. The surfaces were exposed to unstirred 0.1 $mol \cdot dm^{-3}$ NaCl aqueous solution (pH = 5.9) open to the atmosphere.

The polarization curves were obtained starting from the open circuit potential (OCP) and varying the potential up to 400 mV in one set of experiments (anodic branch of the Tafel plot) and varying it down to –400 mV in another set of experiments (cathodic branch of the Tafel plot). The potential scan rate was 5 mV·s^{-1}. The corrosion potential E_{corr} and the corrosion current densitiy j_{corr} were obtained from the Tafel plots. The E_{corr} is the potential at which the current density is zero. The j_{corr} was extrapolated from linear parts of the anodic and cathodic branches of the Tafel plots [21].

The impedance spectra were obtained over the frequency range 100 kHz–10 mHz, with acquisition of 10 points per decade, at an open circuit potential with AC excitation of 10 mV. A potentiostat/galvanostat model PGSTAT30 from Autolab, controlled by an USB-IF030 interface and by the FRA.EXE software both installed in a PC computer, was used to perform these experiments. The EQUIVCRT software developed by the Boukamp group [22] was used to determine the parameters related to the electrical equivalent circuits utilized to describe the electrochemical process occurring on each surface exposed to the aqueous solution containing chloride.

3. Results and discussion

3.1. Electrodeposition of PPy films by cyclic voltammetry

Figure 1 shows the results of the first cycle for the cyclic voltammetry experiments performed in the electrodeposition investigation of PPy from 0.2 mol·dm^{-3} oxalic acid solutions (pH 0.8) and varying the pyrrole concentration between 0.1 and 0.8 mol·dm^{-3}. The curves were obtained by varying the potential from -1.0 to 2.0 V and back to -1.0 V at a sweep rate of 5 mV s^{-1}.

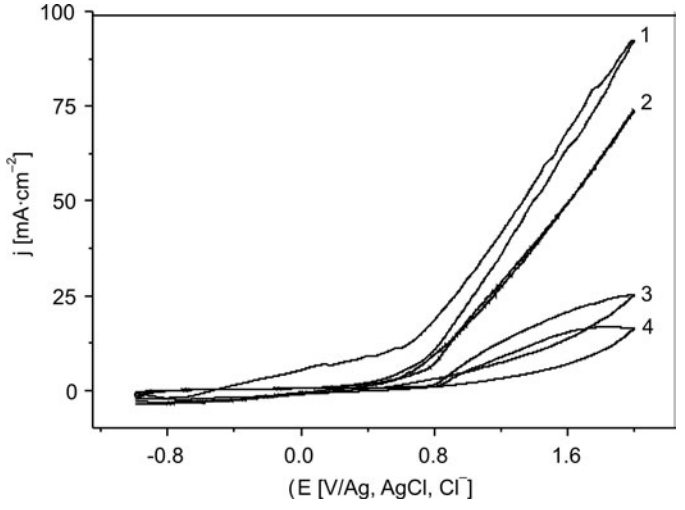

Fig. 1. Voltammetric profiles (first cycle) of PPy growth in 0.2 mol·dm^{-3} oxalic acid medium and pyrrole concentrations of: 1 – 0.8, 2 – 0.5, 3 – 0.2 and 4 – 0.1 mol·dm^{-3}; sweep rate 5 mV·s^{-1}

When the monomer concentration was 0.1 mol·dm^{-3}, the aluminum surface was not completely covered by the polymer. At 0.2 mol·dm^{-3} pyrrole, a homogeneous PPy film was electrodeposited on aluminum. The results in Fig. 1 also show that the potential at which the electropolymerization commences to decrease slightly with increasing monomer concentration. This behaviour may be associated with the diffusion process of pyrrole on the electrode surface which increases with the monomer concentration [5]. The higher the monomer concentration is, the faster the oxidation reaction of pyrrole at the interface aluminum/electrolyte solution, and the lower the potential at which the electropolymerization starts.

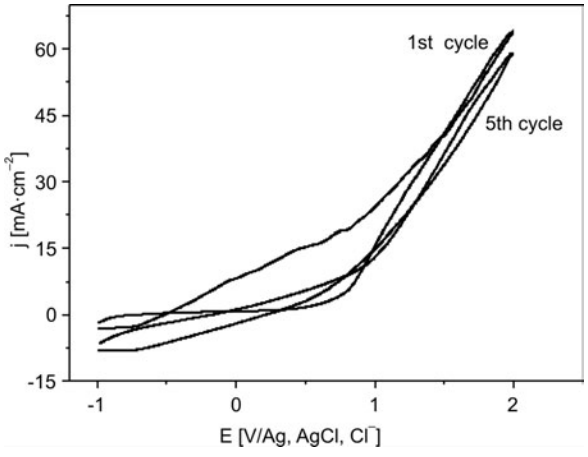

Fig. 2. Successive potentiodynamic growth of polypyrrole on aluminum electrode from aqueous solution containing 0.2 mol·dm^{-3} oxalic acid + 0.5 mol·dm^{-3} pyrrole, pH = 0.8 at the scan rate of 20 mV·s^{-1}

Figure 2 shows the cyclic voltammograms for the first and fifth cycles. The sweep rate of 20 mV·s^{-1} was used in this experiment. The current densities associated with the PPy growth decrease with the number of cycles. This behaviour differs from that reported in the literature for the growth of PPy coatings on AA2024 alloy from oxalic acid, where an increase of the current density was observed with the increase of number of cycles [19]. The behaviour observed in this work was ascribed to the overoxidation process resulting in an increase in the resistance of the coating due to a structural changes of the polymeric chains. This is an irreversible process that results in the shortening of the polymer chain length and/or formation of defects and pores along the PPy chain [23].

3.2. Galvanostatic deposition of polypyrrole films

PPy films were also deposited on aluminum surfaces by chronopotentiometry. Figure 3 shows some time dependences of potential obtained for PPy deposition from

aqueous solutions containing 0.2 mol·dm^{-3} oxalic acid and 0.5 mol·dm^{-3}pyrrole, pH = 0.8 and varying the current densities between 1.0 and 10.0 mA·cm^{-2}.

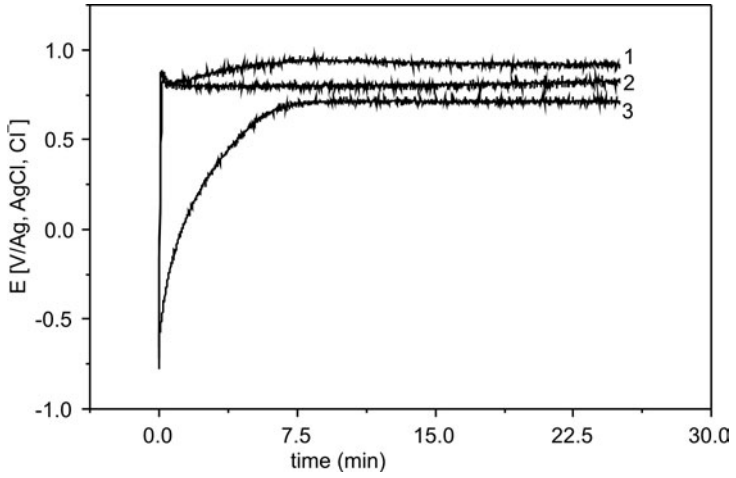

Fig. 3. Time dependences of potential curves for PPy electrodeposition from 0.2 mol·dm^{-3} oxalic acid + 0.5 mol·dm^{-3} pyrrole. The applied current densities (mA·cm^{-2}): 1 – 10; 2 – 5; 3 – 2.5 and 4 – 1.0

At the current density of 1.0 mA·cm^{-2}, the PPy film does not uniformly cover the entire aluminum surface. At 2.5 mA·cm^{-2}, the PPy film is homogeneous and the potential stabilizes at 0.8 V vs. Ag/AgCl and remains constant even after about 2 h after switching on the current. This result is in accordance with that observed in cyclic voltammetry, which showed that the PPy growth commences at 0.79 V vs. Ag/AgCl (curve 2 in Fig. 1). Films easily peeled off from the aluminum surfaces when the current densities higher than 2.5 mA·cm^{-2} were applied. This phenomenon has been observed for PPy films galvanostatically formed using high current densities, and might be associated with the occurrence of side reactions, induced by the high current density, which may result in short chain length or lead to formation of defects along the polymer chain [5]. Increasing the current densities results in a shift of the working potential to more positive values and in an increase of the thickness of the PPy films accompanied by a decrease in their adherence.

3.3. Morphology of PPy films, SEM micrographs

The morphology of aluminum surfaces coated with PPy films was investigated by SEM. The polymeric films were deposited on aluminum electrodes from 0.2 mol·dm^{-3} oxalic acid + 0.5 mol·dm^{-3} pyrrole aqueous solutions (pH = 0.8) by cyclic voltammetry (first cycle) at a sweep rate of 5 mV·s^{-1} and galvanostatically at 2.5 and 10 mA·cm^{-2} using the same deposition charge: 9.10^4 C·m^{-2}. Figure 4 shows these micrographs.

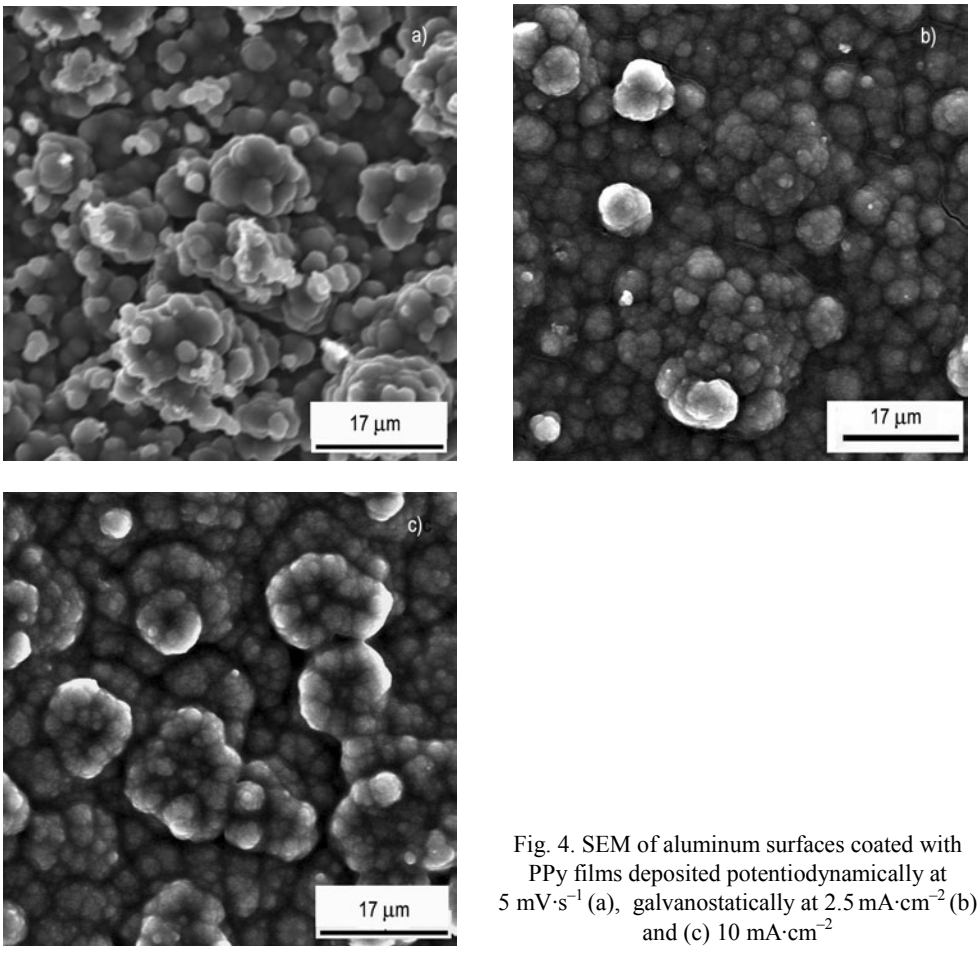

Fig. 4. SEM of aluminum surfaces coated with PPy films deposited potentiodynamically at 5 $mV \cdot s^{-1}$ (a), galvanostatically at 2.5 $mA \cdot cm^{-2}$ (b) and (c) 10 $mA \cdot cm^{-2}$

PPy films formed by cyclic voltammetry are less uniform than those deposited galvanostatically. The latter films are more homogeneous and present a cauliflower-like structure consisting of micro-spherical grains. It has been reported that this cauliflower structure is related to a difficult dopant intercalation in the disordered polymeric chain [24]. PPy films formed at higher current densities (10 $mA \cdot cm^{-2}$) exhibited smaller sized cauliflower-structures, with larger voids between them compared to the films formed at 2.5 $mA \cdot cm^{-2}$. The morphological differences between the films can be explained by side reactions which result in a short chain length, and/or lead to the formation of defects along the polymeric chain.

3.4. Fourier transform infrared (FTIR) spectra

FTIR analyses were used to investigate the composition of the PPy films removed from the aluminum surfaces. Figure 5 shows the FTIR spectra for oxalic acid (curve a)

and for the films formed. The PPy films were formed from 0.2 mol·dm^{-3} oxalic acid + 0.5 mol·dm^{-3} pyrrole containing aqueous solutions, pH = 0.8, by cyclic voltammetry (curve b), by varying the potential from –1.0 to 2.0 V and back to –1.0 V at the sweep rate of 5 mV·s^{-1} and galvanostatically, using the same amount of charge and current densities of 2.5 (curve c) and 10 mA·cm^{-2} (curve d).

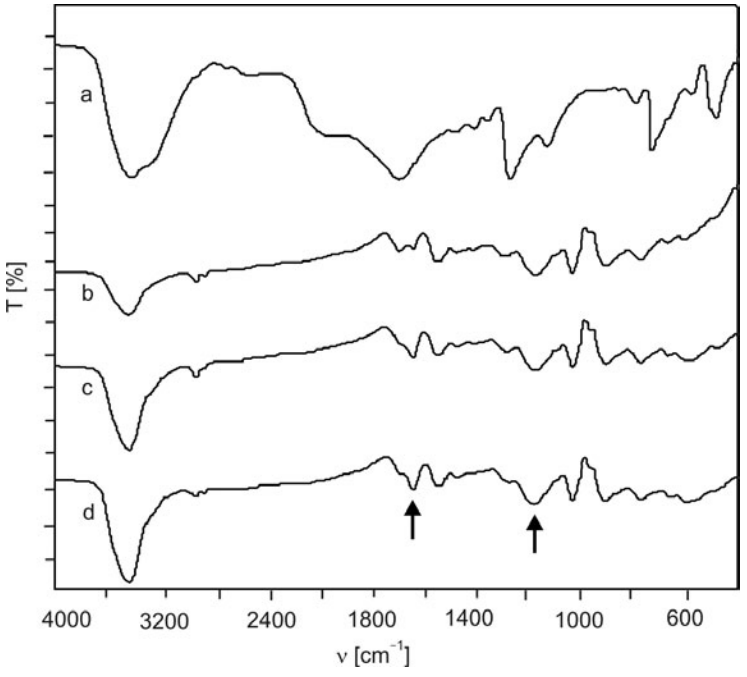

Fig. 5. FTIR spectra of: oxalic acid (a) and PPy films electrodeposited from aqueous solutions containing 0.2 mol·dm^{-3} oxalic acid + 0.5 mol·dm^{-3} pyrrole by cyclic voltammetry at 5 mV·s^{-1}(b), galvanostatically at 2.5 (c) and 10 mA·cm^{-2}(d)

The absorption bands at 1170 and 1630 cm^{-1} in the FTIR spectra of PPy films (marked with arrows in Fig. 5) have been attributed to the bipolaronic species and carbonyl groups that are formed in the overoxidation process of the PPy [25, 26].

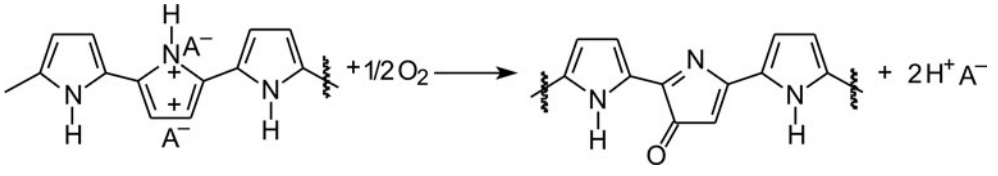

The intense absorption band of the carboxyl group of oxalic acid (at 1700 cm^{-1}) was not observed in the PPy films FTIR spectra. As suggested in the above reaction, overoxidised PPy should not contain significant amounts of oxalic acid.

These results differ from those for PPy films deposited at 2.5 mA·cm^{-2} in tartaric acid-containing medium. For films formed from solutions containing tartaric acid, an

intense band was observed at 1700 cm^{-1} in the FTIR spectrum, indicating that the tartaric acid had been incorporated into the film, and the bands at 1170 and 1630 cm^{-1} have not been observed in the FTIR spectra of the films [16]. This behaviour suggests that the PPy films formed in oxalic acid are more susceptible to the overoxidation process than those formed in tartaric acid.

The results presented in this work also differ from those reported in the literature for PPy films deposited on mild steel from an oxalic acid medium where the presence of an intense band at 1730 cm^{-1} in the FTIR spectrum was attributed to the doping process [27].

3.5. Corrosion tests

Figure 6 presents the potentiodynamic polarization curves obtained in 0.1 $mol \cdot dm^{-3}$ NaCl aqueous solutions (pH = 5.9) for uncoated aluminum surfaces and for those coated with PPy films galvanostatically electrodeposited at 2.5 and 10.0 $mA \cdot cm^{-2}$ from aqueous solutions containing pyrrole and oxalic acid, pH = 0.8.

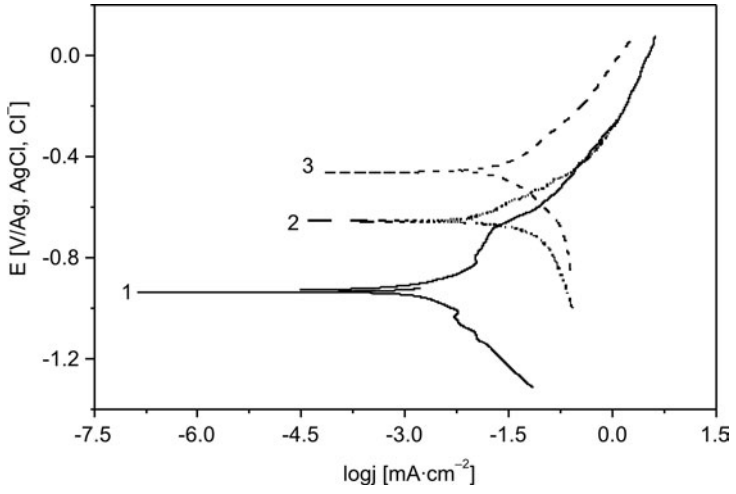

Fig. 6. Polarization curves at 5 $mV \cdot s^{-1}$ in aqueous solution 0.1 $mol \cdot dm^{-3}$ NaCl (pH = 5.9) for polished aluminum surface: 1 – uncoated; and coated with PPy films galvanostatically deposited at: 2 – 10 $mA \cdot cm^{-2}$ and 3 – 2.5 $mA \cdot cm^{-2}$

Table 1 shows the electrochemical parameters obtained from the polarization curves presented in Fig. 6. The corrosion current densities (j_{corr}) of the aluminum surfaces coated with PPy films were higher than those observed for uncoated aluminum surfaces. These results suggest that the PPy films formed in oxalic acid do not protect aluminum surfaces against corrosion.

The PPy coating does not act as a barrier; it does not prevent oxygen and chloride diffusion due to the permeability of the coating. Furthermore, the incorporation of the

chloride ions into the polymer could cause depassivation of the substrate and consequently the corrosion attack.

Table 1. Electrochemical parameters obtained by potentiodynamic polarization curves in NaCl solutions

Aluminum surfaces	Time to reach the OCP in the chloride medium [h]	E_{corr} [V/Ag, AgCl, Cl^-]	j_{corr} [mA·cm^{-2}]
Uncoated	48	–0.93	0.0023
Coated with PPy films deposited at pH = 0.8 and j = 10 mA·cm^{-2}	24	–0.67	0.019
Coated with PPy films deposited at pH = 0.8 and j = 2.5 mA·cm^{-2}	24	–0.46	0.024

Figure 6 shows that the cathodic current densities were higher for the aluminum surfaces coated with PPy than for the uncoated ones. Similar results have been reported in the literature; they have been associated with the reduction of the polymeric matrix, which contributes to an increase in the cathodic currents [28, 29]. A higher overoxidation degree of the PPy films formed at 10.0 mA·cm^{-2} would explain the lower cathodic current densities observed for that surface.

Electrochemical impedance spectroscopy (EIS) was also used to analyze the corrosion of the aluminum surfaces coated with PPy films. Figure 7 presents the Bode plots obtained for aluminum surfaces just polished and coated with PPy film deposited galvanostatically at 2.5 and 10.0 mA·cm^{-2} (maintaining the same deposition charge in 0.1 M NaCl aqueous solution, pH = 5.9).

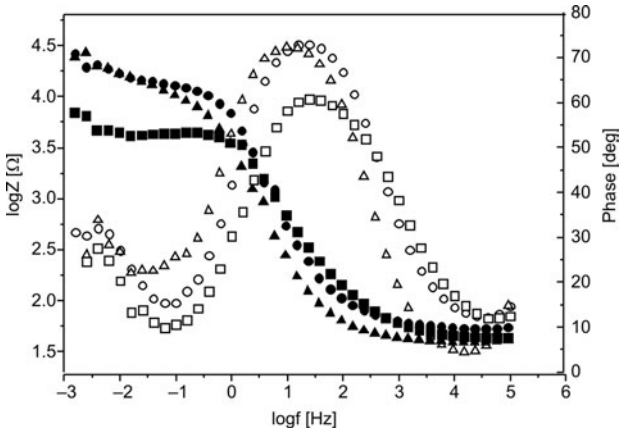

Fig. 7. Bode plot of: aluminum surfaces uncoated (triangles) and coated with PPy films deposited galvanostatically at 2.5 (circles) and 10.0 mA·cm^{-2} (boxes)

In the Bode plot, the ohmic resistance of the electrolytic solution is represented by a high-frequency plateau, while the low-frequency region can give information about the charge transfer resistance (R_{tc}) and film resistance (R_f). The impedance of uncoated

aluminum surfaces is similar to that of surfaces coated with PPy film deposited at 2.5 mA·cm^{-2}. This result confirms the poor performance of PPy film in protecting the aluminum surface against corrosion and it is in accordance with the polarization results presented in Fig. 6. Furthermore, it was observed that the impedance values for the aluminum surfaces coated with PPy film deposited at 2.5 mA·cm^{-2} are higher than those observed for the surfaces coated with film deposited at 10.0 mA·cm^{-2}. This result demonstrates the worst corrosion protection afforded by PPy of the films galvanostatically deposited from oxalic acid containing aqueous solutions at higher current densities (10 mA·cm$^{-2)}$.

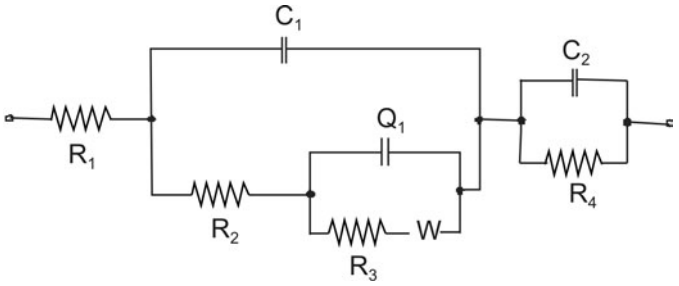

Fig. 8. Equivalent electric circuit model proposed to simulate the electrochemical behaviour of uncoated aluminum surface exposed to chloride medium (see the text for further discussion)

Figure 8 shows the equivalent electric circuit used to simulate the impedance spectrum of the aluminum surface without PPy film. In this model, R_1 represents the electrolyte solution resistance; C_1 and R_2 represent the capacitance and the resistance of the wall pores on the defective aluminum oxide layer; Q_1 and R_3 denote the double layer constant phase element and charge transfer resistance, and W is the Warburg impedance that measures the resistance of the electroactive species to move from the corroding surface to the bulk of the electrolyte, and vice versa. C_2 and R_4 represent the capacitance and resistance of the barrier oxide layer. The constant phase element Q can be interpreted as a deviation of the double layer from an ideal behaviour. This deviation is associated with surface roughness, porosity, mass transport or the presence of a defective oxide film [30–32]. The constant phase element Q is defined by

$$Z_q = (C(j\omega)^n)^{-1}$$

where C is the capacitance of an ideal capacitor. The number n, $0 < n < 1$, represents the deviation of the ideal capacitance behaviour ($n = 1$ represents an ideal capacitor), $j = (-1)^{-1/2}$ and ω is the angular frequency of the AC voltage applied in the electrolyte cell.

Figure 9 presents a comparison between the experimental results (empty circles and plus symbols) and the results of the simulation performed with the proposed equivalent electrical circuit (solid line). It indicates that the model may be used to

explain the behaviour of the aluminum surface exposed to the chloride medium. Table 2 shows the simulated parameter values.

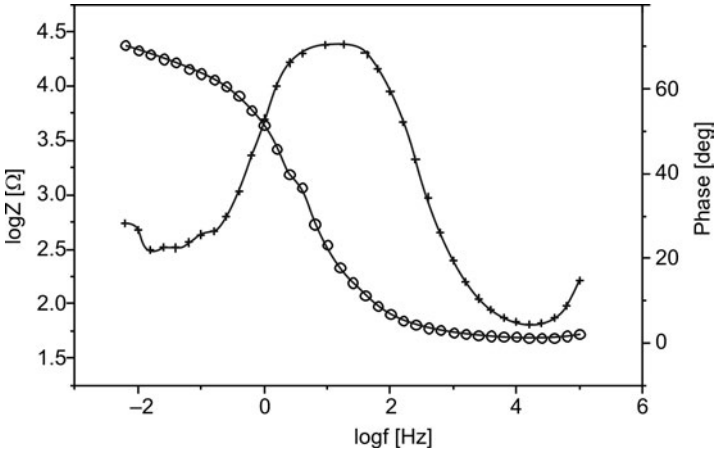

Fig. 9. Bode plot of the aluminum surface without PPy film. An equivalent electric circuit represented by $R_1(C_1[R_2(Q_1[R_3W])])$ (C_2R_4) in Boukamp notation was used to simulate the experimental results

Table 2. Electrochemical parameters obtained by simulation of the EIS results of the aluminum surfaces without PPy films and exposed to chloride medium

C_1	R_2	Q_1	n	$R_3 = R_{tc}$	W	C_2	R_4
2.2 pF	3.0 kΩ	$7.1 \cdot 10^{-2}$ μF	0.91	12.1 kΩ	2.77	31.1 μF	6.8 Ω

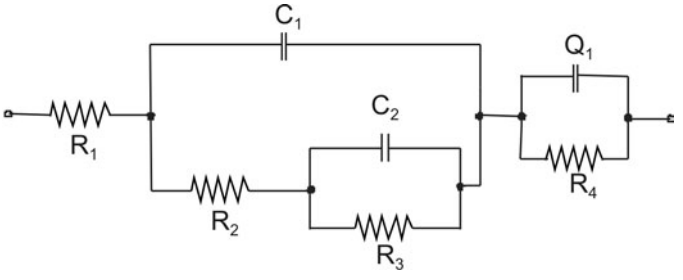

Fig. 10. Equivalent electric circuit model proposed to simulate the electrochemical behaviour of the aluminum surface coated with PPy films

The equivalent electric circuit shown in Fig. 10 was used to simulate the impedance spectra of the aluminum surface coated with the PPy films. In this model R_1 represents the electrolyte solution resistance; C_1 and R_2 represent the capacitance and the resistance of the pores wall of the polymer; C_2 and R_3 represent the capacitance and the resistance of the PPy film. Q_1 and R_4, respectively, denote the double layer

constant phase element and the charge transfer resistance in the interface metal/oxide, respectively.

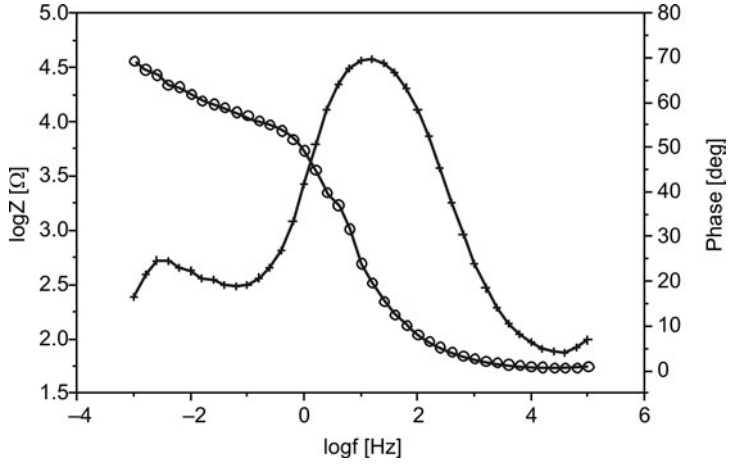

Fig. 11. Bode plot of the aluminum surface coated with PPy film deposited at 2.5 mA·cm^{-2}. An equivalent electric circuit represented by $R_1(C_1[R_2(C_2R_3)])$ (Q_1R_4) in Boukamp notation was used to simulate the experimental results

Figure 11 shows the comparison between experimental data (empty circles and plus symbols) and simulated (solid line) impedance results for aluminum surface coated with PPy film deposited at 2.5 mA·cm^{-2}. This result shows that the proposed model explains the behaviour of the aluminum surface coated with PPy films in chloride medium. Table 3 shows the values of simulated parameters for aluminum surfaces coated with PPy films electrodeposited at 2. 5 and 10 mA·cm^{-2}.

Table 3. Electrochemical parameters obtained by simulation of the EIS results of the aluminum surfaces coated with PPy films and exposed to chloride medium.

Electrochemical parameter	Aluminum surface coated with PPy deposited at 2.5 mA·cm^{-2}	Aluminum surface coated with PPy deposited at 10.0 mA·cm^{-2}
R_1 [Ω]	52.9	52.9
C_1 [μF]	16.7	10.5
R_2 [kΩ]	6.9	3.9
C_2 [mF]	3.9	9.6
R_3 [kΩ]	2.2	3.9
Q_1 [μF]	1.76	0.43
n	0.62	0.71
$R_4 = R_{tc}$ [kΩ]	13.6	1.09

The R_2 values attributed to resistance of PPy pores are higher for films deposited at 2.5 mA·cm^{-2} than for those formed at 10.0 mA·cm^{-2}. This parameter is associated with

defects along the polymeric chain. The smaller the R_2 value is, the higher is the number of defects on the coating.

The R_3 values attributed to the resistance into PPy are higher for the film deposited at 10.0 mA·cm^{-2} than for the film formed at 2.5 mA·cm^{-2}. A higher overoxidation degree for the films formed at 10 mA·cm^{-2} can explain the smaller contribution of reactions on the polymeric matrix. Furthermore, the capacitance of the polymer C_2 was smaller for the film deposited at 2.5 mA·cm^{-2} than for the film formed at 10.0 mA·cm^{-2}. The higher porosity of the latter films, as observed in the SEM micrographs in Fig. 4, explains the higher capacitance observed for this coating.

It was also observed that aluminum surfaces coated with PPy films deposited at 2.5 mA·cm^{-2} showed a smaller charge transfer resistance value R_4 than that observed for surfaces with PPy films deposited at 10.0 mA·cm^{-2}. The presence of larger voids in the film deposited at 10.0 mA·cm^{-2} (Fig. 4(c)) allows the penetration of aggressive ions (chloride) that assists the corrosion process.

Moreover, by comparing the charge transfer resistance values of the uncoated aluminum surfaces with those coated with PPy film, one can confirm the poor performance of PPy film studied in this work to protect aluminum surfaces against corrosion.

4. Conclusions

Films formed by the cyclic voltammetry are much less compact and uniform than those formed galvanostatically. Moreover, films formed at higher current densities are more susceptible to overoxidation than films formed at lower current densities, which was demonstrated by a much smaller microspherical grain size and bigger voids among the grains (SEM results) of PPy formed at higher current densities. This finding is also supported by the FTIR results, which demonstrated that the absorption bands at 1170 and 1630 cm^{-1} may be attributed to the overoxidation process of the PPy.

The polarization curves and impedance results showed that the PPy films presented in this work are not able to protect the aluminum surfaces against corrosion. It was observed that the corrosion current densities of the aluminum surfaces coated with PPy films were higher than those observed for uncoated surfaces. Furthermore, the aluminum surfaces coated with PPy film showed impedance values lower than those observed for the uncoated aluminum. Since higher values of impedance are associated with a higher resistance to corrosion, these results suggest that the coated surfaces present lower corrosion resistance than bare aluminum.

The overoxidation process results in pores and defects along the polymeric structure allowing the penetration of corrosive species and rendering the aluminium surfaces more susceptible to corrosion.

Acknowledgements

The authors thank the Fundação de Amparo à Pesquisa do Estado de São Paulo (FAPESP) for the financial support and the Alcoa Alumínio SA, São Luis, Maranhão, Brazil.

References

[1] INGRAM M.D., STAESCHE H., RYDER K.S., Solid State Ionics, 169 (2004), 51.
[2] AMEER Q., ADELOJU S.B., Sens. Actuators B., 106 (2005), 541.
[3] TALLMAN D.E., SOKINS G., DOMINIS A., WALLACE G.G., J. Solid State Electrochem., 6 (2002), 73.
[4] TRAMONTINA J., MACHADO G., AZAMBUJA D.S., PIANICKI C.M.S., SAMIOS D., Mater. Res., 4 (2001), 95.
[5] WENCHENG S., IROH J.O., Synth. Met., 95 (1998), 159.
[6] WANG L.X., LI X.G., YANG Y.L. React. Funct. Polymers, 47 (2001), 125.
[7] MALINAUSKAS A., Polymer, 42 (2001), 3957.
[8] AYAD M.M., Polym. Int., 35 (1994), 35.
[9] MARTINS N.C.T., MOURA T.S., MONTEMOR M.F., FERNANDES J.C.S., FERREIRA M.G.S., Electrochim. Acta 53 (2008), 4754.
[10] NAOI K., TAKEDA M., KANNO H., SAKAKURA M., SHIMADA A., Electrochim. Acta, 45 (2000), 3413.
[11] LEHR I.L., SAIDMAN S.B., Mater. Chem. Phys., 100 (2006), 262.
[12] BAZZAOUI M., MARTINS J.I., COSTA S.C., BAZZAOUI E.A., REIS T.C., MARTINS L., Electrochim. Acta, 51 (2006), 2417.
[13] SAIDMAN S.B, BESSONE J.B., J. Electroanal. Chem., 521 (2002), 87.
[14] SAIDMAN S.B., J. Electroanal. Chem., 534 (2002), 39.
[15] TSAI M.L., CHEN P.J., DO J.S., J. Power Sources, 133 (2004), 302.
[16] LIU A.S., OLIVEIRA M.A.S., J. Brazil. Chem. Soc., 18 (2007), 143.
[17] AKUNDY G.S., IROH J.O., Polymer, 42 (2001), 9665.
[18]. BRESLIN C.B., FENELON A.M., CONROY K.G., Mater. Des., 26 (2005), 233.
[19] ARENAS M.A., GONZALES BAJOS L., DAMBORENEA J.J., OCON P., Prog. Org. Coatings, 62 (2008), 79.
[20] HULSER P., BECK F., J. Appl. Electrochem., 20 (1990), 596.
[21] ASTM G 102-89, *Practice for Calculation of Corrosion Rates and Related Information from Electrochemical Measurements*, 1994.
[22] BOUKAMP B.A., Solid States Ionics, 1 (1986), 31.
[23] LI Y., QIAN R., Electrochim. Acta, 45 (2000), 1727.
[24] BAZZAOUI M., MARTINS L., BAZZAOUI E.A., MARTINS J.I., Electrochim. Acta, 47 (2002), 2953.
[25] MAZEIKIEN R., MALINAUSKAS A., Polym. Degrad. Stab., 75 (2002), 255.
[26] RODRIGUEZ I., SCHARIFKER B.R., MOSTANY J., J. Electroanal. Chem., 491 (2000), 117.
[27] BRUYNE A., DELPHANCKE J.L., WINAND R., Surface Coatings Techn., 99 (1998), 118.
[28] VILCA D.H., MORAES S.R., MOTHEO A.J., Synth. Met., 140 (2004), 23.
[29] OCON P., CRISTOBAL A.B., HERRASTI P., FATAS E., Corros. Sci., 47 (2005), 649.
[30] BISQUERT J., COMPTE A., J. Electroanal. Chem., 499 (2001), 112.
[31] PAJKOSSY T., KERNER Z., Electrochim. Acta, 46 (2000), 207.
[32] PAJKOSSY T., Solid State Ionics, 176 (2005), 1997.

Received 23 April 2008
Revised 19 December 2008

Materials Science-Poland, *Vol. 27*, *No. 1*, *2009*

A new model for the effect of grain size on the elastic modulus of nanocrystalline materials

ALI SHAFIEI M. *

Department of Materials Science and Engineering,
Sharif University of Technology, P.O. Box 11365-9466, Tehran, Iran

A new model is developed for the structure of nanocrystalline materials. Based on the developed model, a new approach for investigating the effect of grain size on the elastic moduli of nanocrystalline materials is introduced. The predictions of the model are strongly correlated with the experimental results reported in the existing literature.

Key words: *nanocrystalline materials; grain size; elastic modulus*

1. Introduction

The effect of grain size on the non-elastic properties of nanocrystalline materials (NCMs) is quite well understood; however, the effect of grain size on the elastic properties of NCMs is still not known [1, 2]. Some experimental results indicate a decrease in Young's modulus with a decreasing grain size, although some other results show almost no grain size effect [3]. In order to investigate the effects of grain size on the elastic modulus of NCMs, some investigators treated NCMs as composite materials with a grain interior phase and inter-grain phase (sometimes including grain boundaries, triple lines, and quadruple nodes) [3, 4]. Moreover, molecular dynamics simulations (MDS) have also been successfully used to investigate the effect of grain size on the elastic properties of NCMs [1]. Nevertheless, it seems that to investigate the effect of grain size on the elastic properties on NCMs, an accurate concept of the structure of NCMs is needed. Thus, the main aim of this work is an attempt to introduce a new approach to model the structure of NCMs. It is assumed that a nanocrystalline structure could be considered as a layered composite. This can be considered as a novel approach to model the structure of nanocrystalline materials. Moreover, by using this model, a new relation between the grain size and elastic modulus of NCMs is introduced.

* Corresponding author, e-mail: alishland@yahoo.com

2. Model

The concept of NCMs was put forth by Gleiter [5, 6]. In Figure 1 (left) the concept of an NCM structure is schematically shown. Generally, the structure of NCMs can be divided into two parts: grain core and grain-boundary layers. Figure 1 (right) shows how the relative proportions of these two regions vary with the grain size. The important point is that as the grain size decreases into the nanocrystalline region, the grain-boundary layers dominate the structure of NCMs [7].

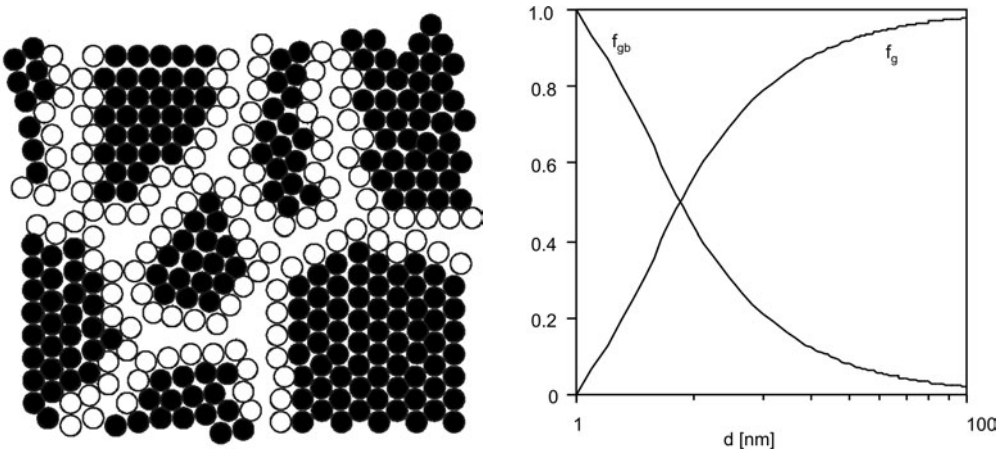

Fig. 1. A simple two-dimensional model of nanocrystalline materials (left). The atoms in the bulk of the grains are indicated in black. The atoms in the grain boundaries are represented as open circles [5]. The volume fraction of grain-boundary layer (f_{gb}) and the volume fraction of crystalline grain (f_g) versus the grain size (d)

According to the conceptual model of NCM structure, as given above, it can be assumed that grain boundaries are like thin layers which bind and fix the nanometer grains. This assumption is more convincing when we consider a considerably high volume fraction of grain boundaries as the grain size decreases into the nanocrystalline region. Our model is based on this assumption. The structure of NCMs can be considered as follows (Fig. 2):

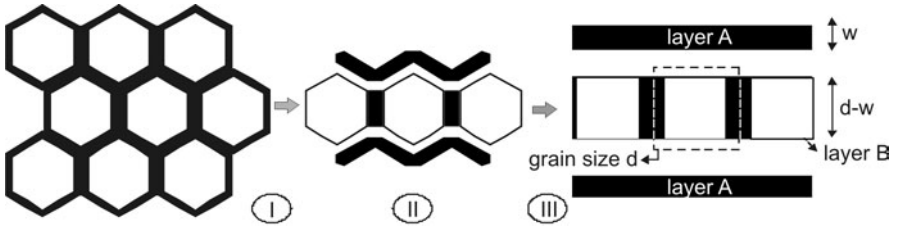

Fig. 2. Models of NCM : I – a simple two-dimensional model, II – model considering grain boundary layers as thin layers which bind and fix the nanometer grains, III – a simple model of the structure of NCMs

We consider NCMs as laminated composites with the following layers (Fig. 2 (III)): Layer A which is a grain-boundary layer with width equal to w (grain-boundary width); layer B which is treated as a fibre-composite layer where the matrix consists of grain-boundary layers, and fibres are grain cores; the width of layer B is equal to d-w ($d - 2w/2$). The model presented in Fig. 2 (III) enables one to predict elastic moduli of NCMs.

3. Elastic modulus

According to Fig. 2 (III) and by applying the laws of classical mechanics to the laminated composite, Young's modulus of NCMs can be evaluated under the assumption that the nanocrystalline bulk is subject to a tensile stress acting in a direction perpendicular to layer A:

$$\frac{1}{E} = \frac{f_A}{E_A} + \frac{f_B}{E_B} \tag{1}$$

where E, E_A and E_B are Young's modulus of the bulk, layer A and layer B, respectively, and f_A and f_B are the volume fractions of layers A and layer B, respectively; Figure 2 (III) shows that f_A and f_B can be expressed as follows:

$$f_A = \frac{w}{w + (d - w)} = \frac{w}{d}, \qquad f_B = 1 - f_A = \frac{d - w}{w + (d - w)} = \frac{d - w}{d} \tag{2}$$

Figure 2 (III) shows that E_A is equal to E_{gb} (Young's modulus of grain-boundary layers) where E_B can be calculated from Eq. (3), assuming that the nanocrystalline bulk and layer B are subject to tensile forces acting in a direction perpendicular to layer B (Fig. 2)

$$E_B = f_M E_M + f_F E_F \tag{3}$$

f_M denotes the volume fraction of matrix (grain-boundary layers) in layer A and f_F denotes the volume fraction of fibres (grain cores) in layer A; E_M is Young's modulus of the matrix in layer A which is equal to E_{gb}; E_F in Eq. (3) shows Young's modulus of fibres in layer A which is equal to E_g (Young's modulus of grain cores). According to Fig. 3, the values of f_M and $f_{g\text{-}B}$ can be calculated by the following relations:

$$\begin{aligned} f_M &= \frac{2\frac{w}{2}(d - w)}{(d - w)^2 + 2 \times \frac{w}{2} \times (d - w)} f_B = \frac{w}{d} \times \frac{d - w}{d} = \frac{w(d - w)}{d^2} \\ f_F &= (1 - f_{gb-B}) f_B = \frac{(d - w)^2}{(d - w)^2 + 2 \times \frac{w}{2} \times (d - w)} \frac{d - w}{d} = \frac{(d - w)^2}{d^2} \end{aligned} \tag{4}$$

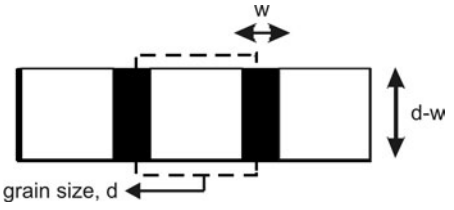

Fig. 3. Scheme of the layer B as used for calculating $f_{gb\text{-}B}$ and $f_{g\text{-}B}$

Therefore the values of Young's moduli of nanocrystalline materials can be calculated by substituting Eqs. (2)–(4) into Eq. (1):

$$\frac{1}{E} = \frac{\frac{w}{d}}{E_{gb}} + \frac{\frac{d-w}{d}}{E_{gb}\frac{w(d-w)}{d^2} + E_g\frac{(d-w)^2}{d^2}} \tag{5}$$

or

$$\frac{1}{E} = \frac{\frac{w}{d}}{E_{gb}} + \frac{d}{E_{gb}w + E_g(d-w)} \tag{6}$$

The important point about Eq. (6) is that it models the change of E with grain size. Equation (7) represents Eq. (6) where E is normalized to E_0 (or E_g) for the perfect crystal lattice

$$\frac{E_0}{E} = \frac{\frac{w}{d}}{\frac{E_{gb}}{E_0}} + \frac{d}{\frac{E_{gb}}{E_0}w + (d-w)} \tag{7}$$

It is generally accepted that the elastic modulus of the amorphous alloy is 60–75% or 70–80% of that of the corresponding equilibrium crystalline alloys [8, 9]. So the ratio E_{gb}/E_g is about 0.7. A similar ratio for E_{gb}/E_g is also assumed in previous works [1–4]. The change of E with grain size has also been modelled by Shen et al. [10] assuming that the modulus is influenced by the grain interior, grain boundary, and grain boundary triple junctions. Different contributions to Young's modulus are estimated according to the rule of mixtures for composite materials by considering their volume fractions. Equations (8) and (9) represent the upper and lower bounds of the rule of mixtures, where E is normalized to the E_0 for a perfect crystal lattice.

$$\frac{E}{E_0} = (1 - V_{gb} - V_{tj}) + Vgb\frac{E_{gb}}{E_0} + V_{tj}\frac{E_{tj}}{E_0} \tag{8}$$

$$\frac{E_0}{E} = (1 - V_{gb} - V_{tj}) + \frac{V_{gb}}{\frac{E_{gb}}{E_0}} + \frac{V_{tj}}{\frac{E_{tj}}{E_0}} \tag{9}$$

V_{gb} and V_{tj} are the volume fractions of the grain boundaries and triple junctions respectively; moreover, Shen et al. assumed E_{gb}/E_0 to be 0.7 and E_{tj}/E_0 to be 0.75. Figure 4 depicts the comparison between Eq. (7), Eqs. (8) and (9) and the experimental data. Figure 4 shows the calculated values of E/E_0 according to $E_{gb}/E_g = 0.7$ and $w = 1$ nm.

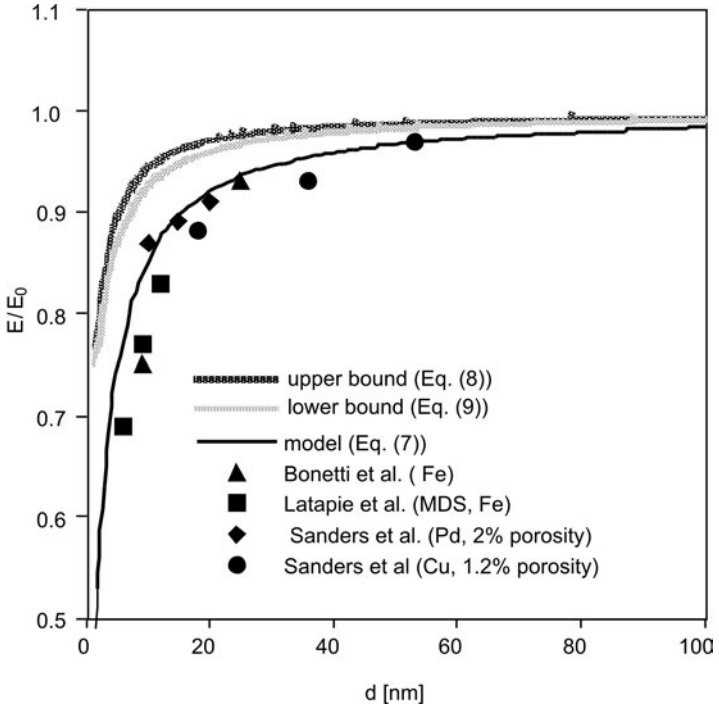

Fig. 4. Dependence of the E/E_0 ratio on the grain size for calculated values and previous works

From Figure 4 it can be concluded that elastic moduli of NCMs are essentially the same as those for conventional grain size materials until the grain size becomes very small (< 20 nm). Because grain boundaries occupy a larger fraction of the total volume in samples with smaller grain sizes, the decrease in E/E_0 could be attributed to the large number of atoms associated with grain boundaries and triple junctions. Since the elastic modulus is a measure of the bonding between the atoms, the reduction of E for both grain boundaries and NCMs can be explained in terms of the increased spacing between atoms in the grain boundaries and triple junctions [1, 13, 14]. The increased spacing between atoms in grain boundaries is schematically shown in Fig. 1 (left).

From Fig. 4 it can be seen that there is a good agreement between the experimental data and the predictions of the model; however, the values predicted from the model are lower than both those from the upper bond model and from the lower bond model. Figure 4 also shows that both the upper bond model and the lower bond model predict higher values than the experimental results. Latapie and Farkas assumed Young's modulus for the grain boundary and triple junction components to be 45% and 50%,respectively, of those of the grain interior, i.e., 45% for E_{gb}/E_0 and 50% for E_{tj}/E_0 [1]. Using these values, the calculated data are situated between the upper and lower bound of the rule of mixtures for composite materials [1]. When the grain size is 1 nm, E/E_0 is 0.75 (Fig. 4), being equal to the assumed value for E_{tj}/E_0. However, according to the presented model, E/E_0 is equal to 0.35 when the grain size 1 nm.

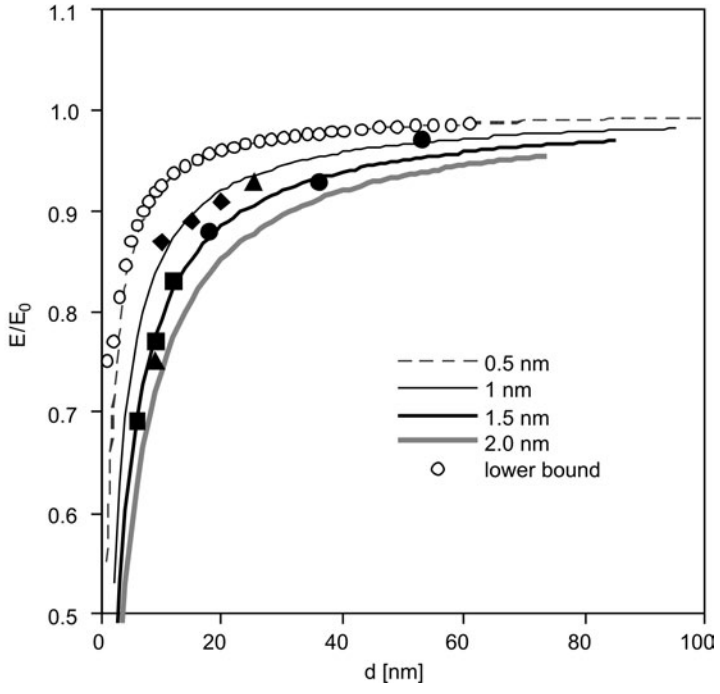

Fig. 5. The effect of grain boundary width on the ratio E/E_0

As an illustration of the effect of grain boundary width on E, Fig. 5 shows the results of calculation using Eq. (7), with w in the range of 0.5–2 nm. It can be seen from this figure that the higher the value of the grain boundary width, the lower the modulus of elasticity. That is because higher grain boundary thicknesses increase the value of f_{gb}. Therefore, the contribution of grain boundaries in the microstructure will be greater, and, because of the lower amount of E_{gb}, E will decrease.

Theoretically, there is a limit to the presented model; according to Fig. 3, the model is valid only for grain sizes (d) higher than grain boundary width (w). Another limit to the developed model is the lowest limit of the crystallite size (d) which leads

to the instability of the crystallite structure with respect to the amorphous structure. Such a crystalline-to-amorphous transition has been found in silicon for a crystallite size of about 30 Å [15]. The thermodynamic criterion of such a transition has been discussed elsewhere [15].

4. Conclusion

A new composite model for the structure of nanocrystalline materials was presented. It was supposed that nanocrystalline materials could be considered as layered composites. Based on the model, a new approach to investigate the effect of grain size on elastic moduli of nanocrystalline materials was introduced. Results show that when the grain size is smaller than 20 nm, Young's modulus of a nanocrystalline material strongly decreases. The predictions of the model were compared with the experimental data, and a strong correlation was observed.

References

[1] LATAPIE A., FARKAS D., Scripta Mater., 48 (2003), 611.
[2] ZHAO S., ALBE K., HAHN H., Script. Mater., 55 (2006), 473.
[3] KIM H., BUSH M., Nanostruct. Mater., 11(1999), 361.
[4] QING X., XINGMING G., Int. J. Solids Struct., 43 (2006), 7793.
[5] GLEITER H., Prog. Mater. Sci., 33 (1989), 223.
[6] GLEITER H., Acta Mater., 48 (2000), 1.
[7] MEYERS M.A., MISHRA A., BENSON D.J., Prog. Mater. Sci., 51 (2006), 427.
[8] POLK D.E., GIESSEN B.C., GARDDNER F.G., Mater. Sci. Eng., 25 (1976), 309.
[9] MATSUMOTO T., MADDIN R., Mater. Sci. Eng., 19 (1975), 1.
[10] SHEN T.D., KOCH C.C., TSUI T.Y., PHARR G.M., J. Mater. Res., 10 (1995), 2892.
[11] BONETTI E., CAMPARI E.G., DELBIANCO L., SCIPIONE G., Nanostruct. Mater., 6 (1995), 639.
[12] SANDERS P.G., EASTMAN J.A., WEERTMAN J.R., Acta. Mater., 45 (1997), 4019.
[13] WELLER M., DIEHL J., SCHAEFER E.E., Phil. Mag. A., 63 (1991), 527.
[14] CHEN D., Mater. Sci. Eng. A., 190 (1995), 193.
[15] VEPREK S., IQBAL Z., SAROTT F.A., Phil. Mag. B., 45 (1982), 137.

Received 12 December 2007
Revised 2 February 2008

Materials Science-Poland, *Vol. 27*, *No. 1*, *2009*

Improvement of $LiCoO_2$ cathodes by using $Ag_2V_4O_{11}$ as an additive

X. CAO*, J. LIU, J. WAN, L. XIE, X. YAN, H. WANG

School of Chemistry and Chemical Engineering, Henan University of Technology, Zhengzhou, 450001 P.R. China

$LiCoO_2/Ag_2V_4O_{11}$ composites were fabricated as cathode materials for lithium ion batteries by mechanical mixing of commercial $LiCoO_2$ and $Ag_2V_4O_{11}$ powders. The underlying principle of this idea was that the metallic silver particles were formed and acted as a conducting matrix when $Ag_2V_4O_{11}$ cathode was electrochemically reduced which could significantly increase the electronic conductivity and decrease the polarization of cathode materials. The structure, morphology and electrochemical performance of bare $LiCoO_2$ and $LiCoO_2/Ag_2V_4O_{11}$ composites were analyzed by XRD, SEM and charge-discharge test of CR2016 coin cells. The results show that a low amount of $Ag_2V_4O_{11}$ additive can effectively enhance the discharge capacity and cycleability of $LiCoO_2$. The composite containing 3 wt. % of $Ag_2V_4O_{11}$ exhibits a higher discharge capacity and better cycle life than bare $LiCoO_2$.

Key words: *lithium-ion batteries; electrochemical performance; $LiCoO_2$; $Ag_2V_4O_{11}$ additive*

1. Introduction

Layered $LiCoO_2$ oxide has been widely applied as cathode active material for Li -ion batteries. Ease of preparation, excellent electrochemical properties and high tap density make it the most commercially used cathode material. In the upcoming years, $LiCoO_2$ will continue to maintain its leading position in terms of market share, despite increasing research into alternative materials such as $LiNi_xCo_{1-x}O_2$, $LiNi_xMn_yCo_{1-x-y}O_2$ and $LiFePO_4$ [1]. However, in general, the maximum delivery capacity of $LiCoO_2$ is around half of its theoretical value (274 mAh/g) due to a large structural change that occurs during the Li^+ deintercalation process [2]. Therefore, how to increase the practical usable capacity of $LiCoO_2$ is a very important and exciting problem.

Nevertheless, the electronic conductivity of $LiCoO_2$ powder is low, and thus $LiCoO_2$ must be well-combined with electro-conductive additives, such as carbon black and acetylene black, for use as active cathode materials. Usually, the total

*Corresponding author, e-mail: caoxy@haut.edu.cn

amount of carbon black and binder must be more than 15% of the total weight of the electrode materials in order to maintain a good conductivity and a mechanical stability of the cathodes [3]. On the other hand, use of excess electro-conductive additives will incur a fall in the energy and power densities for lithium ion batteries. In order to reduce the inert weight of carbon black and improve the electrochemical performance of the cathodes, use of electronically conducting matrices such as polymers, metallic particles and metal fibres has been proposed [3–6].

More recently, Wen et al. [4] developed a novel method with $AgNO_3$ as a starting material to prepare an $LiCoO_2$/Ag composite cathode material for improving the discharge properties such as discharge capacity and rate-capability. It is found that the electronic conductivity of the $LiCoO_2$/Ag composite is significantly enhanced compared with bare $LiCoO_2$, which contributes to a reduced charge-transfer resistance. However, this method greatly suffers from its implementational complexity, because it requires an extra thermal decomposition of the mixture of $LiCoO_2$ and $AgNO_3$ in order to obtain the $LiCoO_2$/Ag composite. It is well known that $Ag_2V_4O_{11}$ is a very important cathode material for lithium primary batteries, and that the Li–$Ag_2V_4O_{11}$ battery system has been used as a power source for implantable cardiac defibrillators (ICDs) [7]. With regard to the discharge characteristics of $Ag_2V_4O_{11}$ cathodes, it is widely acknowledged that metallic silver particles are formed during early states of discharge [7]. However, metallic silver cannot be completely oxidized to Ag^+ and returned to $[V_4O_{11}]$ layers when an $Ag_2V_4O_{11}$ cathode is recharged in terms of ex-situ XRD of cycled $Ag_2V_4O_{11}$ electrode [8]. Considering this fact, we developed a simple technique by mixing the commercial $LiCoO_2$ and $Ag_2V_4O_{11}$ powders and performing a particular charge-discharge regime for improving the charge-discharge properties of $LiCoO_2$. The structure, morphology and electrochemical properties of bare $LiCoO_2$ and $LiCoO_2$/$Ag_2V_4O_{11}$ composites are analyzed by XRD, SEM and a charge-discharge test of CR2016 coin cells.

2. Experimental

Commercial $LiCoO_2$ powder from Hunan Reshine New Material Co., Ltd, China, was used as a bare material for the preparation of $LiCoO_2$/$Ag_2V_4O_{11}$ composites. $Ag_2V_4O_{11}$ and commercial $LiCoO_2$ powders at various weight ratios (3, 5 and 9 wt. % of $Ag_2V_4O_{11}$) were homogeneously mixed by mechanical pestling in an agate mortar. The samples were designated as $LiCoO_2$/$Ag_2V_4O_{11}$-3, $LiCoO_2$/$Ag_2V_4O_{11}$-5 and $LiCoO_2$/$Ag_2V_4O_{11}$-9, respectively.

$Ag_2V_4O_{11}$ powders were prepared by the rheological phase method, as described previously [9]. Stoichiometric ratios of Ag_2CO_3 and NH_4VO_3 were mixed thoroughly by grinding in an agate mortar. The solid-liquid rheological body (muddy state) was obtained by adding distilled water dropwise. Then the rheological body was transferred to a cylindrical, Teflon-lined, stainless autoclave. The sealed autoclave was heated in table-drying and air circulation oven at 90 °C for 5 h and then dried at 120 °C for 8 h. The resulting yellow precursor was obtained by grinding the air-dried

rheological body. Finally, using an alumina crucible as container, the precursor was heated in a muffle furnace (Nabertherm, N7/H) at 500 °C in air for 10 h to obtain the final $Ag_2V_4O_{11}$ powders.

X-ray diffraction (XRD) analysis of the materials was carried out on an XRD-Pert Pro diffractometer (XPERT PRO MPD, Netherlands) with CoK_α radiation (λ = 1.78901 Å). The morphological feature of the so-prepared powders was observed on the SEM- JSM6380LA (JEOL, Japan). The working electrodes were composed of the $LiCoO_2/Ag_2V_4O_{11}$ composite powders, acetylene black and polytetrafluoethylene (PTFE) binder at the weight ratio of 80:10:10. The stainless-steel meshes were used as the current collectors. The CR2016 coin cells were assembled with pure lithium foil as counter electrodes, Celgard-2400 as the separator, 1 mol/dm^3 $LiClO_4$ dissolved in ethylene carbonate (EC) and dimethyl carbonate (DMC) solution (v/v, 1:1) as the electrolyte. All the coin cells were assembled in a dry glove box and tested on a multichannel Neware-battery tester (Neware, Shenzhen) at the ambient temperature. The operational capacity of $Ag_2V_4O_{11}$ is mainly under 3 V but there is hardly any capacity below 3 V for $LiCoO_2$. Therefore, the $LiCoO_2/Ag_2V_4O_{11}$ composite cathode was initially discharged down to a cut-off voltage of 2 V in order to obtain a large number of metallic silver particles. Subsequently, a normal charge-discharge test was cycled at the constant current rate of 30 mA/g (ca. 1.0 mA/cm^2) in the range of 3–4.3 V.

3. Results and discussion

The XRD patterns of the commercial $LiCoO_2$ powder and the $LiCoO_2/Ag_2V_4O_{11}$ composites are presented in Fig. 1. All the characteristic diffraction peaks of $LiCoO_2$ have been marked with asterisks in Fig. 1, curve d, and correspond to a well-defined hexagonal layered structure. Additionally, the characteristic diffraction peaks of $Ag_2V_4O_{11}$ powder are also found, though they are almost submerged by the baselines of XRD patterns due to a relatively higher amplitude of the $LiCoO_2$ diffraction peaks. The inset of Fig. 1d illustrates an expanded view of local XRD patterns of $Ag_2V_4O_{11}$ in the range of 22–40° in 2θ. Obviously, $Ag_2V_4O_{11}$ cannot be doped in the layered structure of $LiCoO_2$, and the $Ag_2V_4O_{11}$ containing specimen was just a composite of the $Ag_2V_4O_{11}$ and $LiCoO_2$ powders.

SEM micrographs of bare $LiCoO_2$ and $LiCoO_2/Ag_2V_4O_{11}$ composites are shown in Fig. 2. Bare $LiCoO_2$ in Fig. 2a clearly demonstrates the original particle shape of $LiCoO_2$, and its surface is smooth. Three composite samples in Figs. 2b–d reveal that the particle shape of $LiCoO_2$ is not changed. Moreover, it is clearly observed that $Ag_2V_4O_{11}$ powders, as submicrometric particles, are highly dispersed on the surface of the $LiCoO_2$ powders. The higher the $Ag_2V_4O_{11}$ content in the powder, the greater is the surface coverage of $LiCoO_2$ by the $Ag_2V_4O_{11}$ particles. The XRD and SEM results confirm the assumption that the addition of $Ag_2V_4O_{11}$ powder does not modify the ordered layer structure of $LiCoO_2$.

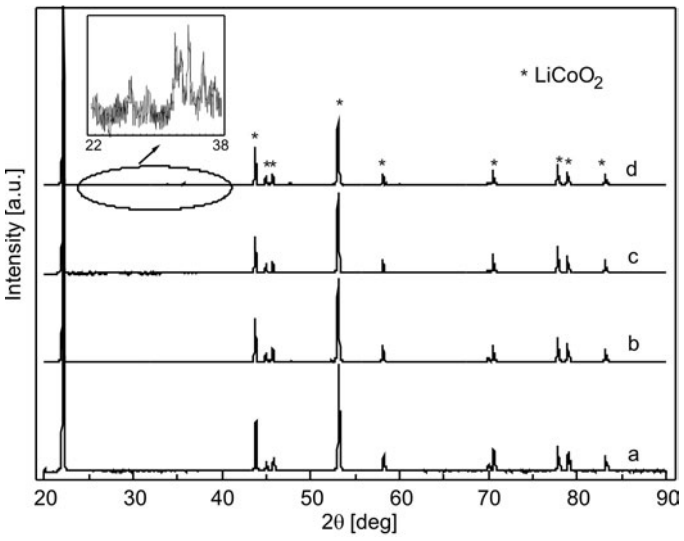

Fig. 1. XRD patterns of bare $LiCoO_2$ (a) and of $LiCoO_2/Ag_2V_4O_{11}$ composites of various $Ag_2V_4O_{11}$ contents: 3 wt. % (b), 5 wt. % (c), 9 wt. % (d)

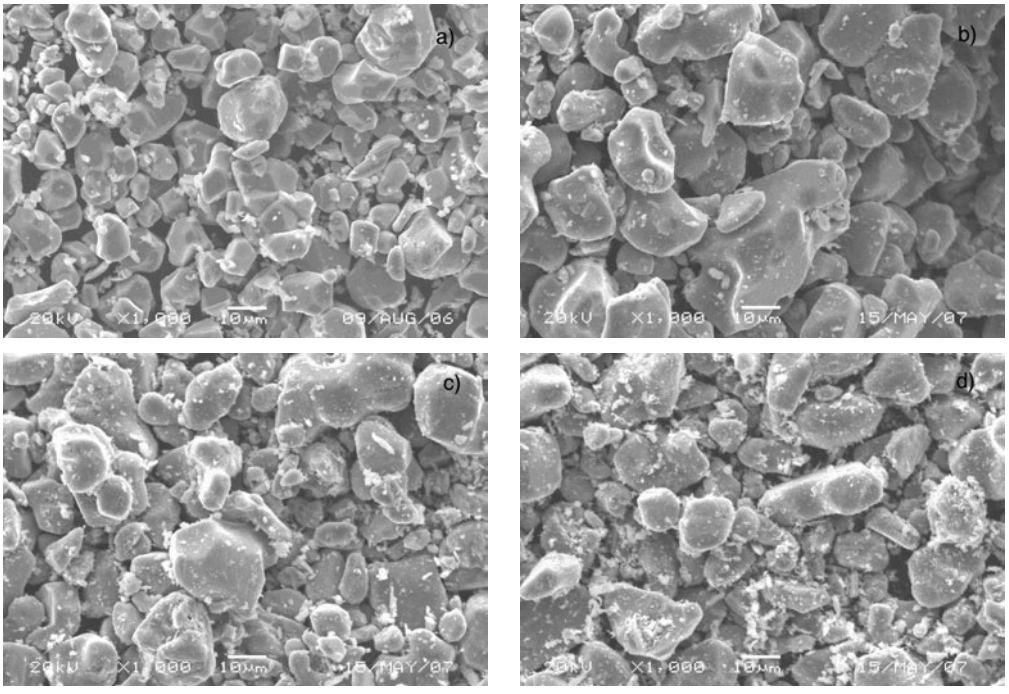

Fig. 2. SEM micrographs of bare $LiCoO_2$ (a) and of $LiCoO_2/Ag_2V_4O_{11}$ composites of $Ag_2V_4O_{11}$ contents: 3 wt. % (b), 5 wt. % (c), 9 wt. % (d)

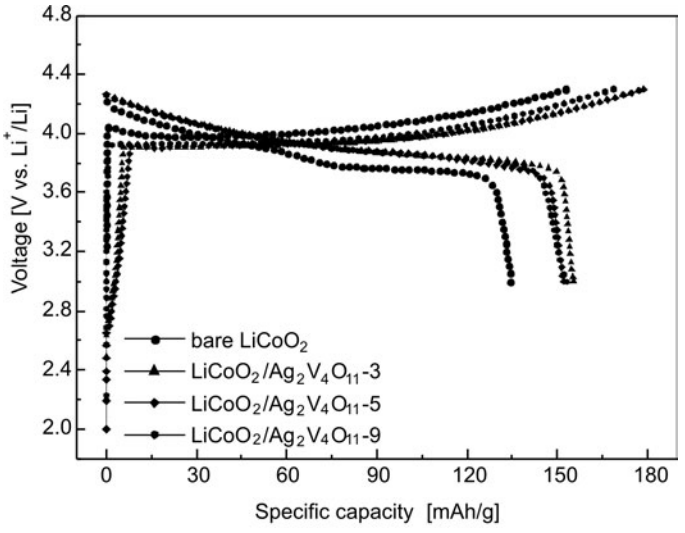

Fig. 3. Initial charge-discharge curves of bare $LiCoO_2$ and of $LiCoO_2/Ag_2V_4O_{11}$ composites of various $Ag_2V_4O_{11}$ contents

Figure 3 shows the initial charge-discharge curves of bare $LiCoO_2$ and of the $LiCoO_2/Ag_2V_4O_{11}$ composites. From the curves, we can see that bare $LiCoO_2$ has an initial discharge capacity of 134.5 mAh/g. However, for the $LiCoO_2/Ag_2V_4O_{11}$-3, $LiCoO_2/Ag_2V_4O_{11}$-5 and $LiCoO_2/Ag_2V_4O_{11}$-9 composites, the initial discharge capacities are equal to 155.4, 152.1 and 153.3 mAh/g, respectively. The initial discharge capacities of the $LiCoO_2/Ag_2V_4O_{11}$ composites are increased in all cases compared with that of bare $LiCoO_2$. In addition, the discharge plateaus of the $LiCoO_2/Ag_2V_4O_{11}$ composites are much higher than that of bare $LiCoO_2$ but, on the other hand, the charge plateaus of the $LiCoO_2/Ag_2V_4O_{11}$ composites are much lower than that of bare $LiCoO_2$. This observation indicates that the $LiCoO_2/Ag_2V_4O_{11}$ composites undergo a depressed electrode polarization during the charge-discharge process. The likely reason for the improved capacity should correspond strongly to the special discharge-charge regime. When the discharge procedure was first performed for $LiCoO_2/Ag_2V_4O_{11}$ composites with a cut-off voltage of 2 V, the metallic silver particles were formed. Such particles uniformly coated on $LiCoO_2$ may act as an electronic conductor, enhancing the surface intercalation reaction and decreasing the polarization of electrodes.

The selective charge-discharge curves of bare $LiCoO_2$ and $LiCoO_2/Ag_2V_4O_{11}$-3 composite are presented in Fig. 4. Charge–discharge curves of bare $LiCoO_2$ display only one plateau, corresponding to the intercalation/deintercalation of Li^+ into/out of the layered $LiCoO_2$. The shape of charge–discharge curves for various cycles is similar, and the discharge capacity of the 10th cycle is 135.3 mAh/g. However, the $LiCoO_2/Ag_2V_4O_{11}$-3 composite exhibits a better charge–discharge performance in comparison with bare $LiCoO_2$. The charge curves of the $LiCoO_2/Ag_2V_4O_{11}$-3 composite for different cycles almost overlap each other and the discharge capacities of the 7th

and 10th cycles are 153.4 and 153.7 mAh/g, respectively, which indicates that the $LiCoO_2/Ag_2V_4O_{11}$-3 composite has excellent electrochemical stability. It is noteworthy that the discharge curves of the $LiCoO_2/Ag_2V_4O_{11}$-3 composite display two plateaus despite its imperceptibility which will be proved later in the differential capacity curve.

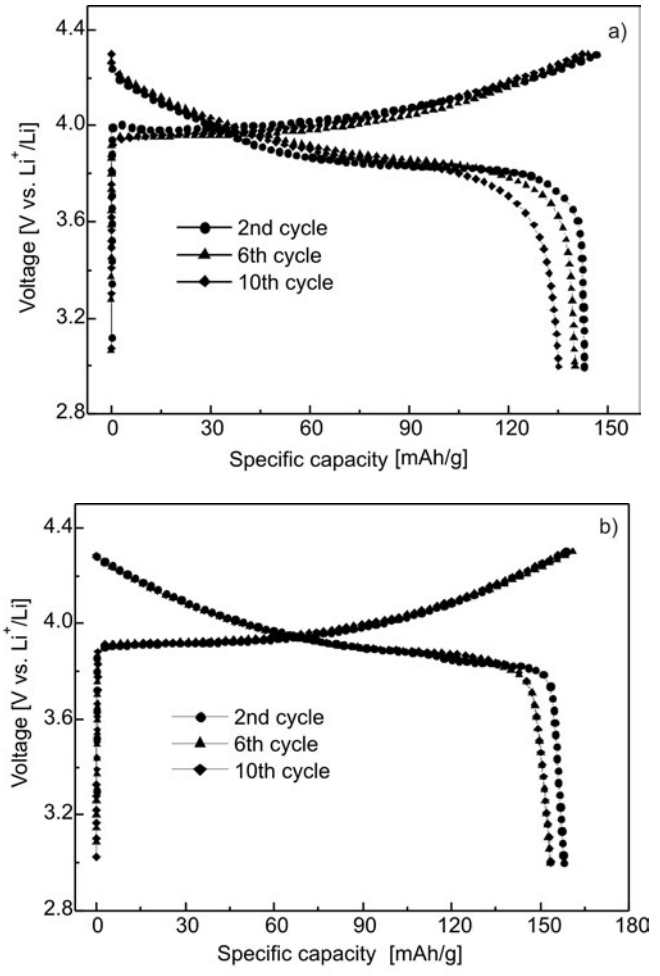

Fig. 4. Selective charge–discharge curves of a) bare $LiCoO_2$, and b) $LiCoO_2/Ag_2V_4O_{11}$-3 composite

The differential capacity curves of bare $LiCoO_2$ and the $LiCoO_2/Ag_2V_4O_{11}$-3 composite calculated from the 2nd charge-discharge curve are shown in Fig. 5, which emphasizes the details of the voltage curves. As shown in Fig. 5, there is one pair of peaks in the differential capacity curves for bare $LiCoO_2$, which is characteristic of the layered $LiCoO_2$ system and corresponds to the plateaus in the charge/discharge curves. It is interesting to observe a well defined reduction peak at about 3.89 V for the Li-

$CoO_2/Ag_2V_4O_{11}$-3 composite. It may be ascribed to the reduction of Ag^+ to Ag, because the redox reaction of the Ag^+/Ag couple still takes place between 3.0 and 4.3 V. This reduction peak is considered to be favourable because the electronic conductivity of $LiCoO_2/Ag_2V_4O_{11}$-3 composite is increased during the discharge. However, the oxidation peak attributed to the Ag^+/Ag couple is not observed in Fig. 5. A detailed investigation into the functional mechanism of $Ag_2V_4O_{11}$ in $LiCoO_2/Ag_2V_4O_{11}$ composites is currently in progress.

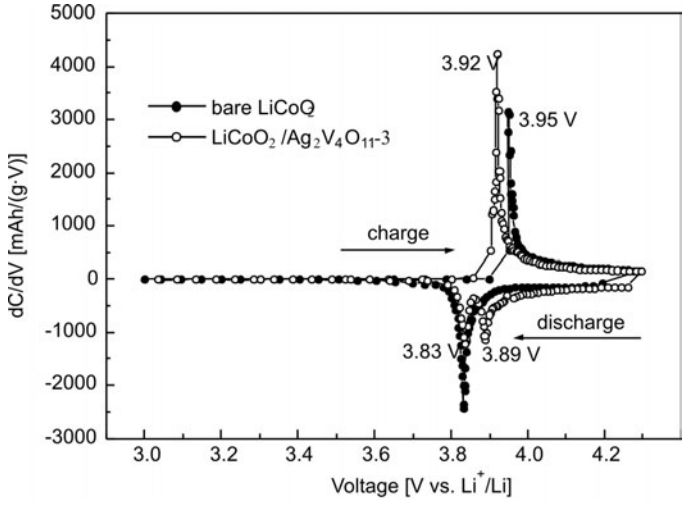

Fig. 5. Differential capacity vs. voltage curves for bare $LiCoO_2$ and $LiCoO_2/Ag_2V_4O_{11}$-3 composite

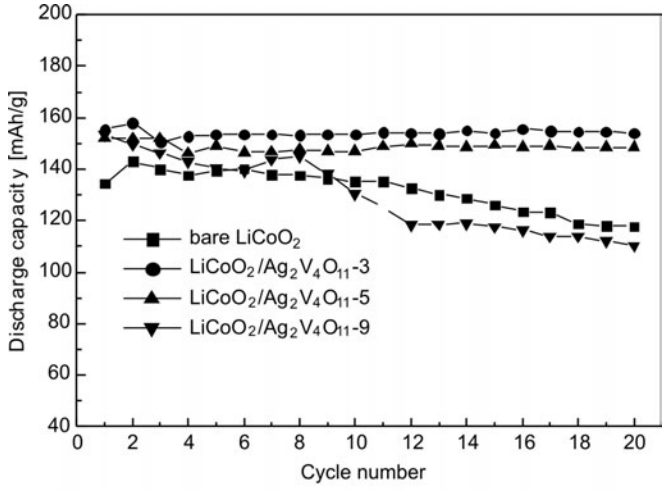

Fig. 6. Galvanostatic cycling of bare $LiCoO_2$ and $LiCoO_2/Ag_2V_4O_{11}$ composites at 30 mA/g between 3.0 and 4.3 V

The dependence of discharge capacity on the number of cycles for the materials collected at the current rate of 30 mA/g between 3.0 and 4.3 V is shown in Fig. 6. The stability of the $LiCoO_2/Ag_2V_4O_{11}$-3 and $LiCoO_2/Ag_2V_4O_{11}$-5 composites is excellent compared to bare $LiCoO_2$, though the profile of the discharge capacity follows a decreasing trend in function of increasing $Ag_2V_4O_{11}$ powder content. The $LiCoO_2$ /$Ag_2V_4O_{11}$-3 composite exhibits a stable discharge capacity of about 153.5 mAh/g within 20 cycles. In comparison, the discharge capacity of the $LiCoO_2/Ag_2V_4O_{11}$-5 composite is decreased but still stabilizes at about 148 mAh/g after 20 cycles. However, cycling the $LiCoO_2/Ag_2V_4O_{11}$-9 composite cell leads to rapid capacity fading after 10 cycles. This phenomenon should be attributed to the charge-discharge characteristics of the $Ag_2V_4O_{11}$ cathode. When the content of $Ag_2V_4O_{11}$ powder is low, the metallic silver particles formed during the discharge serve as a conducting matrix and increase the conductivity of the $LiCoO_2$ material. On the other hand, the structural character of $Ag_2V_4O_{11}$ is a very important factor that affects the electrochemical performance of $LiCoO_2/Ag_2V_4O_{11}$ composite and cannot be neglected when the content of $Ag_2V_4O_{11}$ powder is high. Long-term cycling in the silver reduction-oxidation region incurs a large volume change of cathode material, which probably results in rapid capacity fading [7]. Thus, an appropriate amount of $Ag_2V_4O_{11}$ additive is essential to improve the electrochemical performance of $LiCoO_2$.

4. Conclusions

A novel method is described for the preparation of $LiCoO_2/Ag_2V_4O_{11}$ composites by a simple mechanical mixing procedure. The low content of $Ag_2V_4O_{11}$ additive has been proved to be favourable to the discharge capacity and the cycleability of $LiCoO_2$. The composite containing 3 wt. % of $Ag_2V_4O_{11}$ exhibits the first discharge capacity as high as 155.4 mAh/g in the range of 3.0–4.3 V at the current rate of 30 mA/g and remains at a stable discharge capacity of about 153.5 mAh/g within 20 cycles, which is much higher than that of bare $LiCoO_2$. Therefore, we believe that this method not only provides an alternative to improving the electrochemical performance of $LiCoO_2$, but also is feasible in preparing other improved $LiCoO_2$ composites by adopting other silver vanadium oxides such as $AgVO_3$ and $Ag_{1.2}V_3O_8$.

Acknowledgement

The authors gratefully acknowledge support from the Ph.D. Programs Foundation of Henan University of Technology (No. BS2006011).

References

[1] TARASCON J.M., ARMAND M., Nature, 414 (2001), 359.
[2] ALCANTARC R., LAVELA P., TIRADO J.L., J. Solid State Chem., 134 (1997), 265.
[3] FENG C.Q., CHEW S.Y., GUO Z.P., WANG J.Z., LIU H.K., J. Power Sources, 174 (2007), 1095.

[4] HUANG S.H., WEN Z.Y., YANG X.L., GU Z.H., XU X.H., J. Power Sources, 148 (2005), 72.
[5] CROCE F., EPIFANIO A., HASSOUN J., DEPTULA A., OLCZAC T., SCROSATI B., Electrochem. Solid State Lett., 5 (2002), A47.
[6] AHN S., KIM Y., KIM K. J., KIM T. H., LEE H., KIM M. H., J. Power Sources, 81–82 (1999), 896.
[7] WEST K., CRESPI A.M., J. Power Sources, 54 (1995), 334.
[8] CAO X.Y., Ph.D. Thesis, Wuhan University, China, 2006.
[9] CAO X.Y., ZHAN H., XIE J.G., ZHOU Y.H., Mater. Lett., 60 (2006), 435.

Received 26 December 2008
Revised 2 February 2009

Materials Science-Poland, *Vol. 27*, *No. 1*, *2009*

Dielectric and microhardness studies of methylene blue doped PMMA matrix

A. K. ADIYODI, X. JOSEPH, P. V. JYOTHY, G. JOSE, N. V. UNNIKRISHNAN*

School of Pure and Applied Physics, Mahatma Gandhi University, Kottayam, India–686560

Pure and methylene blue (MB) doped poly(methyl methacrylate) (PMMA) samples were prepared by free radical vinyl polymerization. The effect of methylene blue, which itself is polar in nature, on the glass transition temperature, electric permittivity, and microhardness of the PMMA matrix was studied. It was found that incorporation of the dye increases the electric permittivity and decreases the glass transition temperature of the system. The maximum value of the loss tangent below the glass transition temperature suggests the rotation of the ester side group (β relaxation). MB can also act as a retarder of free radical polymerization causing reduction in the hardness value.

Key words: PMMA; methylene blue; electric permittivity; microhardness

1. Introduction

Organic dye–polymer composites have received considerable attention as a family of potentially new electrooptic materials, because of their interesting dielectric properties such as the ability of an electric field to polarize the material to create electric dipoles. These are basically insulators having the property of storing and dissipating electrical energy when subjected to an electromagnetic field. Organic dyes possess conjugated molecular structures with terminating electron donors and acceptors and large dipole moments, and hence can be oriented in a high static field. The dyes can change the electric permittivity and the electrooptic coefficients of the polymer system [1, 2]. The dye polymers are used in dye lasers, storage materials, capacitors, etc. Many of dye polymer systems have a number of advantages as nonlinear optical materials with high optical quality and processibility. Therefore it is important to understand the effect of the organic dye molecules on the physical, dielectric and mechanical properties of such systems.

The structure of the polymer determines its polarity and hence many of the dielectric properties of the polymer. In polar plastics, dipoles are created by an imbalance in

*Corresponding author, e-mail: nvu50@yahoo.co.in

the distribution of electrons, and in the presence of an electric field the dipoles will tend to align with the field direction. Examples of polar plastics are PMMA, polyvinyl chloride (PVC), polyamide (PA, Nylon), polycarbonate (PC) etc. to name a few. These materials tend to be only moderately good as insulators. The addition of the polar dye such as methylene blue, enables the system to be more polarizable, hence contributing more to the electric permittivity [3]. In addition, such polar dyes can modify the glass transition temperature and microhardnes of the polymer. In view of these facts, we report the effect of methylene blue on the glass transition temperature, electric permittivity, and the hardness of a pure PMMA matrix.

2. Experimental

Five samples A, B, C, D and E with varying concentrations of methylene blue were prepared (Table 1) by bulk polymerization.

Table 1. Compositions and physical parameters of the samples

Parameter	Sample				
	A	B	C	D	E
PMMA V [cm^3]	2	2	2	2	2
Methylene blue c [M]	0	0.5×10^{-3}	1×10^{-3}	1.5×10^{-3}	2×10^{-3}
Thickness [mm]	1.15	0.77	0.90	0.80	1.10
Area [mm^2]	50	67	55	0.65	55

For the preparation of samples, the monomer MMA is mixed with a respective dye dissolved in ethyl alcohol in the ratio 4:1. 1 g of benzoyl peroxide per 100 cm^3 of the solution is used as an polymerization inhibitor. Accurately weighed MB is dissolved in ethanol since it has limited solubility in the monomer MMA. The monomer–alcohol mixture containing the dye and the inhibitor, in a glass test tube were kept in a bath maintained at 50 °C for polymerization. After polymerization the samples were cut into pieces of millimetre thickness using a crystal cutter and then thoroughly polished for further studies. The thickness of the sample was measured with a digital screw gauge. The dielectric measurements were done using an impedance analyzer (Hioki impedance analyzer model 3531). The microhardness measurements of the samples were done using a Vicker's microhardness tester (Lietz). The glass transition temperature of the samples was measured by differential scanning calorimetry (Shimadzu DSC-60) under nitrogen atmosphere.

3. Results and discussion

PMMA is a transparent polymer, used as a shatterproof replacement of glass in a variety of applications. The material is one of the hardest polymers, rigid with

a glossy finish and good weather resistance. PMMA is a synthetic resin belonging to the family of polymeric organic compounds, and is made by free radical vinyl polymerization from the monomer methyl methacrylate (Fig. 1), having the chemical formula $(C_2O_5H_8)_n$. The structure of a PMMA macromolecule is linear with respect to the main carbon chain.

Methylene blue, belonging to a thiazene class of dyes, is also known as methylthionine chloride or 3,7 bis (dimethyl amino) phenothiazin-5-ium chloride or swiss blue. It has the molecular formula $C_{16}H_{18}ClN_3S$ and the molecular mass of 319.85 g/mol and the melting point of about 190 °C. It is stable under ordinary conditions. The structure of PMMA and methylene blue are shown in Fig. 2.

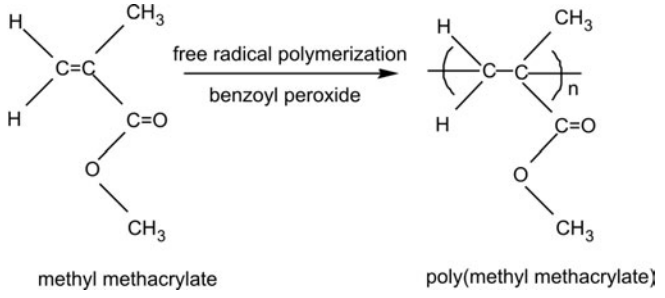

Fig. 1. Polymerization of MMA

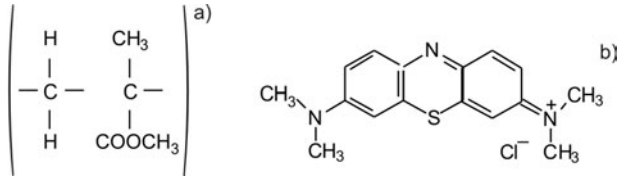

Fig. 2. The structure of PMMA (a) and methylene blue (b)

MB molecule is a polar molecule exhibiting good dielectric properties [4]. Methylene blue can also be used as a photosensitizer in free radical polymerization. The dye can be used as a polymerization inhibitor of several vinyl monomers [5].

Electric permittivity is a measure of the ability of a material to be polarized by an electric field. The dielectric properties of PMMA are determined by the strong electric dipole in the ester side group associated with the orientation of the ester group in the electric field [6, 7]. The electric permittivity decreases with frequency for pure PMMA (Fig. 3). The MB doped samples also show the same behaviour. For polar plastics, the alternating current frequency is an important factor because of the time taken to align the polar dipoles. At very low frequencies the dipoles have sufficient time to align with the field before it changes direction and hence the electric permittivity is high. At high frequencies, the dipoles do not have sufficient time to align before the field changes its direction and hence the electric permittivity is lower [8]. At intermediate

frequencies, the dipoles move but do not complete their movement before the field changes direction and they must realign with the changed field.

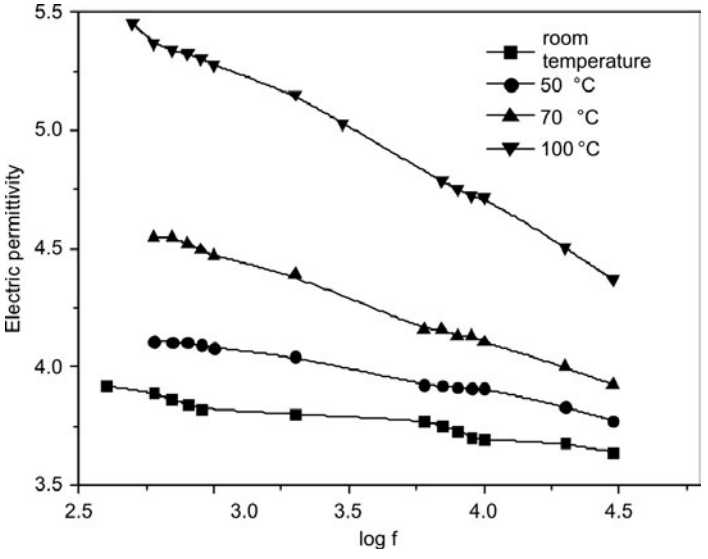

Fig. 3. Dependence of electric permittivity on the frequency of sample A at various temperatures

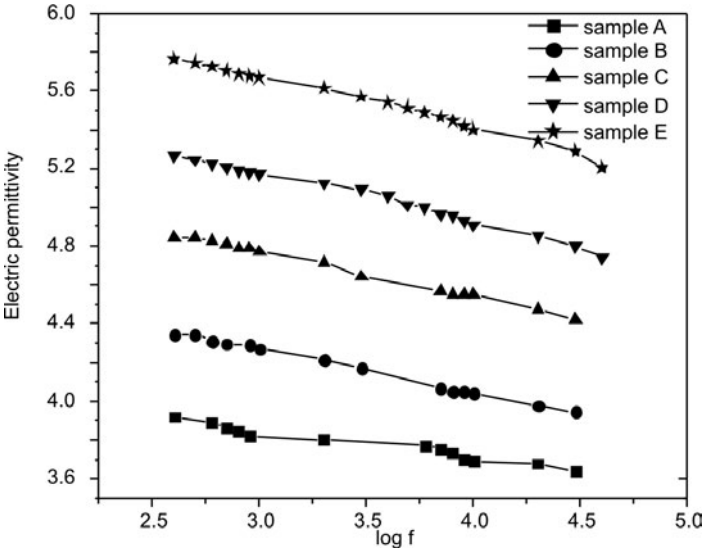

Fig. 4. Dependence of electric permittivity on the frequency of doped and undoped samples at room temperature

Figure 3 shows how the electric permittivity changes with temperature. The increase is due to an increase of polarization arising from the freer molecular motion of

polymer chains which allows orientation of dipolar units in the applied field. The increase is steeper at lower frequencies. At lower temperatures, the dipoles are rigidly fixed and hence the field cannot change the the dipoles. All the five samples exhibit the same behaviour at various frequencies. From Figure 4 it is evident that the electric permittivity increases when the dye is added to the matrix. Since MB is a polar molecule, the addition of the dye causes the number of dipoles to increase, which in turn increases the electric permittivity of the system [3]. The addition of a polar dye enables the system to be more polarizable and enhances the electric permittivity.

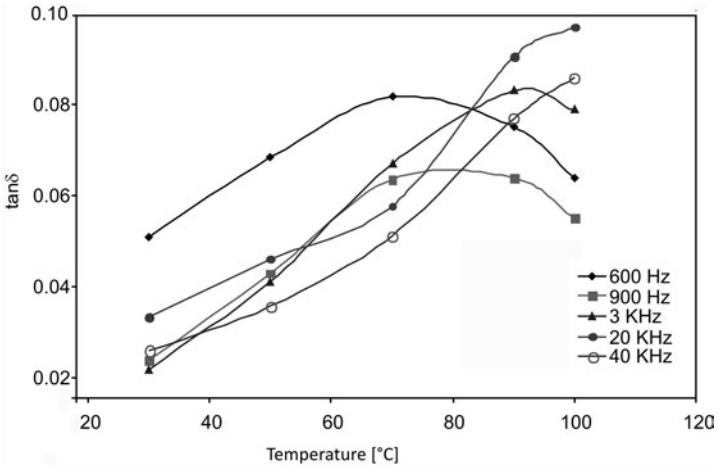

Fig. 5. Temperature dependence of loss tangent on temperature at various frequencies for sample A

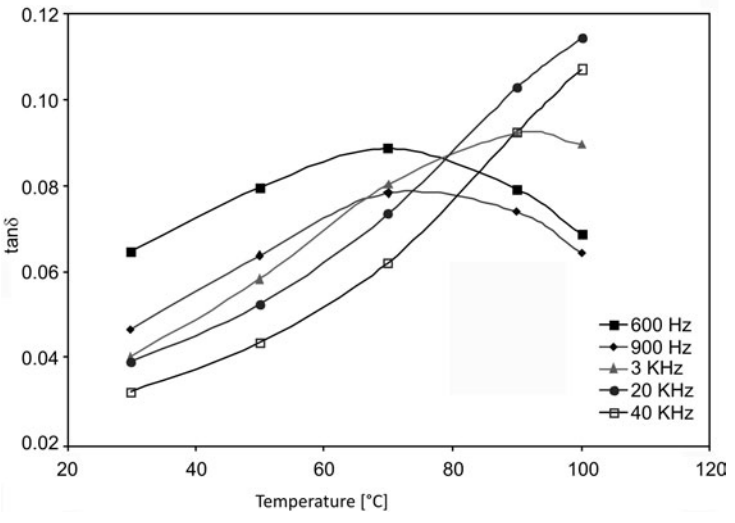

Fig. 6. Temperature dependence of loss tangent on temperature at various frequencies for sample C

The variations of loss tangent with temperature at various frequencies for samples A and C are shown in Figs. 5 and 6. Each tanδ curve has a maximum depending on the frequency of the applied field. In these figures, a loss peak appears at a temperature below the glass transition temperature (108 °C) for lower frequencies. This loss peak is usually associated with β relaxation which occurs at temperatures lower than the glass transition temperature. Here the β relaxation is assigned to the orientation of the ester side group [6]. The maximum values of tanδ shift to a higher temperature with increasing applied frequencies. These shifts of the peak towards higher temperature with increasing frequencies are clearly an indication of the dipolar type of relaxation, which arises due to the relaxation process involving the movements of the dipoles.

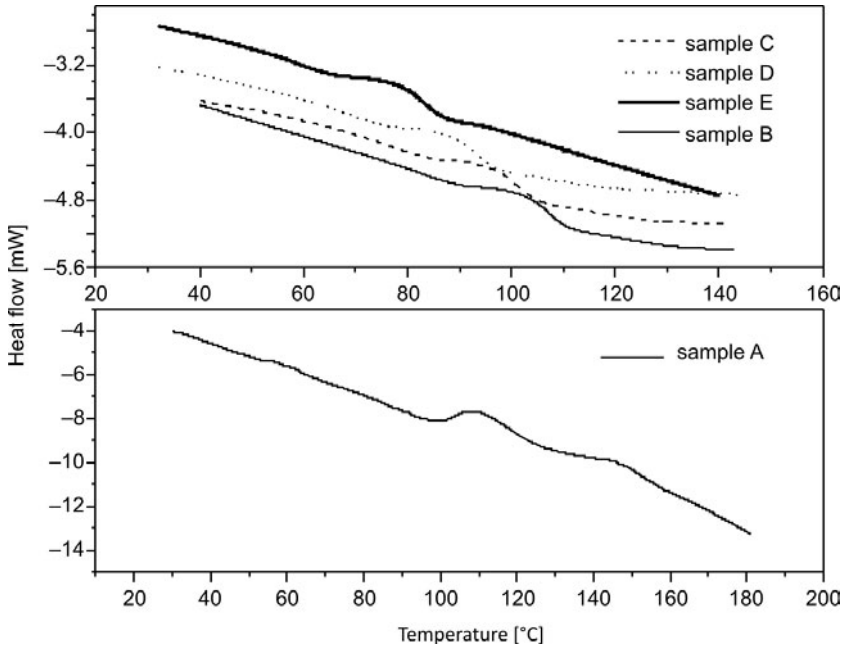

Fig. 7. DSC thermograms of doped and undoped samples

Elastic and plastic properties of polymers depend on the chain length, the degree of cross linking and the crystallinity of the material. Short chains are associated with low modulus and hardness [9]. The DSC curves for doped and undoped samples are shown in Fig. 7. For PMMA, the transition region is 95–120 °C, and the transition temperature is found to be 108 °C. The transition temperature T_g depends on the molecular weight, side branches, steric hindrance, type of bonding within the molecular structure (covalent or non-covalent), presence of plasticizers, copolymers and other physical conditions like pressure [10]. In the case of PMMA doped with MB (5×10^{-4} M), the transition region is 90–110 °C, and the transition temperature is around 103 °C. But for the MB (2×10^{-3} M) doped PMMA sample, the transition region is around 70–83 °C. The transition temperature is 77 °C. The difference in the glass transition

temperature (T_g) between pure and MB doped PMMA is due to the plasticizing effect of methylene blue on the PMMA matrix. Plasticizers are usually low molecular weight non-volatile substances, which, when added to a polymer, improve its flexibility, processibility and hence utility. Here it is an external plastification by the methylene blue in the PMMA matrix, i.e. T_g is lowered by the physical addition of the plasticizer methylene blue. As the polymer becomes softer, the transition temperature also decreases and it will lead to the decrease in the hardness value.

Vicker's hardness H_v is given by

$$H_V = \frac{1.854P}{d^2}$$

where P is the test load [kg] and d is the indentation diagonal length [mm] is measured based on the test load and on the indentation diagonal length. It is an important mechanical property that may be defined as a measure of the resistance of a material to the application of a contact load.

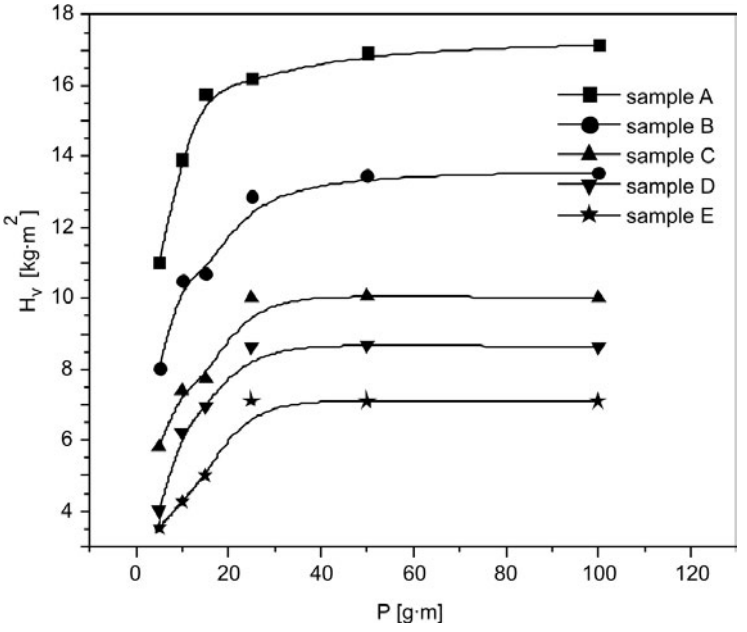

Fig. 8. Vicker's hardness in function of load for all the samples

The dependence of hardness on the load of indentation is shown in Fig. 8. The values of hardness reach saturation around a load of 30 g. The H_V and T_g values for various samples are summarized in Table 2. It is obvious that the hardness is the highest (H_V = 17) for sample A, and the lowest (7) for sample E. Since the dye is a plasticizer, the addition of the dye makes the polymer softer and consequently, as expected, T_g of the dye polymer system is decreased. Such a softening behaviour in the presence

of organic molecules such as DR1 in PMMA [1], lead phthalocyanine in polycarbonate [11], dibutyl phthalate, tricresyl phosphate in PVC [12] and MNA in PMMA [13] is already known. The plasticizers substantially reduce the brittleness of many amorphous polymers by reducing the cohesive forces of attraction between polymer chains. The dye molecules penetrate into the polymer matrix and establish polar attractive forces between it and the chain segments. These attractive forces reduce the cohesive forces between the polymer chains and increase the segmental mobility, thereby reducing the T_g value [12]. Moreover MB is a strong retarder of the polymerization of the vinyl monomer MMA [4]. This may affect the length of the polymeric chain to some extent. This may also be one of the reasons for the softening of the polymer PMMA.

Table 2. Vicker's hardness and transition temperature for various samples

Sample	Hardness [kg/m^2]	Transition temperature [°C]
A	17	108
B	13	103
C	10	95
D	8.5	86
E	7	77

4. Conclusion

The electric permittivity of PMMA samplesis found to increase with temperature and after addition of the dye. It decreases in function of increasing frequency. The dipolar nature of the dielectric relaxation is confirmed by the temperature dependences of the loss tangent at various frequencies. The dye has a plasticizing effect on the polymer which reduces the glass transition temperature of the system. The reduction in the hardness value, in turn, can result in a lowering of the glass transition temperature. These two facts have been substantiated by the DSC and microhardness measurements. MB can also act as a retarder of free radical polymerization, which affects the length of the polymeric chain. This can also be another cause for the reduction in the hardness value.

References

[1] LEI DU, RUNT J., SAFARI A., NEWNHAM R.E., Macromolecules, 20 (1987), 1797.
[2] SINGER K.D., SOHN J.E., LALAMA S.J., Appl. Phys. Lett., 49 (1986), 248.
[3] JAMES HUNT P., FITZGERALD JOHN J., *Dielectric Spectroscopy of Polymeric Materials. Fundamentals and Applications*, Am. Chem. Soc., Washington DC, 1997.
[4] MURTHY V.R.K., PRASADA T.A., SOBHANADRI J., J. Phys.D: Appl. Phys., 10 (1977), 2405.

[5] NIRANJAN K. DAS., BROJA M.MANDAL., Polymer., 23 (1982), 1653.
[6] MAZUR K., J. Phys. D Appl. Phys., 30 (1997), 1383.
[7] NARULA G.K., THRIPATHI A., PILLAI P.K.C., J. Mater. Sci., 26 (1991), 4130.
[8] AKRAM M., JAVED A., RIZVI Z.T., Turk. J. Phys., 29 (2005), 355.
[9] TABOR D., Rev. Phys. Techn., 1 (1970), 145.
[10] MADEKA H., KOKINI J.L., Cereal Chem., 73 (1996), 433.
[11] RANADE A., WANG H., HILTNER A., BAER E., SHIRK S.J., LEPKOWICZ R.S., Polymer., 48 (2007), 624.
[12] GOWARIKER V.R., VISWANATHAN N.V., SREEDHAR JAYADEV., *Polymer Science*, Wiley, 1992.
[13] SUGIARA T., FUJII K., HAGA H., YAMAMOTO S., Appl. Phys. Lett., 69 (1996), 2971.

Received 26 December 2008
Revised 2 February 2009

Materials Science-Poland, *Vol. 27*, *No. 1*, *2009*

The thermal stability, local structure and electrical properties of lithium-iron phosphate glasses

P. JÓŹWIAK[1] , J. E. GARBARCZYK[1*], M. WASIUCIONEK[1],
I. GORZKOWSKA[2], F. GENDRON[3], A. MAUGER[4], C. JULIEN[3]

[1]Faculty of Physics, Warsaw University of Technology, Koszykowa 75, 00-662 Warsaw, Poland

[2]Faculty of Chemistry, Warsaw University of Technology, Noakowskiego 3, 00-664 Warsaw, Poland

[3]Institut des Nanosciences de Paris, UMR-CNRS 7588, Université Pierre et Marie Curie, 140 rue de Lourmel, 75015 Paris, France

[4] Département MPPU, CNRS, Campus Boucicaut, 140 rue de Lourmel, 75015 Paris, France

Amorphous analogues of lithium-iron phosphates (LFP), which are promising cathode materials for Li ion batteries, were prepared by the standard press-quenching method and their thermal stability, as well as structural and electrical properties, were studied for the first time. The glass transition temperature, T_g, determined by the differential thermal analysis (DTA) is composition-dependent and lies in the 492–523 °C range. The local structure, studied by the FTIR absorption spectroscopy, and the thermal stability are found to be almost insensitive to the lithium content. Studies on the electrical properties, carried out by impedance spectroscopy, have shown that the total electrical (predominantly polaronic) conductivity at 450 °C approaches 10^{-2} S·cm^{-1}. The room temperature conductivity of samples after their nanocrystallization (induced by annealing at the temperature of the beginning of crystallization) was higher by a factor of 4–10 (depending on composition) than that of the as-received glass. Therefore, nanocrystallization seems to be a promising way to enhance the electrical conductivity of amorphous lithium-iron phosphates.

Key words: *phospho-olivines; lithium-iron phosphate; glasses; cathode material; nanomaterial; infrared spectroscopy; electron conduction*

1. Introduction

Crystalline olivine-type phases $LiFePO_4$ and $FePO_4$ as well as Li_xFePO_4 solid solutions are under intensive studies worldwide as the most competitive positive electrode-active materials for Li-ion rechargeable batteries. The main advantages of $LiFePO_4$ as a cathode material are that it is a highly stable, inexpensive and environmentally

*Corresponding author, e-mail: garbar@if.pw.edu.pl

friendly material which maintains high theoretical specific capacity of 170 mAh/g and a high discharge voltage of 3.5 V vs. Li [1–5]. Unfortunately, despite all their advantages, olivine-like phases have one serious deficiency – very low electrical (polaronic-type) conductivity - ca. 10^{-9} S·cm^{-1} at room temperature. Many efforts have been undertaken to improve their electrical properties by application of various routes of preparations: the introduction of carbon additives [5, 6], or by doping with supervalent cations [7]. Recently we proposed another, as yet unexplored, way of circumventing the problem of low conductivity of crystalline olivine cathode materials. As a first step we have prepared vitreous analogues of these materials and initiated studies on their local structure [8] and magnetic properties [9]. The second step, being currently under investigation, consists in turning these glasses into nanomaterials by an appropriate thermal treatment. In this respect, we took into consideration our recent experiences with mixed conductive lithium-vanadate phosphate glasses. We found that thermal nanocrystallization of those glasses results in a considerable enhancement of their electronic conductivity [10].

This work reports our most recent results of studies on the thermodynamic, structural and electric properties of lithium-iron-phosphate (LFP) glasses, whose nominal composition can be approximately written as Li_xFePO_4.

2. Experimental

A series of vitreous samples of (nominal composition) Li_xFePO_4 for $0 \le x \le 1$ were synthesized by a press quenching technique. Appropriate amounts of dried precursors: Li_2CO_3 (Aldrich, 99.99 %), $(NH_4)H_2PO_4$ (POCh, 99.5 %) and Fe_2O_3 (POCh, 99 %) were ground and mixed in a mortar. Alumina crucibles filled with the powders were placed in an electric furnace and heated from about 20 °C to 1270 °C in air at the heating rate of 5 °C/min. The molten mixtures kept at 1270 °C were rapidly poured out onto a stainless-steel plate maintained at the temperature close to 25 °C and immediately covered by a second stainless-steel plate. The average thickness of the resulting samples was 0.5–1.0 mm. Chemical analyses carried out by the inductive coupled plasma (ICP) method on the as-received samples have shown that due to evaporation of lithium during the high temperature stage of the synthesis, its content was slightly lower than the nominal one. For low values of x, the difference was negligible. Its maximum value for $x \approx 1$ reached 9%. The amorphous state of all as-quenched samples was confirmed by powder X-ray diffractometry (XRD), using a Philips X'Pert apparatus equipped with a $CuK_{\alpha 1}$ X-ray source and a Ni filter (λ = 1.54 Å). No Bragg peaks were detected in a wide range of 2θ angles between 10° and 80°. The thermal stability of the LFP glasses was studied by the differential thermal analysis (DTA). DTA runs were carried out for ground glass batches of about 130 mg in argon atmosphere at a heating rate 10 K·min^{-1} using a Perkin Elmer DTA-7 analyzer. The local structure of the samples was examined by the Fourier transform infra-red (FTIR) spectroscopy. FTIR absorption spectra of all glasses were recorded in the 150–1500 cm^{-1}

range at room temperature using a Bruker IFS 113v vacuum interferometer. For these measurements, each sample was ground to a fine powder, mixed with CsI in the ratio 1:300, and vacuum pressed into a disk. Electrical conductivity measurements were carried out using a setup based on a Solartron 1260 gain phase/impedance analyzer. The frequency range was 10 MHz–126 mHz. The measurements were carried out in air at temperatures, ranging from room temperature to the initial temperature of crystallization (533–558 °C, depending on composition). Prior to the impedance spectroscopy measurements, platinum electrodes were sputtered onto the opposite faces of the samples. The microstructure of partly recrystallized samples was observed by the field emission scanning electron microscopy (FE-SEM) using a LEO 1530 setup.

3. Results and discussion

3.1. Thermal stability and XRD studies

The differential thermal analysis curves for all glasses are shown in Fig. 1. Up to about 490 °C no thermal events are visible, which points to good thermal stability of the studied materials, especially in comparison with other conductive glasses. A typical run shows a glass transition feature (T_g) followed by an exothermic peak of crystallization, characterized by two parameters: T_{0c} (taken at the onset of the peak) and T_c (taken at the maximum). The first of them corresponds to the beginning of crystallization (nanocrystallization) and the second one corresponds to the end of crystallization (massive crystallization). The values of the glass transition temperature T_g are between 492 °C and 523 °C. The temperatures T_{0c} and T_c are in the 533– 558 °C and 555–579 °C ranges, respectively. A closer look at the asymmetric crystallization peaks reveals that they consist of at least two strongly overlapping peaks (Fig. 1) which are apparently due to different phases present in the crystallized material. Figure 2 shows room temperature XRD powder patterns for samples of three different compositions ($x = 0$, 0.4 and 1) taken after their crystallization. Two patterns are presented for the sample with $x = 0.4$. The upper one was taken after heating the sample up to T_{0c}, corresponding to beginning of crystallization (we refer to this sample as "nano"), and the lower one corresponds to the sample heated up to a temperature slightly above T_c, that means after massive crystallization (labelled "massive"). In the samples studied by DTA, several phases were detected, which could be identified using JCPDS databases [11] and other references [12]. The $x = 0$ sample, besides orthorhombic $FePO_4$ in heterosite form, contained also α-$FePO_4$ (a hexagonal quartz-like structure). The $x = 1$ sample was a mixture of $LiFePO_4$ in triphylite (orthorhombic) form and $Li_3Fe_2(PO_4)_3$ in monoclinic Nasicon-like form. In a case of the $x = 0.4$ sample (referred as "nano"), we also detected a mixture of triphylite and Nasicon-like phases. For that sample we additionally

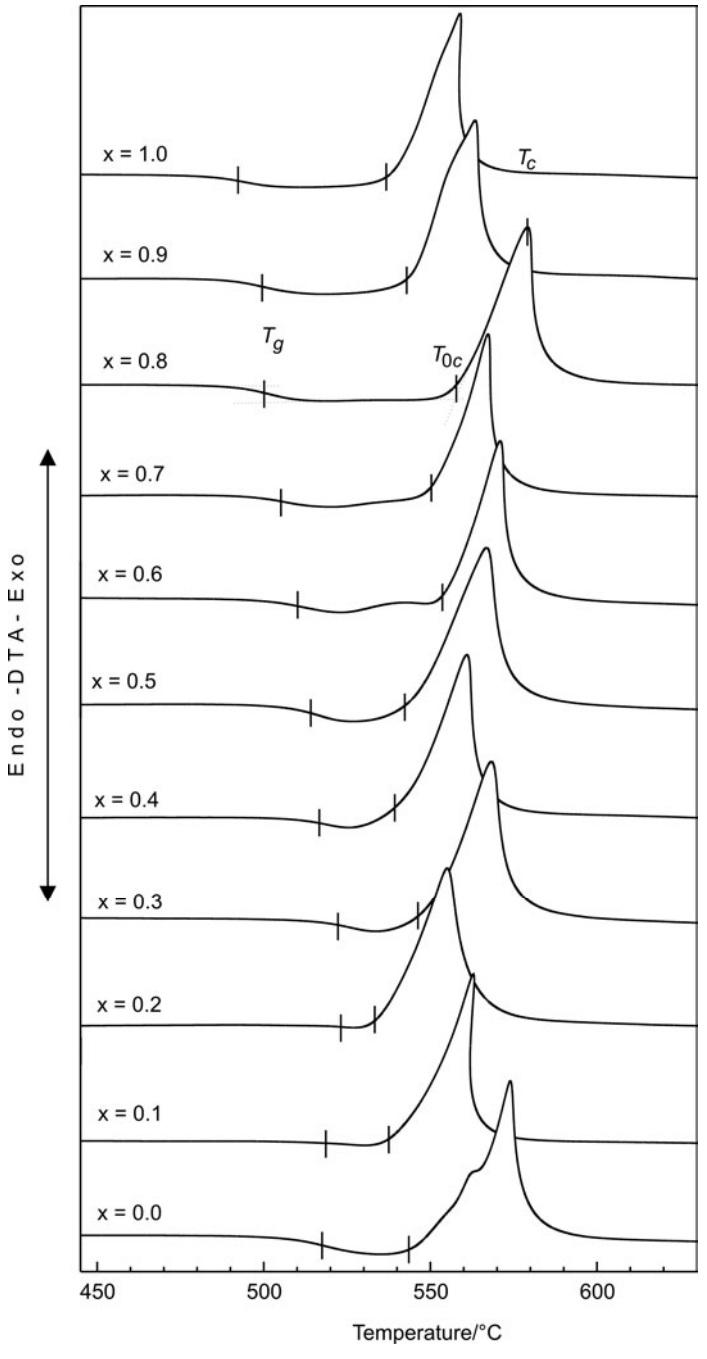

Fig. 1. Differential thermal analysis (DTA) runs
for glasses containing various amounts of lithium

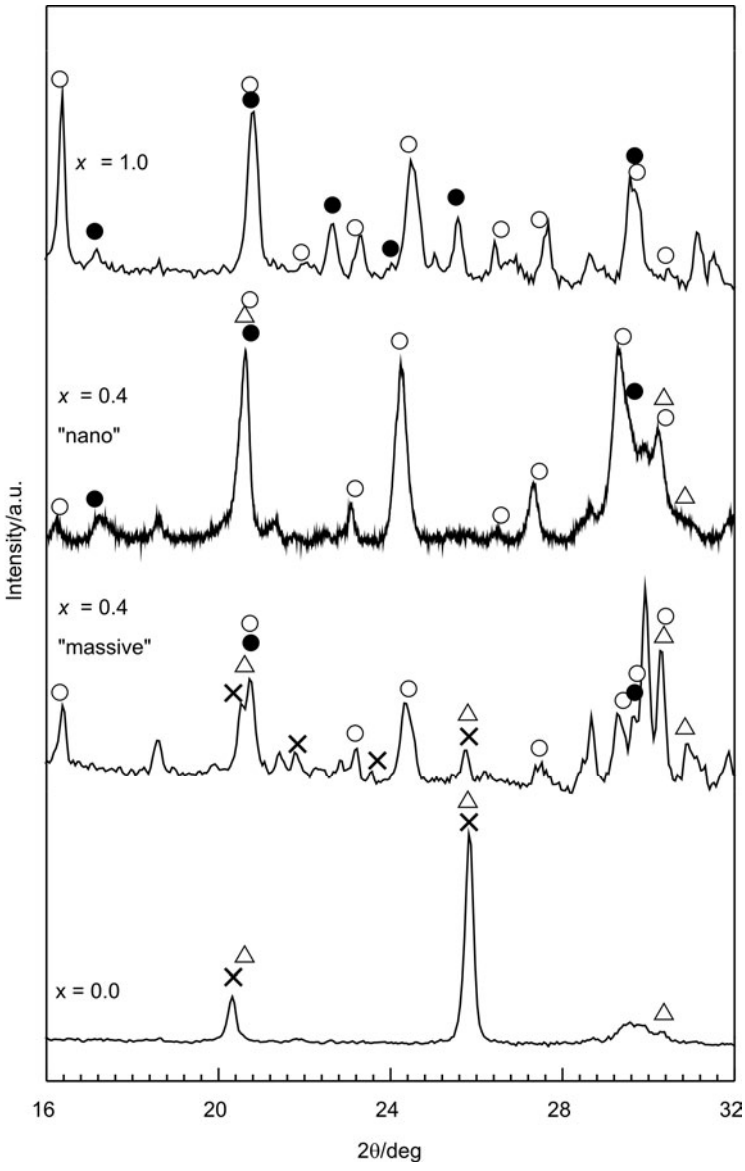

Fig. 2. Room temperature XRD patterns of samples of composition corresponding to: $x = 1$ (top curve), $x = 0.4$ "nano" (after nanocrystallization), $x = 0.4$ "massive" (after massive crystallization) and $x = 0$ (bottom curve). Symbols denote identified crystalline phases: full circles – $LiFePO_4$, open circles – $Li_3Fe_2(PO_4)_3$, triangles – $FePO_4$, crosses – α-$FePO_4$ [11, 12]

observed a broadening of XRD peaks. From the linewidth of the crystalline peaks it was possible to estimate, by a Scherrer formula, that the crystalline particles do not exceed 100 nm in size. Corresponding peaks were much better resolved in the case of

the sample after massive crystallization (Fig. 2). Additionally, in that case we also detected α-$FePO_4$ and heterosite phases.

3.2. Local structure

In order to determine the main features concerning the local structure of the glasses under study, a series of FTIR absorption measurements were carried out. The vibrational spectroscopic data are especially valuable in the case of amorphous systems, for which the natural method of structure determination – X-ray diffractometry – is ineffective.

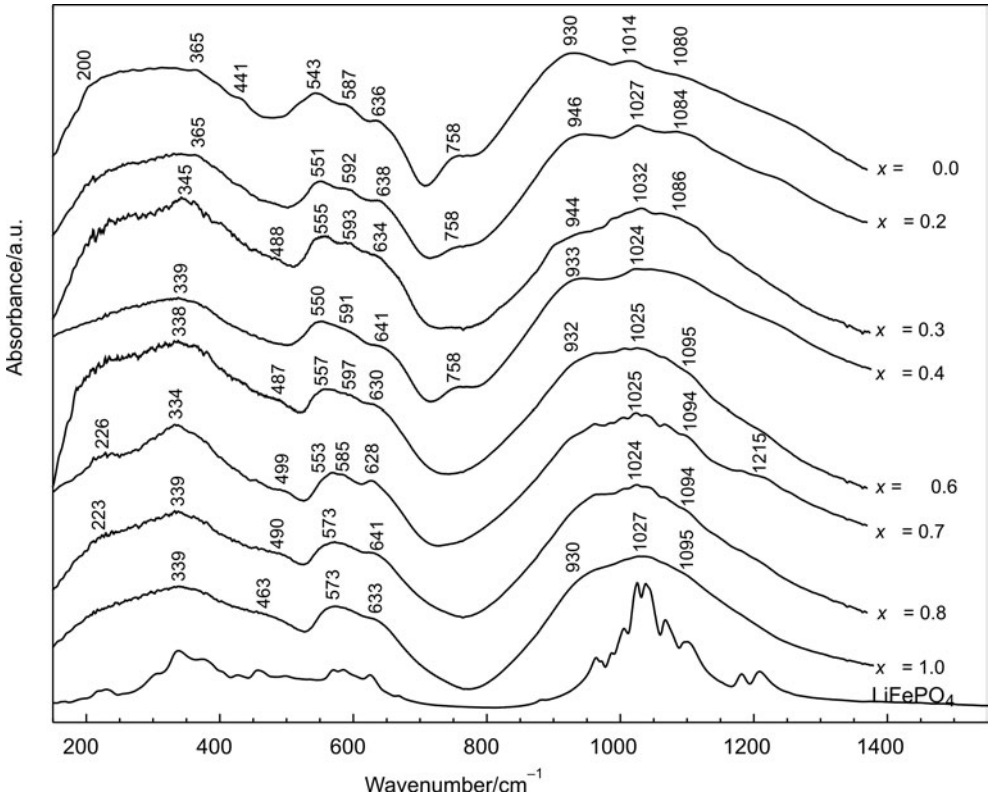

Fig. 3. FTIR absorption spectra of glasses containing various amounts of lithium (the bottom spectrum corresponds to crystalline $LiFePO_4$ [8])

Infrared absorption spectra of studied glassy materials are shown in Fig. 3 and compared with the IR spectrum of $LiFePO_4$ crystal reported in the literature [8, 9, 13–16]. There is a good agreement between the absorption bands of glasses measured in this work and the spectra of the $LiFePO_4$ crystalline phase [8, 16]. Broadening and overlapping of bands recorded for glasses is due to the much higher degree of disorder in

those systems in comparison with crystalline olivine phase. The spectra of the glasses under study can be divided into three wide features centred at about 1050, 600 and 350 cm^{-1}. These bands correspond to symmetric and asymmetric stretching oscillations of PO_4 units, bending oscillations of those units and lattice modes, respectively. Lattice modes (below 400 cm^{-1}) consist primarily of oscillations of oxygen, phosphorus and iron atoms. It is remarkable that, in a high wavenumber range, the IR bands appear exactly at the same positions as that for the crystalline phase. These patterns are consistent with the assumption that the PO_4 tetrahedra have very stable chemical bonds, even when they are the backbone of the vitreous phase. The bands in the spectral range 400–550 cm^{-1} (Li–O oscillations) are weakly dependent on the local lithium environment [9]. The mode at about 640 cm^{-1} is associated with FeO_6 vibrations. The fact that the mode is weaker and less resolved than those of PO_4 provides evidence that the FeO_6 octahedra are substantially disordered in the glasses. At a lower content of lithium ($0 \leq x \leq 0.4$) there are additional weak peaks at 758 cm^{-1} attributed to symmetric stretching vibrations of P–O–P bridging bonds in pyrophosphate $(P_2O_7)^{4-}$ units [17]. Their presence becomes more pronounced in the glasses of compositions which closely resemble $FePO_4$. It is noteworthy that the bands corresponding to the vibration of PO_4 units are almost independent of the lithium content. This indicates that the basic phosphate glass network remains insensitive to the presence of lithium ions.

3.3. Electrical properties

Generally, a lithium-free glass exhibits a typical impedance spectrum composed of a single semicircle characteristic of purely electronic (polaronic) conductors. Electronic conduction occurs via electron hopping between Fe^{2+} and Fe^{3+} ions, which serve as hopping centres for electrons [18]. Impedance spectra of glasses containing lithium consisted of a distorted semicircle, which may indicate phase heterogeneity of the samples or the influence of an ionic component (Li^+) of the total conductivity (strongly overlapped impedance semicircles). Very recent studies by Amin et al. [19] carried out on single crystals of $LiFePO_4$ have shown that the ionic component of electrical conductivity is much lower than the electronic one. Room temperature conductivity of the studied glasses, like in the case of their crystalline counterparts, is relatively low (ca. 10^{-7} $S \cdot cm^{-1}$ for the sample of $x = 1$). However at 450 °C it reaches 10^{-2} $S \cdot cm^{-1}$. The temperature dependences of conductivity for the glasses under study are in accordance with the Arrhenius formula (Fig. 4), with an effective activation energy E_a which slightly increases at about 180 °C. The lowest conductivity was found for the glass $FePO_4$ (not containing lithium). This is apparently due to the predominance of Fe^{3+} centres in such glass, resulting in the smallest concentration of Fe^{2+}–Fe^{3+} pairs essential for electronic hopping. For glasses containing lithium, the concentration of such aliovalent pairs is higher ($LiFePO_4$ introduces Fe^{2+} centres) and therefore their electronic conductivity is higher. Furthermore, those glasses exhibit an ionic component of total conductivity.

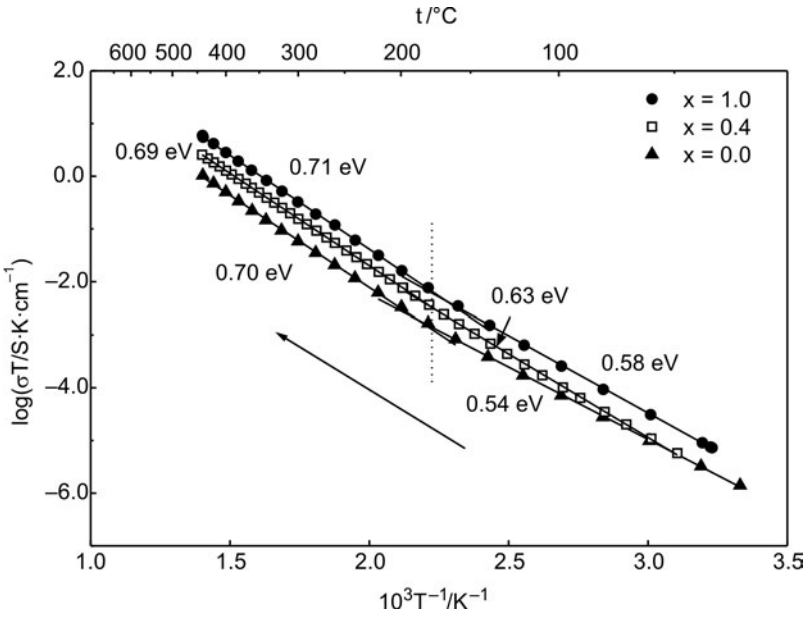

Fig. 4. Temperature dependences of conductivity for glassy samples with three different lithium contents (x = 0, 0.4 and 1)

The activation energies in the low temperature range (up to 180 °C) are equal to: 0.54, 0.63 and 0.58 eV for the glass of compositions corresponding to: x = 0, 0.4 and 1, respectively. It is interesting to note that those values are comparable to activation energies obtained for various crystallographic axes in anisotropic single crystal of $LiFePO_4$ [19]. Above 180 °C, the activation energies are almost independent of composition and are equal to about 0.70 eV (Fig. 4).

3.4. Electrical properties after nanocrystallization

In order to explore a possibility of improving the electrical conductivity of the samples under study by thermal treatment, we carried out electrical measurements at temperatures ranging from room temperature up to the temperature T_{0c} , corresponding to the beginning of the crystallization. Then we cooled the samples down to room temperature. The electrical conductivity of the x = 0 sample reaches its maximum value of 2×10^{-3} S·cm^{-1} at T_{0c} = 540 °C (Fig. 5). On cooling, the conductivity is systematically higher than that on heating, especially at lower temperatures. The increase in the conductivity at room temperature is about one order of magnitude. Also, the activation energies on cooling are different (lower) from those observed on heating. This increase of conductivity was confirmed on repeated heating-cooling cycles performed for some samples. After consecutive heating – cooling cycles there was a further slight increase in the conductivity. The observed changes can be explained based on SEM micrographs. The microstructure of the x = 0 sample, after its heating up to

temperature of the beginning of the crystallization, is shown in Fig. 6. The sample is only partly crystallized, with a substantial share of the amorphous phase still present.

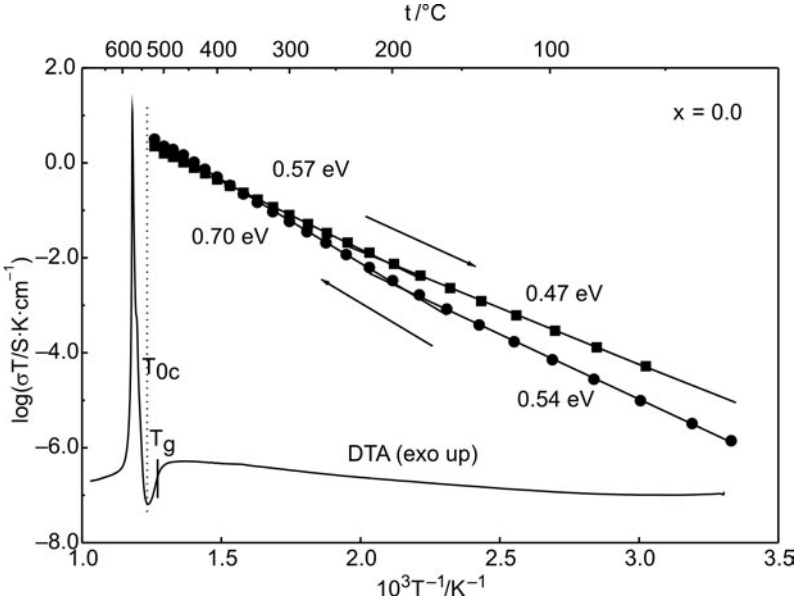

Fig. 5. Temperature dependences of conductivity during heating and cooling for a sample of $x = 0$ combined with DTA run of that sample during heating

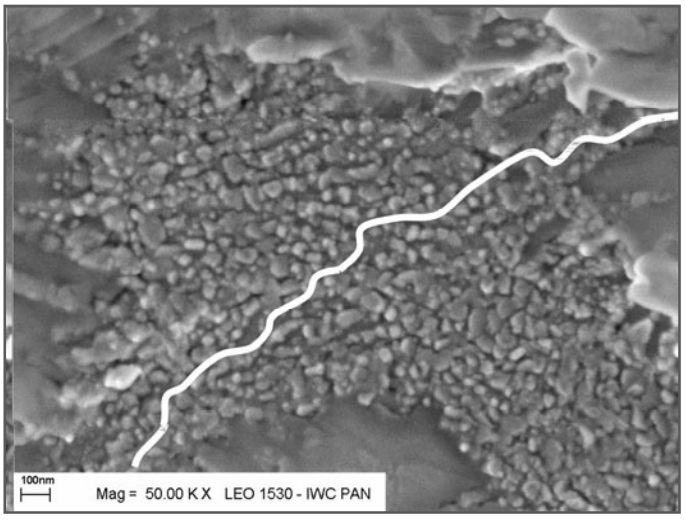

Fig. 6. Scanning electron microscopy (SEM) micrograph of the sample described by $x = 0$ after annealing at T_{0c} = 540 °C. The white line between nanocrystallites depicts an easy conduction path

The heterogeneity of the thermally treated samples may be a cause of the change of the activation energy of the sample on cooling from 0.57 eV above ca. 220 °C to

0.47 eV below that temperature. In Figure 6, one can see a number of isolated nanocrystallites embedded in the glassy matrix. Average grain size does not exceed 100 nm, which corresponds well with the estimates from XRD linewidth analysis. The interface regions between nanocrystallites and amorphous phase are, in our opinion, crucial for the observed conductivity enhancement and the decrease in the activation energy values. One can expect that in the highly defective interfacial regions, the concentration of Fe^{2+}–Fe^{3+} pairs, essential for the electron hopping, would be higher than inside crystallites and within the glassy phase. The density of the interfaces is high enough to form "easy conduction paths" whose conductivity is higher than that of the crystallites and that of the bulk glassy phase. A similar effect, namely a substantial increase in conductivity after nanocrystallization, was observed by us for glasses of the Li_2O–V_2O_5–P_2O_5 system [10].

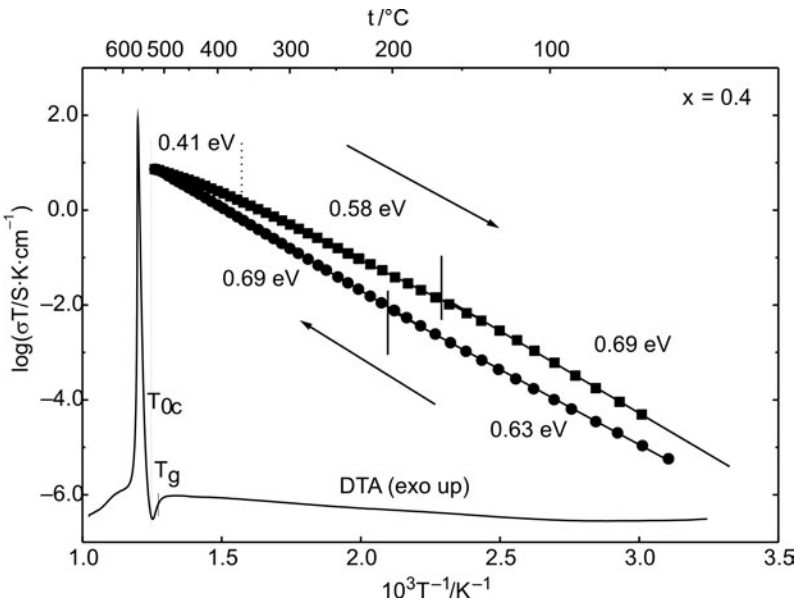

Fig. 7. Temperature dependences of conductivity during heating and cooling for a sample of $x = 0.4$ combined with DTA run of that sample during heating

The temperature dependence of conductivity of the sample corresponding to $x = 0.4$ heated up to $T_{0c} = 530$ °C is shown in Fig. 7. It can be seen that on the cooling run, the conductivity is systematically higher than that on the heating run. The maximum values of the electrical conductivity equal to 1.1×10^{-2} S·cm^{-1} were observed at 530 °C. The conductivity at room temperature of the samples heated up to T_{0c} and cooled down for this sample was increased by factor of 4 from the initial values. This enhancement was due to the nanocrystallization phenomena taking place at temperature T_{0c}. The observed irreversible increase in conductivity is accompanied by a change in the activation energies observed in the cooling stage. The activation ener-

gies start from 0.41 eV in the temperature range 360–530 °C, increase to 0.58 eV in the 160–360 °C range and reach 0.69 eV below 160 °C (Fig. 7). The observed increase of the activation energy values can be attributed to a possible ordering of the emerged crystalline phases. It is known [12] that at temperatures higher than 350 °C crystalline olivines $FePO_4$ and $LiFePO_4$ form solid solutions (disordered phase D). At temperatures lower than 200 °C there are two separate phases: H (heterosite) and T (triphylite). In the intermediate temperature range (200–350 °C) both H and D phases coexist. A similar situation of ordering and separation of the crystalline phases taking place on cooling can occur in our partly crystallized samples. In the case of the composition corresponding to $x = 0.4$, the situation is additionally complicated by the presence of a Nasicon-like phase and residuals of the glassy phase.

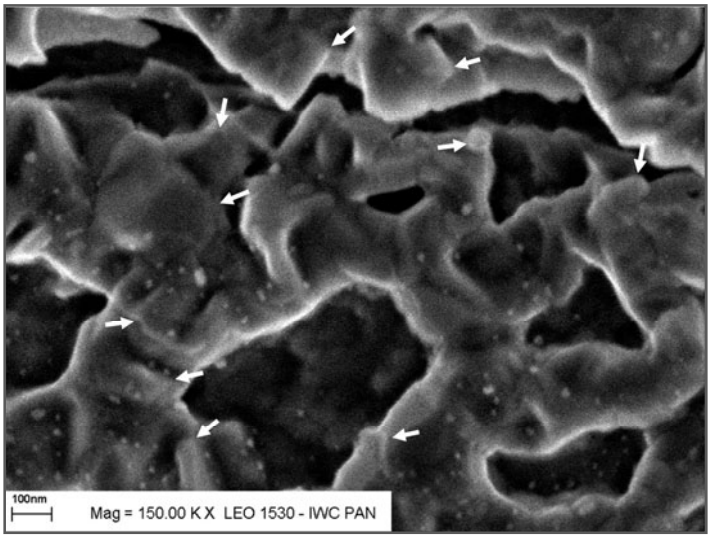

Fig. 8. SEM micrograph of the sample described by $x = 0.4$ after annealing at $T_{0c} = 530$ °C for 0.5 h (arrows show orthorhombic nanocrystallites of re-crystallized glass)

In a SEM micrograph showing a recrystallized region of that sample (Fig. 8) there are visible orthorhombic crystallites (probably triphylite) of approximate size 100 nm embedded in the remaining glassy phase. Both SEM micrographs (Figs. 6 and 8) reveal the substantial porosity of the samples under study after their nanocrystallization. Such porosity and considerable share of nanocrystalline grains in the samples may be useful for eventual application of studied materials as cathodes in lithium batteries.

4. Conclusions

The studies presented here of lithium-iron phosphate (LFP) glasses were, to the best of the authors' knowledge, the first to have been carried out on this subject.

Thermal stability and the local structure are weakly dependent on the composition (lithium content). LFP glasses exhibit mixed electronic-ionic conductivity, with the electronic component predominating. The conductivity reaches its maximum value of 10^{-2} S·cm^{-1} at 450 °C. This work has shown that the re-crystallization of LFP glasses at the nanoscopic scale can be carried out and that it does lead to a significant enhancement in the conductivity. Nanocrystallization seems to be the way ahead for electrical conductivity enhancement of amorphous lithium-iron phosphates.

Acknowledgements

The authors are grateful to Dr. S. Gierlotka, Institute of High Pressure Physics, Polish Academy of Sciences, for the assistance in SEM studies.

References

[1] MANTHIRAM A., GOODENOUGH J.B., J. Solid State Chem., 71 (1987), 349.
[2] PADHI A.K., NANJUNDASWAMY K.S., J.B. GOODENOUGH, J. Electrochem. Soc., 144 (1997), 1188.
[3] ZAGHIB K., STRIEBEL K., GUERFI A., SHIM J., ARMAND M., GAUTHIER M., Electrochim. Acta, 50 (2004), 263.
[4] BYKOV A.B., CHIRKIN A.P., DEMYANETS L.N., DORONIN S.N., GENKINA E.A., IVANOV-SHITS A.K., KONDRATYUK I.P., MAKSIMOV B.A., MELNIKOV O.K., MURADYAN, L.N., SIMONOV V.I., TIMOFEEVA V.A., Solid State Ionics, 38 (1990), 31.
[5] HUANG H., YIN S.C., NAZAR L.F., Electrochem. Solid-State Lett., 4 (2001), A170.
[6] CHEN Z., DAHN J.R., J. Electrochem. Soc., 149 (2002), A1184.
[7] CHUNG S.-Y., BLOKING J.T., CHIANG T.-M., Nature Mater., 1 (2002), 123.
[8] SALAH A.A., JOZWIAK P., ZAGHIB K., GARBARCZYK J.E., GENDRON F., MAUGER A., JULIEN C.M., Spectrochim. Acta, A 65 (2006), 1007.
[9] JOZWIAK P., GARBARCZYK J., GENDRON F., MAUGER A., JULIEN C.M., Mat. Res. Soc. Symp. Proc. 972 (2007), 6.
[10] GARBARCZYK J.E., „JOZWIAK P., WASIUCIONEK M., NOWINSKI J.L., J.„Power Sources, 173 (2007), 743.
[11] *JCPDS database of crystallographic data* (reference codes: $LiFePO_4$ - 00-040-1499, $Li_3Fe_2(PO_4)_3$ – 00-047-0107, α-$FePO_4$ – 01-077-0094).
[12] DODD J.L., YAZAMI R., FULTZ B., Electrochem. Sol. St. Lett., 9 (2006), A151.
[13] PAQUES-LEDENT M.T., TARTE P., Spectrochim. Acta, A 30 (1973), 673.
[14] SALAH A.A., JOZWIAK P., GARBARCZYK J., BENKHOUJA K., ZAGHIB K., GENDRON F., JULIEN C.M., J. Power Sources, 140 (2005), 370.
[15] BURBA C.M., FRECH R., J. Electrochem. Soc., 151 (2004), A1032.
[16] JOZWIAK P., GARBARCZYK J., GENDRON F., MAUGER A., JULIEN C.M., J. Non-Cryst.Solids, 354 (2008), 1915.
[17] NYQUIST R.A., PUTZIG C.L., LEUGERS M.A., *Infrared and Raman Spectral Atlas of Inorganic Compounds and Organic Salts: Raman Spectra*, Academic Press, San Diego, 1997.
[18] MOTT N.F., Adv.Phys., 50 (2001), 865.
[19] AMIN R., BALAYA P., CHEN D.P., LIN C.T., MAIER J., *16th International Conference on Solid State Ionics*, Shanghai, China, July 1- 6, 2007, Book of Program and Abstracts, p. 57.

Received 7 March 2008
Revised 30 January 2009

Materials Science-Poland, *Vol. 27*, *No. 1*, *2009*

Syntheses and characterization of pH-sensitive hydrogel from poly(γ-glutamic) acid

B. YAO[1, 2], C. YANG[1], K. ZHANG[1], C. NI[1], H. SONG[2], Z. NI[1], M. CHEN[1*]

[1]School of Chemical and Material Engineering, Jiangnan University, Wuxi 214122, P. R. China

[2]School of Chemical Engineering, Nanjing University of Science and Technology, Nanjing 210094, P. R. China

Novel pH-sensitive hydrogels were prepared through crosslinking of poly(γ-glutamic) acid (γ-PGA) by using 1,4-butanediol diglycidyl ether as a cross-linker, tetraethylammonium bromide as a catalyst, and reacting in DMSO. The dependence of the swelling ratio of the hydrogels on pH values, ionic strength and cross-linking degree was investigated. It was found that the pH-sensitive range was clearly extended through introducing multiple hydrogen bonds to the hydrogel network during the preparation. The swelling ratios of γ-PGA hydrogels increased with the increase in pH of the aqueous solution from 2 to 9. The swelling of the γ-PGA hydrogels was firstly controlled by the ionization of carboxyl groups in the hydrogels within the pH range from 2 to 5, and then controlled by breaking of the multiple hydrogen bonds in the hydrogels within the pH range from 5 to 9. The swelling ratios of γ-PGA hydrogels were also strongly dependent on the ionic strength of the medium and cross-linking degree of the hydrogels. Increasing the ionic strength and the crosslinking degree resulted in a decrease in the swelling ratio of the hydrogels.

Key words: *poly(γ-glutamic) acid; pH-sensitive hydrogel; crosslinking; swelling*

1. Introduction

Biodegradable polymers are widely used in various fields such as suture materials, bone fixation materials, environmentally friendly materials and drug delivery systems. Recently, further applications of biodegradable polymers have been desired in many situations, such as stimuli-responsible drug delivery systems and tissue engineering, etc. [1–6].

Poly(γ-glutamic) acid (γ-PGA) is a kind of water soluble polyamide which has been extensively investigated due to its biodegradable and biocompatible properties, which are highly desirable for applications [7–16].

Corresponding author, e-mail: mqchen@sytu.edu.cn

It has been reported that γ-PGA hydrogels can be prepared by many methods such as cross-linking following γ irradiation [17, 18] and esterification [19, 20]. In the reported literature, the crosslinked γ-PGA hydrogels were pH sensitive, and their swelling ratios increased with the increase of pH value of the medium, however, the swelling ratio changed little for pH values higher than 5. This was because the pH sensitivity depended only on ionization of carboxyl groups, which were completely ionized at pH = 5.1 [19]. A further decrease in pH had little effect on the swelling. It is evident that due to intermolecular hydrogen bonds, linear γ-PGA had apparent pH sensitivity for pH values higher than 7.4 [20]. Unfortunately, the intermolecular hydrogen bonds were broken during the preparation of crosslinked γ-PGA hydrogels when hydrophobic groups were introduced into the hydrogels [19, 20]. In order to extend the pH sensitivity range in hydrogels, and thereby enlarge their fields of application, we attempted to introduce multiple hydrogen bonds to γ-PGA networks during the hydrogel preparation. Thus, in this study, cross-linked three-dimensional networks of γ-PGA hydrogels were prepared using 1,4-butanediol diglycidyl ether (BDDGE) as a cross-linker, and tetraethylammonium bromide as a catalyst. The esterification reaction took place between the pendent carboxyl groups of γ-PGA and epoxy groups of BDDGE. After the reaction, the hydroxyl groups and ether bonds would be incorporated into the γ-PGA networks. The newly formed hydroxyl and ether groups would form intramolecular multiple hydrogen bonds which functioned as pH sensitive groups. Therefore, the swelling of the novel γ-PGA hydrogel was controlled firstly by ionization of carboxyl groups at a pH between 2 and 5, and then subsequently controlled by breaking the multiple hydrogen bonds at pH between 5 and 9.

2. Experimental

γ-PGA ($M_w = 3.15\times10^5$) was kindly donated by Meiji Seika Kaisya, Ltd. (Tokyo, Japan) and was used without further purification. 1,4-Butanediol diglycidyl ether (BDDGE, Ciba Chemical) and *tetra*-ethylammonium bromide (99.5%, Jiangyin Chengnan Chemical, Jiangyin, China) were used as received. The typical preparation of γ-PGA hydrogel was as follows: 0.2 g of γ-PGA, 16 mg of cross-linker (1,4 butanediol diglicydyl ether, hereafter referred to as BDDGE) and 8 mg of tetraethylammonium bromide were dissolved in dimethyl sulfoxide (DMSO) and placed in a reaction tube. The sealed tube was immersed in a shaking water bath (80 rpm) and kept at 60 °C for 48 h. After gelation, the hydrogels were extracted from the tube and cut into pieces. The γ-PGA hydrogels were washed by immersion in de-ionized water for 5 days: the deionized water was replaced every day to remove the unreacted compounds and linear polymers. Each hydrogel, in the form of a cube, was placed in an excess of deionized water at room temperature. In order to reach swelling equilibrium, the hydrogels were immersed in deionized water for one day. The weight of the swelling hydrogel was determined gravimetrically after eliminating the surface water of the hydrogel with filter paper. The swelling ratios of the hydrogels (Q) were calculated from the following equation:

$$Q = \frac{W_s - W_d}{W_d} \tag{1}$$

where W_s is the weight of the equilibrium swollen hydrogel, and W_d is the weight of the dried hydrogel, respectively.

The γ-PGA hydrogels were immersed in deionized water until the equilibrium swelling had been attained, then the swollen hydrogels were placed in various buffer solutions with pH values ranging between 2 and 10, and in aqueous salt solutions with various sodium chloride and calcium chloride concentrations. KH_2PO_4 buffer and NaOH/HCl solutions were used for adjusting the pH (3.0–9.0), the ionic strength was adjusted with NaCl to 0.1 M. Samples were removed from the aqueous solutions at specific times, and weighted quickly, after having been wiped with filter paper in order to remove excess water from the hydrogel surface. The swelling ratios were calculated from Eq. (1).

3. Results and discussion

3.1. Syntheses of γ-PGA hydrogels

Figure 1 shows the cross-linking scheme of γ-PGA with BDDGE as the cross-linker. The reaction takes place between the pendent carboxyl groups of γ-PGA and the epoxy groups of BDDGE in the presence of tetraethylammonium bromide as catalyst.

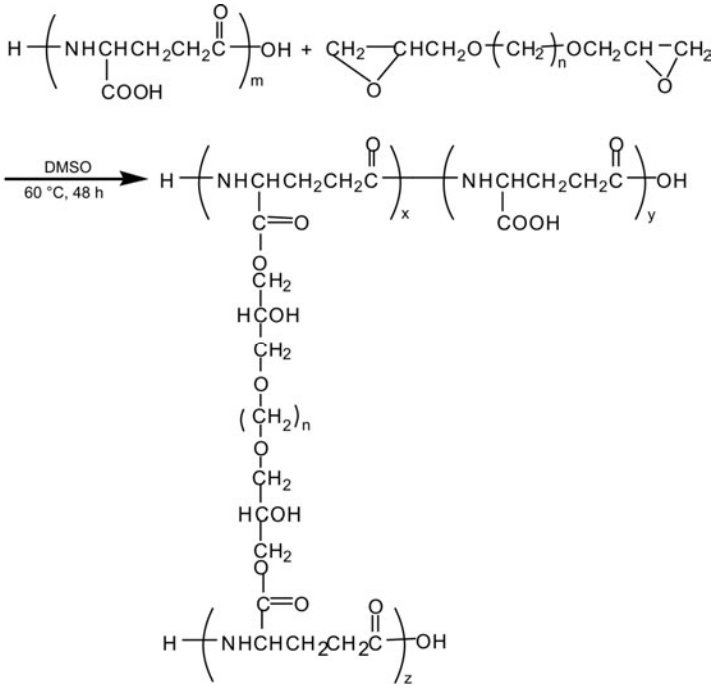

Fig. 1. The cross-linking process of γ-PGA hydrogel using BDDGE as a cross-linker

Table 1. Conditions of synthesis of γ-PGA hydrogel[a]

No.	γ-PGA		BDDGE		BDDGE/COOH molar ratio	Yield [%]
	[mg]	[mmol][d]	[mg]	[mmol]		
1[b]	201	1.56	3	0.015	0.009	–
2	204	1.58	7	0.035	0.022	65
3	198	1.53	10	0.050	0.033	74
4	197	1.53	16	0.079	0.052	84
5	202	1.57	26	0.129	0.082	86
6	196	1.52	39	0.193	0.127	83
7	197	1.53	79	0.612	0.400	89
8	200	1.55	159	0.787	0.507	86
9[c]	199	1.54	203	1.005	0.652	–
10	195	1.51	16	0.079	0.052	69
11[b]	200	1.55	16	0.079	0.052	–
12[b]	193	1.50	15	0.074	0.050	–

[a]Reactions were carried out in DMSO at 60 °C for 48h with tetraethylammonium bromide (4 wt. % of γ-PGA) as a catalyst. The volume of DMSO was fixed at 1 cm^3, except No. 10 (2 cm^3), No. 11 (4 cm^3) and No 12. (6 cm^3).

[b]No gel was obtained.

[c]The gel cracked under swelling in deionized water.

[d]The repeated structure units in the polymer.

In Table 1, the reaction conditions applied for the preparation of γ-PGA hydrogels have been listed. γ-PGA hydrogels can be prepared when the concentration of γ-PGA and the concentration of the cross-linker are higher than their critical values. A similar phenomenon was also reported by Gonzales et al. [24] in the preparation of γ-PGA hydrogel using dihalogenoalkane as a cross-linker. In their study, the critical concentration of γ-PGA was 10 wt. %. In the present study, at the γ-PGA concentration below 15 wt. %, no γ-PGA hydrogels were formed. The concentration of γ-PGA was too low for effective cross-linking, thus no three-dimensional network hydrogel was formed. Additionally, if the molar ratio of BDDGE to [COOH] is below 0.022, then, also, no hydrogel is formed (e.g., No. 1 of Table 1).

It is also found that the mechanical property of γ-PGA hydrogels is related to their cross-linking degree. If the BDDGE content is low (No. 2), γ-PGA hydrogel formed is soft and it is difficult to maintain its shape in the swelling state. Increasing the content of BDDGE will enhance the mechanical strength of the γ-PGA hydrogels. However, if the BDDGE content is high (No. 8), the swelling ratios of γ-PGA hydrogels will be very low and can easily be cracked.

3.2. Swelling behaviour of γ-PGA hydrogels

3.2.1. Effect of the cross-linker content on the swelling ratio of the hydrogels

The cross-linker content has an important effect on the structure of a three-dimensional network (Fig 2). When the cross-linker concentration (the molar ratio of

BDDGE to the repeated structural unit of γ-PGA) is varied from 0.022 to 0.575, the swelling ratio of the hydrogels decreases from 800 to 50. The swelling ratios of the γ-PGA hydrogels decreased with the increase of the concentration of BDDGE, and then remained nearly constant when the concentration of BDDGE exceeded 0.5. This agrees with common observations about hydrogels. Additionally, the –COOH group of γ-PGA hydrogels is the hydrophilic group. The cross-linking reaction between the epoxy group and –COOH group will make the free residual –COOH groups decrease. This might be another reason for the decrease in the swelling ratio of γ-PGA hydrogel with the increase of cross-linking degree.

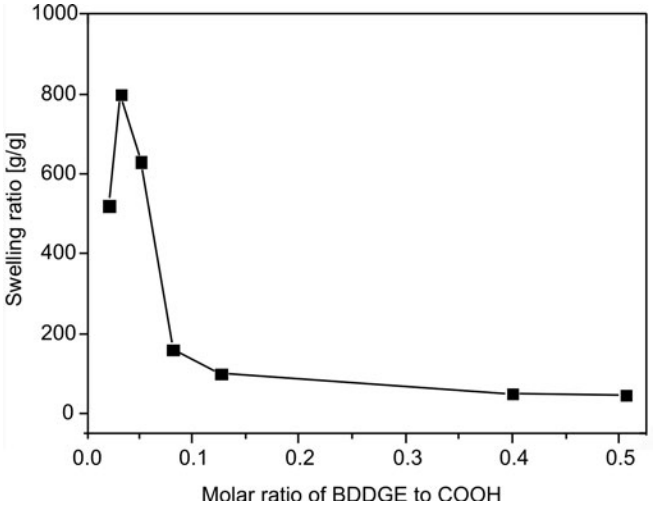

Fig. 2. The plot of the equilibrium swelling ratio of γ-PGA hydrogels in deionized water in function of the molar ratio of BDDGE to the repeated structural unit of γ-PGA. The conditions of hydrogel preparation are indicated in Table 1(from BDDGE/COOH, molar ratio: 0.022 to 0.507)

It was unexpectedly found that the swelling ratio of hydrogel No. 2 has a lower swelling ratio than that of hydrogel No. 3, even though the crosslinking content in No. 2 (0.022) is lower than in No. 3 (0.033). This abnormal result is explained by the fact that a part of the swollen hydrogel is lost in the medium, since the hydrogel is too soft in the low crosslinking state.

3.2.2. Effect of pH on the swelling behaviour of γ-PGA hydrogels

Swelling or contraction in response to pH change is a typical phenomenon of polyelectrolyte hydrogels. The effect of pH value on the swelling ratio of γ-PGA hydrogels is shown in Fig. 3. In this study, the pH values in aqueous solutions are varied from 2.0 to 10.0. It is found that the swelling ratio of γ-PGA hydrogel increases with the increase of the pH value.

The swelling ratio of the γ-PGA hydrogel is about 8 at a pH = 2.0, and sharply increases to 36 at pH = 3.0 (Fig. 3). According to Gonzales et al. [24], the pH corresponding to ca. 50% ionization of γ-PGA was around 2.1. The reason for the low swelling ratio at low pH values could be attributed to the protonation of carboxyl groups which causes greater interaction of the carboxyl groups and hence causes the shrinkage of the γ-PGA hydrogel. Conversely, carboxyl groups will be ionized at high pH values, which results in a higher swelling ratio of the hydrogels. This is due to the ionic repulsion of ionized carboxyl groups. So, the swelling ratio of hydrogel increases with increasing pH.

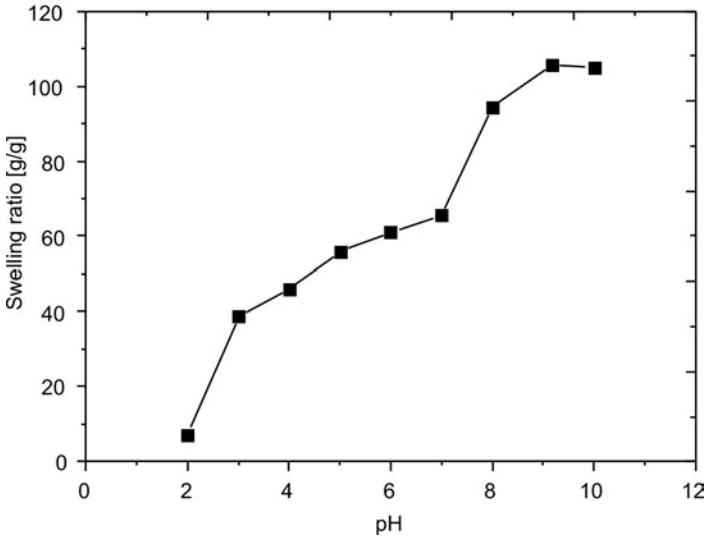

Fig. 3. Dependence of swelling ratio of γ-PGA hydrogel (BDDGE/COOH, molar ratio 0.052, sample 4 in Table 1) in function of pH at a constant ionic strength (0.1 M)

Gonzales et al. [24] and Akashi et al. [25] observed the swelling ratios of γ-PGA hydrogels and γ-PGA propyl hydrogels increased with increasing pH in the 2–5 pH range, but changed little when pH exceeded 5. This phenomenon was attributed to the 100% ionization of γ-PGA at pH = 5.1 [24]. However, in the present study, the swelling ratios of the obtained γ-PGA hydrogels continue to increase from 60 to 105 when the pH changes from 5 to 9. This suggests that the swelling mechanism of γ-PGA hydrogels prepared in the present study may be different from that of the γ-PGA hydrogels prepared by Gonzales et al. [24] and Akashi et al. [20].

Note that linear γ-PGA is insoluble in ultra-pure water, whereas it is soluble in an alkaline solution (pH > 7.4) [20]. This implies that linear γ-PGA can form intermolecular hydrogen bonds. If these multiple hydrogen bonds do not break after the cross-linking of the γ-PGA, they will influence the swelling of γ-PGA hydrogels in aqueous solution. For the γ-PGA hydrogels prepared by Gonzales et al. [24] and Akashi et al. [20], the multiple hydrogen bonds in γ-PGA were broken due to the incorporation of

hydrophobic groups into the gels, therefore the swelling of the obtained γ-PGA only controlled by the ionization of carboxyl groups within the 2–5 pH range. The swelling ratio was no longer obviously affected by pH at pH > 5. However, in this study, some hydroxyl groups and ether bonds are introduced to the γ-PGA network during the cross-linking reaction. As a result, multiple hydrogen bonds in the γ-PGA will form. The breaking of multiple hydrogen bonds is governed by the pH value in the 7.4–9 range. Consequently, we can observe that the swelling ratio clearly increases as pH rises from 7 to 9. Thus the swelling is controlled initially by the ionization of carboxylic groups and then controlled by the breaking of multiple hydrogen bonds. These novel γ-PGA hydrogels have a significantly broader pH-sensitive range, which will enlarge their fields of application.

3.2.3. Effect of ionic strength on the swelling behaviour of γ-PGA hydrogels

It is known that the swelling ratios of polyelectrolyte hydrogels, such as γ-PGA hydrogel, are dramatically dependent on the ionic strength of the medium.

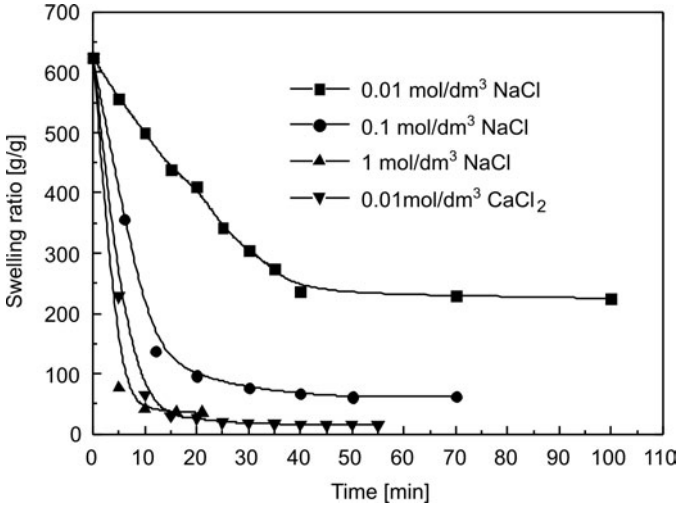

Fig. 4. The contraction curves of γ-PGA hydrogel (BDDGE/COOH, molar ratio 0.052 in Table 1) in various electrolyte solutions

Figure 4 shows the contraction behaviour of γ-PGA hydrogels in salt solutions. When the equilibrium swollen γ-PGA hydrogels are transferred into salt solutions, the γ-PGA hydrogels shrunk due to the ionic screening effect. In the case of NaCl solution, both the contraction velocity and contraction ratio of γ-PGA hydrogels increase with the increase in the NaCl concentration. Figure 4 also indicates that at the same ionic concentration (0.0l mol/dm^3), the equilibrium swelling γ-PGA hydrogels contract more quickly in $CaCl_2$ solution than in NaCl solution and the contraction ratio in $CaCl_2$ solution is higher than that in NaCl solution. When polyelectrolyte hydrogels are immersed in water, an osmotic pressure is established. The osmotic pressure is the

main driving force for the swelling of polyelectrolyte hydrogel. In the present study, the γ-PGA hydrogels adsorb a lot of water in deionized water due to the exerting osmotic pressure of counter ions. When the equilibrium swelling γ-PGA hydrogels are put into salt solutions, the external ions of the γ-PGA hydrogels will diffuse into the hydrogels owing to different salt concentration between the exterior and the interior of the hydrogel, which causes the decrease in the osmotic pressure, and the contraction of γ-PGA hydrogels. Another reason is that when ionic strength increases, the hydrophobic interaction of polymer chains becomes stronger, which makes the hydrogel shrink. The diffusion degree and velocity of ions both increase with the increase in the salt concentration. This may be the reason why the contraction velocity and contraction ratio of γ-PGA hydrogel increase with the increase in the salt concentration. Strong effects are observed by using $CaCl_2$ solution. In this case, the swollen γ-PGA hydrogel exhibits more dramatic contraction than in NaCl solution with the same molar salt concentration. It can be attributed to a difference of ionic strength in NaCl and $CaCl_2$ solutions. Additionally, the ionic interaction between the Ca^{2+} ions and the carboxyl groups inside the hydrogel also had an important role in the shrinkage behaviour.

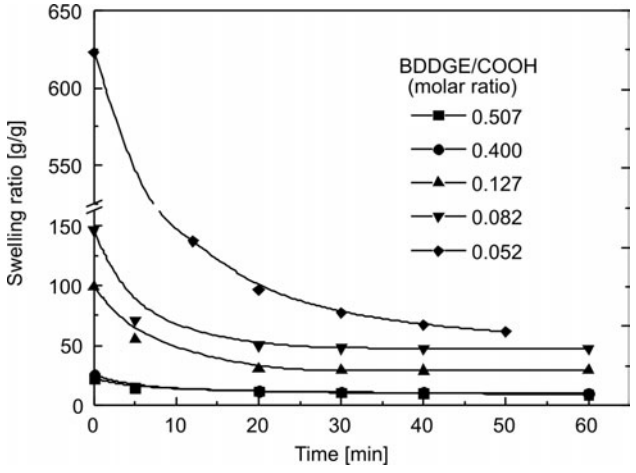

Fig. 5. The contraction curves of γ-PGA hydrogel with various crosslinking degrees in NaCl solution (0.1 mol/dm^3)

The contraction curves of γ-PGA hydrogels with various cross-linking degrees in NaCl solution are plotted in Fig. 5. The γ-PGA hydrogels are swollen in deionized water and subsequently soaked in the 0.1mol/dm^3 NaCl solution. Figure 5 shows that the swelling ratio of γ-PGA hydrogels with low cross-linking degree (No. 4) sharply decreases from 630 to 60 after being soaked in the 0.1mol/dm^3 NaCl solution for 50 min. However, the swelling ratio of the hydrogel (No. 8) with higher cross-linking degree just changes slightly from 22 to 10 during the same period of time. This can be attributed to the difference in the number of residual carboxyl groups in the γ-PGA hydrogels with various cross-linking degrees. It is acceptable that the γ-PGA hydrogels

with lower cross-linking degree have more residual carboxyl groups. So, the external ions have a more noticeable effect on the swelling behaviour of γ-PGA hydrogels.

4. Conclusion

pH-sensitive hydrogels based on poly(γ-glutamic) acid (γ-PGA) were successfully synthesized by the reaction between the pendent carboxyl groups of γ-PGA and the epoxy groups of BDDGE in the presence of tetraethylammonium bromide as a catalyst in DMSO. The swelling ratio of γ-PGA hydrogel is strongly dependent on the pH value and salt concentration of the swelling medium. The pH-sensitive range of the hydrogels has clearly been extended up to pH = 9. This is because multiple hydrogen bonds are formed during the preparation of the hydrogels. This will enlarge the range of possible applications of hydrogels as pH-sensitive materials.

Acknowledgement

This work was financially supported by the National Nature Science Foundation of China, Project No. 50443012, 20671043.

References

[1] ENGELBERG I.,, KOHN J., Biomaterials, 12 (1991), 292.
[2] TOMIHATA K., IKADA Y., Biomaterials, 18 (1997),189.
[3] STUBBE B., MARIS B., DEN MOOTER G.V., DE SMEDT S.C., DEMEESTER J., J. Contr. Release, 75 (2001), 103.
[4] KIKUCHI A., OKANO T., Adv. Drug. Deliv. Rev., 54 (2002), 53.
[5] HOFFMAN A.S., Adv. Drug. Deliv. Rev., 43 (2002), 3.
[6] QIUY., PARK K., Adv. Drug. Deliv. Rev., 53 (2001), 321.
[7] TROY F.A., J. Biol. Chem., 248 (1973), 305.
[8] KUBOTA H., NAMBU Y., ENDO T., J. Polym. Sci. Part. A: Polym Chem, 34 (1996),1347.
[9] TACHABOONYAKIAT W., SERIZAWA T., ENDO T., AKASHI M., Polym J., 32 (2000), 481.
[10] SERIZAWA T., GOTO H., KISHIDA A., ENDO T., AKASHI M. J., Polym. Sci. Part A: Polym. Chem., 36 (1999), 801.
[11] SHIMOKURI T., KANEKO T., SERIZAWA T., AKASHI M., Macromol Biosci., 4 (2004), 407.
[12] MORILLO M., DE.ILARDUYA A.M., GUERRA S.M., Macromo1ecules, 34 (2001),7868.
[13] MORILLO M., DE.ILARDUYA A.M., ALLA A., GUERRA S.M., Macromo1ecules, 36 (2003), 7567.
[14] Melis J., Morillo M., de Ilarduya A. M., Alla A., Guerra S. M., Polymer, 42 (2001), 9319
[15] KUBOTA H., NAMBU Y., ENDO T., J. Polym. Sci. Part A: Polym. Chem., 31 (1993), 2877.
[16] KUBOTA H., NAMBU Y., ENDO T., J. Polym. Sci. Part A: Polym Chem., 33 (1995), 85.
[17] CHOI H.J., KUNIOKA M., Radiat Phys. Chem., 46 (1995), 175.
[18] CHOI H.J., YANG R, KUNIOKA M., J. App. Polym. Sci., 58 (1995), 807.
[19] GONZALES D., FAN K., SEVOIAN M., J. Polym. Sci. Part A: Polym. Chem., 34 (1996), 2019.
[20] SHIMOKURI T., KANEKO T., AKASHI M., J. Polym. Sci. Part A: Polym. Chem., 42 (2004), 4492.

Received 1 July 2008
Revised 2 February 2009

Materials Science-Poland, *Vol. 27*, *No. 1*, *2009*

Crystallization of TeO_2–Nb_2O_5 glasses and their network structural evolution

J. LIN*, W. HUANG, L. MA, Q. BIAN, S. QIN, H. WEI, J. CHEN

College of Materials Science and Engineering, Tongji University, Shanghai 200092, China

TeO_2–Nb_2O_5 glass is a kind of heavy metal oxide glass with a chain-like network structure, in which Nb^{5+} ions connect the Te–O chains and adjust the types of [TeO_x] (x = 3, 4) coordination polyhedra to stabilize the glass network. $(100 - y)TeO_2$–yNb_2O_5 (y = 3–20 mol %) glasses were prepared, the crystallization behaviour and their network structural evolution were studied by means of differential thermal analysis (DTA), X-ray diffraction (XRD) and Fourier transform infrared spectra (FT-IR). The results show that the stabilization of the TeO_2–Nb_2O_5 glass network is greatly influenced by the constitution of Te–O chains and their linkage. The glass structure with lower Nb^{5+} content is inhomogeneous, it is composed of edge sharing Te–O chains, partly edge sharing chains connected by Nb^{5+} ions, apical sharing chains and apical sharing chains connected by Nb^{5+} ions. Crystalline phases of β-TeO_2, $Nb_2Te_4O_{13}$, α-TeO_2 and $Te_3Nb_2O_{11}$ will be formed in turn when the treatment temperature of the glass is increased. When the concentration of Nb^{5+} ions is sufficient to well connect Te–O chains, the glass network will tend to homogenize, only one crystalline phase, $Nb_2Te_4O_{13}$, will be formed. A suitable preheat treatment will also help to homogenize the glass structure and make the glass more stable.

Key words: *glass; tellurite; niobium; crystallization; network structure*

1. Introduction

Tellurite glass is a kind of heavy metal oxide glass with such properties as high refractive index and the third order nonlinear optical property, wide optical window and low phonon energy[1–4]. However, the structure of pure TeO_2 glass is unstable because of its lack of linkage between Te–O chains. Some of the modifier ions such as niobium, zinc, lead and alkali ions, have to be introduced into tellurite glass to improve the linkage between Te–O chains and to connect Te–O chains for stabilizing the glass network [5–8].

Niobium oxide is also a kind of heavy metal oxide with high molecular refractivity and optical nonlinearity. When the Nb^{5+} ions are introduced into the tellurite glass

*Corresponding author, email: lin_jian@mail.tongji.edu.cn

network, they not only connect Te–O chains for stabilizing the glass structure, but also provide some oxygen ions for changing tellurium–oxide coordination polyhedra. As the result, the third order nonlinear optical property of the glass is improved [9]. The stabilization of niobium tellurite glasses and their optical properties are greatly influenced by the composition and network structure of the glasses [10–13]. Therefore, it is important to elucidate details of the structure of Te–O chains and their linkage, for improving the stability of the TeO_2–Nb_2O_5 glasses.

Glasses are ordered in short range and disordered in long range, the short-range structure of the glass is close to that of corresponding crystalline phase. Therefore, the crystallization behaviour of the glasses reflects each short range structure of the glass network. The objective of the present work was to study the crystallization behaviour of TeO_2–Nb_2O_5 glasses by means of DTA, XRD and FTIR, hence deducing the evolution of the glass network structure during crystallization.

2. Experimental

$(100 - x)TeO_2$–xNb_2O_5 (mol %, x = 3–20) glasses were prepared using optical grade TeO_2 and Nb_2O_5 crystalline powders. Well-mixed batches of crystalline raw materials were melted between 750 and 850 °C for 15–20 min in a gold crucible in air. The melt was then cast on cold stainless steel plate. The glass sample was milled for DTA, XRD and FTIR analyses. Some of the glass powders were pretreated between 380 and 560 °C for 10–180 min and then cooled at room temperature.

Thermal properties of the glasses were studied with a Perkin-Elmer DTA-7 device. About 45 to 50 mg of the pretreated glass powder was put in a platinum cup and heated at the rate of 10 °C/min. Crystalline phases in the glasses after heat treatment were analyzed with a D/max-B rotating anode X-ray diffractometer with a CuK_α radiation source. The network structure of the glasses before crystallization was studied with a Equinox 55 FT-IR spectrometer.

3. Results and Discussion

3.1. The network structure of the TeO_2–Nb_2O_5 glasses

The TeO_2–Nb_2O_5 glass belongs to heavy metal oxide glasses with complex structure. $[TeO_4]$ trigonal bipyramids (tbp) and the $[TeO_3]$ trigonal pyramids (bp) link each other to form Te–O chains [14, 15]. Nb^{5+} ions in the glass exist as $[NbO_6]$ octahedra to link the Te–O chains [7]. The melting experiment shows that the TeO_2–Nb_2O_5 glasses were transparent and kept for long period of time when the Nb_2O_5 content was from 2 to 20 mol %.

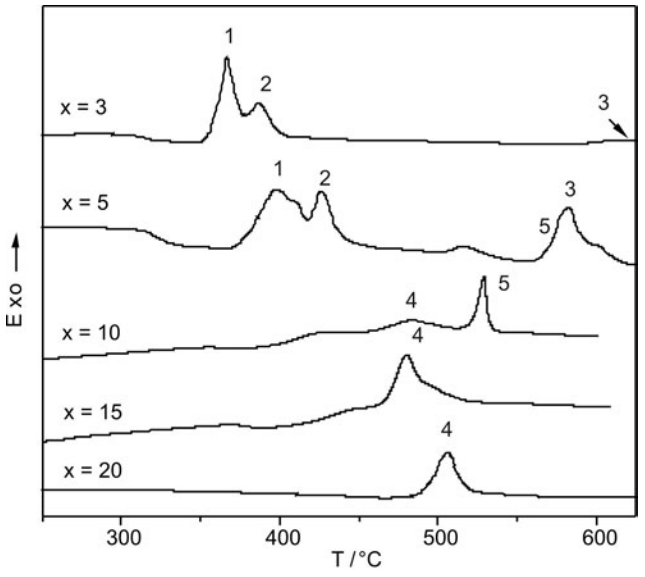

Fig. 1. DTA curves of $(100 - x)TeO_2$–xNb_2O_5 glasses and exothermic peaks corresponding to precipitated crystalline phases: 1 – β-TeO_2(I), 2 – β-TeO_2(II), 3 – α-TeO_2, 4 – $Nb_2Te_4O_{13}$, 5 – $Te_3Nb_2O_{11}$

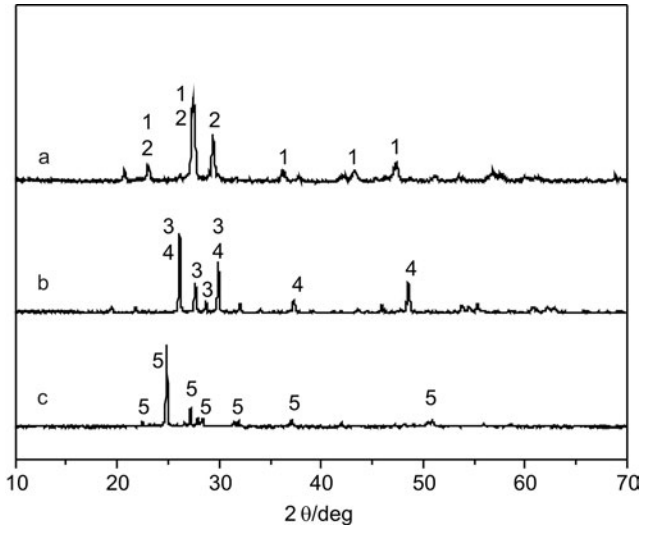

Fig. 2. XRD spectra of $(100 - x)TeO_2$–xNb_2O_5 glasses after heat treatment; curves: a – x = 3, 395 °C, 180 min, b – x = 3, 555 °C, 180 min, c – x = 15, 505 °C, 180 min; 1 – β-TeO_2 (750 882), 2 – β-TeO_2 (090 433), 3 – α-TeO_2 (410945), 4 – $Te_3Nb_2O_{11}$, 5 – $Nb_2Te_4O_{13}$

The DTA patterns of TeO_2–Nb_2O_5 glasses are shown in Fig 1. It was found that the crystallization behaviour of the glasses changed greatly when introducing Nb_2O_5 as the second component. When the Nb_2O_5 content in the glass was 3 mol %, three

kinds of exothermic peaks appeared in the DTA curve for the glass. Some of the XRD results are shown in Fig. 2, they confirm that the β-TeO_2 phase was formed at 350 °C and 380 °C, then a little of α-TeO_2 phase appeared at 620 °C. When the Nb_2O_5 content was 5 mol %, the first exothermic peak was weaker and shifted to higher temperature, and the third one was strengthened and moved to lower temperature. The XRD analysis shows that the $Te_3Nb_2O_{11}$ phase was obtained near 565 °C instead of α-TeO_2. The exothermic peaks in the DTA patterns continued to approach each other when the Nb_2O_5 content was increased, while the $Nb_2Te_4O_{13}$ phase began to be obtained instead of $Te_3Nb_2O_{11}$ and β-TeO_2. When the Nb_2O_5 content was increased to 15 mol%, the exothermic peaks appeared at 465 °C, and the precipitated crystals gradually changed to only one crystalline phase of $Nb_2Te_4O_{13}$.

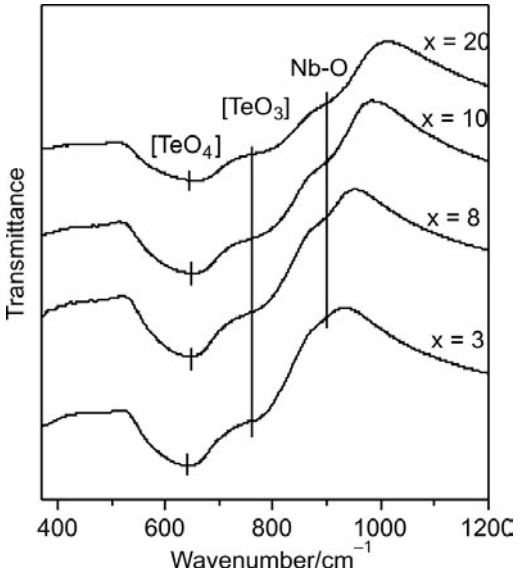

Fig. 3. FT-IR spectra of $(100 - x)TeO_2$–xNb_2O_5 glasses

The FT-IR spectra of the TeO_2–Nb_2O_5 glasses are shown in Fig 3. The band at 638–652cm^{-1} was assigned to [TeO_4] tbps. It slightly shifted to higher frequencies when the Nb_2O_5 content was increased. The shoulder at 760 cm^{-1}, which belonged to [TeO_3] bps, was improved with increasing Nb_2O_5 content. The band at 900 cm^{-1} was assigned to the vibration of Nb–O bonding, though its origin from [NbO_6] or [NbO_4] groups was in dispute [10, 16]. The absorption coefficient ratio of the [TeO_4] and the [TeO_3], and the absorption coefficient of the Nb–O band are shown in Fig. 4. The ratio of [TeO_4]/[TeO_3] decreased with increasing Nb_2O_5 content, accompanied with increasing content of Nb–O groups. It can be concluded that the introduced Nb_2O_5 changes some of [TeO_4] tbps into [TeO_3] bps, while the Nb^{5+} ions connect Te–O chains as [NbO_6] octahedra.

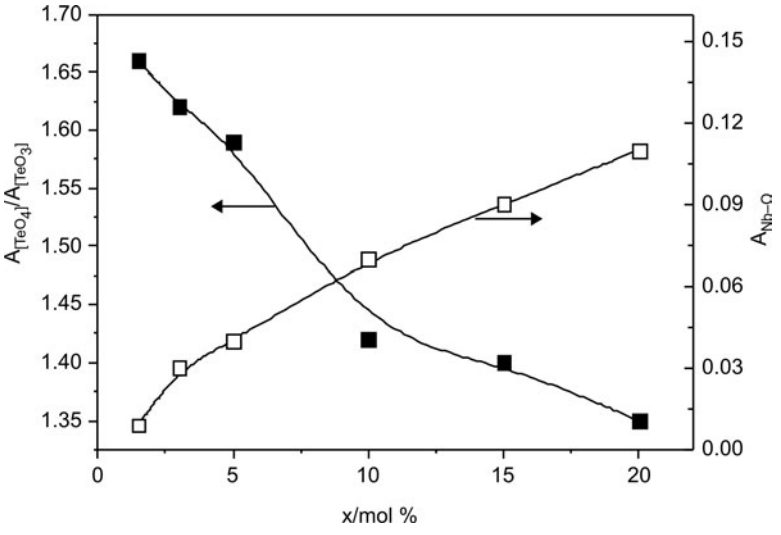

Fig. 4. The absorption coefficient of coordination polyhedra and their ratio in $(100 - x)TeO_2$–xNb_2O_5 glasses

The network structure of the TeO_2–Nb_2O_5 glasses changes with the content of Nb^{5+} ions. When the Nb_2O_5 content is lower, most of Te^{4+} ions exist as $[TeO_4]$ tbps and form Te–O chains, the $[TeO_4]$ tbps link each other both in apical sharing and in edge sharing, only a few of $[TeO_3]$ bps exist in the glass network. The Nb^{5+} ions exist as $[NbO_6]$ octahedra to link the chains as shown in Fig 5. Due to insufficient linkage of the Te–O chains because of insufficient amount of Nb^{5+} ions in the TeO_2–Nb_2O_5 glass, the glass network easier loses its stability. Therefore, the metastable edge-sharing $[TeO_4]$ tbps will first form edge-sharing β-TeO_2 phase at lower temperature. The apical-sharing $[TeO_4]$ tbps are more stable than the edge-sharing ones, they will form α-TeO_2 phase with similar structure at higher temperatures. Te–O chains connected with Nb^{5+} ions are more stable, they will form $Te_3Nb_2O_{11}$ phase with apical-sharing structure [17] at much higher temperatures.

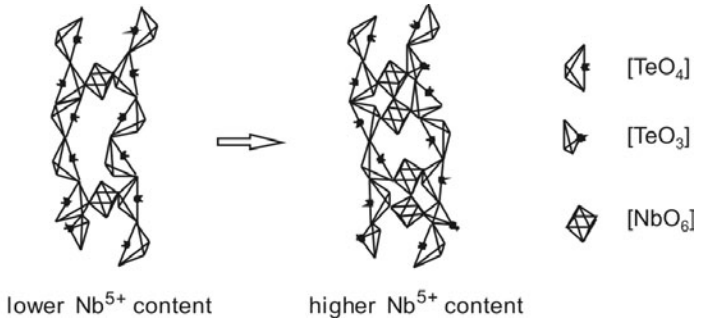

Fig. 5. Schematic diagram of the TeO_2–Nb_2O_5 glass network

When the Nb_2O_5 content in the glass is increased, more and more Nb^{5+} ions will connect Te–O chains as [NbO_6] octahedra, just like the [NbO_6] octahedral chain between [TeO_4] tbp chains in the $Nb_2Te_4O_{13}$ crystal, in which some of the polyhedra are linked by edge sharing [18]. The introduced Nb_2O_5 will also provide oxygen ions to change more [TeO_4] tbps into [TeO_3] bps. It seems that the glass network is strengthened by enhancing the linkage of Te–O chains. The tellurite network will also come to homogenization, because of uniform distribution of Nb^{5+} ions among the Te–O chains, though some of the tellurium-oxide polyhedra still link each other in edge sharing. Therefore, the precipitated crystals will contain only one crystalline phase, such as $Nb_2Te_4O_{13}$ phase.

3.2. The structural evolution of the TeO_2–Nb_2O_5 glasses under preheat treatment

The heat treatment will also affect the network structure of the TeO_2–Nb_2O_5 glasses. The DTA curves of the $90TeO_2$–$10Nb_2O_5$ glass after preheat treatment at 470 °C for various times are shown in Fig 6. Three kinds of crystallization peaks were found, which belonged to the crystalline phase of β-TeO_2, $Nb_2Te_4O_{13}$ and $Te_3Nb_2O_{11}$. This means that the glass structure consists of three kinds of Te–O chains: partly edge-sharing [TeO_4] chains, partly edge-sharing [TeO_4] chains connected by Nb^{5+} ions and apical-sharing [TeO_4] chains connected by Nb^{5+} ions. When the glass was preheat treated at 470 °C, some of the crystals were nucleated or formed from the glass before DTA analysis, it resulted in weakening crystallization peaks and in the fall of crystallization temperature in DTA patterns.

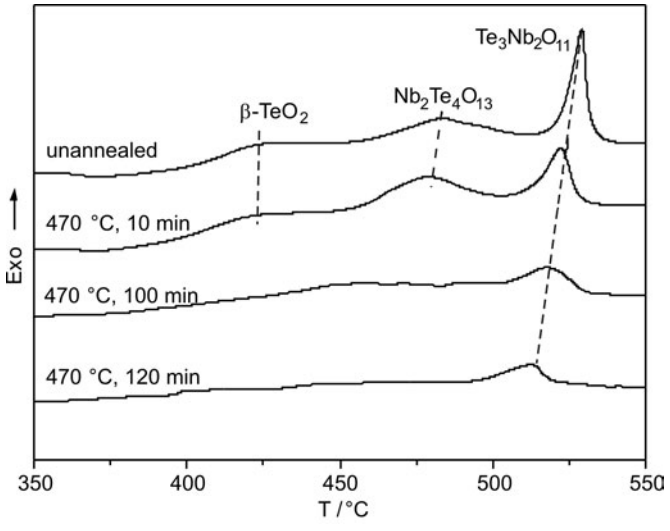

Fig. 6. DTA curves of the $90TeO_2$–$10Nb_2O_5$ glass after heat pretreatment

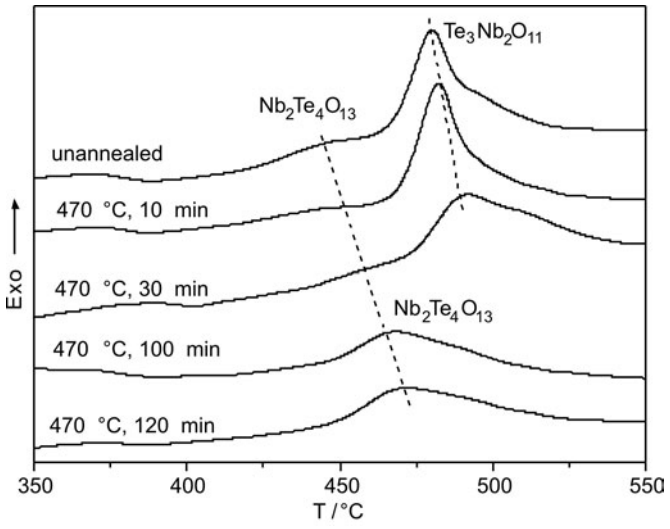

Fig. 7. DTA curves of the $85TeO_2$–$15Nb_2O_5$ glass after heat pretreatment

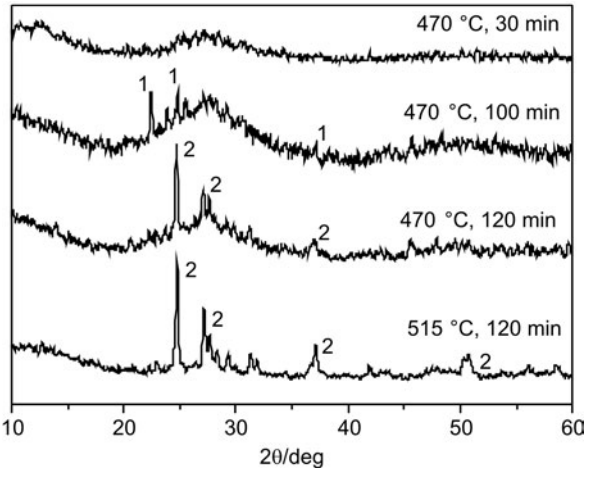

Fig. 8. XRD spectra of the $85TeO_2$–$15Nb_2O_5$ glass after heat pretreatment

The crystallization characteristic of the $85TeO_2$–$15Nb_2O_5$ glass is different from that of the $90TeO_2$–$10Nb_2O_5$ glass. The DTA curves of the $85TeO_2$–$15Nb_2O_5$ glass after pretreating at 470 °C are shown in Fig 7. The exothermic peak, attributed to β-TeO_2, disappeared. The first peak from $Nb_2Te_4O_{13}$ was strengthened and shifted towards higher temperatures at a prolonged pretreatment time, while the peak from $Te_3Nb_2O_{11}$ was weakened and shifted to higher temperatures as well. The XRD spectra of the $85TeO_2$–$15Nb_2O_5$ glass under various heat treatment conditions are shown in Fig 8. When the glass was heat treated at 470 °C for 30 min, no crystals were found. If the pretreatment time was extended to 100 min, the $Te_3Nb_2O_{11}$ phase was formed. When the pretreatment time was prolonged to 120 min, the crystalline phase was

changed into $Nb_2Te_4O_{13}$. It can be concluded that $Nb_2Te_4O_{13}$ will first be formed from partly edge-sharing [TeO_4] chains connected by Nb^{5+} ions, and then $Te_3Nb_2O_{11}$ from apical sharing [TeO_4] chains connected by Nb^{5+} ions. If the number of Nb^{5+} ions in the glass is sufficient to well connect Te–O chains, the crystalline phase of TeO_2 will not be formed from the glass without cooperation of Nb^{5+} ions. It seems that the preheat treatment at 470 °C would homogenize the network structure of $85TeO_2$ $–15Nb_2O_5$ glass and make the glass more stable.

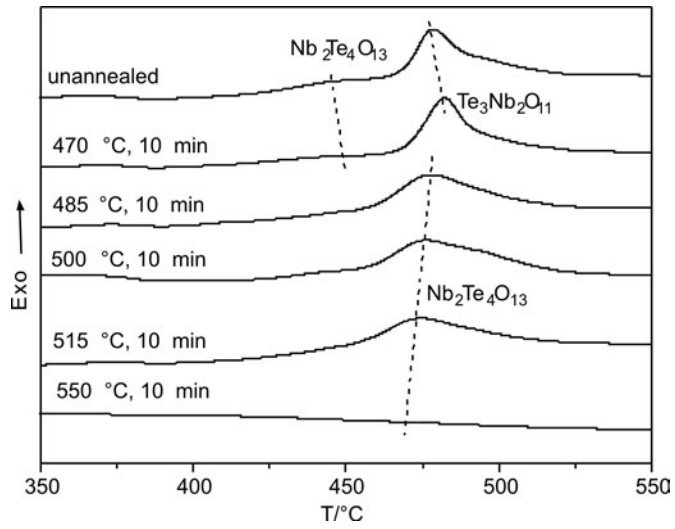

Fig. 9. DTA curves of the $85TeO_2$–$15Nb_2O_5$ glass after heat pretreatment

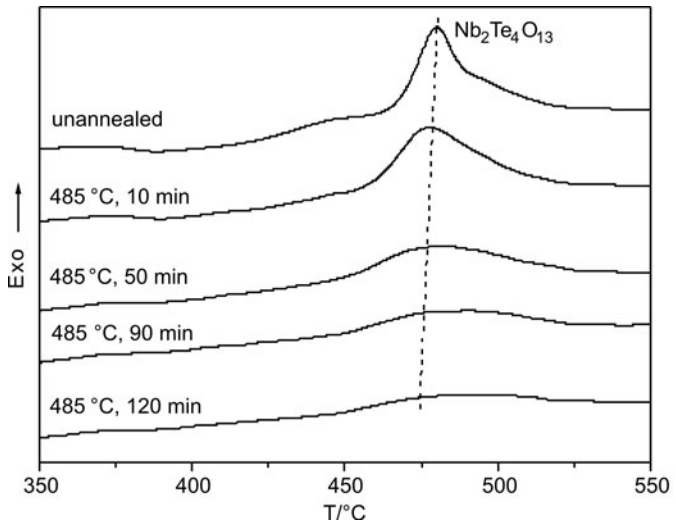

Fig. 10. DTA curves of the $85TeO_2$–$15Nb_2O_5$ glass after heat pretreatment

The effect of pretreatment temperature on the DTA curves for $85TeO_2$–$15Nb_2O_5$ glass is shown in Fig. 9. The exothermic peaks attributed to the crystalline phase of $Te_3Nb_2O_{11}$ and $Nb_2Te_4O_{13}$ shift to higher temperatures. When the pretreatment temperature is increased to 485 °C, the crystallization peaks merge into one peak attributed to the $Nb_2Te_4O_{13}$ phase, and then this peak shifts to lower temperature with increasing pretreatment temperature. The influence of the pretreatment time on the DTA patterns at 485 °C is shown in Fig 10. The crystallization peak was weakened and shifted towards lower temperatures with the increasing pretreatment time. This means that a suitable heat pretreatment will homogenize the glass network structure and make it more stable. However, the overheat treatment will result in partial nucleation and crystallization in preheat treatment and make the glass structure less stable.

4. Conclusions

The network structure of the TeO_2–Nb_2O_5 glasses consists of Te–O chains, most of $[TeO_4]$ tbps connect each other in apical sharing, whereas a few of $[TeO_4]$ tbps link in edge sharing. When Nb_2O_5 is introduced into the glass network, it provides oxygen ions to change some of $[TeO_4]$ tbps into $[TeO_3]$ bps, and the introduced Nb^{5+} ions connect the Te–O chains. The insufficient linkage between Te–O chains results in an inhomogeneous tellurite glass network. The glass will lose its stability in the edge-sharing Te–O chains during heat treatment at first, and then in the partly edge-sharing chains connect by Nb^{5+} ions, and at last in the apical-sharing Te–O chains.

When the Nb_2O_5 content in the glass is increased, more and more Nb^{5+} ions will connect Te–O chains. The introduced oxygen ions from Nb_2O_5 will also increase the content of $[TeO_3]$ bps, while the edge-sharing pyramids still exist in the glass structure. The sufficient number of Nb^{5+} ions will connect the Te–O chains, homogenize the glass network, and increase the structure stability. The structural evolution results in only one crystalline phase of $Nb_2Te_4O_{13}$ representing the partly edge-sharing Te–O chains connected by Nb^{5+} ions, being formed during heat treatment. Furthermore, a suitable preheat treatment at 470 °C will help in homogenization of the glass structure.

Acknowledgements

Owing to the support from the Chinese National Nature Science Foundation (approved No. 50572069) and Shanghai Science and Technology Commission (approved No. 0652nm002), this work could be completed. Some of this work was supported by Professor Richard K. Brow (Missouri University of Science and Technology).

References

[1] KIM S., YOKO T., SAKKA S., J. Am. Ceram. Soc., 76 (1993), 2486.
[2] EL-MALLAWANY R., Mat. Chem. Phys., 60 (1999), 103.
[3] WANG J., PATTNAIK R.K., TOULOUSE J., JAIN H., PRASAD S., SPIE, 5597 (2004), 136.
[4] WANG J.S., VOGEL E.M., SNITZER E., Opt. Mat., 3 (1994), 187.

[5] OVECOGLU M.L., OZALP M.R., OZEN G., ALTIN F., KALEM V., Key Eng. Mat., 264-268 (2004), 1891.
[6] SLIVA M.A.P., MESSADDEQ Y., RIBEIRO S.J.L., POULAIN M., VILAIN F., BRIOIS V., J. Phys. Chem. Solids, 62 (2001), 1055.
[7] LIN J., HUANG W., SUN Z., RAY C.S., DAY D.E., J. Non-Cryst. Solids, 336 (2004), 189.
[8] LIN J., HUANG W.H., WANG H.B., JIN C., LUO L.Q., Chin. J. Mat. Sci. Eng., 22 (2004), 827.
[9] CANIONI L., MARTIN M.O., BOUSQUET B., SARGER L., Opt. Commun., 151 (1998), 241.
[10] AHMAD M.M., YOUSEF E.S., MOUSTAFA E.S., Physica B, 371 (2006), 74.
[11] CAPOBIANCO J.A., VETRONE F., BOYER J.C., SPEGHINI A., BETTINELLI M., SPIE, 4829 (2003), 81.
[12] ZHAO C., ZHANG Q.Y., PAN Y.X., JIANG Z.H., Chin. Phys., 15 (2006), 2158.
[13] CHEN D.D., LIU Y.H., ZHANG Q.Y., DENG Z.D., JIANG Z.H., Mater. Chem. Phys., 90 (2005), 78.
[14] EL-MALLAWANY R., Mat. Chem. Phys., 63 (2000), 109.
[15] YAMAMOTO H., NASU H., MATSUOKA J., KAMIYA K., J. Non-Cryst. Solids, 170 (1994), 87.
[16] VILLEGAS M.A., FERN'ANDEZ NAVARRO J.M., J. Eur. Ceram. Soc., 27 (2007), 2715.
[17] GALY J., LINDQVIST O., J. Solids State Chem., 27 (1979), 279.
[18] BLANCHANDIN S., CHAMPARNAUD-MESJARD J.C., THOMAS P., J. Alloys Compds., 306 (2000), 175.

Received 30 May 2007
Revised 22 August 2008

Materials Science-Poland, *Vol. 27*, *No. 1*, *2009*

Silicon oxide nanowires and spheres grown by hydrothermal deposition

L.Z. PEI*

School of Materials Science and Engineering, Key Lab of Materials Science and Processing of Anhui Province, Anhui University of Technology, Ma'anshan 243002, PR China

Silicon oxide nanowires and spheres were prepared via a simple hydrothermal deposition using silicon powder as the starting material. Field emission scanning electron microscopy (FESEM), transmission electron microscopy (TEM), energy dispersive spectra (EDS) and high-resolution transmission electron microscopy (HRTEM) were used to observe the structure and morphologies of the products. The results show that the average diameter of silicon oxide nanowires with an amorphous structure is about 500 nm, and that smooth silicon oxide spheres have a definite diameter distribution ranging from several hundred nanometers to several micrometers. The growth process of the silicon oxide nanowires and spheres is discussed.

Key words: *hydrothermal deposition; nanoscale materials; silicon oxide nanowires and spheres*

1. Introduction

Preparation of one-dimensional nanowires has attracted a wide attention since the discovery of carbon nanotubes (CNTs) in 1991 [1]. Silicon oxide, one of the best candidates for photoluminescence materials, has been actively studied for a long time. Great efforts have been devoted to the preparation of silicon oxide nanowires because of their potential application in high-resolution optical heads of scanning near-field optical microscopy, nanointerconnection and microphotonic devices due to their intensive light emission ability [2, 3]. Silicon oxide nanowires have been prepared via different routes such as laser ablation, chemical vapour deposition (CVD) and template method according to the vapour–liquid–solid (VLS) growth mechanism, oxide-assisted growth mechanism and template confinement mechanism [2, 4–9]. Hydrothermal synthesis of CNTs and other one-dimensional nanomaterials [10–15] demonstrates their potential for preparing one-dimensional nanomaterials. As previously reported [16, 17], self-assembled silicon nanotubes and silicon carbide nanotubes have been prepared by a simple hydrothermal method using silicon monoxide, silica and

*Corresponding author, email: lzpei@ahut.edu.cn.

silicon carbide as the starting materials, respectively. Recently, we attempted to deposit one-dimensional nanostructures on silicon substrates in order to study the effect of silicon powder as starting material on the formation of one-dimensional silicon-based nanomaterials under hydrothermal conditions. It is very important to prepare large one-dimensional silicon-based nanomaterials for understanding their nucleation and growth mechanisms under hydrothermal conditions and future applications. In the paper, we report that silicon oxide nanowires with an average diameter of about 500 nm were prepared by hydrothermal deposition on silicon substrates using silicon powder as a starting material. At the same time, silicon oxide spheres with the diameter distributions ranging from several hundred nanometers to several micrometers were also deposited on silicon substrates.

2. Experimental

The experiments were performed in a conventional autoclave. The main features of this autoclave are the following: maximum pressure 22 MPa, maximum temperature 500 °C, volume 1000 cm^3, power 1.5 kW and stirring velocity 0–1000 rpm. 1.25 g of Si powder (purity: $\geqslant$ 99%, average particle size: ca.42 μm) was mixed with 48 cm^3 of distilled water. The mixture was placed in the autoclave. The silicon substrate, of dimensions of 4×2 cm^2, was cleaned in distilled water for 10 min using a supersonic wave apparatus. Then, the latter was fixed in the stainless steel bracket situated in the centre of the autoclave. The autoclave heated to 470 °C, was set to a pressure of 6.8 –8.2 MPa, and the rotational speed of the stirrer was 200 rpm. The temperature and pressure were maintained for 24 h. Subsequently, the autoclave was cooled to room temperature in air. Finally, the silicon substrate with bulk light grey deposit was obtained after the experiment.

SEM observation was performed using JEOL JSM-5600LV FESEM with 1 nm point-to-point resolution operating under a a 15 kV accelerating voltage. TEM and HRTEM samples were prepared by administering several drops of solution with samples onto a standard copper grid with a porous carbon film after the samples were dispersed into distilled water and treated for about 10 min using a supersonic wave apparatus. TEM and HRTEM observations were performed using a JEOL JEM 3010 transmission electron microscope with a 1.7 Å point-to-point resolution operating with a 300 kV accelerating voltage with a GATAN digital photography system.

3. Results and discussion

Bulk light grey deposit can be observed on the silicon substrate. SEM observations reveal an abundant number of nanowires and spheres. Figure 1a is the general SEM image of silicon oxide nanowires and spheres. The diameter of spheres ranges

from several hundred nanometers to several micrometers, and can even be greater than ten micrometers The length of the silicon oxide nanowires deposited on the spheres is about several micrometers, and can even be greater than ten micrometers. The SEM image of silicon oxide nanowires under higher magnification (Fig. 1b) shows that the silicon oxide nanowires have a relatively narrow diameter distribution, and that the average diameter is around 500 nm. The surface of silicon oxide nanowires is very smooth. It is obvious that the growth tips of the silicon oxide nanowires are closed semi-circular structures. So the growth tips are similar to those of silicon nanowires prepared by oxide-assisted growth [18–21].

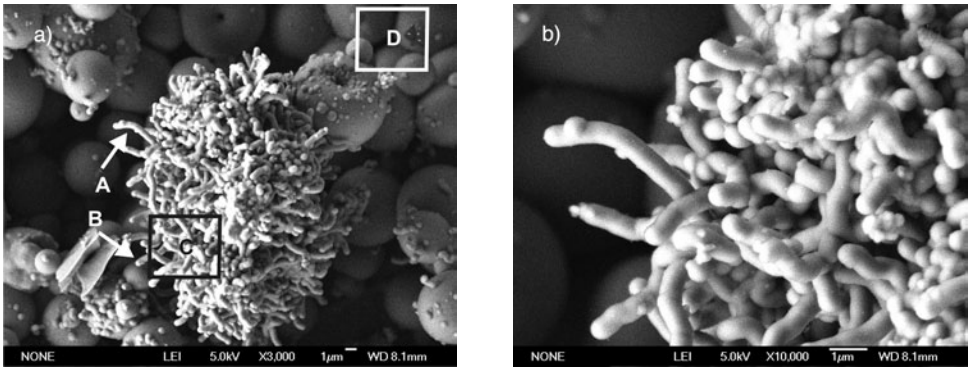

Fig. 1. SEM images of: a) the obtained sample, b) silicon oxide nanowires under higher magnification

The results demonstrate that no metallic catalyst particles exist in the silicon oxide nanowires. The production ratio of silicon oxide nanowires to spheres estimated by further SEM observations is about 1:9. EDS spectra of the nanowires and spheres are measured in order to determine the end product composition. The point, line and plane EDS spectra of the nanowires (Figs. 2a–c) show that the nanowires are composed of only silicon and oxygen. The corresponding quantitative analyses of the chemical composition of these samples using SEM-EDS experiments were performed by the software applied in the Link ISIS300 EDS. The atomic ratio of Si:O of silicon oxide nanowires is about 1:1.9 (point scanning and line scanning) and 1:1.8 (plane scanning), respectively, showing that the silicon oxide nanowires are SiO_x (x between 1.8 and 1.9) nanowires. Such a result also reveals that the element distribution of Si and O in the silicon oxide nanowires is uniform. The plane scanning EDS spectrum performed on spheres (Fig. 2d) reveals that the spheres are also composed of silicon and oxygen. The corresponding atomic ratio of Si:O is about 1:1.6 showing that the O content of the spheres is less than that of the silicon oxide nanowires.

Figure 3a is a general TEM image of silicon oxide nanowires. Different from the SEM results, some silicon oxide nanowires with a smaller diameter of about 200 nm are observed showing that silicon oxide nanowires with smaller diameters can be formed under present hydrothermal deposition conditions. In addition, similar to the

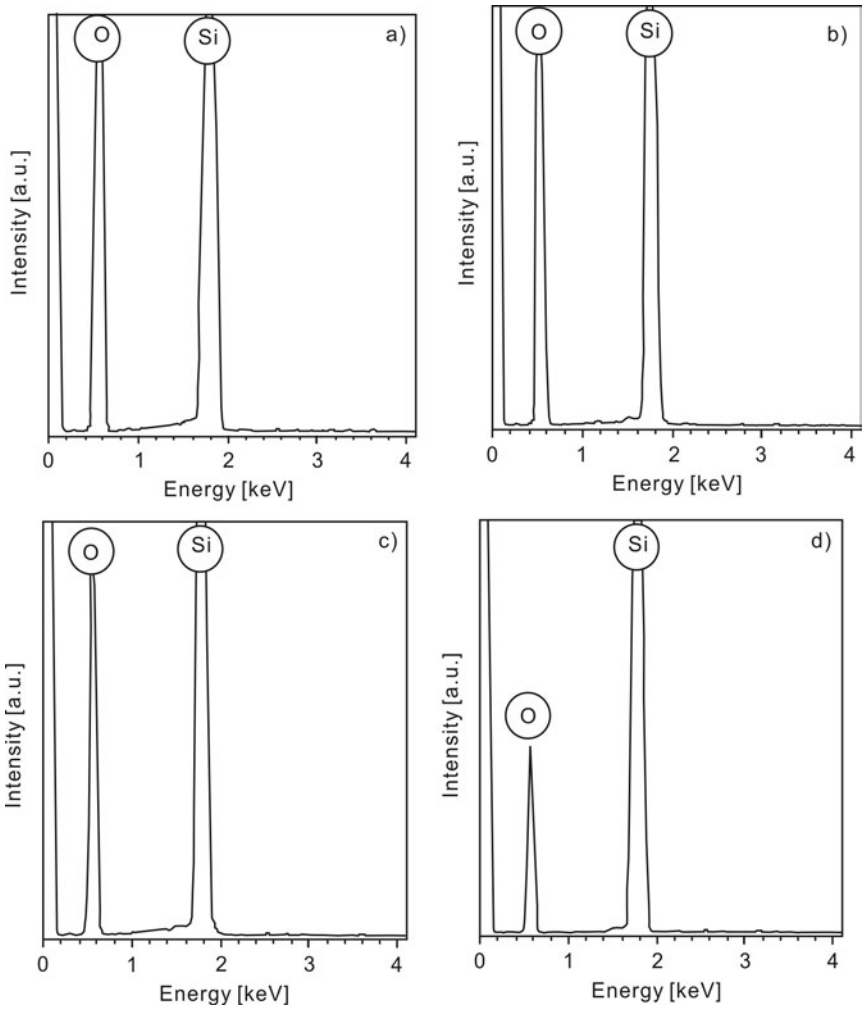

Fig. 2. Results of the EDS analysis of the sample shown in Fig. 1a: a) the point scanning EDS spectrum of the nanowire tip pointed by A, b) the line scanning EDS spectrum of the nanowire pointed by B, c) the plane scanning EDS spectrum of the nanowires pointed by C, d) the plane scanning EDS spectrum of the silicon oxide spheres pointed by D

SEM observation, the growth tips are mainly composed of semi-circular closed caps. The highly diffusive ring obtained from the electron diffraction analysis shown in the inset of Fig. 3a, reveals that these silicon oxide nanowires are amorphous, similarly to those synthesized by other methods [2, 4–9]. The surface of a nanowire is smooth, according to the TEM image of a single silicon oxide nanowire (Fig. 3b). The HRTEM image (the top-right of Fig. 3b) reveals an amorphous structure which is in agreement with the selected area electron diffraction (SAED) result. Spherical structures are also observed from the TEM image (Fig. 4a). The corresponding SAED pattern shown in the inset of Fig. 4a is a kind of highly diffusive ring. The result demon-

strates that the silicon oxide spheres are also amorphous. The HRTEM image of silicon oxide spheres (Fig. 4b) further substantiates the SAED result.

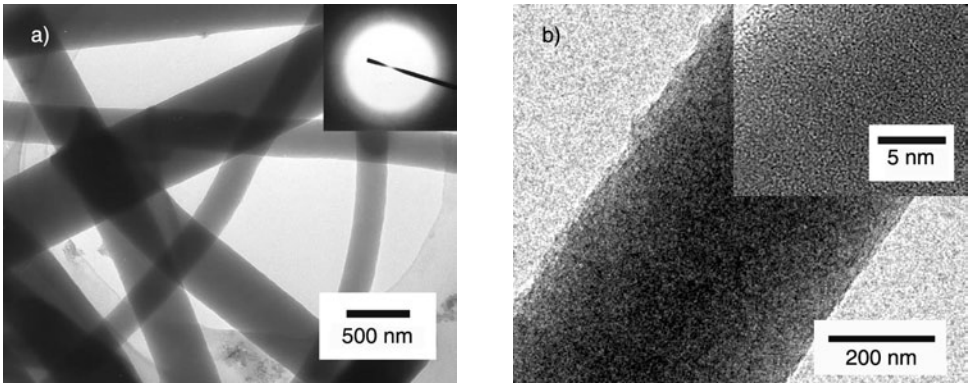

Fig. 3. TEM image of the silicon oxide nanowires (a), the inset is the corresponding SAED pattern and TEM image of a single silicon oxide nanowires (b), the inset is the corresponding HRTEM image

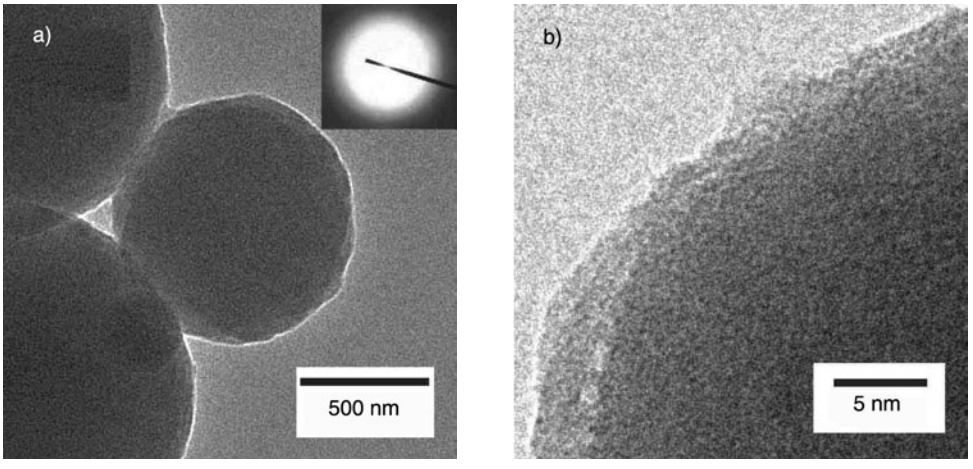

Fig. 4. TEM image of silicon oxide spheres (a), the inset is the corresponding SAED pattern and a HRTEM image of the silicon oxide sphere (b)

The obtained silicon oxide nanowires and spheres are composed of silicon and oxygen. The amount of O is greater than that of Si. Therefore, much oxygen exists in the sample. The amount of O in the starting material is measured in order to determine the origin of the oxygen. Thus, the EDS analysis was performed with the energy spectrometer (Fig. 5). A small amount of oxygen is observed in the plane scanning EDS spectrum. The quantitative analysis with the software applied in the Link ISIS300 EDS shows that the content of O in Si powder is 2.37wt. % which is far less than that of the end-products. The result demonstrates that only a part of the oxygen in the sample comes from the starting material of silicon. Silicon oxide exists mainly in the form

of silicon monoxide because the content of oxygen is far lower than that of Si in the sample. Thus it is reasonable to conclude that only a small amount of oxygen originates from the Si powder. Si is a stable monoatomic element under the standard atmospheric conditions and at room temperature. Thus, silicon oxide cannot be formed from Si under atmospheric pressure and the present experimental temperature. Si is also difficult to gasify. But the deposition process takes place under the pressure of 6.8–8.2 MPa and at the temperature of 470 °C being higher than the critical temperature of water (374 °C [22]).

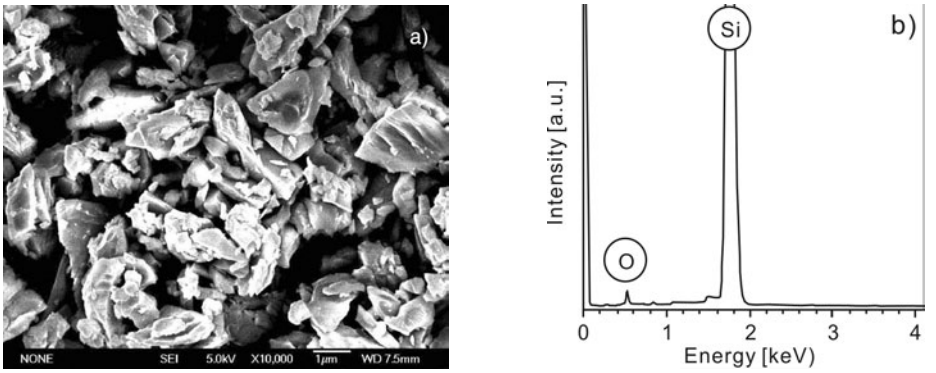

Fig. 5. SEM image of Si powder (a) and plane scanning EDS spectrum (b) corresponding to Fig. 5a

Therefore, the experiments are considered as having been conducted under supercritical conditions. Supercritical water enjoys a different status under high pressure such as sufficient density to dissolve materials, a higher diffusivity than in liquid state, a low viscosity facilitating mass transport, and high compressibility allowing easy changes in density and dissolving power [22]. Thus the supercritical hydrothermal conditions may play an essential role in the gasification of Si. Considering all these, the possibility of the reaction between Si gas and water gas is investigated by calculating the temperature dependence of the Gibbs energy under atmospheric pressure. Si gas possibly reacts with H_2O to form H_2, such as according to the following reaction:

$$\mathrm{Si(gas)+2H_2O(gas) \rightarrow SiO_2(solid) + 2H_2(gas)} \tag{1}$$

The Gibbs energy of these materials can be described by [23]:

$$G_i(T) = -R_G T\left(\frac{C_{i,1}}{T^2} + \frac{C_{i,2}}{T} + C_{i,3} + C_{i,4}T + C_{i,5}T^2 + C_{i,6}\ln T\right) \tag{2}$$

where G_i is the Gibbs energy of the system which consists of two materials, i.e., Si and H_2O and $R_G = 8.314$ J·mol^{-1}·K^{-1} is the gas constant. $C_{i,1}$–$C_{i,6}$ are the coefficients for the two materials. The $G_i(T)$ values of various materials are given in the literature [24]. The ΔG value is lower than -5.5×10^5 J·mol^{-1} at 400 °C according to the calculation. The result demonstrates that the reaction can occur in accordance with the thermodynamics. The hydrothermal pressure can also enhance the reaction rate according to the

chemical reaction theory. Therefore, Si and H_2O gases can react with each other to form SiO_2 and H_2 according to Eq. (1) under the aforementioned supercritical hydrothermal conditions under the pressure of 6.8–8.2 MPa. Thus a large amount of oxygen in the sample originates from the reaction of gaseous Si and H_2O. In addition, the existence of gas in the autoclave when its temperature decreased to room temperature also confirms that an abundant quantity of hydrogen can indeed be generated under high temperate, high pressure conditions.

Silicon oxide is known to play a large role in the nucleation and the growth of silicon oxide nanowires. Therefore, the formation of silicon oxide nanowires is based on the oxide-assisted growth mechanism [18, 21]. The melting point of the starting material, silicon, is 1414 °C [25]. Therefore, the starting material cannot be gasified under the specified experimental temperature and atmospheric environment. The temperature of the formation of silicon oxide nanowires is lower than that in other methods [2, 26–28] which may contribute to the supercritical hydrothermal conditions under the pressure of 6.8–8.2 MPa. Some of the silicon is gasified, forming silicon gas, with the increase of temperature and pressure in the autoclave. Water vaporization reacts with the gasified silicon, forming silica nanoscale clusters. The nanoclusters are suspended in the supercritical hydrothermal environment and are stirred continuously. The melting temperature of these nanoclusters may be reduced, due to their nanoscale size and the effect of a supercritical hydrothermal environment [16, 17, 19, 22]. The nanoclusters might be liquid-like, which can be called semi-molten or in a molten state under the specified hydrothermal conditions. These semi-molten or molten nanoclusters deposit into silicon substrates continuously with the overflow of the atmosphere in the autoclave. The molten or semi-molten silicon oxide at the tip of the initial silicon oxide liquid droplets absorbs a large amount of silicon oxide, resulting in a continuous growth of silicon oxide nanowires. The formation process of silicon oxide spheres is different from that of silicon oxide nanowires. The amorphous structure of the silicon oxide spheres is also different from the crystalline structure of silica nanospheres synthesized by the Stöber–Fink–Bohn method [29]. It is believed that more nanoclusters collide with each other, forming the clusters with larger size and depositing in silicon substrates. A small amount of silicon oxide nanospheres with amorphous structure are formed with diameters measuring several hundred nanometers: these diameters are smaller than those of micro-spheres observed from the SEM experiment. Silicon oxide spheres with different diameter distribution form, owing to the surface tension effect of the liquid-like clusters. The formation process is similar to that of the silicon oxide nanospheres prepared by hydrothermal deposition using silicon and silica as the starting materials [30]. Therefore, fewer silicon oxide nanowires were synthesized out of spheres.

4. Conclusions

In summary, a simple and easily controllable hydrothermal deposition method has been used to prepare silicon oxide nanowires and spheres. The amorphous silicon ox-

ide nanowires have a smooth surface, an average diameter of about 500 nm and the length of a few micrometers, and can even exceed ten micrometers in length. The as-synthesized spheres with the amorphous structure also have smooth surfaces and the diameter distribution ranging from several hundred nanometers to several micrometers. The supercritical hydrothermal conditions are believed to play an important role in the formation and growth of silicon oxide nanowires and spheres. A possible growth process of silicon oxide nanowires is proposed based on the oxide-assisted growth mechanism.

Acknowledgement

This work was supported by the Natural Science Foundation of Anhui Provincial Education Department of China under Grant No. KJ2007B077.

References

[1] IIJIMA S., Nature, 354 (1991), 56.
[2] YU D.P., HANG Q.L., DING Y., ZHANG H.Z., BAI Z.G., WANG J.J., ZOU Y.H., QIAN W., XIONG G.C., FENG S.Q., Appl. Phys. Lett., 73 (1998), 3076.
[3] TONG L.M., LOU J.Y., GATTASS R.R., HE S., CHEN X.W., LIU L., MAZUR E., Nano Lett., 5 (2005), 259.
[4] PAN Z.W., BAI Z.R., MA C., WANG Z.L., J. Am. Chem. Soc., 124 (2002), 1817.
[5] ZHANG M., BANDO Y., WADA K., KURASHIMA K., J. Mater. Sci. Lett., 18 (1999), 1911.
[6] NI H., LI X.D., GAO H.S., Appl. Phys. Lett., 88 (2006), 043108.
[7] HU J.Q., JIANG Y., MENG X.M., LEE C.S., LEE S.T., Chem. Phys. Lett., 367 (2003), 339.
[8] TEO B.K., LI C.P., SUN X.H., WONG N.B., LEE S.T., Inorg. Chem., 42 (2003), 6723.
[9] TONG L., GATTASS R.R., ASHCOM J.B., HE S., LOU J., SHEN M., MAXWELL I., MAZUR E., Nature, 426 (2003), 816.
[10] GOGOTSI Y.G., NICKEL K.G., Carbon, 36 (1998), 937.
[11] SUCHANEK W.L., LIBERA J.A., GOGOTSI Y., YOSHIMUR A.M., J. Solids State Chem., 160 (2001), 184.
[12] WEI H.Y., WU Y.S., LUN N., HU C.X., Mat. Sci. Eng. A, 393 (2005), 80.
[13] CHEN X.Y., WANG X., AN C.H., LIU J.W., QIAN Y.T., Mater. Res. Bull., 40 (2005), 469.
[14] GAO G.X., SONG X.Y., YU H.Y., FAN C.H., YIN Z.L., SUN S.X., Mater. Res. Bull., 41 (2006), 232.
[15] PROKES S.M., CARLOS W.E., SEALS L., LEWIS S., GOLE J.L., Mater. Lett., 54 (2002), 85.
[16] TANG Y., PEI L.Z., CHEN Y., GUO C., Phys. Rev. Lett., 95 (2005), 116102.
[17] PEI L.Z., TANG Y., CHEN Y., GUO C., LI X.X., YUAN Y., ZHANG Y., J. Appl. Phys., 99 (2006), 114306.
[18] LEE S.T., WANG N., ZHANG Y.F., TANG Y., MRS Bull., 24 (1999), 36.
[19] PEI L.Z., TANG Y., CHEN Y., GUO C., ZHANG W., ZHANG Y., J. Cryst. Growth, 289 (2006), 423.
[20] MA D.D.D., LEE C.S., AU F.C.K., TONG S.Y., LEE S.T., Science, 299 (2003), 1874.
[21] LEE S.T., ZHANG Y.F., WANG N., TANG Y., BELLO I., LEE C.S., CHUNG Y.W., J. Mater. Res., 14 (1999), 4503.
[22] CUMMINGS P.T., COCHRAN H.D., SIMONSON J.M., MESMER R.E., KARABORNI S., J. Chem. Phys. 94 (1991), 5606.
[23] SHI W.S., PENG H.Y., XU L., WANG N., TANG Y., LEE S.T., Adv. Mater., 12 (2000), 1927.
[24] LIANG Y.J., CHE Y.C., LIU X.X., LI N.J., Inorganic Thermodynamic Data Book, Northeastern University publishers, Shenyang, China, 1993.
[25] ZHANG Y., TANG Y., WANG N., LEE C.S., BELLO I., LEE S.T., J. Cryst. Growth, 197 (1999), 136.
[26] HU J.Q., JIANG Y., MENG X.M., LEE C.S., LEE S.T., Chem. Phys. Lett., 367 (2003), 339.

[27] YANG Y., TAY B.K., SUN X.W., FAN H.M., SHEN Z.X., Physica E, 31 (2006), 218.
[28] SUN S.H., MENG G.W., ZHANG M.G., QIAN Y.T., XIE T., ZHANG L.D., Solid State Commu., 128 (2003), 287.
[29] MÍGUEZ H., MESEGUER F., LÓPEZ C., MIFSUD A., MOYA J.S., VÁZQUEZ L., Langmuir, 13 (1997), 6009.
[30] PEI L.Z., Mater. Charact., 59 (2008), 656.

Received 21 November 2007
Revised 2 February 2009

Contents

Instructions for Authors

1. Submission of Manuscripts

Manuscripts can be sent by e-mail or by conventional mail. Submission of a manuscript to *Materials Science-Poland* implies that it is not being considered for publication elsewhere, and the authors have a necessary authorisation to publish the material contained in the paper.

1.1. First Submission

1.1.1. By Electronic Mail

Authors are encouraged to submit electronic versions of the manuscript to the e-mail address of the journal (*vide infra*). A single PDF file containing text, references, figures, tables etc. should be sent. When the size of such a file exceeds acceptable limits, the manuscript can be split into a few files (this should be clearly indicated in the covering letter). **Files in the DOC or RTF formats will be accepted only exceptionally.**

1.1.2. By Conventional Mail

The manuscripts can also be submitted by conventional mail. Authors are requested to send a CD with a PDF file containing a complete manuscript (text, references, tables, figures, etc.). The disk, accompanied by a covering letter, should be mailed to the Editor-in-Chief at his address given below.

1.2. Final Submission

After the manuscript has received preliminary acceptance, the authors will be requested to send the following material:

– A PDF file containing the complete manuscript (text, literature, tables, figures, etc). The file should be carefully checked as it will serve as a hard copy in case of doubts.

– A DOC or RTF file containing the text, references, tables and figure captions. The content of the file should be identical with that of the hard copy, and should exactly match the version seen and accepted be the referee(s).

– File(s) in appropriate formats containing figures. **Please consult Section 2.5 of this document.**

The files should be preferentially sent by e-mail, to the address of the Journal (*vide infra*), or by conventional mail, on a CD, to the Editor-in-Chief.

– **Additionally, the corresponding author is requested to send a copyright transfer form. The form should be copied from the web page of the Journal, filled out, signed and mailed to the Editor-in-Chief via conventional mail.**

2. Organisation of the Manuscript

The hard copy of the manuscript, submitted as a PDF file, should contain the material that can be reproduced in the A4 or letter size format, double spaced with ample margins throughout. All pages of the manuscript should be numbered consecutively, including references, figure captions and tables.

2.1. The First Page

The first page should be organised as follows:

Title of the paper

J.A. White[1], T.J. Brown[2*], M. Green[2**]
[1]Affiliation 1
[2]Affiliation 2
E-mail (only the corresponding author)

Abstract

An abstract of no more than 200 words

Key words

3 to 5 keywords, separated by semicolons (;)

* (**)Footnote(s)

2.2. Headings, Sub-headings

These should be placed in the main text as appropriate. The authors are encouraged to conform to the standard sequence of sections (e.g., Introduction; Experimental; Results; Discussion; Conclusions; etc.)

2.3. References

In the main text, references should be numbered consecutively by Arabic numerals in square brackets (e.g., [1]; [3, 4]; [7–11]). **Each reference should contain names of all authors**. The list of references should follow the main text and should be of the following format:

For a paper in a journal:

[1] KITAMURA T., YOKOYAMA M., J. Appl. Phys., 69 (1991), 821.

For a book:

[2] SWALIN R.A., *Thermodynamics of Solids*, Wiley, New York, 1962.

For a chapter in a book:

[3] WILD U.P., RENN A., *Spectral Hole-Burning*, [in:] H. Dürr and H. Bouas-Laurent (Eds.), *Photochromism. Molecules and Systems*, Elsevier, Amsterdam, 1990, p. 930.
Journal abbreviations should be in accordance with the standards of *Chemical Abstracts*.

2.4. Equations

Equations referred to in the text should be numbered consecutively at the right hand margin with Arabic numerals in parentheses.

2.5. Figures

All artwork will be reproduced in black and white. All figures should be numbered with Arabic numerals, have descriptive captions, and be mentioned in the text. An approximate position for each figure should be indicated in the text. The required formats of the drawings (plots, schemes of technological processes) must be vector files such as XLS, OPJ, cdr (Excel, Origin, CorelDraw) which may also be exported as EPS, EMF or WMF files. **Drawings submitted in tiff or jpg formats (bitmaps, raster graphics) even if exported as EPS, EMF or WMF files, will not be accepted**. They are acceptable only in the case of photographs (samples, laboratory equipment, etc.). The photographs (only in grayscale) should have the resolution not lower than 300 dpi (estimated for the size in which they are expected to be reproduced).
The figures may be embedded in the text or their approximate positions should be indicated. **In any case, they should also be attached separately as original files.** The list of figure captions should follow the list of references at the end of the text.

2.6. Tables

Tables should be numbered consecutively with Arabic numerals. Each table should be given a descriptive caption. If the tables are grouped at the end of the main text, then an approximate position of each table should be indicated in the text. The tables should be planned so as their final widths do not exceed 13 cm.

Electronic versions of the manuscripts should be sent to:

MatSci@pwr.wroc.pl

Material sent by conventional mail should be addressed to:

Professor Juliusz Sworakowski
Politechnika Wroclawska
I-30
Wybrzeże Wyspiańskiego 27
50-370 Wrocław
Poland

Web page of Materials Science-Poland: www.MaterialsScience.pwr.wroc.pl